Proceedings of:

The Seventh Annual Meeting

The American Society for Precision Engineering

October 18-23, 1992

Grenelefe Resort & Conference Center

Grenelefe, Florida

The American Society for Precision Engineering (ASPE) is a multidisciplinary professional and technical society concerned with research and development, design, manufacture and measurement of high accuracy components and systems. ASPE activities encompass relevant aspects of mechanical, electronic, optical and production engineering, physics, chemistry, and computer and materials science. Membership is open to anyone interested in any aspect of precision engineering.

Founded in 1986, ASPE provides a new focus for a diverse but important community. Other professional organizations have covered aspects of precision engineering, always as a sideline to their principal goals. ASPE is based on the core of generic concepts necessary to achieve precision in any application; independent of discipline, ASPE intends to be the focus for precision technology —and to represent all facets from research to application.

ASPE — The American Society for Precision Engineering
401 Oberlin Road, Suite 108
P.O. Box 10826
Raleigh, NC 27605-0826
Phone (919) 839-8444 Fax (919) 839-8039

Precision manufacturing is becoming a critical issue for international competitiveness. In this context, precision engineering plays a central role for both research and development of new technologies. Scientific advances have increased the potential for design and manufacturing into the regime of nanotechnology, thus requiring increased emphasis on metrology, machine design, control systems and material fabrication processes. Because of advanced applications for mechanical parts (bearings and gears), electronics (VLSI and electro-optics), materials (ceramics and electronic), adaptive control and system integration, the expectations for and the diversity of precision engineering will expand in the 90's. The mission of the American Society for Precision Engineering (ASPE) is to serve as a focus for the profession, and to emphasize the need for information exchange among the many disciplines participating in this critical area.

We are pleased to present the program for the Seventh Annual Meeting of the ASPE. The meeting provides an international forum for the exchange of ideas, for the discussion of solutions to challenging problems, and for the presentation of new research results and technological developments. The precision engineering community includes professionals from universities, government laboratories and private industry. The meeting offers an ideal format for the exhibition of new products from a wide range of companies.

The program reflects the vitality of the ASPE and the relevance of its Annual Meeting.

Welcome to the Grenelefe.

1992 ASPE Meeting Organizing Committee

Ronald O. Scattergood, Chairman
North Carolina State University

Thomas G. Bifano, Boston University
Kenneth L. Blaedel, Lawrence Livermore National Laboratory
Norman Bobroff, IBM Thomas J. Watson Research Center
William J. Bryan, 3M Company
Jeffrey W. Carr, IBM Thomas J. Watson Research Center
Thomas A. Dow, North Carolina State University
Peter J. Falter, Westinghouse Electric Corporation
Anthony E. Gee, Cranfield Institute of Technology
Donald Golini, Litton ITEK Optical Systems
Robert J. Hocken, UNC-Charlotte
Kenichiro Horio, Saitama University
Don A. Lucca, Oklahoma State University
Jay K. Lunzer, Lunzer Industrial Diamonds
Dan E. Luttrell, Precitech
Richard L. Rhorer, Los Alamos National Laboratory
Phillip E. Russell, North Carolina State University
David H. Youden, Rank Pneumo

1992 Annual Meeting

Contents

Foreword — Organizing Committee ..... *ii*

Preface — Corporate Members ..... *iv*

Cooperating Sponsors — Technical Exhibitors ..... *v*

Program ..... *vi*

Commercial/Forum/Distinguished Lecturer *1*

Technical Paper Index *2-7*

Technical Papers *11-200*

Poster Papers *203-393*

Author Index *395-396*

Preface

This book comprises the proceedings of the 1992 Annual Meeting. The contributions reflect the authors' opinions and are published as presented to ASPE, without change. Their inclusion in this publication does not necessarily constitute endorsement by the ASPE, or its editorial staff.

Individual readers of this book and nonprofit libraries acting for them are permitted to make fair use of the material contained in this book to be used in teaching or research; provided they copy said paper in total, as written by the author. Permission is granted to quote excerpts from the scientific or technical works in this book with proper acknowledgment of the source to include: the author's name, the book name, and the ASPE tag line. Reproduction of figures and tables is likewise permitted from the contents of this book, provided that the same acknowledgment of the same source and content is printed.

Any other type reproduction, systematic copying or multiple reproduction of any material in this book is expressly prohibited except with the written permission of the ASPE editorial staff, addressed to the Society's headquarters.

Printed in the United States of America
AMERICAN SOCIETY FOR PRECISION ENGINEERING

Corporate Members of the ASPE

COMPANY	CONTACT	LOCATION
3M Company	William J. Bryan	Petaluma, CA
ADE Technologies, Inc.	Michael A. Bahtiarian	Newton, MA
Acteron Corporation	Patrick Burt	Redwood City, CA
Aerotech, Inc.	Stephen A. Botos	Pittsburgh, PA
Bausch & Lomb	Michael J. Clark	Rochester, NY
Brown & Sharpe Manufacturing Co.	Michael L. Majlak	North Kingstown, RI
Chardon Tool & Supply Co., Inc.	Weldon Bennett	Chardon, OH
Charmilles Technologies Corporation	Harry C. Moser	Lincolnshire, IL
Contour Fine Tooling, Inc.	Stuart E. Galer	Marlborough, NH
Cranfield Precision Engineering, Ltd.	Patrick A. McKeown	Cranfield, England
Dover Instrument Corporation	John R. Hero	Westboro, MA
IBM - T.J. Watson Research Center	Norman Bobroff	Yorktown Hts., NY
Micro Encoder, Inc.	Kim Atherton	Kirkland, WA
Moore Special Tool	E. Ray McClure	Bridgeport, CT
Professional Instruments Co.	Ted J. Arneson, Jr.	Minneapolis, MN
Rank Pneumo	John Blocker Byrd, III	Keene, NH
Tencor Instruments	Graham J. Siddall	Mountain View, CA
Zygo Corporation	Carl A. Zanoni	Middlefield, CT

Cooperating Sponsors

Brown & Sharpe

Butterworth-Heinemann

Laser Focus World

Photonics Spectra

Rank Pneumo

Technical Exhibitors

A.G. Davis Gage & Engineering Co.
Acteron Corporation
ADE Technologies, Inc.
Aerotech, Inc.
Alson E. Hatheway, Inc.
Brown & Sharpe Manufacturing Co.
Chardon Tool & Supply Co., Inc.
Charmilles Technologies Corporation
Contour Fine Tooling, Inc.
Cranfield Precision Inc.
Fabreeka International, Inc.
Lanxide Corporation
Lion Precision
Park Scientific Instruments
Precision Engineering Center — N.C. State University
Precision Engineering Laboratory — University of N.C. at Charlotte
Polytec Optronics, Inc.
Professional Instruments Co., Inc.
Queensgate Instruments
Rank Pneumo
Schott Glass Technologies, Inc.
Surface Finishes Co., Inc.
Tencor Instruments
WYKO Corporation
Zygo Corporation

Program

1992 ASPE Annual Meeting

Time	Sun., Oct. 18	Mon., Oct. 19	Tues., Oct. 20	Wed., Oct. 21	Thurs., Oct. 22	Fri., Oct. 23
8:00			Continental Breakfast	Continental Breakfast	Continental Breakfast	
9:00	Tutorial	Tutorial	Technical Session 1	Technical Session 4	Technical Session 6	Tours: 1) Martin Marietta 8:00-3:00 2) Kennedy Space Center 8:00-3:00
10:00			Break + Poster Session	Break Technical Session 5	Break Technical Session 7	
11:00						
12:00			Lunch + Committee Meetings	Lunch + Business Meeting	Lunch	
1:00						
2:00	Tutorial	Tutorial	Technical Session 2	Exhibits	Technical Session 8	
3:00			Break		Break	
4:00			Technical Session 3		Technical Session 9	
5:00						
6:00	Board Meeting	Welcome Reception	Dinner			
7:00			Distinguished Lecture	Commercial Session/ Open Forum		
8:00			Hospitality Suite			
9:00				Hospitality Suite		
10:00						

Other Technical Sessions

Distinguished Lecturer

Tuesday, October 20, 7:00

Calvin Quate

Calvin Quate has been Professor of Applied Physics and Electrical Engineering at Stanford University since 1961. Prior to joining Stanford, he was employed at Bell Laboratories and Sandia Corporation and his work centered on acoustic wave signal processing. After landmark achievements in this field, he then turned his attention to imaging technologies. In the mid-seventies he invented the acoustic microscope and this was followed, about a decade later, with the invention of the Atomic Force Microscope (with Binning and Rohrer).

Professor Quate is a Member of the National Academy of Engineering, the National Academy of Sciences and is a Fellow of IEEE and of many other societies. He has authored or co-authored over 180 publications. For his outstanding achievements in science and technology, Professor Quate has received many awards, including the IEEE Medal of Honor (1988) and culminating, in June of this year, with the President's 1992 National Medal of Science.

Commercial Session and Open Forum

Wednesday, October 21, 7:00-9:00

Commercial Session Chair: William J. Bryan, 3M Company

Open Forum Chair: Robert J. Hocken, University of North Carolina - Charlotte

The commercial and open forum sessions will be held on Wednesday, October 21. In this special evening session, company representatives are being invited to make brief presentations on new products associated with precision engineering. You will have the opportunity to hear about limitations on performance of existing approaches, new approaches relevant to precision engineering and advances that can be expected in the future.

The open forum was created to encourage dissemination of new and significant results, as well as observations on precision engineering subjects. All interested conference participants can sign up at the Conference Registration Table for short, informal presentations.

Technical and Poster Paper Index

The technical program for the 1992 ASPE Annual Meeting contains over 90 papers on current research from Asia, Australia, Europe, India, South America and the US. Authors from national laboratories, universities and industry will share their ideas and conclusions on a wide variety of topics.

Papers that lend themselves to significant verbal interaction, concise but important discoveries, or strongly visual or tactile subjects have been selected for the poster session. This year the poster papers will be close to both the exhibits and the technical sessions for the duration of the conference, and authors will be present to discuss their work on Tuesday, October 20, from 10:00 am to 12:00 pm.

In addition to a total of ten technical sessions, an Open Forum will be offered where recent results can be discussed, as well as a Commercial Session where manufacturers will give an update on their most recent innovations.

Session I
Ultra-Precision Machining I

Tuesday, October 20, 1992, 8:30 - 10:00 am — *Session Chair: Don Lucca (Oklahoma State University)*

1. ***Turning of Fresnel Lens Mold — Turning by Newly Developed Diamond Turning Machine***
   Y. Yamazaki and K. Nakamura (OMRON Corporation) and H. Hashimoto (Kanagawa Institute of Technology) ..... page 11
2. ***Optimized Tool Path Descriptions for Aspherical Surface Generation***
   M. Gerchman (Rank Taylor Hobson, Inc.) ..... page 15
3. ***A Nanometric Precision Non-contact Toolsetting System***
   P. Morantz (Cranfield Precision Engineering) ..... page 18
4. ***Tool Force, Tool Edge, and Surface Finish Relationships in Diamond Turned Aluminum***
   J. Drescher and T. Dow (NC State University) ..... page 22
5. ***LIDAR Project: Diamond Turning Mirrors in a Panic Situation***
   R. Rhorer (Los Alamos National Lab.) ..... page 26

Session II
Modeling

Tuesday, October 20, 1992, 1:30 - 3:00 pm — *Session Chair: Irving Stowers (Lawrence Livermore National Lab.)*

1. ***Fracture Mechanics Applied to the Ductile Machining of Brittle Materials***
   G. Hiatt and J. Strenkowski (NC State University) ..... page 29
2. ***Simulation of Micro-Indentation Using Molecular Dynamics Modeling on the Connection Machine***
   P. Scagnetti, T. Bifano, R. Nagem and G. Sandri (Boston University) ..... page 33
3. ***Fracture Toughness Effects in Precision Grinding of Ceramics***
   S. Smith and R. Scattergood (NC State University) ..... page 37
4. ***Toward an Eclectic Model of Brittle Materials Machining***
   J. Duduch (University of Sao Paolo) and A. Gee (Cranfield Institute of Technology) ..... page 41
5. ***Simulation of Diamond Turning of Silicon Surfaces***
   D. Boercker, J. Belak, I. Stowers, R. Donaldson, and W. Siekhaus (Lawrence Livermore National Lab.) ... page 45

Session III
Ultra-Precision Machining II

Tuesday, October 20, 1992, 3:30 - 5:00 pm — *Session Chair: David Youden (Rank Pneumo)*

1. ***Effect of the Tool-Workpiece Interface on Energy Dissipation in Ultra-Precision Machining of Aluminum***
   D. Lucca, Y. Seo (Oklahoma State University) and R. Rhorer (Los Alamos National Lab.) ..... *page 49*
2. ***Diamond Tool Wear During the Single Point Diamond Turning of Copper***
   W. Larson, J. Drescher, J. Strenkowski and T. Dow (NC State University) ..... *page 53*
3. ***Cryogenic Diamond Turning: Theory and Experiment***
   C. Evans, S. Polvani and E. Whitenton (National Institute of Standards and Technology); R. Lundin and D. Stewart (Los Alamos National Lab.) and E. Paul (Stockton State College) ..... *page 57*
4. ***Influence of Machining Parameters to Residual Stresses Remaining in Diamond Cut Surfaces***
   K. Horio, T. Kasai and Y. Ogata (Saitama University) ..... *page 61*
5. ***Ultraprecision Vacuum Fixturing for Thin Walled Parts***
   M. Powell (Atomic Weapons Establishment) ..... *page 65*

Session IV
Ultra-Precision Grinding

Session Co-Chairmen: Thomas Bifano (Boston University) and Kenichiro Horio (Saitama University)

Wednesday, October 21, 1992, 8:30 - 10:00 am

1. ***Study on the Ductile Mode Grinding of Silicon Single Crystal (The Effect of Temperature and Load Rate on Brittle-Ductile Transition)***
   T. Wu, N. Morita and Y. Yoshida (Chiba University) ..... *page 69*
2. ***Influence of Microstructure in Precision Grinding of Fine Ceramics***
   E. Brinksmeier and P. Roth (University of Hannover) ..... *page 73*
3. ***Ceramic Mirror Grinding: Using Extremely Fine Grit Diamond Wheel***
   L. Zhou, K. Syoji and T. Kuriyagawa (Tohoku University) ..... *page 79*
4. ***Cleaning Technique for Super Abrasive Grinding Wheel with FRP Cleaner***
   K. Abe and N. Yasunaga (Nippon Steel Corp.) ..... *page 83*
5. ***Preparing Ultraprecision Grinding Wheels****
   R. Polvani and C. Evans (National Institute of Standards and Technology)

Session V
Materials & Processing

Wednesday, October 21, 1992, 10:30 am - 12:00 pm — *Session Chair: Anthony E. Gee (Cranfield Institute of Technology)*

1. ***Machinability/Material Property Correlations in Hydrogel Polymers***
   D. Mackay and P. Lingard (Eycon Lens Laboratories Pty. Ltd.) and Y-W. Mai (University of Sydney) ..... *page 87*
2. ***Ultra Thin Bonded Single Crystal Silicon-On-Insulator Wafers Using MeV Ion Implanted Precision Etch Stops***
   P. Pronko and A. Ezis (UES, Inc.) ..... *page 92*
3. ***Surface Characteristics of Ion Milled CVD Sic***
   S. Fawcett and R. Rood (Optical Systems Branch, NASA), T. Drueding and T. Bifano (Boston University) and C. Egert (Oak Ridge National Lab.) ..... *page 96*
4. ***Part Machining Revisited***
   P. Hannah, D. Stewart and F. Garcia (Los Alamos National Lab.) ..... *page 100*
5. ***Surface Microstructure of Single Point Diamond Machined Polymers****
   S. Molis (IBM East Fishkill Facility) and J. Carr (IBM T.J. Watson Research Center)

** Paper not available at press time.*

Session VI
Machine Design and Control I

Thursday, October 22, 1992, 8:30 - 10:00 am — *Session Chair: Richard L. Rhorer (Los Alamos National Lab.)*

1. ***An Active Lead Screw Mechanism — A Lead Screw with Backlash Control for Ultra Precision Positioning***
   K. Sato, Y. Murayama, S. Imada, A. Shimokohbe (Tokyo Institute of Technology) ..... *page 112*
2. ***Capstans or Lead Screws? Comparing the Performance of Diamond Turning Machines Under Operating Conditions***
   D. Youden (Rank Pneumo) ..... *page 116*
3. ***Characterization and Control of a Traction Drive System***
   G. Rao and R. Ro (NC State University) ..... *page 122*
4. ***A Study on Frictional Characteristics of Slide-Way in Microdynamics***
   A. Kanai, M. Miyashita, and H. Nishihara (Ashikaga Institute of Technology) and J. Yoshioka (NUTR K.K.) ..... *page 126*
5. ***Non-Optical, Miniature, Precision Diamond Turning***
   P. Hannah, L. Forman, P. Gobby, S. Armstrong, J. Bartos, D. Hatch, L. Salzer and B. Henneke (Los Alamos National Lab.) ..... *page 130*

Session VII
Novel Metrology

Thursday, October 22, 1992, 10:30 am - 12:00 pm — *Session Chair: Jeffrey Carr (IBM Thomas J. Watson Research Center)*

1. ***A Proposed Design for an Unpolarised Optical Interferometer System with Sub-nanometric Sensitivity***
   M. Downs and W. Rowley (National Physical Lab.) ..... *page 142*
2. ***An Interferometric Rough Surface Displacement Sensor with 10nm Resolution and 40mm Measuring Range***
   D. Tang and M. Akabane (Tokyo Seimitsu Co. Ltd.) and E. Zhang, K. Yasuda, K. Sato and A. Shimokohbe (Tokyo Institute of Technology) ..... *page 145*
3. ***Sampling Strategies for Circles in Coordinate Measuring Machines***
   O. Odayappan, J. Raja, R. Hocken and K. Chen (UNC-Charlotte) ..... *page 149*
4. ***Long Range Constant Force Profiling: Initial Results and Ongoing Developments***
   L. Howard (UNC-Charlotte) and S. Smith (University of Warwick) ..... *page 153*
5. ***Smart Grinding Balls and Smart Bearings for On-Line Process Supervision***
   R. Gao, M. Bhandiwad and R. Warrington (Louisiana Tech University) ..... *page 157*

Session VIII
Surface Topology and Scanning Microscopies

Thursday, October 22, 1992, 1:30 - 3:00 pm — *Session Chair: Michael Downs (National Physical Lab.)*

1. ***Boundary Evaluation of an Indentation by Scanning Tunnelling Microscope Data***
   G. Barbato and G. Picotto (C.N.R. Turin) and G. Murari and G. Podda (Politecnico di Torino) ..... *page 161*
2. ***Optical Profilometry of Mechanically Inaccessible Surfaces***
   M. Visscher and K. Struik (Eindhoven University of Technology) ..... *page 165*
3. ***A New Unified Approach to Surface Texture Instrumentation***
   P. Scott (Rank Taylor Hobson Ltd.) ..... *page 169*
4. ***A Near-Field Scanning Optical Microscope Module***
   B. Boudreau, T. Cloninger, J. Raja, J. Patten and R. Hocken (UNC-Charlotte) ..... *page 173*
5. ***Scanning Probe Metrology***
   D. Grigg and P. Russell (NC State University) and J. Griffith, G. Kochanski and M. Vasile (AT&T Bell Labs) ..... *page 178*

Session IX
Machine Design and Control II

Thursday, October 22, 1992, 3:30 - 5:00 pm — *Session Chair: Dan Luttrell (Precitech, Inc.)*

1. ***A Kinematically Coupled Magnetic Bearing Test Fixture***
   T. Poovey, M. Holmes and D. Trumper (UNC-Charlotte) ..... *page 181*
2. ***A High Precision Five-Degree-of-Freedom Micropositioner Based on Electromagnetic Driving Principle***
   W. Wang and I. Busch-Vishniac (The University of Texas at Austin) ..... *page 185*
3. ***Robust H ∞ Control System Design of a New 3-DOF Magnetic Micro-Levitation Robot***
   A. Mohamed (Assiut University) and B. Vestgaard and I. Busch-Vishniac (The University of Texas at Austin) ..... *page 189*
4. ***Precise Positioning Mechanism with Surface Motor***
   Y. Tomita, F. Sato and Y. Koyanagawa (Sumimoto Heavy Industries Ltd.) ..... *page 193*
5. ***Analytical/Experimental Methods Supporting an "Error Budget"-Based Design of the PATS/PFMS***
   J. Bennett, R. Rhorer and R. Stevens (Los Alamos National Lab.) ..... *page 197*

Poster Session

Tuesday, October 20, 1992, 10:00 am - 12:00 pm

Fabrication Processes

Grinding

1. ***Analysis of the Kinematics and Workpiece Quality in Rotation Grinding of Monocrystalline Silicon***
   E. Brinksmeier and M. Klein (University of Hannover) ..... *page 203*

Diamond Turning

2. ***High Precision Turning of Hardened Steel — a Challenge for a New Generation of Machine Tools***
   M. Weck, J. Luderich and A. Wieners (Fraunhofer IPT) ..... *page 207*
3. ***Orthogonal Ultra-Precision Machining of Single Crystal Germanium***
   D. Lucca and T. Oquin (Oklahoma State University) ..... *page 211*
4. ***Single Point Diamond Turning of (111) CdTe for Epitaxial Film Growth***
   D. Lucca and Y. Seo (Oklahoma State University) ..... *page 214*
5. ***Nanometer Tool Centering for Diamond Turning Applications***
   A. Miller and J. Cunningham (Oak Ridge National Laboratory) ..... *page 216*
6. ***Evaluation of Environmentally Safe Cleaning Agents for Diamond Turned Optics***
   L. Theye, R. Day and M. Scott (Los Alamos National Lab.) ..... *page 220*
7. ***Investigation of Tool Wear in Metal Cutting Using Acoustic Emission***
   H. Ravindra, Y. Srinivasa and R. Krishnamurthy (Indian Institute of Technology - Madras) ..... *page 224*

Polishing

8. ***Pressure-Controlled Micropolishing of Glass***
   Y. Yamada and T. Kurobe (Kanazawa University) ..... *page 228*
9. ***A Study on Correcting Techniques for Recovering Accuracy of Deteriorated Lapping Plate Using a Correcting Carrier***
   K. Ichikawa and A. Kajikura (Fujikoshi Machinery Co.) and K. Ishikawa and H. Suwabe (Kanazawa Institute of Technology) ..... *page 232*
10. ***Observations on the Mechanisms of Polishing***
    R. Parks (University of Arizona) and C. Evans (National Institute of Standards and Technology) ..... *page 236*
11. ***The Effect of Polishing Particle Size on the Finish and Sub-Surface Damage of Glass***
    C. Lee (University of Nottingham) and D. Bell (Optical Surface Technologies) ..... *page 240*

Other Novel Processing

12. ***Ion Figuring System for Segmented, Adaptive Optics***
S. Fawcett and R. Rood (Optical Systems Branch, NASA, Marshall Space Flight Center) ..... page 244

13. ***A Basic Study on Cutting Characteristics and Lifetime of Wire Tool Electrodeposited Diamond Grains***
K. Ishikawa, H. Suwabe and K. Kanayama (Kanazawa Institute of Technology) ..... page 248

14. ***Laser Photo-etching Method for a Maskless Fabrication of a New Type Amorphous Silicon Solar Cell Submodule***
S. Kiyama, Y. Yamamoto, H. Hosokawa, R. Suzuki, M. Osumi, H. Nishiwaki, S. Sakai, S. Matsumi, M. Ohnishi, S. Tsuda, S. Nakano and Y. Kuwano (Sanyo Electric Co. Ltd.) ..... page 252

15. ***High Speed Milling Improves Machining Results***
M. Shimanovich (New Jersey Institute of Technology) and R. Pessolano (General Machine & Instrument Co., Inc.) ..... page 256

Metrology

Scanning Metrologies

16. ***A Comparison of Stylus, Interferometric and Scanning Probe Measurements***
T. McWaid, J. Fu, T. Vorburger and J. Song (National Institute of Standards and Technology) ..... page 259

Interferometry

17. ***Comparison of Optical Figure Measurements by Mechanical and Interferometric Methods***
R. Schenz, R. Donaldson, D. Owens and S. Patterson (Lawrence Livermore National Lab.) ..... page 263

18. ***A Scanning Differential Interferometer to Measure Index Heterogeneity***
N. Bobroff, A. Rosenbluth and M. Hatzakis, Jr. (IBM Thomas J. Watson Research Center) ..... page 269

19. ***Direct Phase Conversion for Very Low Frequency Measurand Detection in a Fiberoptic Interferometric Sensor***
L. Giulianelli, A. Seltzer and A. Buckman (Research Applications, Inc. and the University of Texas at Austin) ..... page 275

20. ***Intercomparison of Commercial High Resolution Linear Scales with a Laser Interferometer****
B. Damazo and C. Evans (National Institute of Standards and Technology)

Novel Metrology Systems

21. ***A New Strategy for Inspecting Roundness Features***
L. Carpinetti and D. Chetwynd (University of Warwick) ..... page 281

22. ***A New Measuring Method of Central Position of Spindle Rotation (1st Report: Steel Ball Method)***
N. Ozawa, K. Takeuchi and T. Sugano (Mechanical Engineering Laboratory, Ibaraki) ..... page 285

23. ***Linear Detection of High-Precision Optical Surface Sensor and its Function of Optical Skid***
T. Kohno, S. Mutoh and T. Miyai (Tokyo Metropolitan Institute of Technology) and E. Satoh (Olympus Optical Co. Ltd.) ..... page 289

24. ***On-Machine Measurement of Large Mirror Profile***
W. Gao and S. Kiyono (Tohoku University) ..... page 293

25. ***Investigation of Optical Non-Contact Measuring System for Gear Geometry — Measurement of Pitch Errors and Tooth Profiles***
E. Okuyama and H. Moritoki (Akita University) and S. Kiyono (Tohoku University) ..... page 297

26. ***Computer Integrated Error Calibration System for a CMM of CNC Type using Calibrated Mechanical Artefacts and Touch Probe***
H. Pahk and J. Kim (Pohang Institute of Science and Technology) ..... page 301

27. ***The Application of a Knowledge Based System for Surface Metrology****
D. Stevens (Rank Taylor Hobson Ltd.) and R. Parkin (De Montford University)

28. ***Self Calibration of Displacement Sensors***
S. Kiyono, M. Morishima and T. Sugibuch (Tohoku University) ..... page 305

29. ***A Fully Automatic High Precision Length Measuring Machine for Calibrating Optical Line Scales***
M. McCarthy (National Physical Laboratory) and A. Gee (Cranfield Institute of Technology) ..... page 309

* *Paper not available at press time.*

Surface Topography

30. ***Comparison of the Conformity of Surface Topography Measured by Optical and Stylus Instruments***
W. Dong, L. Blunt and K. Stout (University of Birmingham) ..... page 313

31. ***The Specification of a Flexible File Format for Storage and Retrieval of Engineering Topographic Data***
P. Sullivan and K. Stout (University of Birmingham) ..... page 317

32. ***Determination of Proper Sampling Spacing for 3D Topography Measurement of Machined Surfaces Using Power Spectral Analysis***
T. Lin, K. Stout and P. Sullivan (University of Birmingham) ..... page 324

33. ***Non-Contact Surface Roughness Measuring System of Magnetic Disk***
Y. Zheng (Tsinghua University, Beijing) and L. Zhu (Huazhong University of Science and Technology, Wuhan) ..... page 328

Machine Design

34. ***A Sphere and Cylinder Alignment System***
R. Rhorer (Los Alamos National Lab.) ..... page 332

35. ***A Study on the Static and Dynamic Characteristics of Externally Pressurized Air Bearings***
D. Han, S. Park, W. Kim and J. Kim (Seoul National University) ..... page 336

36. ***Evaluation and Improvement of Thermal Characteristics of a Thrust Air Spindle***
N. Mishima, K. Mizuhara and Y. Okazaki (Mechanical Engineering Laboratory, AIST) ..... page 340

37. ***Study on Tightening Techniques of Plastic Parts by Means of Tapping Screws***
K. Ishikawa, R. Hori and N. Unno (Kanazawa Institute of Technology) ..... page 344

38. ***Pressure Profiles Within Various Arrangements of Externally Pressurized Aerostatic Flat Pad Bearings****
K. Stout, S. El-Ashkar and P. Sullivan (University of Birmingham)

39. ***Characteristics Identification of a Mechanical Dynamic System***
J. Mandak (Slovak Metrological Society) ..... page 348

40. ***A Study of the Characteristics of Herring Bone Air Bearings for Polygon Mirror Laser Scanners***
G. Lin and R. Warrington (Louisiana Tech University) and Y. Ue and T. Satomi (Tokyo Denki University) ..... page 352

41. ***Design Concept of Ultraprecision and High Stiffness Feed System Based on Differential-Force Operation, and the Application***
M. Miyashita and A. Kanai (Ashikaga Institute of Technology) and J. Yoshioka (NUTR K.K.) ..... page 359

42. ***Power-Efficient Linear Motor for Precision Motion Control***
D. Trumper, T. Nguyen and M. Williams (UNC-Charlotte) ..... page 363

43. ***Ball Screw Nonlinearity and Dynamic Slideway Performance***
J. Cuttino and T. Dow (NC State University) ..... page 367

Controls

44. ***A Study On Dynamic Performance of Closed-loop Commuted Stepping Motor to Improve Precision Motor Control***
K. Yung (Hong Kong Polytechnic, Kowloon) and H. Liu (Tsinghua University, Beijing) ..... page 372

45. ***Accuracy Improvement of Machine Tool by Workpiece-Referred Control***
T. Kohno, A. Morita and H. Nagano (Tokyo Metropolitan Institute of Technology) and Y. Uda (Nikon Corporation) ..... page 376

46. ***Using a Single Chip Microprocessor to Compensate the Transmission Error of Gear Hobbing Machines***
Y. Li and Z. Chen (Huazhong University of Science and Technology) ..... page 380

Materials

47. ***Depth of Reluctant Uncut and Deformed Part in CFRP Cutting***
T. Kaneeda (Okayama University of Science) ..... page 386

48. ***The Effect of the Interaction of Abrasive Grains on the Deformation and Fracture Behavior of Brittle Materials***
N. Morita, T. Wu and Y. Yoshida (Chiba University) ..... page 390

* *Paper not available at press time.*

Technical Papers

TURNING OF FRESNEL LENS MOLD
-TURNING BY NEWLY DEVELOPED DIAMOND TURNING MACHINE-

1992 Annual Meeting of American Society for Precision Engineering

Y. Yamazaki* , K. Nakamura* and H. Hashimoto**
* Manufacturing Technology R&D Laboratory, OMRON Corporation
Shimokaiinji, Nagaokakyo-city, Kyoto, 617 JAPAN
** Kanagawa Institute of Technology
Shimoogino, Atsugi-city, Kanagawa, 243-02 JAPAN

1. Introduction

Recently, as equipmen has become smaller, integration of optical components has advanced, and requests for thinning and high-precision of lenses are increasing. Among others, the Fresnel lens, which is easily thinned and can obtain excellent optical characteristics, is remarkable.

Conventionally, Fresnel lenses have been manufactured by means of the electron-beam lithography method, which had, however, the drawback that deep patterns could not be processed and much time was consumed.

To solve these problems, therefore, a diamond turning machine is developed on which a metal mold for Fresnel lenses is turned out. Further, with this metal mold, Fresnel lenses are mass-produced through injection-molding. This paper describes the structure and performance of the diamond turning machine, and reports on the profile accuracy of metal molds machined on the turning machine as well as the optical characteristics of Fresnel lenses molded by injection.

2. Development of Diamond Turning Machine

To machine a metal mold for Fresnel lenses, a diamond turning machine is designed and manufactured according to the specificatiions shown in Table 1. Main elements of the turning machine (Fig. 1) are mounted on a granite base with air-damper, enabling to delete high-frequency vibrations over 2.5HZ in order to avoid interference of external vibrations during machining. Further, X- and Z-axes are arranged independently and orthogonally in "T-bar structure" so that the height between the base and machining point can be reduced and both axes can maintain individual performances without interference.

On the X-slide a diamond tool holder is mounted and on the Z-slide a main shaft air spindle driven by an AC servo-motor. The slide and spindle are

Table 1 Main specification of the machine

Characteristics	Specification
Slide ways	
Travel	x-axis 50mm
	z-axis 63mm
Positioning resolution	20nm
Spindle	
Speed range	100-1800rpm
Radial accuracy	50nm
Test piece	
Profile accuracy	0.2μm
Surface roughness	Ra0.002μm

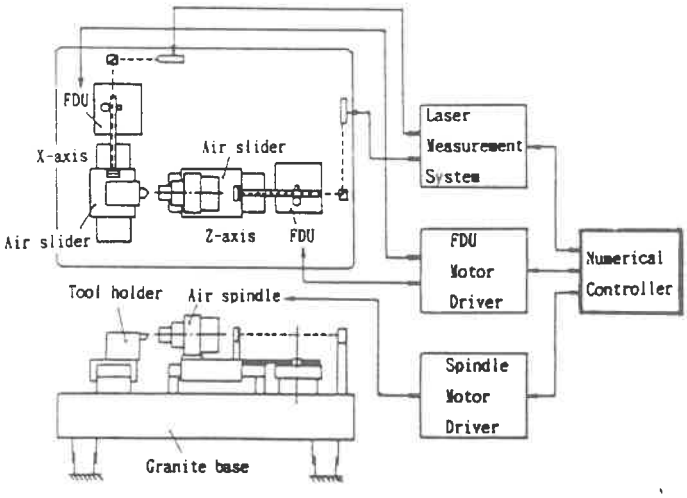

Fig. 1 Schematic diagram of the diamond turning machine

equipped with aerostatic bearings, which move smoothly and generate very little heat. Measurements indicate that pitching and yawing of the slides is 0.3 seconds each and the rotating accuracy of the spindle is 0.05μm in radial direction.

A friction drive unit (FDU) is applied; direct drive is carried on by means of a seven-phase AC servo-motor. A positioning control system consists of a position-servo loop according to the laser measurment system with a measuring resolution of 1.25nm and of a velocity-servo loop of FDU motor. Each axis is controlled by a NC unit with a minimum resolution of 10nm.

Fig. 2 illustrates a structural view of the friction drive unit. A drive rod between the drive shaft directly connected to the servo-motor and the back-up roller is pushed on by means of rotation of the drive shaft through friction force and moved straight ahead. This rod is connected to the slide and the slide can be positioned by controlling the rotating speed of the drive shaft. To drive the shaft, a seven-phase AC servo-motor for ultra-low speed, the speed variation is 0.6% even at a speed as low as 3rpm, is employed.

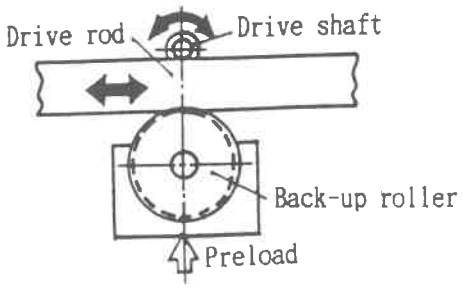

Fig. 2 Friction drive unit

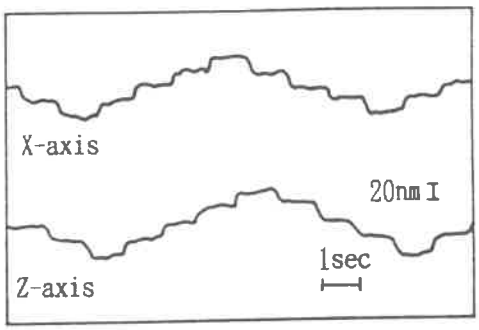

Fig. 3 20nm step responses by FDU

3. Performance Evaluation of Diamond Turning Machine

Positioning accuracies of X- and Z-axes of the turning machine are evaluated. Giving a 20nm-step command to each axis of the turning machine. corresponding step responses of the slide are measured with a capacitance gage. Measuring results are shown in Fig. 3. Step responses of 20nm are found, but non-linear characteristics such as hysteresis or backlash are not found.

To evaluate performance of the entire turning machine, a PMMA resin is turned flat and spherical. Machining conditions are: cutting depth 1μm, feed rate 1μm/rev , and rotations of main shaft 1800rpm. A single-crystal diamond tool with a nose radius of 0.5mm is used. Workpiece is measured on a measuring instrument of tracer type. As a measuring result, a surface roughness of Ra 0.002 μm for flat workpieces and a profile accuracy of 0.2μm for spherical workpieces are obtained.

4. Required Profile Accuracy and Machining of Metal Mold for Fresnel Lenses

Fig. 4 shows the mold, which is sawtooth-shaped, 60μm in depth and 29μm in minimum width. Optical characteristics of the lens designed here are NA 0.47, focal length 1.1 μm, and lens diameter 1.855mm.

If the focal length of Fresnel lenses slips out, the response output of the sensor fluctuates. To keep the fluctuation in an allowable range, the focal position of

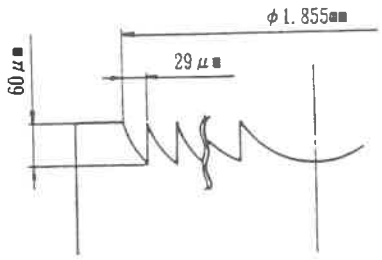

Fig. 4 Dimension of the Fresnel lens mold

Fresnel lenses must be within an error of 40μm. In view of these optical characteristics, it is necessary to keep the machining profile accuracy of the mold for the lens below 5μm.

The way of machining of metal mold for Fresnel lenses are described as the following. The diamond tool used for machining is 5 μm in edge width with a 20° edge angle. Feeding the tool in X-direction and positioning the slides of X- and Z-axes of the turning machine by numerical control so that a workpiece can be moved forward and backward in synchronization with the movement of the tool, a pattern for the metal mold is formed. Machining conditions are : cutting depth 1 μm, feed rate 0.3μm/rev , and main shaft rotations 1800rpm. Also lubricating oil is used to cool workpiece and remove chips.

Radial accuracy of the metal mold is measured noncontactly by scanning laser microscope. It is found that radial error of machined pattern is within 3 μm, satisfying a required machining profile accuracy.

Roughness of the machined surface of mild copper alloy mold is measured with a surface indicator of tracer type. Fig. 5 shows the measured results which a mirror surface Ra0.009μm was obtained.

5. Manufacture of LED with Fresnel Lens

To evaluate the injection-molded Fresnel lens, its focusing characteristics are measured by LD incident beam. As shown in Fig. 6, the focused beam spot is 2μm in diameter, which is nearly coincident with the theoretical value. Moreover, focal length measured is 1.124mm (designed value: 1.1mm), the error of focusing position is kept within 40.μm as designed object value.

LED with Fresnel lens can be manufactured by inserting LED chip during the process of injection-molding of the lens. A structural view of the LED with Fresnel lens is illustrated in Fig. 7. By coupling with the Fresnel lens, thickness of the LED is reduced by 70%, and volume by 50%.

To throughly evaluate the performance of the LED, the optical characteristics of a conventional LED are compared with those of a LED with

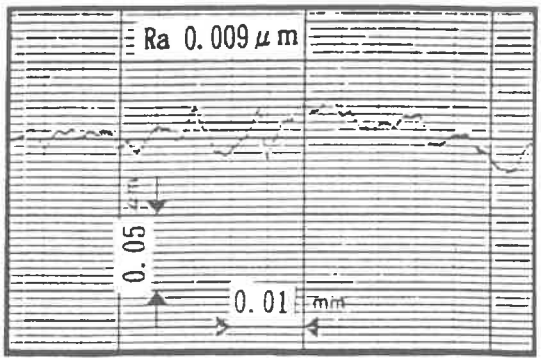

Fig. 5 Surface roughness of the Fresnel lens mold

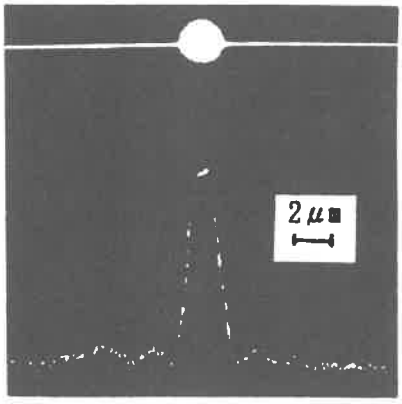

Fig. 6 Optical characteristics of the molded Fresnel lens

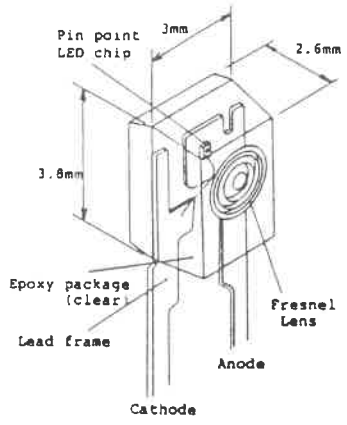

Fig. 7 LED with Fresnel lens

Fresnel lens. Using the same LED chip as the light source, light quantities collimated by a spherical lens and a Fresnel lens are measured with a photo-transistor, and the light quantities are compared. The comparision is indicated in Fig. 8. Upon experiments, the light quantity of a LED with Fresnel lens is three times as much as that of a conventional LED using spherical lens.

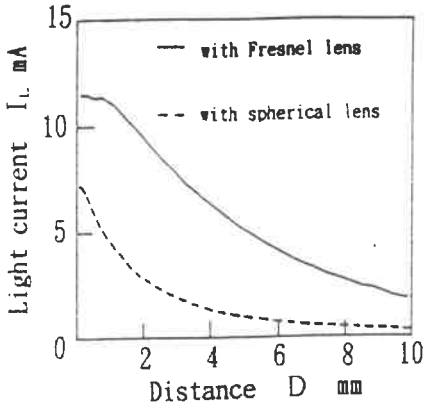

Fig. 8 Optical characteristics of LED with Fresnel lens

6. Conclusions

To mass-produce Fresnel lenses featuring thin and highly desirable optical characteristics through injection molding, a diamond turning machine was designed and manufactured, and a metal mold for Fresnel lenses was machined on the turning machine. The following results were obtained:

(1) A feed mechanism employing a friction drive unit was developed, and a fine positioning resolution of 20nm was obtained on the X- and Z-axes of a diamond turning machine.

(2) A diamond turning machine having the machining performance of a profile accuracy of 0.2μm was developed.

(3) A metal mold of a radial accuracy 3μm was machined, satisfying a required machining accuracy of 5μm.

(4) Using the injection-molded Fresnel lens the LD beam was focused in a 2μm diameter circle, reaching close to theoretical value.

Optimized Tool Path Descriptions For Aspherical Surface Generation

Mark Craig Gerchman
Rank Taylor Hobson Inc.
Keene, New Hampshire USA 03431-0543

The modern ultra-precise machine tool is capable of producing aspherical surface geometries to demanding tolerances. Many factors (*e.g.* machine tool accuracies, environmental effects, and machining dynamics) influence the accuracy of the surfaces generated. One factor that directly influences surface geometry is the description of the tool path used by the machine tool's numerical control system. This paper will describe a new algorithm for the optimization of the tool path description for aspherical surface generation.

Various interpolation schemes are used by ultra-precise machine tool control systems to "smooth" tool path descriptions. These interpolation schemes include linear, circular, polynomial, spline and machine specific descriptions. Simple linear interpolation has remained the preferred choice for the ultra-precision community since the use of multiple points provides for greater user control over path definition and compensation for residual form errors.[1]

Current software, that use a linear interpolation scheme to describe tool paths, define a series of points that are equally spaced along the desired theoretical curve and offset to account for tool tip geometry. These points are used by the machine tool control system to position the machine such that the relative positions of the tool and work piece follow the described straight line segments between these points and approximate the desired curve (see figure 1). The number of points used to define the curve must be selected to maintain a maximum difference between the linear segment and the theoretical curve below some specified tolerance limit.

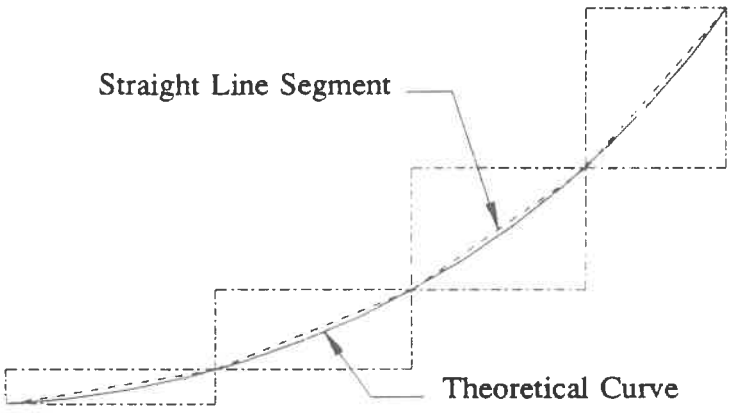

Figure 1 - Linear Interpolation Scheme

The current software algorithms begin this process with a functional description of the surface to be generated. This functional description is required to permits the calculation of first and second derivatives. From these, the instantaneous radius of curvature can be calculated for any point within the range of the aspherical surface. By evaluating the instantaneous radius of curvature over this range a minimum instantaneous radius can be found. Using this radius and a maximum interpolation error the spacing of points that form the linear segments is determined. Thus, the total number of points required can be approximated by dividing the curve length by this linear segment length. The effects of finite tool tip geometry is then calculated for each of

these points and applied to create the tool path. When this fit is required to be improved a smaller linear interpolation error is used and a more dense selection of points results. The limit on the number of points used has been the machine control system's processor speed (update considerations) and data memory storage.

During recent work on the description of machine tool motions for the *LAST* test[2] it was found that reducing the linear interpolation error did not necessarily improve the accuracy of the tool path description. The argument that more and more points increases accuracy is based on a mythical machine tool control system that permits infinite position programmability. Real machine tool control systems restrict the definition of these points to a grid of minimum programmability. A machine tool position can only be specified to a finite number of significant digits. This quantization will adversely effect the tool path's accuracy when the linear interpolation error becomes smaller than this programmability level. Figure 2 shows how shorter segments provide a less accurate fit to a theoretical curve than a more widely spaced set of points in the limit of quantized programmability.

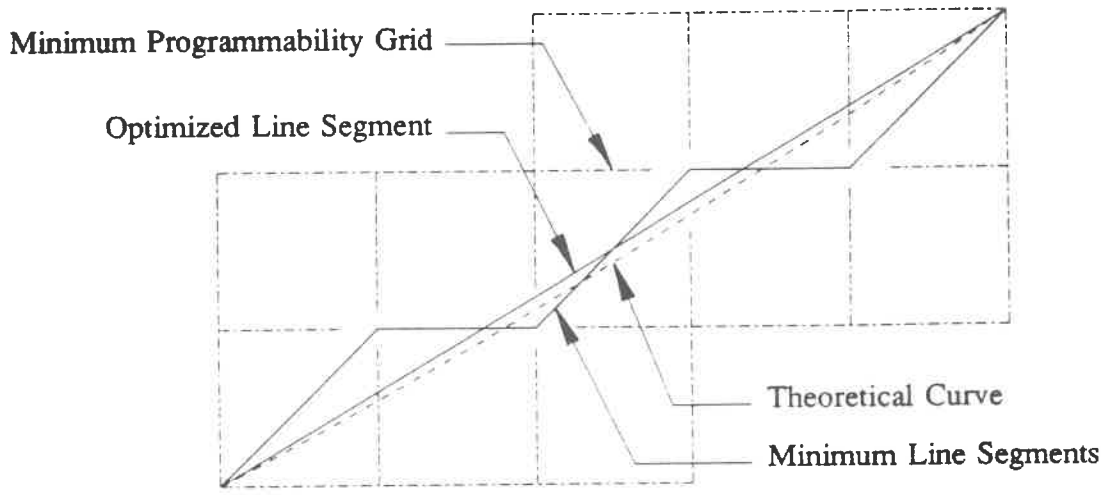

Figure 2 - Minimum Programmability Effects On Optimized Tool Path Descriptions

A new algorithm has be constructed that takes this quantized programmability into account. This algorithm searches along the theoretical curve in the vicinity of the usual end point (but always to shorten the segment) for the closest intersection between the curve and the grid of minimum programmability. When the closest point is found this point then becomes the end point for the current straight line segment and the starting point for the next segment. When the algorithm is applied after tool tip compensation the search is performed in an iterative fashion since the straightforward functional relationship becomes transcendental.

To demonstrate the benefits of this new algorithm consider the following example which for simplicity neglects tool tip compensation. Consider the generation of a paraboloid of revolution with a focal length of 125 mm and a diameter of 75 mm on a machine tool with 10 nm programmability and a maximum interpolation error of 1 nm. The functional form for this surface is given in equation 1. From this functional description derivatives can be determined and the functional form of the instantaneous radius of curvature expressed.

$$z = z(x) = \frac{x^2}{4f} \quad , \quad r(x) = \frac{\left(1 + \left[\frac{\partial z}{\partial x}\right]^2\right)^{\frac{3}{2}}}{\frac{\partial^2 z}{\partial x^2}} = 2f\left(1 + \frac{x^2}{4f^2}\right)^{\frac{3}{2}} \tag{1}$$

By evaluating this function over the aspherical curve, the smallest instantaneous radius of curvature is found at the vertex of the curve and is equal to twice the focal length ($r_{min} = 2f$). Using this value for the minimum radius and the maximum interpolation error (ε) a minimum segment length is determined from equation 2 and calculated to be 0.0447 mm.

$$s \approx \sqrt{8 r_{min} \varepsilon} = \sqrt{16 f \varepsilon} \tag{2}$$

Equation 3 describes the length along the aspheric curve. Solving this expression over the range of x values from the centerline to 37.5 mm (half the diameter) yields a distance along the curve of 37.64 mm. Dividing this value by the minimum segment length gives the approximate number of segments required to define the tool path, which is calculated to be 842.

$$L = \int_{x_{min}}^{x_{max}} \sqrt{\left(\frac{\partial z}{\partial x}\right)^2 + 1}\ \delta x = \int_{x_{min}}^{x_{max}} \sqrt{\frac{x^2}{4f^2} + 1}\ \delta x \tag{3}$$

Using the point selection algorithm without the search feature the average distance between the theoretical curve and these 842 linear segments is 2.05 nm. This error is larger than the maximum interpolation error and is approximately half of the rounding error due to minimum programmability restrictions. Applying the new algorithm with a search length of one percent of the segment length results in a need to only increase the total number of linear segments in the path description by 4, but with an increase in the accuracy of the curve definition such that the average error is only 0.72 nm. This is a threefold improvement in the tool path description with a negligible increase in the number of points required!

The new search algorithm has proven to consistently improve the accuracy of tool path descriptions over a wide variety of aspherical surface forms. Because the algorithm creates the tool path description off-line and prior to surface generation it does not impact surface generation time. As the tolerances for surface accuracies improve this algorithm will provide a means to optimize the tool path descriptions for aspherical surface generation.

---

[1] Gerchman, Mark Craig, "Compensation of residual form errors in precision machined components", Proc. SPIE vol. 1573 (1991).

[2] Gerchman, Mark Craig and David H. Youden, "An evaluation of ultra-precise machine tool contouring performance: the Low Amplitude Sine Tracking (*LAST*) Test", Progress in Precision Engineering, Springer-Verlag (1991).

A NANOMETRIC PRECISION NON-CONTACT TOOLSETTING SYSTEM

P. Morantz
Cranfield Precision Engineering
Cranfield Institute of Technology
Bedford, MK43 0AL, UK

An optical toolsetting technique for diamond tools has been devised. This achieves nanometric precision without contacting the tool edge, thus avoiding tool damage which is known to occur with contact probing.

Introduction

The manufacturing process of diamond turning has become of significant importance in high precision manufacture. Severe demands are placed on the precision with which surfaces must be produced - in a variety of shapes and materials.

In order to meet these demands, many machining parameters must be optimized: workpiece quality and holding technique, machine dynamic characteristics, accuracy of axis motions, etc. Most important for consideration here are the relative position of workpiece and cutting point.

The most recent generation of aspheric generators [1] are now capable of the required precision in motion - at the nanometre level; but in order to exploit this machine precision, it is essential that registration of tool position / orientation to machine axes, and qualification of tool shape, can be achieved at an equivalent level of precision.

Toolsetting

In order to make accurate parts, the tool cutting point must follow the programmed path, despite unknown tool shape and orientation errors. There are two ways this can be achieved:

Without a tool setting system, accurate positioning of a tool can only be achieved by an open-ended iterative approach. This is because new tools cannot be accurately replaced in a tool holder (only to a few microns at best). This iteration involves three steps: machining operation, component profile measurement and subsequent tool resetting.

A tool setting system allows the position of the tool edge to be known relative to the machine axes, by measuring the tool position prior to a cut. This knowledge is crucial. If there is an offset between the actual and assumed position of the tool, the edge's cutting point will not follow the correct trajectory. The toolsetting operation allows this offset to be removed; compensating for errors in tool holding, edge profile and long period (e.g. thermal) effects.

Contacting probe toolsetting

Existing high precision toolsetting systems are normally contacting. For example, systems using air-bearing LVDT's can achieve extremely fine resolution, and repeatability at the micro-inch (25 nm) level.

All contacting systems however, have serious disadvantages. These are a consequence of the finite contacting force. At the moment of contact between probe and tool tip, which are both hard materials, there is an extremely high impact force, which is known to cause damage[2]; particularly to the fine diamond tool tip.

This has inevitable consequences for surface finish and form. Even if damage can be minimized, by using exceptionally low forces and closing speeds, there is a further effect on toolsetting repeatability from the 'machining' of the probe material by the harder diamond tool tip.

Another serious difficulty with contacting probes is the influence of dirt on the repeatability of measurement. Contamination of the tool edge, or of the probe tip, can lead to inaccurate and inconsistent results - seriously affecting the overall system (machining) performance.

Optical non-contact toolsetting

The use of non-contacting toolsetting systems (in particular optical systems) overcomes the problems stated above, and confers significant additional advantages. Problems with tool tip impact damage are completely avoided. Problems with tool tip contamination can be significantly reduced; as will be shown below. An optical system gives a visual indication (to the operator, or an automatic system) of tool condition / quality i.e. the occurrence of chips.

The basic configuration, shown in figure 1, is that of a high magnification optical microscope. The image (viewable on a TV monitor, see figure 9) is processed by a sophisticated computer system integrated with the machine control system. The mechanical / optical system embodies design features specific to this application: design for low thermal coefficients and high stability - and for low heat dissipation.

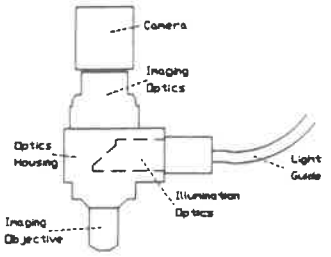

Figure 1. The optical system.

Achieving nanometric precision

Optical toolsetting is in regular use, but setting repeatability in the optical object plane has normally been limited to around ½ micron[3][4]. In direct visual systems, this limit is a consequence of the diffraction limited resolving ability in visible light.

A very high magnification system and with CCD and computer image analysis can yield much higher resolution and repeatability. The very sensitive focus discrimination of the system may also be employed as a setting determinant for tool height.

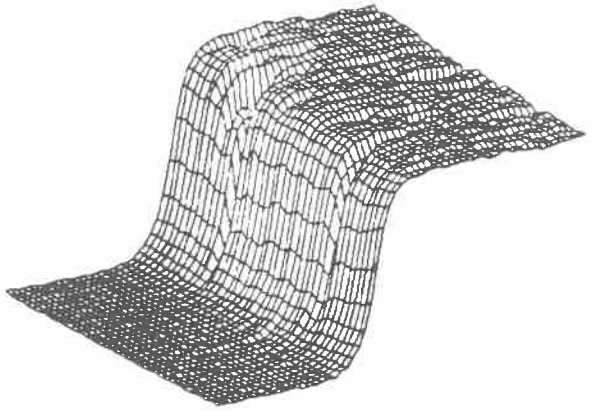

Figure 2. Mesh plot of sharp focus edge.

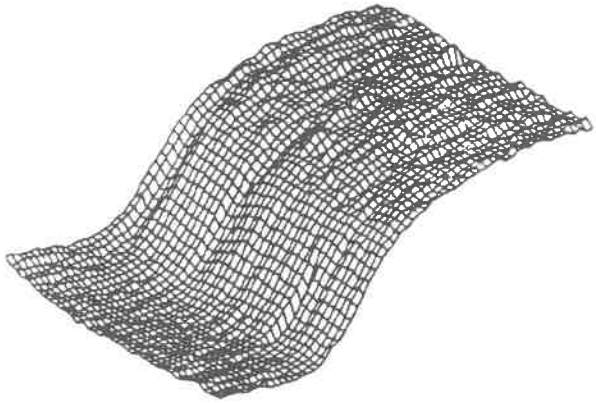

Figure 3. Mesh plot of out of focus edge.

Figures 2 and 3 show intensity mesh plots representing segments of images on a CCD array, of a sharply focussed and de-focussed edge respectively. Each mesh intersection represents the intensity received at a CCD pixel. It is the function of the image analysis to cope with varying image intensity, contrast, focus, noise (surface debris), tool geometry (profile and rake), illumination conditions etc. and still produce measurements of nanometre range repeatability, so that toolsetting can function at the level required.

Integration within the control system for the machine confers particular advantages. The ability of the optical system to act as a highly sensitive probe in three directions, allows movement of the tool under machine control so that the entire cutting edge is mapped relative to machine axes, using the machine motions for metrology. This gives not only an accurate measure of tool 'radius' but a complete understanding of tool shape (edges seldom follow circular arcs) yielding parameters of the ellipse shape, indication of wear and damage, a

measure of rake - in fact a complete description of the tool edge. This can be used for tool shape compensation where tool indexing is not possible, or for accurate cutting point determination otherwise.

Figure 4 shows the principle of the optical toolsetting operation with the diamond turning machine. The tool edge traverses the field of view under machine control. Successive measurements are taken, each one yielding positional information in three orthogonal directions. For each separate measurement, accurate automatic focussing of the image, by tool height adjustment, allows a sensitive setting of tool height. A complete map of the tool edge is built up in three dimensions.

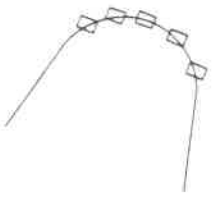

Figure 4. The measurement strategy.

Results of evaluation

In order to provide a searching evaluation of the performance limit of the system, its resolution and repeatability were evaluated against a precise metrology machine, capable of nanometric positional increments. Figure 5 shows the results of comparing 1 nanometre positional increments of the diamond tool on the metrology machine against the position of the tool measured by the optical toolsetting system. The tool is being moved normal to its edge, in the plane of its top rake. These measurements, taken over a period of 3 hours, span 1.6 microns actual tool movement. The scatter from the expected straight line (shown on an expanded scale in figure 6) includes not just measurement errors in the optical toolsetting system but also positional errors of the metrology machine (thermal drift etc.). Nevertheless, it can be seen that the standard deviation of the combined error is still less than 10 nm.

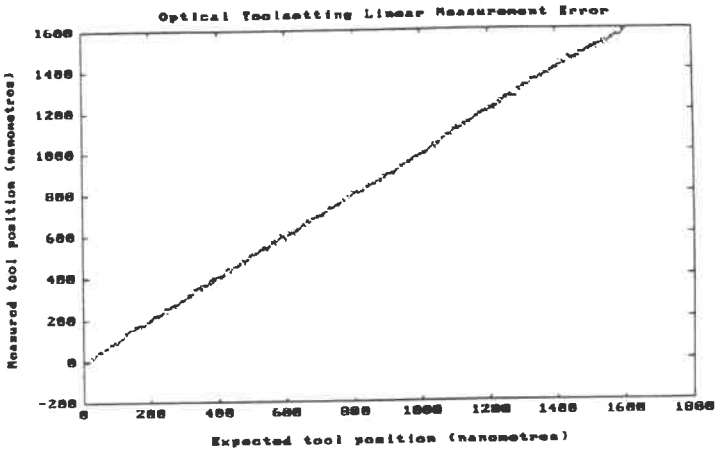
Optical Toolsetting Linear Measurement Error
Measured tool position (nanometres)
Expected tool position (nanometres)

Figure 5.

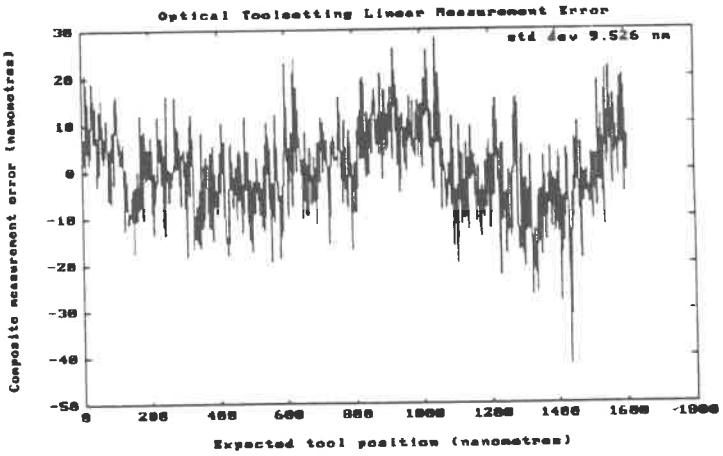
Optical Toolsetting Linear Measurement Error
std dev 9.526 nm
Composite measurement error (nanometres)
Expected tool position (nanometres)

Figure 6.

Measurements taken over a shorter period of time, encompassing less thermal drift, show an even lower standard deviation ~5 nm in figure 7. This is a good way of characterizing the repeatability performance of the system.

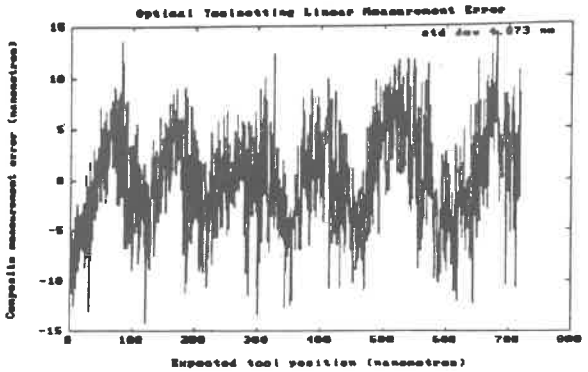

Figure 7.

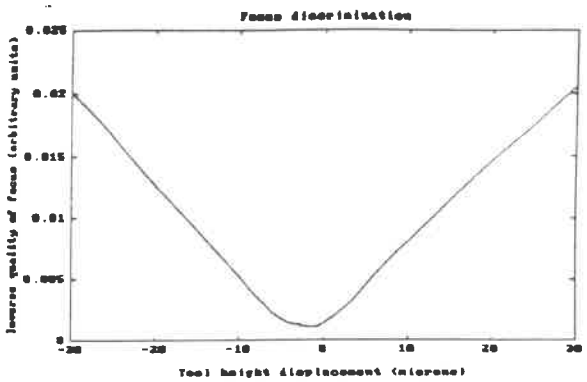

Figure 8.

The height measurement capability is shown in figure 8. A machine controlled scan of the tool edge through focus, enables a determination of correct (in-focus) tool height to be made, to a precision of around 0.2 micron.

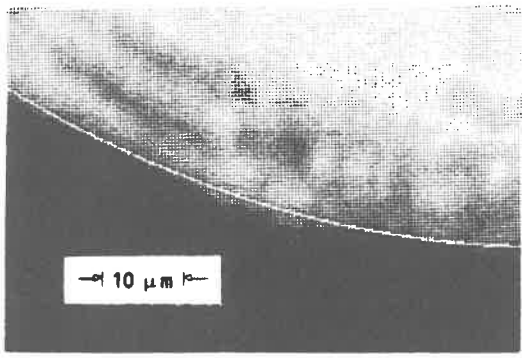

Figure 9.

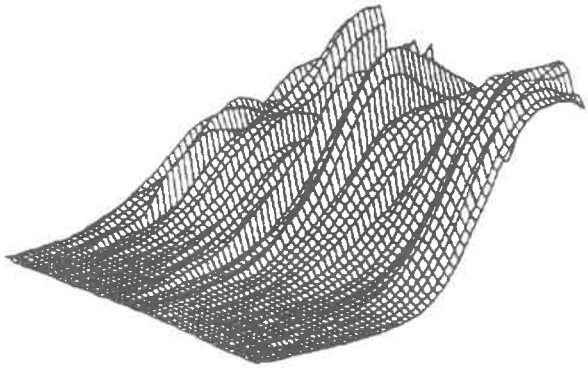

Figure 10.

Measurements indicate a very useful degree of immunity to surface contamination. Figure 9 shows the 'one-shot' measured edge profile along a dirty and de-focussed tool edge. This is a most taxing edge condition for metrology, but the bright white line indicates the system's measure of actual edge profile, derived from this image. The same edge is shown in intensity mesh plot in figure 10.

The capability of the system for handling de-focussed images allows similarly accurate probing of high top-rake tools. The limit on acceptable rake (around 35°) is currently set by the nature of the illumination, which is coaxial with 0.6 N.A.

Further development, particularly of the optical / CCD system is expected to improve the repeatability of measurement by as much as a factor of 2.

This system was developed as part of a DTI (UK) Link Nanotechnology Ultra Precision Machining Research project with additional funding from Cranfield Precision Engineering Ltd., DeBeers Industrial Diamond Division (PTY) Ltd., Framatome, S.A. and IBM (UK) Laboratories Ltd.

References

1. Carlisle, K., P. Shore, Proc 6th IPES, 85 (1991).
2. Myler, J.K., R.A. Parker and A.B. Harrison, Proc SPIE, 1333, 58 (1990).
3. Wills-Moren, W.J., H. Modjarrad and R.F.J. Read, Annals of CIRP Vol. 31/1/1982.
4. Doiron, T.D., Precision Engineering, 1989, p231-238.

TOOL FORCE, TOOL EDGE, AND SURFACE FINISH RELATIONSHIPS IN DIAMOND TURNED ALUMINUM

Joseph.D. Drescher*, Thomas A. Dow
Precision Engineering Center
North Carolina State University, Raleigh, NC 27695-7918

INTRODUCTION

The theoretical surface finish for diamond turned ductile metals is much smaller than the surface roughness actually achieved. For typical cutting conditions, the calculated peak-to-peak roughness is less than 5nm while in practice, the measured surface roughness is greater by at least a factor of two. Many effects contribute to the discrepancy between theoretical and measured peak to peak roughness including spindle motion, slide vibration, and material imperfections. Changes in the sharpness of the tool edge condition can also contribute to larger than expected values. As improving machine designs reduce the other contributions to surface roughness, the effects of the diamond tool geometry will become increasingly important. This aspect is significant to process control since the tool edge condition can be assessed through force measurement.

It has been shown that measured tool force in diamond turning can be an indicator of the tool edge condition. Since the condition of the tool edge also affects the surface finish, the possibility exists for using tool force to predict the surface finish as a component is produced. This requires a clear understanding of the relationships between the tool edge, tool force, and surface finish.

EXPERIMENTAL PROCEDURE

A series of experiments were performed to determine the relationship between the components of tool force, the wear of the tool, and the surface finish. A 200 mm diameter disk of aluminum (6061-T6) was faced by a diamond tool and at selected cutting distances the tool forces were measured, the surface finish was determined, and the tool edge was inspected. The conditions for these wear experiments were as follows.

- Tool: 750 µm radius, 0° rake, 10° clearance
- Depth of Cut: 20 µm
- Feed Rate: 1.25 µm/rev to 5 µm/rev
- Surface Speed: 0-20 m/s (2000 rpm)
- Coolant: mineral oil

Tool Forces

At specific cutting distances during the wear experiments, a prescribed cut was made in the aluminum and the forces in the cutting and thrust directions were measured for a 5 µm/rev infeed and a 15 µm depth of cut. The ratio of thrust to cutting force was calculated from this data and is shown in Figure 1. The force ratio appears to approach a maximum value near the end of the experiments. The quadratic curve fit shown on the plot is an excellent match to the measured data.

* Currently at United Technologies, Pratt & Whitney, East Hartford, CT

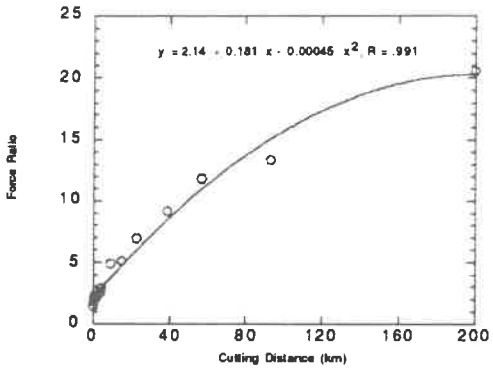

Figure 1 Force ratio (thrust force/cutting force) vs. cutting distance in aluminum 6061-T6 from 0 to 200km

Tool Edge Condition

The tool was examined periodically with a light microscope as well as a scanning electron microscope (SEM). Flank wear on the clearance face of the tool was measured from Nomarski photographs and the edge radius was obtained from SEM images at various stages of wear.

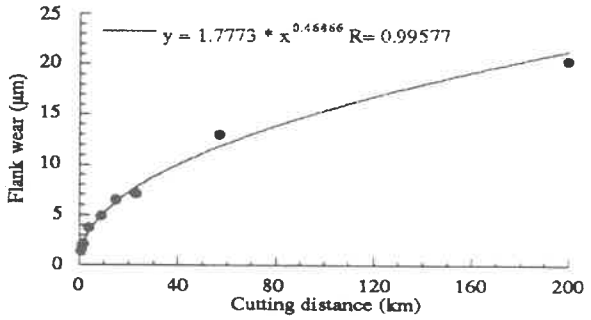

Figure 2 Flank wear vs. cutting distance in cutting of aluminum 6061-T6

Figure 2 shows the measured flank wear vs. cutting distance. These values can be represented by a power law curve fit with initial flank wear of 1.8 µm and a final flank wear of 21 µm after 200 km of cutting. Figure 3 shows the edge radius of the tool increased quickly before leveling to approximately 1 µm after 200 km cutting distance. A logarithmic model fit this data best.

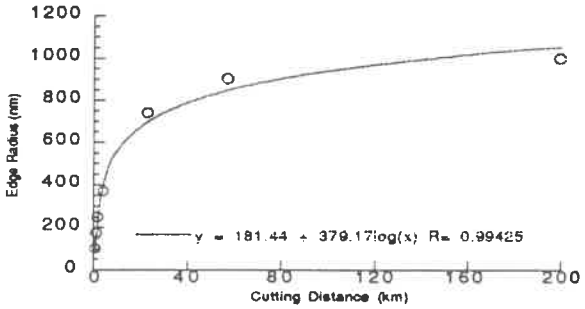

Figure 3 Measured edge radius vs. cutting distance in aluminum 6061-T6

Surface Finish

Sample surfaces were cut at the various stages of tool wear using a 5 µm/rev infeed and 10 µm depth of cut. These surfaces were examined with an optical interferometer at 10X magnification (0.6 x 0.8 mm field of view) and peak-to-peak roughness values were measured. Figure 4 gives the results of roughness plotted as a function of the log of the cutting distance. The 10X magnification was selected to include the influence of the particulates in this aluminum alloy, and to a lesser extent, lower spatial frequency components in the surface finish. The behavior shown in Figure 4 may give some quantitative explanation of the commonly observed wear-in period of diamond tools in the cutting of aluminum.

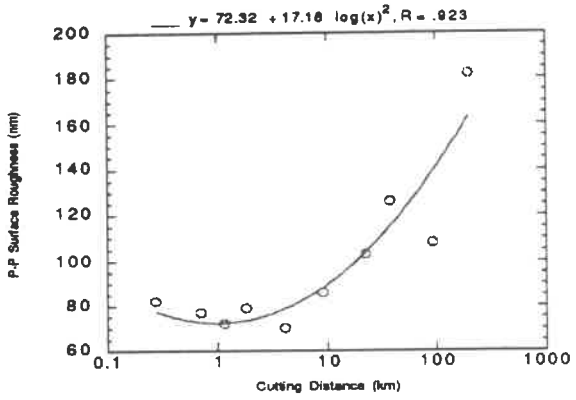

Figure 4 Peak to peak surface roughness vs. cutting distance.

Initially, the surfaces are characterized by scratches which originate at the particles as illustrated in Figure 5. A very sharp tool encountering such a particle tends to remove it from the surface leaving a hole, or drag it along resulting in the scratch.

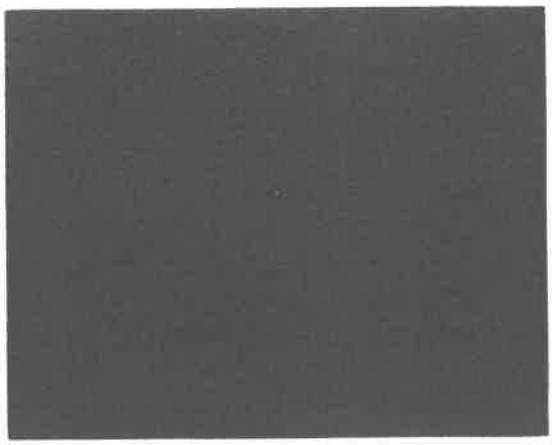

Figure 5 Micrograph of machined 6061-T6 Al with new tool (500x)

As the edge radius grows, the tool has a burnishing effect. While the resulting surface has pits where particles were apparently removed, there is less scratching and when particles are removed the surface is smoothed over. As the edge radius becomes even larger the density of particulates on the surface appears to increase as shown in Figure 6; that is, a higher percentage of particles remain on the surface resulting in a larger roughness.

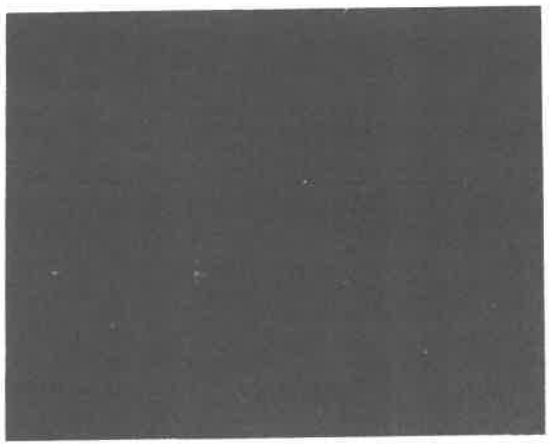

Figure 6. Micrograph of machined 6061-T6 Al after 200km cutting distance (500x)

TOOL FORCE/TOOL EDGE RELATIONSHIPS

The edge radius is plotted as a function of the measured force ratio in Figure 7. The best fit model to this data was a quadratic polynomial. For edge radii less than about 400 nm, the force ratio is independent of the edge radius. However, wear of the tool beyond this value has a significant effect. The force ratio becomes a very sensitive indicator of the edge radii beyond about 600 nm.

The relationship between the force ratio and measured flank wear is shown in Figure 8. A straight line provided an excellent fit for the

data. Since the thrust force increased as tool contact area in the thrust direction (flank wear) increased while the cutting force (related to material removal rate) remained relatively unchanged, this relationship was as expected.

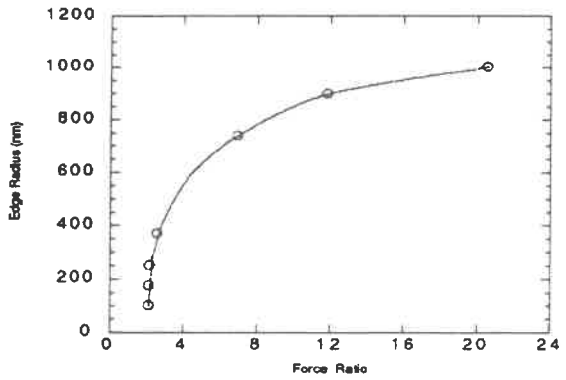

Figure 7 Measured edge radius vs. force ratio (thrust force/cutting force) from 0 to 200km cutting distance

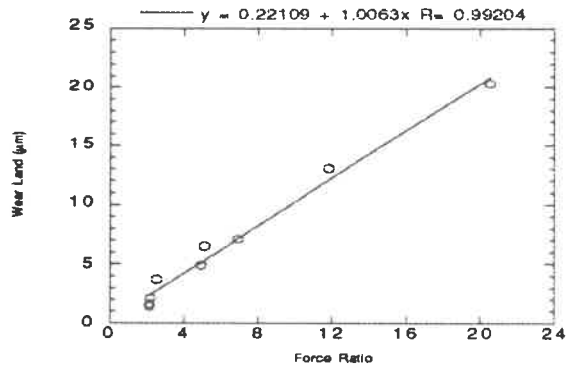

Figure 8 Measured flank wear vs. force ratio from 0 to 200km cutting distance

Since both tool force and surface finish are related to the tool edge, the force ratio can be related directly to the surface finish. The plot of Figure 9 shows this relationship for the experiment conducted. The best fit curve is a monotonically increasing function raising the possibility that the tool force ratio can be used as a sensor to measure the resulting surface finish for a given depth of cut.

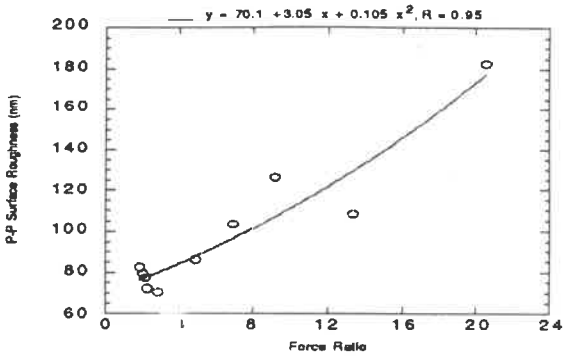

Figure 9 Surface Roughness vs. Tool Force Ratio

CONCLUSIONS

- Tool wear increased rapidly in the initial cutting stages. Flank wear continued to increase in a more gradual manner while the edge radius approached a value of approximately 1 µm.
- The peak to peak surface finish improved for the initial stages of tool wear but increased with increasing cutting distance. The edge rounding was identified as the principle wear characteristic responsible for the measured roughness values.
- A dimensionless tool force ratio of thrust force to cutting force increased with cutting distance. The increase in the force ratio was principally due to flank wear.
- The monotonically increasing relationship between the tool force ratio and surface roughness can be used to predict the resulting surface finish and lead to real-time control strategies.

LIDAR Project:
Diamond Turning Mirrors in a Panic Situation

Richard Rhorer
Los Alamos National Laboratory
Los Alamos, New Mexico 87545

Introduction

The manufacturing of diamond turned optics is common for many infrared applications, and the diamond turning shop at Los Alamos has made many optical elements in the past fifteen years. In December 1990 a unique challenge was presented to the employees of this shop -- to fabricate a series of large optical elements in less than two weeks. This two week period included designing, purchasing materials, roughing the blanks, diamond turning, testing and coating. Responding to this challenge produced some degree of panic; however, we were able to manufacture a system that would have been impossible without diamond turning technology.

The acronym LIDAR (LIght Distance And Ranging) is used to describe a system similar to RADAR, except light waves are used instead of radio waves. The basic idea is to send out a pulse of radiation, and then analyze the reflected radiation. An optical system is needed to collect the radiation and focus it into a detector. This optical system needs to be a large enough diameter to focus a reasonable amount of energy on the detector.

The LIDAR Project at Los Alamos was initiated to support the Desert Storm war effort. The product from the LIDAR project was to have an airborne capability to detect aerosols in the atmosphere up to 40 kilometers away. The system designers estimated that a 24 inch diameter telescope and associated scanner was needed to accomplish the requirements. The optical components were completed on December 31, 1990, and the completed LIDAR was airborne and tested by the end of the first week of January 1991. The LIDAR system was ready, but was not needed in Desert Storm.

Building the LIDAR System Optics

The LIDAR telescope designs called for a 24-inch diameter elliptical primary and a spherical 6-inch diameter secondary. Telescope mirrors were fabricated from stock 6061-T6 aluminum. The primary mirror was designed to be held in a 3-point fixture that had been used for a smaller mirror previously. The mirror blank was produced by milling pockets to lighten the overall weight of the telescope. The primary mirror blank was made in 5 days, including heat treat, and the final diamond turning done in one day. When assembled, the F/2 telescope was good to about two waves when tested with a visible light interferometer. This was judged to be completely acceptable for the infrared collecting application.

The scanner mirror is optically simple, but presented a particular challenge because of the size and weight concerns. The 24 x 36 inch, flat surface mirror had to be mounted on a rotary table to allow the LIDAR to scan out through an aircraft door. This mirror was fabricated from a 4-inch thick piece of 6061-T6 aluminum plate . The back side of the scanner is shown in figure 1, and the front surface is shown in figure 2.

By machining the pockets in the back side, the weight of the blank was reduced from about 375 pounds to less than 100 pounds. The mirror was held during machining by the same 3-point mount as used for the telescope mirror; however, an adapter plate was bolted on the back side of the blank. This 1-inch thick plate was heat treated and then turned flat on a precision lathe while held with the three mounting bolts we used on the

completed mirror. After milling the pockets in the back side of the scanner, heat treating, and lapping the back surface, the adapter plate was bolted on and used to hold the mirror during diamond turning.

The preparation of the scanner blank included about 80 hours of actual milling time, diamond turning was completed in about 6 hours. After diamond turning, the scanner was tested in an interferometer and determined to be within about three waves (visible light) over the center 18 inches. This scanner mirror exceeds the specifications for flatness required in the infrared system.

Lessons Learned

In completing this LIDAR project, and now looking back, I suggest we can learn something for future "fast prototyping".

1. An accurate scale drawing should be maintained and updated continuously to insure that mechanical components interface when building a complicated system.

2. A "full service" shop is needed to build a complete high precision system in a very short time.

3. A tremendous amount of work can be done in a very short time when it is not necessary to wait for decisions and approvals.

4. A rule-of-thumb design approach (as used on the diamond turned mirror blanks) is possible when you are not trying to advance the state-of-the-art in any of the critical technologies involved.

Acknowledgments

There were many people at Los Alamos that made vital contributions to this LIDAR project. Over eighty people were included in a Los Alamos Distinguished Performance Award presented in May 1991 -- and we probably missed some contributions in this award. The building of the mirror blanks for diamond turning would not have been possible without the efforts of George Zakar. George arranged for the right shop people, the materials, and the equipment to deliver the mirror blanks, and he worked continuously with almost no sleep for the last week of the project. Erich Baumgartner, who had run the diamond turning shop for 15 years, completed the telescope mirrors his last day of work before retirement. Felix Garcia diamond turned the scanner mirror, and his advance preparations allowed the final operation to be accomplished successfully in a very short time. Phil Hannah advised us, beginning with the initial conversation about the mirrors, on all aspects of the diamond turning and reassured us the job could be done. A special acknowledgment is also due Bob Karl who asked us to diamond turn the mirrors and had faith that we could get them done on time.

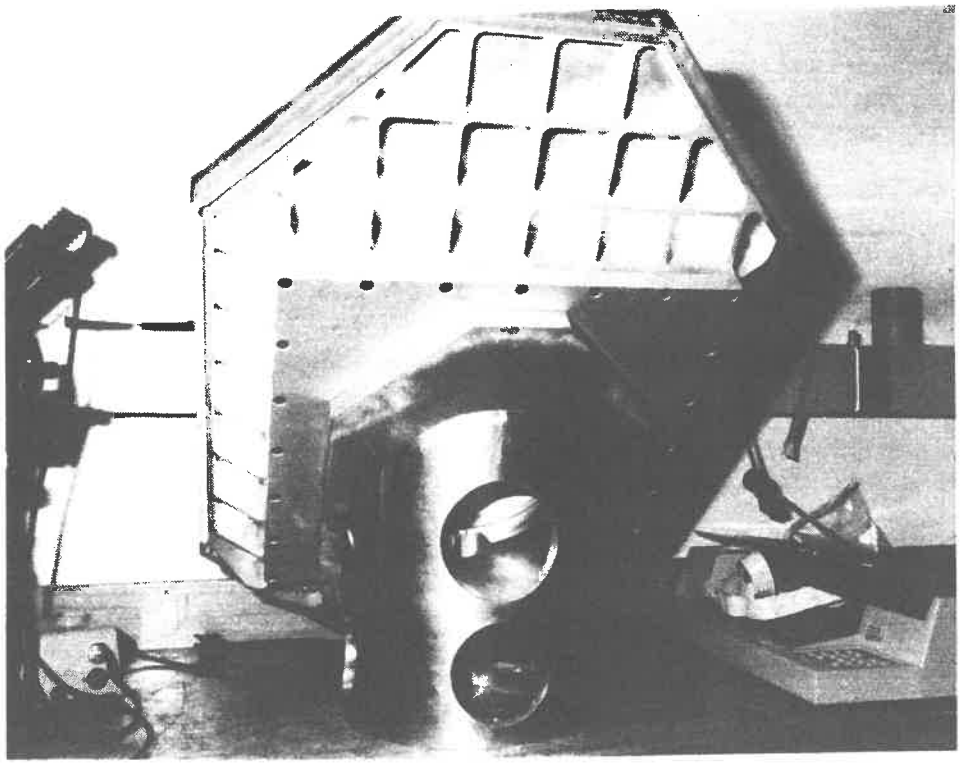

Fig. 1. Back Side of Scanner Mirror

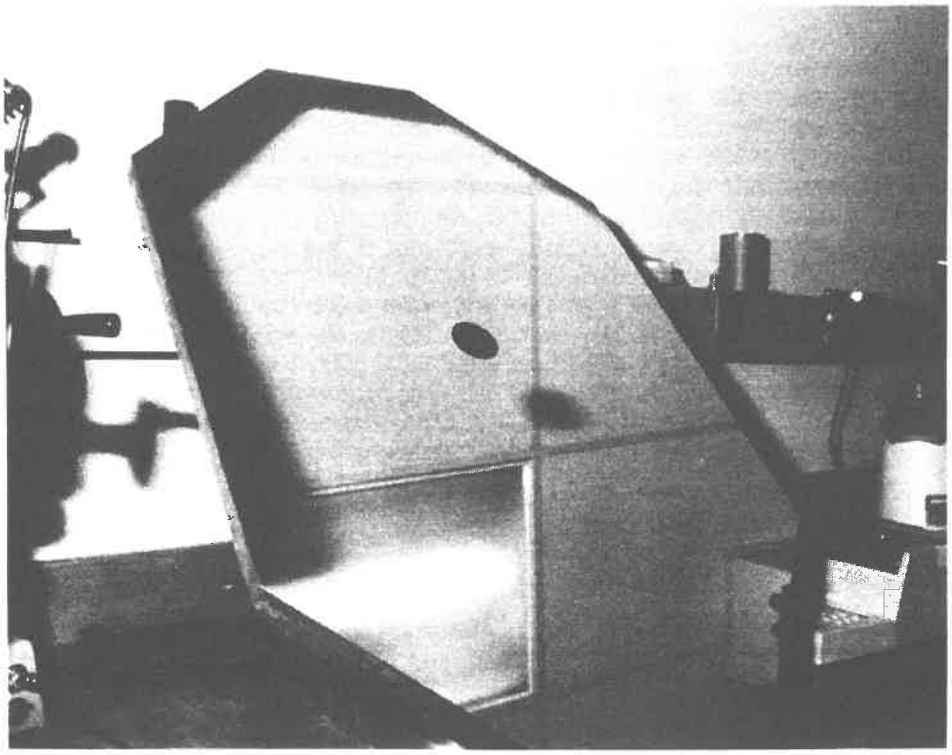

Fig. 2. Front Side of Scanner Mirror, 24 x 36 Inches

FRACTURE MECHANICS APPLIED TO THE DUCTILE MACHINING OF BRITTLE MATERIALS

G.D. Hiatt, J.S. Strenkowski
North Carolina State University
Raleigh, N.C.

Previous work has shown that ductile-regime cutting of brittle materials is highly dependent on the cutting conditions[1,2]. In those studies, a critical depth of cut parameter was identified and measured experimentally for germanium and silicon. The critical-depth of cut was measured using a radiused tool and was defined as the local chip thickness at the location where surface fracture was first observed. It is defined as that thickness above which fracture will occur in the chip and below which ductility dominates. This parameter defines the transition from plastic flow to fracture that occurs along the tool nose.

To consistently obtain a fracture-free surface, it is necessary to understand how different material properties and machine parameters interact to influence crack propagation during the machining of brittle materials. The likelihood that a brittle material can be machined in a ductile manner is a strong funcion of the stress and temperature distributions resulting in the workpiece from the cutting process. In this paper, a fracture mechanics model for single point diamond turning (SPDT) of the brittle materials silicon and germanium is described that can be used to predict the critical-depth parameter at which damage occurs in a brittle material. For a given cutting speed, rake angle, clearance angle, and tool edge radius, an arbitrary depth of cut is chosen for the orthogonal model. The stresses from the cutting model are then used to compute the stress intensity factor in the machined workpiece surface. If the stress intensity factor is less than the fracture toughness of the workpiece material, then it can be concluded that fracture will not occur. The advantage of this approach is that the stress state in the workpiece can be related to the cutting tool geometry and cutting conditions. Therefore, cutting conditions can be identified for which ductile regime cutting of a brittle material can be accomplished.

Eulerian Finite Element Cutting Model

During machining the elastic deformation is small compared to the viscoplastic deformation, so the equations that govern viscoplastic flow of solids can be written in a manner similar to that of incompressible elasticity. Following the development for orthogonal cutting developed by Strenkowski and Carroll[3,4], and Strenkowski and Moon[5], the stress and strain-rate are related through a viscosity coefficient μ

$$\mu = \frac{\sigma_f}{\sqrt{3}\dot{\bar{\varepsilon}}} + \bar{\mu} \tag{1}$$

where $\dot{\bar{\varepsilon}}$ is the second invariant of the strain-rate tensor or the effective strain-rate, σ_f is the flow stress, and $\bar{\mu}$ accounts for work hardening of the workpiece.

Material Model

Machining involves extremely high temperature and strain-rate gradients which cause the material and thermal properties to vary throughout the workpiece. Accurate material prop-

erties are required for the model to give useful results. Strain-rate has a significant effect on material properties such as the yield stress and fracture toughness. In general, flow stress decreases with temperature but increases with strain-rate.

One way of combining the temperature and strain-rate effects on the flow stress is through the so-called Zener-Hollomon parameter[6]. The flow stress for silicon and germanium can be expressed in terms of the temperature and strain-rate as[7]

$$\dot{\gamma} = \bar{c}\tau^{n}\exp(-Q/\bar{K}T) \qquad (2)$$

where $\dot{\gamma}$ is the shear strain rate, $\bar{c}$ is a constant, τ is the flow stress, Q is the activation energy, and $\bar{K}$ is Boltzmann's constant. With this form of the Zener-Hollomon parameter, the combined effects of temperature and strain-rate can be simulated for silicon and germanium.

The Zener-Hollomon parameter is introduced into the cutting model through the viscosity relationship in Equation (1). The flow stress is determined from the current temperature and strain-rate with the Zener-Hollomon parameter. Therefore, the combined effect of both elevated temperature and high strain-rate can be directly incorporated into the cutting model, which is then used for predicting the stress distribution in the workpiece for various cutting conditions.

Fracture Model for Cutting

The principal of superposition as outlined by Broek[8] was used to analyze fracture of the workpiece. Using superposition, the stress intensity of the workpiece is equal to that of the workpiece in which tractions previously transmitted by the unfractured material are applied to the faces of the crack. This superposition concept can be applied to other stress distributions and geometries if the appropriate stresses are applied to the crack faces.

For the machined silicon and germanium, the stresses in the unfractured workpiece were calculated with the finite element cutting model as those stresses that would exist in the absence of a crack. The principal stresses were calculated and cracks of different sizes were then placed at the location of the greatest principal stress behind the tool with the crack aligned perpendicular to the direction of the maximum principal stress. Then non-zero tractions were applied to the crack faces so that the appropriate boundary conditions were maintained. The stress intensity factor was then calculated with the appropriate equations as given by Tada[9] for a constant stress applied over an edge. Then the crack was extended by the length of another element, the stress intensity factor calculated again, with the entire procedure repeated until the stress intensity reached a maximum and began to decrease.

SPDT with a Round Nose Tool

The finite element cutting model was used to simulate the machining of silicon and germanium with a diamond tool. The tool edge was assumed to have a constant radius of 70 nm

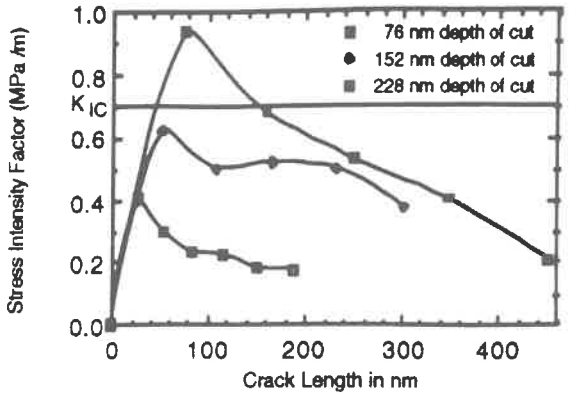

Figure 1: Variation of stress intensity factor with crack length for three depths of cut for silicon (-10° rake angle).

as estimated by Miyamoto et al. For example, for the machining of silicon with a -10° rake angle, 16° clearance angle, and cutting speed of 2.1 m/s, three depths of cut were simulated corresponding to 76, 152, and 228 nm. These were chosen because Blake found that the critical-depth parameter at which damage occurred was 152 nm for these cutting conditions. Figure 1 shows the variation of K with crack length for the three depths of cut. The critical stress intensity factor K_{IC} is included for comparison. For silicon, K_{IC} was assumed to be $0.7 MPa\sqrt{m}$. This figure demonstrates that an existing crack will not propagate regardless of its length for the smallest depth of cut (76 nm). The calculated stress intensity factor for the intermediate depth (152 nm) nearly reaches K_{IC}. For the 228 nm depth of cut, the calculated stress intensity is sufficiently large to propagate a crack. These findings are consistent with Blake's experimental results.

When the rake angle is increased to -30°, similar results are obtained in which the critical depth of cut was found to be 446 nm. These results are also consistent with Blake's results. Note that as the rake angle becomes more negative, the critical depth parameter becomes larger. This is because the tensile stresses do not extend as deeply into the surface, and so the stress intensity factor for a crack of a given length is reduced.

It was found that cutting speed had little effect on the surface damage arising from fracture. For the highest speed of 16.8 m/s there was only a small reduction in the stress intensity factor. However, this reduction suggests that higher speeds than this could possibly lower the amount of fracture due to the increased temperature.

The effect of the tool edge radius on the quality of the finished workpiece becomes significant when the radius is comparable to the depth of cut. Because the depths of cut are small in precision machining, a small edge radius can have a significant effect on the plastic formation of the chip, the surface deformation, and the residual stresses. When the depth of cut is small compared to the edge radius, the rake angle appears to become more negative. The cutting edge radius for sharp diamond tools has been estimated to be 70 nm by Miyamota for a tool with a a small amount of wear.

Three different edge radii were used to study the effect of the cutting edge radius on fracture during machining. For a -10° rake angle, 2.1 m/s cutting speed, and a 51 nm depth of cut, the stress becomes less tensile as the edge radius becomes larger. Also, the tensile stresses do not extend as far into the workpiece and are smaller in magnitude for the more

negative rake angles. Thus the effect of increasing the cutting edge radius is similar to decreasing the rake angle. However, it was found that the peak stress intensity factor was similar for all three radii. Therefore, this indicates that the edge radius has little effect on ductile machining of germanium.

To allow a more direct comparison with the orthogonal cutting model, a more simplified tool geometry was also used to verify the fracture mechanics analysis developed in this thesis. A straight edge -10 degree rake angle, 6 degree clearance angle tool was chosen to machine germanium for 25, 38, 50, 64 and 76 nm depths of cut. The finite element model correlated well with the experimental results.

In conclusion, the technique described in this paper shows great promise for predicting the cutting conditions for which brittle materials can be machined in a ductile manner. Although the test conditions in this research were somewhat limited, all of the predicted critical depths of cut were consistent with diamond turning experiments for both round and straight-edge diamond tools. This technique can be used to choose those cutting conditions that will lead to reduced surface damage in the machined surface of brittle materials.

References

1 Blake, P. N., "Ductile-Regime Turning of Germanium and Silicon", Ph.D. Thesis, North Carolina State University, Raleigh, NC, 1988.

2 Blackley, W.S., "Single Point Diamond Turning of Brittle Materials", M.S. Thesis, North Carolina State University, Raleigh, NC, 1990.

3 Strenkowski, J. S., and Carroll, J. T., "A Finite Element Model of Orthogonal Metal Cutting", *Journal of Engineering for Industry*, Vol. 107, 1985, pp. 346-354.

4 Strenkowski, J. S., and Carroll, J. T., "An Orthogonal Metal Cutting Model Based on an Eulerian Finite Element Method", *Manufacturing Processes, Machines and Systems, Proceedings of the 13th NSF conference on Production and Research Technology*, 1986, pp. 261-264.

5 Strenkowski, J. S., and Moon, K., "A Thermo-Viscoplastic Model of the Cutting Process Including Chip Geometry and Temperature Prediction", *NSF Manufacturing Systems Conference Proceedings*, January, 1989.

6 Zener, C., and Hollomon, J.H., "Effect of Strain Rate Upon Plastic Flow of Steel", *Journal of Applied Physics*, Vol. 15, 1944, pp. 22-32.

7 Schroter, W., Brion, H.G., and Siethoff, H., "Yield Point and Dislocation Mobility in Silicon and Germanium", *Journal of Applied Physics*, Vol. 54, No. 4, 1983, pp. 1816-1820.

8 Broek, D., *The Practical Use of Fracture Mechanics*, 4th ed., Martinus Nijhoff Publishers, Dordrecht, The Netherlands, 1986.

9 Tada, H., *The Stress Analysis of Cracks Handbook*, Del Research Corporation, Hellertown, Pennsylvania, 1973, p. 8.4.

SIMULATION OF MICRO-INDENTATION USING MOLECULAR DYNAMICS MODELING ON THE CONNECTION MACHINE

PAUL A. SCAGNETTI, THOMAS G. BIFANO
RAYMOND J. NAGEM and GUIDO V. H. SANDRI
DEPARTMENT OF MECHANICAL ENGINEERING
BOSTON UNIVERSITY

INTRODUCTION: Molecular dynamics modeling of material deformation holds great potential as a means of simulating precision machining processes and understanding the atomistic mechanisms of material deformation. Such models are well suited for problems involving plastic flow and fracture at a microscopic scale[1,2]. The current challenge is to develop methods for calculating macroscopic quantities such as stress, strain, and constitutive relationships. Initially, such quantities can be used to verify the models against analytical solutions and experimental data. More importantly, plastic deformation can be described in terms of these quantities, which would improve the understanding and development of material processing techniques.

BACKGROUND: Since an analytical solution for the elastic stress field under a circular indentor is known[3], an MD simulation of this problem provides a useful check upon the macroscopic calculations. The plastic deformation indentor problem is less well understood, particularly in terms of the constitutive relationship between stress and strain.

Molecular dynamics is a technique in which a material is modeled as a system of interrelated discrete point masses. We have developed a nano-meter scale, two-dimensional model of micro-indentation using 8192 molecules in a hexagonal lattice, and a hybrid potential (Lennard-Jones and Embedded-Atom)[4]. Such a model has been proposed as a suitable representation of metals[5]. The simulations have been carried out on a massively parallel computer[6] with each processor responsible for one molecule. The particle trajectories are followed through a Verlet numerical integration routine. The temperature of the system is maintained at approximately 1/4 of the melting temperature with the use of thermostats.

Using continuum definitions, we have developed methods of calculating the stress and the strain tensors in MD models which are defined at each lattice point. Thus a relationship between stress and strain can be computed within the vicinity of each molecule. This relationship will be examined before and after dislocations occur near a given point.

---

[1]W.G. Hoover, A.J. DeGroot, C.G. Hoover, I.F. Stowers, T. Kawai, B.L. Holian, T.Boku, S. Ihara, J. Belak, **Large-Scale Elastic-Plastic Indentation Simulation via Nonequilibrium Molecular Dynamics,** *Physical Review A*, 10 (42), 1990, pp.5844-5853.

[2] J. Belak, I.F. Stowers, **Molecular Dynamics Studies of Surface Indentation in Two Dimensions,** Atomic Scale Calculations of Structure in Materials, Vol 193, San Francisco, CA, Apr 16-21, 1990.

[3]S.P. Timoshenko, J.N. Goodier, **Theory of Elasticity**, McGraw-Hill Book Co. New York, 1970, pp 409-413

[4]B.L. Holian, A.F. Voter, N.J. Wagner, R.J. Ravelo, S.P. Chen, W.G. Hoover, C.G. Hoover, J.E. Hammerber **Effects of Pairwise versus Many-Body Forces on High-Stress Plastic Deformation,** Physical Review A, 6(42), 1991, pp. 2655-2661.

[5] S.M. Foiles, M.I. Baskes, and M.S. Daw, **Embedded-Atom -Method Functions for the FCC Metals Cu, Ag, Au, Ni, Pd, Pt, and other Alloys**, *Physical Review B*, 12(33), 1986, pp. 7983-7991

[6] Thinking Machines Corporation, CM-2

CALCULATING STRESS: Stress in continuum mechanics is defined at a point as the force per unit area in the limit as the area is reduced to zero. In plane strain simulations, the stress tensor is calculated as a force per unit width per unit line length as the line length is reduced to zero. For MD models, the stress is more difficult to calculate because the force on a line segment is neither continuous nor uniform, and the stress does not smoothly approach a set value as the line length is reduced to zero. Therefore, the definition of stress and it's calculation must be carefully constructed. We model stress in the following way. A line segment, centered on a particular molecule, is extended to intersect several molecules on either side. This line is chosen as the line of interest. The forces on one side of the line segment are summed, and divided by the length of the line in order to arrive at a stress in the neighborhood of the center molecule.

In order to establish the length of the line needed to ensure sufficient statistical information, a material property such as density can be calculated using various cutoff distances. Since larger cutoff distances will ensure proper density, the line can be reduced until the density varies substantially. Simulations performed indicate that a line length of approximately $5r_o$ is sufficient. In simulations performed to this point, stress has not been calculated on the boundary molecules.

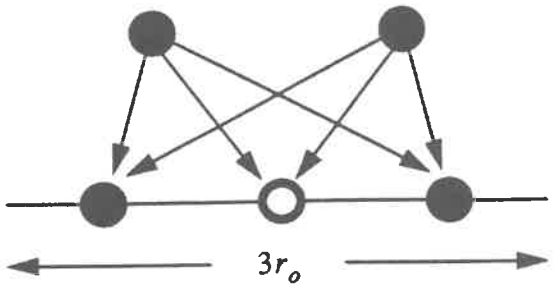

Diagram of forces required to calculate stress on white molecule, r_o is the bond length between two molecules.

CALCULATING STRAIN: The strain tensor can be computed using purely geometric information. In continuum mechanics, the strain tensor is defined as the rate of change of displacement with respect to position. Using the nearest neighbors within a hexagonal lattice, this definition can be applied directly to discrete models. The displacement of each molecule is calculated as the difference between the initial and the current position. Then the strain-displacement relations, which involve a derivative, can be computed using finite difference methods. In order to increase the accuracy of such computations, the algorithm involves all six of the neighbors, and includes nonlinear terms.

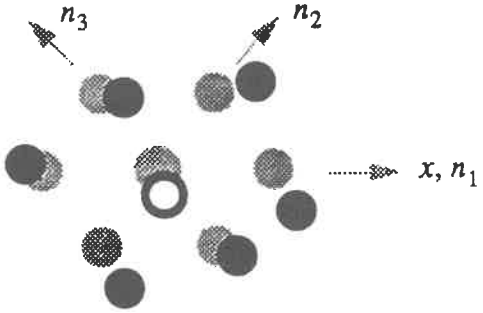

Diagram of displacement field used in calculating strain on white molecule. Gray molecules indicate initial positions.

RELATING STRESS AND STRAIN: For linearly elastic materials, the relationship between stress and strain follows Hooke's law:

$$\sigma_{xx} = (\lambda + 2\mu)\,\varepsilon_{xx} + \lambda\varepsilon_{yy}$$

This same relationship can be tested throughout the MD lattice. Though there will be fluctuations the constants should remain fairly uniform throughout the stages of elastic deformation. As the deformation becomes plastic, the relationship will no longer hold.

RESULTS: For the simulations performed thus far, the following observations are made. First, plastic deformation starts to occur as the indentor reaches a depth of about $1.5r_o$. Second, the maximum stresses throughout the lattice do not increase as the deformation becomes plastic. Rather, a slip line forms, and the stress remains at the maximum elastic value. In this sense, the slip acts to relieve any further stress by propagating dislocations.

The behavior of the system is particularly dependant upon two conditions. First the initial configuration has a strong effect on the type of dislocations that occur. Since our simulations were started with a evenly spaced lattice, the slip lines were straight for more than 10 bond lengths. If the lattice had been started in a less regular configuration, the slip lines would probably have been shorter. Second, the behavior of the system showed a heavy dependance upon the thermostating techniques. After running the simulations at various temperature levels, it was observed that plastic flow occurred more at higher temperatures. In the low temperature simulations, the workpiece demonstrated more vacancies than dislocations, and behaved in a more brittle manner.

The initial elastic phase, which occurs early in the indentation, agreed qualitatively with the analytical stress and strain field descriptions. Beyond the elastic indentation, our simulations describe the dislocation activity and vacancy generation which occur in plastic deformation. As the indentor moves into the workpiece, dislocations begin with a line a molecules which reach the yield stress. These molecules form a slip line which acts to relieve the stress.

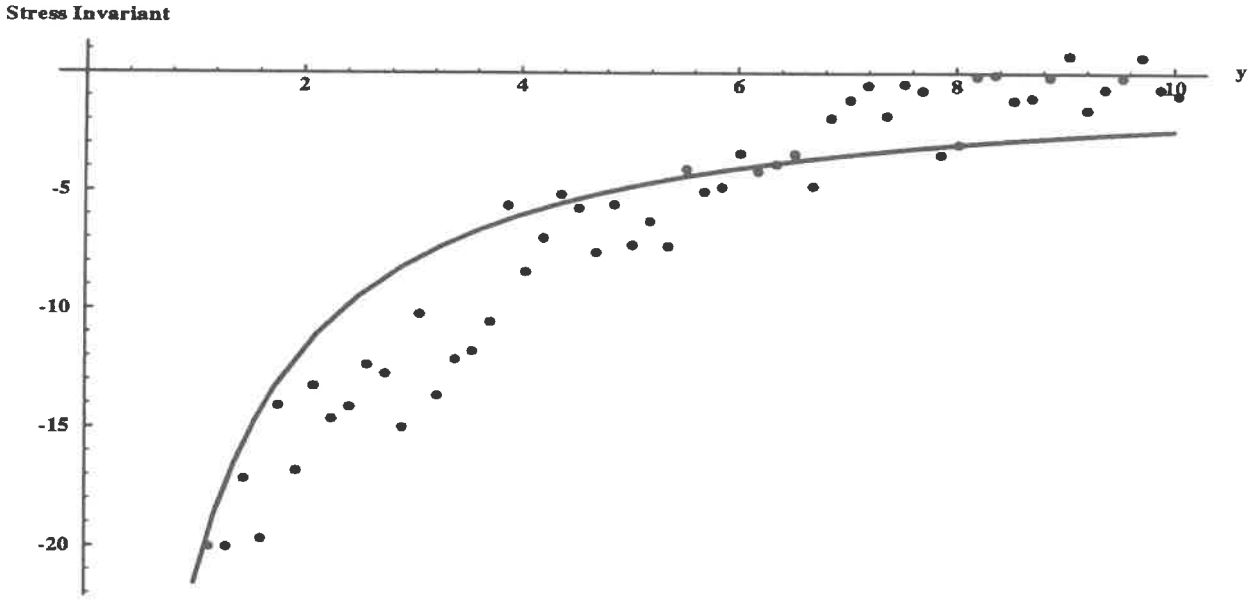

Plot of stress invariant $\sigma = (\sigma_{xx} + \sigma_{yy})/2$ *as a function of depth along the centerline of the indentor. The solid line indicates the analytical solution, the points indicate values calculated from the molecular dynamics simulation. The analytical solution is plotted in terms of the applied load. The discrete stress field is expressed in terms of the bond energy and molecular spacing.*

Figures on Following Page: *Maps of the Stress Invariant* $\sigma = (\sigma_{xx} + \sigma_{yy})/2$ *for a two-dimensional simulation of a* $32r_o$ *diameter, rigid indentor, moving at* $0.001r_o/\tau$, *where* τ *represents a typical molecular oscillation period. Images shown are taken at the following indentation depths;* $1.5r_o$ *(top), and* $10r_o$ *(bottom). The top image corresponds qualitatively to the elastic stress field solution for a circular indentor. The bottom image demonstrates the slip lines which act to relieve the stress. The images are taken from the central section of a 8192 molecule simulation which was maintained at 1/4 of the melting temperature. Darker areas indicate more compressive stress.*

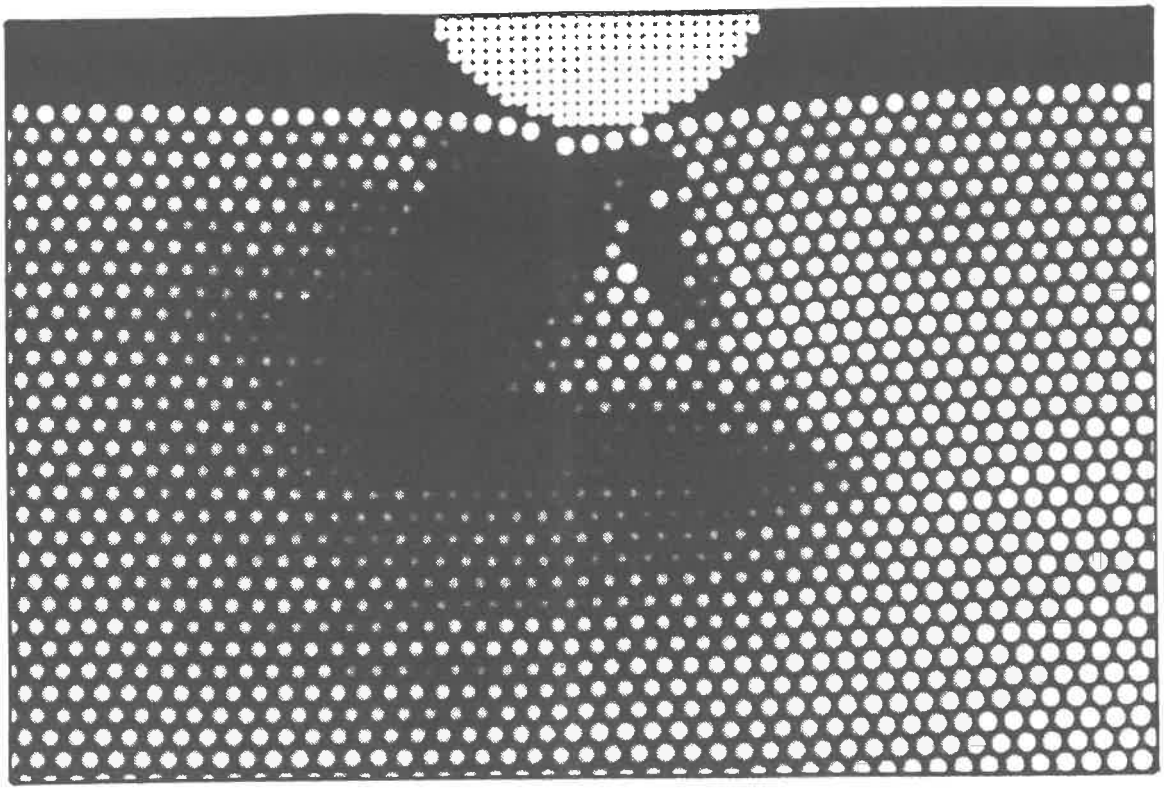

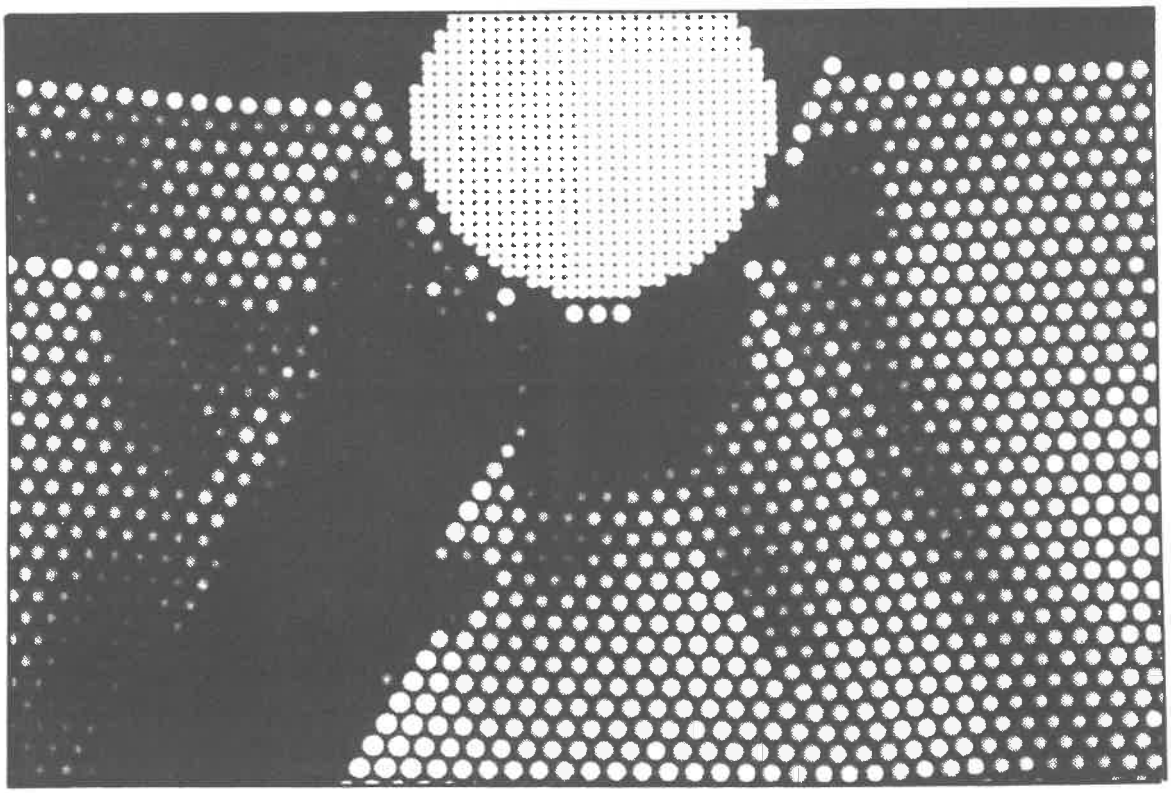

Fracture Toughness Effects in Precision Grinding of Ceramics

Stanley M. Smith and Ronald O. Scattergood
North Carolina State University
Raleigh, NC 27695-7918

INTRODUCTION

Fracture toughness values for short cracks are important in situations where small crack-size scales limit fabrication and performance. For precision grinding applications the fracture damage can be on the order of microns in size scale. A problem arises with many ceramic-based materials because the toughness is not constant, but instead increases with increasing crack size [1]. Standard procedures for fracture toughness testing of ceramics are based upon the production of a straight, through-section precrack in a test specimen. However, it is difficult, if not impossible, to produce straight precracks having crack lengths below about 1 mm. Therefore it is essential to develop new methods for characterizing fracture toughness at size scales relevant for precision grinding. Indentation methods using Vickers or Knoop hardness indenters have been used to generate short precracks for toughness testing. Indentation cracks as small as 20-50 μm can be produced for most ceramics and glasses. Two important aspects complicate the use of indentation cracks. First, the stress intensity factor due to the indentation plastic zone must be incorporated into the analysis. This requires the introduction of a residual-stress factor χ, which scales indentation load to the crack driving force. Second, the geometry of the indentation crack must be known. The method for short-crack toughness measurement adopted here involves the in situ measurement of indentation crack length during bend testing. The factor χ can be independently determined as part of the test procedure for the particular material of interest. Using critical depth concepts [2], predictions of grinding performance based on fracture toughness variations can be made. The short-crack toughness is a basis for selecting and optimizing ceramic-based materials for precision grinding.

BACKGROUND-FRACTURE MECHANICS

The stress intensity factor K acting on an indentation crack subjected to an applied stress σ_a is given by

$$K(c) = \psi \sigma_a c^{1/2} + \frac{\chi P}{c^{3/2}} \qquad (1)$$

where ψ is a shape factor for a surface crack, c is crack length, and χ scales the strength of the indentation residual-stress field to the indentation load P. Stable crack growth occurs prior to failure because of the $c^{-3/2}$ dependence of the residual-stress driving force [3]. For conditions of

mechanical equilibrium, K(c) equals the fracture toughness T(c), and Eq. (1) can be rearranged to give

$$\sigma_a c^2 = \frac{T(c)}{\psi} c^{3/2} - \frac{\chi P}{\psi} \qquad (2).$$

For the case of constant toughness, a plot of $\sigma_a c^2$ vs. $c^{3/2}$ allows determination of T and χ independently from the least-squares slope and intercept, provided ψ is known. Alternatively, if the material exhibits an increase in fracture toughness with crack length (T-curve behavior), the plot of $\sigma_a c^2$ vs. $c^{3/2}$ will show some curvature, in which case nonlinear fitting of the data is required to obtain the T-curve.

EXPERIMENTAL PROCEDURE

Disks of Canasite* (a glass-ceramic) nominally 25 mm in diameter and 2 mm thickness were indented in their centers using Vickers indentation loads between 10 and 200 N and dwell time of 10 s. A drop of silicone oil was placed on the prospective indentation site to minimize environmental effects during indentation. Indented disks were stressed in biaxial flexure by a ring-on-three-ball loading fixture mounted on an inverted microscope [4]. All in situ tests were carried out in a dry nitrogen environment. Three separate runs were made for each indentation load.

RESULTS AND DISCUSSION

Figure 1 shows a typical plot of $\sigma_a c^2$ vs. $c^{3/2}$ with the upward curvature indicative of T-curve behavior. The functional form of the T-curve is not known a priori, however a general representation of the T-curve can be given by

$$T(c) = a_1 + a_2 c + a_3 c^2 + \ldots + a_n c^{n-1} \qquad (3).$$

Eq. (2) then becomes

$$\sigma_a c^2 = \frac{1}{\psi}\left(a_0 + a_1 c^{3/2} + a_2 c^{5/2} + \ldots + a_n c^{n+1/2}\right) \qquad (4)$$

where $a_0 = -\chi P$. $\psi = 1.29$ for half-penny median/radial cracks was used. A first order determination of the T-curve was obtained by using the first two terms of Eq. (3) and fitting the $\sigma_a c^2$ vs. $c^{3/2}$ plots via Eq. (4) using the general method of least squares to obtain a_0, a_1, and a_2. Use of more than two terms in the expansion resulted in values of the coefficients which lacked

* Provided by Gordon Shafer, Jr., Corning, Inc.

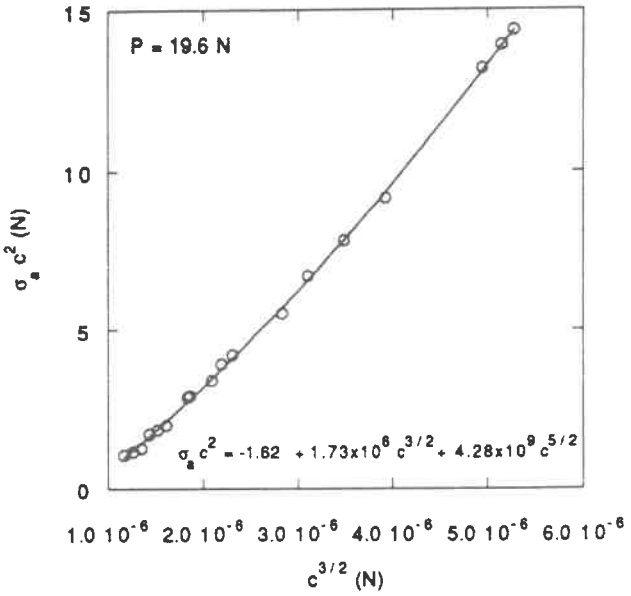

Figure 1: In situ results for Canasite.

physical significance. This was due in part to limitations in the curve-fitting routine. An important advantage of the in situ technique is that the residual-stress factor χ is determined independently from the T-curve. Figure 2 shows the variation of χ with indentation load. There was no systematic trend in χ with indentation load, the average value over all indentation loads being 0.11. Figure 3 shows plots of fracture toughness versus crack length for each indentation load calculated from the average values of a_1, and a_2. The T-curve rises from about 2.5 MPa$\sqrt{m}$ ($c \sim 70$ μm) to about 5.5 MPa$\sqrt{m}$ ($c \sim 900$ μm).

The strong T-curve behavior exhibited by Canasite has important implications for its grinding performance. The critical depth of cut characterizing the brittle to ductile transition is proportional to the square of the ratio of toughness to hardness. The short-crack toughness relevant to precision grinding is significantly lower than the long-crack toughness, thus grindability predictions must be based on the short-crack value. Work in progress is aimed at extending these tests to other ceramics and correlating the results with grinding tests.

REFERENCES

1. R. F. Cook, B. R. Lawn and C. J. Fairbanks, J. Am. Ceram. Soc., **68** [11], 604 (1985).
2. T. G. Bifano, T. A. Dow and R. O. Scattergood, Proc. SPIE, **966**, 108 (1988).
3. P. Chantikul, G. R. Antis, B. R. Lawn, D. B. Marshall, J. Am. Ceram. Soc., **64** [9], 539 (1981).
4. S. M. Smith and R. O. Scattergood, J. Am. Ceram. Soc., **75** [2], 305 (1992).

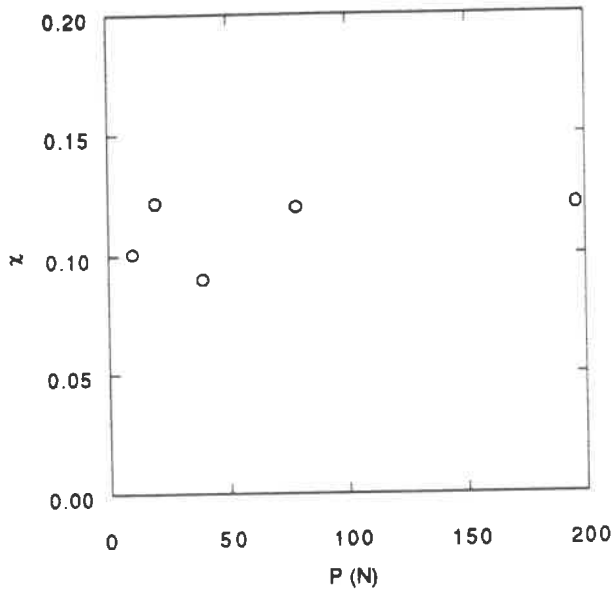

Figure 2: Variation of χ with indentation load.

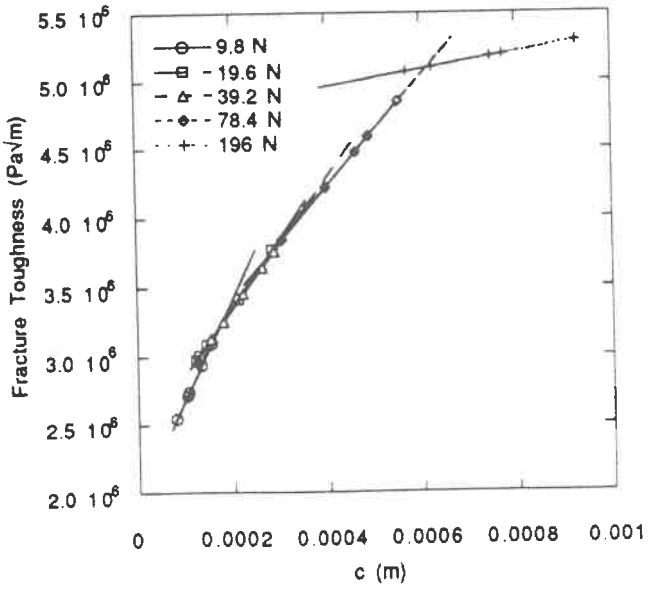

Figure 3: Variation of fracture toughness with crack length for the indicated indentation loads.

Toward an Eclectic Model of Brittle Materials' Machining

J G Duduch[a,b] and A E Gee[a]

[a] School of Industrial and Manufacturing Science
Cranfield Institute of Technology,
Cranfield, Bedford, MK43 0AL, UK
[b] On leave from Dept Engenharia Mecanica,
Univ Sao Paulo, Sao Carlos, SP, 13560, Brazil

1 Introduction: History and Origins

To increase the range of manufacturing materials, the requirement to deterministically machine brittle materials is now well-established. Because of critical sub-micrometre depth requirements (for low surface damage), machining processes are perforce of high precision.

Research into the deterministic machining of brittle materials has yielded results which conform with observations of other modes of material deformation and/or removal[1]. An overall model embracing the range of such observations offers a route to understanding by providing models in one mode which may serve to explain phenomena in another.

2 Contributing Processes

Retained-abrasive wheel-grinding is of considerable interest but intrinsic difficulties of access arise for in-process experimental observation or study of the effects of individual grits, (as is the case for free-abrasive optical lap-grinding and polishing). It is possible, however, to examine the actions of individual grits preset respectively by position and load in single point turning[2,3] and ruling[4].

These four fundamental machining conditions form a 2x2 matrix[4] with variables of tool singularity/multiplicity and tool setting/loading. Although not a machining process, microindentation may be added to yield five potential areas for model-study.

3 Microindentation

At low indenter loads and depths (gram/micrometre order), plastic pile-up without cracking is observed around microindentation in glasses[5] and other brittle materials. Above critical loads/depths, median radial vents open up and lateral cracking occurs of multimicrometre scale[6].

4 Ruling

Twyman[7] observed a "... continuous thread of glass shaved away from the polished surface by a lightly-loaded diamond in the ruling of a fine line..." and shows an interferogram of a smooth groove in glass. It is known that ruling in glass has been employed as an initial process in producing grazing-incidence X-ray gratings.

It transpires that ruling is able to provide controllable experimental conditions for multiple (parallel) observations of the transition between brittle and ductile conditions. With a small increase in loading, smooth, plastically-formed grooves of 1um section, can be shown to lead to brittle

chipping of perhaps 10-20um depth in the same machine-stroke, with little observable gradation between plastic and brittle conditions[3,8].

5 Single Point Machining

Puttick et al[2] showed that, machining at speeds of less than about $0.01ms^{-1}$, a single point diamond tool held with large magnitude negative rake-angle at sub-micrometre depths, generated grooving with little sign of chips or debris. At higher speeds ($>0.1ms^{-1}$), shearing and residual stress gave rise to 'trailing wake' long chip-formation. With depth reduction (to 150nm) classical (front-face) cutting with near-zero tool-rake has recently been demonstrated[8,9].

6 Free Abrasive Grinding and Polishing

Lens surfaces have been manufactured using free-abrasive laps free to move in five degrees of freedom over the (spherical) surface being generated with the two held in contact by a preload. The process is intrinsically shape-convergent for 'nesting' surface forms with two areal degrees of freedom between workpiece and lap (ie flat, cylindrical and spherical) and so laps may be large. Used over seven centuries[7], the process provides post-process knowledge but, like wheel-grinding, does not lend itself to in-process experimental observation of grit conditions or actions. The degree of skill required is perhaps indicative of the empirical nature of the understanding. (This, together with requirements for other surface forms and high volumes, is an incentive for alternative, more deterministic, processes).

Three sub-processes are involved:

(i) hard-lap rough-grinding for economic volume removal;
(ii) fine hard-lapping to reduce surface roughness;
(iii) soft (pitch) lap polishing.

As brittle processes, (i) and (ii) produce surfaces with roughness in the 1-10um+ ranges. Final polishing (iii) produces a specularly reflective surface with (perforce) sub-wavelength roughness amplitude (see Section 9). It follows that, during final polishing, no grit is impressed into the workpiece to greater than the critical plastic/ductile depth. Sub-micrometre polishing particles may be employed but, for reasons of speed and economy, larger sizes are used with pitch laps to produce polished finishes. From this it may be postulated that transition to ductile polishing is attributable not primarily to grit size but to the action of the soft lap. Examination of hard and soft lap actions is therefore appropriate.

To provide for a link between known actions of hard and soft lap free abrasive grinding/polishing processes and those of single-point/grit processes (microindentation, ruling and single-point machining), a postulate model of the action of individual grits under the laps is required; this is addressed in Sections 7 and 8.

7 Hard Lap Action: Commencement with Three-grit Model

When a hard lap brings to bear a preload upon a matching nesting glass workpiece surface via an interfacial layer of grit-particles, the lap/workpiece will kinematically come to bear first upon three of the proudest non-colinear grits; these will share the applied load and indent and brittle-crack the glass workpiece surface. Lateral working will cause these trapped grits to roll or scratch the surface, causing conchoidal pitting. Each grit

can rotate until, in a weak orientation, its component of the preload force causes it to break; the load is then redistributed among adjacent proud grits. Load-bearing grits may also locate into pits, allowing others to share the load.

These actions may be expected to continue until sufficient grits exist within a size range spread (of the order of the surface roughness - see section 9) to share the preload that no further individual grit suffers a breaking force. Thereafter, resultant larger grits may be expected to dominate abrasive effects. Increasing the load would be expected to require more grits in order to sustain it stably without breakage, thus reducing the size of the dominant grits and 'fining' the hard-lapping process (as occurs). Washing down and using smaller grits would be expected to cause preferential abrasion of surface peaks as force cannot be brought to bear on the bottom of a pit deeper than the largest grit diameter.

8 Soft Lap Action: Extension of the 3-point Single Particle Commencing Model

With a soft-lap bearing upon a (nesting-form) workpiece surface through polish particles, initial contact will be made through three proudest particles. These will be pushed, (unbroken), into the pitch of the soft lap (at rates which are functions of force, pitch-viscosity and grit area/shape), until a fourth particle comes into contact with both surfaces. The load will be redistributed to the four, reducing the force per particle and thence the sink-rate. This process of load sharing and sink-rate reduction will continue until very many particles are simultaneously being pushed into the pitch at a sink-rate deemed negligible within working time-scales. Subjected only to low forces, particles will indent the glass workpiece without cracking.

Lateral working of a sharp-pointed particle engaging with associated indentations can be expected to rotate it (analogously to a rack-and-pinion) until a face bounded by large internal angles is exposed to the workpiece with insufficient indentation-slope to generate the torque required to rotate the grit further (cf. teeth missing from rack and pinion). Invoking ruling/single-point machining sub-models, lateral working would be expected to cause plastic grooving, pile-up and shearing. It might also be expected to generate local frictional heating around a proud grit, thereby softening the pitch and promoting preferential sinking and rotation.

From the foregoing, a model of a pitch-lap may be postulated in which the peaks of a large number of particles come quickly to a uniformly proud layer protruding from the pitch, each grit offering a parallel face bounded by highly negatively-raked adjacent faces. In this condition a situation transpires very similar to that of the truncated diamond-grits exposed by electrolytic dressing[10] whose actions are also likely to be those observed with single-points[2,4].

9 Surface Roughness: Relationship to Forming Action

Ruling (Section 3) showed that, when single-point brittle fracture occurs, a pit of 10-20um scale is formed. In hard-lapping (Section 7), grits of up to this diameter could exist unloaded in pits; larger grits will protrude above the peaks and so be preferentially loaded. Large grit hard-lap free abrasive grinding can therefore be expected to generate this order of roughness (as it does[1]). A postulate-process explaining fining of hard-lapping is given in Section 7.

In respect of polishing, diffractive scatter effects require that roughnesses

are of the order of 10nm or less, some two orders of magnitude less than that resulting from brittle abrasion.

10 Conclusions

Microindentation results (Section 2) can be extrapolated to explain observations of plastic-action grooving of brittle materials obtained in single point ruling (Section 3) and turning (Section 4) experiments. From these it is possible in turn to postulate hard and soft lap action commencing with kinematic three-point first contact conditions. Consideration of the viscous, frictional and thermal effects on a grit partly-immersed in pitch provides a model for a highly autonomous self-organising mechanism capable of aligning multiple polish-grit particle faces to within a narrow range of protrusion heights. This corresponds with polishing requirements, to be able to plastically work a glass surface to the required two orders of magnitude lower surface roughness than that obtainable with the hard-lap.

From the foregoing it might be inferred that deterministic machining will ideally require geometrical control to a similar order of magnitude.

11 References

1 Brown N J "Lapping, Polishing and Shear Mode Grinding" J Japan Soc Prec Eng, 1990, **56**(5), 800-805

2 Puttick K E, Rudman M R, Smith K J, Franks A and Lindsey K "Single-point Diamond Machining of Glasses" Proc Roy Soc Lond A, 1989, **426**, 19-30.

3 Gee A E, Spragg R C, Puttick K E & Rudman M R "Single-point diamond form finishing of glasses and other macroscopically brittle materials" Proc SPIE, 1991, **1573**, 39-48 [SIRA Conf 'Commercial Applications of Precision Manufacturing at the Sub-micron Level', London, Nov 1991].

4 Chao C-L & Gee A E "Investigation of Brittle/Ductile Transition in Single Point Machining of Glassy Materials Using a Ruling Engine" Proc IPES5/ASPE Conf., Monterey CA Sept 1989, pp259-263.

5 Taylor E W "A Hardness Table for Some Well-known Types of Optical Glass J Sci Instrum, 1949, **26**(9), 314-316.

6 Lawn B R and Wilshaw R, "Indentation Fracture: Principles and Applications" J Mat Sci, 1975, **10**, 1049-1081.

7 Twyman F *Prism and Lens-making* (2nd ed) Hilger, London 1952, (reprinted Adam Hilger, Bristol 1990); see pp9,51-52 & Fig 209b.

8 Chao C-L, PhD Thesis, Cranfield Inst Tech, 1991.

9 Chao C-L & Gee A E, "Material Removal Mechanisms Involved in the Single-point Diamond Turning of Brittle Materials" Proc ASPE Conf, Santa Fe, Oct 1991 pp 259-263.

10 Ohmori H, Takahashi I & Nakagawa T, "Mirror Surface Grinding by Metal Bonded Super-abrasive Wheel with Electrolytic In-process Dressing" in Seyfreid P, Kunzmann H, McKeown P & Weck M (eds) *Progress in Precision Engineering* (Proc IPES6/UME2 Conference, Braunschweig, Germany, 1991) Springer, Berlin, 1991, pp153-165.

12 Acknowledgements

The authors would like to thank Prof K E Puttick (University of Surrey) and Dr C-L Chao of Chung-Chen Institute of Technology, Tao-Yuan, Taiwan, ROC, (formerly of Cranfield Institute of Technology) for useful discussions.

One of us (JGD) is in receipt of a research studentship from the Government of Brazil.

Simulation of Diamond Turning of Silicon Surfaces

D. B. Boercker, J. Belak, I. F. Stowers, R. R. Donaldson, and W. J. Siekhaus

Lawrence Livermore National Laboratory, Livermore, CA 94550

The ability to machine precisely figured silicon surfaces is central to the successful construction of various sophisticated optics systems. Diamond turning is a well established technique for producing high-quality optical surfaces. Unfortunately, the tribochemical interactions between carbon and silicon present some serious difficulties. Recent experiments have been done to study both the nature of tool wear and of surface damage during the diamond turning of silicon surfaces. A round-nosed tool wears most at its shoulder and to a lesser extent at the tip, with relatively little wear in between. An important aspect of the surface damage is a transition from ductile behavior at the base of the cut to brittle fracture up the shoulder of the cut which occurs whenever the uncut chip thickness exceeds a critical value. By changes in the cutting conditions, such as feed rate and rake angle, the transition point can be moved up the shoulder to the point that fracturing does not penetrate below the base of the cut, leaving an undamaged finished surface.

In order to gain insight into the tribochemical mechanisms of importance to this process, we have performed molecular dynamics (MD) simulations of the machining of a silicon surface with a diamond tool. The basic MD method is the same as that used by Belak *et al.*[1] to simulate the orthogonal cutting of copper. These simulations are performed in the rest frame of the cutting tool and follow the detailed, microscopic motions of the atoms both in the tool and in the work piece as it moves under the tool. Such simulations give good qualitative descriptions of chip formation and dislocation propagation. In order to apply this same technique to the cutting of silicon requires an accurate model of the interatomic bonding and chemistry involved. To this end we have implemented the interatomic potentials for silicon and carbon proposed by Tersoff,[2] which include angular dependent forces that are very important in covalent materials. We have performed two types of simulations, each designed to look at a different aspect of the problem. One type is designed to look in detail at possible wear mechanisms for the tool, such as graphitization and carbide formation. The other simulates orthogonal cutting and focuses on chip formation and surface damage mechanisms.

In both types of the simulation, the silicon work piece is a large slab containing 20160 atoms oriented with the (001) face up. Most of the atoms in the work piece move freely

according to Newton's laws. A relatively few atoms near the upstream boundary and the lower boundary have additional constraint forces which maintain their temperature at about 300° K.[3] Finally, a constant velocity boundary condition is imposed on the lowest atoms in the slab. Atoms leaving the simulation cell at the "downstream" end are destroyed and new ones are periodically produced at the "upstream" boundary. Performing the calculation in the rest frame of the tool allows the simulation of cutting over lengths which are many times the computational cell dimension without having to follow the motion of a prohibitively large number of atoms.

FIG. 1. Wear of diamond asperities. The darker spheres represent two diamond asperities moving across a (001) silicon surface at 540 m/sec. Several silicon atoms have combined with carbon atoms to form SiC.

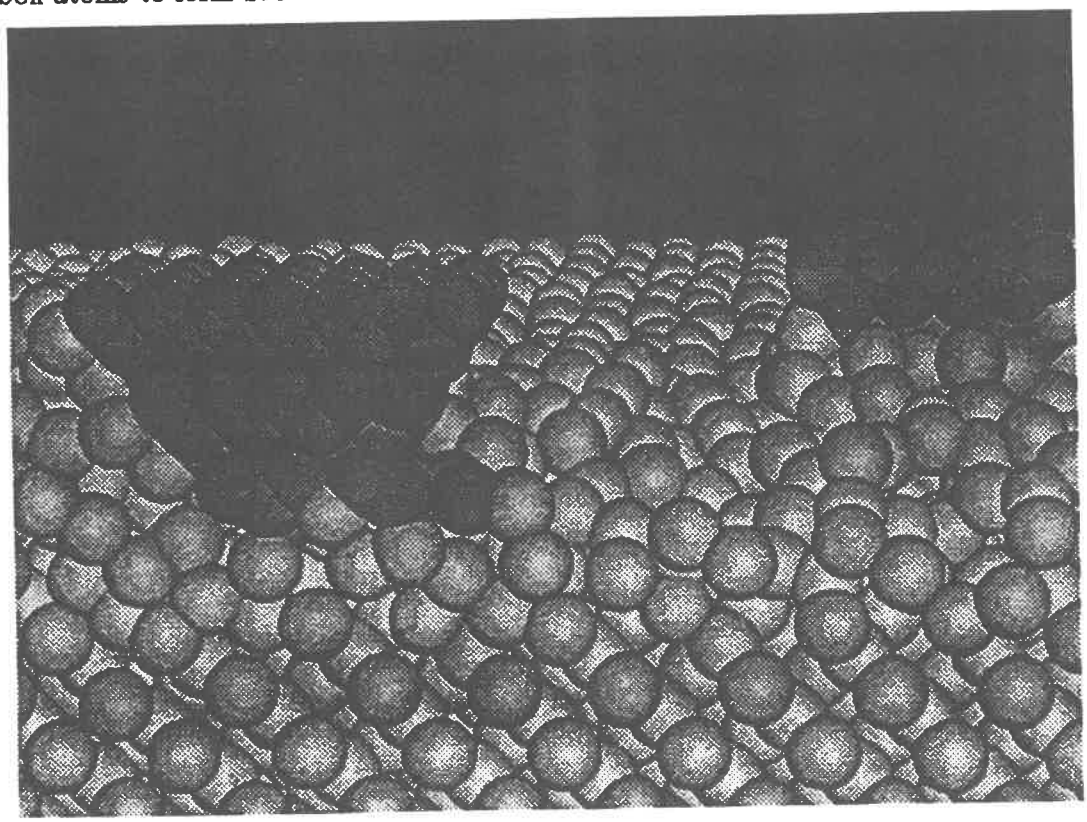

Tool wear is simulated by suspending two small carbon asperities from a flat diamond surface and observing their interaction with the silicon work piece. The asperities differ in size, but are both shaped as square pyramids with the four triangular faces being (111) surfaces. The square base of the larger pyramid contains 64(=8x8) atoms, while the base of the smaller one contains 36(=6x6) atoms. All of the atoms in both asperities are free to

move as Newton's equations dictate. The bases of the pyramids are (001) planes that are attached to the bottom (001) plane of a rectangular diamond slab that is 4 atomic layers thick. The atoms in the bottom two layers of the slab also move according to Newton's equations, but their temperature is controlled. The atoms in the top two layers are kept in a rigid lattice which initially moves downward at a constant velocity, but stops after the desired penetration is obtained. After that time these atoms are held fixed in space.

A three dimensional "snap shot" showing the two asperities with the upper slab removed for clarity is shown in figure 1. The smaller asperity is in the background and the larger one is in the foreground, with half its atoms stripped away to allow visibility below the surface. The silicon is moving from left to right in the figure at about 540 m/sec. While there is very little damage being done to the pyramids above the surface, it is clear that the atoms in the tip of the larger asperity have begun to break away and some are being replaced by silicons. Later in the simulation, a graphitic cluster of six carbon atoms appears at the surface on the downstream side of each asperity. No other damage, except for a build-up of silicon on the pyramid faces, was visible during the simulation time of about 10 picoseconds.

FIG. 2. Orthogonal cutting of silicon with a diamond wedge at a cutting speed of 540 m/sec. Silicon atoms are clinging to both faces of the diamond. The silicon in the chip and in about the first 5 layers below the cut surface is amorphous.

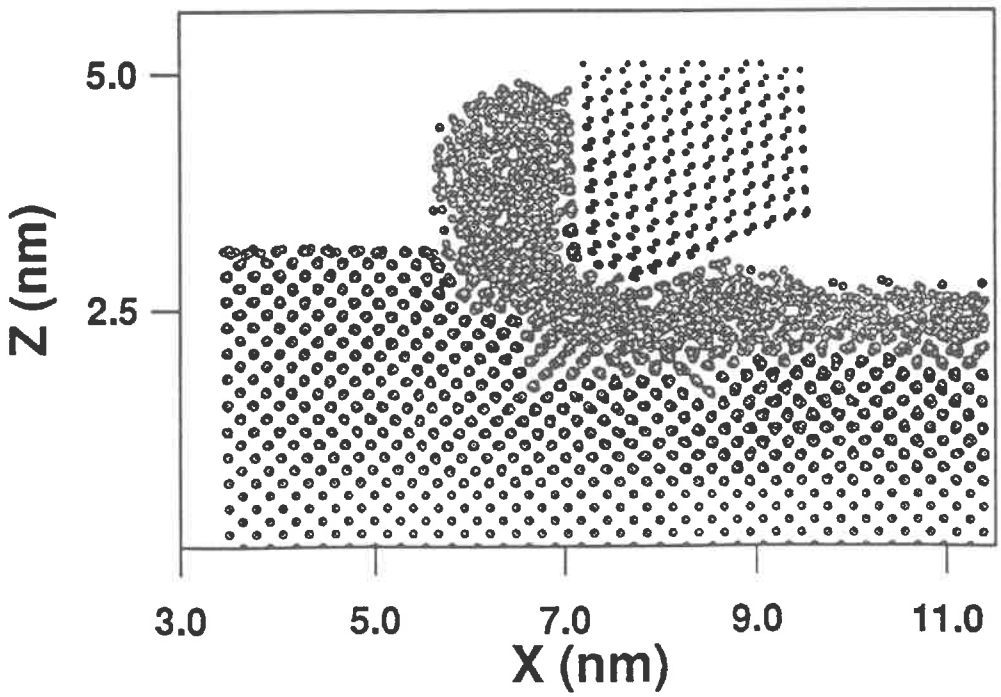

Orthogonal cutting of silicon by diamond is simulated by creating a wedge-shaped tool with a (111) cutting face, and imposing periodic boundary conditions in the direction parallel to the surface and normal to the cutting direction. As in the previous simulation, the lower atoms in the tool are free to move according to their force laws, while the uppermost atoms are held rigid. Atoms just below the rigid layers are maintained at room temperature. A two-dimensional projection of the cutting along the periodic direction is shown in figure 2. Once again the workpiece is moving at about 540 m/sec from left to right. The first thing to notice is that there appears to be very little damage done to the wedge as yet. In addition, there is a boundary layer of silicon clinging quite tightly to both the rake and clearance faces of the tool, so that most of the actual cutting is being done by this layer. Finally, the silicon atoms in the chip and in about the first 5 layers below the trailing surface of the workpiece appear to be amorphous and possibly even to have melted.

This work was performed under the auspices of the U. S. Department of Energy by Lawrence Livermore National Laboratory under Contract No. W-7405-Eng-48.

---

[1]J. Belak and I. F. Stowers, *A Molecular Dynamics Model of the Orthogonal Cutting Process*, Proc. of the 1990 Annual ASPE Meeting.

[2]J. Tersoff, *Modeling Solid-state Chemistry: Interatomic Potentials for Multicomponent Systems*, Phys. Rev. B **39**, 5566 (1989).

[3]W. G. Hoover, *Canonical Dynamics: Equilibrium Phase Space Distributions*, Phys. Rev. A **31**, 1695 (1985).

Effect of the Tool-Workpiece Interface on Energy Dissipation in Ultra-Precision Machining of Aluminum

D.A. Lucca, Y.W. Seo
Oklahoma State University
Stillwater, OK 74078

and

R.L. Rhorer
Los Alamos National Laboratory
Los Alamos, NM 87545

Introduction

Advances in both the efficiency of the ultra-precision machining process and the quality of the final workpiece are being limited by our incomplete understanding of the governing process physics. Of late, there have been increased efforts to extend this understanding. Our work has focused on the development of physical models of the mechanical energy dissipation and resulting temperatures when machining at depths of cut less than several micrometers. Our approach has been to attempt to accurately identify the regions of mechanical energy dissipation in the tool-chip-workpiece zone, and subsequently equate mechanical work to heat for a prediction of the temperatures which result. Initial work [1] indicated that in the orthogonal ultra-precision machining of copper, the total specific energy increased dramatically at small depths of cut, consistent with results reported for the micro-cutting of copper [2] and with the classical works on the "size effect" [3]. An overall energy balance indicated that at depths of cut below several micrometers, shearing in the shear zone and rake face friction are unable to account for the observed energies. For depths of cut below several micrometers, tool flank face rubbing due to workpiece material elastic recovery and plowing due to the tool edge radius take on increased roles as mechanisms of mechanical energy dissipation. A contribution towards quantifying these dissipative effects is presented here.

Experimental Study

In the present study, orthogonal flycutting of 6061-T6 aluminum was performed. A flat nose, single crystal diamond tool was rotated 76.2 mm off axis to provide the cutting motion, and a rectangular workpiece (1 mm wide, 15 mm long) was fixed atop a Kistler 9251A piezoelectric dynamometer which allows for the measure of the cutting and thrust forces. The workpiece was positioned with its length tangent to the tool motion, also 76.2 mm off axis. The rotating tool's constant infeed rate corresponded to the depth of cut. The magnitude of the off axis dimension compared to the length and width of the workpiece allowed for orthogonal "planing" of the workpiece to be achieved. A constant infeed assured a known depth of cut, independent of any elastic recovery of the material behind the tool edge. The procedure for collecting the cutting and thrust force data has been reported elsewhere [1, 4].

The single crystal diamond tool was characterized in two dimensions by SEM examination. The tool was coated with approximately 5 nm of AuPd and then examined. Since the tool was flat-nosed, it was positioned in the SEM with the line of sight along the cutting edge. Normal viewing could be assured by slightly tilting the tool such that both the rake and flank faces appeared as lines. The edge radius was measured before cutting and was estimated at 0.2 μm.

Results and Discussion

Observed Force Behavior

The magnitudes of the cutting and thrust forces were obtained from the average heights in the cyclic force signals over a range of depths of cut from 0.01 to 20 μm. The results are shown in Figs. 1-3. In Fig. 1, cutting and thrust forces are shown as a function of depth of cut for two specimens. The curves show the same trends as for the ultra-precision machining of copper [1, 2, 4], viz, a linear decrease in both cutting and thrust force down to 1-2 μm and a cross-over of the cutting and thrust force curves. Fig. 2 shows the direction of the resultant force vector calculated from the ratio of thrust to cutting force as a function of depth of cut. This result is calculated using the average of the two specimens in Fig. 1. A severe rotation of the resultant force vector downward towards the workpiece as depth of cut decreases is observed. The thrust force becomes the dominant force component for depths of cut below 0.1 μm. Here the force system resembles that of sliding indentation. The cutting/thrust force cross-over may be viewed as the point at which the process transitions from a cutting dominant to sliding/plowing dominant process. Fig. 3 shows the total specific energy calculated from the cutting force. The overall trend of increasing specific energy with decreasing depth of cut is consistent with the results of Furukawa [5] for aluminum. This trend is consistent with previous studies on copper [1, 4]. Recent work [6] indicates that asynchronous spindle motion may call into question results for depths of cut below 30 nm, however the repeatability of results in this range was seen to be quite reasonable.

Effect of Edge Radius on Specific Energy

A series of force components were obtained using a new tool which was characterized as having a 0.2 μm edge radius. After machining a few kilometers in cutting distance, another series of cuts was performed. The results of the specific energies based on the measured cutting forces are shown in Fig. 4. At depths of cut above 0.4 μm, both results show the same trend. However, below 0.4 μm, the specific energy resulting from the worn tool increased considerably. This shift in energy dissipated may be due to a change in the tool edge condition since other cutting conditions remained the same. Characterization of the tool edge after cutting could confirm this, however, accurate 3D tool edge characterization has been shown to be a formidable task.

Measurement of Contact Length

The flank face of the diamond tool was given a flash coating of AuPd of about 5 nm in thickness, and then cutting at a prescribed depth was performed. Cutting and thrust forces were measured and the tool flank face was examined under the SEM. The minimum distance from the tool edge to the no-coating/coating interface was taken as the contact length. Five experiments were performed at each of three depths of cut, viz, 0.01, 0.1 and 1 μm. The measured contact length and thrust force at each depth of cut are shown in Fig. 5. The contact length is seen to decrease with decreasing thrust force and depth of cut, and also follows the general trend of thrust force. The results indicate that at a depth of cut of 1 μm, the apparent contact length is on the order of the depth of cut, and at a depth of cut of 0.01 μm, the apparent contact length is two orders of magnitude greater than the depth of cut. Whereas the measured length of the worn-off coating can be viewed as an upper bound for the contact length, calculating a length based on the measured thrust force, and assuming an interface pressure equal to 3 times the uniaxial yield strength could be considered a lower bound. At a depth of cut of 0.01 μm, using a measured bulk yield strength of 36.3 kg/mm^2 for aluminum, this estimate would indicate an apparent contact length of 0.49 μm as compared to 1.03 μm which was inferred by the AuPd coating technique. The above reasoning would indicate that the contact length would still be between about 50 to 100 times the depth of cut at 0.01 μm. Here it is seen that the predicted contact stress based on the measured contact length ranged from 1.45 to 1.88 times the uniaxial yield strength of aluminum when the

apparent area is assumed equal to the actual area, which would suggest that the measured contact lengths lie in a reasonable range.

Elastodynamic Subsurface Stress Fields of the Workpiece

Due to the nature of the measured force system and the fact that the tool-workpiece contact may dominate the length scale at submicrometer depths of cut, the ultra-precision machining process may be idealized as a sliding indentation problem. For an estimate of the elastic-plastic boundary layer thickness, a model of a loaded rigid slider on an elastic semi-infinite body was used. The elastodynamic stress fields were obtained using a Fourier integral transform technique. Normalized von Mises equivalent stress contours with respect to the uniaxial yield strength of 6061-T6 aluminum machined at 0.1 μm depth of cut are shown in Fig. 6. The axial distance and depth from the surface are normalized with respect to the measured half contact length. At 0.1 μm depth of cut, the thickness of the elastic-plastic boundary is estimated to be about 0.9 μm, 9 times the depth of cut. At 0.01 and 1 μm depth of cut, the thickness was estimated at about 40 and 2 times of the depth of cut respectively. We are currently extending this elastic solution to the elasto-plastic case which will allow for a calculation of the energy dissipated in the workpiece subsurface due to the sliding at the tool-workpiece interface.

Conclusions

The dissipation of mechanical energy in the orthogonal flycutting of 6061-T6 aluminum was examined by measuring the cutting and thrust forces with depth of cut. The overall trend of the resultant forces with depth of cut was seen to be consistent with recently reported results on aluminum and copper. The observed value of minimum specific energy was also seen to agree well with results reported in the literature. At submicrometer depths of cut, the machining process may be viewed to transition from a cutting dominant to sliding/plowing dominant process. A change of tool edge condition due to wear during machining was observed to have a significant effect on energy dissipation. Contact length at the tool-workpiece interface was measured, and appears to be the dominant length scale at submicrometer depths of cut. The subsurface elastic-plastic boundary layer, based on the measured force components and the contact length, has been estimated. Extension of this model to the elasto-plastic case will allow for a calculation of the energy dissipated in the workpiece subsurface.

Acknowledgements

The authors gratefully acknowledge the kind support of this work by the National Science Foundation, Division of Design and Manufacturing Systems, the Oklahoma Center for the Advancement of Science and Technology, and the Department of Energy.

References

1. Lucca, D. A., Rhorer, R. L. and Komanduri, R., "Energy Dissipation in the Ultraprecision Machining of Copper", Annals of the CIRP, 40, 1, 1991, 69-72.
2. Moriwaki, T. and Okuda, K., "Machinability of Copper in Ultra-Precision Micro Diamond Cutting", Annals of the CIRP, 38, 1, 1989, 115-118.
3. Nakayama, K. and Tamura, K., "Size Effect in Metal-Cutting Force", Trans. ASME, J. Eng. Ind., 1968, 119-126.
4. Lucca, D. A., Seo, Y. W. and Rhorer, R. L., "Energies in the Ultra-Precision Machining of Ductile Materials", Proceedings of the 1992 NSF Design and Manufacturing Systems Conference, Georgia Institute of Technology, Atlanta, Georgia, Jan. 8-10, 1992, 123-129.
5. Furukawa, Y. and Moronuki, N., "Effect of Material Properties on Ultra Precise Cutting Processes", Annals of the CIRP, 37, 1, 1988.
6. Lucca, D. A. and Rhorer, R. L., "Unpublished data", 1992.

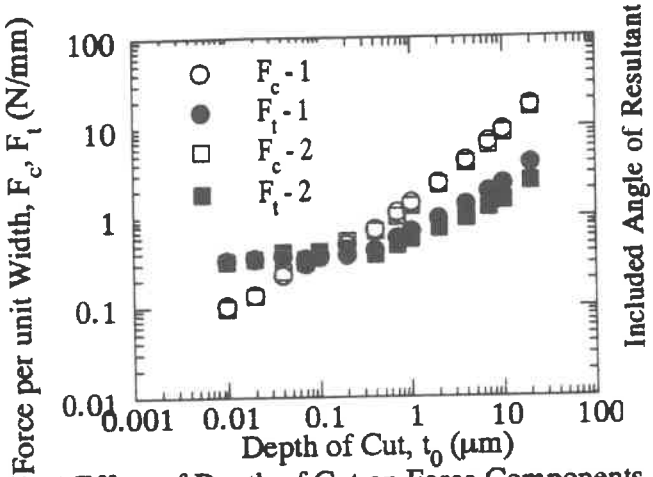

Fig.1 Effect of Depth of Cut on Force Components in Orthogonal Flycutting of Al 6061-T6

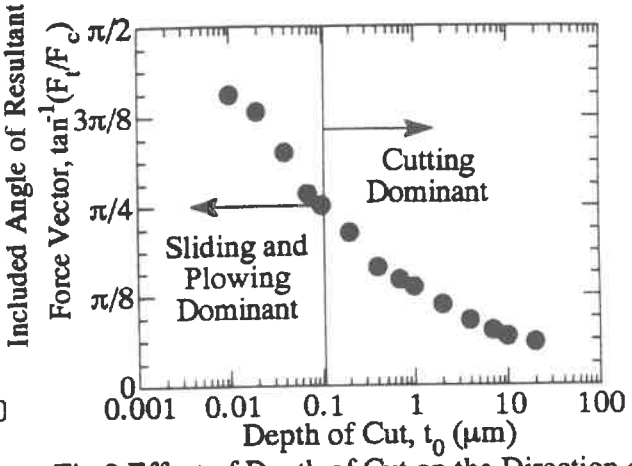

Fig.2 Effect of Depth of Cut on the Direction of Resultant Force in Orthogonal Flycutting of Al 6061-T6

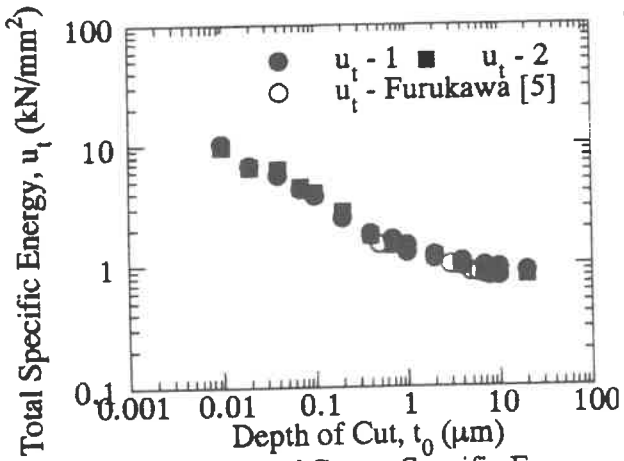

Fig.3 Effect of Depth of Cut on Specific Energy in Orthogonal Flycutting of Al 6061-T6

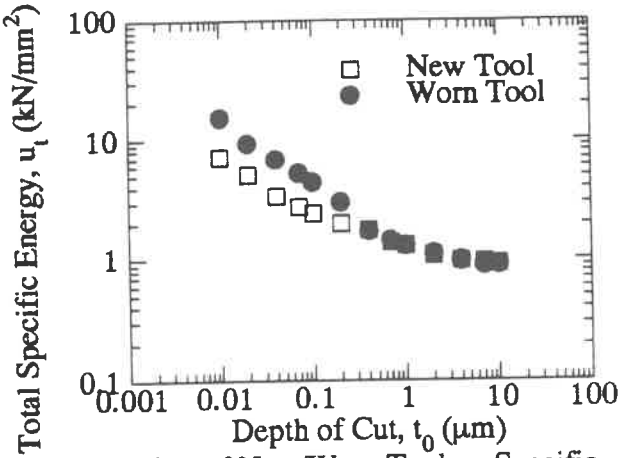

Fig.4 Effect of New/Worn Tool on Specific Energy in Machining of Al 6061-T6

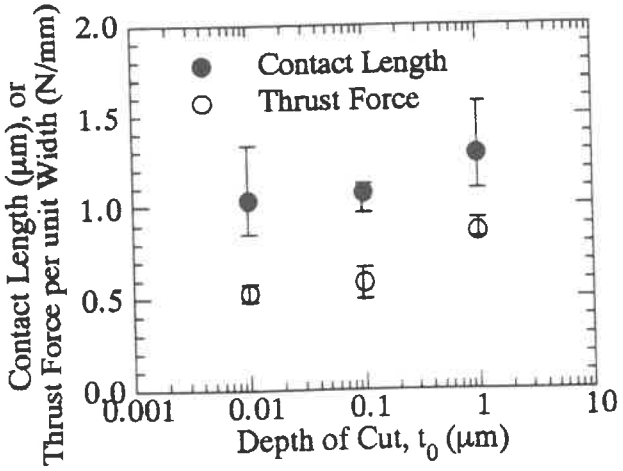

Fig.5 Measured Contact Length and Thrust Force in Orthogonal Flycutting of Al 6061-T6

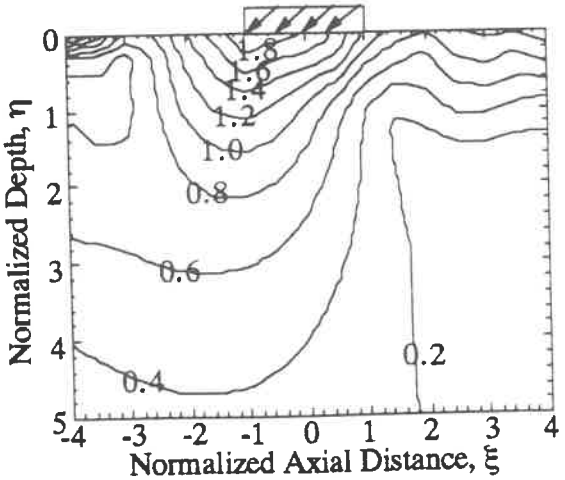

Fig.6 Normalized von Mises Equivalent Stress with respect to Uniaxial Yield Strength in Machining of Al 6061-T6 at 0.1 μm

DIAMOND TOOL WEAR DURING THE SINGLE POINT DIAMOND TURNING OF COPPER

W. C. Larson, J. D. Drescher,
J. S. Strenkowski, and Thomas A. Dow
Precision Engineering Center
North Carolina State University
Raleigh, NC 27695-7918

INTRODUCTION

Changes in the geometry of a diamond tool during machining can have a significant impact on the figure and finish of machined surfaces. If the mechanisms causing wear of single point diamond tools during precision machining can be identified, cutting conditions can be chosen to minimize wear, extend tool life, and improve surface finish.

EXPERIMENTAL MEASUREMENTS OF TOOL WEAR

Experiments with worn diamond tools have been carried out in which changes along the cutting edge and clearance face have been measured. A straight edge tool with a 0° rake angle and a 6° clearance angle was used to plunge cut a plated copper workpiece to a depth of 1 μm. The width of the cut was 1 mm. The wear was determined by directly measuring the wear land and indirectly determining the tool edge radius from measured tool forces. Wear land length, tool edge radius, rake angle, and clearance angle allow computation of tool geometry, which can then be used to compute the wear volume. Table 1 summarizes the changes in the tool geometry as a function of the cutting distance in copper. The change in tool geometry is shown schematically in Figure 1.

Distance (Km)	Edge Radius (μm)	Wear Land Length (μm)
1	0.1	0.9
2	0.18	1.2
4	0.59	1.8
7	0.84	2.65
10	0.95	3.3

Table 1: Tool Geometry Variation

The volume worn away can be converted to wear rate $\dot{W}$ by:

$$\dot{W} = AwV/d \qquad (1)$$

where A is the measured wear area, w is the width of cut, V is cutting velocity, and d is the distance cut between measurements. Using equation (1) and a 10 m /s cutting speed and a cutting width of 1 mm, Table 2 summarizes the wear rates for various elapsed distances.

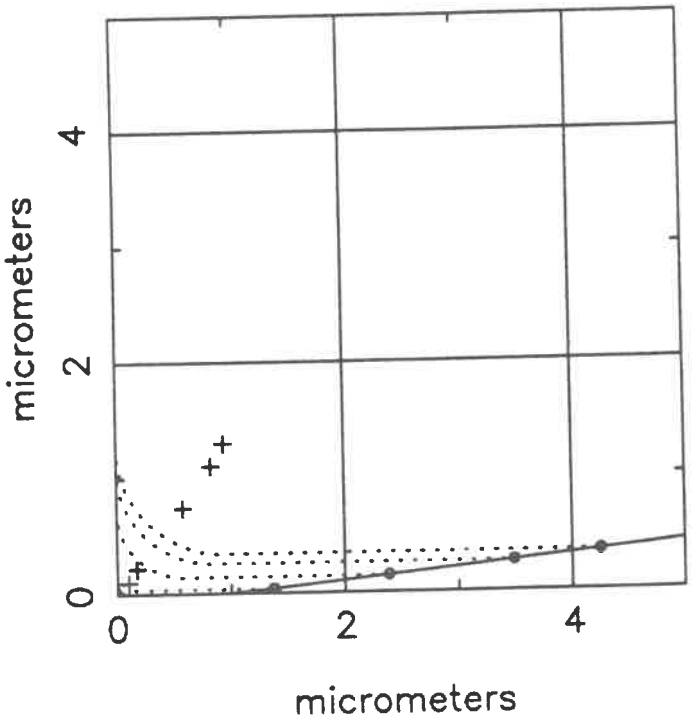

Figure 1: Tool Geometry

Case	Elapsed Distance (Km)	Total Area (μm^2)	Wear Rate (10^{-12} mm^3 / s)	Normalized Wear Rate (10^{-9} mm^2 /s)
1 Km - 2 Km	1	0.0536	536	450
2 Km - 4 Km	2	0.315	1580	837
4 Km - 7 Km	3	0.698	2330	791
7 Km - 10 Km	3	0.964	3120	830

Table 2: Tool Wear Rates

The last column of Table 2 shows the wear rate divided by the average wear land length. Note that the relatively constant normalized wear rate implies a wear process that is dependent on the area of contact.

WEAR MECHANISMS

The experimental measurements have been compared with a theoretical model which includes abrasive and chemical effects. The model includes a thermo-viscoplastic finite element model to predict the forces and the resulting temperature distribution in the chip, workpiece, and tool for a copper workpiece. The temperature obtained from the finite element model is consistent with previous experimental work. The abrasive wear rate is estimated by using measured tool forces, predicted wear land length, and published wear coefficients for diamond sliding on copper. The chemical wear mechanism proposed is that of solid state diffusion of carbon atoms into the workpiece material.

Abrasive wear. The high speed flow of workpiece material across the flank is an ideal condition for abrasive wear. Abrasive wear is governed by Archard's wear law :

$$W = K_1 \, P \, S \tag{2}$$

where W is the wear, P is the load, S is the sliding distance and K_1 is the wear per unit load per unit sliding distance or coefficient of wear. This equation can be used to find the wear rates by replacing the sliding distance S by the relative sliding velocity. Using values for K_1 determined by Crompton, Hirst, and Howse[1] and measured thrust force, abrasive wear rates of 6.02 to 17. x 10^{-12} mm^3 / s are predicted by equation (2). The range of values of K_1 are due to the uncertainty in the crystal orientation of the diamond tool. Note that these computed wear rates are more than an order of magnitude lower than the measured wear rates.

Chemical Wear. Solid state diffusion of carbon atoms from the diamond tool to the workpiece is governed by Fick's First law, which includes a diffusion coefficient with an exponential dependence on temperature. This type of temperature dependence allows wide variations in wear rate (a 6° C change in temperature doubles the wear rate). By further assuming that the carbon concentration gradient can be estimated by setting the separation between the tool and the workpiece to be equal to the atomic lattice parameter and by setting the concentration of carbon atoms in the tool to zero, the temperature (T_{req}) necessary to account for the observed wear can be calculated:

$$T_{req} = \frac{\frac{-\Delta E_D}{R}}{\log\left(\frac{d_{wear}\, l_{dia}}{t_{mach}}\right) - \log D_o} \qquad (3)$$

where D_o is the frequency factor, ΔE_D is the activation energy, l_{dia} is the lattice parameter of diamond, d_{wear} is the depth of wear damage, t_{mach} is the machining time, and R is the universal gas constant. Equation (3) can be applied to the wear experiment by setting R = 1.98 cal / mole K, t_{mach} = 900 sec, and l_{dia} = 0.35 nm. Note that the values for the interstitial diffusion of carbon atoms into copper as given by Bergner[2] are D_o = 74. x 10^{-6} m^2 / s and ΔE_D = 37.9 kcal / mole. The solution to equation (3) predicts a required temperature of 290 ^{0}C along the flank face of the tool to account for the observed wear from 1 to 10 Km.

DISCUSSION

Only a small percentage of the measured wear is due to abrasion. The bulk of the wear must be accounted for by another mechanism. Thermal degradation of the tool can also be eliminated as a possible wear mechanism due to the high temperatures required to initiate oxidation or graphitization of the tool (500 ^{o}C)[3]. A chemical wear mechanism that requires much lower temperature to cause significant wear is solid state diffusion. While the temperature predicted by the wear model is higher than that measured by Iwata[4], his measurements only gave the average interface temperature. Temperature profiles predicted by a finite element cutting model confirm that temperatures high enough to cause significant diffusion wear are possible. Therefore, solid-state diffusion of carbon from the diamond tool seems to be a plausible mechanism for flank face wear.

REFERENCES

1. Crompton, D., W. Hirst, and M.G.W. Howse, *The Wear of Diamond*. Proc. R. Soc. Lond. A., 1973. **333**: p. 435-454.

2. Bergner, D., *Diffusion of Heavy Interstitials in Metals*. Metallurgia I Odlewnictwo, 1986. **12(4)**: p. 379-400.

3. Wilks, J. and E. Wilks, *Properties and Applications of Diamond*. 1991, Oxford: Butterworth-Heinemann Ltd.

4. Iwata, K., T. Moriwaki, and K. Okuda, *A Study of Cutting Temperature in Ultra-High Precision Diamond Cutting of Copper*. 15TH North American Manufacturing Research Conference Proceedings, 1987 SME Manufacturing Technology Review, 1987. **2**: p. 510-515.

CRYOGENIC DIAMOND TURNING: THEORY AND EXPERIMENT

Chris J. Evans[1], Ralph L. Lundin[2], Edwin S. Paul[3], Robert S. Polvani[1], Delbert D. Stewart[2], and Eric Whitenton[1]

Single point diamond turning is a mature technology applied to a wide range of products. Very rapid tool wear, however, renders the process inapplicable to a number of materials, notably ferrous metals. Many authors have attributed this rapid wear to chemical processes, although there has been little agreement in the literature about the exact nature of the chemical interactions.

The rate of chemical reactions increases exponentially with temperature. Thus, a reduction of tool tip temperature should result in reduced wear rates. We have constructed diamond turning and fly-cutting systems in which both tool and workpiece may be chilled using enclosed flows of liquid nitrogen. There are considerable experimental difficulties associated with measurement of the actual cutting temperature (ie the temperature at the diamond-work interface), T_i. We assume, however, that:

$$T_i = T_b + T_f$$

where T_b is the bulk temperature and T_f is a "flash" temperature, or local temperature rise related to the local shear, sliding friction etc. The aim of the cryogenic systems we have developed is to reduce T_i by reducing T_b for both tool and work. We recognize that T_f may be affected by the temperature dependent changes in workpiece material properties and by changes in the cutting mechanics. An overall reduction in T_i, however, should produce a reduction in the chemical components of diamond tool wear.

Experimental

All the experimental work to date has been performed on diamond turning machines built on Moore #3 Measuring Machine bases. The first cryogenic system, built at Los Alamos National Laboratory, was fitted on a machine with a double-

[1] National Institute of Standards and Technology, Gaithersburg, Md 20899

[2] Los Alamos National Laboratory, Los Alamos, NM 87544

[3] Stockton State College, Pomona, NJ 08240

hemisphere porous graphite air-bearing with an integral AC motor. This system was designed solely for on-center turning.

The system for cooling the part is based around a reservoir mounted on the spindle face plate. The part is mounted to this reservoir which is attached to a relatively large bore pipe which rotates with the spindle. Liquid nitrogen is pumped along a stationary small bore pipe which passes down the axis of the spindle; the liquid nitrogen strikes the front face of the reservoir and is flung out centrifugally, filling the reservoir. Boil-off returns along the annulus between stationary and rotating pipes, to be exhausted at the rear of the spindle. Flow rate is adjusted, either manually or using a control loop based on a thermocouple sensing exhaust temperature, to minimize liquid phase in the exhaust. The tool is cooled by conduction along the shank from a liquid nitrogen reservoir.

The second system, built at NIST, is designed to allow both on-center turning and flycutting experiments. In this case the machine uses a belt-driven Blockhead 10B air bearing spindle which can be configured with a mercury-wetted slip ring system to allow measurements of local temperature. Typical operating temperature of tool and work-piece in both systems is approximately 120K.

These measured temperatures are in reasonable agreement with simple thermal models of the system. The models show, however, the ultimate temperatures reached on both tool and work-piece are dominated by (a) contact resistance at mechanical joints; and (b) air-side convective heat transfer.

Contact resistance in mounting the part to the spindle reservoir has been addressed two ways. The first approach is to minimize resistance by maximizing contact area. In this case the front surface of the reservoir was been copper plated and then diamond turned in situ; the back of the part is lapped. The alternative approach is to use gallium soldering; as long as the reservoir and part are of similar materials (eg both 400 series stainless steel or both 300 series stainless), this works well.

Even in the very low humidity environment at Los Alamos, the operating temperatures cause a rapid build up of a fine grained ice layer on the work. This layer we believe is a good insulator, helping to reduce convective heat transfer. However, it makes it difficult to locate the part surface by traditional techniques, such as "visual" touch-off. In single point turning we have used both accelerometers and acoustic pick-ups of the form commonly used in jig grinding. In flycutting configurations we have used a piezo-electric dynamometer. Ice build-up may be eliminated by operating in a dry gaseous environment.

The work material for the bulk of the experiments to date has been 440V stainless steel, a powder metallurgy analog of 440C but with much finer carbides (typically

2-4 micrometers). This material was chosen primarily to reduce the affect of abrasive wear, chipping and fatigue.

Results

Preliminary results supported the original hypothesis. A number of 35 mm diameter samples were diamond turned at Los Alamos using a spindle speed of 780 rpm with a nominal depth of cut of 1.25 micrometers and a feed rate of 1 micrometer per revolution. Natural diamond tools with 0.5 mm diameter nose radius, 0° rake, 8° clearance were used. Surface finish of 25 nm Ra and flatness better than 700 nm P-V were achieved. Surface finish was dominated by two features; a waviness associated with the servo performance and interactions between carbides in the workpiece and the tool. Very low tool wear was observed.

In a second series of experiments using larger depths of cut (5 micrometers), tool wear has been measured when diamond turning 440V stainless steel and 99.998% pure iron at room temperature and under cryogenic conditions. Reductions in tool wear are observed in both cases. Under cryogenic conditions, however, tool wear on the pure iron is higher than on the stainless steel while the reverse is true under normal (ambient) conditions. This observation tends to support the idea that there may be more than one wear mechanism taking place, and that the dominant mechanism is a sensitive function of conditions.

Two important mechanisms appear to be diffusion and catalyzed graphitization. Transitions between dominant mechanisms would provide a reasonable explanation for the experimental observations.

Discussion

Studies of coal gasification, diamond wettability, and diamond tool fabrication all offer clues to the chemical mechanisms in tool wear. A simplified model of the chemical tool wear process is based on the formation of either metal-carbon or metal-carbon-oxygen complexes. These complexes are unstable, and very short lived; the next reaction step may be:

* reversion to the diamond lattice;
* graphite formation;
* reaction with the environment (hydrocarbons,oxygen etc);
* diffusion of carbon into the metal; or
* carbide formation

Rate constants for each of these mechanisms may be written as an Arrhenius function:

$$k = A \cdot e^{(-E/RT)}$$

For any given system, higher temperature leads to higher wear. Note however, that a change in temperature may affect one mechanism more than another, changing the balance between them. Thus at cryogenic temperatures diffusion may dominate and the carbon content of the steel will reduce diffusion rates, giving lower wear than when machining pure iron. At higher temperatures, graphitization and/or reactions may be more important; the higher hardness of the steel should result in higher local temperatures and, hence, higher wear rates.

The first step in all these reaction mechanisms is the formation of the metal-carbon or metal-carbon-oxygen complex. Evidence from a number of sources indicates that metals that form complexes easily have unpaired d-shell electrons. Table 1 lists the number of unpaired d-shell electrons for a range of elements of interest.

Table 1: Number of unpaired d electrons in the ground state

0	1	2	3	4	5
Mg	U	Ti	V	Fe	Cr
Al	Pt	Ni	Co	Nb	Mn
Cu		Rh	Ru	W	Mo
Zn			Ta		Re
Ge			Ir		
Ag					
Pd					
In					
Sn					
Au					
Pb					
Be					
Si					
Pu					

The correlation between unpaired d electrons and "diamond turnability" is striking, although the exceptions grouped at the bottom of the table need further investigation. In the case of Pu, the explanation may be that the f-shell, which is energetically close to the d shell, is incomplete.

Influence of Machining Parameters to Residual Stresses Remaining in Diamond Cut Surfaces

Kenichiro HORIO, Toshio KASAI, Yoshiharu OGATA
Saitama University
255 Shimo-okubo, Urawa, Japan

1. Introduction

In ultraprecision cutting with a single crystal diamond tool, a problem of surface integrity has not drawn our attention so much. However the problem will not be bypassed when more severe specification is required to components and improved performance of the technique is needed [1].

One of the most important matter of the surface integrity is a damaged layer remaining just under the surface after machining. As it is supposed to be very thin because of small feed rate and small depth of cut, transmission electron microscope (TEM) is necessary to evaluate [2]. But it is so difficult and troublesome to make a specimen for the TEM inspection. Thus we noticed residual stresses remaining after the ultraprecision cutting.

In this paper the plate deformation method on face cutting is taken because the method can supply the information about the minute vertical distribution of residual stresses. And the effect of machining parameters or diamond tool cutting-edge radius to the residual stress have been investigated.

2. Measurement of residual stresses

2.1. Measuring procedure

Fig.1 shows a flow of residual stress measurement. The procedure consists of preparing workpiece without residual stress, diamond cutting, repetition of removal of damaged layer and curvature measurement, and calculation of residual stress distribution along normal direction

2.2. Equations for calculation

A equation required for the stress calculation is as follows. Though the equation is for x-direction, that for y-direction (perpendicular to x) is very similar. The equations were derived from consideration of anisotropic effect within workpiece and elastic effects caused by residual stress. The elastic deformations are bending and contraction or extension [3].

$$\sigma_{xr}(a) = \frac{E}{6(1-\nu^2)}\left\{(h-a)^2\frac{\mathrm{d}(1/\rho_x)}{\mathrm{d}a}+\nu\frac{\mathrm{d}(1/\rho_y)}{\mathrm{d}a}-4(h-a)(\frac{1}{\rho_x}+\nu\frac{1}{\rho_y})\right.$$
$$\left.-2\int_a^h(\frac{1}{\rho_x}+\nu\frac{1}{\rho_y})\mathrm{d}a\right\}-\frac{E(h-a)}{1-\nu^2}\cdot(\Delta\frac{1}{\rho_x}+\nu\cdot\Delta\frac{1}{\rho_y}) \quad (1)$$

where,

$$\frac{1}{\rho_x}=\frac{1}{\rho_x(a)}-\frac{1}{\rho_x(0)},\ \Delta\frac{1}{\rho_x}=\frac{1}{\rho_x(a_0)}-\frac{1}{\rho_x(0)},\ \frac{1}{\rho_x(a)}=\frac{8\delta_x(a)}{4\delta_x(a)^2+d^2+4\delta_x(a)(h-a)} \quad (2)$$

$\frac{1}{\rho_x(a)}$	:	curvature of workpiece after a etched	a	:	depth from surface
h	:	thickness of workpiece	d	:	diameter of workpiece
$\delta_x(a)$	:	deflection of the specimen	a_0	:	thickness of damaged layer
E	:	Young's modulus	ν	:	Poisson's ratio

2.3.Experimental conditions

Table 1 shows the machining conditions in experiment. Workpiece material was Al-Mg alloy for magnetic disks and fly cutting by a diamond tool with 5mm nose radius were executed. The new (just now polished) tool with sharp edge were prepared and cutting tests were repeated to make the tool worn. Thus evaluation of edge radius effect to residual stresses could be realized.

Fig.2 shows our definition of directions. The cutting direction is almost parallel to tool trace and the feeding direction is perpendicular to the cutting direction. The anisotropic effect can be evaluated by measuring along these directions.

Underlined factors in each column in Table 1 are standard experimental conditions. Influence of factor such as cutting speed, feed, depth of cut, coolant or edge sharpness of tool, to the residual stresses was evaluated.

3.Experimental results

3.1.Anisotropic effect

Fig.3 shows the measuring result of the specimen's curvature along each direction during repetition of etching after ultraprecision cutting with dull (worn) tool. Moreover Fig.4 shows the residual stress distribution calculated from the data of Fig.3 and those in the case of fresh (sharp) tool. In almost all cases the stress was compression. Etching was done by phosphorus acid mixed with acetic acid and nitric acid.

In Fig.3 and Fig.4 there are slight difference between the two directions. The residual stress along the cutting direction is rather higher than that along the feeding direction.

3.2.Effect of machining factors

(1) Cutting edge radius

Fig.4 also shows the comparison of residual stress distribution between sharp tool and dull tool. Edge radius of the sharp tool was almost 50nm by means of the SEM having two detectors [4] and that of the worn tool was almost 350nm. Although in the magnitude of surface roughness there is not any significant difference between them, the depth of existing residual stress layer is different so much. In the case of sharp tool, it is found that the damaged layer is very thin.

(2) Feed

In machining with sharp tool, feed affects the existing depth of residual stress (Fig.5). Small feed generates deep residual stress. On the other hand, in machining with dull tool, the feed does not affect the residual stress at all.

(3) Cutting speed

In machining with sharp tool, cutting speed slightly affects magnitude of residual stress along cutting direction. High cutting speed generates large stress. There is also not any change in residual stress distribution in machining with dull tool.

(4) Depth of cut

Even in machining with sharp tool or dull tool, there is not any influence of the depth of cut to residual stress at all.

(5)Coolant

In machining with sharp tool and without coolant, totally different phenomena occurs. As in Fig.6, the stress along cutting direction is tension just under the surface, decreases with depth and changes compression at a certain amount of depth. Moreover maximum of the stress along feeding direction, which maintains compression, is not at the surface like others but at a certain amount below. It is interesting that in machining with dull tool (Fig.7) there is not any difference so much between with and without the coolant.

4.Conclusion

The residual stress distribution at ultraprecision cut surface can be derived by the deformation method. The magnitude of the stress along the cutting direction is bigger than that along the feeding direction. The cutting edge radius of diamond tool is very sensitive to the residual stress distribution. Some machining parameters affect the residual stress distribution.

References

(1) Ikawa,N., Donaldson,R.R., Komanduri,R., König,W., McKeown,P.A., Moriwaki,T., Stowers,I.F., 1991, Ultraprecision Metal Cutting - The Past, the Present and the Future, Annals of the CIRP, 40/2 :587-594

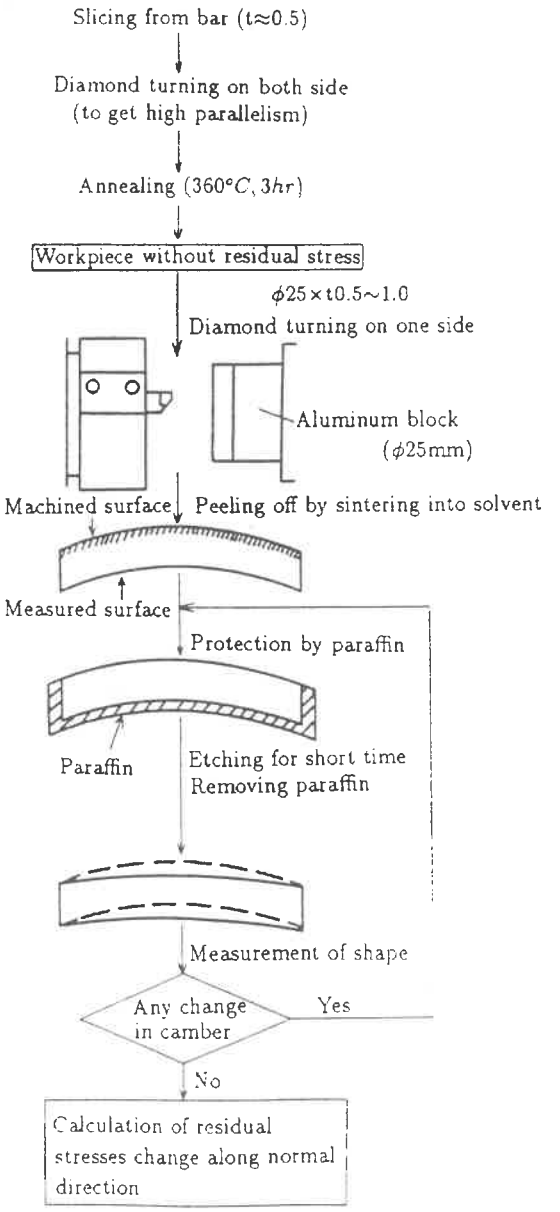

Fig.1 Measuring procedure

Table 1 Machining conditions

Workpiece	Al-Mg Alloy(φ25mm,t≈0.5mm)
Tool	Single crystal diamond tool
Nose radius	5mm
Cutting method	Fly cutting
Cutting speed	500,600,700mm/min
Feed	2,5,10μm/rev
Depth of cut	2,5,10μm
Coolant	Kerosene spraying,None

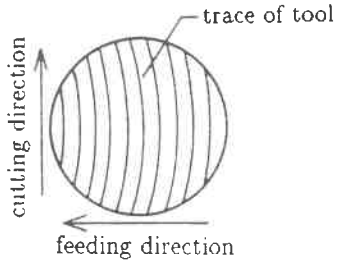

Fig.2 Definition of direction

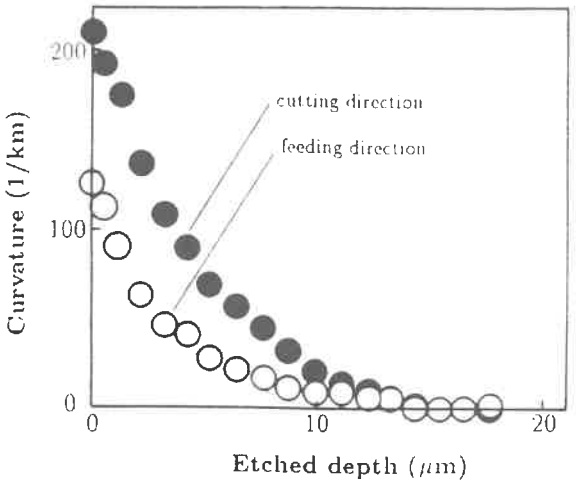

Fig.3 Relation between etched depth and curvature of workpiece (in case of machined with worn tool)

(2) Sugano,T., Takeuchi,K., Goto,T., Yoshida,Y., 1987, Diamond Turning of an Aluminum Alloy for Mirror, Annals of the CIRP, 36/1 :17-20

(3) Horio,K., Kasai,T., Ogata,Y., Kobayashi A., 1992, A Study on Damaged Layer Remaining In Diamond Mirror Cut Surface, Annals of the CIRP, 41/1 :137-140

(4) Asai,S., Taguchi,Y., Horio,K., Kasai,T., Kobayashi,A., 1990, Measuring the Very Small Cutting-Edge Radius for a Diamond Tool Using a New Kind of SEM Having Two Detectors, Annals of the CIRP, 39/1 :85-88

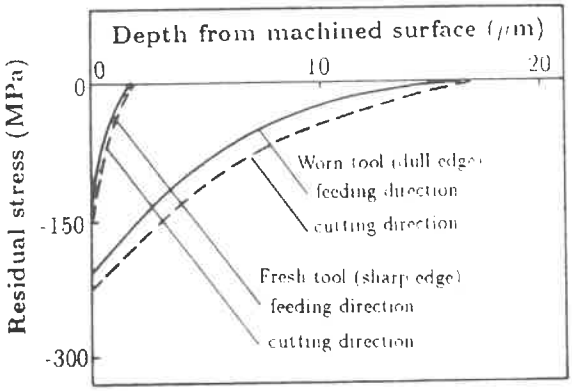

Fig.4 Residual stress distribution along normal direction

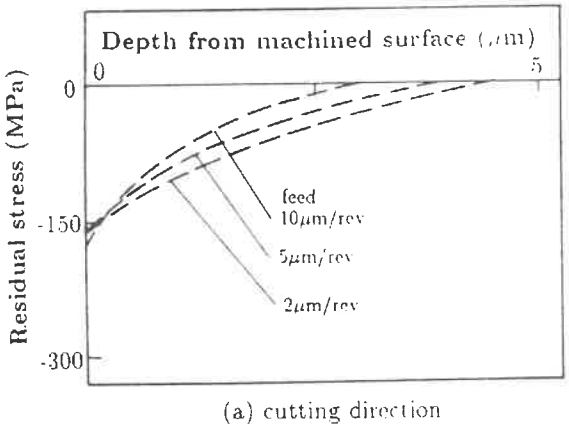

(a) cutting direction

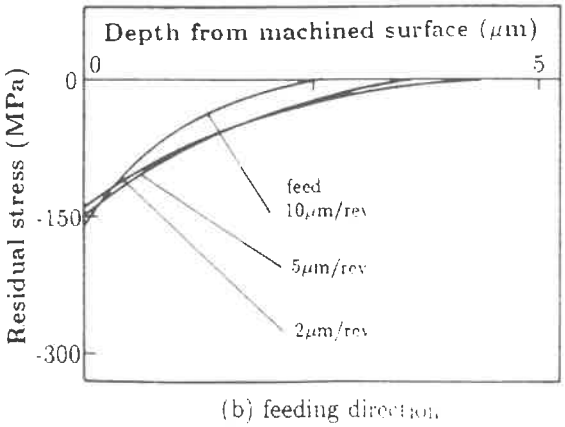

(b) feeding direction

Fig.5 Influence of feed to residual stress distribution

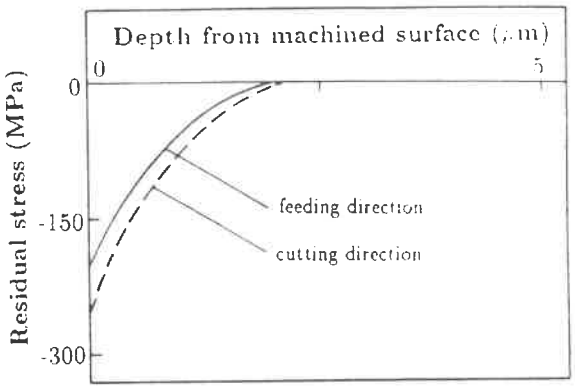

(a) with kerosene spraying

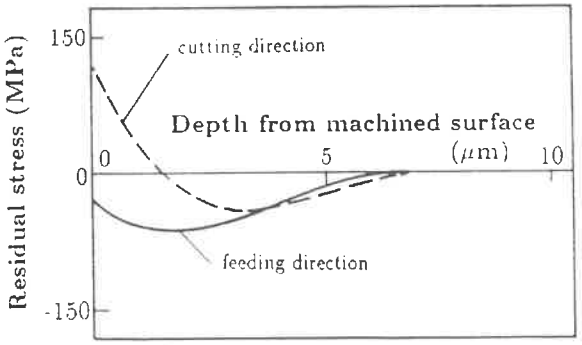

(b) without kerosene spraying

Fig.6 Influence of coolant to residual stress distribution (Sharp tool)

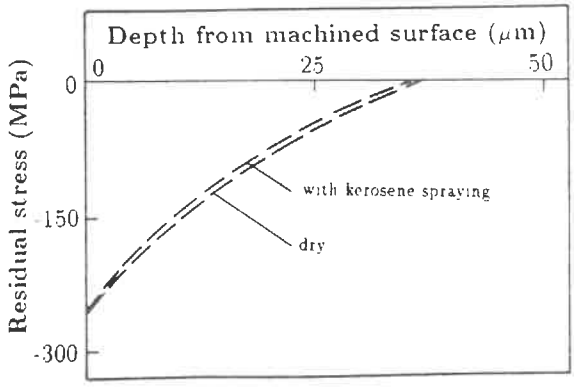

(a) cutting direction

Fig.7 Influence of coolant to residual stress distribution (Dull tool)

Ultraprecision Vacuum fixturing for thin Walled Parts

Martin Powell
Atomic Weapons Establishment
Aldermaston, UK

Introduction

The Ultra Precision machining of thin walled parts presents unique requirements as they can easily be distorted by the holding fixture. The result being that although the part may have been perfectly machined it will deform on release from the holding fixture.

A well known method of applying a uniform holding force over most of the surface of a delicate or shaped part is by Vacuum chuck. The uniform distribution of the holding force ensures wide spread small deformation of the part, rather than localised large deformations, as with mechanical clamping techniques.

Present Vacuum Chucks

The majority of vacuum chucks currently being used, draw vacuum through a single spiral groove or a number of linked concentric grooves of equal width.

An analysis of part deformation (Flat Copper Plate) over such chucks is shown in figure 1.

Thin Component Deformation over Vacuum Chuck

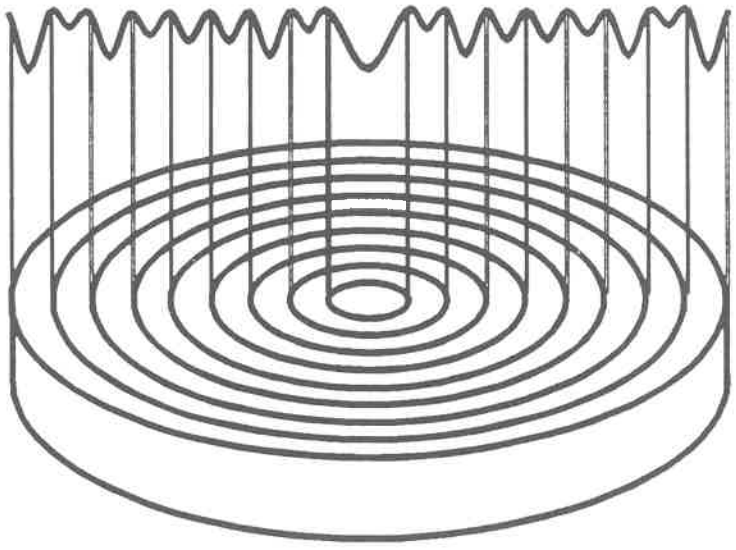

Figure 1

Figure 2 shows magnified, the deformation that occurs from the centre to the edge of the flat part indicating three areas of interest:

(i) Central Hole

(ii) Inner Grooves

(iii) Outer Groove

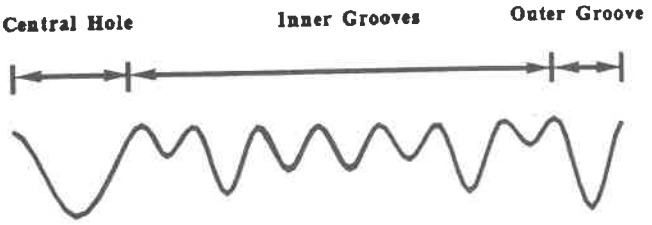

Figure 2

When uniform size grooves and central hole radius are used, large deformations of the part occur at the edge and centre of the chuck. This then affects the magnitude of the deformations over adjacent grooves in a decaying manner between successive grooves. The deformations over the outer and inner grooves for groove widths between 15mm to 22.5mm have been confirmed experimentally.

These deformations can be attributed to three support conditions.

Central Hole Deformation

This being analogous to a disc clamped around its periphery.

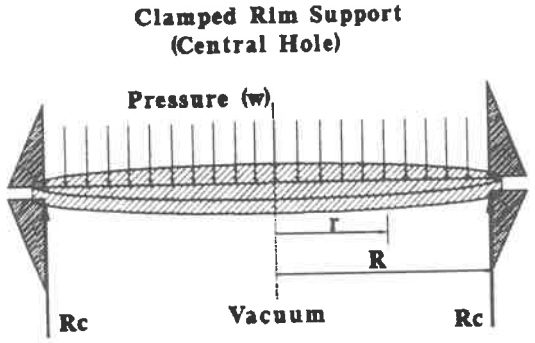

Figure 3

V = Deformation

$$V = \frac{wR^4}{64F} = \frac{3wR^4(1-\nu^2)}{16Et^3}$$

Equation 1 (Hearn)

Inner Groove Deformation

This being analogous to a beam clamped at each end.

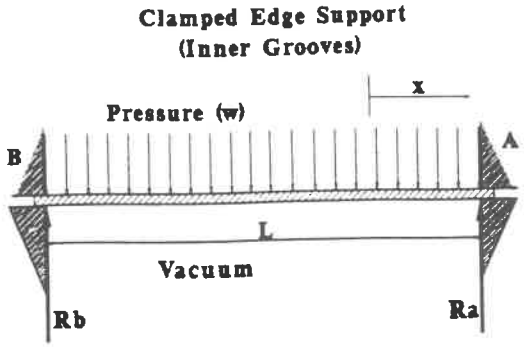

Figure 4

V = Deformation

$$V = \frac{w}{24EI}(2Lx^3 - x^4 - L^2x^2)$$

Equation 2 (Redford)

Outer Groove Deformation

This being analogous to a beam clamped at one end but simply supported at the other.

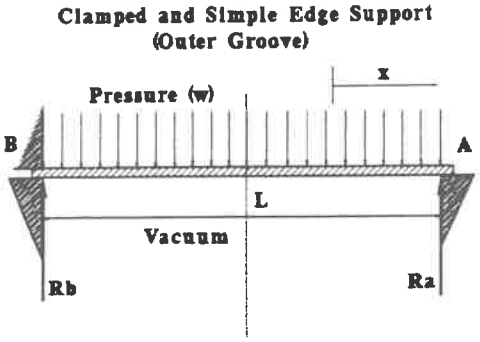

V = Deformation

$$V = \frac{w}{48EI}(3Lx^3-2x^4-L^3x)$$

Equation 3 (Redford)

Figure 5

By determining a hole diameter and outer groove width that will produce the same maximum deflection as the inner grooves, part deformation magnitude over voids can theoretically be made uniform as in figure 6. Also referred to as "tuning" the central hole and outer groove.

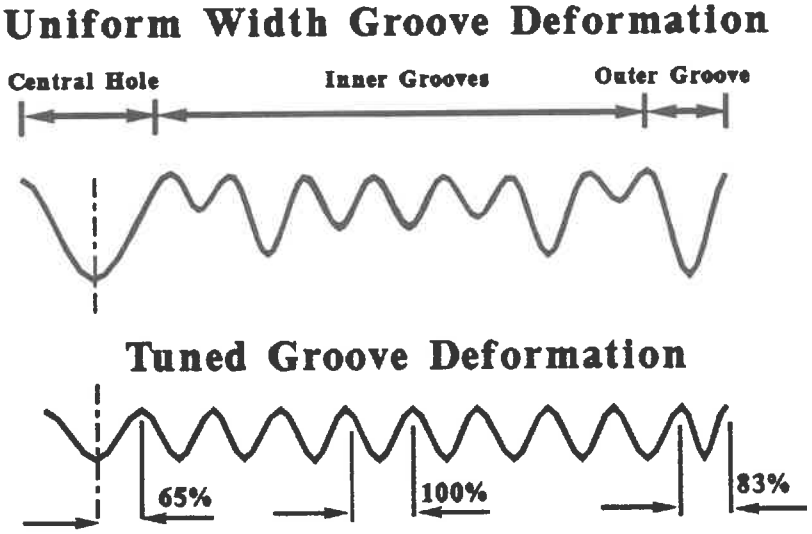

Figure 6

From bending theory calculations, there is a constant ratio of hole radius and outer groove to inner groove width.

Taking - Inner groove width = 100%

Then; Central hole radius ≈ 65%

Outer groove width ≈ 83%

Analysis of grooves using FEA indicates that for groove width to part thickness ratios less than 15:1, bending theory becomes inaccurate. However the above figures can still be used as a good approximation as shown in figure 7 for 3mm grooves using a finite element model.

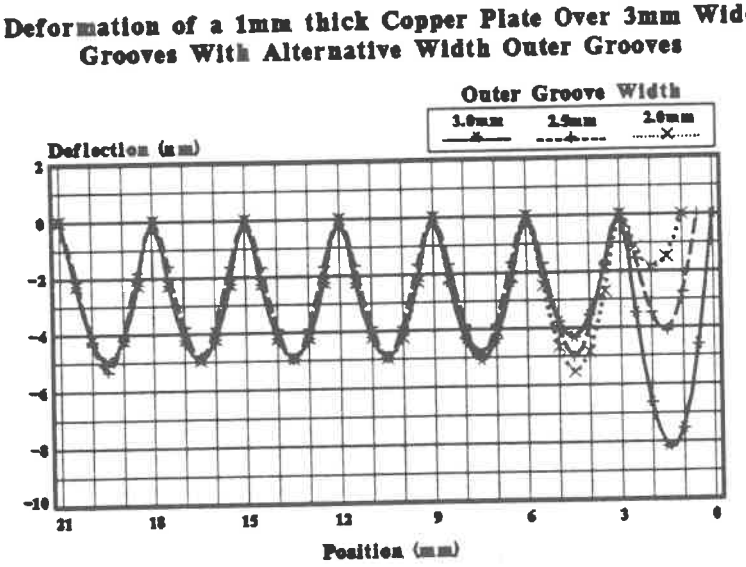

Figure 7

Although a 2.5 mm groove (83.33%) does not give an identical deformation at the outer groove to those of the inner grooves, it does provide an approximate 37% improvement in total deformation magnitude.

References

HEARN E.J. 1977, MECHANICS OF MATERIALS. Pergamon.

REDFORD G.D
Rimmer J.G.
Titherington D. 1971 MECHANICAL TECHNOLOGY. (Macaulay's Method) MacMillan Press.

Study on the Ductile Mode Grinding of Silicon Single Crystal
(The Effect of Temperature and Load Rate on Brittle-Ductile Transition)

Tung-Chung WU, Noboru MORITA and Yoshitaro YOSHIDA
Chiba University
Chiba-Shi,Japan

During the machining process of brittle materials,the variation of the machining mode,from the ductile to the brittle mode,is related to the machining conditions and the tool's shape in addition to material properties. However, the micro-mechanism of the variation has not been totally understood yet. As we knew,the dislocation movement is the most important plastic flow mechanism of crystalline materials. The dislocation movement of brittle materials will be much more active at high temperatures, and on most occasions,the material fracture toughness increases as a result. It is known that silicon single crystal is a kind of material with no crack defect; B-D-T emerges in a very narrow range of temperatures; and the B-D-T temperature rises with the increase of load rate. From these facts, it is obvious that B-D-T is directly affected by the dislocation movement,which is initiated by the inherent effects of the properties of crystal material,and has nothing to do with the slip and the phase of grain boundary.[1] Hirsch's study[2] indicated, when the temperature is below brittle-ductile transition temperature Tc(about 815° K) ,only brittle fractures occur,and there is no connection between fracture stress and temperature. At the point of transition,brittle fractures are brought about exclusively by extremely high stress.When the temperature is above Tc,the specimen is in all plastic deformation and develops into the ductile mode. Tc is highly sensitive to the strain rate ε,and rises with the increase of strain rate. The dislocation velocity V depends on temperature T and load $f(\sigma)$ (as shown in Fig.1),which means the following relation can be established[3]:

$$V=f(\sigma)\exp\{-E/(kT)\} \qquad (1)$$

On the other hand,it is meaningful to infer that there is a fixed ratio between the dislocation velocity of B-D-T and load rate dw/dt. Therefore,the following relation between transition temperature Tc and load rate dw/dt is expected:[1]

$$dw/dt \propto \exp\{-E/(kT)\} \qquad (2)$$

In other words, B-D-T can be decided once load rate dw/dt is decided.Essentially,it seems that B-D-T in grinding has something to do with dislocation movement ,which is affected by temperature. From this point of view, physical factors such as the material's temperature and load rate are taken as two of the grinding conditions to probe into the phenomenon of B-D-T in grinding.

In this study,in order to realize the influence of temperature and load rate (dN/dt) on B-D-T,the indentation and the scratching experiments by means of silicon single crystal are carried out at various temperature. The indentation experiment of silicon single crystal is to realize the micro-mechanism of B-D-T . Fig.2 is the schematic diagram of the experimental set-up. The specimen is heated by CO_2 laser beam ,and indentation is made with a diamond pyramid indenter and a conic indenter on the specimen surface . The temperature of the specimen is controlled by laser power and measured with a thermal couple and an infrared thermometer . The indenting load is measured by a piezoelectric dynamometer. The relation between load and time is analysed with a dynamic

signal analyzer. Three kinds of indenting speed 8.3, 16.6, and 33.2 μm/s are used. Fig.3 shows the relationship between the indenting load and the projection area of indentation . The projected area of indentation increases with the amount of load and the rising of temperature. This shows that the dislocation movement is more active at high temperatures and plastic flow becomes easier. Fig.4 shows the indentation shape , cracks and slip lines being observed on the heated specimen. The slip lines around the indentation are characteristic of material with diamond crystal structure. To apply a load to the plane (100), a weaker cleavage plane (111) is produced.[9] Therefore, taking the indented area as center , the four adjacent planes (111) formed square slip lines. At high temperatures the dislocation movement is more active;slip lines are obvious. When using a pyramid indenter at a high temperature, the cracks appear not only along the diagonal direction but also at the intersection of the slip lines caused by dislocation. Fig.5 shows the relationship between indenting load and crack length when using a pyramid indenter at different temperatures and indenting speeds. Crack length, proportional to the indenting load, will be shorter while applying a low indenting speed at high temperature. The special thing is that cracks can hardly be seen above 600° C. This shows that load rate and material temperature are the factors resulting in B-D-T. Fig.6 shows the relationship between load rate and crack at various temperatures. Load rate, defined as

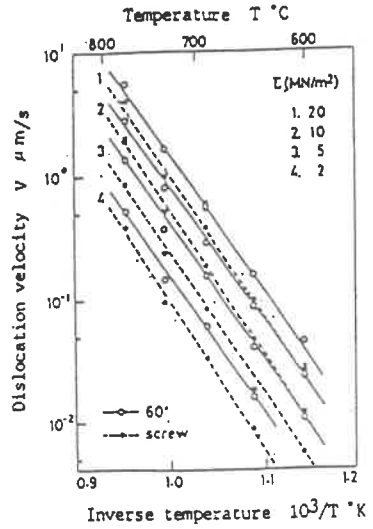

Fig.1 Relationship between temperature and dislocation velocity under various load

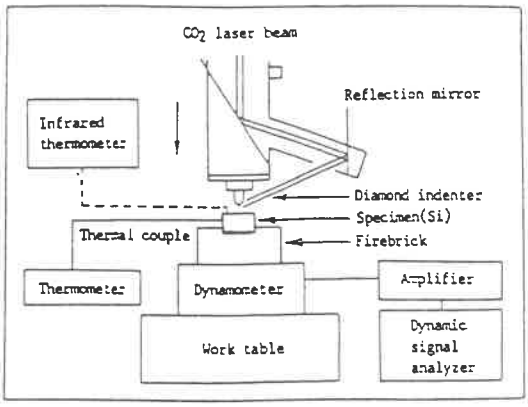

Fig.2 Schematic diagram of experimental set-up

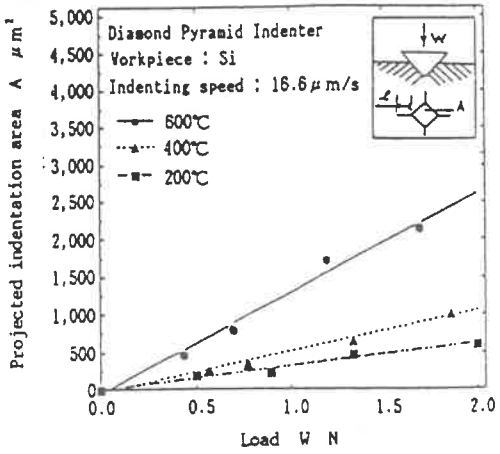

Fig.3 Relationship between load and projected indentation area under various temperature

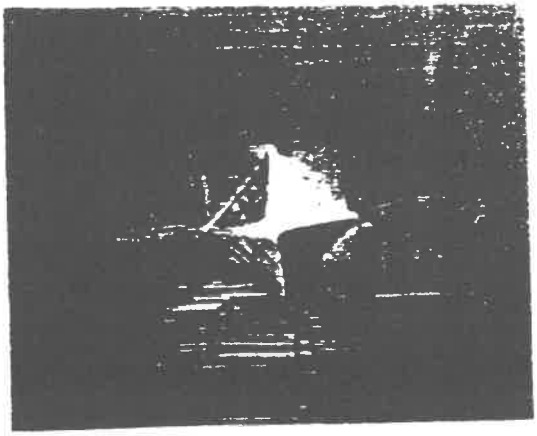

Fig.4 Indentation with pyramid indenter at 400 °C (×500)

dN/dt, becomes smaller under the conditions of light load, high temperature and low indenting speed. From the figure, we learn that crack length becomes shorter as load rate is decreasing and no crack occurs at temperature above 600°C, and a load rate of about 2 N/s. Fig. 7 shows the influence of indenting speed on crack length at various temperatures. The fracture toughness is small with low temperatures, at which brittle fracture is induced; therefore crack length is longer. On the other hand, no crack happens at the temperature of 600°C. Base on data of Fig. 6 and Fig. 7, we infered that B-D-T occurs at 600°C as load rate is about 2 N/s. Since equation (2) also shows that the relation between load rate and transition temperature is acceptable, according to the result of the experiment, we inferred material temperature and load rate are the controlling factors to B-D-T, and when load rate is larger than dislocation velocity at the same temperature, brittle fracture occur.

The scratching experiment of silicon single crystal is carried out by means of a diamond pyramid indenter. The experiment is to make the indenter move on the 5/1000 incline surface of the specimen to form scratching. Considering the result of the indenting experiment, we selected a scratching speed of 16.6 μm/s to meet the condition of B-D-T. Moreover, we change the temperature of the specimen to measure the variation of cutting force with time. It is realized that the distance from the begining point of cutting to the occurrence of brittle fracture becomes longer in accordance with the rising of temperature, which means the ductile mode machining is expected to be accomplished at 400°C if the depth of cut is less than 1 μm . Under this condition, the normal force is below 50 mN. Fig. 8 shows the effect of temperature on load rate dF/dt under the variation of scratching force. dFt/dt and dFn/dt are derived from the variation of normal force and tangential force during scratching. In the figure, the white dot indicates the begining point of scratching, and the black dot indicates the end point of scratching. The arrow shows the increase of dF/dt. The black line is the linking line of dF/dt which shows the occurrence of B-D-T at various temperatures. It shows the area of plastic deformation or elastic deformation below the line. dFn/dt is bigger than dFt/dt, therefore, it can be inferred that B-D-T is controlled mainly by normal force. And dF/dt becomes smaller at high temperatures. It seems that a low dF/dt makes the occurrence of B-D-T most possible. To compare dF/dt under the same temperature, we can see that dF/dt is getting bigger approximately from the starting point of scratching. This clearly indicates that

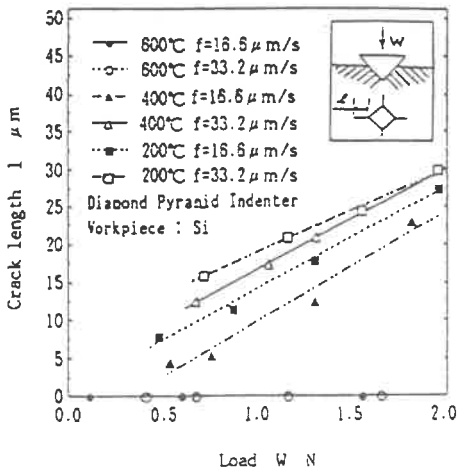

Fig.5 Effect of various conditions on crack length

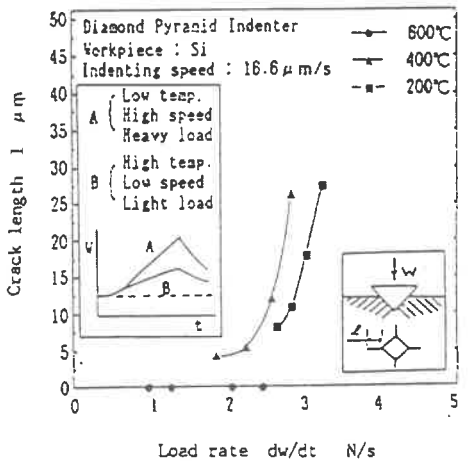

Fig.6 Relationship between load rate and crack under various temperature

temperature and dF/dt control the value of dc directly. In the scratching experiment, B-D-T is also controlled directly by the material temperature and load rate (dF/dt). Deductively, cutting load and cutting speed have strong connection with B-D-T.

The indentation and the scratching experiments with silicon single crystal shows that B-D-T and the value of dc are directly affected by material temperature and load rate. That is , B-D-T is affected by the rising of material temperature and the load rate. In the actual grinding, it is proper to consider that the heat of friction between grains and material provides sufficient temperature for the generation of B-D-T. Therefore, high speed grinding, which will cause a very high rise in temperature, and the distribution of grains are very important.

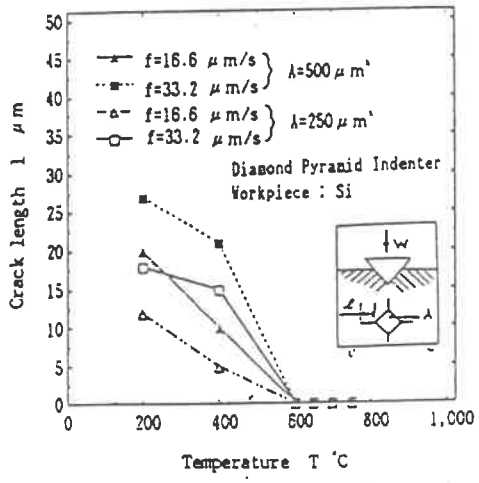

Fig.7 Influence of indenting speed on crack length under various temperature

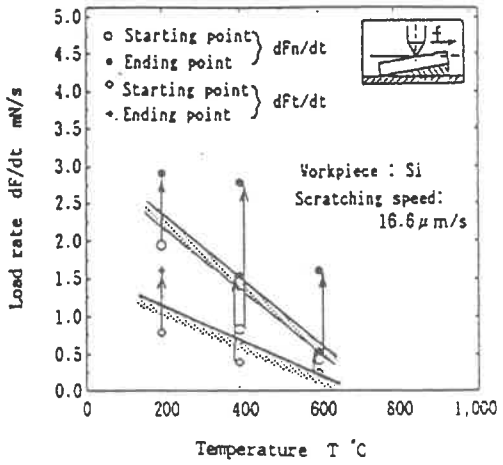

Fig.8 Effect of temperature on load rate dF/dt under the variation of scratching force

ACKNOWLEDGEMENTS

Special thanks for asistance in research are due to: Kawasaki Steel Corp. and Okamoto Machine Tool Co., JAPAN. This research was sponsored and supported by the Mechanical Industry Research Laboratories, ITRI, Taiwan, ROC.

REFERENCE:

1)K.Maeda, S.Fujita, H.Nishioka and T.Narita, Brittle-Ductile Transition in Covalent Crystals, JIM, Vol.29, No.12 (1990) 999

2)P.B.Hirsch, Fundamentals of the Brittle-Ductile Transition, JIM, Vol.29, No.1(1990)5

3)M.Imai and K.Sumino, In situ X-ray topographic study of the dislocation mobility in high-purity and impurity-doped silicon crystals, Philosophical Magazine A, Vol.47, No.4 (1983)559

4)G.C.Rybicki and P.Pirouz, Indentation Plasticity and Fracture in Silicon , NASA Technical Paper 2836(1988).

INFLUENCE OF MICROSTRUCTURE IN PRECISION GRINDING OF FINE CERAMICS

Dr. E. Brinksmeier, P. Roth
Institute for Production Engineering and Machine Tools (IFW)
Hannover, Germany

Abstract

This paper presents the results of grinding experiments with various grades of alumina ceramics. While equivalent in chemical composition, these ceramics differ in microstructure and mechanical properties due to varied sintering conditions. When machined identically, the materials reveal systematical differences in grindability. Material removal mechanisms depend strongly on the microstructure of the materials with grain size identified as one dominant parameter. Ductile as well as brittle behaviour of ceramics under compressive load and/or elevated temperaures can be identified in grinding. Over a wide range of machining conditions, grain and pore sizes can limit the obtainable surface finish.

Experimental procedure and results

While the aspects of machining parameters and tool specifications in grinding of ceramics have been examined closely [1-6], it is of equal interest to study the influence of varying microstructure with ceramic materials. For this purpose, a series of five high-purity alumina ceramics has been produced under controlled conditions[1] (99.98% Al_2O_3). Their properties are given in table 1.

Material type	Sintering temp. T_s [°C]	Grain size d_g [µm]	Hardness HV 10	Fracture toughn. K_{Ic} [MPa·m$^{1/2}$]	Bending strength σ_{4b} [MPa]
TM 30	1300	0.83	1960	3.70	320
TM 40	1400	2.2	1920	3.80	380
TM 50	1500	4.4	1770	4.10	340
TM 60	1600	7.8	1650	4.15	300
TM 70	1700	12.2	1590	4.05	300

Table 1: Material properties

[1] Materials were processed by Dr. R. Telle, PML/MPI fuer Metallforschung, Stuttgart, Germany.

According to the sintering temperatures the alumina grades were named TM 30...70. Densities superior to 99% were obtained in all cases without any additives. With sintering temperature, average grain sizes rise from 0.8 to 12 µm while hardness and bending strength decrease. Higher values of ISB fracture toughness are measured with the coarser alumina grades.

Surface grinding tests were performed using a 1A1 D91 C50 resin bond diamond grinding wheel at v_c = 30 m/s with oil as a coolant. Grit depth of cut h_{cu} was varied via the wheel depth of cut, a_e, to study the brittle/ductile transition in material removal. As suspected, the five alumina varieties behave very differently in grinding [7]. Figure 1 gives SEM views of ground surfaces.

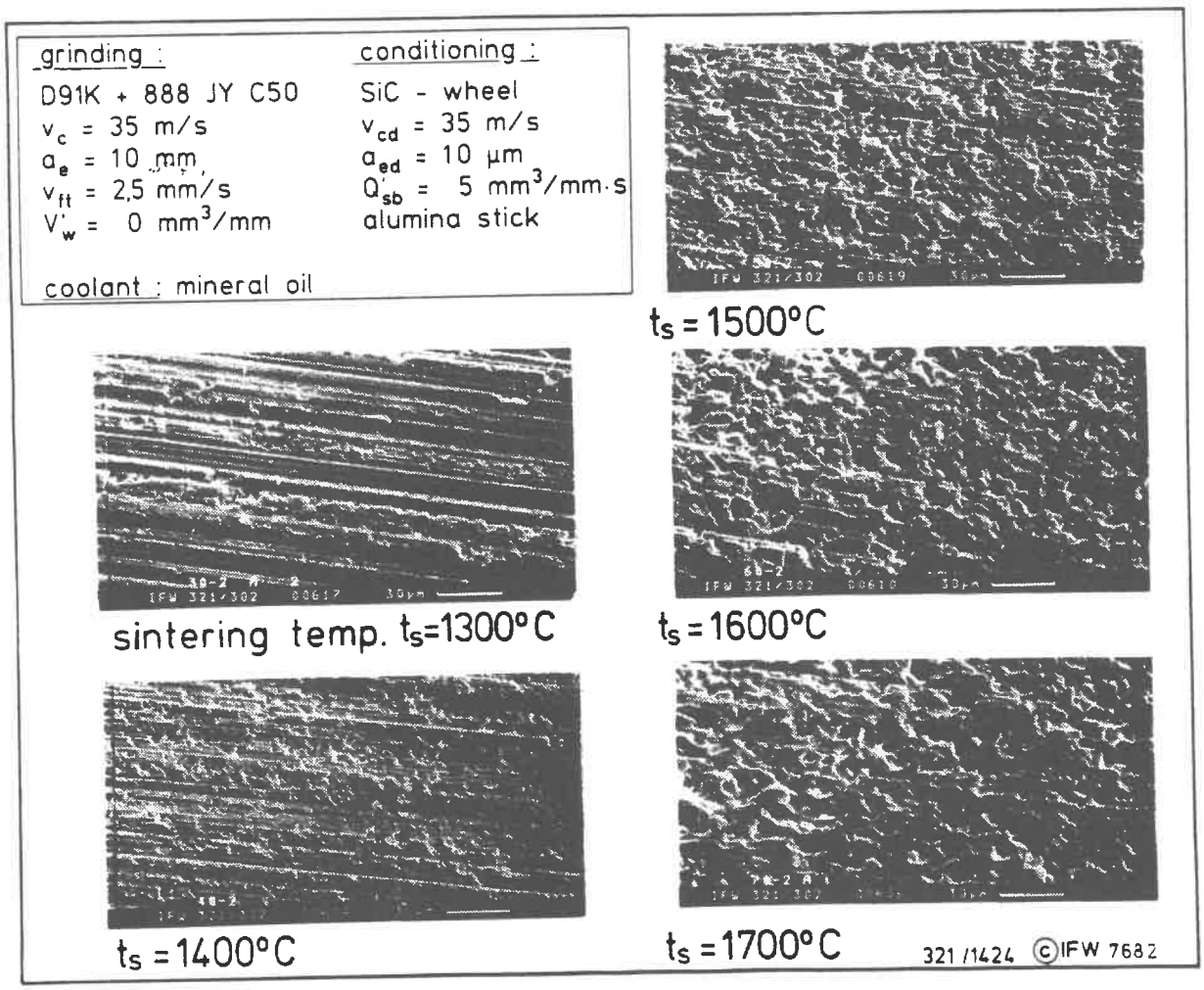

Fig. 1: Surfaces of various alumina ceramics ground under identical conditions

With the fine-grained varieties (TM 30 and 40), ductile material behaviour dominates surface formation. The ground surfaces are covered with smooth grooves. Some pile-up of displaced material can be observed. The regular groove pattern is broken by two different types of cavities. Small pores form as grains are broken from the surface under the action of a grit. Larger, flakelike particles are removed by chipping. Some of these have only partly separated from the substrate and remain on the surface close to their original position.- With the increase in grain size, the removal of complete grains takes over. The surfaces of coarse alumina varieties reveal many near-perfect grain facets uncovered by intergranular fracture in micro-brittle material behaviour. Some remaining plateaus bear traces of plastic deformation as with fine-grained material.

Surface roughness was measured as an indicator of the prevailing mechanism of material removal. Generally, very little influence of machining conditions is found. Surface finish is only about 20% better in creep feed grinding. Instead, material grain size dominates the roughness of ground surfaces. Figure 2 gives the roughness R_z of the various materials relative to feed direction.

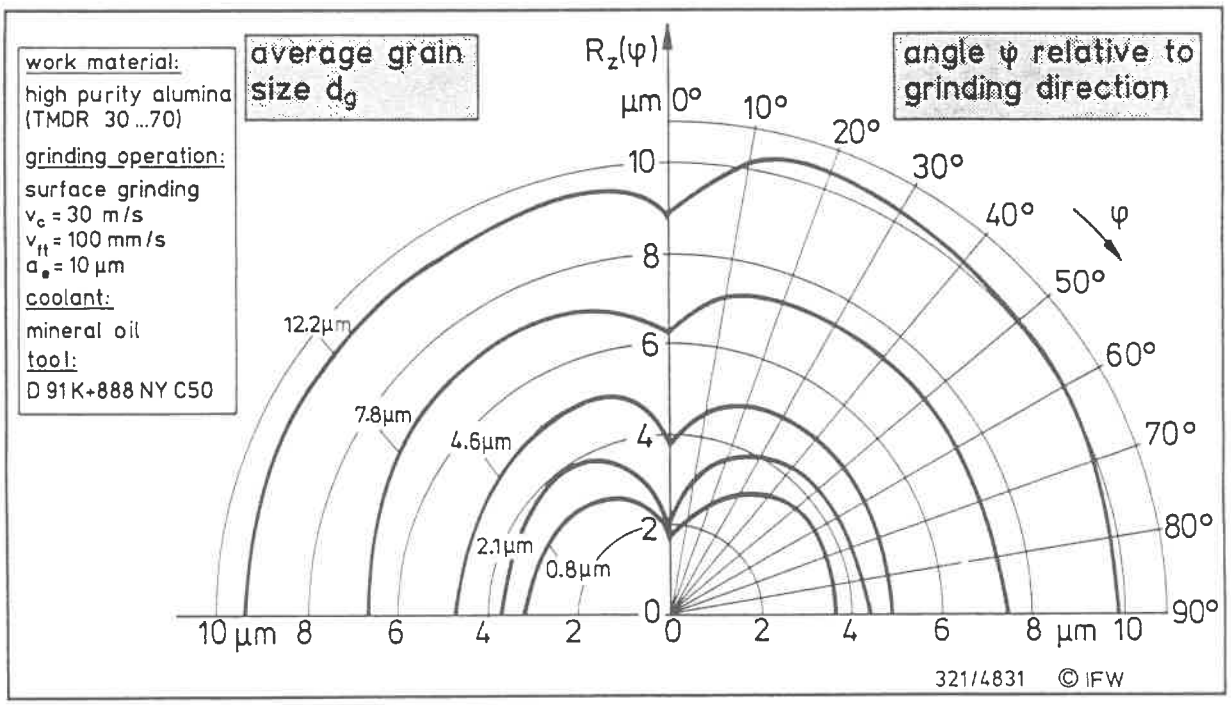

Fig. 2: Directivity of surface roughness

While the fine-grained aluminas exhibit marked differences in roughness along and across feed direction, the influence of feed direction is almost lost with coarse grain. As can be gathered from SEM observation (see above), fracture dominates with coarse microstructures while the surfaces of fine-grained aluminas appear covered with a layer

of deformed material less than 1 µm thick. In the latter case, the roughness is determined by the traces of the grits.

The specific grinding energy e_c is a useful quantity to assess the effectivity of a grinding process [8-10]. It denotes the energy necessary to remove a unit volume of material. It is derived from the tangential grinding force F_t, grinding and feed speeds, v_c and v_{ft}, and the wheel width b by

$$e_c = (F_t \cdot v_c) / (a_e \cdot b \cdot v_{ft}),$$

The specific grinding energy has been shown to vary inversely with the undeformed chip thickness h_{cu} [7, 11]. In grinding of ceramics, e_c indicates the relative importances of brittle and enrgy-consuming ductile material behaviour. The results represented in figure 3 now show the close connection of the grinding energy with workpiece grain size. The two sets of graphs refer to different grinding conditions typical for surface and creep feed grinding. All cases exhibit the same trend, namely an inverse correlation between energy demand and grain size. Between the finest-grained and the coarsest alumina varieties, ratios of up to four in e_c are found. In particular, grinding energy is related to the square root of d_g by a near-exponential function.

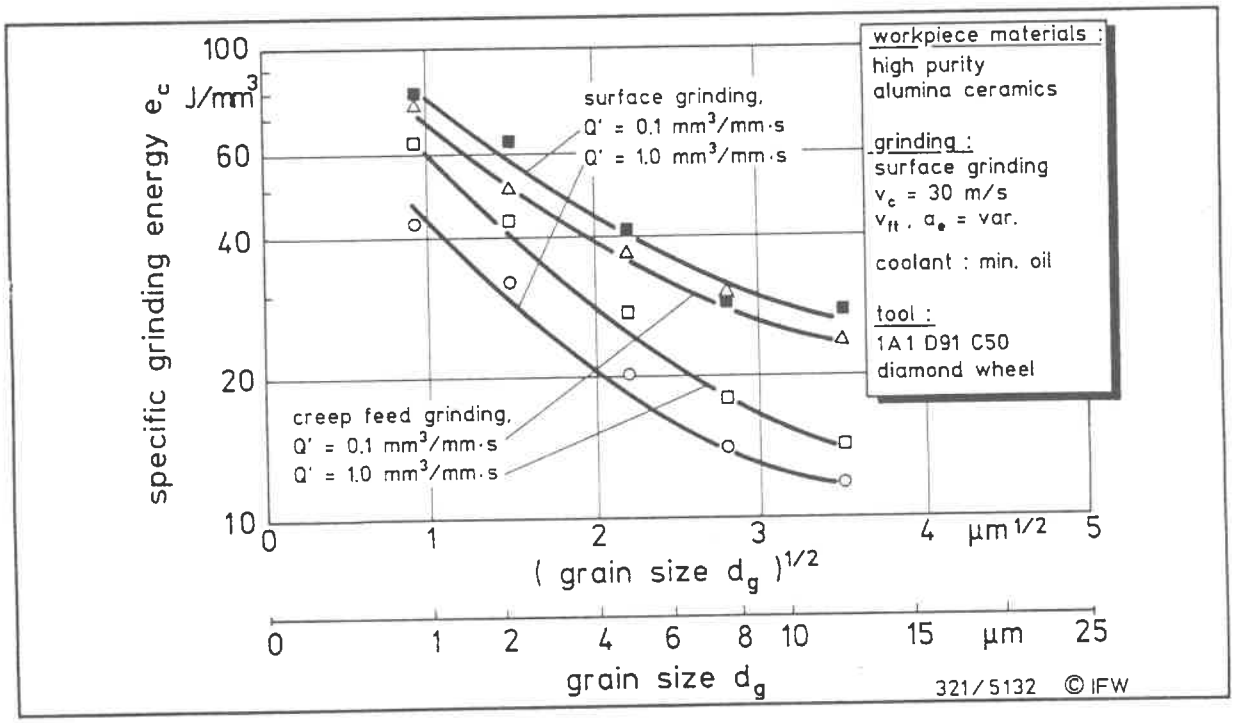

Fig. 3: Specific grinding energy e_c vs. workpiece grain size d_g

These results point at a significant amount of micro-brittle behaviour in material removal. Fracture mechanics can explain the dependence of grinding force on grain size: The grain boundaries must be regarded as defects in ceramic microstructure, especially if, as in this case, the remaining porosity forms rows of pores along them. The linear dimension of the individual grain boundaries is a fraction of the grain size. With the boundaries acting as cracks, the strength of the material in resisting the tangential grinding force is thus indirectly controlled by grain size. Furthermore, the measured increase in energy demand reflects the larger amount of rubbing and ploughing in material removal found with fine-grained workpiece materials. This is documented by figure 4.

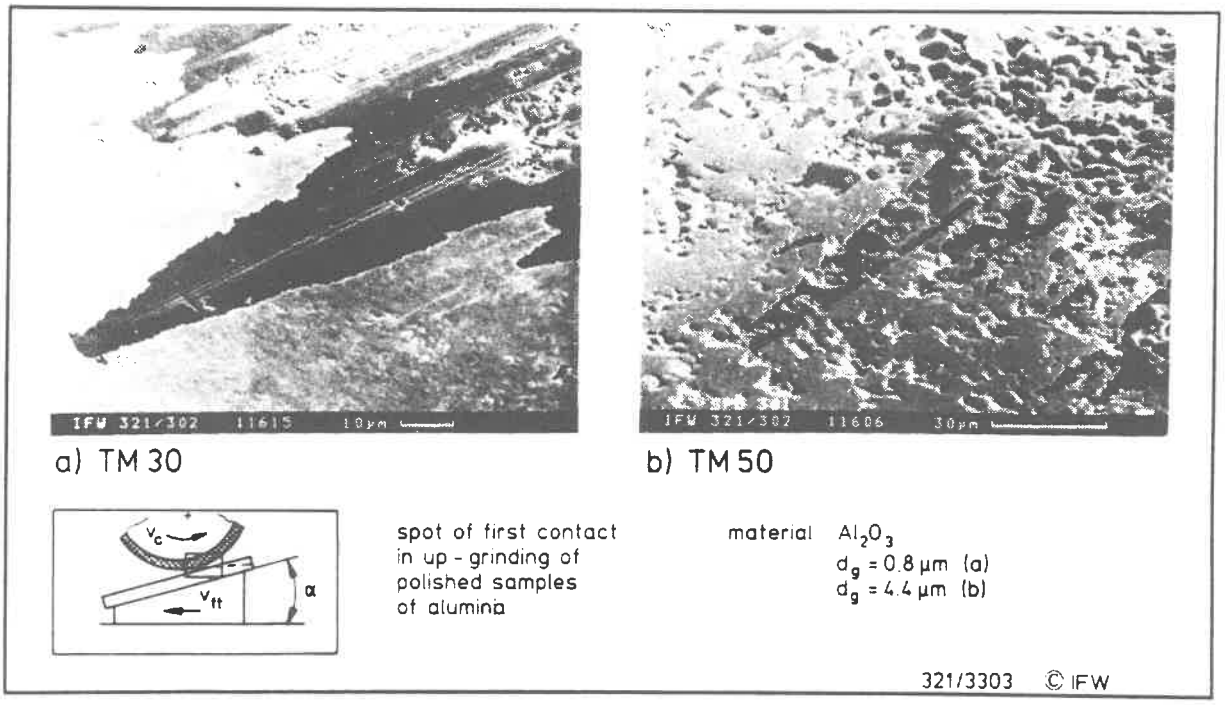
a) TM 30
b) TM 50
spot of first contact in up - grinding of polished samples of alumina
material Al_2O_3
d_g = 0.8 µm (a)
d_g = 4.4 µm (b)
321/3303 © IFW

Fig. 4: Traces of rubbing, cutting and ploughing actions of the grit

The micrographs demonstrate the reaction of two different workpiece materials, TM 30 and 50, to grinding with a constantly increasing grit depth of cut, realized by tilted specimens. As they contact the polished surface, sharp cutting edges immediately start removing material in the ductile mode (cutting). Duller grits remove the sputtered gold coating in elastic contact (rubbing) and then displace material sideways in plastic deformation (ploughing). With increasing depth of cut, micro-brittle fracture sets in and leads to material removal by cracking. The two workpiece materials are clearly distinguished by their different degree of ductility. While with TM 30, heavily deformed layers of material are smeared along the grooves, grain break-out sets in much earlier in TM 50.

References

[1] Tönshoff, H.K, G. Warnecke, H.-Z. Choi;
Der Beitrag der Forschung zum Sägen von Stein; IDR 11(19)1, 5-11

[2] Kirchner, H.P., J.C. Conway;
Mechanisms of Material Removal and Damage Penetration during Single Point Grinding of Ceramics; Machining of Ceramic Materials and Components, Vol. 17; ASME, New York, 1985, 53-61

[3] Tönshoff, H.K, E. Brinksmeier;
Abrasives and their Influence on Force, Temperature and Surface; SME International Grinding Conference; Philadelphia, June 10-12 (19)

[4] Saljé, E., H. Möhlen;
Prozeßoptimierung beim Schleifen keramischer Werkstoffe; IDR, 21(1987)4, 243-247

[5] Saljé, E., H. Möhlen;
Material Removal in Grinding of Advanced Ceramics; SME Technical Paper MR88-498, 1988, 1-19

[6] Blake, P., T. Bifano, T. Dow, R.O. Scattergood;
Precision Machining of Ceramic Materials; Ceramic Bulletin, 67(1988)6, 1038-1044

[7] Tönshoff, H.K, R. Telle, P. Roth;
Chip Formation and Material Removal in Grinding of Ceramics; SME Techn. Paper MR90-539, 1-18

[8] Zheng, H.W., G.Q. Cai, S.X. Yuan;
An Experimental Study on Mechanism of Cermet Grinding; Annals of the CIRP; 38(1989)1, 335-338

[9] Liao, T. Warren, G. Sathyanarayanan;
An Investigation into Creep Feed Grinding of Alumina Ceramic; Transactions N. Am. Manuf. Res. Inst. of SME (NAMRC XVII); 17(1989)1, 175-184

[10] Akbari, J., Y. Ichida, K. Kishi, T. Machida;
Grinding Energy of Fine Ceramics; Proceedings of the First International Conference on New Manufacturing Technology; Chiba, 1990, 323-328

[11] Inasaki, I.;
High Efficiency Grinding of Advanced Ceramics; Annals of the CIRP, 35(1986)1, 211-214

CERAMIC MIRROR GRINDING:
Using Extremely Fine Grit Diamond Wheel

Libo ZHOU, Katuso SYOJI and Tsunemoto KURIYAGAWA
Dept. of Mechatronics & Precision Eng., Tohoku University
Sendai, 980, Japan

Introduction

Ceramics are extremely hard to machine using typical methods. Usually, mirror finishing of these hard-brittle materials requires the use of diamond abrasives. Grinding in particular, when compared with lapping or polishing, efficiently produces excellent geometric form. With the recent improvements in manufacturing technology, it is now possible to produce high quality micron or sub-micron grit diamond wheels. With the use of these extremely fine grit wheels, mirror grinding technology will play an important role in the future of ultra-precision machining. This paper describes a truing device and a grinding machine specially designed for performing the precision grinding. The equipment's fundamental characteristics and high level of performance will also be discussed.

Grinding machine and truing device

According to the previous research on resinoid-bonded diamond wheels[1], diamond grains sinking into the bond materials during the grinding process, causes a steep decline in grinding performance. In order to reduce the load on all cutting edges, it is important to reduce the depth of cut and the spindle run-out as much as possible. **Fig.1** is a schematic diagram of the cylindrical grinding machine developed for this study. This machine uses a hydrostatic bearing to improve the rotating accuracy of the spindle. The grinding force can be determined in-process by monitoring the oil pressure variation in the hydraulic pocket. The main feature of this machine is the infeed system shown in **Fig.2**. The mechanism governing coarse motion consists of a high response DC servo motor and a precise ball screw with a resolution of *0.4μm/pulse*. For fine infeed motion, four layered piezo electric transducers (each of which can create a maximum pushing force of *3500N*) are installed between the screw bush and the spindle unit at a pre-load of *350N*. Each transducer is driven by a *12bit* D/A converter with a theoretical resolution of *2.4nm/bit*. The fine infeed motion is used to control the depth of cut, and the coarse motion is used to compensate for the expansion of the piezo electric transducers when they are charged to *100V*. **Table 1** gives further specifications of the infeed system. To produce a smooth infeed motion, a

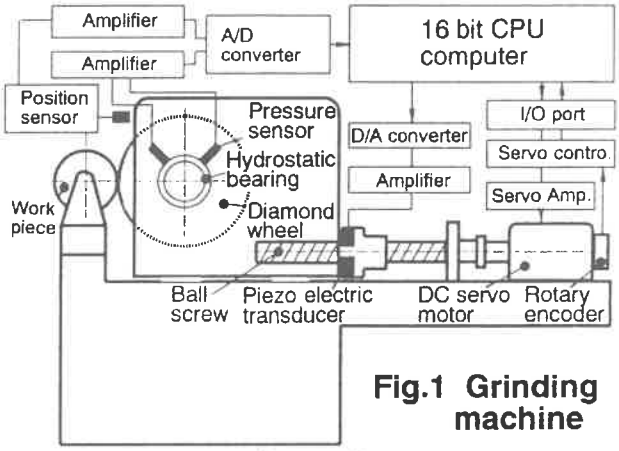

Fig.1 Grinding machine

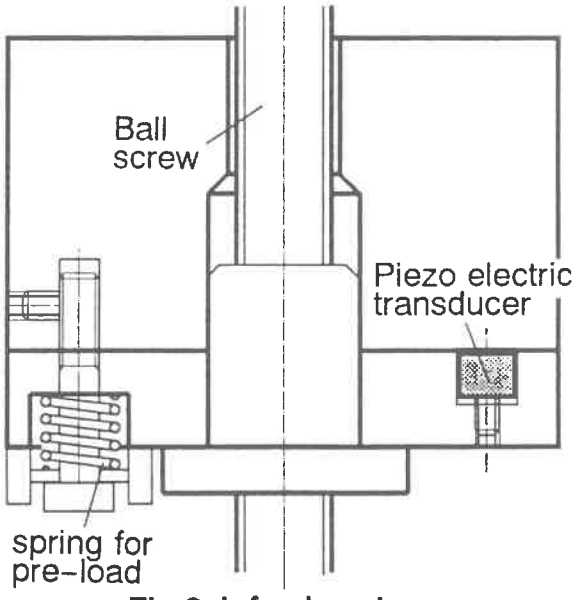

Fig.2 Infeed system

Table 1 Specifications of infeed system

Motor	Power[kW]	0.25
	Torque[$kg \cdot cm$]	24
Encoder	Output pulse[P/R]	2500×1,2,4
Ball screw	Lead[mm]	4
	Stroke[mm]	50
	Resolution[$\mu m/P$]	0.4
Piezo electric transducer	Size[mm]	10×10×9
	Operating voltage[$V \cdot DC$]	0~100
	Expension(at 100V) [μm]	6.3
	Resolution[nm]	2.4
	Max. pushing force[N]	3500
	Pre-load[N]	350

hydrostatic bearing guide was utilize in the slide ways.

An alternative approach to reducing the excessive load exerted on cutting edges, is to improve the geometric accuracy (namely, truing accuracy) of the grinding wheel. For this purpose, a special truing device (**Fig.3**) was designed such that the cup-type GC grinding wheel can make reciprocating movements while revolving about its axis. The truing device performs both truing and dressing even though the matrix-type diamond wheels do not necessarily require dressing after truing. Furthermore, by using two rotary tables to control the relative inclination of the GC wheel's axis to the wheel surface, the diamond wheel can be adjusted to a desired cross-sectional profile as described below. **Table 2** gives detail specifications of the GC-cup truing device.

Experimental results

Table 3 shows the truing and grinding conditions used in the experiments. The truing device, being different from traditional tools, does not make any traverse motions. Consequently, not only is it able to true a straight wheel very precisely, but by changing the inclination of the GC wheel axis, it is also able to true a concave or convex wheel. For example, in **Fig.4**, the cross-sectional profile of the diamond wheel is plotted as a function of the inclination of the GC wheel axis. Because the profile is also in agreement with the profiles of GC wheel loci analyzed theoretically, the truing device is qualified for form-grinding applications.

Fig.5 shows truing efficiencies at various infeed rates, f_t, per reciprocation of GC wheel. Generally, the efficiency increases with

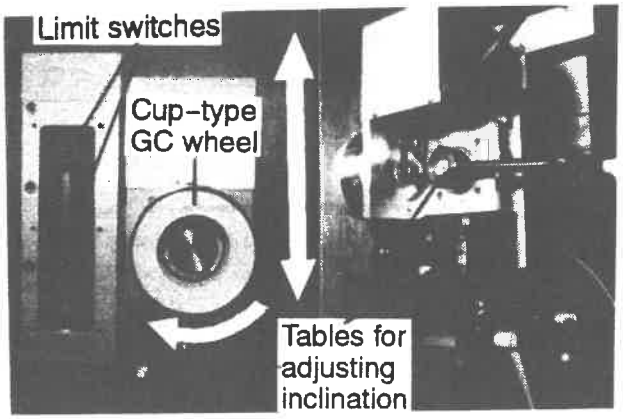

Fig.3 Truing device

Table 2 Specification of GC cup-truer

GC wheel & rotation	Size[mm]	$90^D \times 55^H \times 20^T$
	Power[W]	15 (AC motor)
	Speed[rpm]	90~1400
Up-down reciprocation	Power[W]	30 (DC motor)
	Stroke[mm]	10~150
	Speed[m/min]	0.18~18
Table for adjusting inclination	Max. angle[°]	-15~+15
	Resolution[°]	0.03
Weight	Cup-truer[kg]	17
	Power unit[kg]	11.5

Table 3 Experiment conditions

Diamond wheels	SD1500,3000,5000, (Concentration=125)	
	(Size=$350^D \times 12^T \times 5^X$)	
GC Truers	GC400H~GC6000H ($90^D \times 55^H \times 20^T$)	
Truing conditions	Wheel speed	$350m/min$
	Truer speed	$1000rpm$
	Reciprocation speed	$1m/min$
Grinding conditions	Wheel speed	$1000m/min$
	Workpiece	ZrO_2 ($\phi 100 \times W10$)

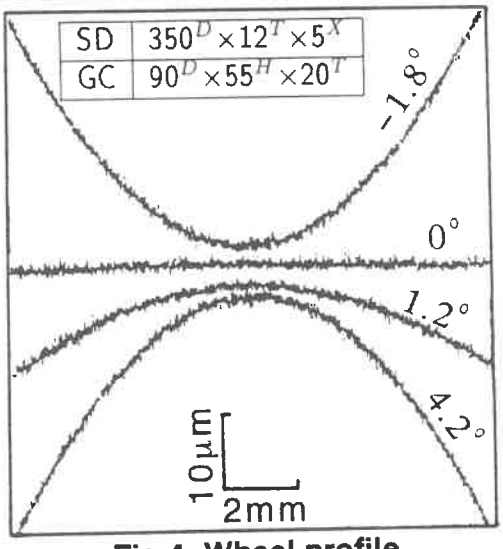

Fig.4 Wheel profile

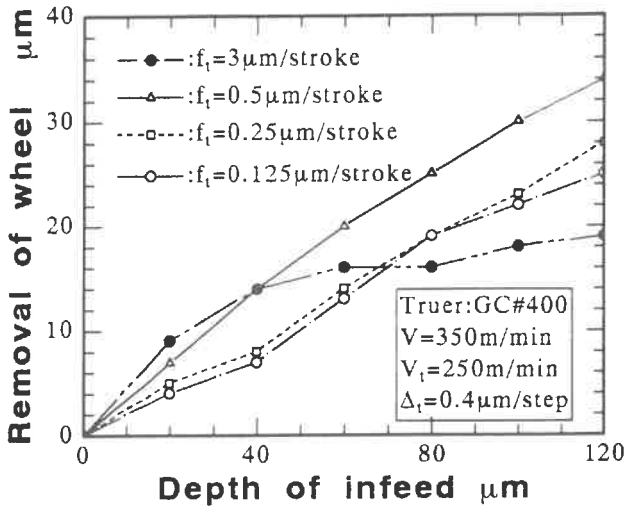

Fig.5 Truing efficiency

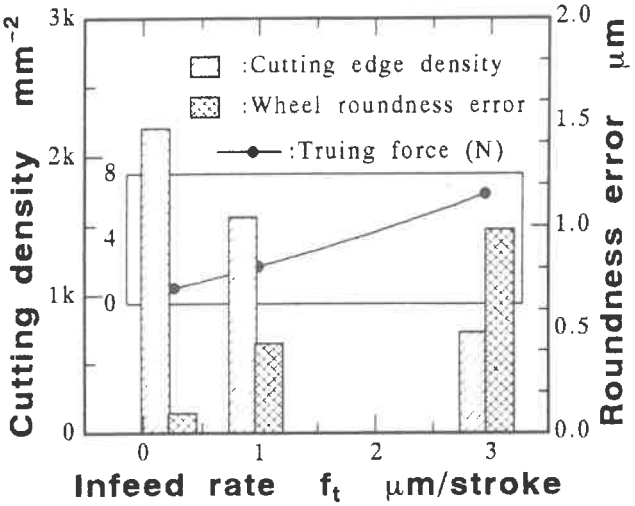

Fig.6 Effect of truing force

increasing f_t. However, an excessive f_t setting reduces the capacity of diamond wheel removal. In fact, truing with this device is carried out by a lapping action between the diamond wheel and GC grains that are broken off the GC wheel. If a high f_t value is used, a large number of diamond grains will fall off the wheel surface, resulting in fewer cutting edges. Therefore, the diamond wheel loses the grinding ability necessary to break off enough GC grains for effective truing. **Fig.6** illustrates that in the above situation, the truing force does increase sharply. The vibration caused by the truing force leaves chatter marks on the wheel surface after truing, and consequently deteriorates its roundness. Evidently, using optimum truing conditions is the key to successful truing of extremely fine grit diamond wheels.

As mentioned above, the grinding force can be measured in-process. The grinding machine can function at both a force-controlled mode and a motion-controlled mode. The grinding experiments in this research were carried out in the motion-controlled mode which is handled by the piezo electric transducers. **Fig.7** shows the influence of the depth of cut on the grinding force and surface roughness. In cases where the depth of cut was too small, the results were irregular due to ploughing of cutting edges. Generally, by reducing the depth of cut, both the grinding force and the surface roughness decreases. Consequently, a fine infeed system is essential for achieving effective grinding with extremely fine grit diamond wheels.

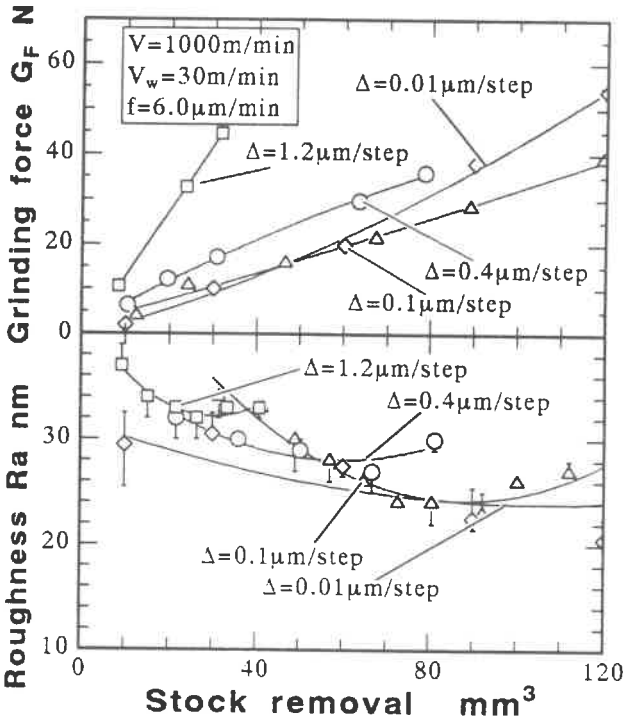

Fig.7 Effect of depth of cut

Fig.8 shows the influence of infeed rate, *f*, on grinding at a depth of cut of *0.01μm/step*. As the feed rate decreased, the roughness improved markedly, regardless the machining efficiency. Furthermore, mirror surfaces of *Rmax=120nm* and *Rmax=40nm* were obtained after grinding with *SD3000B* and *SD5000B* respectively. **Fig.9** is an example of mirror surface

obtained. In addition, it should be noted that the above experiments were conducted at infeed grinding without any spark-out. Further improvement in the surface roughness is expectable if traverse grinding is applied.

Conclusion

The aim of this study is to establish a technique for applying extremely fine grit diamond wheels to ceramic mirror grinding. A device employing a GC-cup type grinding wheel was developed for truing and dressing. Diamond wheels trued with this device were efficiently formed into the desired profile with excellent roundness and damage-free cutting edges. A mirror surface was successfully formed through grinding with the machine equipped with a fine infeed system.

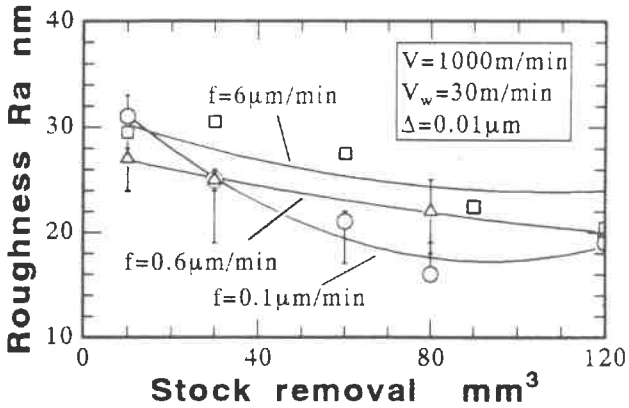

Fig.8 Effect of infeed rate

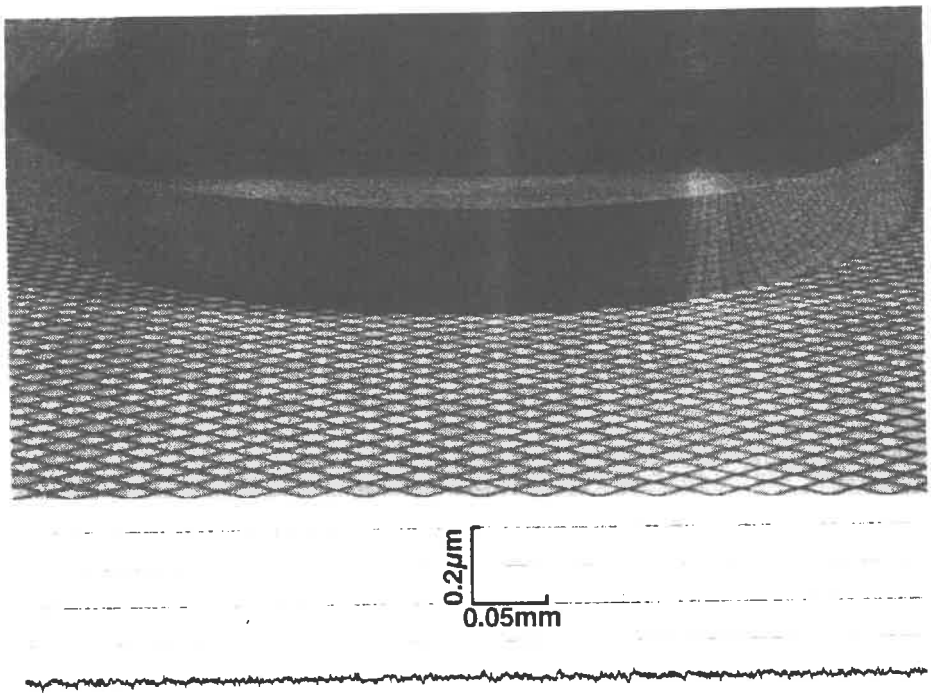

Fig.9 The surface after grinding with *SD5000*

Reference

1) *Libo Zhou, T.Kuriyagawa and K.Syoji*: Truing, Dressing and Grinding Characteristics for Very Fine Grit Diamond Wheels, Proceedings of CIRP Conference on PE & MS, Sept. 1991

Cleaning Technique for Super Abrasive Grinding Wheel with FRP Cleaner

Kohzo Abe , Nobuo Yasunaga
Nippon Steel Corporation
1618 Ida Nakahara-ku, Kawasaki 211, Japan

1. Introduction

This paper proposes a diamond wheel cleaning technique, which is designed to remove only ground chips attached to wheel surface and to leave little damage in abrasive grains and bonds. Conventional truing and dressing techniques keep the grinding wheel surface fresh and maintain the cutting ability of the wheel by crushing the abrasive grains, but have an undesirable feature that the bond material is excessibly removed.

Cleaning can be practically realized by a FRP (Fiber Reinforced Plastic) cleaner, which consists of long glass fibers with diameters about 13 microns unidirectionally bonded with epoxy resin. The effectiveness of the FRP cleaner was verified by diamond wheel grinding experiments of SIALON (Si-Al-O-N) ceramics which is known as a difficult-to-grind material.

2. Cleaning test of loaded diamond wheel by stick method

We tried to remove the adhered chips on a diamond wheel after grinding SIALON using a FRP stick and observed the wheel surface by a scanning electron microscope. The closs sections of the FRP Cleaner and GC (Green silicon Carbide) dressing stick used in this experiment are shown in Fig.1. Figure 2 shows the state of the diamond wheel surfaces. It is clearly seen that the FRP cleaner removed only ground chips attached to the wheel surface, where diamond grains are left in truncated state. In case of conventional GC dressing stick, we can observe fractured and fresh diamond grains. This indicates that GC stick removed not only adhered chips but also abrasive grains and bonds together.

3. High-efficient cutting off of SIALON ceramics with in-process cleaning

Cut-off grinding of SIALON ceramics was carried out with in-process cleaning. Fig.3 shows the experimental system. To clean the grinding wheel steadily during cutting, we sticked SIALON ceramics specimen on a plate of the FRP cleaner and cut both plates together in process of grinding. Table 1

shows experimental conditions. The stock removal rate Z' was set very high at 13 $mm^3 \cdot mm^{-1} \cdot sec^{-1}$.

Figure 4 shows 'vertical grinding force' on the SIALON specimen receiving from grinding wheel. When the FRP cleaner was used Fig.4 (a), the grinding force was about 170N and the average grinding ratio exceeded 300, as shown in Fig.5. It is also indicated that cyclic cutting proceeded in a stable condition. When no cleaning was added, the grinding force which is seen in Fig.4 (c) rapidly increased in proportion to the number of cutting owing to loading and exceeded 500N at the fourth cutting. It is obvious from these results that the FRP cleaner is effective in cleaning grinding wheel surface. In case of the GC dresser of Fig.4 (b), since diamond abrasive grains are forcibly fractured and released in short cycles, the grinding ratio significantly decreased about 40, although sharp abrasive grains are always exposed to the surface and the grinding force becomes stable at low levels about 110N.

4. Cleaning mechanism of FRP Cleaner

Bottom of cut grooves were observed by a SEM (Fig.6 and Fig.7). In case of FRP cleaner, it can clearly be seen that the snapped glass fiber has come away from the bottom surface. In the GC dresser, it was confirmed that there were many destructions of vitrified bond and falling down of whole SiC grains.

From these observations, we suppose the mechanism of FRP cleaning and GC dressing as illustrated in Fig.8. A diamond grain will fracture the glass fiber of the FRP cleaner to small size and the yielded soft fiber-chips remove only ground chips. In case of GC dresser, a diamond grain will break the vitrified bond on the boundary of sintered SiC grain, so that the fallen-off SiC grains give much mechanical damage to diamond grains because of its hardness.

5. Conclusions

1) Cleaning can be realized for diamond grinding wheel with FRP cleaner.
2) Truncated diamond grains are observed in FRP cleaning test.
3) FRP cleaner enables high-efficiency and high-grinding-ratio grinding of difficult-to-grind materials.

The cleaning technique is thus effective in grinding difficult-to-grind materials, and will be suitably applied to ultra precision grinding processes.

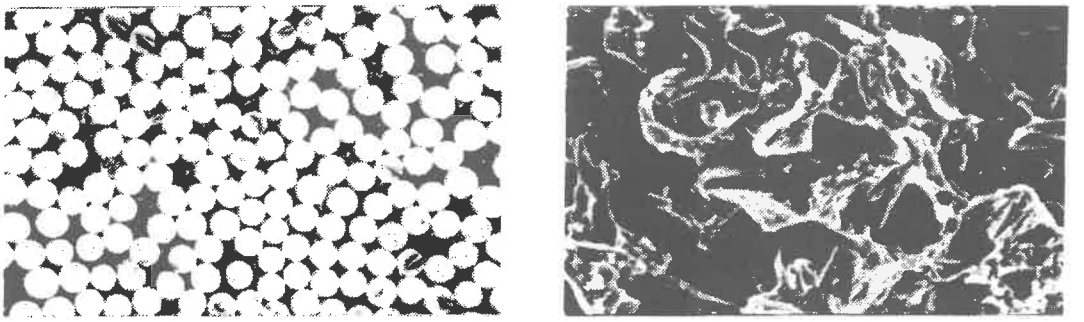

(a) FRP Cleaner (b)GC dresser 50 μm

Fig.1 SEM photograph of the closs section

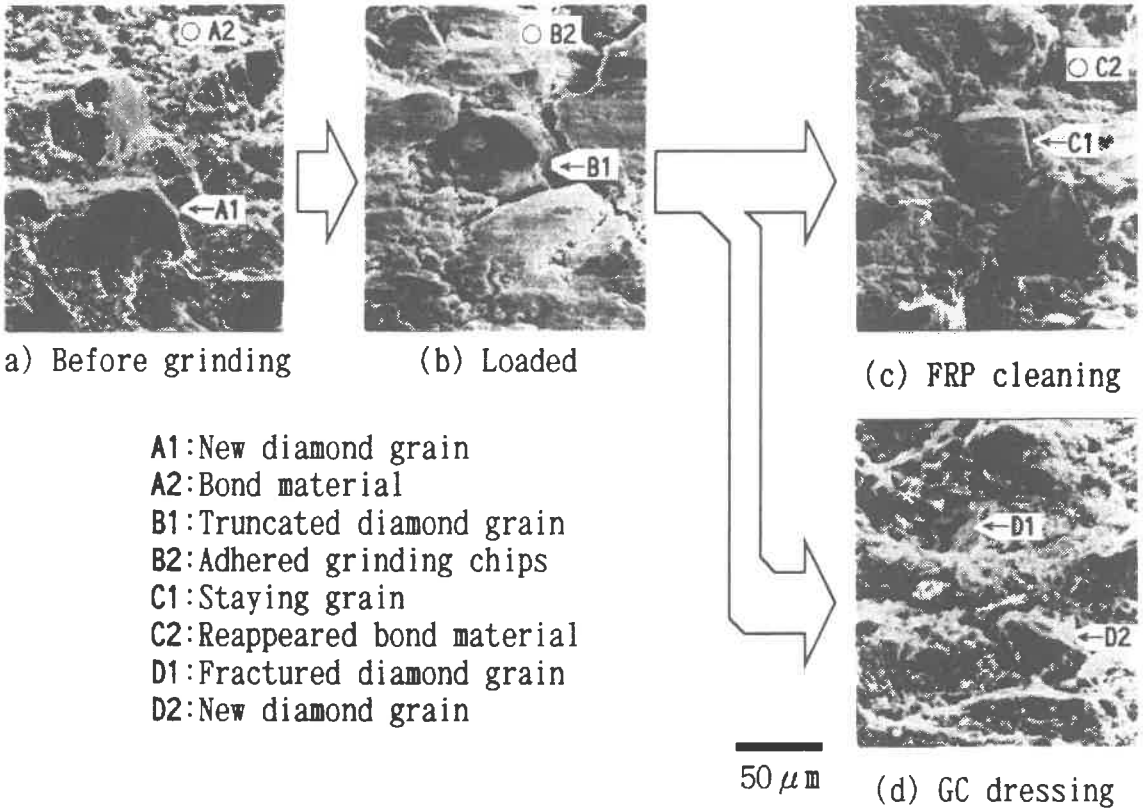

(a) Before grinding (b) Loaded (c) FRP cleaning (d) GC dressing

A1:New diamond grain
A2:Bond material
B1:Truncated diamond grain
B2:Adhered grinding chips
C1:Staying grain
C2:Reappeared bond material
D1:Fractured diamond grain
D2:New diamond grain

Fig.2 Comparison of diamond wheel surfaces

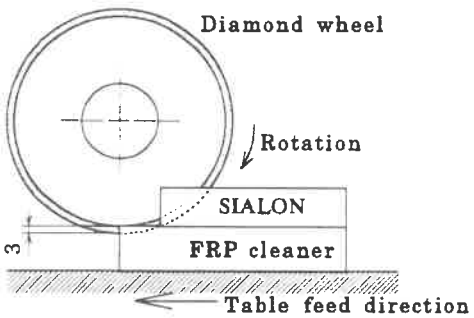

Fig.3 Experimental system

Table 1 Experimental conditions

Diamond wheel	SDC140N100B
Work piece	SIALON ceramics
Adhesive	Wax
Creep feed grinding	Down cut
Table feed rate	80mm/min
Peripheral speed	1000 m/sec
Coolant flow rate	45 l/min

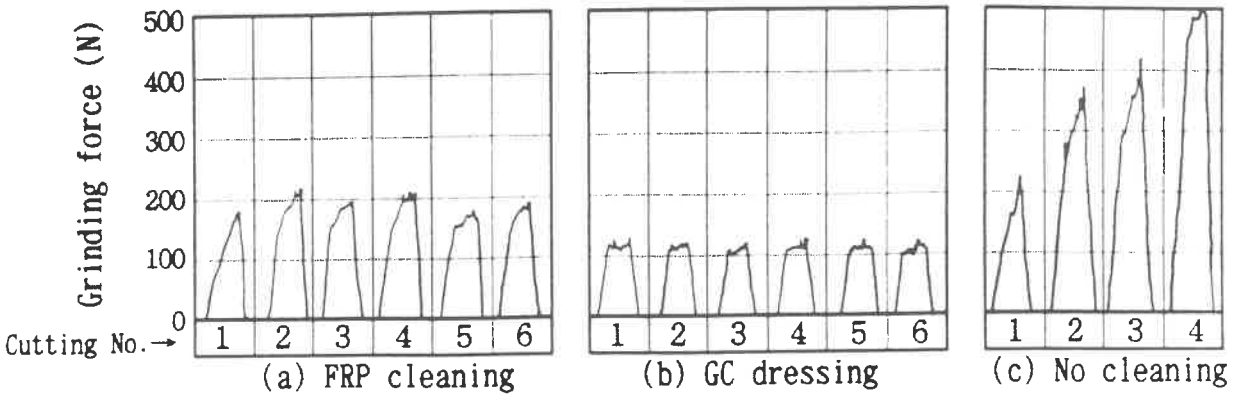

(a) FRP cleaning (b) GC dressing (c) No cleaning

Fig.4 Comparison of grinding force

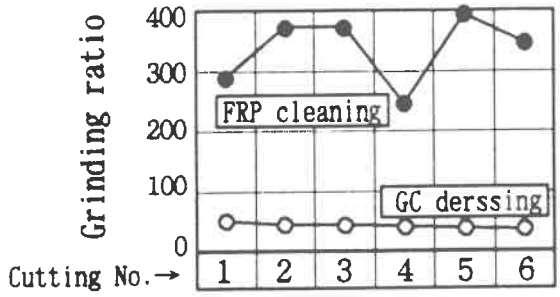

Fig.5 Comparison of grinding ratio

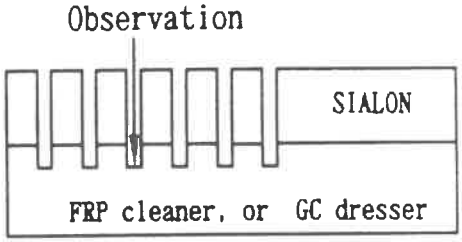

Fig.6 Observation direction

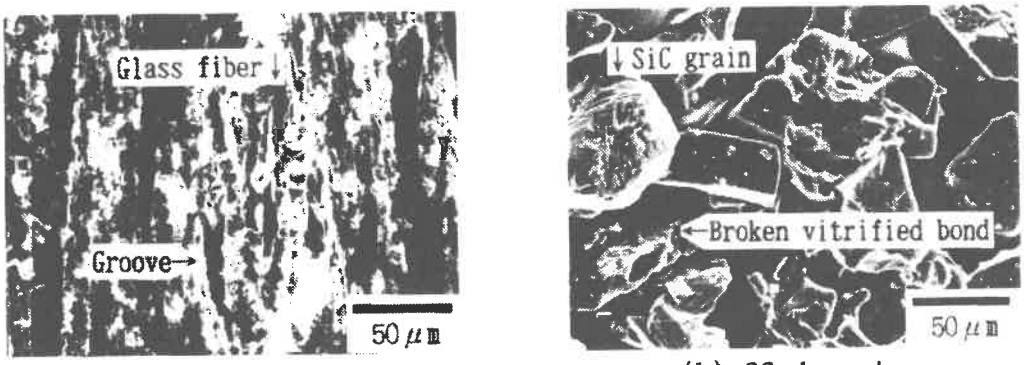

(a) FRP cleaner (b) GC dressing

Fig.7 SEM observation of groove bottoms

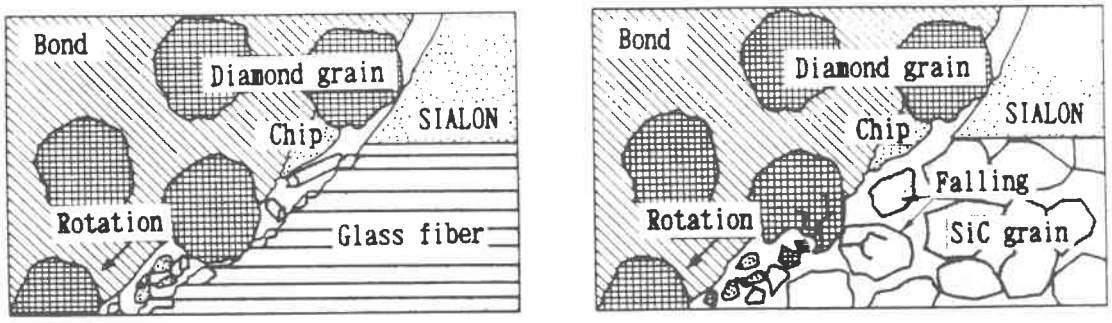

(a) FRP cleaner (b) GC dressing

Fig.8 Comparison of mechanism

MACHINABILITY/MATERIAL PROPERTY CORRELATIONS IN HYDROGEL POLYMERS

D.B. Mackay*, Y-W. Mai+ and P.S. Lingard*
* Eycon Lens Laboratories Pty Ltd, Lane Cove NSW 2066
+ Department of Mechanical Engineering, The University of Sydney NSW 2006 AUSTRALIA

Introduction

pHEMA Hydrogel based polymers and co-polymers are commonly used in contact lens manufacture by diamond turning. Although machining optimisation studies have been reported for engineering polymers [1;2;3], such as PMMA, there has been no reported work on hydrogel polymers for opthalmic use.

In contact lens manufacture an optical finish is obtained on the lens surface by diamond turning and polishing. Many factors affect the machinability of hydrogels.

We are here concerned with optimising the machining conditions for several hydrogel polymers, i.e feed rate, depth of cut, rake angle and linear cutting velocity. We also examine whether critical rake angles apply for hydrogels as reported by Kobayashi during orthogonal machining [1] and whether there is a critical depth of cut as reported by Puttick et al. [4].

Hydrogel polymers are available in a range of hydrated water content and are machined dry in manufacture, allowance being made for dimensional changes upon hydration. It seemed possible that with increasing hydrated water content, the dry polymers might become increasingly brittle, limiting the range of machining conditions within which ductile machining occurs. In this report the results of material machinability testing are correlated with mechanical properties of the hydrogels.

Experimental Methods

Mechanical Property Testing

Mechanical testing of a range of hydrated water content hydrogels was carried out in the dry state. From these tests information on Young's modulus, compressive yield strength, fracture toughness, tensile strength and hardness was collected. Additionally, glass transition temperatures were found using a DSC.

Machinability Study

A manually operated production lathe was instrumented to allow precise control of the machining parameters. This lathe possesses a precision roller bearing spindle drive with a magnetic coupling. The lathe was computerised to control feed rate, depth of cut and cutting speed, as well as recording cutting forces in three orthogonal

directions, using a three axis force transducer with specially designed tool post. A precision servo-driven x-y table replaced the quadrant of the production lathe (positioning accuracy ±0.1 μm). The cuts were performed as a facing operation using a diamond tool of 0.75 mm nose radius. Rake angle was varied between tests.

As cutting forces for diamond turning of hydrogels were below 10 N, force measurement to below 0.1 N was required. Thermal insulation as well as cross-talk correction were necessary in order to achieve accurate measurement from the force transducer.

Surface finish of the machined specimens was measured using a Talysurf 5 instrument, and their surfaces inspected using scanning electron microscopy.

Results

For the majority of tests the cutting forces did not vary by more than 20% between materials although some mechanical properties varied considerably (Table 1).

Rake angle

Increasing rake angle from -10° to +18° causes cutting forces to decrease by 30% in the direction of cut, while the normal force drops by 50%. Forces in the direction of traverse were constant for all rake angles. The critical rake angle, defined by Kobayashi [1] as the tool rake angle where the normal cutting force is zero, was not found for the range of rake angles used. As we are using a facing cut rather than an orthogonal cut, rake angle variation does not have as great an effect. Additionally, large positive rake angles were not achievable due to problems in obtaining a sharp edge on a diamond with this geometry.

The surface roughness is not significantly affected by changes in rake angle unless pitting occurs due to brittle fracture. Some of the more brittle hydrogels exhibited this brittle fracture at large positive rake angles (Fig 3(b)).

Depth of Cut

Cutting forces increase linearly with depth of cut for all the tested materials while the surface roughness remains fairly constant. Depths of cut greater than 1 mm generate large amounts of heat leaving a cloudy, slightly burnt surface.

Feed rate

Increasing the feed rate also increases cutting forces linearly. Surface finish is improved by reducing the feed rate. Between 45 and 65 μm/rev the Ra (average surface roughness) is approximately the same as the theoretical surface roughness. Theoretical Ra depends only on tool nose radius r and feed rate f [5]:

$$Ra = f^2/32r$$

With decreasing feed rate the Ra approaches a minimum, beyond which further decrease in feed rate will not improve the surface finish (Fig. 1). A Minimum surface roughness of 25 - 35 nm was obtained with most of the materials. This is limited by spindle vibrations, tool sharpness and material properties.

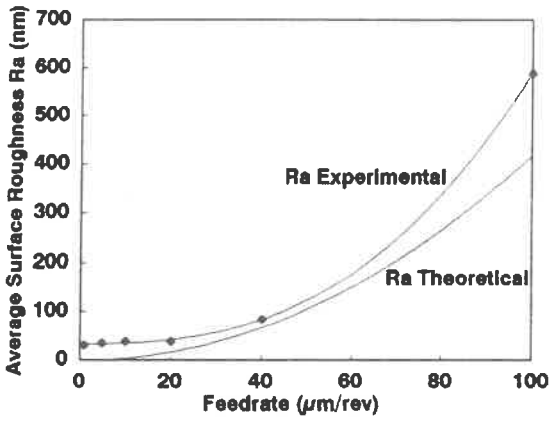

Figure 1 Theoretical and experimental Ra values

Linear Cutting Speed

Cutting speeds of up to 265 m/s applied during testing. The cutting force is independent of cutting speed for a constant feed rate. Surface finish was not significantly affected by cutting speed.

Size effects and brittle fracture

A considerable amount of work has been done in the area of ductile-brittle transitions in ceramics [7;8], however brittle polymers have largely been overlooked. When machining brittle materials it is important that material is removed via ductile flow processes rather than by brittle fracture [9]. Puttick et al. [4] proposed a critical linear dimension of stressed volume of material d_c , based on size effects [6] , below which brittle fracture will not occur, ie:

$$d_c=\alpha ER/\sigma_y{}^2$$

Where E is Young's Modulus, R the fracture toughness and σ_y the yield stress for plastic flow. α is a numerical parameter dependent on the type of test.

Table 1 shows the properties of the different hydrogels and their experimental critical linear dimension for brittle fracture. In a facing cut the feed per revolution (f) is the dimension corresponding to d_c, but the depth of cut also influences brittle fracture. α is dependent on the machining conditions and averaged 0.36 in this study.

The relationship between the predicted critical linear dimension (d_c) and the experimental values, are shown in Figure 2 for several hydrogels and PMMA. Polymers with high fracture toughness and low compressive yield strength are less susceptible to brittle fracture and therefore higher feed rates can be used. Those with low fracture toughness must be machined at low feed rates. Figure 3 shows typical SEM micrographs of machined surfaces. When the feed rate is less than the critical feed rate (Fig 3a), no brittle fracture occurs and when the feed rate exceeds the critical

feed rate the characteristic pits of brittle fracture occur (Fig 3(b)).

Table 1

Material	Water Content %	E Young's Modulus (GPA)	σ_y Yield Stress (MPa)	R Fracture Toughness (J/m^2)	Theoretical Critical Feed Depth (μm/rev)	Experimental Critical Feed Depth (μm/rev)
V38H	38	2.82	129	94	6	8
V55H	55	3.54	146	140	8	10
V60	60	2.96	64	785	204	100
V75H	75	3.82	148	224	14	20
PMMA	0	3.50	60	640	224	115

Conclusion

A correlation has been drawn between the mechanical properties of hydrogels and their machinability, in terms of the critical linear dimension for brittle fracture d_c. Cutting forces and surface roughness have been analysed. From these tests a range of optimum machining conditions were found for different hydrogels.

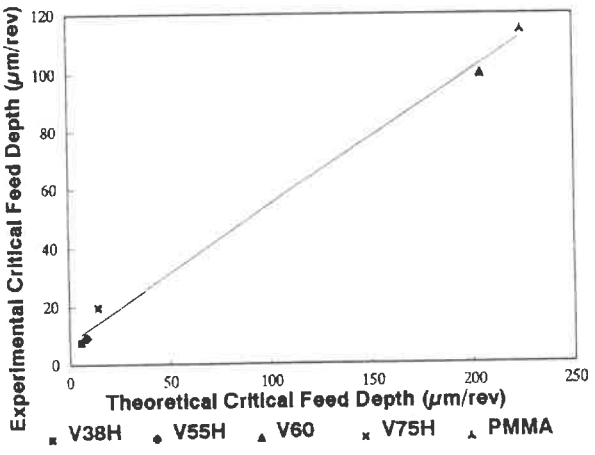

Figure 2 Theoretical and experimental critical feed rate

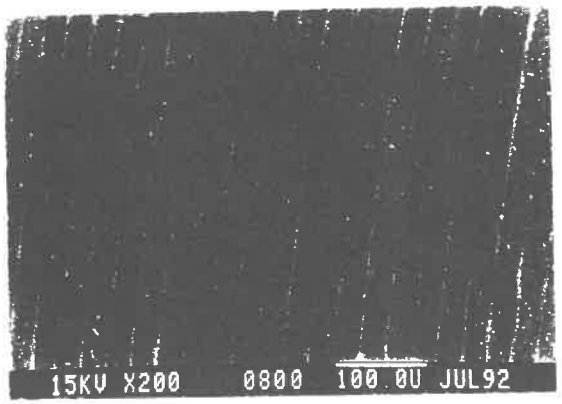

a

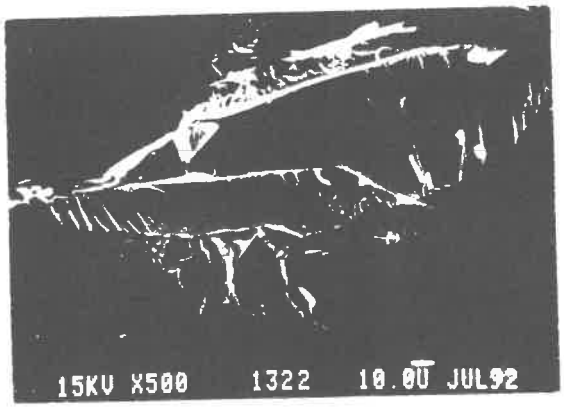

b

Figure 3 (a) Surface obtained from elastoplastic flow (b) Surface obtained due to elastic fracture

Acknowledgements

This project was made possible through financial support from the Commonwealth National Teaching Company Scheme.
The authors are grateful to Steve Payor for his contributions to the machine control software, and the mechanical design and construction of the NC machinery.

References

1) Kobayashi, A. Machining of Plastics, New York : McGraw Hill, 1967.

2) O'Brien, P., Thompson, W. and Russel, J.K. "A statistical model for predicting surface texture of machined thermo plastics," *Annals of the CIRP*, 1977, **25**, 339-344.

3) Young, A.E and Wilson, J.H. "The critical rake angle in the machining of plastics," *Plastics and Rubber: Processing*, September, 1978, 77-84.

4) Puttick, K.E., Rudman, M.R., Smith, K.J., Franks, A. and Lindsey, K. "Single point diamond machining of glasses," *Proc. R. Soc. Lond.*, 1989, **A 426**, 19-30.

5) Whitehouse, D.J., Vanherck, P., de Bruin, W. and van Luttervelt, C.A. "Assessment of surface typology analysis techniques in turning," *Annals of the CIRP*, 1974, **24** , 265-273.

6) Atkins, A.G. and Mai, Y-W. Elastic and Plastic Fracture, Chichester : Ellis Horwood, 1985.

7) Schinker, M.G. "Subsurface damage mechanisms at high-speed ductile machining of glasses," *Precision Engineering*, 1991, **13**, 208-218.

8) Becker, K. "Single point diamond turning of brittle and hard materials," Presented at the 5th International Precision Engineering Seminar, Monterey, CA, September 18-22, 1989.

9)Nakasuji, T., Kodera, S., Hara. S. and Matsunaga, H. "Diamond turning of brittle materials for optical components," *Annals of the CIRP*, 1990, **39**, 89-92.

ULTRA THIN BONDED SINGLE CRYSTAL SILICON-ON-INSULATOR WAFERS USING MeV ION IMPLANTED PRECISION ETCH STOPS

P. P. Pronko and A. Ezis
UES, Inc.
Dayton, OH 45432

Full 100 mm diameter wafers with a nano-structured layer of high quality single crystal silicon-on-insulator (SOI) are fabricated using bonded wafer technology in conjunction with mechanical thinning and a new approach to the placement of precision etch stops. Definitive chemical etch stop action is provided by the use of raster scanned MeV ion implantation for the precise placement of uniform high concentrations of boron that act as P^{++} barriers to the etch process. This technique eliminates the use of a more conventional approach that might involve the use of a combination of doped and undoped epitaxial layers with their associated poorer thickness uniformity. Increasing interest has been expressed in the use of SOI material for integrated circuits if a high degree of thickness uniformity in the layered silicon material and its underlying oxide can be achieved. The semiconductor chip community makes use of such SOI material for ultra-fast, high density and radiation hardened circuits. A process sequence has been developed in our lab which has as its goal SOI material with thickness parameters of approximately 100 ±5 nm ultra high quality single crystal silicon on silicon dioxide of comparable thickness. Figure 1 is a diagram of this final structure.

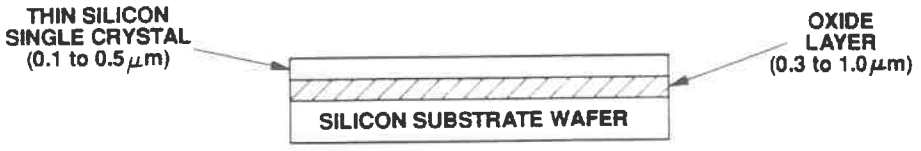

Figure 1. Silicon-on-Insulator Structure.

The method being described uses a double high energy (MeV) ion implantation sequence for placing appropriate etch stops. The second, or retro MeV implant, is applied after the first stage of etch back and stop process as a method for improving the uniformity of the final SOI film. The need for a double implant approach is associated with the shape of the MeV boron depth profiles and the need for a low concentration of boron in the final thinned silicon layer. Figure 2(a,b) is a schematic diagram of how the double implant technique is utilized. The first high energy boron implant provides a dose of 6×10^{15} cm^{-2} at an energy of 2.5 MeV. This produces an etch stop boron peak at approximately 3.2 μm below the oxide-silicon interface. After the silicon is thinned, first with mechanical thinning, and then in an EPW etch (ethylenediamine-pyrocatechol and water) to this 3.2 μm level, a second implant from the back side (i.e., through the etched surface) with 1.7 MeV boron to a dose of 6×10^{15} ions/cm^2 provides a new etch stop at a depth of approximately 0.8 μm below the oxide-silicon interface. The first implant carries a direct topographic image of the original silicon surface which is at the SiO_2-Si interface. The second implant is in registry with this, and, therefore, reproduces the front surface topography. After arriving at this level with a second EPW etch, the material is further thinned with a selective etch of 1-3-8 ($HF:HNO_3:CH_3CO_2H$) to remove the P^{++} layer. This etch stops at a P^+ boron concentration that is approximately 500 nm from the silicon - SiO_2 interface. Further thinning and smoothing of the silicon is accomplished with an oxidation stripping procedure which provides for careful control of the final thickness of the silicon device film. Optimization of this procedure is expected to ultimately provide 100 nm ±5% uniformity.

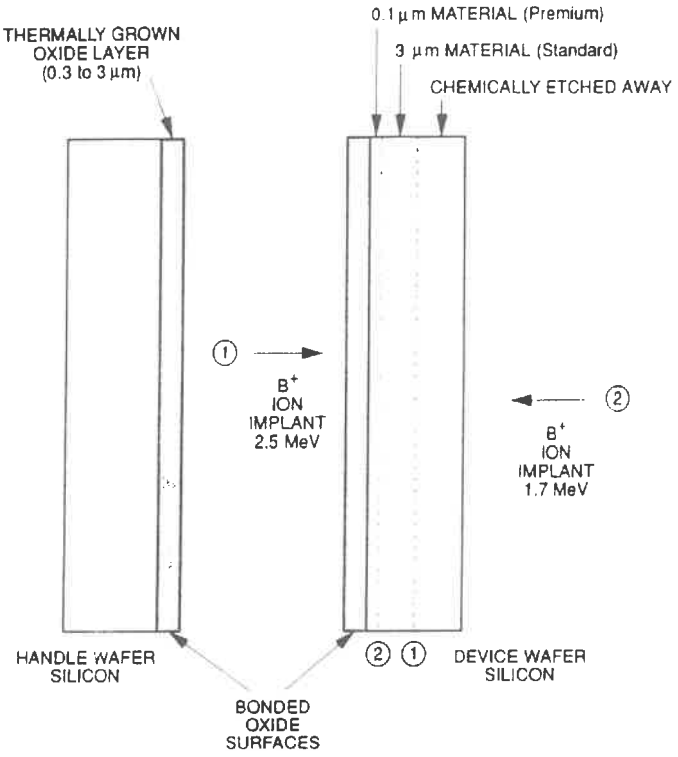

Figure 2a. Retro-Implant Procedure. 1) Denotes First Implant and Placement of Etch Stop, 2) Denotes Second Implant and Placement of Etch Stop.

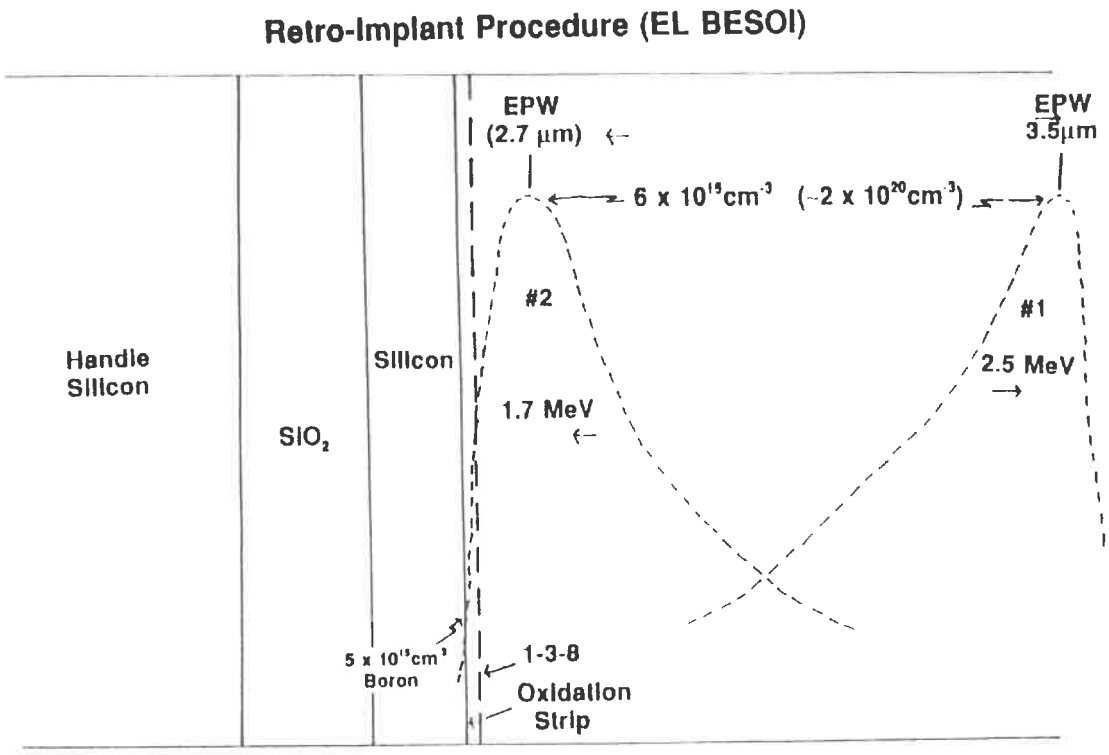

Figure 2b. MeV Implant Profiles as Depicted in Figure 2a.

Figure 3 is a cross-sectional transmission electron micrograph (TEM) of the silicon wafer material in the region where the MeV implant occurred. The figure shows the material after annealing at 1100°C for 2.5 minutes. Prior to annealing it is observed that there is a finely dispersed band of tiny defect clusters centered around 3.5 μm in depth having a distributional full width of about 0.5 μm. This represents the end of range damage for the 2.5 MeV implant. The presence of this high boron level (maximum concentration of 2×10^{20} cm^{-3}) introduces sufficient lattice strain after annealing (due to the undersized radius of boron compared to silicon) to cause plastic deformation of the silicon in the region of the peak boron concentration. When the material is annealed at 1100°C, as shown in Figure 3, the radiation damage from the ion implant process is removed, the boron takes up electrically active substitutional lattice sites, and the silicon undergoes limited strain-relief plastic deformation to accommodate the internal stresses from the boron. The resulting array of localized dislocation loops is seen in the post annealing micrograph of Figure 3. It is also noted that between the region where this defect band exists and the surface of the material, where the final thinned material will reside, there are no observable residual defects.

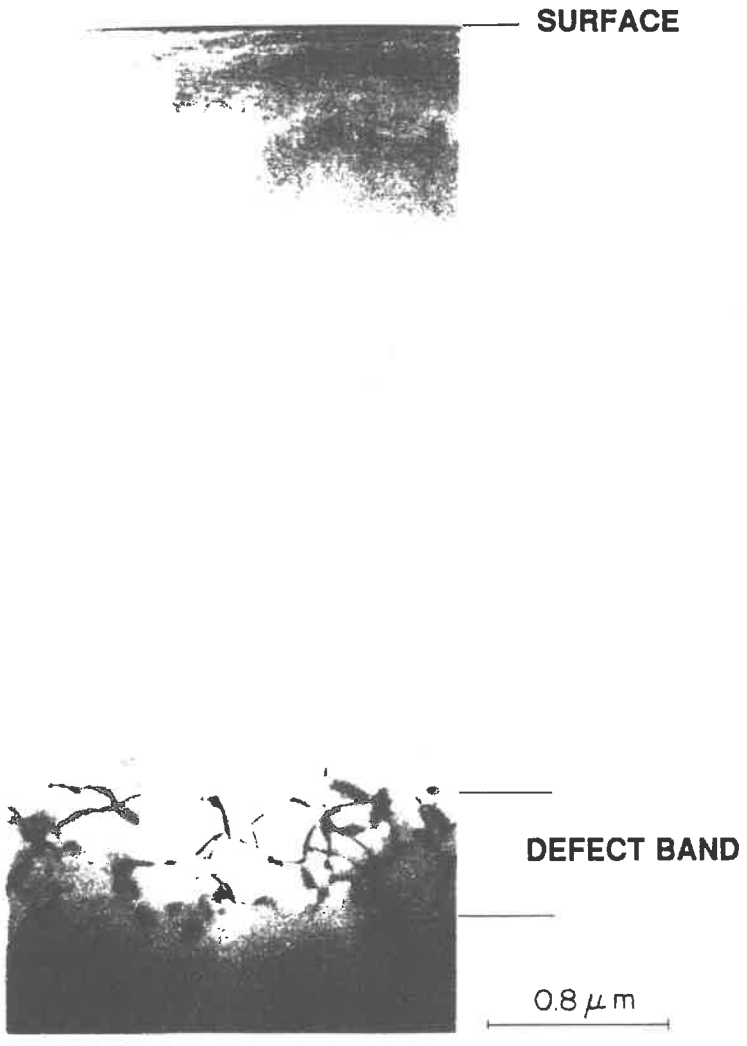

Figure 3. Cross-sectional TEM after High Temperature Anneal (1100°C for 2.5 min.).

The fabrication sequence employed in making our ultra-thin laminated structures uses a combination of mechanical and chemical thinning techniques. The following sequence describes our process and the thinning stages achieved at each major processing step.

1. Two identical silicon wafers are first oxidized with the substrate or handle wafer being given an oxide approximately ten times thicker than that of the machined or device wafer. Usually 3000Å vs. 300Å of SiO_2, respectively.
2. The device wafer is ion implanted with a P^{++} etch stop such as boron at 2.5 MeV to a dose of approximately 6×10^{15} cm^{-2} and annealed to activate the dopant. The peak of the boron distribution will reside at about 3.2 μm below the oxidized surface (Figure 2b).
3. The wafers are bonded by physically joining the SiO_2 surfaces face to face then annealing to sinter the interface into a continuous material.
4. The back side of the wafer is then mechanically lapped to a thickness of 50 μm using diamond tipped stops on the lapping carrier. This is followed by a polishing step to remove approximately 4 μm additional material to clean, smooth and remove lapping damage from the surface of the sample.
5. Chemical etching is performed in a refluxed EPW bath at 120°C under inert atmosphere which provides a removal rate of approximately 1.5 μm/hr. This material removal step abruptly terminates when the retreating surface reaches the peak of the ion implanted boron profile which represents a transition from high resistivity silicon to heavily doped P^{++} silicon. The thickness uniformity of the etched material is critically dependent on the placement precision of the boron etch stop. Uniformity of the lateral concentration and depth of implant is critical in this regard. Since the depth of the first implant carries a topographic image of the original silicon surface, the back side after etching will also carry this same image after etching.
6. A second implant is then performed through the etched back surface at 1.7 MeV to a total fluence of 6×10^{15} cm^{-2} producing the second etch stop profile as shown in Figure 2b. The symmetry of this second profile is the reverse of the original implant and provides a very sharp drop off in boron concentration near the final surface of the sample.
7. After thermal annealing, to activate the boron, a final etch is performed with KOH/IPA down to the peak of the second implant where upon it too abruptly terminates. Further controlled removal of material is accomplished with a selective 1-3-8 ($HF\text{-}HNO_3\text{-}CH_3CO_2H$) etch which leaves an etched thickness of approximately 500 nm at approximately 10^{18} cm^{-3} concentration of boron.
8. Final thickness control and finish is obtained through a carefully monitored oxidation process which consumes silicon in a ratio of 1 SiO_2 to 0.45 silicon. This oxide layer is then stripped in HF to provide the final thin SOI of 100 nm thickness. The selectivity and precision of the various etching steps will determine the final thickness uniformity.

To date our material has been made to a thickness of 484 nm with a standard deviation ±4 nm. We are actively pursuing the goal of 100 ±5 nm, and expect to achieve that in the near future. These results are to be compared with data obtained on similar material fabricated using boron doped epitaxial layers that are strain compensated with germanium to eliminate threading dislocations in the final high resistivity silicon layer. In that case we obtain thicknesses of final SOI material that are measured, with 1σ variations, at 413 ±7.5 nm. The consequence of thickness variations in an engineering application require that uniformities be quoted in 3σ rather than 1σ values. This is the difference between 99.7% and 68% confidence limits on actual material. Thus, total thickness variations across the material at 3σ will be 150 Angstroms variation in our 5 nm (1σ) material.

Characterization of the material manufactured by the above method is now underway. Breakdown voltage of the buried oxide is occurring at 300 volts compared to 325 volts for a dry oxide standard. Further evaluation of material quality relative to pin holes, dislocations, or residual etching effects are under study as is the materials response under ionizing irradiation. Use of this material for radiation hardened circuits is a major applications area.

Surface Characteristics of Ion Milled CVD SiC

Steven C. Fawcett and Robert W. Rood

Optical Systems Branch, EB23
National Aeronautics and Space Administration
Marshall Space Flight Center, AL 35812

Thomas W. Drueding and Thomas G. Bifano

Aerospace and Mechanical Engineering
Boston University
Boston, MA 02215

Chuck Egert

Optics Modil
Oak Ridge National Laboratory
Oak Ridge, TN 37831

Introduction

Ion figuring of optical components is a relatively new technology that can alleviate some of the problems associated with traditional contact polishing. Because the technique is non contacting, edge distortions and rib structure print through are not a problem. This investigation was aimed at determining some of the basic parameters involved with using ductile grinding in combination with ion figuring to produce finished optical components. The primary areas of consideration were the material removal rates and the resulting surface finishes. Multiple chemical vapor deposited silicon carbide (CVD SiC) samples that have been polished or ductile ground to angstrom level surfaces were characterized to determine the topographic surface information. The surface evaluation consisted of stylus profilometry, interferometry, optical and scanning electron microscopy. These surfaces were then ion machined at specific material removal depths. The finished surfaces were characterized to evaluate the effects of the ion machining process with respect to the material removal rate and the previous processing technique. This study provided some of the information required to effectively utilize a combination of ductile grinding followed by ion machining as a primary figuring procedure for optical components.

Machining Rate

The apparatus used in the ion figuring experiments is described in a separate article [1]. This equipment consisted of a 3 centimeter diameter ion source and a translation stage system within a vacuum environment. The initial experiments were performed on the substrates to determine the material removal rates for given beam parameters. The ions were produced from Argon gas with the parameters listed in Table 1.

The CVD SiC samples used in these experiments were obtained from Morton International Advanced Materials and were 3 mm thick. The polished samples were 3 cm diameter and the ductile ground samples were 6 mm wide rectangular pieces. The polished samples were processed by lapping with an oil based diamond compound. The lapping was done in steps starting with 15 µm diamond and proceeding through 9, 6, 3 and 1/2 µm. The processing only continued as long as required to remove the visible scratches from the previous steps. The final polishing at the smaller grit sizes was continued for the times and grit sizes listed in Table 2.

The ductile ground samples were sliced from pieces of CVD SiC from the same batch as the polished samples. They were then mounted on steel sample holders and ground in the ductile regime. The grinding was performed by Yuan Yi at the Ultraprecision Grinding Research Laboratory at Boston University. A 4 - 8 µm resin bonded diamond wheel (with the

exception of samples "9" and "10" which used a 180 μm bronze bond diamond wheel) running at 3600 RPM with deionized water coolant was used throughout. The other grinding parameters for each sample are summarized in Table 3.

Parameter	Value
Cathode Current	4.3 A
Discharge Current	0.6 A
Discharge Voltage	40 V
Beam Current	40 mA
Beam Voltage	1000 V
Accelerator Current	2 mA
Accelerator Voltage	150 V
Neutralizer Current	50 mA
Filament Current	4.1 A
Source Distance	8 cm
Pressure	1.4×10^{-4} torr

Table 1 Ion source operating parameters.

Sample	Grit Size	Time
A	1/2 μm	35 min
B	1/2 μm	10 min
C	3 μm	*
D	1/2 μm	40 min
E	1/2 μm	60 min
F	3 μm	*

Table 2 CVD SiC polishing parameters (* time not recorded, processed to remove visible scratches from 6 μm step).

Sample	# of cuts	Infeed	Crossfeed Rate
5	5	250 nm	2.6 μm/rev
6	6	200 nm	2.6 μm/rev
7	6	250 nm	5.2 μm/rev
8	7	250 nm	3.5 μm/rev
9*	15	500 nm	5.2 μm/rev
10*	7	250 nm	3.5 μm/rev

Table 3 CVD SiC ductile regime grinding parameters (* ground in the brittle regime).

Machining Rate

The initial experiments were performed to determine the beam current profile and hence the relative material removal rates with respect to its center. In this experiment, a circular sample was located beneath the ion beam so that the edge of the sample would correspond with the point of maximum intensity. One half of the sample was masked to provide a reference surface for step height measurements. After the sample was ion machined for a specified period the relative height differences between the surfaces was measured and normalized with respect to time. Figure 1 shows a plot of the measured machining rate versus the distance from the beam center. This gaussian profile was used to provide varying depths for the surface characterization study.

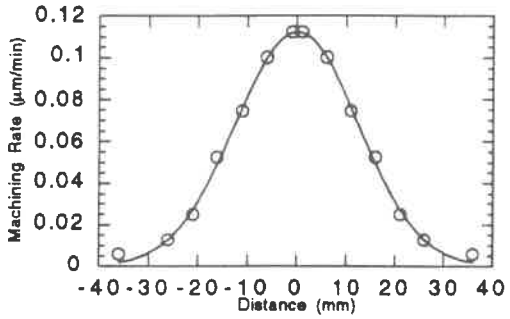

Figure 1 Machining profile of 3 cm ion source.

Surface Characterization

Once the samples were polished or ground, surface characterization measurements were made. Unmagnified, visual examination revealed no scratches or pits in any of the samples (with the exception of the brittle ground sample "9"). Optical microscopy to 400 X only revealed an occasional fracture location and the grooves caused by the grinding crossfeed. Also, the samples were viewed with a scanning electron microscope (SEM). These pictures again revealed the grinding crossfeeds and occasional fracture sites. There were small (≈ 100 - 200 nm diameter) discontinuities visible in the SEM

micrographs of the ductile ground samples. On all the polished samples, small (≈ 100 nm wide) scratches became visible. The two samples that were not processed with the 1/2 μm diamond (samples "C" and "F") revealed a significantly greater amount of polishing marks. It should be noted that the marks on sample "C" were oriented in a certain direction while on sample "F" the marks were random. The directionality of the features on "C" may be due to a error in processing where the sample failed to rotate during lapping.

All the samples were measured to determine the surface roughness parameters prior to ion machining. An initial attempt to use a Talysurf for these initial measurements proved futile when it was determined that the surfaces finish of the samples was better than the resolution of the instrument. The initial measurements were then made on a Wyko optical profilometer to determine the surface roughness. Multiple measurements were made for each sample and the results averaged. The RMS values ranged from 7.56 Å to 12.77 Å for the polished samples and from 12.87 Å to 35.68 Å for the ductile ground samples. The brittle ground sample ("9") had an average RMS roughness of 321.5 Å.

Results

After evaluation, the samples were ion machined in a static position so that the total depth profile would correlate with the profile of Figure 1. Various times were used so that a range of total depths would be achieved. The polished samples all revealed visible scratches after only a few minutes under the beam. When examined under an optical microscope, some of the samples showed extensive damage at the larger machining depths which tapered off as the total depth was decreased. The damage is shown in Figure 2. This micrograph reveals the hemispherical pits uncovered by the ion machining process.

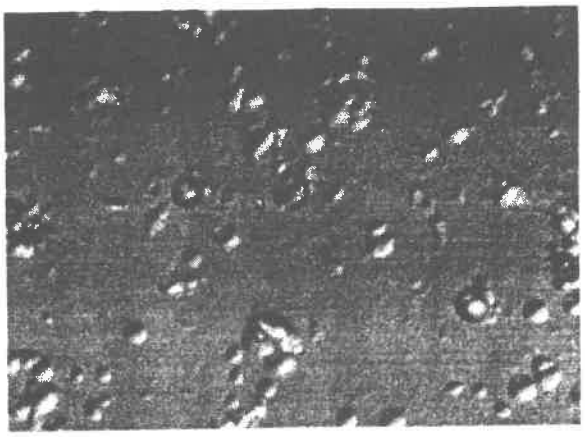

Figure 2 Optical micrograph of polished CVD SiC ion machined to a depth of 4.5 μm (Sample "B" at 400 X).

The pits in Figure 2 are believed to have been formed at the sites of sub-surface damage caused by the loose abrasive polishing with the larger grit diamond. The size of the pits are approximately 10 to 20 μm diameter which corresponds to the fracture size expected from the initial polishing stage with 15 μm diamond. Because of the lack of a controlled polish, it is likely that the fractures from previous grit sizes was not completely removed in subsequent steps and was left as sub-surface damage. This damage was then uncovered by the ion figuring. The almost perfect hemisphere shape of these pits initially led the investigators to believe that these features were actually re-deposited material which coalesced on the substrate. After much deliberation and numerous profilometry traces, it was determined that the features were indeed pits. It is believed that these sites are formed when the lateral cracks caused by the forces of the individual diamond grits are uncovered. The initial lateral cracks may potentially propagate under the thermal loading inherent with the ion figuring process. The areal density of these fracture sites appears to directly correlate with the density of the ion beam current and hence with the machining depth.

The ground samples were also evaluated optically. The samples ground in the ductile regime showed only a few fracture sites in discrete areas of the samples. These areas appeared to correspond with areas which may have undergone some scratching during the grind and an example is shown in Figure 3. However, most of the areas were free of fracture as can be seen in the bottom portion of Figure 3. The pits shown range from 3 to 8 μm diameter which also seems to correspond to the diamond grit size of 4 to 8 μm. The brittle ground sample "10" showed a small amount of hemispherical pitting similar to what was shown in Figure 2 for the polished sample.

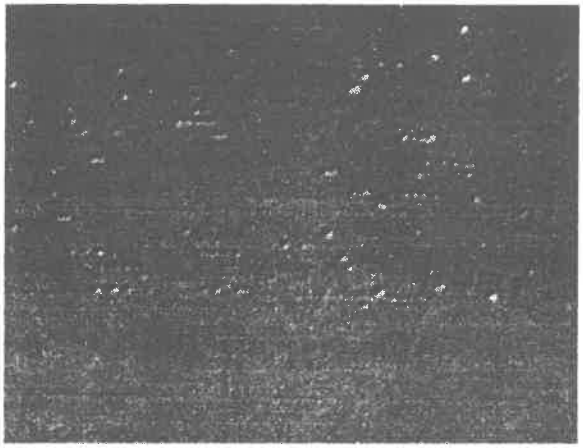

Figure 3 Optical micrograph of ductile ground CVD SiC ion machined to a depth of 3 μm (Sample "5" at 400 X).

Surface roughness measurements were also made on the figured samples. The samples with a large amount of pitting could not be measured with the optical profilometry. Therefore, all samples were measured with a Talysurf stylus profilometer. The results of these measurements are shown in Figure 4. This data was collected in four linear, 20 mm traces of the samples with no filtering. The RMS deviation from a linear fit was calculated over a 1 mm length of data which was then shifted in 0.5 mm steps over the entire 20 mm length. The 40 individual RMS data points from each trace were averaged and correlated with machining depth to arrive at the points of Figure 4. A linear fit to the data is also shown for visual clarity.

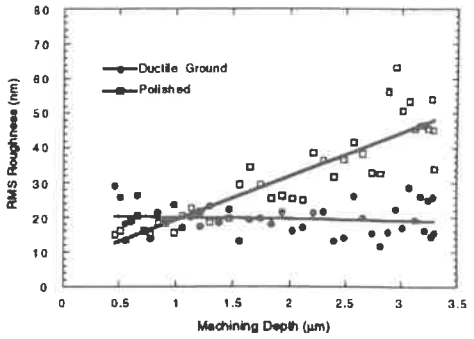

Figure 4 Surface roughness variation with ion machining depth. Polished sample "A" and ductile ground sample "5" ion figured 30 min.

This plot reveals that there is a significant increase in the surface roughness as a function of machining depth for the polished samples and no measurable increase for the ductile ground samples. This increase for the polished sample is primarily due to the subsurface damage sites which were opened as was shown in Figure 2. However, it should be noted that the resolution of the Talysurf is of the same order of magnitude as the measurements of the ductile ground samples (≈ 10 - 20 nm). It is felt that these measurements are therefore in the noise of the device and can not reveal the true variations of these ductile ground surfaces. Further studies of these surfaces are warranted.

References

1. Fawcett, S.C. and R.W. Rood, "Ion Figuring System for Segmented, Adaptive Optics", American Society for Precision Engineering Annual Meeting Conference Proceedings, October 1992.

PART MOUNTING REVISITED

P. Hannah, F. Garcia, D. Stewart
Los Alamos National Laboratory

Having been involved with single point diamond turning since the 1960's; I share with others of my age, a unique perspective of the craft. I am amazed at how the fundamentals seem to be forgotten or misplaced, and need to be re emphasized and re learned. Each new precision machine operator not only needs to re learn (many times the hard way), these fundamentals, but seems to inherit all the folklore; good and bad, from his predecessor. Let me explain.

I spend some of my time as a consultant to the shops' division at the Los Alamos National Laboratory, at which there are five precision turning machines divided between two buildings. The main shop area houses an old friction way (hydrodynamic) turning Machine. The base of this turning machine is made from the base of an old Moore measuring machine. The air bearing spindle, a "Red Head" was made by the Heald Machine Tool Co. With the addition of an Allen-Bradley Numerical control system, this machine has become a work horse, used primarily to make smooth flat surfaces in the fly-cutting mode (Fig.1).

Recently, I became involved in the evaluation and repair of the machine as it no longer produced smooth surfaces. Smooth surfaces are not the point of this narrative, accurate geometry however is.

In order to evaluate our progress, and provide a diamond turned part for comparison, we selected a piece of 6061 aluminum (Fig.2). We had it lathe turned to a diameter of 3.5 inches, and a thickness of approximate 1 inch. A groove 0.200 inches wide was turned 0.150 inches deep, 0.170 inches from the back surface. This continuous lip at the back of the part is used for clamping. The test part is then attached to the machined surface of a cast iron "precision" setup block, or knee. This then is mounted on the X-Axis table (Fig.1).

The fly-cutter assembly is mounted on the air bearing spindle, which usually holds the part as in "on axis" turning. Cutting is achieved by moving the X-Axis table past the rotating fly-cutter. Infeed (depth of cut) is achieved by moving the Y-Axis.

The operator attached the test part to the mount with 2 clamps 180 degrees apart. The clamps were strips of aluminum 1 inch wide and about one eighth of an inch thick. A hole was provided in each clamp so that by tightening the 2 bolts pressure could be applied to the clamps, and thus to the part (Fig.3).

Having no reason to check the operators work, the test part was cut for the evaluation of the machine repair. After cutting, the part was measured. Surface texture data and an interferogram were provided. The cosmetic quality was good for a fly-cutter, about 200 Å. P-V. However the interferogram showed the test part to be astigmatic with 2.2 λ of cylinder (Fig.4).

Suspecting distortion due to the mounting, we took the part to a surface plate and rubbed its back on a piece of fine lapping film. This revealed that the back surface was concave with 2 high spots or contact areas 180° apart (Fig.5). Laying the part on its face, we used a dial indicator to measure the back's concavity, which at it's deepest was 0.0013 inches. Further examination of the diamond turning marks on the front surface showed that the mounting clamps were placed by chance, exactly on the high area's axis, (The area not in contact with the mounting surface).

Now I am sure that this story, to many of you, may seem to belabor the obvious, but bear with me. The operator lapped the back of the test part flat until there was 360° of contact around the part's edge (Fig.6). The suggestion was made that due to the low cutting forces and shallow depth of cut (0.00005") maybe the mounting bolts did not have to be made quite so tight. Now the story gets more interesting.

You might think that based on the corrections to the part mounting that the next machine evaluation cutting test would go better. You would expect the part to be flatter, right? Wrong, this time the part had 2.5λ of cylinder (Fig.7). It turns out that "just snug" is not a quantitative term, and does not mean the same to every one. And what about the surface of the mounting knee?

As it turned out the knee was concave about 0.0005 inches, which is in the wrong direction. Let's see if any of you are awake, did you catch the potential flaw in our thinking? We lapped the part's back flat with 360° of contact at the edge only. The back should have been made flat over its entire area. Completely lapping the back and using a torque wrench solved the problem, as the part had less than a wave of cylinder after the next cutting. We should mention that on critical parts heat treatment is also a good idea.

Moving to another example we take a look at the use of the vacuum chuck. We were diamond turning Zinc Selenide domes that are used as the spherical protective IR window on the front of the Maverick missile (Fig.8). Zinc Selenide, although glass like, can be diamond turned. In fact the diamond turned material is stronger,

due to (we feel) less subsurface damage than conventionally ground and polished material.

The Zinc Selenide is vapor deposited on a spherical mandrel. This rough shell is then ground on an optical curve generator with a diamond cup wheel. It is this ground shell that we have to diamond turn. The first operation is to hold the part on a convex, male vacuum chuck (Fig.9). At this point the part is thick (aprox. 0.375 inches) and distortion is not a problem. The part's convex outer surface is now diamond turned. In the next machining we use a concave vacuum chuck, as the part is held on its diamond turned convex surface.

One would think that if we used the same N/C machine program on the same diamond turning machine on which we cut our part, with only the sign changed (convex to concave), we would get 2 surfaces that were very close to matching, and our part should be uniformly supported. It is at this point that we enter our story. After machining our concave "pot" we machined in several circular concentric and axial grooves that act as channels for the vacuum (Fig.10). After careful deburing of all the machined edges our chuck was ready for production machining, or so we thought. We had obtained a convex master optical 6 inch diameter "test plate" and monochromatic light source that we would use to measure the part's smoothness and radius on its concave surface. The test plate's size allowed us look at a large area of the diamond turned surface.

Armed with this measurement capability we carefully placed the part into the "pot chuck" and turned on the vacuum pump and started machining. As soon as the surface cleaned up (machined all over) we looked at it with the test plate. We thought that we would see circular fringes but were greeted with fringes that were anything but round. We were close to the specified radius as there were only a few fringes, but the non roundness showed that there was a serious distortion problem. The operator re machined the chuck several times before he gave up and called for help. Being a well-trained machinist he had tried every trick in the book, many of which like shimming, was not the thing to do!

One of the first things that we found was that the 2 surfaces were trying to go into optical contact but due to areas of "dirt" the contact was not uniform thus causing some part distortion. We began to see this as we introduced a controlled leak into the system (pulled less than an atmosphere). We soon realized that what we needed was indeed less vacuum. We machined an "O" ring groove near the outer edge of the chuck, and inserted a low durometer rubber "O" ring. By adjusting a "leak" valve we were able to

maintain about one quarter of an atmosphere and were able to successfully machine the part. This is made in part possible by the fact that the part was axially symmetric (centrifugal forces' uniform) and that the cutting force was also very low (a few grams at most).

This brings us back to the point of this whole story. It is so easy for us to assume that the machine operator, technician, or even an engineer understands the new set of rules' one must play by in the field of precision engineering. The answer is careful training and good communication. It is so easy to create a mythology, especially in a relatively new technology. Once learned this folklore is very hard to unlearn and if you are not careful will bite you when you least expect it.

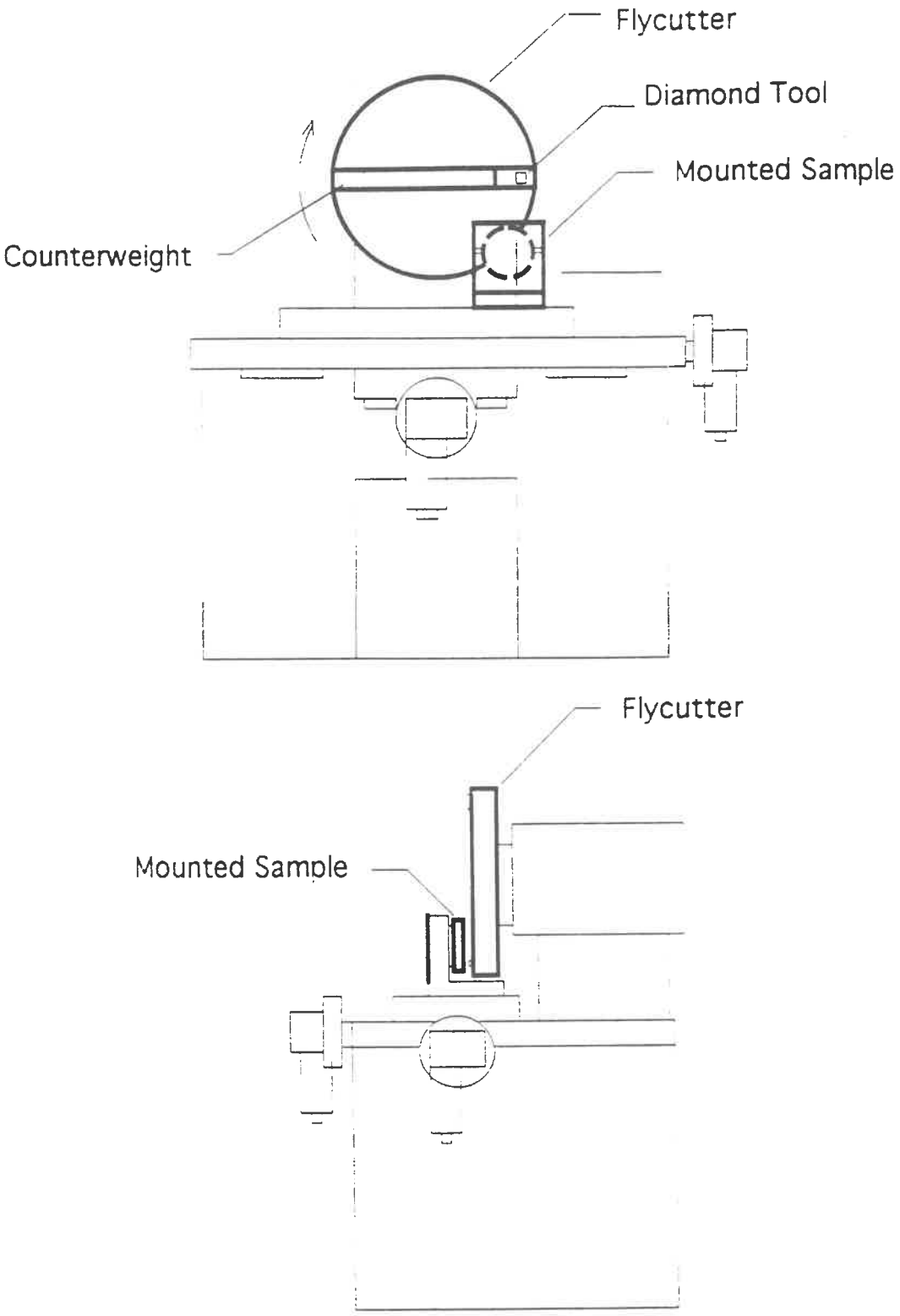

Diamond Turning
Machine Set-up

Figure 1

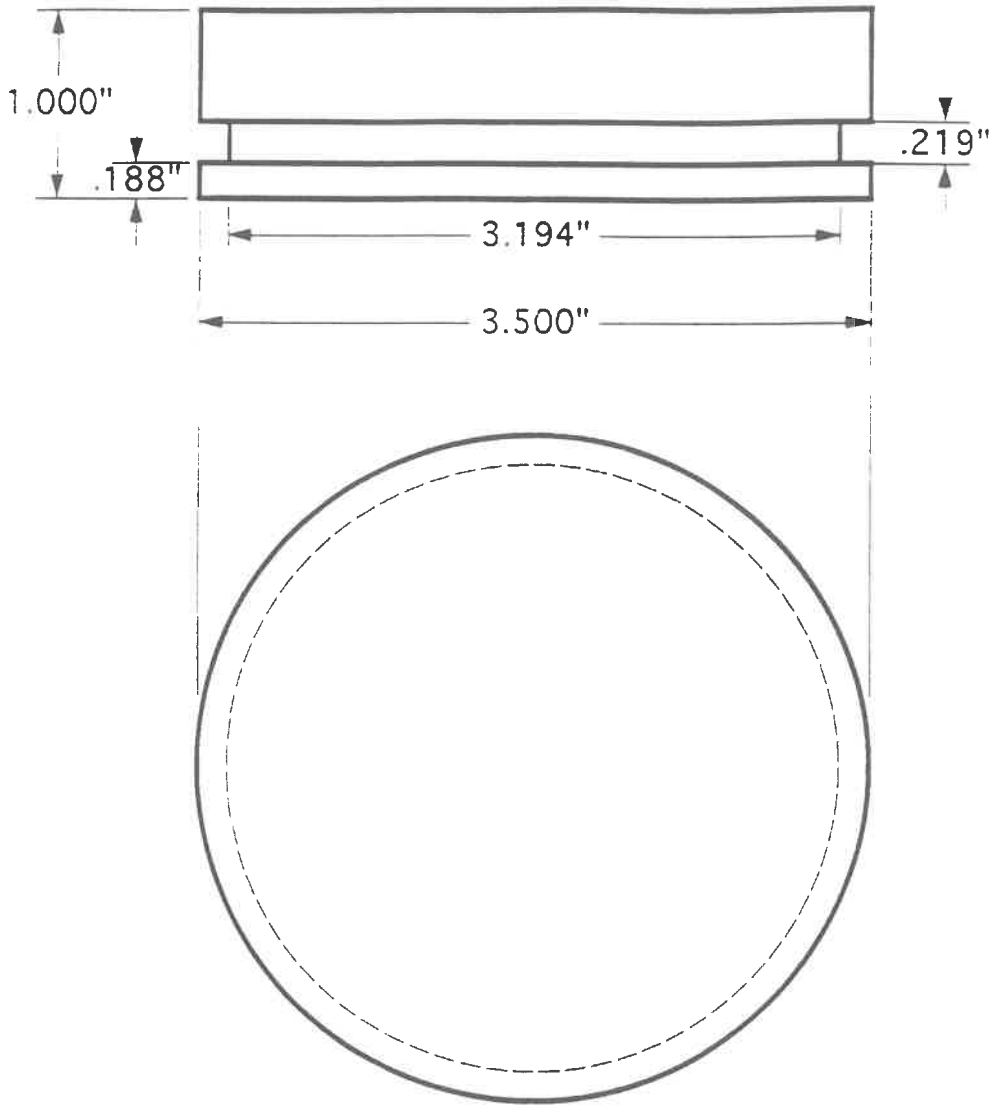

6061-T6 Aluminum test part

Figure 2

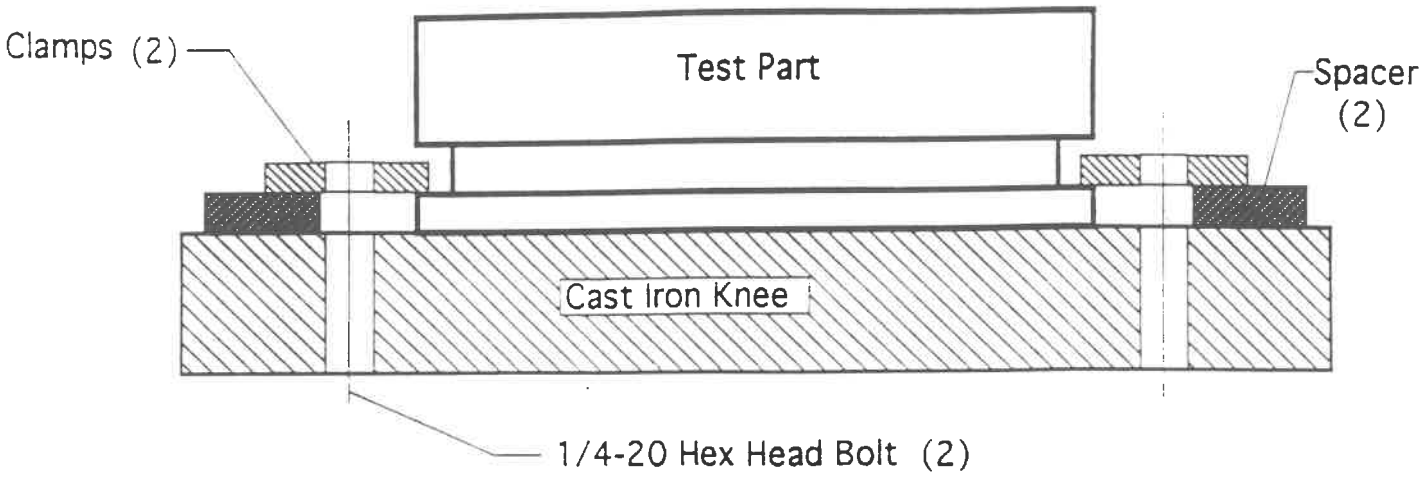

Part Mounting 1st. Test
Figure 3

LANL '92 PRH

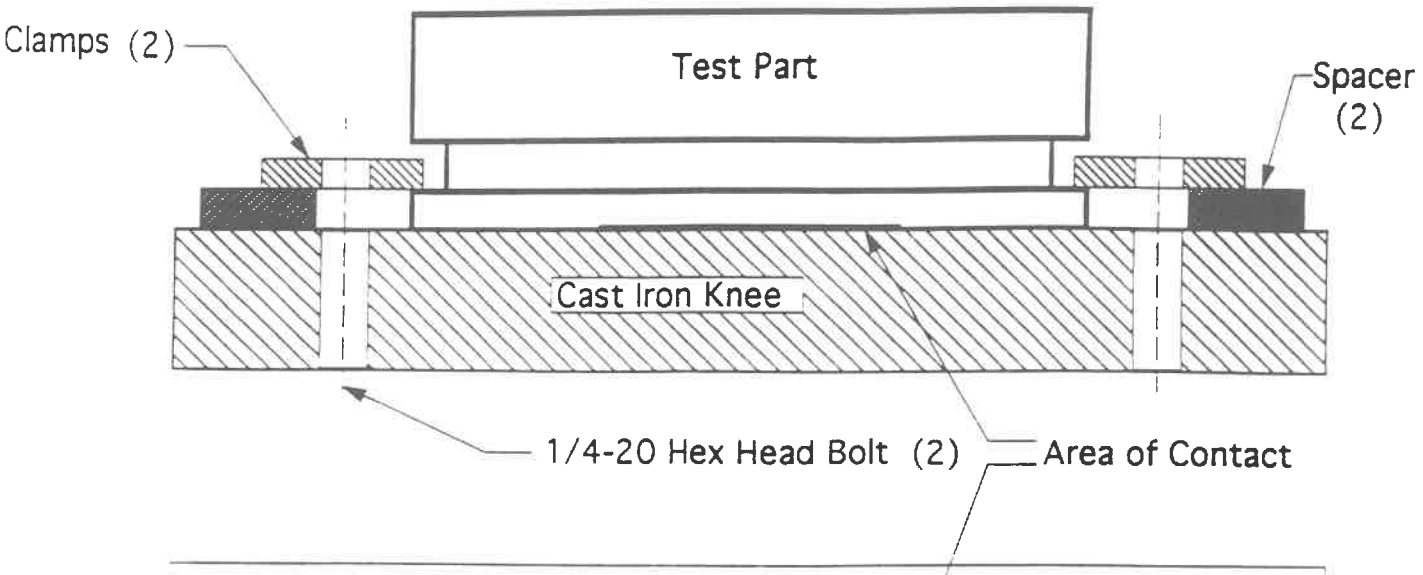

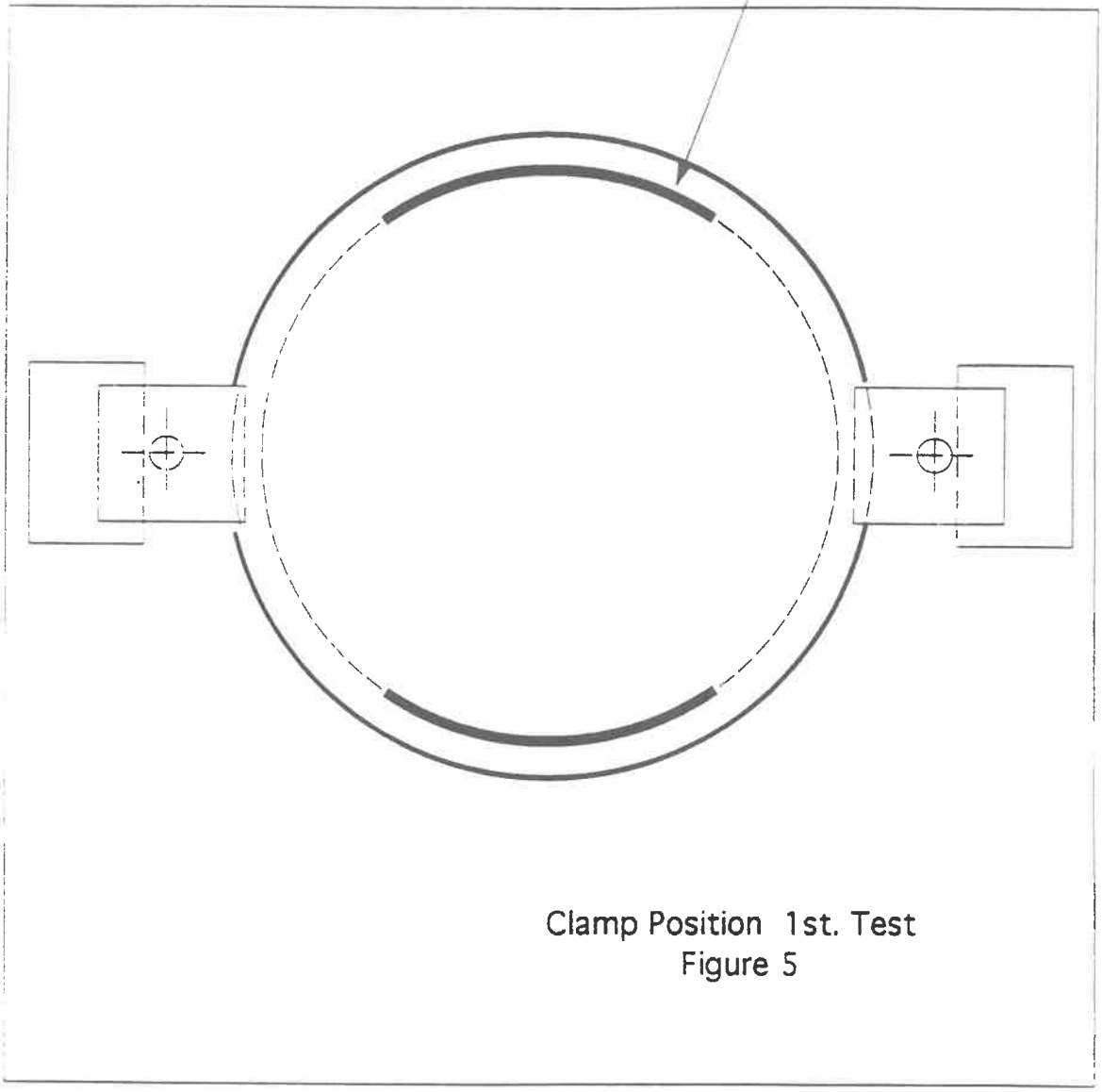

Clamp Position 1st. Test
Figure 5

LANL '92 PRH

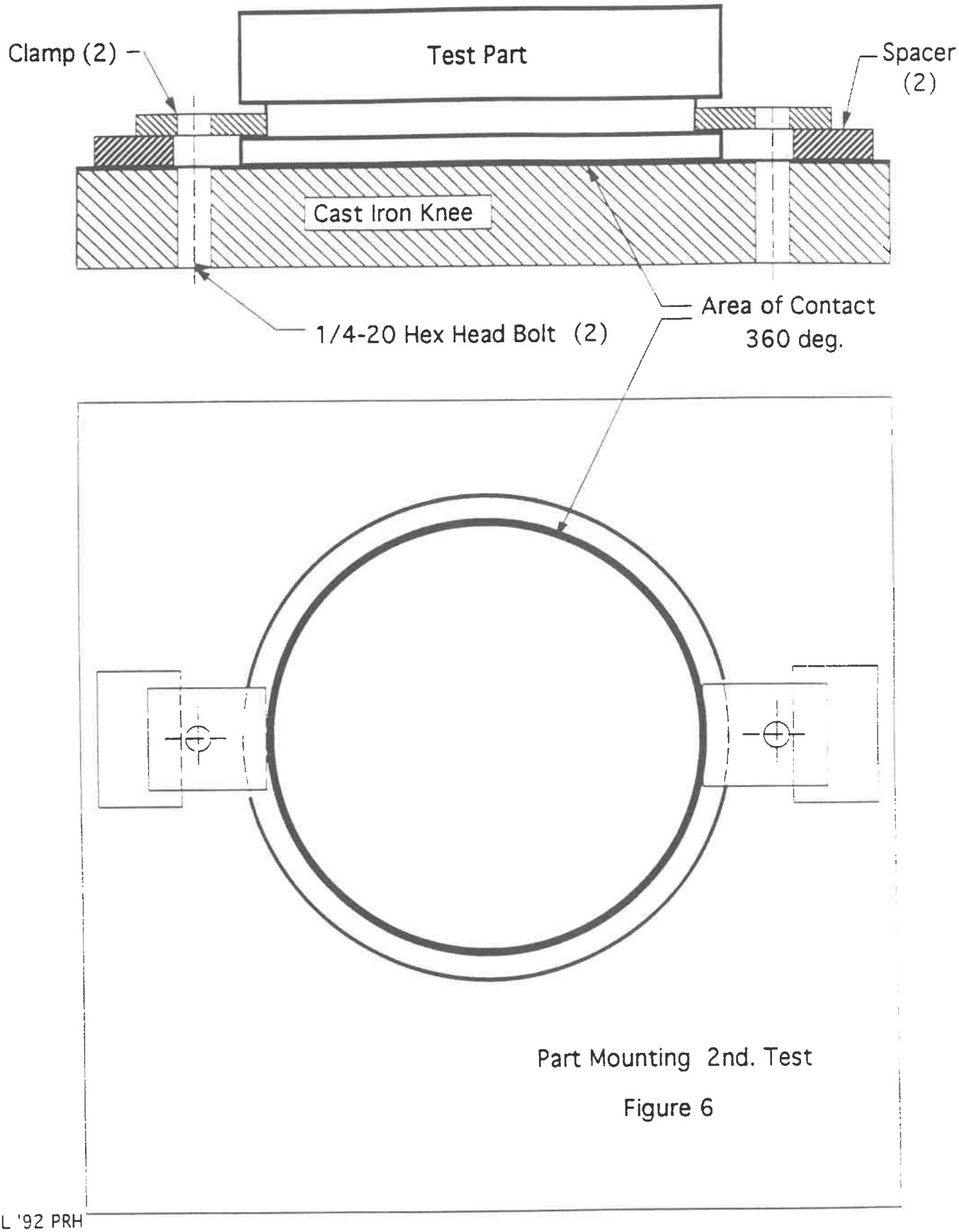

Part Mounting 2nd. Test

Figure 6

LANL '92 PRH

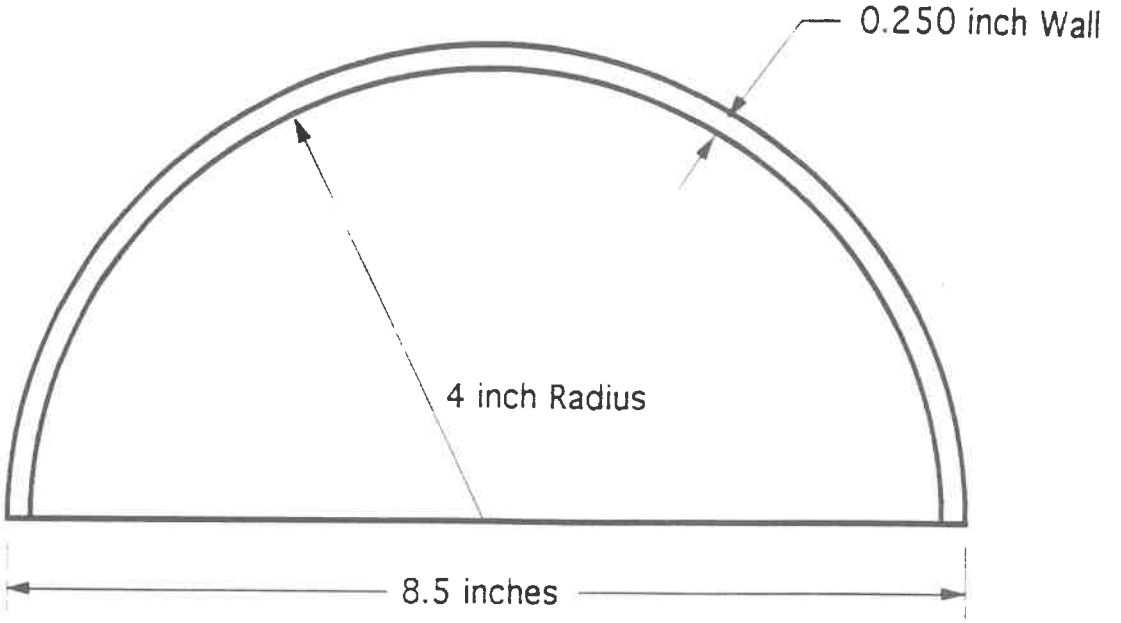

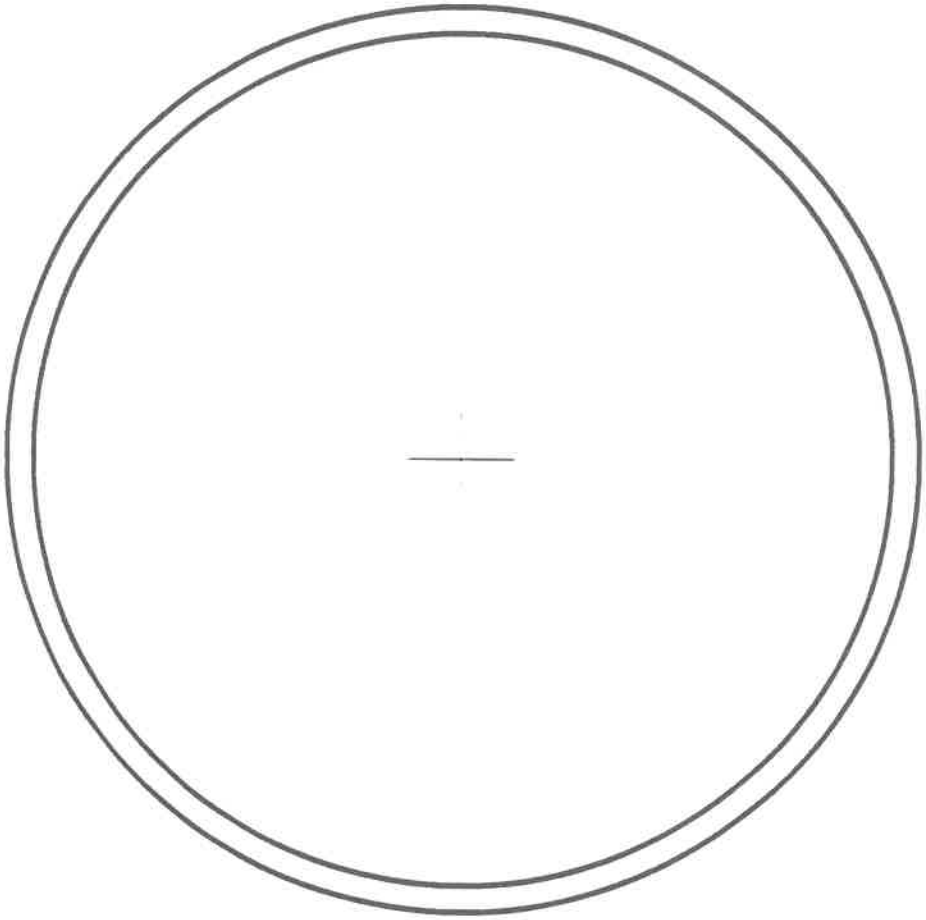

Typical "MAVERICK" IR Window
Matl. Zinc Selenide
Figure 8

LANL '92 PRH

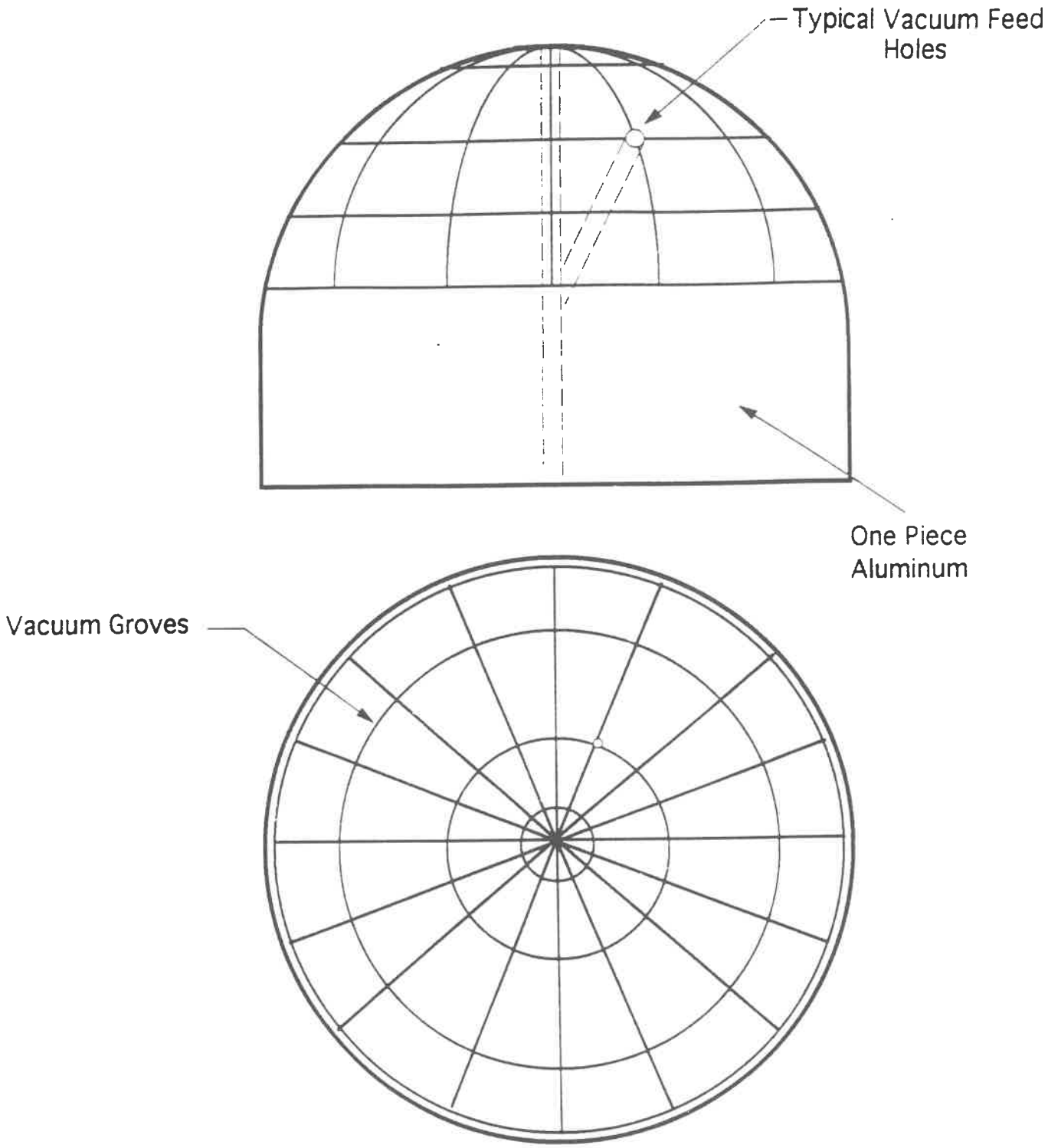

Convex Vacuum Chuck

Figure 9

LANL '92 PRH

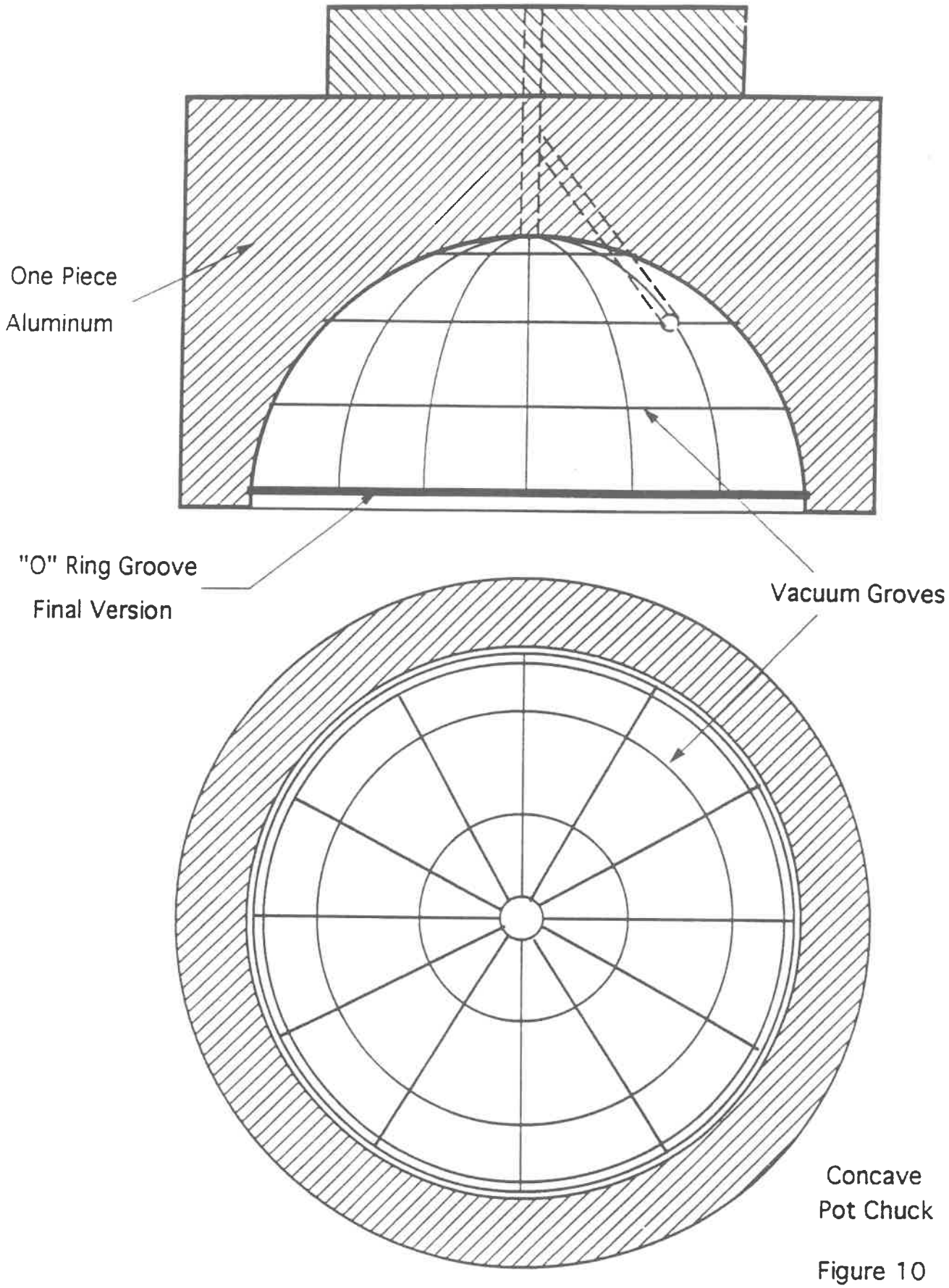

Figure 10

LANL '92 PRH

AN ACTIVE LEAD SCREW MECHANISM - A LEAD SCREW WITH BACKLASH CONTROL FOR ULTRA PRECISION POSITIONING

Kaiji SATO, Yoshihisa MURAYAMA, Shigehiko IMADA and Akira SHIMOKOHBE
Precision and Intelligence Laboratory, Tokyo Institute of Technology
4259 Nagatsuta, Midori-ku, Yokohama 227, Japan

Key words: positioning, lead screw, active control, backlash, piezoelectric actuator

Introduction

Conventional lead screws are often used in precision driving mechanisms with a long working range[1][2]. In the mechanisms, lead screws have to drive tables fast and position them precisely. For the first role, a sufficient backlash between a screw and a nut is necessary because the frictional force between them makes the table motion slow, causes noises and produces heat. For the second role, the backlash is not preferable to the frictional force, because the backlash causes chattering vibration and long positioning time.

In many practical cases, the backlash is adjusted to zero by using, for example, a doublenut. However, a large frictional force in the doublenut causes a positioning error, i.e. a static deviation. Namely, lead screw mechanisms have to satisfy the following inconsistent requirements; a sufficient backlash for driving an object fast, and zero backlash but a little frictional force for positioning the object precisely.

The authors propose an active lead screw mechanism (ALSM) which can satisfy above inconsistent requirements. The ALSM is able to not only control the backlash but also position a table by piezoelectric actuators (PEAs).

Principle of ALSM

Figure 1 shows the principle of the ALSM which comprises a lead screw, two nuts, two PEAs and a table. The table is connected to the nuts through the PEAs so that they can control not only the backlash but also the position of the table. The ALSM has the following capability:

(1) *Coarse and fast positioning with full-backlash* : When the table is to be driven fast and coarse-positioned by a motor, the lengths of the PEAs are adjusted so that they give an enough backlash between the screw and nuts to produce little frictional force (Fig.1(a)).

(2) *Backlash elimination* : After the coarse-positioning, the PEAs are elongated or shortened to eliminate the backlash, which gives the ALSM sufficient stiffness (Fig.1(b)).

(3) *Fine-positioning without backlash* : The

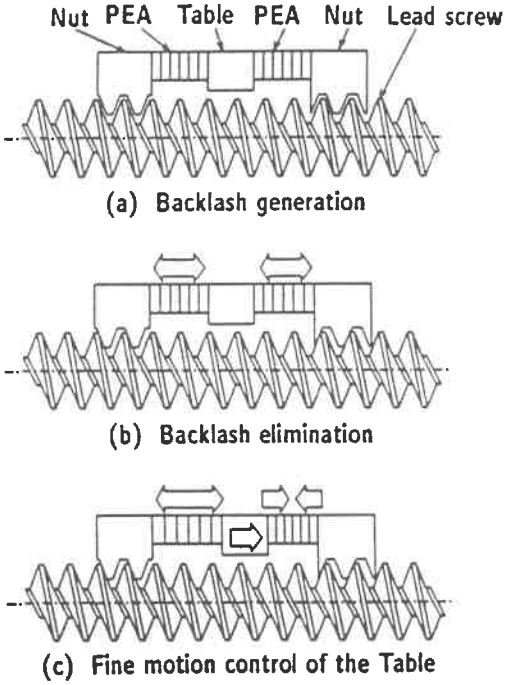

Figure 1 Principle of the ALSM

push-pull drive of the PEAs enables them to fine-position the table with sufficient stiffness and zero backlash.

Experimental mechanism

An experimental ALSM is set up using six PEAs, a conventional sliding screw rotated by an electric motor and two nuts. Figure 2 shows the nut configuration of the experimental ALSM. The dimensions of the lead screw are shown in Table 1. Each of the nuts is connected to the table through three PEAs and three coil springs. The springs keep the PEAs in contact with the table and the nuts.

Figure 3 shows a schematic of the ALSM. A laser position transducer (resolution; 10nm) measures the table position and a rotary encoder (14400P/R) detects the rotation angle of the lead screw. The ALSM is designed to have the maximum backlash when all PEAs are at their shortest length. To eliminate the backlash, the PEAs have to be elongated by an amount equal to the backlash which changes depending on the table position. Therefore, the ALSM has to have a set of backlash data or be capable of the real time measurement of the backlash. In this paper, the backlash was measured as a function of the rotation angle of the lead screw (backlash function) with the laser position transducer and stored into a controller computer.

Table positioning method

The table positioning method consists of the following three steps:
(1) First, the PEAs maximize the backlash. In this state, the table can be driven fast and coarse-positioned by the motor. Broken lines in Fig.4 represent this step. The coarse-positioning control is considered to be accomplished when a positioning error less than $\pm 5\mu m$ lasts for more than 5ms.
(2) After the coarse-positioning, the rotation angle of the lead screw is measured with the

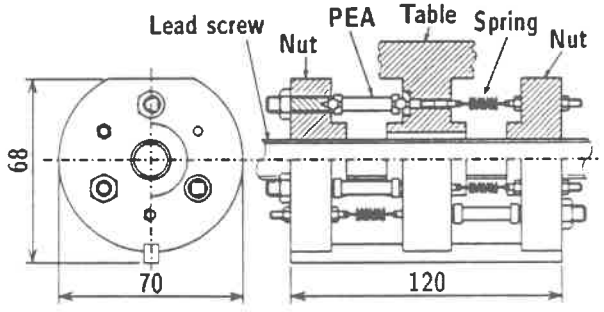

Figure 2 The nut configuration of the experimental mechanism

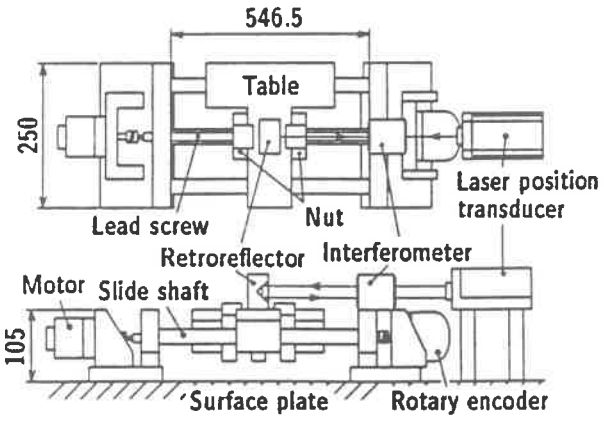

Figure 3 Schematic of the ALSM

Table 1 Profile of the lead screw

Trapezoidal lead screw	
Thread angle	30°
Lead	4mm
Major diameter	16mm

rotary encoder and the backlash is interpolated using the stored backlash function. The PEAs are elongated by an amount equal to the backlash to make it zero. Chain lines in Fig.4 represent this step. This step continues a few or more milliseconds which includes the time not only for elongating the PEAs but also for waiting for the residual vibration of the table to calm down.

(3) The table is fine-positioned by the push-pull drive of the PEAs. Solid lines in Fig.4 represent this step.

Figure 5 shows a block diagram of the control system for the steps (1) and (3). As the coarse controller, P element is used for F1 and D element, for F2 (P-D controller, equation(1)). Similarly, PI-D controller (equation(2)) is used as the fine controller.

$$\left.\begin{aligned} F_1 &= \beta_{1c} \\ F_2 &= \alpha_{2c}\, s \end{aligned}\right\} \quad \cdots\cdots\cdots (1) \qquad \left.\begin{aligned} F_1 &= \beta_{1f} + \frac{\gamma_{1f}}{s} \\ F_2 &= \alpha_{2f}\, s \end{aligned}\right\} \quad \cdots\cdots\cdots (2)$$

These controllers are implemented on a digital computer. The control parameters of the coarse- and fine-positionings are determined independently of each other. In the step(2), the PEAs are elongated with an open-loop method.

Experimental results

Figure 6 shows the backlash between the screw and nuts (backlash function). The backlash was measured at every 90° of the screw rotation and stored in a controller computer. The dynamic models of the ALSM in steps (1) and (3) were examined and model parameters were identified experimentally to design the control parameters.

Figure 7 shows the experimental and calculated coarse-positioning responses of the table to 2mm, 5mm and 10mm step inputs. Figure 8 shows the experimental and calculated fine-positioning responses of the table to a 2μm step input. In the figures, both responses agree

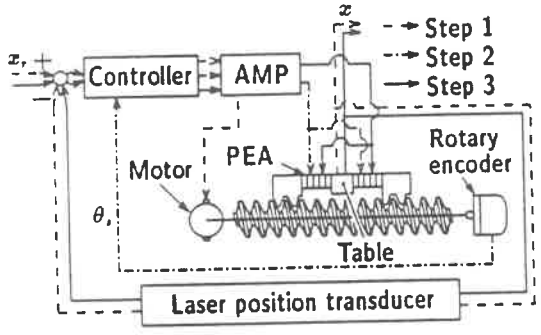

Figure 4 Table positioning algorithm

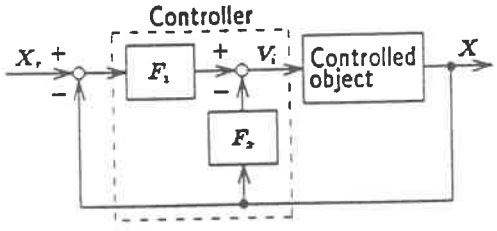

Figure 5 Control system

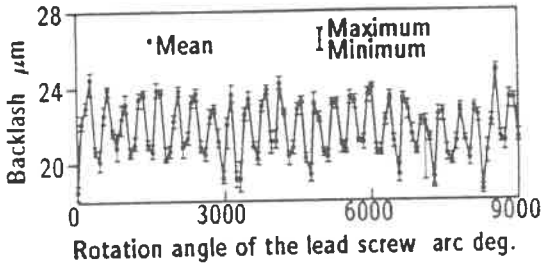

Figure 6 The measured backlash

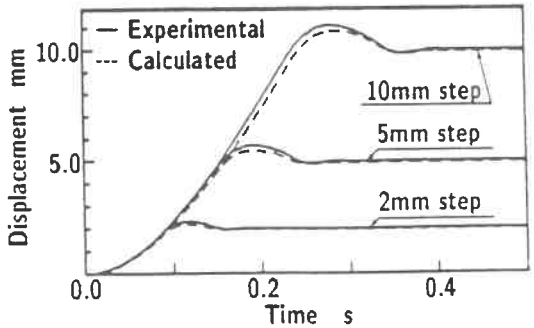

Figure 7 Step responses with coarse positioning

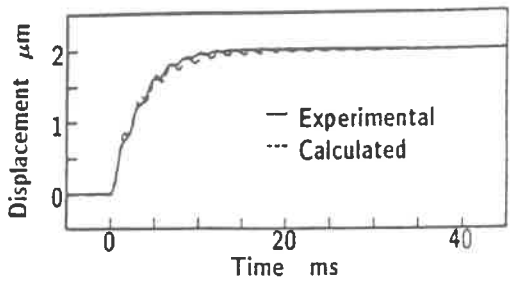

Figure 8 Step responses with fine positioning

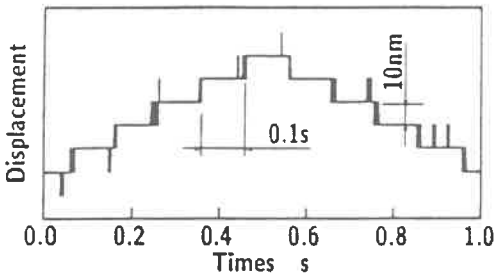

Figure 9 Positioning resolution (10nm)

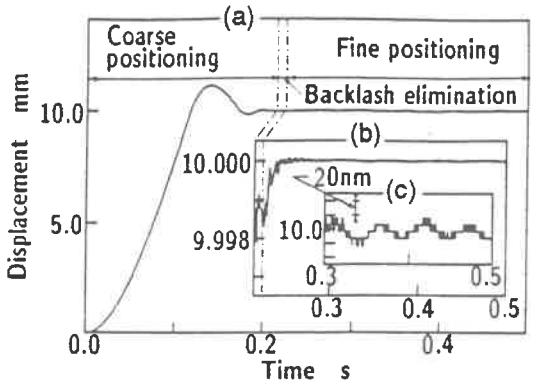

Figure 10 The coarse- and fine-positioning of the table to a 10mm step input

well with each other. Figure 9 shows the resolution of the fine-positioning. The result proved that the ALSM had the resolution better than 10nm.

Figure 10 shows the coarse- and fine-positioning of the table to a 10mm step input. Fig.10(a) shows that the step(1) required 215ms and the maximum table speed was 130mm/s. The step(2) continued for 10ms and a 1.8μm position error remained (Fig.10(b)). The step(3) is shown in Figs.10(b) and (c) which show that the error is reduced quickly except the residual vibration of a constant period (52ms). This vibration was caused by the mass of the surface plate on which the ALSM was set and the stiffness of the table support. So in this paper, positioning is deemed to be accomplished when the error($x_r - x$) keeps less than $\pm$10nm over this period. From this point of view, the time required for the step(3) was 118ms. The total amount of time to position the table in Fig.10 was then 343ms. The average of 20 similar positionings was 370ms.

Conclusions

The ALSM is proposed as an ultraprecision positioning mechanism with a high speed. The experimental mechanism of the ALSM had 130mm/s maximum table speed, 10nm positioning resolution which is equal to the resolution of the laser position transducer used as a feedback sensor and 370ms positioning time for a 10mm step input. Next steps are the real time measurement of the backlash and improvement of the coarse- and fine-positioning control strategy to realize faster positioning.

References

1 D.E.Luttrell and T.A.Dow "Development of a high speed system to control dynamic behaviour of mechanical structures," *Precision Engineering* 1987, **9**, pp.191-200

2 H.Yonezawa and H.Sasai "Positioning Table with High Accuracy and High speed," *Annals of the CIRP* 1990, **39**, pp.433-436

Abstract

CAPSTANS OR LEAD SCREWS ?

Comparing the Performance of Diamond Turning Machines
Under Operating Conditions

David H. Youden
RANK PNEUMO
A Division of Rank Taylor Hobson Inc
P.O. Box 543, Precision Park
Keene NH 03431-0543

Capstan drives have received a considerable amount of attention over the last several years A number of well known organizations have invested time and effort designing diamond turning machines which use these drives for slide translation.

Capstan drives are generally felt to be superior to ball screws because they eliminate the cyclic errors often associated with screws and because they lower the frequency of tachometer ripple to a point where it falls within the bandwidth of the servo controller. Capstan drives also have very low coulomb friction compared to ball screws.

Capstan drives, however, have a low mechanical advantage which limits the thrust force available from the device. The low mechanical advantage also causes the tachometer signal to be vanishingly small, limiting the usefulness of velocity feedback.

The author has had the unique opportunity to analyze the performance of, and produce diamond turned parts on, two ultra-precision diamond turning machines which are mechanically identical except for the slide drives. One machine has slides that have preloaded ball screw drives and the other has air bearing capstan drives.

Capstan drive slide design

The slides on the capstan drive machine are hydrostatic box slides. The traction drive bar is attached to the slide by a small, spring steel reed. The reed serves to decouple the slide from any small vertical motions of the drive bar, and to ease the alignment of the traction drive to the slide in the vertical plane. Figure 1 illustrates the construction of the slide and the location of the traction drive roll assembly.

The capstan drive bar is tee shaped in cross section. The top of the bar is about 50 mm wide and the bottom is 25 mm wide. The bottom of the bar runs on the drive roll. The bar is preloaded against the drive roll by an air bearing that operates on the top surface of the drive bar, forcing it against the roll with about 1800 Newtons.

The capstan drive roll is supported by two air journal bearings. There is no thrust bearing as the roll is located axially by the drive bar which, in turn is located by the slide itself. A DC servo motor and tachometer are mounted on one end of the drive roll. Figure 2 shows the construction of the drive roll assembly.

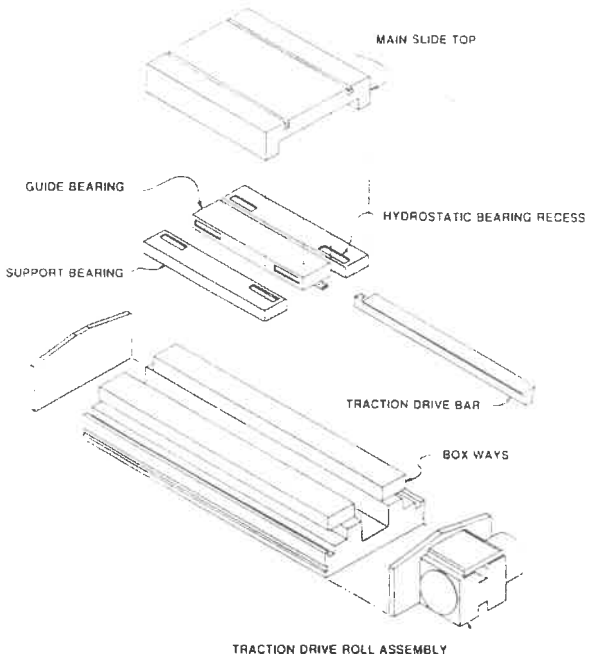

Figure 1: Capstan drive slide assembly

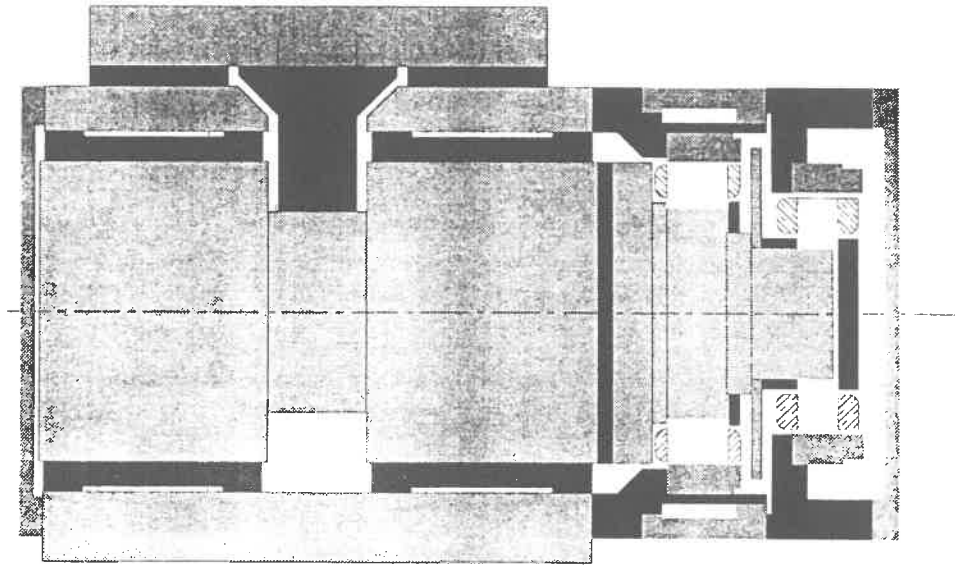

Figure 2: Section through capstan drive roll assembly

Lead Screw Slide Design

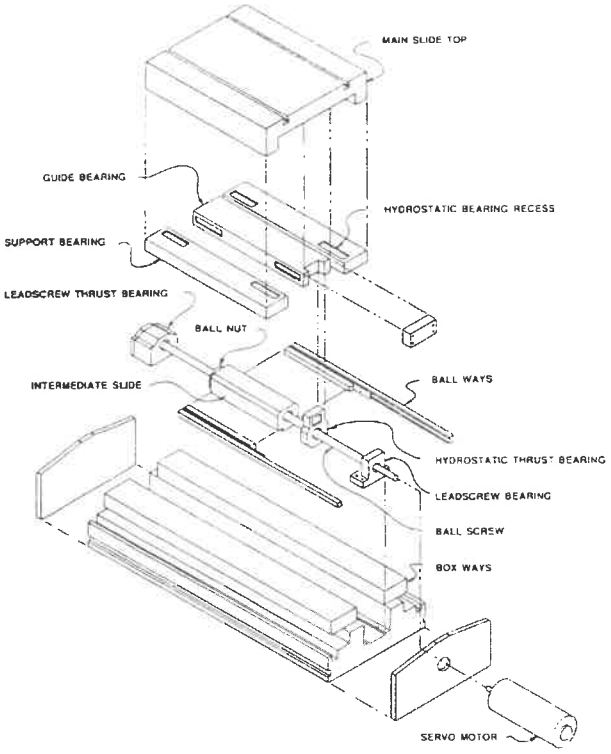

HYDROSTATIC BOX SLIDE DESIGN

Figure 3: Lead screw driven slide assembly

The slides used on the lead screw driven machine are similar in appearance to those on the capstan drive machine and, the way system is identical on both sets of slides. The slide drive system is, obviously, quite different. These slides have a 5 mm pitch ball screw with a preloaded nut located below the slide on its center line. The screw is supported by preloaded ball bearings with the thrust bearings located on the end of the screw nearest to the nut when the slide is in the machining theater. A DC servo motor/tachometer is attached to the screw through a flexible coupling. The ball nut is attached to an intermediate slide. This slide is about 100 mm square in cross section and 300 mm long.

The intermediate slide moves on preloaded ball ways. On the opposite end of the intermediate slide (Away from the ball nut) is a hydrostatic thrust bearing which protrudes up above the intermediate slide and engages a recess in the end of the main slide guide way. This bearing serves to transmit thrust from the lead screw to the main slide while effectively decoupling the main slide from pitch, roll, and yaw of the intermediate slide. The technique is so effective that cyclic errors in straightness caused by the ball screw are reduced to less than 10 nanometers peak to valley. Figure 3 illustrates the construction of the lead screw driven slides.

LAST Test Results

Prior to cutting parts, a Low Amplitude Sine Tracking (LAST) test[1] was run on each machine to verify that the machine servos were properly adjusted. In the LAST test, for a 10 nm programming resolution machine, one axis moves in a sinusoidal fashion with a peak to valley amplitude of 500 nm and a period of 60 seconds while the other slide moves first in one direction and then in the other direction at

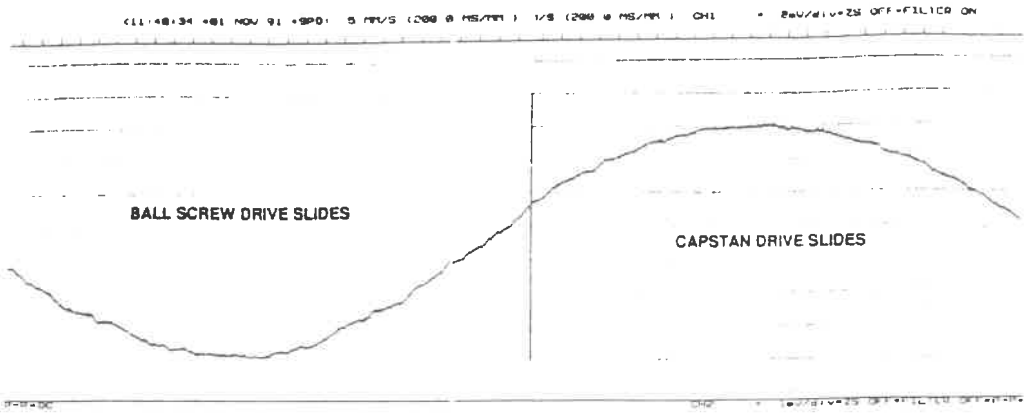

Figure 4: Sections of LAST test data from two different slides.

2.5 mm/sec. The position of the first slide is recorded throughout the 3 minute test. Improperly adjusted servos manifest themselves as artifacts on the trace at or near the reversal points on the sine wave. Figure 4 shows that the LAST tests on the two machines were very similar in appearance.

Cutting tests

The parts used for our cutting tests were made of Furukawa A-5486 aluminum, a material which we have found gives excellent results when diamond turned. Each part was 76 mm in diameter and about 25 mm thick. The parts were held on vacuum chucks and a 254 mm spherical radius was turned under the following conditions:

Spindle speed	2000 RPM
Finish depth of cut	.002 mm
Feed rate	2.5 mm/min
Coolant	Odorless mineral spirits (Spray mist)

Results

The parts were measured on an RTH Talystep over a scan length of at least 150 microns. Roughness data was taken using a filter cut-off of 0.33 Hz and waviness data was taken using a filter cut-off of 25 Hz. The data was assessed over each successive 50 micron window. The data from two represenative parts, one from the capstan driven machine, and one from the lead screw driven machine is presented below.

Part designation	LEAD SCREW DRIVES A	CAPSTAN DRIVES B
Roughness, nm	7.0	7.5
R_t	7.0	8.5
	7.5	9.0
Waviness, nm	5.9	9.6
R_t	7.3	9.9
	10.2	12.6

The parts were also inspected using an S-5 Form Talysurf which produced the following results:

Part designation	LEAD SCREW DRIVES A	CAPSTAN DRIVES B
R_a, nm	4.3	6.1
R_t, nm	33.6	66.6
W_a, nm	5.3	5.4
W_t, nm	23.8	26.3

Further testing was done using a Zygo Mark 2 interferometer with a phase measuring attachment. This instrument produced the following data:

Part designation	LEAD SCREW DRIVES A	CAPSTAN DRIVES B
P-V, λ	0.15	0.16
RMS, λ	0.022	0.030

Although these parts are all within the machine performance specification, it is clear that the parts cut on the machine with lead screw driven slides are somewhat superior to those cut on the other machine.

In addition to part cutting tests, there is the question of drive system stability under different operating conditions. The machine slides have a mass of about 180 Kg and the mass of the spindle is about 135 Kg making the total moving mass of the X axis just over 300 Kg. The work piece can add up to 125 Kg of additional mass. It was found that capstan drives were more sensitive to changes in the driven mass than lead screw drives. In order to maintain peak performance, the servo drives required retuning if massive work pieces were to be machined to the accuracy obtainable on the machine used for the test cutting.

Conclusion

Retuning the servo drives is not a long nor a complex task. The requirement that it be done, however, in addition to the fact that there is no improvement in cutting results, has lead us to the decision to continue to use lead screw drives until such a time when the advantages of capstan drives can be more clearly demonstrated.

1. Gerchman, Mark Craig and Youden, David H. "An Evaluation Of Ultra-Precise Machine Tool Contouring Performance: The Low Amplitude Sine Tracking (LAST) Test" Proc. 6th International Precision Engineering Seminar. Proc 2nd International Conference On Ultra-Precision In Manufacturing Engineering Pub. by Springer-Verlag, Berlin 1991 pp 124-127.

Characterization and Control of a Traction Drive System

Ganesh S. Rao
Paul I. Ro
Precision Engineering Center
North Carolina State University
Raleigh, NC 27695-7918

Introduction

Modern machining is placing greater demands on its positioning systems. In order to meet those needs, new systems are being investigated. One of these promising new systems is the traction, or capstan drive. Traction drives have very low friction and no backlash. However, they tend to be more sensitive to noise and mechanical disturbances. This paper presents some preliminary work performed on a Rank-Pneumo traction drive, including a simple analytical model and the results of using a digital PID controller to control position.

Setup

The system consists of an Inland QT-3802 DC motor with a roller attached to the shaft. A drive bar is preloaded onto the roller. Both the bar and the roller are made of stainless steel. Air bearings support the roller and maintain the preload on the bar. A Dover air bearing slide is attached to the drive bar with a rigid coupling. The position of the slide is measured with an ADE Microsense capacitance gage. Input to the motor comes from a 286 PC with a Data Translation DT-2823 I/O board. The board is connected to a Kepco amplifier and a current controller which helps maintain a constant torque in the motor. A diagram of the setup is given in Figure 1.

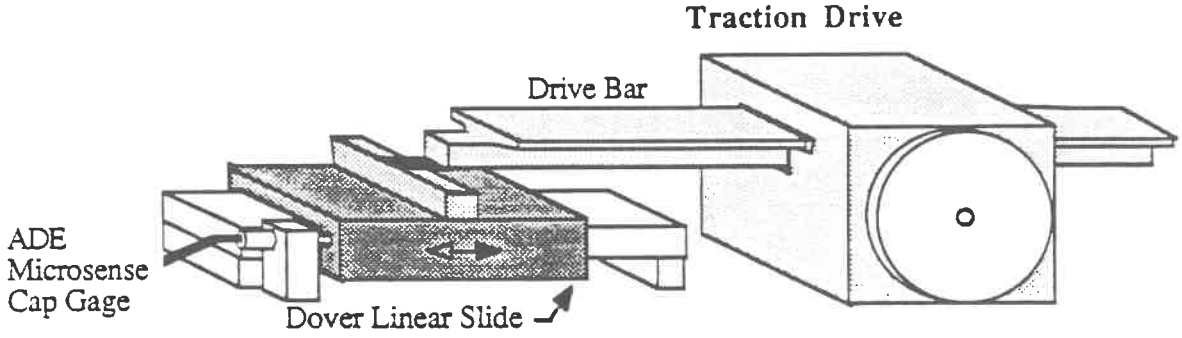

Figure 1: Diagram of the Traction Drive setup

Analytical Model

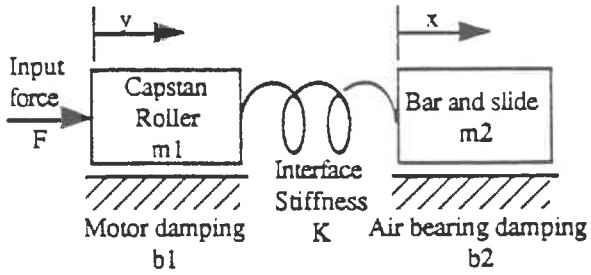

Figure 2: Analytical model of the traction drive

A simple, intuitive model of the traction drive is given in Figure 2. It consists of two masses connected by a spring. The two masses represent the capstan ($m1$) and the bar and slide assembly ($m2$). The bar and slide can be combined into one mass as the coupling between them is rigid. The spring represents the interface stiffness of the rolling contact between the bar and the roller. The roller has a damping associated with the motor ($b1$) and the bar and slide have a damping ($b2$). The input is a force on the roller (F) and the output is the displacement of the slide (x). Summing the

forces around each block and taking the Laplace transform gives:

$$m_1\ddot{y} = F - b_1\dot{y} - K(y-x) \Rightarrow m_1s^2Y = F - b_1sY - K(Y-X)$$
$$m_2\ddot{x} = -K(x-y) - b_2\dot{x} \Rightarrow m_2s^2X = -K(X-Y) - b_2sX \quad [1]$$

Further simplification gives the following transfer function. As the bar and slide are supported by air bearings, the damping *b2* can be neglected.

$$\frac{X}{F} = \frac{K}{s^4(m_1m_2) + s^3(m_2b_1) + s^2K(m_1 + m_2) + s(Kb_1)} \quad [2]$$

The size of the contact patch between the bar and the roller can be calculated given the preload force (1.78 kN) and the material properties of the bar and roller. The length of the contact is equal to the width of the bar which is 2.54 cm. Using the equations for a contact between a cylinder and a plane, the width of the patch was found to be 315.2 μm. From this, an approximate interface stiffness of 196.5 MN/m was calculated for very small applied torques.[1] The values for the other system parameters are given in Equation [3]. The rotational elements were converted into their linear equivalents.

$$m1 = \frac{J}{r^2} = 1.8826 \text{ kg}$$
$$m2 = 12.799 \text{ kg}$$
$$b1 = \frac{b}{r^2} = 164.076 \frac{\text{N-sec}}{\text{m}}$$
$$b2 = 0 \quad [3]$$

Using these values, the system poles were found to be at -37.989 $\pm$ 10932i, -11.1758 and 0. The peak in the Bode plot occurs at 1740 Hz. Therefore, the interface stiffness affects higher frequency dynamics which are beyond the range of interest for control. In order to obtain an accurate model of the system, the actual characteristics were obtained experimentally for a 200 Hz frequency range.

Experimental Model

A Wavetek FFT analyzer was used to study the response of the system. The goal was to obtain a transfer function for the system from the input (torque) to position. Pseudo-random noise was used as input. The noise was generated by a C program and the amplitude of the noise was adjusted so that the output displacement was within 150 nm. The frequency range was 0 to 200 Hz.

The resulting system frequency response looked like that of a simple second order system. Using the data points of the transfer function and a curve fitting algorithm, a transfer function with 2 poles and no zeros was obtained.[2] This is the simplest model that adequately matched the data. The transfer function is given in Equation [4] and a Bode plot in Figure 3. The peak at 40 Hz may be caused by the dynamics of the amplifier and current controller.

$$Gp = \frac{5887.917}{s^2 + 105.563\,s + 7.362378\times10^4} \quad [4]$$

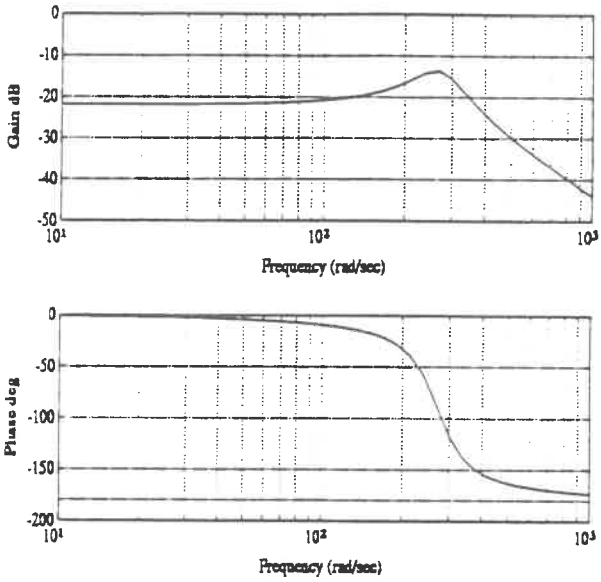

Figure 3: Bode plot of actual system response

Digital PID Control

The continuous time PID gains were calculated to give a critically damped response and a 1 second settling time. The gains were tuned on the actual system so that a satisfactory control was achieved.

The digital PID gains can be calculated from the continuous time gains.[3] The control input u must be calculated given K_P, K_I, K_D and the position error e. This is done using a trapezoidal approximation for the integral term

and a backward difference for the derivative term. The resulting control equation, Equation [5], was implemented in a C program on the 286 PC using the DT-2823 board.

$$u(t) = u(t-1) + \left(K_P + \frac{K_I T_s + K_D}{2T_s}\right) e(t) - \left(K_P - \frac{K_I T_s + 2K_D}{2T_s}\right) e(t-1) + \frac{K_D}{T_s} e(t-2) \qquad [5]$$

Results

A closed loop system with the plant of Equation [4] was simulated on Simulab. The results matched well with the actual system output under PID control. The simulated output for a 100 nm step with ±20 nm of noise is given in Figure 4 below. Discrepancies start to show up when the input amplitude is large. This is because the model was obtained for small motions and is linear. The actual system is nonlinear and the model cannot account for the changes as the input amplitude increases.

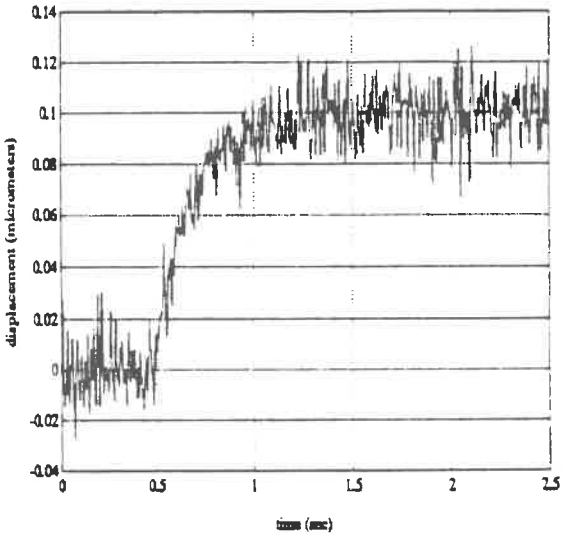

Figure 4: Simulated response for a 100 nm step with ±20 nm of noise

The actual control worked well for position commands between 70 nm and 2 μm. The overshoot for a 1 μm step is only 3% (30 nm). Figures 5 and 6 below show the actual system step response for steps of 100 nm and 1 μm. The system's good disturbance rejection properties can be seen in Figure 7 where the control returns the system to zero after a series of 1 μm impulse disturbances. There is, however, a noise problem. The noise amplitude is ±20 nm. Most of the noise seems to be coming from the A/D converter on the DT-2823 board. A buffer circuit may have to be built to reduce this noise. A finer level of control will be impossible until this noise is reduced.

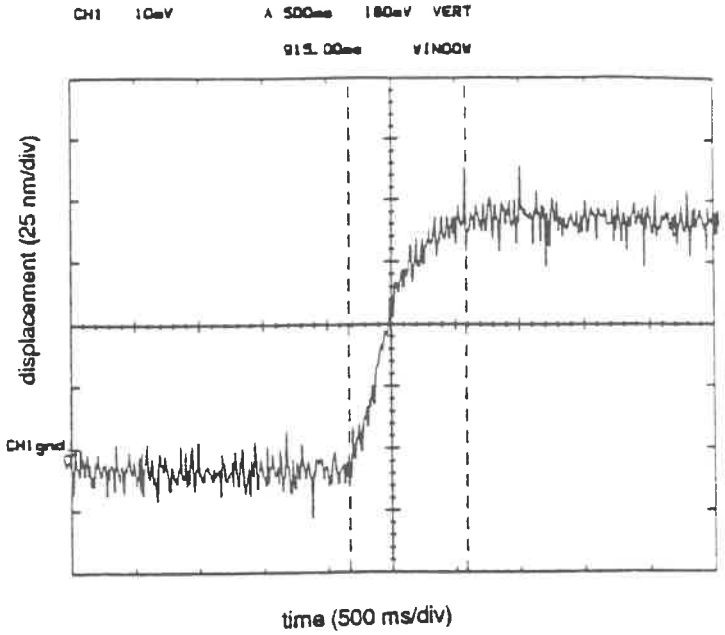

Figure 5: Actual system response to a 100 nm step

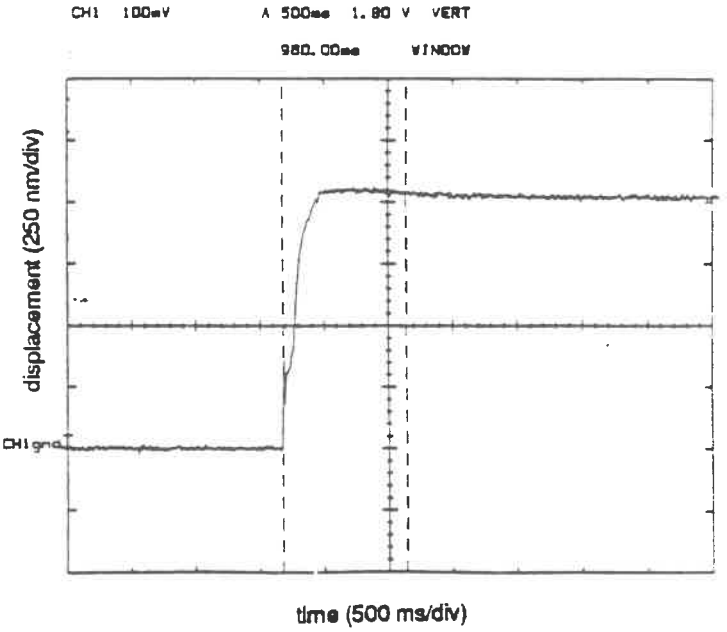

Figure 6: Actual system response to a 1 μm step

There is also an interesting phenomenon that occurs when the system is disturbed. The system overshoots in certain predictable directions when the bar is hit. This can be seen in Figure 7. Here, the bar is initially at -500 nm when it is commanded to zero. Then, given a positive impulse disturbance, the bar moves in the positive direction before being brought back to zero by the controller. On the next impulse disturbance, however, the bar jumps back in the opposite direction. On every succeeding disturbance, the direction in which the bar deflects alternates. The direction of the impulse disturbance is immaterial.

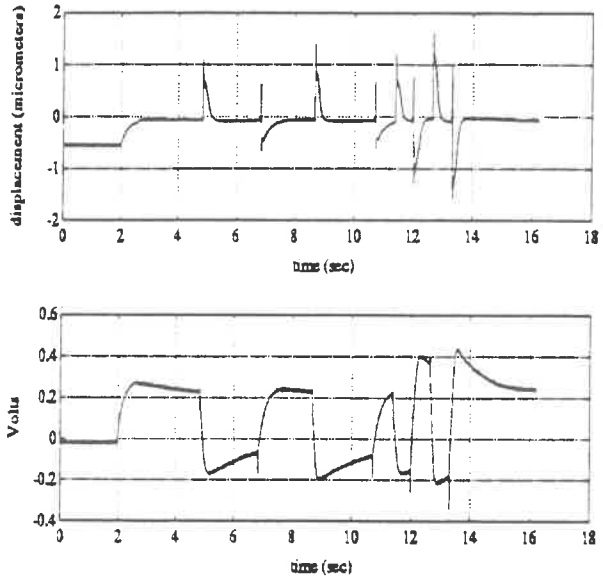

Figure 7: Response of system to impulse disturbances

The initial condition of the bar seems to affect the next deflection. If the bar moved positively to reach the set point, the following deflection will be positive and vice versa. This appears to be a system property and not a result of the control as the bar would sometimes move opposite the direction of a disturbance with the motor off. This behavior may be the result of oil which was blown into the system during a compressor failure. Once this condition has been remedied, the analysis will have to be repeated.

Conclusions and Future Work

Using a simple PID control scheme, the traction drive is capable of sub-micrometer motion. This leads to the hope that a finer level of control can be achieved when the noise problems have been properly dealt with. The system also exhibits some peculiar behavior that has not yet been fully explained. Further work should shed some light on this an provide a more complete analytical model of the system.

References

1. Slocum, A.H., *Precision Machine Design*. 1992, Englewood Cliffs, NJ: Prentice-Hall. 750.

2. Sanathanan, C.K. and J. Koerner, *Transfer Function Synthesis as a Ratio of Two Complex Polynomials*. IEEE Transactions of Automatic Control, 1962. : p. 56-58.

3. Miller, M., *Design of Three Axis Diamond Turning Machine Controller*. 1991, North Carolina State University:

A Study on Frictional Characteristics of Slide-Way in Microdynamics

A. Kanai*, M. Miyasita*, H. Nishihara*, J. Yoshioka**
* Ashikaga Institute of Technology, Ashikaga, Tochigi 326, Japan, ** NUTR K.K.

1. Introduction

A feed and frictional load characteristics of a 150 kg carriage on plain bearings with a differential-force operated hydraulic actuator in a travel range of nanometer is studied. In the present paper, experiences on the test rig in a frictional load characteristics are reported for a reciprocating travel of 4 μm at constant feed rate and ten steps of various feed per step in reciprocation, and also under the bearing pressure of 50, 89 and 130 kPa.

2. Test rig

Fig. 1 is the test rig. The feed system is composed of a hydraulic servovalve, a differential-force operated hydraulic actuator with no seal involved and a capacitive feedback sensor A located close to the driving point along the plain bearing guideway. Another capacitive sensor B is attached along the guideway away from the sensor A by 400 mm for comparing the displacement at A and B.

Carriage: 150 kg mass and $500^{\text{Length}} \times 300^{\text{Width}}$ mm.
Hydrostatically supported horizontally.
supported by plain bearing vertically with the under side and the hydrostatic pads on the top side are attached for making variable the bearing pressure.

A feed characteristics of the feed servo system[1] is as follows:

Feed resolution : better than 1 nm
Max. feed stiffness : more than 60 N/nm
Band width : 100 Hz

Fig. 2 is a cross section of the feed mechanism.

Plain bearing area : 295.6 cm^2
Effective area of hydrostatic pads : 120.6 cm^2

The piston of actuator is hydrostatically supported without any seal, and the pressure difference between the two cavities generates the driving force. In the range of lower feed rate, the pressure difference enables to calculate the frictional load.

3. Experimental results.

3.1 Feed and frictional load characteristics in reciprocating motion.

Fig. 3 is an example of the test results on the feed and frictional load characteristics at the feedback sensor A in the travel range of 4 μm in reciprocating motion. (a) is the frictional load and (b) is the displacement of the carriage. A series of the experiments under the following conditions were forwarded:

Bearing pressure, P_s : 50, 89, 130 kPa
Feed rate, V : 100, 200, 400 nm/sec

In Fig. 3 the bearing pressure is 50 kPa and the feed rate 100 nm/sec.
As shown in Fig. 4, the frictional load characteristics is separated into two domains, the transient and the stationary. And the characteristics shows a high repeatability and the transient after reversing the feed direction also has a good coincidence in reciprocating motion.
Here, a displacement of α and a increase of frictional load β in the transient in Fig. 4 can define an effective spring constant. Fig. 3 shows a soft spring characteristics.
Fig. 5 and 6 are examples of the test results for stepwise feeds.
A series of the experiments under the following conditions were forwarded:

Stepwise feed, S : 1, 2, 5, 10, 20, 50 and 100 nm/step

In Figs 5 and 6 the bearing pressure is 50 kPa.
From these test results, the frictional load characteristics is composed of two domains, the

transient and the stationary as modeled in Fig. 4 and shows a soft spring characteristics.

3.2 Frictional load characteristics in the stationary domain.
Fig. 7 is an example of the test results on the stationary frictional load at the feed rate of 100 to 400 nm/sec. The frictional load is almost not influenced by the feed rate in this range. An increase of the frictional load during the displacement of 1 to 3 μm is only 1.6 to 3.4% of the stationary frictional load.
The stationary frictional load in the stepwise feed experiments is different from the test results at a constant feed rate as shown in 3.4 later.

3.3 Frictional load characteristics in the transient domain.
As parameters representing the frictional load characteristics in the transient domain, the displacements of γ and δ shown in Fig. 8(a) are introduced. These are the displacement from the point of reversing feed direction, at which the friction arrives at 63.2% or 80% of the stationary friction respectively. (a) shows the experimental results of parameters γ and δ. (b) is the averaged effective spring stiffness for the displacements of γ and δ. The averaged effective spring stiffness during the travel of 50 nm after reversing feed direction is 5 to 7 N/nm and then, the requirement for a lost motion free feed system is esteemed to be extraordinary high stiffness.

3.4 Comparison of frictional load characteristics for constant rate and stepwise feeds.
Fig. 9 (a) is an example of the comparison of frictional load characteristics experimentally obtained. (b) shows the summary of the test results on stepwise feed experiments. They say that the stationary frictional loads in the stepwise feed of 20, 50 and 100 nm/step are almost 70% of the stationary load at each feed rate. The comparison will reflect the difference of contact mechanism between them. CNC machines have to take care of this difference in design.

3.5 Comparison of displacement at feedback point and another part on carriage.
Fig. 10 is a comparison of the detected displacement by the feedback sensor A and additional sensor B shown in Fig. 1. In the stationary domain no relative displacement between sensors A and B, but in the transient after reversing feed direction a small amount of relative motion such as 0.1 μm can be observed. At present it is not clear what causes the relative displacement, but the tension and the compression of the carriage along the guideway can be mentioned as one of the reason.

Reference
(1) Kanai,A., Sano,H., Yoshioka,J., Miyashita,M., Nanotechnology 2.1(1991)

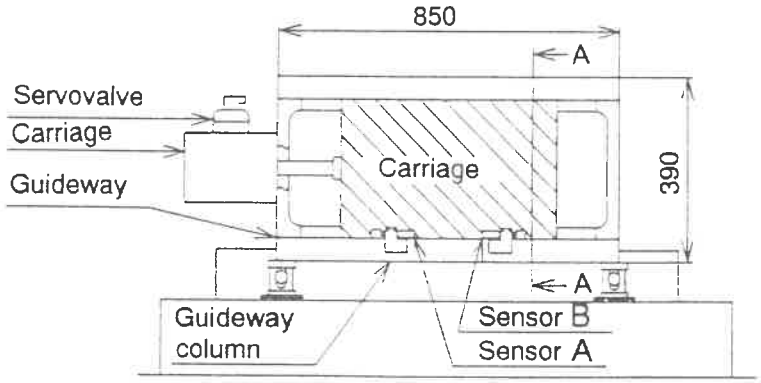

Fig. 1 Construction of the test rig

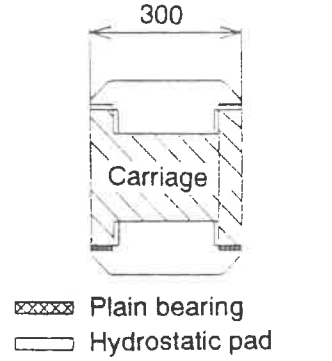

Fig. 2 Sectional view (A–A)

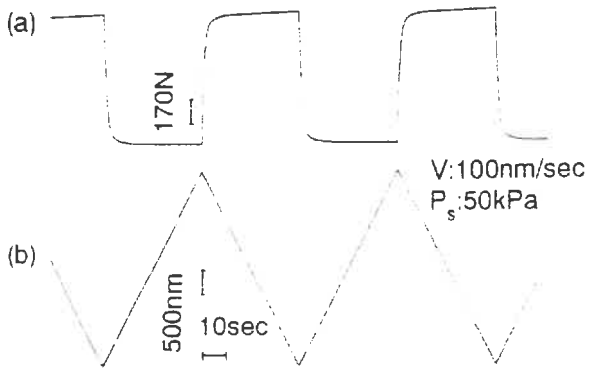

Fig. 3 Frictional load (a) and displacement of carriage (b) for the constant feed rate

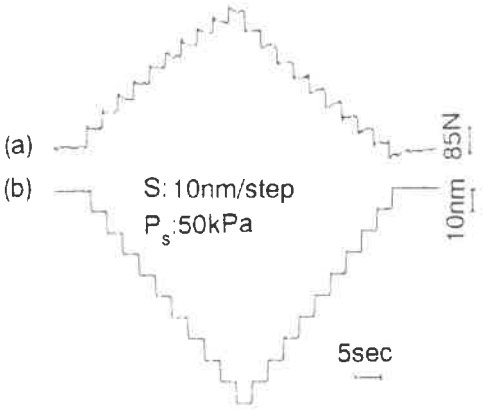

Fig. 5 Frictional load (a) and displacement of carriage (b) for the stepwise feed

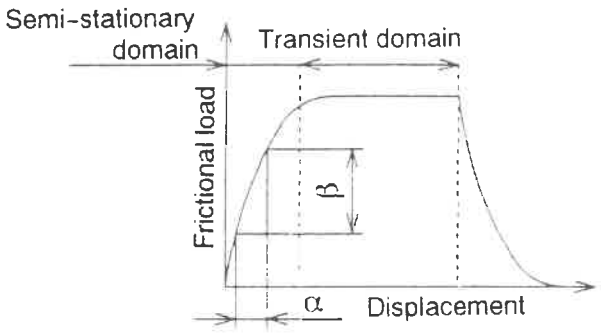

Fig. 4 Two domains in frictional load characteristics

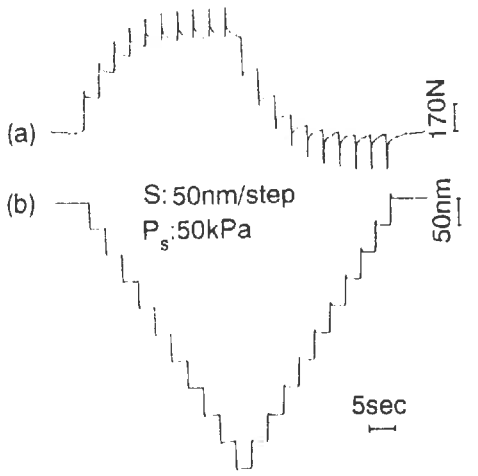

Fig. 6 Frictional load (a) and displacement of carriage (b) for the stepwise feed

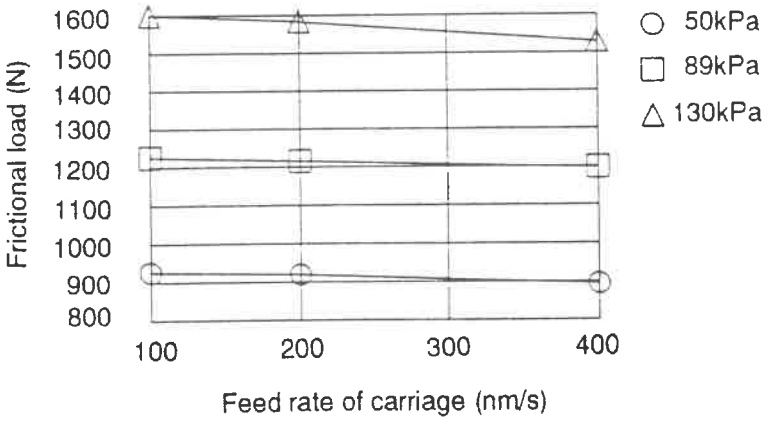

Fig. 7 Frictional load in stationary domain

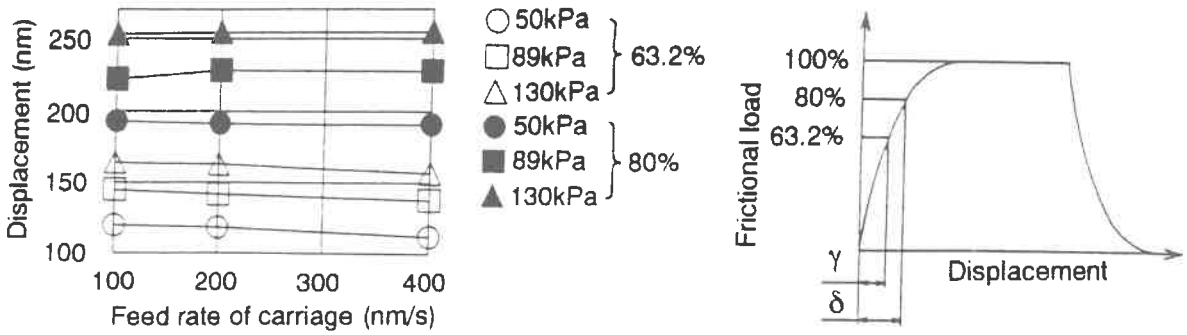

Fig. 8 (a) Transient domain for constant feed rate

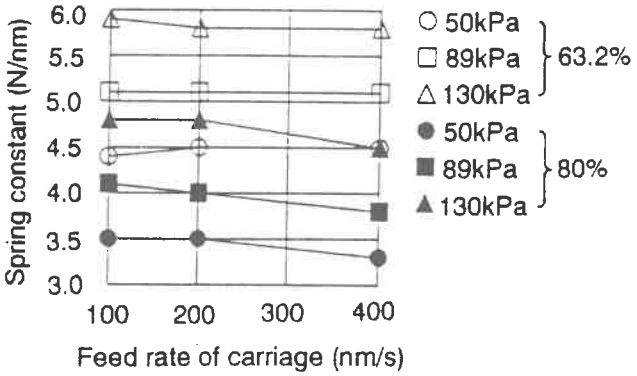

Fig. 8 (b) Effective spring constant in the transient domain for constant feed rate

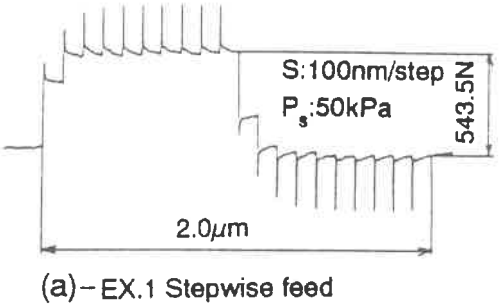

(a)－EX.1 Stepwise feed

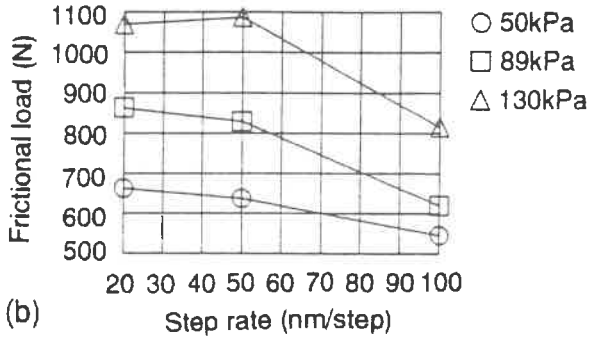

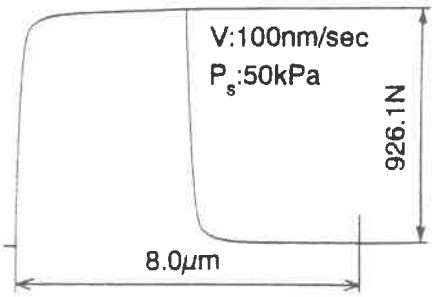

(a)－EX.2 Constant rate feed

Fig. 9 Frictional load in the stationary domain for stepwise feed

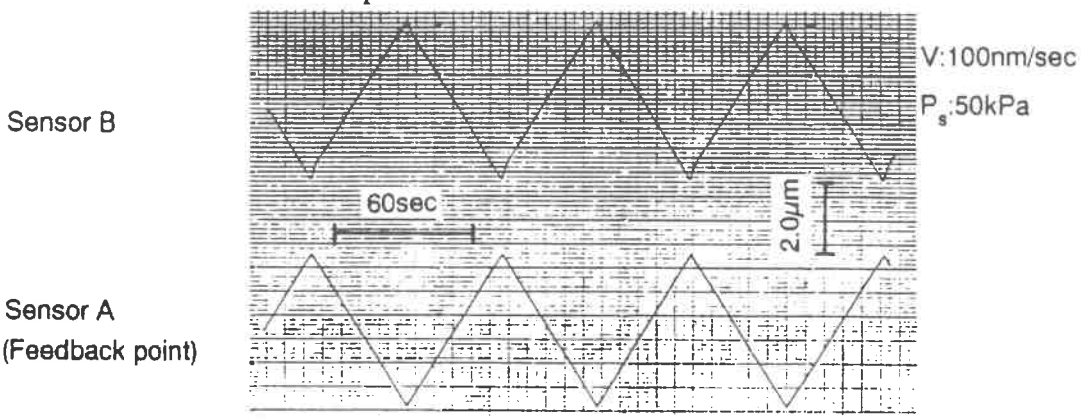

Fig.10 Displacement at the point away from the feedback point by 400mm

Non-Optical, Miniature, Precision Diamond Turning

P. Hannah, L. Forman, P. Gobby, S. Armstrong,
J. Bartos, D. Hatch, L. Salzer, B. Henneke
Los Alamos National Laboratory

If we go back in time and precision engineering history about thirty years, we find a turning point in the long history of the use of diamond as a cutting tool. The development of very sharp diamond tools and the availability of aerostatic and hydrostatic bearings, precision lead screws and slides led to the rise of single point diamond turning. The laser interferometer and the computer numerical control system have also helped bring this technology to the point we are at today. Experimenters during this recent period have come a long way, not only in the diversification of the turning process itself, but in the understanding of the physics of the process, chip science, material/diamond interaction, machine tool dynamics, etc. The single point diamond turning process over the last thirty years has grown into a mature technology that has been widely adopted by many industries for the manufacture of precision components. Many diamond turning process and machine users are still making optical parts, but others have found different uses for these geometrically accurate, specular surfaces, and it is to these other uses that we address this paper.

Imagine a cylindrical can, open on one end, closed on the other, with a small hole through the wall of this closed end (Figure 1). To this can we now add a machined plastic filling or plug, and our small hole in the closed end gets a disc of a third material.

This sounds rather straightforward until we look at the dimensions and materials (Figure 1a). Our "Can" is made of gold, and is only about 400μm (0.016") in diameter by 200μm (0.008") long with a wall only 25μm (0.001") thick. The plastic "Plug" is made of Delrin and fits inside the can. Our small hole "Disc" is made of 25μm (0.001") thick aluminum, with a diameter of about 100μm (0.004"). This assembly is a target for the laser fusion program. The next view graph (Figure 1b) is a simple scale comparison, to better give you a feel for how small these parts are.

Now that we have established the parts' size and materials the job becomes more complex. How do we machine or fabricate these parts? How do we hold parts so small? How do we assemble such a small component? Although single point diamond turning plays an

important part in the making of these components there are other processes or steps that are used also. They are: Physical Vapor Deposition (PVD), Electroplating, Plastic Coating, Microscopic Assembly and Manipulation.

Back to our target. The first operation is to diamond turn a mandrel (Figure 2, step 1). Bear in mind that the center machined section, which becomes the ID of our can, is only 400µm (0.016") in diameter by 200µm (0.008") long. With parts this small material quality, especially homogeneity, becomes very important; small voids, normally not a problem, become chasms on parts this small. On small parts like this we found that even OFHC copper was not suitable as it can have microscopic voids, however we do use it for larger parts. We finally settled on Silicon Bronze welding rod. It diamond turns well and seems to be void free. By diamond turning the mandrel we insure that the internal surface of the gold can will be specular. A feducial mark or reference step must be placed on or machined into the mandrel shank, as once plated, the mandrel surfaces become obscured. The end of the mandrel is now plated with gold (step 2). By careful masking and control of the plate thickness we minimize the machining waste of an expensive material. After plating (step 3), the OD of the Can and mandrel are diamond turned down to the desired diameter. Then the end of the mandrel is turned down until uniform wall thickness of the Gold Can is achieved. The last step (step 4) in the making of our Can is to leach away the bronze mandrel leaving our finished product. Leaching is achieved by using a bath of warm 50% nitric acid. After leaching the cans must be handled with care as gold dents and abrades easily.

We now move to the making of the small aluminum Disc (Figure 3). I would remind you that this Disc is only 100µm (0.004") in diameter, and 25µm (0.001") thick. First a small round copper blank is diamond turned on both sides, as is the flat face of the vacuum chuck that will be used to hold the part. Now a layer of aluminum is plated onto the copper blank. Then the face of the aluminum is diamond turned to the final required thickness, in this case 25µm. The plated blank is now offset so the axis of rotation falls on a circle about half way from the center to the edge. The tool is now moved away from this offset axis of rotation 50µm, then through a series of plunge cuts, each deeper and closer to the finished diameter, the part is machined. After the required diameter is reached the parts are literally "popped" off of the coated copper blank. It seems that the two metals do not diffuse into each other,

but form a weak bond, strong enough for machining but weak enough to permit careful mechanical removal of the finished parts.

This brings us to the 400µm (0.016") diameter Delrin plug. First a piece of Delrin rod is mounted in a collet and then diamond turned (Figure 4, step 1) to the finished diameter and height 200µm (0.008")+.

In order to provide machining support, the part is potted in a rigid wax (step 2). The wax and the Delrin are machined as in (step 3). When the wax is melted you are left with the small Delrin plug.

Before discussing assembly, we would like to mention that the diamond tools required to make these small parts in some cases are special. They may require dead sharp tips; radii of a few microinches are not uncommon. Diamonds with their cutting edges facing to the right or left are also used and most tool manufacturers are willing to work with their customers on tool design etc.

We would like to spend just a minute, and tell you how the preceding parts were assembled. Note: All the following assembly would be done with the assistance of a stereo microscope.

The gold can would be stood, open end up in a small glass Petri dish with cover. The dish and cover are important, as a sneeze or bump could be disastrous. The Delrin plug is then picked up with tweezers and placed or pushed into the gold can. Interestingly a small No.11 scalpel is frequently used as an assembly tool. The parts are so small that the scalpel's edge, both sharp and flat, makes a great pushing tool. If you noticed, the Delrin plug's thickness dimension had a plus after it. If you know the depth of the Gold Can, and you make the plug longer by a known amount, you can determine when the plug is seated. We typically use a shadowgraph for these measurements. Also there is sufficient friction between the Can and Shell to hold the parts together. Glue is not used in this step.

The Can/Plug assembly is now turned over, so the disc hole is exposed. Using a vacuum probe the aluminum disc is picked up and placed in or on the hole. The scalpel is used to gently push the part into the hole. The shadowgraph is used to insure that the disc is flush with the Can surface. These Discs can be slightly undersized, thus, loose in the hole. This being the case, a very small amount of 5 minute epoxy would be applied with a probe made with a single hair. It's hard for me to imagine applying any amount of epoxy to a part this small.

I would like to move to the making of a more complex part (Figure 5). In this view graph we see the mandrel, and in this case we are using OFHC copper as our part is a bit larger. It is similar to the one we made for the previous target with the exception of a

longer first section (step 1). This first section is machined oversize to insure that after gold plating and during the machining step that all of the gold will be removed from the copper. Step 2 simply shows the mandrel end plated with gold. Step 3-This diameter having been left oversized is now turned to its final dimension. In the next step (Figure 6, step 4) we are adding another coating. Parylene, a plastic material, overcoats the whole mandrel end, completely covering the gold and the copper. In this machining step (5) the parylene is cut from the end of the mandrel and from its sides exposing the copper. Leaching removes the copper, leaving the gold/parylene assembly as shown in (step 6). We now have a gold Can with a parylene coating covering the gold and forming a tube for the next step. Our assembly now gets a partial plug of AL(Aluminum) or PPS(Polyphenylsulfide).
Both of these materials can be diamond turned and are rigid enough so as not to require special chucking or mounting. As in all of the previous turning steps, the use of the precision diamond turning machine with its ability to move in steps as small as a microinch makes possible the very accurate part dimensions required. After machining the plug, a small insert tube is used to push the plug into the assembly. The last operation is to fill the tubular Parylene section with foam which is cured with an ultra-violet lamp.

This completes our look at some rather unique uses for precision diamond turning. Quite frankly without this process we are not sure how these very small components would be machined, much less to tolerances of microinches! Chris Evans in his book[1] quotes E.R. McClure then of Lawrence Livermore National Laboratory as saying "There was no place in the physicists' equations for tolerances."

It certainly seems true, that in the world of target physics at least, that near perfect parts are required. Precision single point diamond turning and the machines that have been[1] and are being developed have certainly gone a long way toward achieving this goal.

---

[1] Evans C. "Precision Engineering: an Evolutionary View" Cranfield Press 1989
1

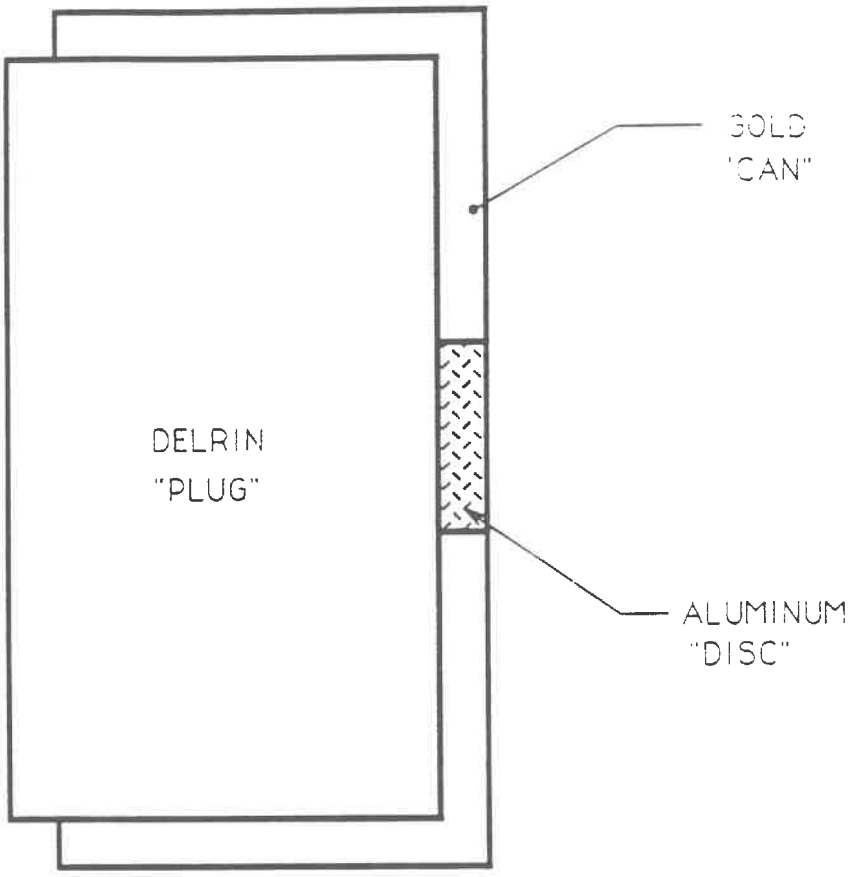

LASER TARGET

Figure 1

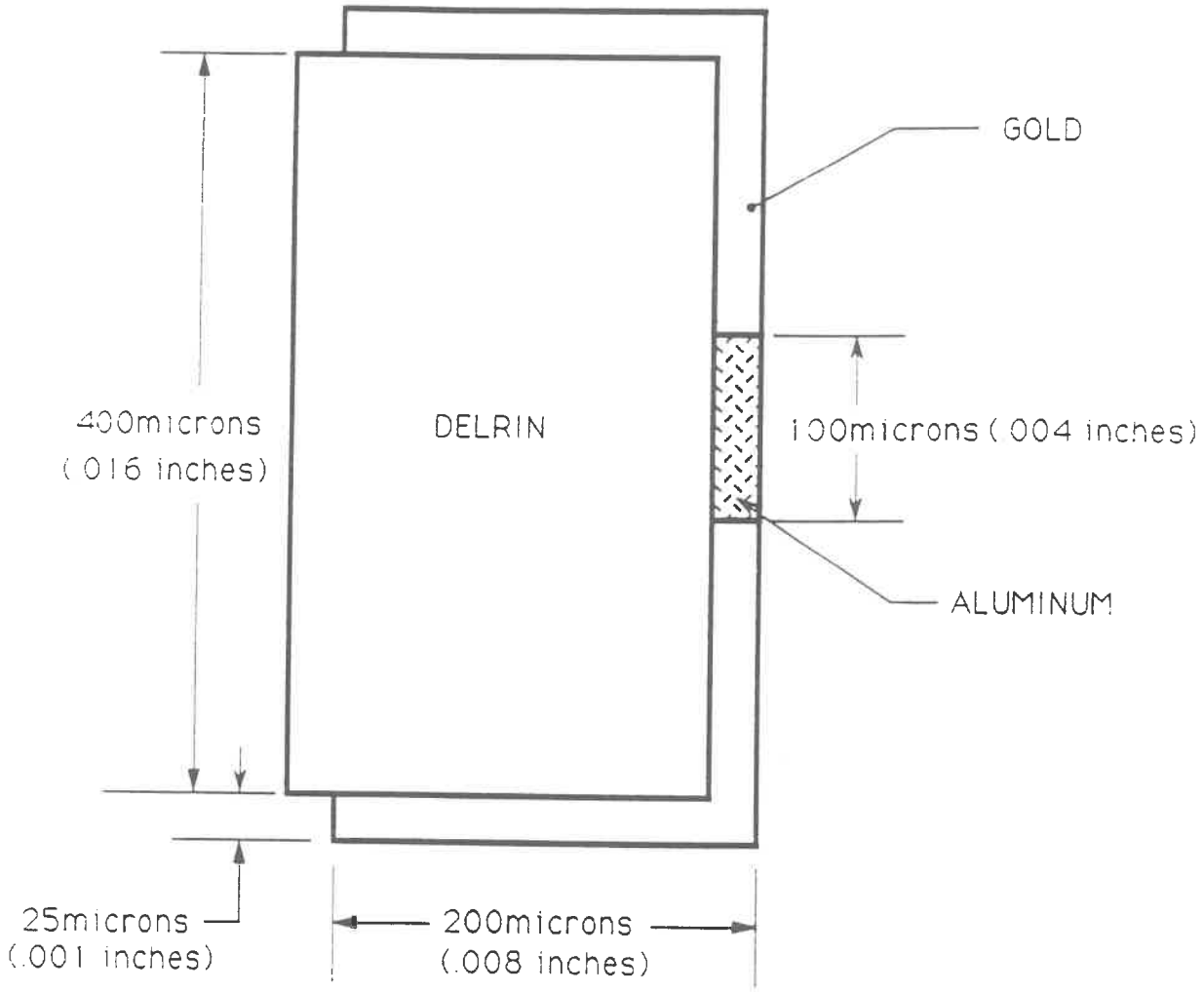

LASER TARGET

Dimensions

Figure 1a

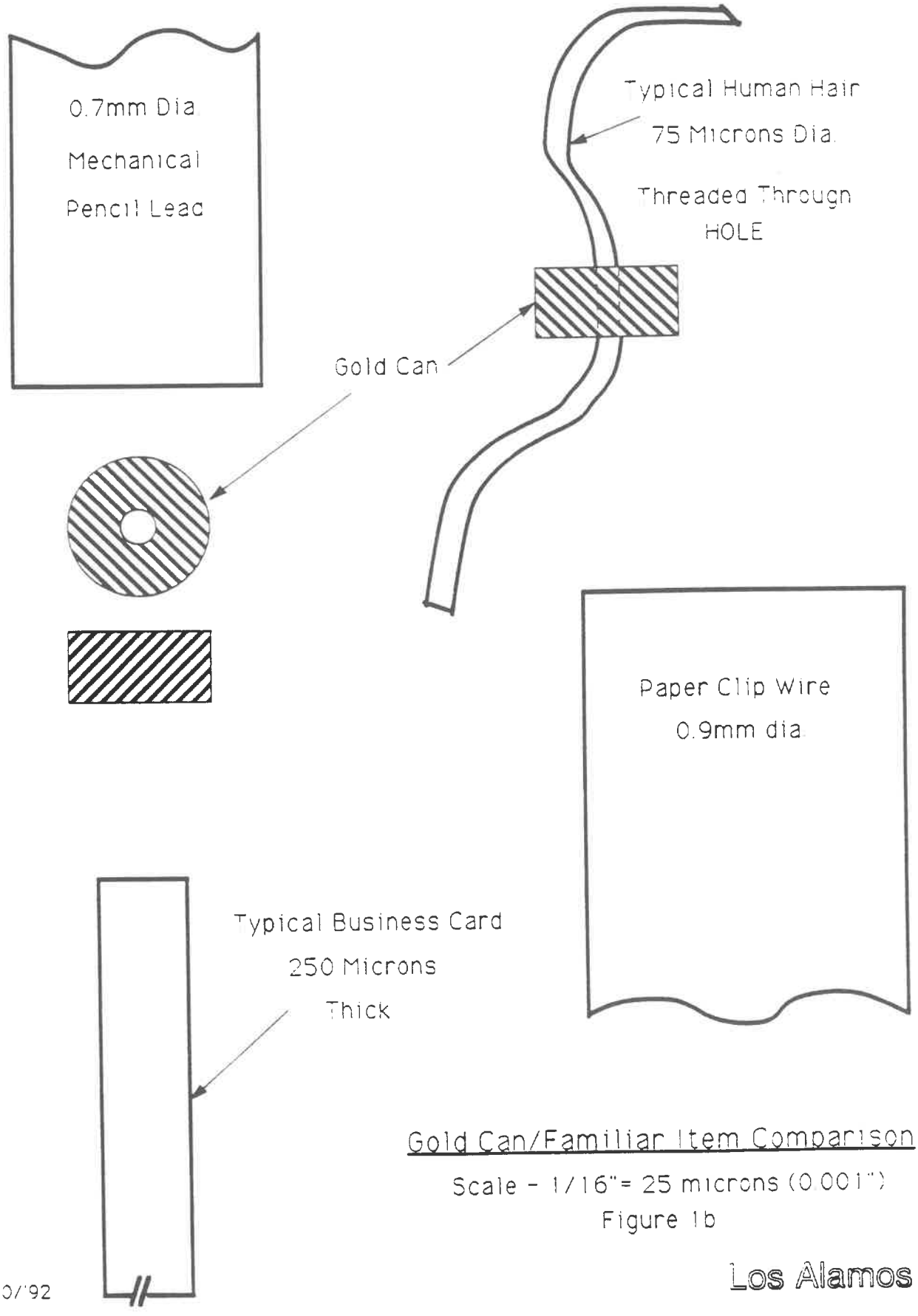

Gold Can/Familiar Item Comparison

Scale - 1/16"= 25 microns (0.001")

Figure 1b

PRH 6/30/'92

Los Alamos

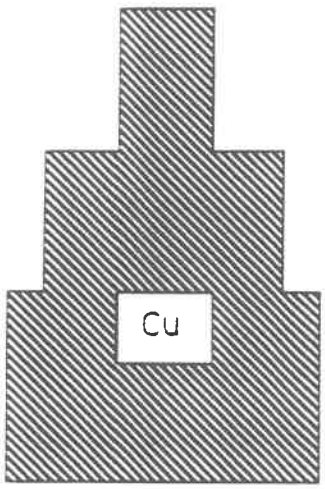

Step 1

Diamond Turn Cu Mandrel

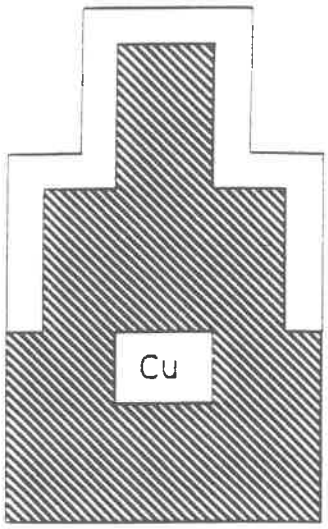

Step 2

Gold Plate Cu Mandrel

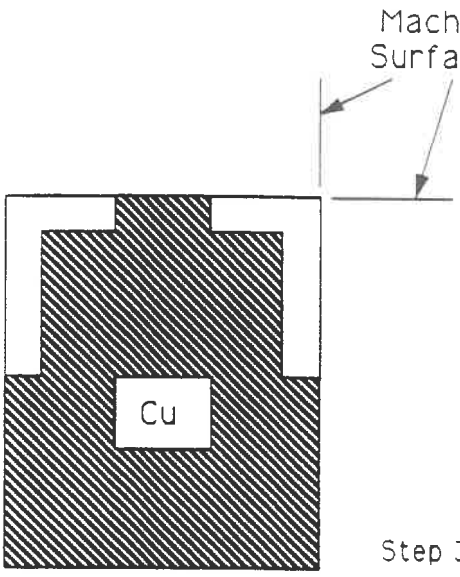

Step 3

Diamond Turn Cu and Au
then
Leach Cu Mandrel

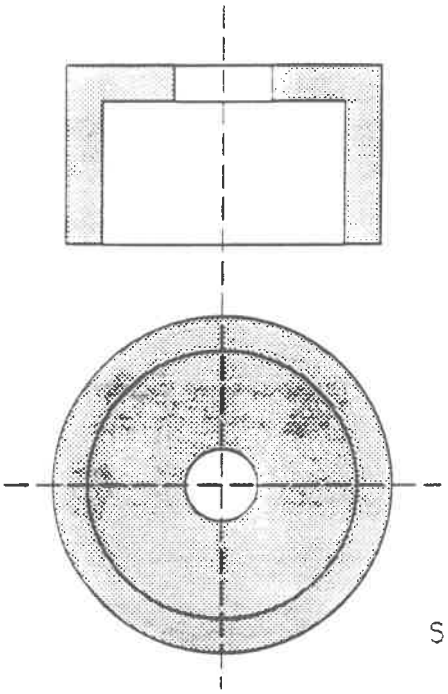

Step 4

Finished Au Can

LASER TARGET

Gold Can Fabrication
Figure 2

PRH '92 LANL

Los Alamos

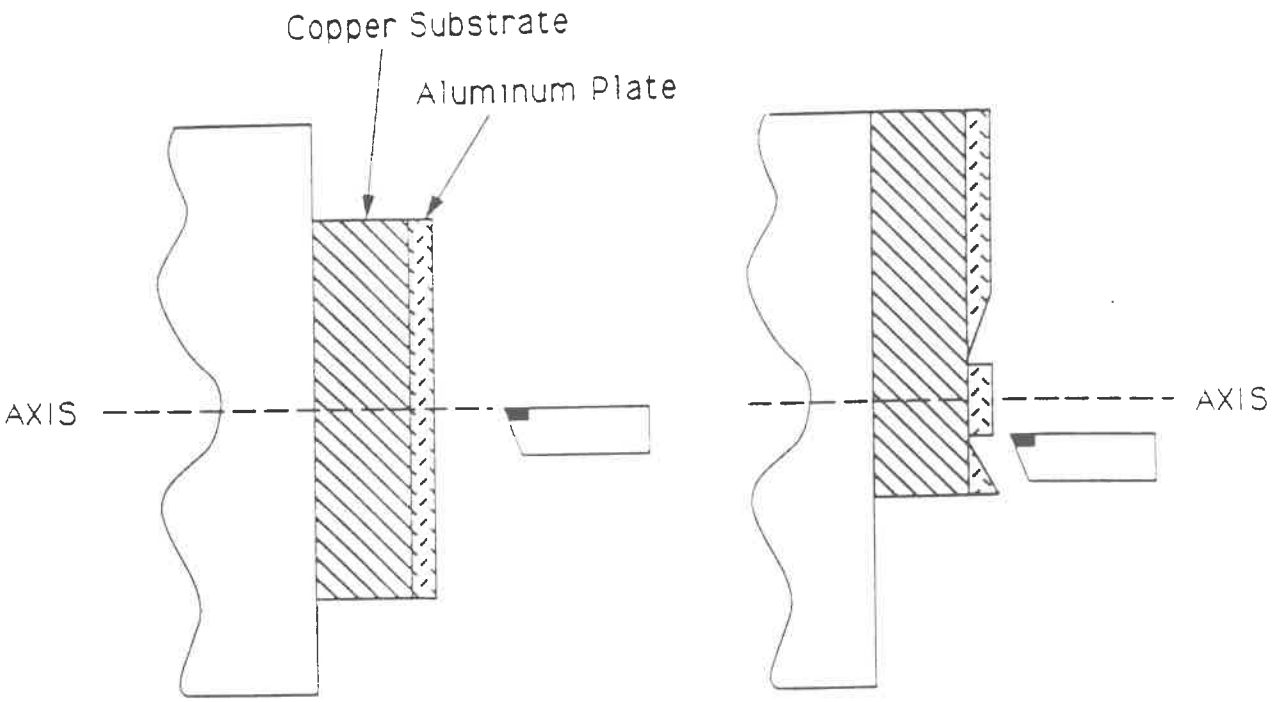

1st. Operation

Diamond Turn Aluminum (flat)

2nd. Operation

Eccentric Turning of Discs

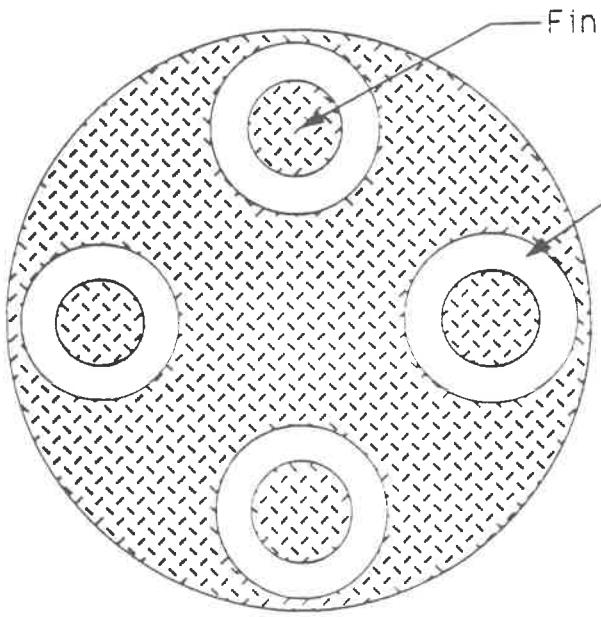

Finished Discs

LASER TARGET

Aluminum Disc Turning

Figure 3

PRH '92, LANL

Los Alamos

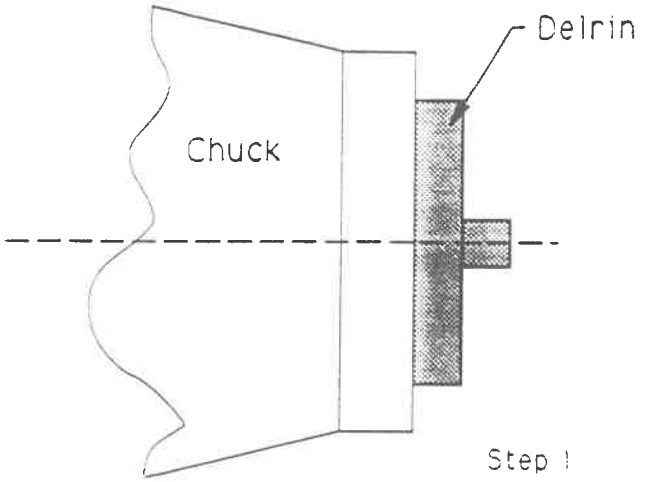

Delrin Turned from Solid

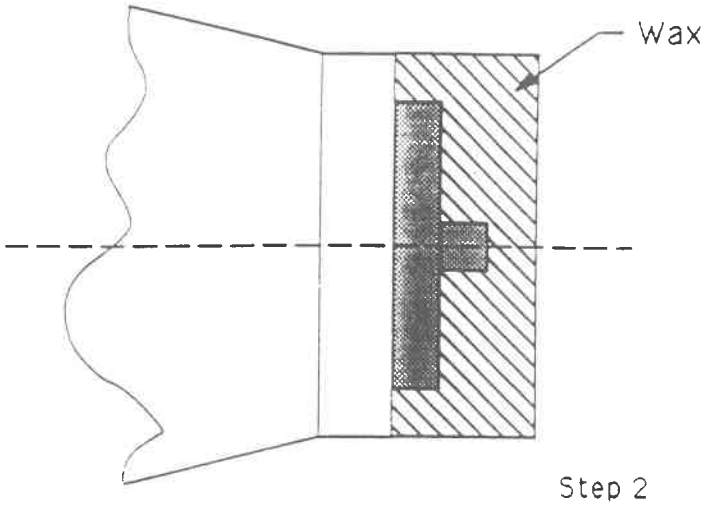

Wax Potting

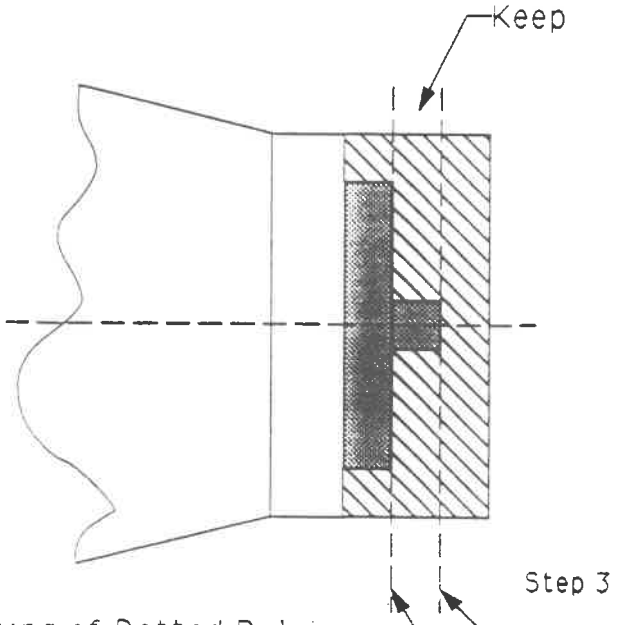

Machining of Potted Delrin

Melt Wax

Finished Delrin Part

LASER TARGET

Delrin Plug Fabrication

Figure 4

PRH 92 LANL

Los Alamos

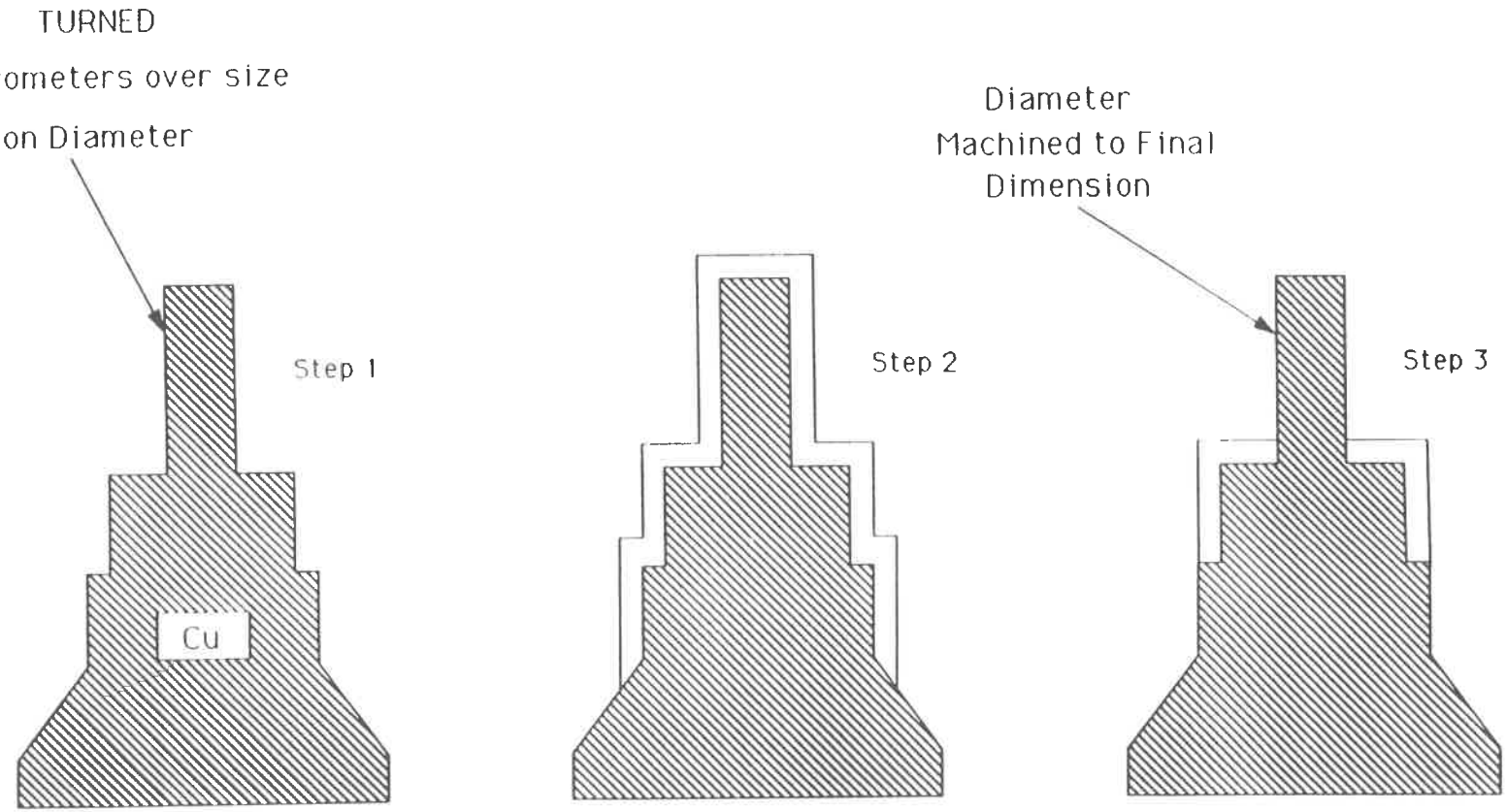

LASER TARGET

Machining Sequence

Figure #5

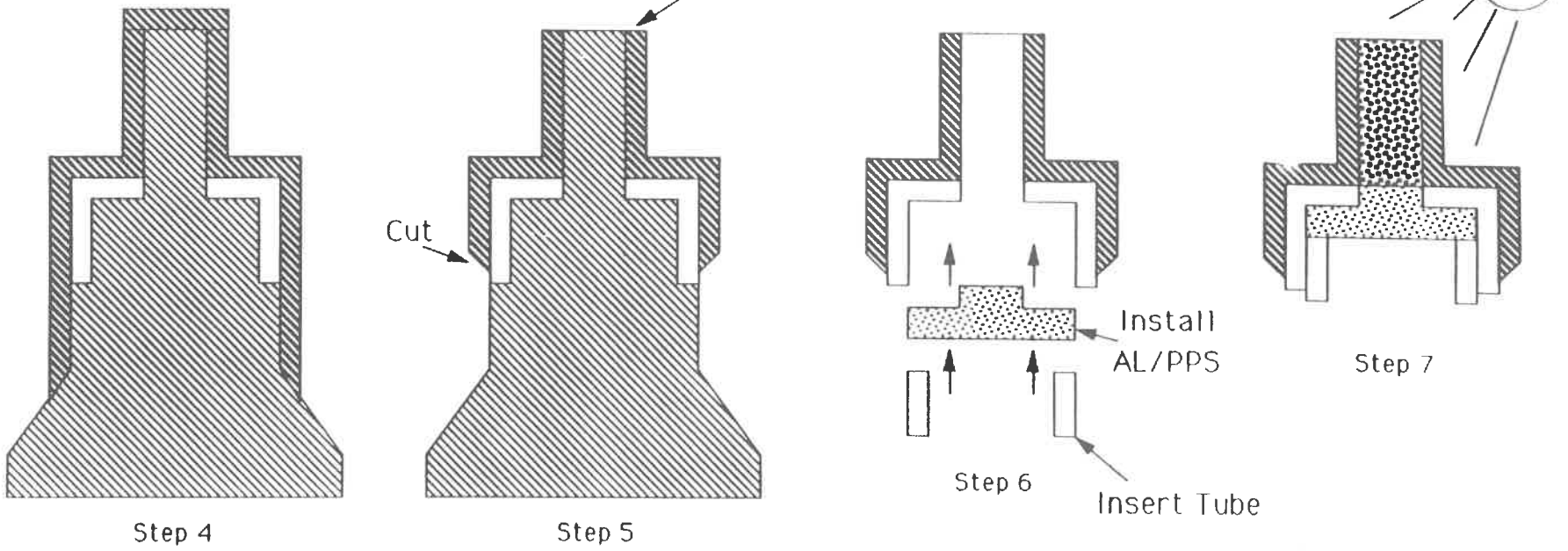

PARYLENE COAT

MACHINE PARYLENE
and
LEACH Cu MANDREL

LASER TARGET
Machining Sequence

Figure #6

A PROPOSED DESIGN FOR AN UNPOLARISED OPTICAL INTERFEROMETER SYSTEM WITH SUB-NANOMETRIC SENSITIVITY

M J Downs and W R C Rowley

Division of Mechanical and Optical Metrology
National Physical Laboratory

ABSTRACT

Optical interferometry is widely used for the precise measurement of length and the coherence of laser radiation permits fringe-counting systems with measurement ranges in the free atmosphere of up to 50 metres. The most commonly used radiation sources are frequency stabilised Helium-Neon lasers. These devices are readily available commercially and experience has shown that their frequencies do not usually change by more than a few parts in 10^8 over the lifetime of the laser tube. By using electronic systems to analyse the sinusoidally varying path length signals generated from the interferograms, sub-nanometric resolutions can be realised in certain applications.

The most commonly employed two beam interferometric measuring systems are based on designs by Michelson and Jamin. Bi-directional counting techniques are used to automatically correct for vibration or retraced motion, ensuring that the fringe count represents the displacement of the moving reflector. For optimum performance the fringe counting and fractioning electronics require two signals with constant average dc levels and sinusoidal components, related to the optical path difference in the interferometer, that are in phase quadrature. The counter logic is set to respond each time one of the signals passes through its average value. Unfortunately in practice this dc level is subject to variations. For example, its value is dependent on the intensity of the light source. Removal of the dc component by capacitance coupling, so that the average signal level is always zero, is not completely effective because the frequency of the sinusoidal component may be very low and, indeed, zero if the corner cube retro-reflector attached to the workpiece is stationary.

It is common practice either to employ some form of modulation of the interferometer signal or to maintain the average signal level at zero volts by an electronic subtraction

process which removes variations in the average signal level from the photodetector signals and avoids the need for modulation. However, instruments using these methods involve the use of polarisation techniques, introducing a 90° phase difference between the signals obtained from two orthogonally polarised components by means of a phase retardation plate. This results in the imposition of alignment requirements on the polarisation azimuths of the optical components in the interferometer system and the radiation source and, in addition, makes the system sensitive to polarisation effects which can result in a non-linear relationship between the measured phase difference and the respective path difference.

The interferometers described in this paper do not employ any form of modulation and generate two signals varying sinusoidally with path length by viewing the two outputs produced by the optical system. An example of this is the NPL sub-nanometric interferometer shown in the diagram. A phase difference of 90° is introduced between these signals by using an interferometer beamsplitter design utilising semi-transparent metal films. This has the significant advantage of completely removing the alignment constraints for the polarisation azimuths of the system and reducing the optical components required for an interferometer to a beamsplitter and retro-reflector. Electronic alignment and control is performed automatically by a processor which continuously analyses and modifies the two signals to obtain a high level of performance from these instruments.

The interferometers described avoid the problems encountered when measuring sub-nanometric path differences with instruments employing polarisation techniques and can be used for precision measurement with any radiation source suitably coherent for the application.

Instruments constructed using the technique are cheap to produce and easy to apply in practice as they require only a limited amount of optical alignment and all of the electronic adjustments required are automatically controlled by the electronic processor.

Interferometer beamsplitter characteristics

R_S = Reflectance (substrate/film interface)

R_A = Reflectance (air/film interface)

T = Transmittance

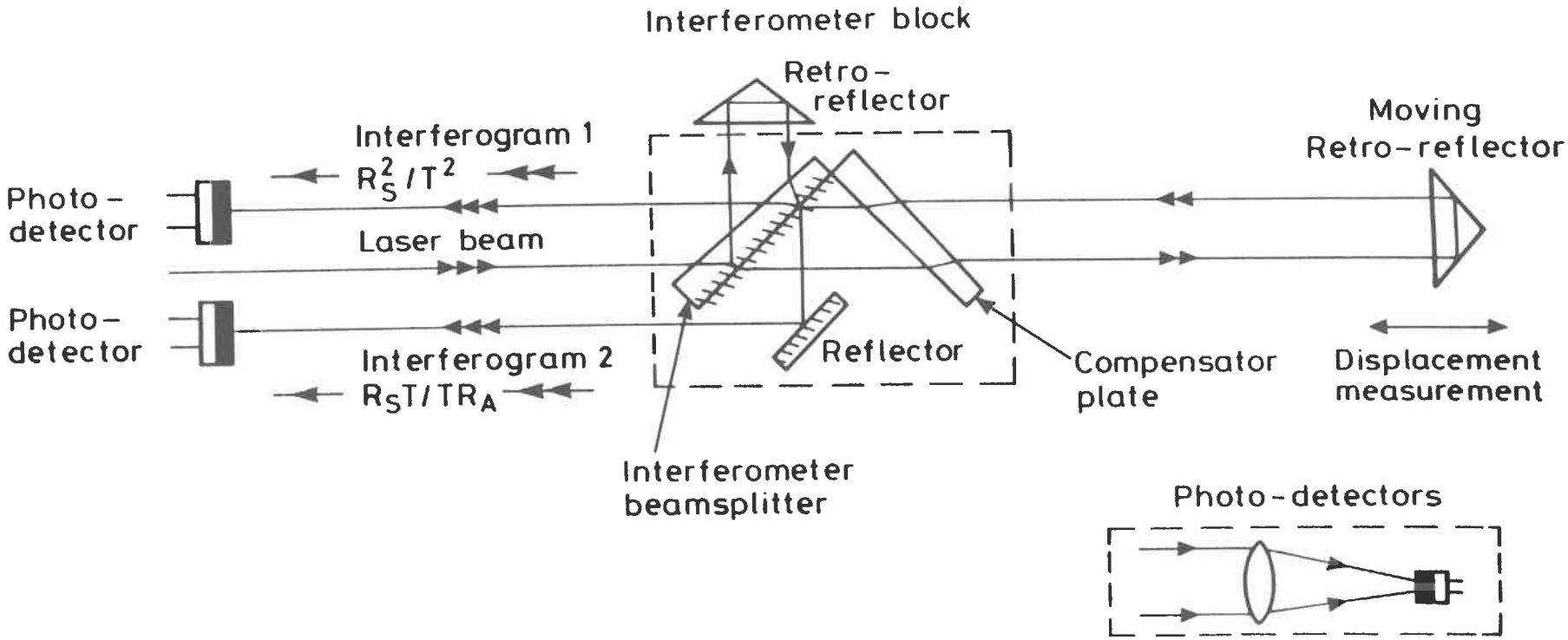

Cube Corner

Length measuring interferometer

AN INTERFEROMETRIC ROUGH SURFACE DISPLACEMENT SENSOR WITH 10nm RESOLUTION AND 40mm MEASURING RANGE

Donglei TANG*, Enyao ZHANG, Katsuhiko YASUDA**,**
Kaiji SATO, Akira SHIMOKOHBE** and Masahiro AKABANE***
*: Tokyo Seimitsu Co. LTD, 2968-2 Ishikawa-cho, Hachioji, Tokyo 192
**: Tokyo Institute of Technology, 4259 Nagatsuta-cho, Midori-ku, Yokohama 227

key words: optical sensor, noncontact sensor, laser diode, optical fiber coupler, selfoc lens, frequency modulation, heterodyne interferometer

1. Introduction

Recently there has been increasing demand for noncontact sensors in fields such as three-dimensional measuring machines, in-process measurements and robotics. However, there is still no method for rough surface displacement measurements which has: (1) no need for attachment of a retro-reflector or a mirror to rough surfaces, (2) a large measuring range of more than several milimeters, and (3) a high resolution of some ten nanometers.

This paper introduces a heterodyne interferometric optical fiber sensor for the displacement measurement of rough surfaces. The feature of laser diodes that their frequency can be modulated by the injection current is used[1].

2. Sensor setup and principle

2.1 Sensor setup

Figure 1 shows the basic setup of the sensor. It consists of the following subsystems:

2.1.1 Optical setup

The optical setup constitutes a Fizeau-type interferometer. It consists of a single-mode laser diode LD, a collimating lens L1, an optical isolator, a microscope objective lens L2, a single-moade optical fiber coupler, a selfoc lens SFL and two photodetectors, PD1, and PD2.

2.1.2 Electronic circuits

Electronic circuits are designed for generating the triangular modulation current and processing signals.

2.1.3 LD temperature controller

Since the wavelength of the LD is changed by the temperature fluctuation, a LD temperature controller using a Peltier heating element is used to stabilize the LD cavity temperature.

2.2 Principle

2.2.1 Interferometry

The light emitted by the LD is channeled into fiber 1 by L1 and L2. Light from fiber 1 is divided into two beams by the fiber coupler. One beam is transmitted by fiber 3 and its power is detected by the PD2. The other beam is transmitted by fiber 2 to the SFL, which is attached to the end of fiber 2. Light from fiber 2 is collimated by the SFL. A small part of the light reflects at the SFL exit end, while the remainder emerges from the SFL and illuminates the object surface. A fraction of the light scattered by the object surface is collected by the SFL. The beams reflecting at the SFL exit end (the reference beam) interfers with the beam collected by the SFL (the object beam). The two beams are transmitted back through fibers 2 and 4. The interference power is detected by the PD1.

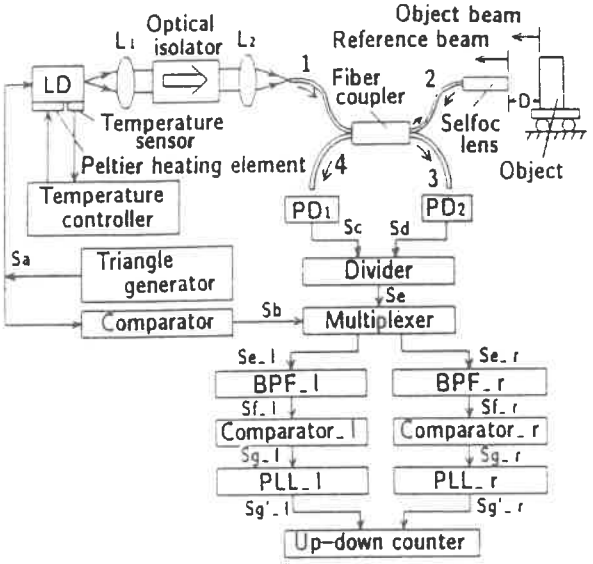

Fig.1 Basic setup of the interferometric rough surface displacement sensor

2.2.2 Signal processing

Figure 2 shows waveforms of electric signals when the object is stationary (Fig.2(a)) and moves away from the sensor (Fig.2(b)). When the LD is injected by the triangular modulation current Sa (Fig.2), the frequency ω and the power I of the reference and the object beams change as Fig.3. Since there is a time delay τ between the two beams due to the distance D from the SFL exit end to the object surface, a frequency difference ω_b between two beams occurs. The sign of ω_b in the front half of the modulation period is opposite to that in the back half.

PD1 detects the beat signal Sc whose amplitude is modulated undesirably by Sa. This effect is removed by dividing Sc by PD2 output, Sd. The divider output Se is time-multiplexed into Se_l and Se_r to process separately the signals according to the sign of ω_b. The first half of Se_l and the second half of Se_r change their frequency and phase when D changes. To eliminate the effect of the frequency change, two bandpass filters (BPF_l and BPF_r) extract only the fundamental components of modulation frequency, Sf_l and Sf_r. The phases of Sf_l and Sf_r remain proportional to the distance D.

However, conventional phase detectors can not measure the dynamic phase change over 2π and do not have a enough resolution. So, in this paper, the phase change is measured from the integration of the frequency deviation. Digital signal processing is used as shown in Figs 1 and 2 where the frequencies are multiplied to realize a higher resolution by the PLLs. The outputs Sg'_l and Sg'_r are fed into a up-down counter. The ouput of the counter denotes the object displacement from an arbitrary reference position.

In Fig.2(a), the object is stationary and the frequencies of Sg'_l and Sg'_r are the same. Therefore, the output of the up-down counter remains constant. However, as shown in Fig.2(b), when the object moves away from the sensor, the frequency of Sg'_l increases while the frequency of Sg'_r decreases. Then the up-down counter output increases. Similarly, when the object approachs the sensor, the counter output decreases.

2.2.3 Mathematical description

In the time of , $\tau \leq t \leq Ts/2$, the injection current Sa (Eq.(1)) modulates the LD

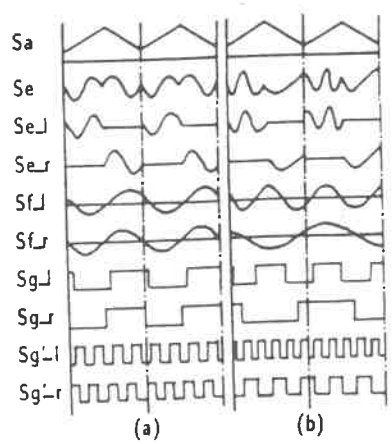

Fig.2 Waveforms of the electric signals.
(a) the object is stationary,
(b) the object moves away from the sensor

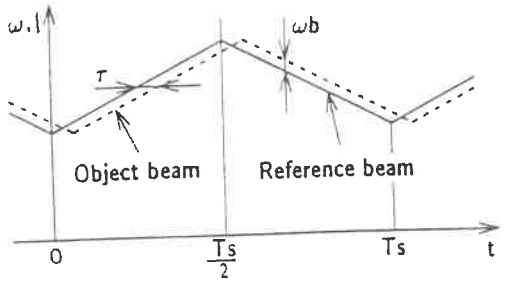

Fig.3 Frequencies and powers of the reference and object beams

frequency ω as Eq.(2).

$$Sa(t) = i_0 + \frac{2\Delta i}{T_s}t, \qquad (1)$$

$$\omega(t) = \omega_0 + \frac{2\Delta\omega}{T_s}t = \omega_0 + \alpha t, \qquad (2)$$

where i_o is the bias current, Δi is Sa amplitude, ω_o is the LD frequency when LD is driven by i_o, $\Delta\omega$ is the magnitude of LD frequency modulation, and α is the rate of the frequency modulation, $\alpha = 2\Delta\omega/Ts$.

The time delay τ between the reference and object beams is $\tau = 2D/C$ (C: velocity of light).

The optical fields of the reference beam $E_r(t)$ and the object beam $E_o(t-\tau)$ can be expressed by

$$E_r(t) = \sqrt{\beta_r I(t)}e^{j[\omega_o t + \alpha t^2 + \phi(t)]}, \qquad (3)$$

$$E_o(t-\tau) = \sqrt{\beta_o I(t)} e^{j[\omega_o(t-\tau)+\alpha(t-\tau)^2+\phi(t-\tau)]}, \quad (4)$$

where the powers of the reference and object beams are denoted by β_rI(t) and β_oI(t), respectively. Here, ϕ(t) is the LD random phase fluctuation.

The output of the PD1 is given by

$$\mathrm{Sc(t)} = \mathrm{K}\{[\mathrm{E_r(t)} + \mathrm{E_o(t-\tau)}] \cdot [\mathrm{E_r^*(t)} + \mathrm{E_o^*(t-\tau)}]\rangle$$

$$= \mathrm{KI(t)}[\beta_r+\beta_o+2\sqrt{\beta_r\beta_o}\mathrm{e}^{(\frac{-\tau}{2\tau_{coh}})}\cos(\omega_b t+\phi_b-\alpha\tau^2)], \quad (5)$$

where K is a constant, $\langle\ \rangle$ denotes a time average, $\star$ is the complex conjugation and τ_{coh} is the LD coherence time. The frequency ω_b and phase ϕ_b are proportional to the distance D as

$$\omega_b = 2\alpha\tau = 2\alpha\frac{2D}{C}, \quad (6)$$

$$\phi_b = \omega_o\tau = 2\pi\frac{2D}{\lambda_o}, \quad (7)$$

where λ_o is the LD wavelength corresponding to ω_o as $\lambda_o = 2\pi C/\omega_o$.

In Sc(t), since τ is small, $\alpha\tau^2 \doteq 0$, exp(-$\tau/2\tau_{coh}$) $\doteq 1$. The term I(t) is removed by the divider and the DC component, $\beta_r+\beta_o$, is removed by an ac-coupling in the divider output onto the multiplexer. Thus Se can be simply described as

$$Se(t) = 2K\sqrt{\beta_r\beta_o}\cos(\omega_b t + \phi_b). \quad (8)$$

Since Se_l is a periodic signal, it is composed of a fundamental and several harmonic components as

$$Se\_l(t) = \sum_{n=1}^{\infty} B_n \cos(n\omega_s t + \phi_b), \quad (9)$$

where the amplitude Bn is

$$B_n = K\sqrt{\beta_r\beta_o}\,\mathrm{sinc}[\frac{(\omega_b - n\omega_s)T_s}{2\pi}], \quad (9)$$

where sinc(x) is a sinc function.

The fundamental frequency component Sf_l obtained by the BPF_l is

$$Sf\_l(t) = B_1\cos(\omega_s t + \phi_b). \quad (11)$$

Similarly, Sf_r obtained by the BPF_r is

$$Sf\_r(t) = B_1\cos(\omega_s t - \phi_b). \quad (12)$$

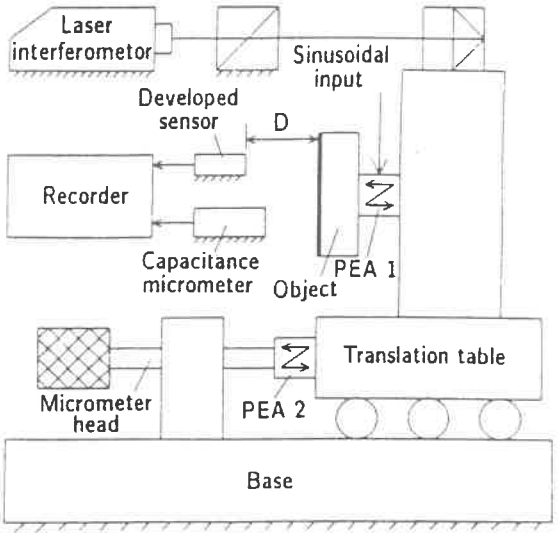

Fig.4 Experimental setup to examine the sensor

If the phase change of Sf_l, or Sf_r, is measured, the displacement of the object ΔD can be obtained by $\Delta D = \Delta\phi_b/(4\pi)\lambda_0$.

3. Experimental setup

3.1 Constructed sensor

A 10mW laser diode (Hitachi, HL7802G) is used. The fiber coupler is made of single-mode fibers of 6μm core and 125μm cladding, and its dividing ratio is 50:50. The SFL is 0.25 pitch in length and 1.8mm in diameter. The SFL is not AR-coated, which allowes about 4 percent of light to reflect at the exit end.

The bias injection current of LD is 55mA. The frequency of triangular modulation current is 10kHz and the amplitude is 1.2mA. The up-down counter changes 80 pulses for every 2π change of ϕ_b. One pulse corresponds to $\lambda_o/80$ which approximately equals to 10nm displacement.

3.2 Experimental setup

Figure 4 shows the experimental setup to examine the sensor. The distance D between the sensor and the object surface is changed by a micrometer head and a piezoelectric actuator (PEA2). A HP laser interferometer and an ADE capacitance micrometer are used as reference sensors.

4. Experimental results

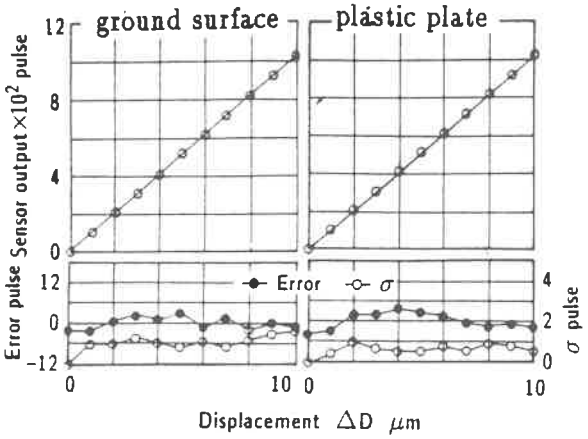

(a) range 10μm

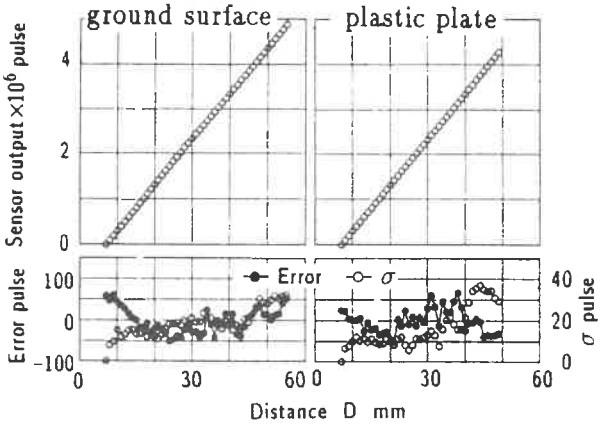

(b) range 50mm

Fig.5 Displacement measurement results

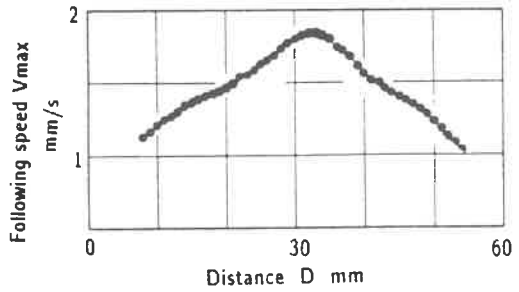

Fig.6 Following speed V_{max} vs distance

4.1 Displacement measurements

Figure 5 shows the experimental results of two rough surfaces (a ground metallic surface, R_a=2.04μm, R_{max}=17.0μm, and a brown plastic plate, R_a=0.11μm, R_{max}=2.84μm). In the ranges of 10μm (Fig.5(a)), 50mm (Fig.5(b)), output pulses of the sensor relative to the reference sensors are tested. Errors from the least squares straight lines and the standard deviation for 6 repetitions of the measurements are calculated. When the distance of the object from the sensor is less than 7mm, or greater than 50mm, the output of BPFS become too small and the measuring range is limited.

Figure 5 indicates that the measuring range, linearity and standard deviation are almost constant in spite of the different surface features.

4.2 Vibration measurements

The object is vibrated sinusoidally the PEA1. The vibration is detected by the sensor and the the ADE capacitance micrometer simultaneously. The amplitude A_m of the vibration is constant (A_m=1μm). When the vibration frequency f is low, the outputs of the sensor and ADE capacitance micromenter are the same. However, when the frequency f is increased, the sensor becomes unable to measure the vibration correctly, which indicates the limit of the sensor following speed. This following speed limit is due to the bandwidthes of BPFs. Figure 6 is the measured results of the sensor following speed V_{max} ($V_{max}=2\pi f_{max}A_m$, f_{max}: maximun measurable vibration frequency) relative to distance D. Since the amplitudes of the BPFs change with D, the measured following speed V_{max} also changes with D. The maximum following speed of the sensor is 1.8mm/s.

5. Conclusions

An optical noncontact displacement sensor was introduced. The sensor proved itself to have a large measurement range of displacement for rough surfaces. The measuring range, resolution and accuracy were sufficient for practical use. The next step of the study is to improve the following speed.

References

1) A.Dandridge: Current-induced frequency modulations in diode laser, Electron. Lett. 18, 302(1982).

SAMPLING STRATEGIES FOR CIRCLES IN COORDINATE MEASURING MACHINES

O. Odayappan, J. Raja, R. J. Hocken, and K. Chen
Precision Engineering Group, UNC Charlotte
Charlotte, NC 28223

1.0 INTRODUCTION

The increasing need for tighter tolerances, emphasis on process control in manufacturing to achieve high quality, and the trend towards automation has resulted in the need for fast and accurate dimensional and form measurement systems. Co-ordinate measuring machines (CMMs) have been designed to satisfy the measurement needs in modern manufacturing, and in recent years CMMs have become the instrument of choice for dimensional measurement. CMMs are capable of providing detailed dimensional data on most machined part surfaces and also give the relationship between various part features. This is achieved by taking discrete sample points on surfaces and establishing substitute geometry based on the sampled points.

One of the major tasks for the CMM operator is to decide the sampling strategy - how many points are necessary and how to distribute these points. There is theoretically a minimum number of points required for determining each geometric entity, but in the presence of measurement error and manufacturing error, more points are necessary to detect the departure from the nominal form. Taking more points than needed might be uneconomical due to increased inspection time and computational performance. Hence, there should be a recommended, statistically-based number of points and a recommended distribution for CMM measurement. UNCCharlotte, National Institute of Standards and Technology, National Physical Laboratory (U.K.) and Physikalisch-Technische Bundesanastalt (Germany) have active research projects in this area. The British Standard BS 7172 [1] addresses this problem for the most important geometric entities usually measured, namely, lines, planes, circles, spheres, cylinders and cones. Their recommendations for the number of points are given in the table in Figure 1.0. The distribution of these points are also covered in the standard.

These recommendations can be refined by taking into account other factors like the tolerance requirements, different types of form errors, noise in the data, effect of sampling using different algorithms, etc. This paper reports a part of the results from a project sponsored by Computer-Aided Manufacturing International (CAM-I). The project was carried out by first identifying the parameters that could influence the measurement and then conducting computer experiments to study their effect on measurement strategy. The following sections provide a brief summary of the research work carried out to arrive at a decision table for measurement of circles in a CMM.

2.0 PARAMETER IDENTIFICATION, COMPUTER SIMULATION AND ANALYSIS

Identifying the parameters that affect the measurement process and the measuring system is an essential prerequisite for developing a measurement strategy. The various parameters that could influence the measurement strategy of a circular profile are given in Figure 2.0.

In order to develop the best measurement strategy, numerous experiments had to be conducted to study the influence of different parameters on the measurement strategy. Considering the large number of experiments and the associated cost and time, computer-

simulated test cases were used for this study. The simulation was verified using data from real parts. A typical three-lobed part was selected and measured using a CMM. This part was compared with a three-lobed, computer-generated part to validate our data generation procedure.

The computer generated data, representing different manufacturing conditions were used to fit a circle using substitute geometry algorithms(Least Squares, Mini-Max, Maximum Inscribed and Minimum Circumscribed) and the parameters (radius, center coordinates and out-of-roundness) of the circle are obtained. The simulation is repeated 100 times for the same part by taking the same number of points, i.e., the same part is measured repeatedly by sampling at different locations in the same plane. Sample sizes of 3 to 20 points were studied. This is done for different parts with commonly encountered form errors, such as lobing(2-9 lobes). Figure 3.0 gives the results from a computer experiment for a three lobed computer generated part and a real part. Results from the computer experiments were analyzed, and used to arrive at a decision table for the measurement of a circle in a CMM. The decision tables provide recommendations for number of points and sampling method based on the expected nature of form error and measurement error.

3.0 CONCLUSION

In this research project, rules were developed for measuring circles. Initially all the parameters that could influence the measurement of circles were identified. Computer programs were developed to simulate parts with different types of error similar to the ones obtained from different manufacturing processes. The simulated parts were sampled in the computer with different sampling schemes, and the data were processed with least-squares, minimum zone, minimum circumscribed, and maximum inscribed circle algorithms. The results were analyzed to arrive at recommendations to measure the circles.

From our experiments we observed that whenever the number of points is equal to the number of lobes, center values converge to the true solution values (True solution is the solution obtained by sampling 360 points.) but the size and form error detected deviated from the true solution values. When the number of points sampled is one more than the number of lobes, the center of the fit circle is shifted, though the size is equal to the true solution value. When a common factor exists between the number of lobes and the number of sampling points, the form error detected varies considerably.
Based on extensive experimentation, the number of points to be sampled for different lobing characteristics of the part for different algorithms were deduced. The results were summarized in the form of decision table.

4.0 REFERENCES

1. BSI, "Assessment of Position, Size and Departure from Nominal Form of Geometric Features", British Standards Institution, BS 7172,1989.

2. Odyappan, O. "Development of Methodologies for Measurement of Circles on a Coordinate Measuring Machine", M. S. Thesis, UNCCharlotte, NC, Aug., 1992.

Element	Minimum Number of Points		Comment Regarding Recommended Minimum Number of Points
	Mathematical	Recommended	
Line	2	5	
Plane	3	9	Approximately three lines of three points.
Circle	3	7	To detect up to six lobes.
Sphere	4	9	Approximately three circles of three in parallel planes.
Cylinder	5	12	Circles in four parallel planes for information on straightness.
		15	Five points on each circle for information on roundness.
Cone	6	12	Circles in four parallel planes for information on straightness.
		15	Five points on each circle for information on roundness.

Figure 1 The mathematical minimum number of points and the recommendations as given in BS 7172 [1].

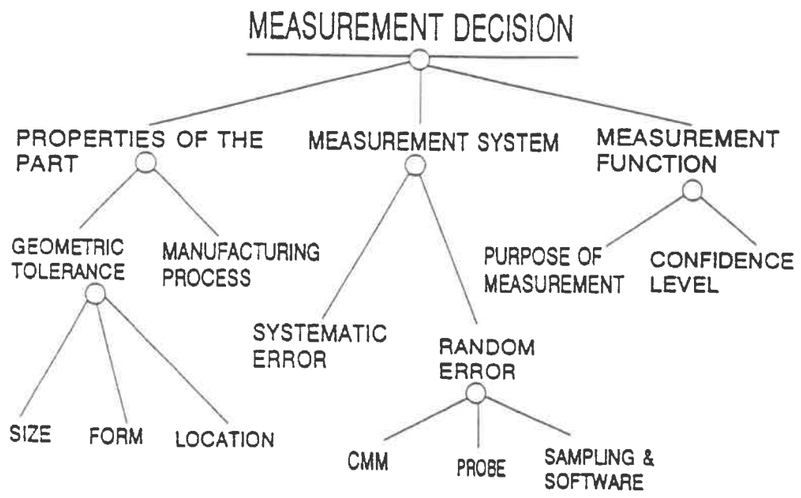

Figure 2 Parameters influencing the measurement strategy.

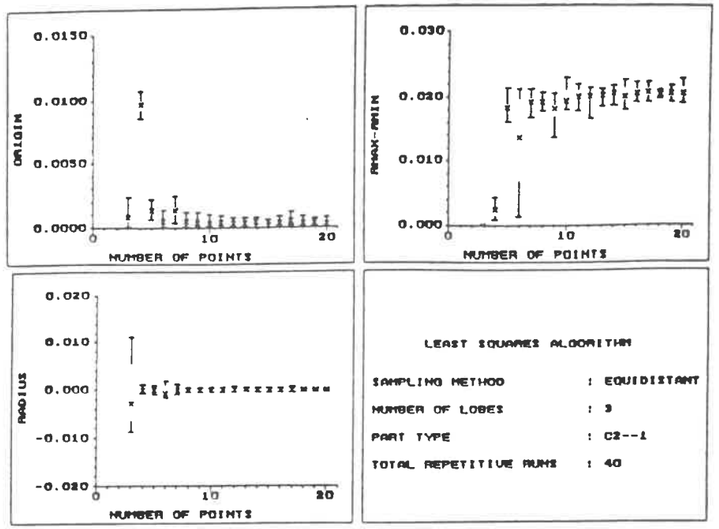

Figure 3a Results of the least-squares algorithm for a three-lobed turned part with 10 m lobe amplitude and 2.5 m random error using equidistant sampling.

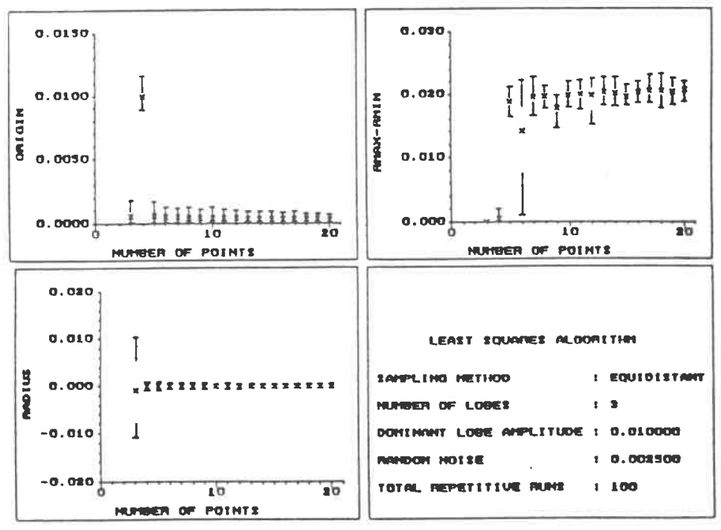

Figure 3b Results of the least-squares algorithm for a computer generated three-lobed part with 10 m lobe amplitude and 2.5 m random error using equidistant sampling.

LONG RANGE CONSTANT FORCE PROFILING: INITIAL RESULTS AND ONGOING DEVELOPMENTS.

Lowell P. Howard and Stuart T. Smith*

University of North Carolina at Charlotte
Precision Engineering Laboratory
Charlotte, NC 28223, USA

* University of Warwick
Centre for Microengineering and Metrology
Coventry CV4 7AL, England

INTRODUCTION

There is some evidence [Garratt, 1990] that high resolution stylus profilers with small radius styli (< 1 μm), contact the surface with enough pressure to "plow" through small surface features, while still following the macroscopic profile of the surface. This process has been likened to removing a layer of topsoil from a golf course with a bulldozer [Thomas, 1978]. While the bulldozer may leave behind an ugly scar, the lay of the land (or fidelity of the stylus measurement) remains unchanged. Unfortunetly, the scattering properties of most optics are defined by these same fine striations that conventional stylus profilers plastically deform.

So, while the fidelity of stylus form measurements has been proven, it is self-evident from the growth of non-contacting surface finish instrumentation markets that metrologists are indeed very concerned about surface damage effects from profiler styli. Consider now atomic force microscopes, which have taken stylus measurements almost to their physical limits. While AFMs have evolved into atom resolving commercial instruments, their widespread application to tasks traditionally reserved for stylus instruments has been hampered by at least two factors:

- Lack of international standards for measurement cantilevers or microscope components. Conversely, stylus instruments have been studied for decades and are supported by many international standards.

- There as yet exists no faculty for continuous long scans over several hundred micrometers. International standards for stylus instruments specify the cutoff wavelength for most engineering surfaces to be in the range of 0.8 mm with a traverse length of around 5 mm.

We endeavored to take some of the best elements of stylus profilers (probe knowledge, standards and long traverse length) and blend them with some of the best elements of AFMs (low force operation, high-speed scanning) to produce a hybrid metrology tool.

CONSTANT FORCE PROFILING [Howard and Smith, 1992]

Recently, experiments were performed that significantly improved both the contact force and scanning speed of a stylus instrument. To summarize:

• A force sensor capable of utilizing standard ISO styli was constructed from low thermal expansion coefficient materials (Fig. 1). The sensor's glass cantilever spring is air damped by the squeeze film of air between the electrodes, providing controllable dynamics.

• The force on the cantilever was monitored by a capacitance gage which was used to control a piezoelectric stack in a closed loop configuration. By maintaining a constant capacitor gap, the stylus was forced to follow a contour of constant force (Fig. 2). This contact force is adjustable by changing the control system's setpoint.

• A precision carriage and slideway (Rank Taylor Hobson Nanostep) was used to translate the sample under the stylus. This slideway has excellent thermal expansion characteristics, is dimensionally stable with time and has a noise level on the order of picometers (Fig. 3).

• Nanometer sensitivity was achieved over traces many tens of millimeters long while profiling at a constant force of approximately 0.1 μN (Fig. 4).

ADVANCED FORCE PROFILER

Currently under development is an improved instrument which will be used to undertake force/damage and compatibility studies with existing stylus profilers. This instrument will be host to several systems designed specifically for these studies:

■ A low-cost kinematic carriage and slideway system, utilizing low-cost BK-7 glass components in such a way to produce a nearly perfect vee shaped slideway system (Fig. 5).

■ A simple polarization interferometer to measure carriage and sample displacement (Fig 6). This interferometer allows us to sample the profiler output at constant **spatial** rather than **temporal** intervals. Since each sample is recorded with displacement information, repetitive scans at various forces are much easier to cross-correlate for further study.

■ A custom capacitance bridge to measure the force sensor's cantilever deflection. Computer automated nulling of this high frequency bridge is currently being developed.

ACKNOWLEDGEMENTS

The Authors most graciously acknowledge the support of the National Science Foundation, Queensgate Instruments, Rank Taylor Hobson, Bob Hocken, Jay Raja, Derek Chetwynd, Salam Harb and the technical staff at the Centre for Microengineering and Metrology.

REFERENCES

Garratt, J.D. and Bottomley, S.C., Nanotechnology, 1(1), p. 38, 1990.
Howard, L.P. and Smith, S.T., Rev. Sci. Instrum., at press (Oct., 1992).
Thomas, T.R., Mecanique Materiaux Electricite, No. 337, p. 17, Jan. 1978.

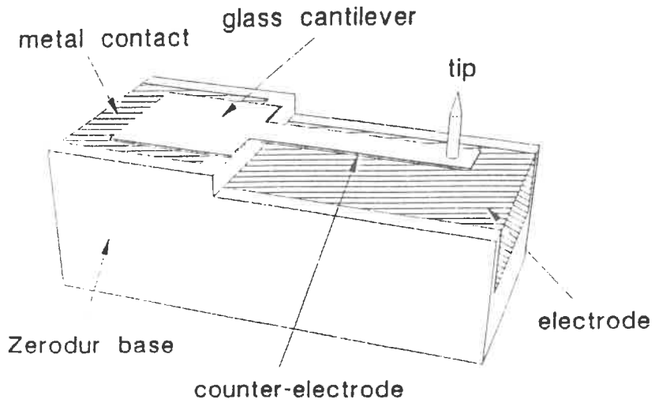

Figure 1. Zerodur and Glass force probe with diamond stylus.

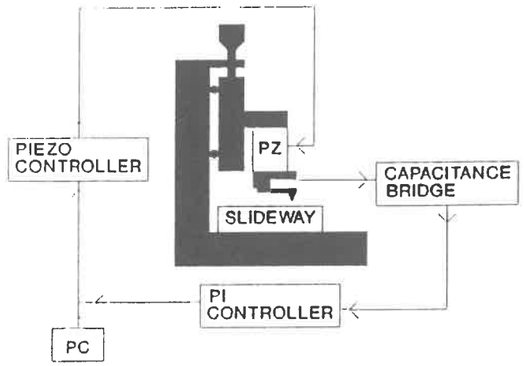

Figure 2. System block diagram for constant force profiling.

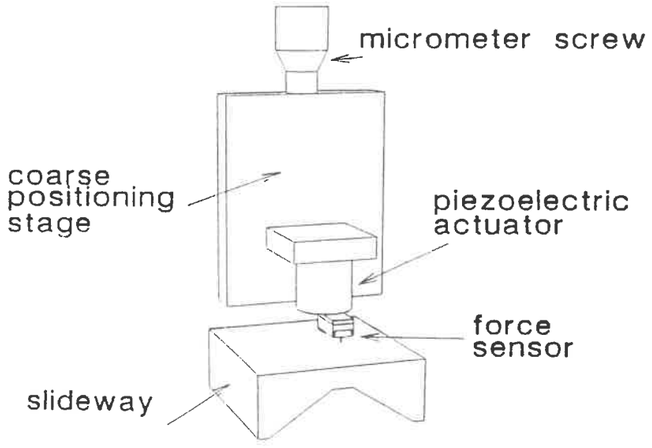

Figure 3. Drawing of apparatus showing force probe on profiler.

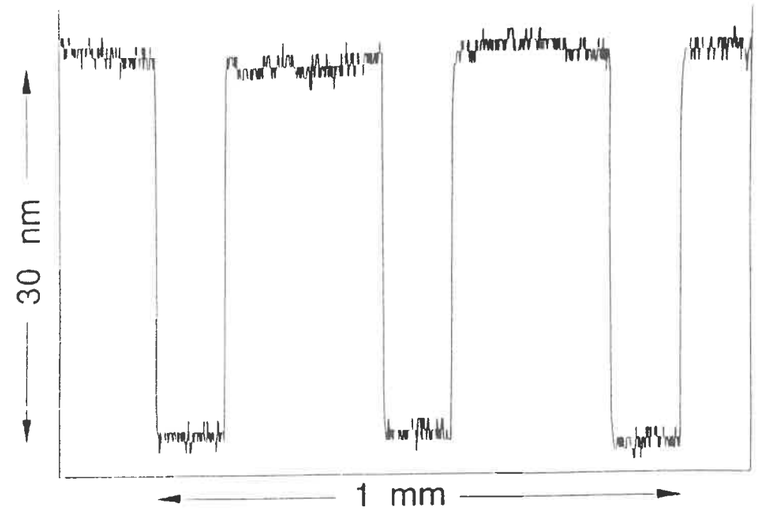

Figure 4. Profile of 30nm step height standard on silica glass.

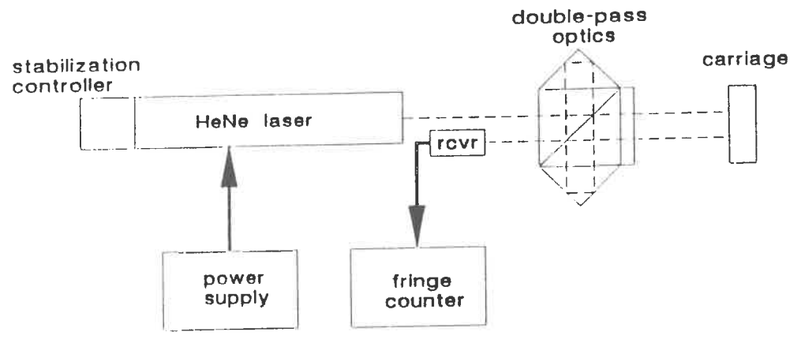

Figure 5. Carriage interferometer system under development.

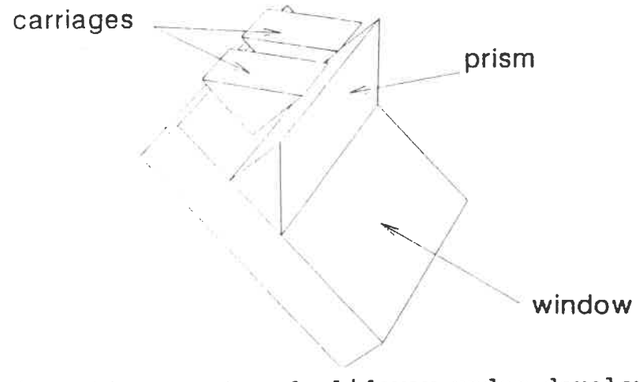

Figure 6. Kinematic vee-shaped slideway under development.

SMART GRINDING BALLS AND SMART BEARINGS FOR ON-LINE PROCESS SUPERVISION

Robert X. Gao, Manoj V. Bhandiwad and Robert O. Warrington
Louisiana Tech University
Ruston, LA 71272

In many branches of industry, mechanical or chemical processes have to be carried out in a closed apparatus environment. This often leads to restraints in obtaining evident information regarding the dynamics and working status of the process. In consequence, it's difficult to realize a timely inspection and adjustment of the products quality. A typical example hereto is the mechanical grinding of raw and fine materials by using ball mills. Within the rotating mill chamber, charge media (mineral aggregate, coal, ore, etc.) and metal grinding balls are subject to constant collisions, shears and rubs with each other. These result in crushing down of the charge media to a desired grain size after a certain period of time. Due to the characteristic random load application, the energy efficiency of this grinding method is amazingly low - about 1/10 of a defined grain crushing. Besides, the energy consumption of each grinding process is not constant but follow distribution functions determined by the physical properties of the materials to be ground. Furthermore, the huge mechanical and thermal loadings prevent an easy and effective on-line grinding effects supervision during the process. Thus, ball milling is traditionally regarded as a black box system, and mill operation parameters for achieving a desired grain size (grinding cycle, ball geometry, charge media ratio, etc.) are determined on a empirical basis.

To enable an energy saving grinding, it is essential to create a mill operation parameters pattern which generates specifically the desired impact and energy distribution needed for a given type of material in order to achieve the required grinding results within the shortest possible time. For this purpose, realistic, real-time data on load distributions inside the mill must first be obtainable, which will require an on-line, in-process measurement. A straightforward yet ideal solution is to implant a microtransducer with dynamic force sensing element and signal processing electronics into the normal grinding balls to build a set of self-contained, autonomous "smart grinding balls" [1]. These balls will then be put into the grinding chamber to become a part of the charge media. During the grinding process they register the intensity of each impact they were subject to as well as the frequency of impacts of each intensity group. With the operational parameters varied, different data will be registered. This way, a wide range of data on the realistic stress distributions inside the mill chamber can be obtained which will adequately serve the need for mill operation studies. On the whole, following aspects must be considered for the smart ball design and construction: 1) They should have the same size, mass and surface characteristics as the normal grinding balls to simulate fully their motion and stress behavior; 2) In view of the realistic mill operations and to allow easy ball charge handling during the experiment, the maximum ball diameter should not exceed 60 mm. 3) The ball instrumentation must withstand a combined mechanical and thermal impact of estimated up to 450 g and 350 K; 4) The ball surface must be dust- and waterproof to prevent damages from grinding media to the electronics.

Spectrum analyses show that impact signals due to grinding ball collisions are mostly within the frequency range of ≤ 15 kHz. This fits properly into the application range of piezoelectric sensors. Due to the geometrical restraints for the ball instrumentation, no commercial model could be applied directly for the signal pick-up. Instead, a thin piezoceramic disc (about 0.5 mm thick and 15 mm in diameter) is chosen as the primary sensing element. This disc is glued inside the ball to the butt end of a plunger whose other end forms a defined measuring area of the ball surface. To protect the ball instrumentation from the mechanical and thermal stress, the ball instrumentation with electronics and battery are fully accommodated by a cylindrical metal housing. This cage is then covered by two steel shells which are fastened together through a set of fine screws. Regarding the electronics implantation there are two versions developed for batchwise and on-line data processing on the mills. The basic version contains the following functional modules:

- Charge Amplification: high impedance charge signals (Q) from the piezosensor are converted into proportional voltage output (U_{out}) through a JFET operational amplifier which is configured as a current integrator ($|U_{out}| = Q/C$). The output is independent of capacity fluctuation of the input cabling.
- Signal Conditioning: active lowpass filter with impedance converter reduces signal distortion by attenuating high frequency noise components.
- Data Conversion: each voltage signal is converted by a set of LinCMOS voltage comparators (2.5 µs response time) into a digital bit number. The reference voltages are provided by a precision FET current source together with a resistor array.
- Data Storage: the converted bit combinations are latched into memory units temporarily for late processing. The units have a data capacity of 64K.
- I/O Interface: through output buffers and a customized connector (12 x 12 mm) which is fixed on the circuits board, data registered in the memory units can be transferred to the host computer for statistical analysis, graphics display and other purposes.

Based on these modules, the modified on-line version of the smart balls have an additional circuitry for real time data modulation and transmission. A microsize SAW-transmitter (Surface Acoustic Wave) with 433 MHz nominal frequency is pulse modulated by a data modulator which is further connected to an impact counting unit. Whenever a predetermined number of impacts of a certain intensity group has been registered, the modulator will be triggered and data transmission will begin.

Conclusions from the mechanical strength analyses for realistic grinding process shows that only a volumetric space of about 2 cm^3 is allocable for the electronics implantation in the smart balls. Thus, the circuits miniaturization becomes a crucial task. Basically, there exist three types of technologies in the microelectronics area which can be applied for this purpose: ASIC (Application Specific Integrated Circuit), SMD (Surface Mounted Devices) and Hybrid (thick and thin film). To achieve a low cost, high degree of integration of both analog and digital components and yet leave sufficient flexibility for parts modification, a combination of SMD and thick film techniques is chosen. For the basic version of the smart balls, the whole electronics are integrated on a ceramic chip of 20 mm x 22 mm x 2 mm. Similarly, the on-line version is comprised of two chips. The chips are soldered on a circular board which in turn is fixed on the metal housing in the balls. The minimum diameter of the basic version balls is 40

mm. For on-line version, it is 60 mm. In Figure 1, the basic components of a smart ball are shown.

To verify the applicability of the smart balls, systematic grinding experiments are carried out in a mill of 800 mm inner diameter and 400 mm length. The grinding media void ratio Φ_m, which denotes the relationship between the bulk volume of the grinding media to that of the balls: $\Phi_m = V_{Mg} / (\varepsilon_l * V_{Mk})$, is set to be 0, 0.6, 0.8 and 1.0, where $\Phi_m = 0$ means grinding test without charge media. The mill rotational speed n_k is selected to be 40%, 60%, 80% and 100% of the critical rotating speed, at which the centrifugal acceleration at the inner wall of the mill chamber equals that of the gravitation. Through variation and combination of Φ_m and n_k, 16 different test patterns can be realized. To reduce measurement errors due to the random motion behavior of the balls as well as to confirm the reproducibility of the data acquisition, 6 smart balls are applied for each grinding process. For a clear comparison of test results under various conditions, an "impact frequency H_i" is introduced which denotes how many times a ball has been impacted during each mill rotation: $H_i = N_k * F_f / 2 U_n$, with N_k the registered impacts, U_n the number of total mill rotations and F_f the ratio of the measuring area to the whole ball surface. Data analysis shows that by all the grinding tests with or without charge media, there always exists a maximum of H_i within the speed range of n_k = 60% - 80%. The decrease of H_i in high speed range can be explained by the fact that due to the increasing centrifugal force, a portion of balls will adhere to the mill chamber walls. Consequently, less balls can participate effectively in the grinding process. Hence, less impact will then be registered. Another observation is that with the impact intensity (which correlates to higher grinding energy), the frequency maximum (H_i) tends to shift in the direction of higher speed range. This explains the phenomena that at higher mill speed, the ball charge will loosen up so that more stronger impacts can be generated.

Error and grinding effects analyses show that the maximum random error of the experiments is less than 8.5% [2]. Systematical errors caused by fabrication tolerance in mechanical structures and electronic circuits can be compensated through calibration before the balls are applied. The impact distributions measured coincide with conclusions from computational simulations. Through variation of the operational conditions, specific data on energy distributions can be obtained. These values can be correlated to the individual grinding requirement for a given material to derive guidelines for an energy saving mill operation. Besides, the developed implantation technique is generally applicable for parameter measurement and registration on free moving objects as well as for other types of on-line process supervision.

Similar to the development described above, smart ball bearings with self-diagnostic and error reporting capabilities are now being developed. Bearing is one of the widely used fundamental machine components whose failure due to overloading or overheating has great influence on the manufacturing precision. Based on the conception that an overall process supervison can only then be reached, when as many as possible traditional "passive" parts of the machining system become actively involved in the supervision frame, microtransducer is being constructed to be integrated into the bearing's environment. An alarm signal will be transmitted cordless to the machine monitoring system outside the bearing, each time when critical force and/or temperature fluctuations are registered. To properly implement the alarm generating function, bearing modelling under static and dynamic loadings are being made. In static

case where bearing is under a combined redial (F_r) and axial (F_a) loading, the critical load P_{max} beyond which static failure occurs is first determined by considering the static load capacity C_s. This will then be consistently compared to the force signal measured by the integrated sensor. In case that the measured force amplitude is greater than that of the calculated one, an alarm signal for static failure will be given. Analysis of dynamic loading is more complex, since the ball contact angle increases at the inner raceway and decreases at the outer one, as a result of the centrifugal force F_c and gyroscopic moment M_g acting on the bearing balls. Numerical computation shows that, similar to the static case, current loadings acting on the ball-raceway interface can be analytically determined. When the calculated force value is exceeded by the measured one, a dynamic failure will be indicated. Besides overloading analyses, the temperature effect on the bearing is also studied which results in an analytical determination of the current temperature t_o of a bearing under normal lubrication conditions. This will then be used as criterion for overheating signal generation. The modelling conducted provides design guidelines for developing microtransducers which will enable a completely cordless and autonomous real-time bearing loading status supervision.

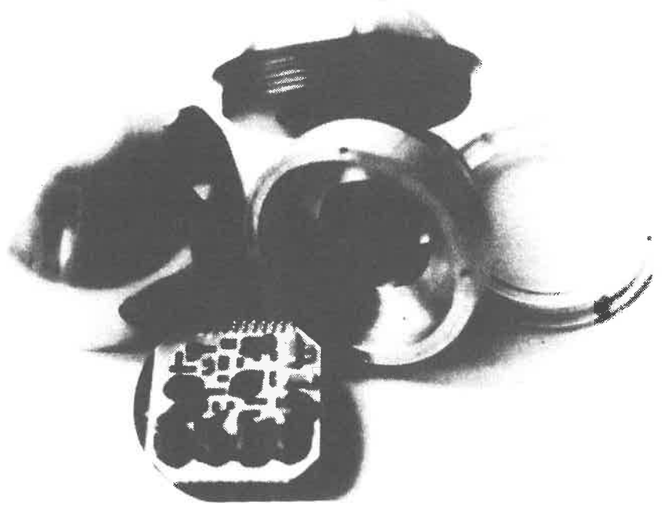

Fig. 1. Basic components of a smart grinding ball

References

[1] Thelen, W., Gao, X. and Rolf, L., 1989, "Technology for measuring energy distribution in ball mills", in *Proc. International Exhibition and Conference for Industrial Measurement* (in German), Wiesbaden, Germany, pp. 428-434.

[2] Gao, X., 1991, "Development of a measuring technique for determing the stress intensity distributions in ball mills", *PhD. thesis* (in German), Technical University of Berlin, Germany.

BOUNDARY EVALUATION OF AN INDENTATION BY SCANNING TUNNELLING MICROSCOPE DATA

G. Barbato, G. Murari(*), G.B. Picotto and G. Podda(*)
C.N.R Turin, Italy
(*) Politecnico di Torino, Italy

The Scanning Tunnelling Microscope (STM) [1,2] has become a powerful tool for studying the topographical surface structure of materials at the submicron scale. The STM is the most promising technique for overcoming the present limitations of traditional microhardness measurement methods. The hardness of the solid is defined as the force required for an indenter to penetrate the solid divided by the area of the base of the residual indentation. Microhardness measuraments have been made for many years and usually rely on reflected-light microscopy to measure the size of the indentation. At the submicron scale the STM is required.

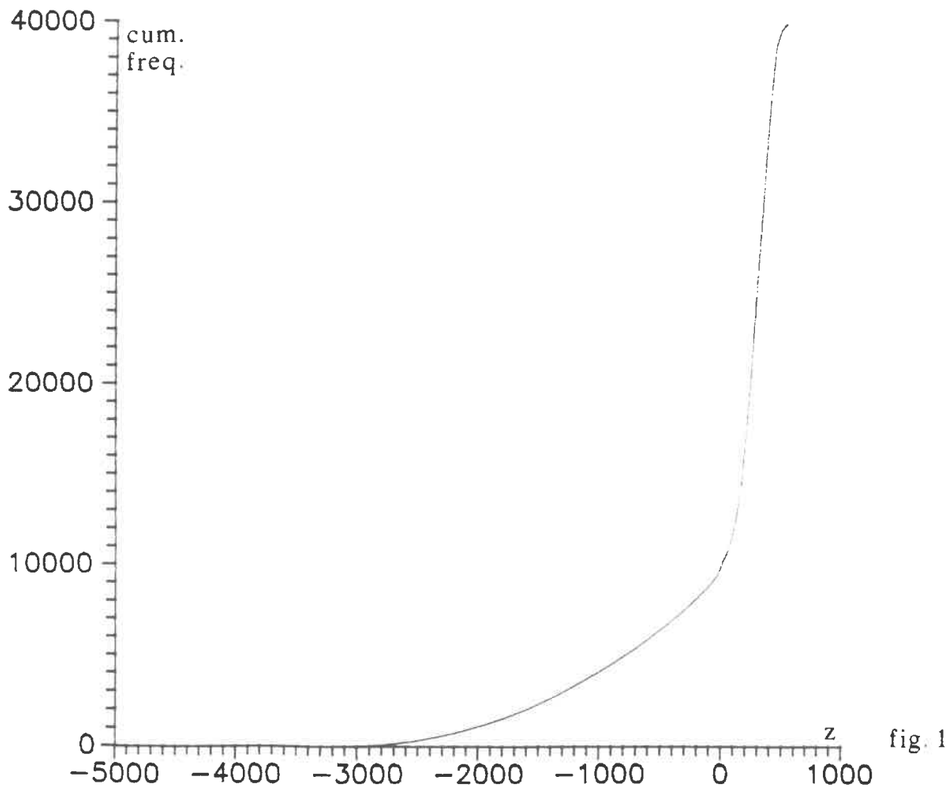

fig. 1

A preliminary investigation was described [3] by Barbato et al., who defined the boundary of the indentation as the intesection between the indentation itself and the "main original plane" of the block surface. The depth of the indentation, i.e. the distance of its bottom from this plane, was taken as a good parameter for the evaluation of microhardness.

In the present research work the 200×200 array of data $z = f(x, y)$ directly obtained from the STM is used to calculate a frequency table with data grouped in classes and to build the corresponding cumulate frequency diagram (fig. 1).

The inflection of this diagram provides the value of z which corresponds to the indentation boundary, so that reference to some main original plane of the block surface can be dispensed with. In fact, the cumulate frequency is nominally proportional to the depth of the indentation and suddenly changes its curvature when the actual surface is reached. The value of z corresponding to the minimum of this curvature is chosen to evaluate the indentation depth.

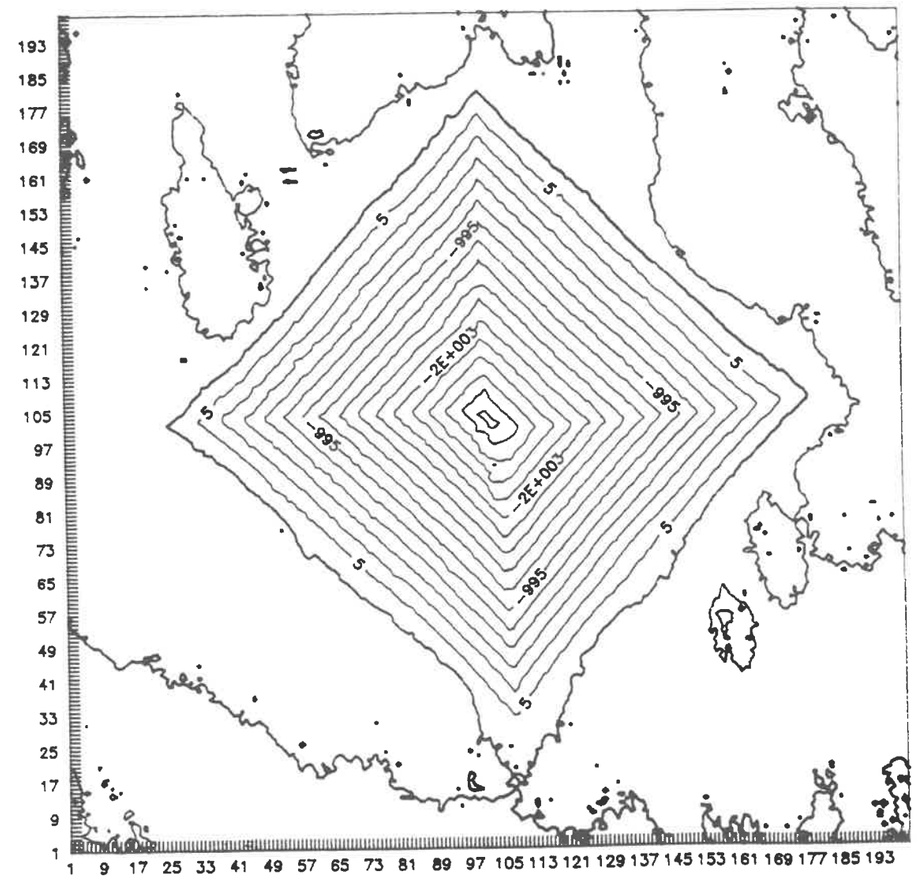
193
185
177
169
161
153
145
137
129
121
113
105
97
89
81
73
65
57
49
41
33
25
17
9
1
1 9 17 25 33 41 49 57 65 73 81 89 97 105 113 121 129 137 145 153 161 169 177 185 193
5
-995
-2E+00
-2E+00
-995
5
-995
5
5
5

The contour map of the indentation shows a series of closed, squared and concentric curves followed by a series of other curves. The evaluated indentation depth should correspond closely to the z value of the last of the closed, squared and concentric curves (fig. 2). The cumulate frequency diagram was found to be insensitive to the choice of class intervals.

In fact, the block surface after indentation is neither plane neither, generally, horizontal. Then for any choice of class intervals, the cumulative frequency is heavily affected by the entries that lie outside of the indentation. As a consequence, the above calculation method does not provide an indentation depth which corresponds to the z value of the last of the closed, squared and concentric curves.

A different method was developed to overcome this difficulty. For each z the entries of the array that are less or equal to z are selected and represented in a raster bilevel display. A filling algorithm is applied from the interior of the indentation and the color of the background is selected. As long as the pixels of the indentation are not 8−connected with those of the exterior, the corresponding boundary curve is closed. This is shown by the fact that the filling stops at the indentation boundary. Otherwise the filling continues to delete all 8−connected pixels.

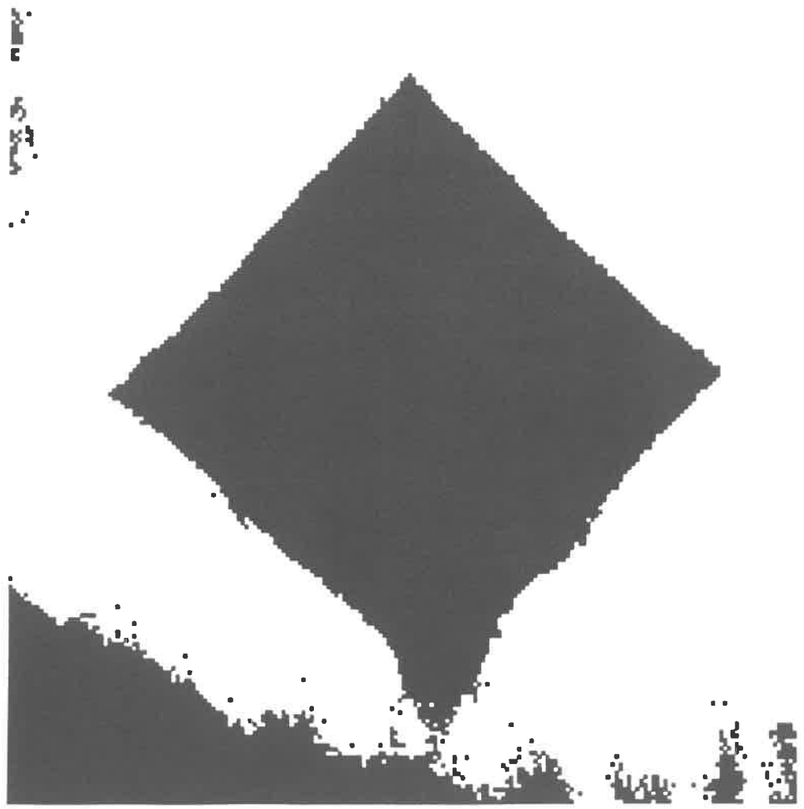

fig. 3

In our experience, it is proved generally possible to find a z corresponding to a closed indentation curve, while the indentation curve was not closed for $z+1$. This situation is shown in fig. 3 and in fig. 4.

In fig. 3, at a certain depth z, the indentation is closed and it disappears after the filling, while no external pixel is removed. In fig. 4, corresponding to a depth $z+1$, the indentation is 8−connected in the lower part to some external pixels, which disappear with the indentation itself after the filling.

The difference between the total number of the entries that are less or equal to z and the pixels that remain after the filling yields the area of the largest closed indentation curve. Its diagonal can be extimated by assuming that the curve is a perfect square.

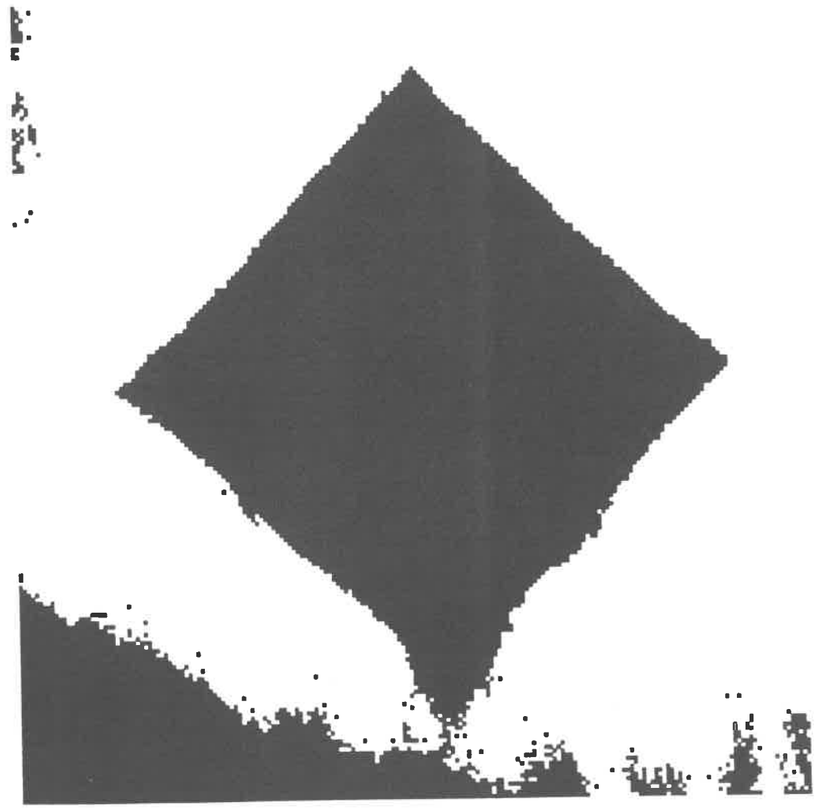

fig.4

References

[1] Binning G., Rohrer C.H. and Weibel E., 1982, *Phys. Rev. Lett.* **49** 57–58.

[2] Miyamoto I., Ezawa T. and Itabashi K., 1991, *Nanotech.* **2** 52–56.

[3] Barbato G., Desogus S., Germak A. and Picotto G.B., 1991, *Digests of Int. Conf. Scanning Tunnelling Mycroscopy*, Interlaken, Switzerland, Aug. 12–16.

OPTICAL PROFILOMETRY OF MECHANICALLY INACCESSIBLE SURFACES

M. Visscher and K.G. Struik
Eindhoven University of Technology

1 Introduction: Optical profilometry

During the last decade optical profilometers have been developed for e.g. surface roughness measurements. An example of such a profilometer, based on the so-called pupil obscuration method (see Braat 1987 section 2.5.2), is shown in fig. 1. When the surface is in focus, all four photodiodes (B_1, A_1, A_2 and B_2) receive the same amount of light. If, otherwise, the surface is in a higher position than the focus, the outer diodes (B_1 and B_2) receive more light than the inner diodes (A_1 and A_2) and if the surface is in a lower position than the focus, B_1 and B_2 receive less light than A_1 and A_2. This difference is detected by the so-called **focus error signal** (*fes*), reading

$$fes = \frac{(A_1+A_2) - (B_1+B_2)}{(A_1+A_2) + (B_1+B_2)} \qquad (1)$$

(A_1 and B_1 being the signals from the diodes A_1 and B_1 respectively)

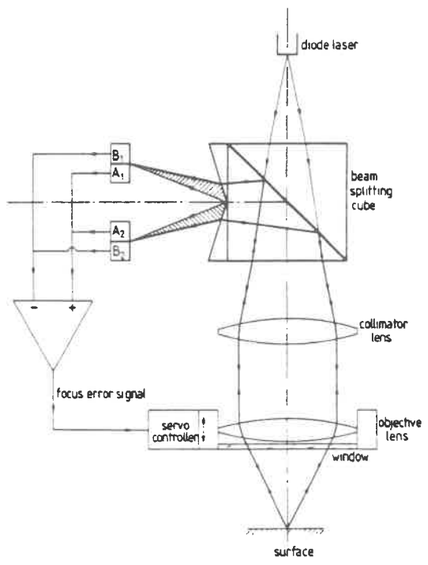

Figure 1 Optical profilometer

A servo controller can be used to focus the objective lens onto the surface, i.e. the lens is moved to the position where the focus error signal is zero. Scanning a rough surface, the height variations can be determined by continuous measurement of the lens position.

Compared with mechanical profilometers, optical devices have the advantage of contactless scanning, thus avoiding deformation and possible damage of soft surfaces. Also optical profilometers can in principle be used to scan surfaces which are not accessible for mechanical devices, e.g. profile measurement through a transparent layer, measurement on the backside of a transparent plate, or in the situation that one is interested to measure the roughness texture of one surface in contact with another, transparent, surface (fig. 2). Such a measurement can e.g. be performed to determine the deformation of the roughness texture at different loads.

In the following, a profile measurement on the contact of a rough elastomer and a smooth glass plate will be described. The influence of the glass plate, through which the elastomeric surface is scanned, will be discussed. This influence is mainly caused by two factors:
- Spherical aberration caused by the

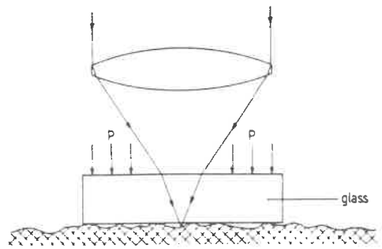

Figure 2 Scanning through a glass plate on the surface

refraction on the glass surfaces. This aberration reduces the focus spot quality;
- Introduction of two additional reflecting surfaces.

It will be shown how the influence of these factors can be reduced to obtain proper measurements. Finally, some measurements will be presented to demonstrate the potential of optical profilometry for the scanning of mechanically inaccessible surfaces.

2 Spherical aberration

When aberration free lenses are used, the wave front of the focused beam is spherical and the resulting focus spot is diffraction limited. However, the wave front of the beam transmitted through the window is not spherical due to the light refraction on the window surface (fig. 3). Consequently the focus spot diameter is larger than for the spherical wave front and the resolving power of the profilometer is reduced. A criterion for the maximum spherical aberration, at which the focus spot is still diffraction limited, is

$$\frac{n^2 - 1}{8n^3}\, t\, (NA)^4 \;\leq\; 0.95\ \lambda \qquad (2)$$

(see e.g. Visscher 1992 pp. 164ff.) in which n is the index of refraction of the window, t is the window thickness, NA is the numerical aperture of the objective lens and λ is the wavelength of the radiation. In practice, n is in the range of roughly 1.4 to 1.7 and λ is about 800 nm (diode lasers). Therefore the aberration criterion can be written as

$$NA \;\leq\; 2\, t^{-1/4} \qquad (t \text{ in } \mu\text{m}) \qquad (3)$$

The focus error device shown in fig. 1 is derived from a Compact Disc transducer (Struik and Chang, 1987), in which a special objective lens (NA = 0.45) is applied which compensates for the aberration of the 1.2 mm thick protective layer of the CD. In normal roughness measurements, such a layer does not exist on the scanned surface. Therefore, a 1.2 mm thick window is fixed near the objective lens to substitute the layer optically. In our experiments presented in section 4 below, an elastomeric surface will be scanned through a 1.2 mm thick glass plate on the surface, after the window near the objective lens is removed.

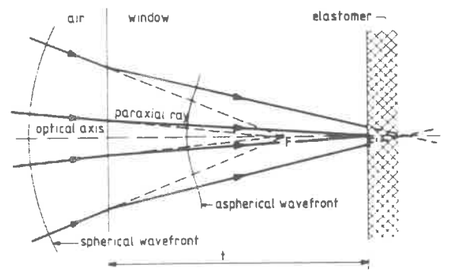

Figure 3 Spherical aberration due to refraction on the window surface

3 The reflection on the glass surfaces

Scanning a surface through a glass plate on it (fig. 2), the light from the diode laser reflects on three surfaces:
- The elastomeric surface: this reflection is needed for the surface scanning;

- the upper glass surface;
- the lower, contacting glass surface.

Visscher (1992 p. 43ff.) found that the reflection on the upper glass surface, which is it a relatively large distance from the focus, has no significant influence on the measurement. Otherwise, the reflection on the lower surface has a large influence. It was initially expected that the measured roughness height would be smaller than the real roughness height, because the objective lens would be focused between both reflecting surfaces. However, experiments showed larger height variations in the roughness profiles instead of smaller. The origin of this result is not understood at the moment and it is therefore decided, that a liquid must be present in the contact area for proper measurements: No reflection occurs on the lower window surface, when the index of refraction of the liquid equals the index of refraction of the glass plate and the reflectance influence is then of course eliminated (see Visscher, 1992 pp. 168ff.).

4 Example of a measurement

An example of surface scanning through a transparent body will be given below, which originates from the reciprocating seal research project at Eindhoven University. Kanters (1990 chapter 6) found that the seal's surface roughness has a significant influence on the leakage and friction. This influence was not as expected, due to asperity flattening in the lubricated contact which already occurred when the surfaces were fully separated by the lubricant film. Further research therefore focuses on the roughness deformation in the contact area. The practical significance of this investigation is the aim to develop high precision hydraulic and pneumatic cylinders. This requires better insight into the frictional behaviour of the seals to enable the development of seals which operate with constant friction.

The example shown below concerns the roughness deformation under static load, which is of importance for pneumatic applications, where the seals are generally hardly lubricated. Another example, presented by Visscher (1992 chapter 4), deals with the lubrication problem at sliding motion between the elastomer and a transparent rigid body, which is of importance for hydraulic seals.

In the measurements under static load, a glass plate is pressed onto a polyurethane surface (fig. 2) and the deformed roughness texture is measured with the device shown in fig. 1. The diameter of the measurement spot is about 1 μm and the sample distance is 2 μm in both directions. The data was not additionally filtered.

A scan of the undeformed roughness texture is shown in fig. 4. The standard deviation (σ or R_q value) of the roughness height distribution is about 0.66 μm. Fig. 5 shows the deformed roughness texture in the loaded contact. A liquid is present in this measurement, eliminating the reflection on the lower glass surface. Now some flattened areas (indicated by A, B and C) are found and the R_q value is hardly reduced ($R_q \approx 0.63$ μm). Increase of the load hardly affects the roughness

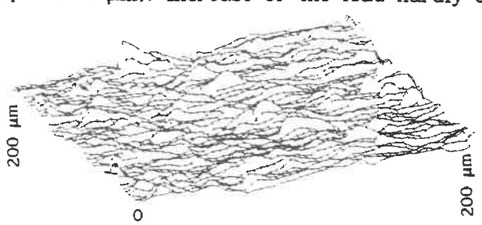

Figure 4 Undeformed roughness texture of the polyurethane test plate

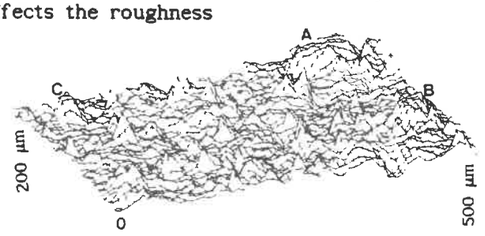

Figure 5 Roughness texture at an average contact pressure of 0.03 MPa (measurement with liquid in the contact)

texture: both the roughness height and the dimension of the flattened areas are not changed at increase of the contact load (Visscher 1992 pp. 82ff.), which indicates that the load is largely supported by the liquid and not by asperity contact.

Further measurements were performed on the dry contact of the same polyurethane and glass plate and the results are shown in fig. 6. Now much more roughness flattening is found and the deformation clearly increases with increasing load. The roughness height can not be derived from these measurements, because of influence of the lower glass surface reflectance (see section 3), but the real area of contact can in principle be derived.

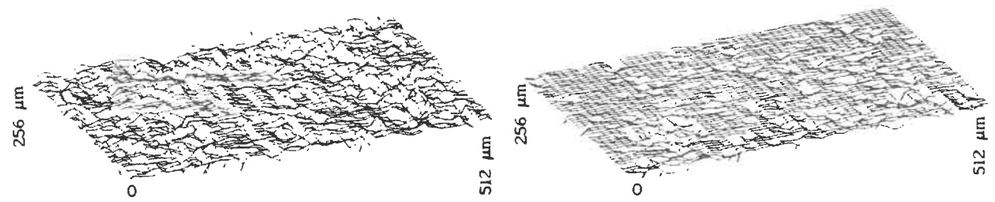

Figure 6 Deformed roughness texture of the polyurethane test plate (measured on the dry contact)
a. Average contact pressure = 0.06 MPa **b.** Average contact pressure = 0.12 MPa

5 Conclusions

Optical profilometers can be used to scan surfaces which are mechanically inaccessible, when measures are taken to prevent too much spherical aberration and to prevent influence of reflection on the window surface near the scanned surface.

Acknowledgement

We thank Mr. A.C.M.E. van Kalmthout, Mr. J.W. Versteeg and Mr. J.A. Peels for their technical support and Dr. J.J. Baalbergen and Prof. J.J.M. Braat (both of Philips Research Laboratories, Eindhoven) for their advise.

The measurements presented in section 4 were obtained in cooperation with Mr. C. Hendriks. Financial support was given by the Technology Foundation STW.

References

Braat, J.J.M., 1987, "Read out of optical discs", chapter 2 in "*Principles of optical disc systems*" by Bouwhuis, G. and others, Adam Hilger Ltd., Bristol, 3rd. ed. (1st. ed. 1985), ISBN 0-85274-785-3

Kanters, A.F.C., 1990, "*On the calculation of leakage and friction of reciprocating elastomeric seals*", Ph.D. Thesis, Eindhoven Univ. of Tech.

Struik, K.G., and **Chang, M.F.**, 1987, "Measurement of shape and roughness by a modified compact disc sensor coupled to a personal computer", *Proc. 4th. Int. Seminar on Prec. Engng.*, Cranfield Inst. of Tech., UK, pp. 81-90

Visscher, M., 1992, "*The measurement of the film thickness and the roughness deformation of lubricated elastomers*", Ph.D. thesis, Eindhoven Univ. of Tech.

A NEW UNIFIED APPROACH TO SURFACE TEXTURE INSTRUMENTATION

Dr Paul J. Scott
Rank Taylor Hobson Ltd
2 New Star Road
Leicester LE4 7JQ
ENGLAND

INTRODUCTION

Discrepancies between the "correct" values of standard surface texture parameters measured on different instrumentation is a common cause of dispute. Differences between manufacturers and their customers over the functional suitability of components has occurred because parameter values are in tolerance on one instrument and out of tolerance on another. In most cases it is not a question that one instrument is right and the other wrong. They may both conform to National and International Standards and so their results are equally valid.

To overcome the above problems the ISO 9000 series on "Quality Systems"[1] requires unique procedures to be defined to characterize quality. For surface texture there are many different instrumental techniques that can be used to explore/measure surface texture, e.g. mechanical stylus, optical methods, AFM, capacitance methods, acoustic etc. For measurement results to have any "absolute" interpretation, the measuring instrumentation must be precisely defined, since measurement results are not only an assessment of the artifact under examination but are also an assessment of the instrument used in that examination.

One approach to satisfy ISO 9000 requirements is to choose one measuring technique/instrument and define this as a reference method to which all other instruments shall be compared. This approach I believe would be unacceptable to most in surface texture measurement. Fortunately a more flexible approach to surface texture instrumentation is currently being considered.

REFERENCE SURFACE MEASURING INSTRUMENT

The concept of a "reference surface measuring instrument" is being adopted by the international metrology community to address the problem of specification of surface texture instrumentation[2]. Initially only profile measuring instrumentation are being considered since a vast majority of surface texture instrumentation in the field are of this type. The reference surface measuring instrument philosophy is easily generalised from profiling instruments to areal instrumentation.

The reference surface measuring instrument is a mathematically well defined theoretical instrument and is the preferred surface measuring instrument. A schematic diagram outlining the main features of the reference profiling instrument is given in figure 1. The "probe" is guided across the surface under examination to produce the "probe generated profile", that is a profile defined by the interface of the probe with the surface. The transducer produces a signal that is the difference between the "probe generated profile" and a "reference or datum profile". The "reference profile" is typically generated as part of the guiding mechanism of the instrument.

After the transducer the signal is converted into a digital signal via an Analogue to Digital converter. At this point the signal only contains the vertical or Z-component of the profile. The horizonal or X-component, generated by the traversing mechanism, is combined with the Z-component when the total profile is filtered to remove the short wavelength component of the profile in a mathematically defined way. The resulting profile is called the "Primary Profile". The Primary profile represents the basis for (digital) profile recording, profile processing by means of profile filter, calculation of profile parameters and digital output, as covered by International Standards. A further profile filter separates the longer wavelength component (Waviness profile) from the shorter wavelength component (Roughness profile) in the Primary profile. Finally Waviness and Roughness algorithms are applied to these profiles respectively to produce various profile displays and parameter results. It should be stressed that though figure 1 contains all the main features of the reference instrument other configurations are possible which produce identical measurement results.

The key feature of the reference surface measuring instrument is that of standardized transmission bands for the wavelength content of the measurement[3]. All surface texture instruments limit the wavelength content of their measurement. The short wavelength limitation is currently not defined but left to various arbitrary instrumental factors such as the characteristics of the probing system, the characteristics of the analogue to digital converter, the data sampling scheme etc. It is the variability in the transmission band of measurement between instruments that is one of the main causes of the discrepancies in measured results.

It is proposed to define the short wavelength and long wavelength limits in the measurement transmission band for Roughness profiles by the wavelength transmission characteristics of low and high pass Gaussian profile filters respectively (see figure 2). The Gaussian profile filter is so named because the associated filter weighting function has the equation of the Gaussian density function. Profile filters are identified by their cut-off wavelength value, that is the wavelength of a sinusoidal profile of which 50% of the amplitude is transmitted by the profile filter. The band of sinusoidal profile wavelengths which are transmitted by greater than 50% by the reference instrument, are defined by the values of the short wavelength cut-off λ_s and long wavelength cut-off λ_c. The standardized values of λ_s and λ_c are to be taken from the following series:-

... 0.0025; 0.008; 0.025; 0.08; 0.25; 0.8; 2.5; 8.0 mm; ...

The standardized ratio of λ_c:λ_s is approx 300:1 (e.g. λ_c=0.8mm & λ_s=0.0025mm); though there is provision made for the selection of other preferred ratios, these being 100:1 & 1000:1. These ratios should give sufficient scope to accommodate a wide variety of functional requirements from research through to general measurement. By seeking to standardize both the upper and lower transmission characteristics of the instrumentation, the inter-comparison between instruments and between surface is more accurately assessed.

The Reference Surface Measuring Instrument does not confine instrumentation to one technology, such as stylus base instrumentation, but allows the full range of probing techniques (such as AFM, optical, stylus etc) to be utilised. For a given standardized transmission band, the instrument designer shall select instrumental attributes (such as the probing system,

transducer, analogue to digital converter etc.) whose characteristic effects lie outside the chosen transmission band (see figure 2). That is to say any technology that allows the specified transmission band to be faithfully reproduced can be used and will give comparable results to any other instrument with the same transmission band.

Engineered surface measuring instruments will always be an approximation to the mathematically defined reference surface measuring instrument. Given the degree of approximation other instrumental attributes can also be deduced. Take for instance the rate of sampling of the measured points in the primary profile. Due to the short wavelength limit there will be a smallest effective wavelength contained in the primary profile. The Nyquest criteria can be utilised to determine a theoretical maximum spacing between measurement points on this profile. For example if the smallest effective wavelength of the primary profile is taken as the 1% point on the transmission curve of the low pass Gaussian profile filter defined by λ_s then it can be shown that the theoretical maximum spacing between adjacent sampling points is approximately $\lambda_s/5$.

What is not so well understood is that the reference surface measuring instrument framework also allows the user to choose an appropriate measuring instrument for each metrology application. First stage is to decide which wavelengths on the surface are not required for measurement. Next one of the standardized transmission bands should be chosen to contain the remaining wavelengths. Finally a measuring instrument capable of measuring the given transmission band is selected. This procedure will greatly reduce many of the problems of differences in results when measurements are taken on different surface measuring instruments.

CONCLUSIONS

The reference surface measuring instrument provides a reference against which actually engineered instruments can be compared and also indicates the conditions under which comparisons between different instrument types are meaningful. It is envisaged that surface measuring instruments designed using the reference instrument philosophy will greatly benefit the end user with an improvement in quality of surface texture measurement.

REFERENCES

1 ISO 9001 - 1987
Quality systems - Models for quality assurance in design/development, production, installation and servicing.

2 ISO/TC57/SC1/WG1 N36
Second Draft Proposal for the revision of ISO 3274 "Stylus instruments for the measurement of surface roughness using a digitally stored profile for the calculation of parameters and the recording of the profile".

3 ISO/TC57/SC1/WG1 N37
Metrological characterization of phase corrected filters and transmission bands for use in contact (stylus) instruments.

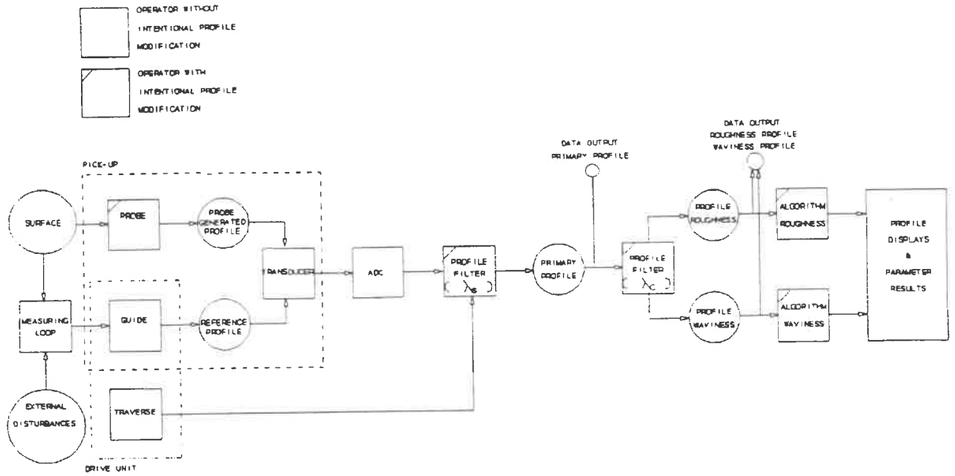

Figure 1 Outline Schematic of Reference Profiling Measuring Instrument

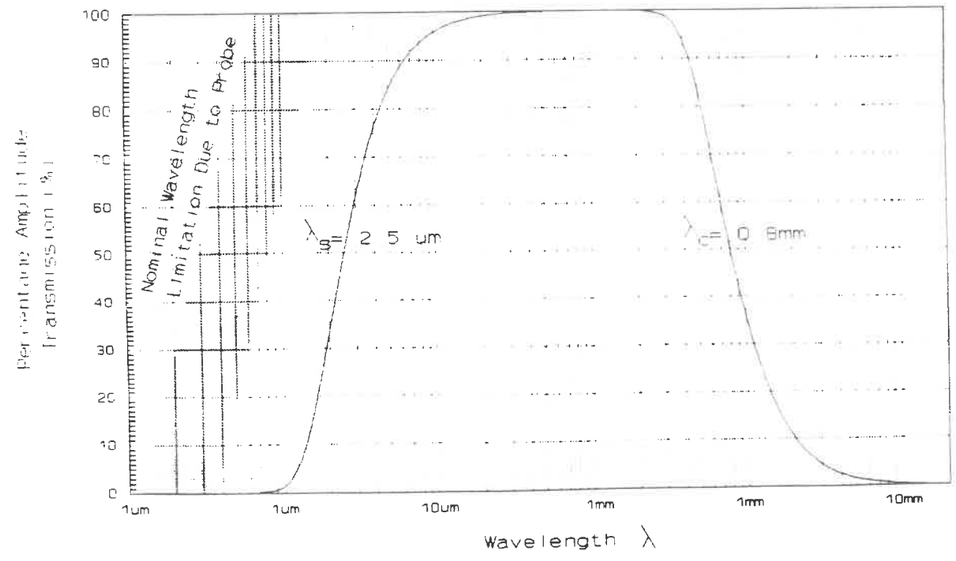

Figure 2 Example of a Standardized Transmission Band

A NEAR-FIELD SCANNING OPTICAL MICROSCOPE MODULE

B.D. BOUDREAU, T. CLONINGER, J. RAJA, J. PATTEN AND R.J. HOCKEN

DEPARTMENT OF MECHANICAL ENGINEERING AND ENGINEERING SCIENCE
UNIVERSITY OF NORTH CAROLINA AT CHARLOTTE
CHARLOTTE, NC 28223

1.0 INTRODUCTION

Non-destructive imaging of objects on the nanometer scale is becoming important in many disciplines. Conventional microscopy with its far field optics is diffraction limited to a spatial resolution of 200nm. A relatively new technique called near-field microscopy [1,2] utilizes the non-diffracted illumination emanating from a sub-wavelength aperture to image objects. When imaging an object the aperture must be kept within 100nm of the surface as it scans the area of interest. The transmitted light is collected by a microscope objective and measured. By using this technique, near-field microscopy circumvents the diffraction limit enabling it to achieve spatial resolution on the order of 20nm.

The near-field scanning optical microscope (NSOM) developed for this study was designed as a module that replaces the positioning table of a standard optical microscope. This configuration combines the low magnification, large field of view capabilities of the conventional microscope with the high magnification, small range capabilities of a near-field microscope to produce an instrument with an expanded range of magnification. Additionally, the standard microscope serves as the collection and aiming optics of the near-field microscope. However, the integral nature of this module requires it to be compact and yet provide three separate orthogonal axes of motion required for operation and alignment.

2.0 NEAR-FIELD MICROSCOPY

"Near-field" (figure 1) refers to the distance between the object being imaged and the plane where the image is produced. "Quantitatively the near field can be defined as the distance from a screen wherein the initially collimated radiation emanating from an aperture diverges by less than 20%."[2] Conventional microscopy is limited by far-field diffraction due to the relatively large distance between the object and its image. In an NSOM the light used to image an object must pass through a small aperture (typically 500 to 100nm diameter) near the object (figure 2). In order to obtain optimal resolution, the distance between the aperture and the object must be less than the radius of the aperture. As the aperture is scanned over an object, the intensity is recorded and used to build a raster image of the object. Under these circumstances, the resolution of the microscope is within an order of magnitude of the aperture size regardless of the illumination wavelength.

The apertures used in near-field microscopy are constructed using micro-pipette techniques developed for biological applications. In the fabrication process an optical fiber is heated while under tension. This results in the fiber necking and breaking, forming a very small tip. The resulting tip is then coated with 200nm of aluminum to form a small aperture at the end. The sole purpose of these apertures is to either illuminate or collect light from

a small region of the object. In either case, the transmitted light is guided to a detector. The long slender nature of these probes makes them ideal for imaging even rough surfaces.

3.0 NEAR-FIELD MICROSCOPE MODULE

The module developed in this study is patterned after a similar module developed by Betzig [3]. The significance of the module design is that it simultaneously provides the user with observation and transmitted light collection capabilities. Our module has been designed to include orthogonal horizontal and vertical pipette positioning adjustments. These have been included to bring the imaging area within range of the piezo tube. Coarse adjustments are also available to align the pipette with the optical system of the microscope.

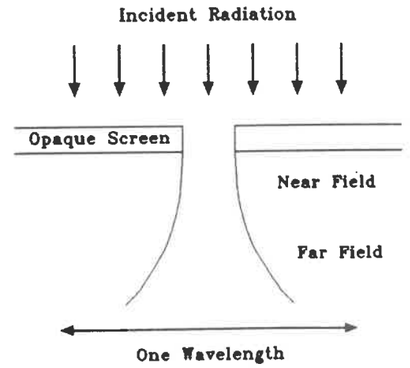

Figure 1 - Illumination from a sub-wavelength aperture.

3.1 PLACEMENT AND MOUNTING

The near-field microscope module is designed to replace the positioning table of a Finescope FS100 manufactured by Mitutoyo (figure 4). It mounts on the microscope using a Maxwell type kinematic mount. The use of this mount simplifies removal and replacement to within a few micrometers. Implementing the near-field microscope in this way provides several advantages; namely, we take advantage of a high quality, expertly designed, optical system, and the availability of reflection and transmission illumination sources. This arrangement also provides the ability to observe and record a feature using both the conventional and near-field microscopes.

3.2 APERTURE POSITIONING

Adequate positioning capabilities are the first requirement of a flexible easy to use microscope. A conventional microscope requires only one set of positioning components (X-Y positioning stage and focusing). However, in a near-field microscope the fiber probe must be aligned with the object and collection optics and, then scanned to form an image. To satisfy these requirements our microscope has been designed with two coarse and one fine positioning devices.

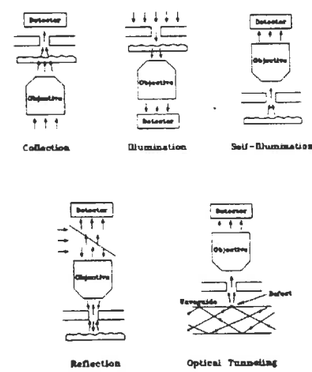

Figure 2 - Near-field illumination modes.

Operation and design of both rough X-Y positioning devices (figure 3) is similar to that of the lens centering mounts manufactured by Oriel [4]. The design consists of an inner ring or cylinder which rests on three hemispheres and an outer cup on which the three hemispheres and two positioning screws are mounted. The two positioning screws are mounted radially outward from the side of the cup and form an orthogonal coordinate system. Two spring loaded plungers are used to hold the center ring tightly against the positioning screws. The position of the center ring can be adjusted along either axis by turning one of the positioning screws. The three hemispheres provide the flat datum and sliding surfaces over which the center ring will move. The center ring has been slightly beveled to provide a downward force which holds the mount together.

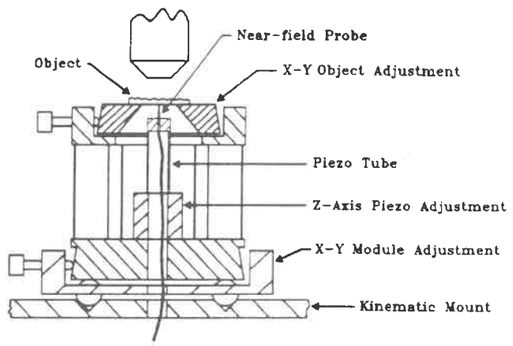

Figure 3 - Near-field microscope module.

The upper positioning system (sample and piezo adjustments in figure 3) are used to bring the area to be imaged within range of the fine motion system. During imaging, the object of interest rests on the center ring of the upper positioning system. Its X-Y position relative to the pipette is controlled by manipulating the positioning screws. The aperture to object distance is regulated by adjusting the Z position of the piezo tube. The module X-Y adjustment is used to align the pipette and collection optics. In this positioning system, the microscope module structure serves as the center ring. The height or focusing adjustment is performed as in a conventional microscope using the table height adjustment knob.

The sub-nanometer aperture positioning is performed with a standard scanning tunneling microscope (STM) type piezoelectric tube [5,6,7]. As in scanning tunneling microscopy area scanning is achieved by mounting the fiber probe on the piezo tube and varying the electrode voltages in pre-set patterns. We have designed and built a high voltage amplifier circuit which converts the computer control signals to the required electrode voltages.

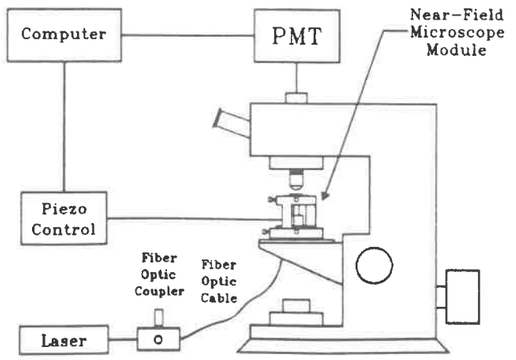

Figure 4 - Overall system diagram.

3.3 ENVIRONMENTAL STABILITY

Perturbations in the environment surrounding any precision

measuring device can adversely affect the results. These effects can manifest themselves as an increase in the noise level (reduced clarity) or unexpected offset (intensity shift). Vibrations and temperature variations are typical sources for noise interference. Fortunately, there are methods for reducing the effects of these noise sources.

Design and isolation are the two primary ways of eliminating or reducing vibrational effects. Our microscope will be isolated from the floor and building by placing it on an air table. To prevent transmitted vibrations, all wires connected to the microscope will be grounded to a solid object and subsequently connected via a flexible loosely hanging wire. Vibrational effects can be minimized by reducing the mass and increasing the stiffness such that the natural frequency of the structure is well above any drive frequencies present in the environment. Aluminum was used to reduce the mass of the structure while the stiffness was increased by using arched structures (no cantilevers).

Using a single construction material is the best method of reducing thermal effects. In our module we have tried to approximate this approach by using a single material wherever possible. The materials in the structural loop are the steel spheres in the X-Y positioning mounts, the probe, the piezo tube, and aluminum structure. Considering the small time frame required to collect an image, we do not anticipate any problems with the use of dissimilar materials.

4.0 CONCLUSIONS

An easy to use, near-field microscope module has been designed and built incorporating two orthogonal alignment devices and a fine motion piezoelectric scanning tube. Characterization and application of this microscope continues; construction of a similar module for use with infrared radiation will begin soon.

ACKNOWLEDGEMENTS

This research effort is being supported by a three year National Science Foundation Grant: DDM-9019776. The authors wish to thank E. Betzig and J. Trautman of AT&T Bell Labs for their suggestions and help in the areas of fiber probe fabrication and microscope design. Construction of this microscope was aided by the efforts of undergraduate assistants: Ralph Colborn, Josh Cloninger and Hiren Surti.

REFERENCES.

1. D.W. Pohl, Advances in Optical and Electron Microscopy, Academic Press, pp. 243-312, (1991).

2. A. Harootunian, E. Betzig, M. Issacson, and A. Lewis, "Super- Resolution Fluorescence Near-Field Scanning Optical Microscopy", Appl. Phys. Lett. **49**, (11) 674 (1986).

3. R.E. Betzig, AT&T Bell Labs, Personal Communication, July 1991.

4. Product Catalog, Oriel Corporation, Stratford CT.

5. G. Binnig and D.P.E. Smith, "Single-tube Three-Dimensional Scanner for Scanning Tunneling Microscopy", Rev. Sci. Instrum. **57**, (8) 1688 (1986).

6. G. Binnig, and H. Rohrer, "Scanning Tunneling Microscopy", IBM J. Res. Dev. **30**, (4) 355 (1986).

7. E. Betzig, "Non-Destructive Optical Imaging of Surfaces With 500 Angstrom Resolution", Ph.D. dissertation, Cornell University, (1988).

Scanning Probe Metrology

D. A. Grigg and P.E. Russell
North Carolina State University
Material Science & Engineering
Raleigh, NC

J. E. Griffith, G.P. Kochanski and M. J. Vasile
AT&T Bell Laboratories
Murray Hill, NJ

Because of their ability to provide high resolution, three-dimensional images, scanning probe microscopes (SPM) are natural candidates for performing precision measurements of surface topography.[1] Cross-sectional and perspective views can be generated from any direction once an image has been acquired. Errors in SPM can be divided into position errors and probe-shape errors. A position error is the difference between a probe's true position and the demanded position. Probe shape errors arise from uncertainties in the probe shape and from the nonlinear interaction between the probe and sample.

The design of a scanning probe microscope suitable for metrology applications must include solutions to several errors. The principal sources of error in SPMs are the nonlinearities in the piezoelectric actuators, the probe shape and the effects of contaminants at the probe-sample interface. Actuator errors can be large because of nonlinear behavior, but this can be solved by independently monitoring the actuator's motion. The probe must be shaped properly for a given measurement, and it must be characterized to allow interpretation of the measurement. For use in metrology, we have developed probe microscopes with position monitors[2] and a rocking beam force sensor.[3] We have also developed probe sharpening[4,5] and *in-situ* probe shape characterization[6,7] techniques.

We have implemented a capacitance-based monitor[2] to measure the probe's position in all three axis. Additional errors originate from angular changes in the tube scanner. We have measured the angular change as a function of displacement and report errors as great as 25% for a 5 mm length probe. The errors are a linear function of probe length and lateral displacement and are easily corrected.

The ability to handle non conductive surfaces makes scanning force microscopy (SFM) an important tool for probe metrology. Recent papers have reported large interaction forces in scanning tunneling microscopy

(STM) [6,8,9] capable of deforming the probe and sample. We have chosen to use the rocking beam force balance sensor developed by Joyce and Houston [10] and Miller et al.[3] The rocking beam force sensor allows us to measure large, conductive and non conductive surfaces in air and vacuum. The rocking beam force sensor can operate at a high stiffness without compromising its sensitivity ($\approx 10^{-8}$N). This technique is vacuum compatible and allows the measurement of probe-sample interactions in a dual force/tunneling current mode.[9] This takes advantage of both techniques simultaneously when measuring a surface.

The shape and size of the probe determines the amount of topographic information that is accessible. The probes must be sharp enough to reach down into the features of interest. We have developed methods to controllably fabricate sharp tungsten and iridium probes with a Ga^+ focused ion beam (FIB). [4,5] These probes typically have 5-6 nm radii and cone angles between 12° and 15° over the first two microns from the apex.

Accurate measurement of surface topography requires knowledge of the probe shape. This is particularly true when extracting line-widths or measuring surface roughness. The probe may change during its use because of large interaction forces and surface contaminants.[6,9] Therefore, measurement of the probe shape before and after scanning is required. We have developed a simple *in-situ* method to characterize the probe shape using lithographically shaped structures of known dimensions.[6,7] If the probes are too slender they may flex under the influence of lateral forces generated by contaminants on the sample's side walls.[6] We have also studied the effects of surface forces on these probes and how ambient conditions may affect measurements.[9]

When measuring surface roughness, a blunt probe can cause a surface to appear either smoother or rougher than it really is, depending on the circumstances. Narrow cracks in the surface may not appear in the scan, while protrusions can appear too large. We have studied the effects of probe shape on surface roughness calculations. Our findings show large differences between the true surface roughness and the measured surface roughness obtained with a typical probe. The analysis includes surface wavelengths from 5 nm to 300 nm.

1) J. E. Griffith, D. A. Grigg, M. J. Vasile, P. E. Russell, and E. A. Fitzgerald, "Scanning Probe Metrology", J. Vac. Sci. Technol., A, July/August 1992.

2) J. E. Griffith, G. L. Miller, C. A. Green, D. A. Grigg, and P. E. Russell, "Scanning Tunneling Microscope with a Capacitance-Based Position Monitor", J. Vac. Sci. Technol., B 8, pp. 2023-2027, 1990.

3) G. L. Miller, J. E. Griffith, E. R. Wagner, and D. A. Grigg, "A Rocking Beam Electrostatic Balance for the Measurement of Small Forces", Rev. Sci. Instrum., **62**, pp. 705-709, 1991.
4) M. J. Vasile, D. A. Grigg, J. E. Griffith, E. A. Fitzgerald, and P. E. Russell, "Scanning Probe Tips Formed by Focused Ion Beams", Rev. Sci. Instrum, **62**, pp. 2167-2171, 1991.
5) M. J. Vasile, D. A. Grigg, J. E. Griffith, E. A. Fitzgerald, and P. E. Russell, "Scanning Probe Tip Geometry Optimized for Metrology by Focused Ion Beam Milling", J. Vac. Sci. Technol., **B** 9, pp. 3569-3572, 1991.
6) J. E. Griffith, D. A. Grigg, M. J. Vasile, P. E. Russell, and E. A. Fitzgerald, "Characterization of Scanning Probe Microscope Tips for Linewidth Measurement", J. Vac. Sci. Technol. **B** 9, pp. 3586-3589, 1991.
7) D. A. Grigg, P. E. Russell, J. E. Griffith, M. J. Vasile, and E. A. Fitzgerald, "Probe Characterization for Scanning Probe Metrology", Ultramicroscopy, May, 1992.
8) M. Salmeron, D. F. Ogletree, C. Ocal, H. C. Wang, G. Neubauer, and W. Kolbe, "Tip-Surface Forces During Imaging by Scanning Tunneling Microscopy", J. Vac. Sci. Technol. **B** 9, pp. 1347-1352, 1991.
9) D. A. Grigg, P. E. Russell, and J. E. Griffith, "Tip-Sample Forces in Scanning Probe Microscopy in Air and Vacuum", J. Vac. Sci. Technol., **A** July/August, 1992.
10) S. A. Joyce, and J. E. Houston, "A New Sensor Incorporating Force-Feedback Control for Interfacial Force Microscopy", Rev. Sci. Instrum., **62**, pp. 710-715, 1991.

A Kinematically Coupled Magnetic Bearing Test Fixture

Tony Poovey, Mike Holmes, and David Trumper
Precision Engineering Laboratory
The University of North Carolina at Charlotte
Charlotte, North Carolina 28223

One of the current areas of research at the University of North Carolina at Charlotte involves the use of electromagnetic actuators as linear magnetic bearings in the development of an extremely high resolution positioning stage. Precision motion control at the nanometer level is necessary for precision applications such as diamond turning and photolithography. Initial research in the area of high precision motion control using magnetic suspension concluded that the electromagnet actuator force characteristics should be measured directly for linearization and implementation into the controller design [1]. Classical magnetic circuit theory can closely model the actuator force characteristics at low flux densities. However, as the actuators approach saturation, the behavior deviates from theory and experimental measurement is required. This paper describes the development and testing of a magnetic bearing test fixture designed for such actuator calibration.

The electromagnet test fixture consists of a fixture body and platform, three adjustable platen support columns with ball-and-groove kinematic couplings, three capacitance probes, and a target platen as shown in Figure 1. The electromagnet consists of E-shaped nickel-iron alloy blanks laminated and wound with 400 turns of #26 wire and housed within a mounting cartridge. The electromagnet cartridge is mounted inside the test fixture body in an inverted position with its pole faces exposed upwards towards the target platen as shown in Figure 1. A laminated iron target is attached to the underside of the target platen such that it is attracted towards the electromagnet. Located at 120 degree intervals around the perimeter of the fixture body are the three support columns; each consisting of a micrometer head, a load cell, and a kinematic ball/cylinder coupling. In the original design, the ball/cylinder kinematic coupling is a modified ball/vee groove design where the traditional flat vee groove is replaced by a pair of parallel hardened steel cylinders . In an improved test fixture design to be discussed later, the ball/cylinder coupling is replaced by a gothic arch vee groove and a larger diameter ball both fabricated from silicon carbide for increased stiffness. The micrometer heads are used to adjust the height of the platen above the electromagnet, while the load cells measure the attractive force between the electromagnet and the target platen. Three capacitance probes mounted to the top perimeter of the fixture body are used to sense the distance between the electromagnet and three datum pads on the target platen. The platen makes two points of contact in each of three grooves thus providing control of six degrees of freedom with the minimum number of constraints possible. This type of coupling, commonly referred to as a Maxwell mount, has the ability to provide sub-micron repeatability if properly designed [2]. The kinematic adjustability of the target platen facilitates the measurement of both force and torque as a function of target separation gap. Torque can be generated by the pitch and roll rotation of the target platen and will be the subject of further study.

The objective of the test software is to characterize the relationship between actuator force, current, and target separation gap as shown in Figure 2. In a control application, it is desirable to linearize the nonlinear force-current relationship in order to determine the current required to obtain a desired force at the given separation gap [3]. The data collected from the test procedure allows the development of a two dimensional look up table which permits such a linearization.

A block diagram for the system is shown in Figure 3. The user first initializes the actual air gap between the electromagnet face and target. Through a digital-to-analog converter, the test software outputs a sinusoidal control voltage with an amplitude of 10 volts. This sine wave is fed to the power amplifier which outputs a current proportional to the input voltage. The power amplifier output drives the electromagnet which applies a corresponding force to the target platen. The force, f(I,G), is a function

of input current and target separation gap. The load cells transduce this force into a proportional charge which is amplified and converted to a voltage by the charge amplifier. Both the electromagnet current and the load cell output voltage are logged into the computer via analog-to-digital converters for storage. After data is taken for one separation gap, the gap is adjusted to a new value and the test procedure is repeated for each gap setting. Afterwards, a two dimensional look up table of force versus current at the designated target separation gaps is built. The integrity of the look up table is verified by a separate routine which uses the look up table to vary the commanded force while simultaneously measuring the actual force. The result is a commanded force versus actual force comparison as shown in Figure 4 in which the straight line shows that the force can be accurately commanded to the desired value.

The electromagnets are intended to be tested at frequencies as high as 2000 Hz however, during initial testing, a resonance peak was encountered at 629 Hz. A kinematic coupling analysis program [4] verified this result with a resonance prediction of 628 Hz. Through a systematic evaluation of component stiffnesses throughout the test fixture, a compliance was traced to the ball/cylinder kinematic couplings supporting the target platen. Thus an improved kinematic coupling, shown in Figures 5 and 6, was designed with the aid of the coupling analysis software. The improved coupling design, made of silicon carbide, features a gothic arch vee groove with a larger radius of curvature than before and utilizes a greater preload. This results in an increase of coupling stiffness by a factor of 5.8 based upon calculations from the coupling design program. In addition, the effective mass of the system can be reduced by isolating the test fixture base from the table with a closed-cell foam pad. This essentially changes the system model from a single-mass/spring vibrating system to a double-mass/spring vibrating system. Frequency response test results of the fixture with and without vibration isolation were in good agreement with the theoretical results. In order to further improve the bandwidth of the test fixture, the system mass was reduced by a factor of two by constructing a target platen made with carbon fiber and foam core construction.

To conclude, an improved test fixture has been built and tested using the redesigned kinematic couplings, lighter target platen, and other changes described above. Frequency response results show an increase in system resonant frequency to 1630 Hz which compares with a predicted resonant frequency of 2273 Hz using the analysis software. Part of this discrepancy can be attributed to form errors in the fabrication of the gothic arch coupling which more realistically resembled a flat vee groove coupling. In addition, a stray compliance which reduces the collective stiffness of the remainder of the components to approximately the same value as the coupling alone may be resident within the structural loop of the system thereby reducing the stiffness significantly. The faulty couplings are being rebuilt to original specifications and an improved fixture body design is under development.

References

1. Trumper, D.L., "Magnetic Suspension Techniques for Precision Motion Control," Ph.D. Thesis, Dept. of Electrical Engineering and Computer Science, M.I.T., Cambridge, MA, Sept., 1990.

2. Slocum, A.H., and Donmez, A., "Kinematic Couplings for Precision Fixturing - Part 2: Experimental Determination of Repeatability and Stiffness," *Precision Engineering*, 10 (3), July, 1988, pp.115-122.

3. Trumper, D.L., Sanders, J.C., Nguyen, T.H., and Queen, M.A., "Experimental Results in Nonlinear Compensation of a One Degree-of-Freedom Magnetic Suspension," NASA International Symposium on Magnetic Suspension Technology, Hampton, VA, August 19-23, 1991.

4. Slocum, A.H., "Design of Three-Groove Kinematic Couplings," *Precision Engineering*, 1992, 14 (2), April, 1992, pp. 67-76.

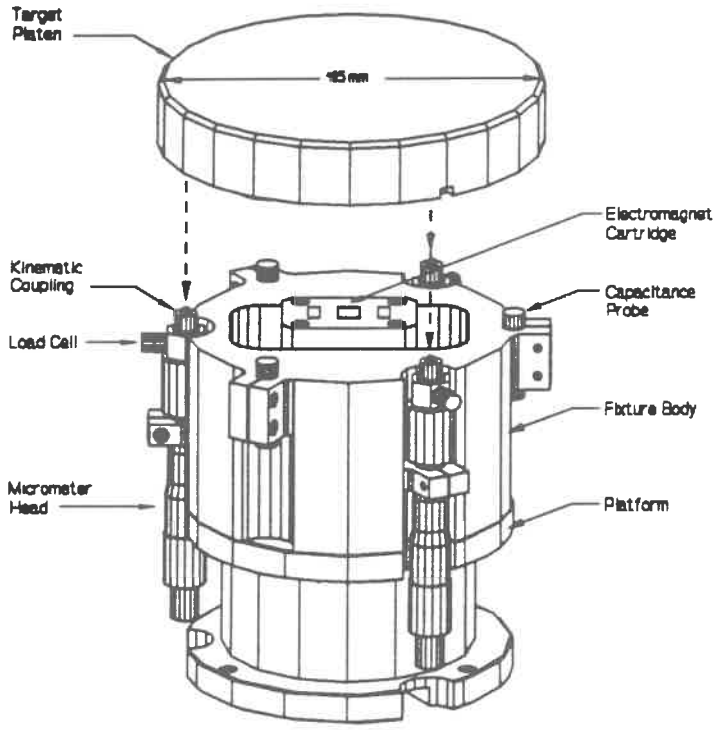

Figure 1 Solid model representation of the original test fixture design

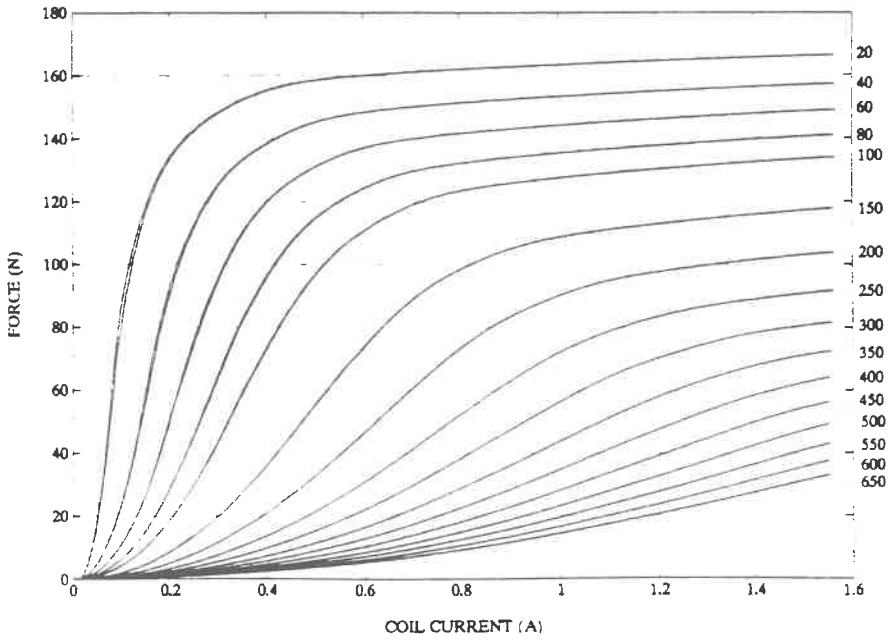

Figure 2 Force versus current at various separation gaps for a electromagnet with 400 turns of #26 wire

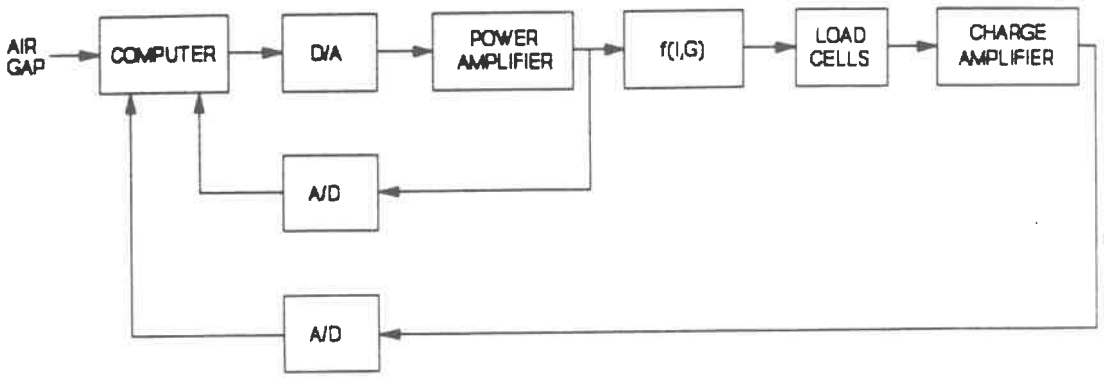

Figure 3 Block diagram of electromagnet testing procedure

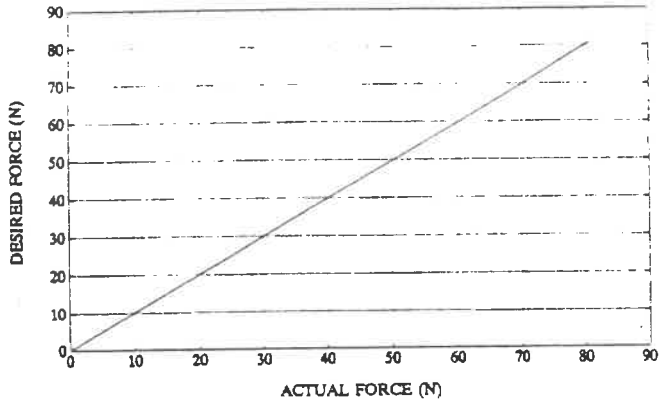

Figure 4 Desired force versus measured force at a 300 micron separation gap

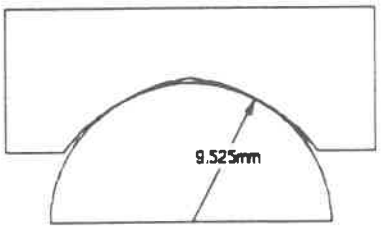

Figure 5 Gothic arch kinematic coupling

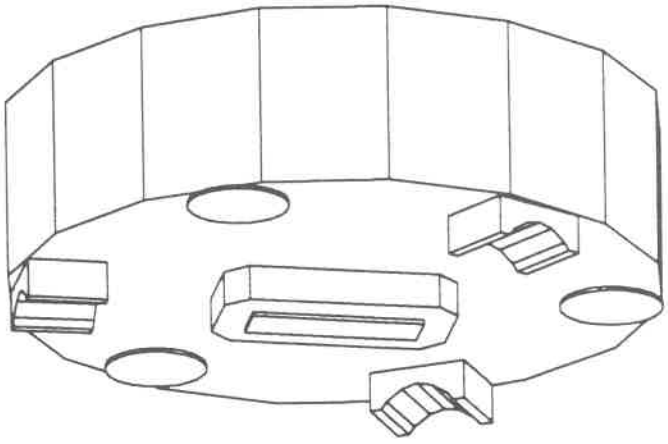

Figure 6 Carbon fiber platen with gothic arch kinematic couplings

A High Precision Five-Degree-of-Freedom Micropositioner Based on Electromagnetic Driving Principle

Wanjun Wang and Ilene Busch-Vishniac
Department of Mechanical Engineering,The University of Texas at Austin
Austin,Texas 78712

Abstract

This article describes a new micropositioner which is driven magnetically and in which the manipulator is attached to springs. The advantage of this approach over magnetic levitation approaches is that passive stability is ensured while friction is eliminated.

1. System Design and Operation

A high precision five-degree-of-freedom micropositioner is being developed in the Department of Mechanical Engineering, The University of Texas at Austin. The device has a linear spring suspension and is driven electromagnetically. Because mechanical friction has been one of the most important factors limiting the resolution and accuracy of positioning devices, magnetic levitation technology has been used by some researchers to eliminate friction and achieve high resolution [1,2]. Since a magnetically levitated, free-floating positioning device is inherently unstable without closed loop control, its accuracy and resolution are limited by the sensing system and would require fast computation for digital control. To have the advantages of a free-floating system (magnetically driven and friction free) and avoid its disadvantages (such as inherent instability, sensor limitations, and the computation burden), the new system is suspended by specially-shaped flat springs and is driven electromagnetically. The system consists of four parts: spring suspension, moving part (manipulator), a group of permanent magnets, and the sensing system.

Shown in Fig. 1 is the basic design of the system. The manipulator is suspended by two beryllium-copper flat springs. The springs are specially designed as shown in Figure 2b. The springs are fixed on the chassis at the four corners and are connected together by the rigid manipulator at their centers. Three groups of coils are fixed on the connector which forms a rigid body suspended between the two springs. The coils are reinforced

mechanically against bending. Each group of coils and its holder is referred to as an "arm". As shown in Figure 1, there are two translational arms and one rotational arm. The translational arm coils are arranged electronically so as to ensure uniform fields in all of the x-direction coils and in all of the y-directional coils. The permanent magnets on the manipulator are held by iron brackets to form U-shaped magnetic "shoes" with two magnets facing each other in opposite poles as shown in Figure 2(a). A very thin layer of soft steel is fixed on the surface of the permanent magnet to help to achieve a uniform magnetic field in the air gaps of the magnetic shoes.

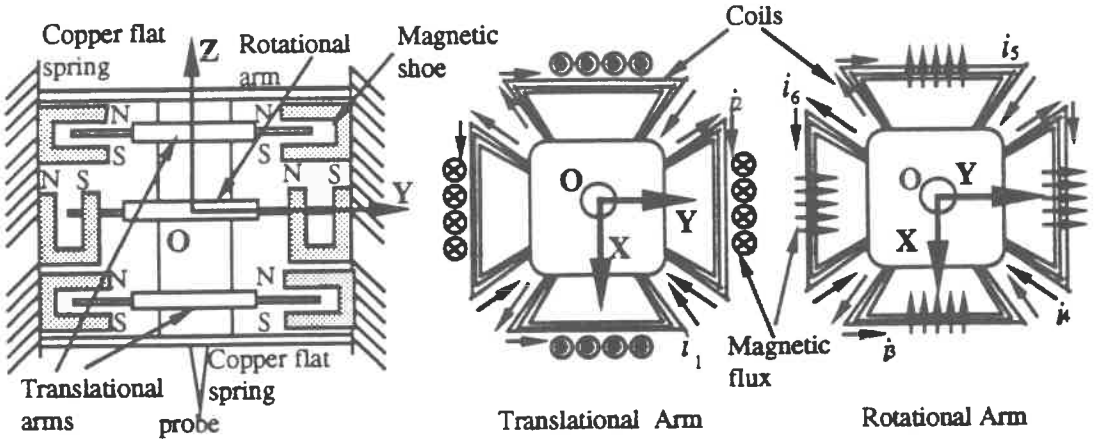

Figure 1: Diagram of the Device

When electrical currents are supplied to the coils, Lorentz forces exerted in the two translational arms drive the positioner to translate in the x and y dimensions. The Lorentz forces developed in the rotational arm translate the manipulator in the z direction and rotate (ϕ and ψ) it out of the $X-Y$ plane. By controlling the electrical currents to the coils, the manipulator motion can be controlled in five degrees-of-freeedom.

Three lateral effective PSDs (position sensitive detectors) and three LEDs are used for the sensing system with the LEDs fixed on the manipulator and the PSDs fixed on the chassis. As the manipulator moves, the light beams from the LEDs move on the surfaces of the PSDs. Better than $0.1\mu m$ position resolution has been achieved over a working space of 2 mm by 2 mm using this sensing system.

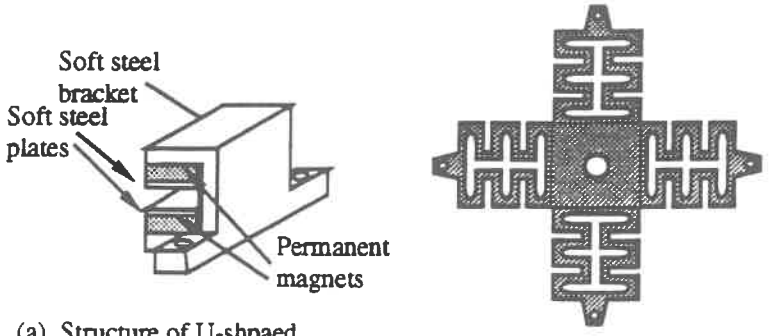

(a) Structure of U-shpaed magnetic "shoe"

(b) Flat beryllium-copper spring

Figure 2: a. U-shaped Magnetic Shoe and b. Flat Beryllium-Copper Spring

2. Mathematical Model of The Manipulator

The electrical coils and the magnetic shoes have been designed to eliminate dimensional crosstalk and avoid nonlinearity, thus keeping the system control straightforward. To simplify the modeling of the system, the following assumptions were made: the magnetic fields in air gaps are uniform; the manipulator is a rigid body and is symmetric with respect to the system coordinate system $X-Y-Z$; there is no rotation within the $X-Y$ plane; and finally the fringe effects and damping are negligible. With these assumptions the following equations can be obtained for the system:

$$\frac{d^2X_0}{dt^2} + \frac{K_X}{M}X_0 = \frac{4BNL}{M}i_2 + \frac{BNL\sin\psi}{M}(i_4 + i_6), \tag{1}$$

$$\frac{d^2Y_0}{dt^2} + \frac{K_Y}{M}Y_0 = \frac{4BNL}{M}i_1 - \frac{BNL\sin\phi}{M}(i_3 + i_5), \tag{2}$$

$$\frac{d^2Z_0}{dt^2} + \frac{K_Z}{M}Z_0 = \frac{BNL}{M}(i_3 + i_4 + i_5 + i_6) \tag{3}$$

$$\frac{d^2\phi}{dt^2} + \frac{K_\phi}{I_{XX}} = \frac{BNLD}{I_{XX}}(i_4 - i_6), \tag{4}$$

and

$$\frac{d^2\psi}{dt^2} + \frac{K_\psi}{I_{YY}} = \frac{BNLD}{I_{YY}}(i_5 - i_3). \tag{5}$$

Here B is the flux density in the air gap of the magnetic shoes; M is the mass of the manipulator; K_X, K_Y, K_Z, K_ϕ, and K_ψ are the spring constants

in the X, Y, Z, ϕ, and ψ dimensions; i_1, i_2, i_3, i_4, and i_5 are the electrical currents supplied to the coils 1, 2, 3, 4, and 5 respectively (See Fig. 1); N is the number of turns in each coil; L is the length of each coil contained in the air gap of the magnetic shoes; D is the distance from the geometric center of the rotational arm to the straight portion of the coils; and I_{xx} and I_{yy} are the moments of inertia with respect to body coordinate system $x - y - z$.

3. Control of the System

From Eqs. (1)-(5), it can be seen that there exists little dimensional crosstalk. The rotation ψ is only dependent on the currents i_3 and i_5, the rotation ϕ is only dependent on the currents i_4 and i_6, and i_1 and i_2 control the X and Y tranlations respectively. The advantage of this dimensional separation is that each type of motion can be independently controlled, either in parallel or series.

We have implemented a digital controller using an IBM PC-AT with analog to digital (A/D) and digital to analog (D/A) conversion capabilities. Power driving circuits are used to drive the electrical coils and the position and the orientation of the manipulator are monitored by the sensing system and fed back to the computer controller.

Since the system is inherently stable and there is no mechanical friction, the resolution and accuracy of the system are theoretically limited by the A/D and D/A boards. Potentially, the device can be used for high precision microprobing, cellular biology, microsurgery, and industrial work in the micromechanical area.

References

1. M. C. Jeong and I. J. Busch-Vishniac, "A Magnetic Micro-Levitation Robot," **ASME Dyn. Sys. and Control**, DSC-Vol. 19, 69-81 (1990).

2. M. C. Jeong and I. J. Busch-Vishniac, "A Submicron Accuracy Magnetic Levitation Micromachine with Endpoint Friction," **Sensors and Actuators**, 19, 225-234 (1992).

Robust H_∞ Control System Design Of A New 3-DOF Magnetic Micro-Levitation Robot

Abdelfatah M. Mohamed†, Bard Vestgaard and Ilene Busch-Vishniac

Mechanical Engineering Dept., The University of Texas, Austin, TX 78712

Introduction

Many operations in manufacturing require high precision motions and delicate forces. Such operations have resisted automation because friction generally limits the repeatability and resolution of a robot and other automated tools. Micromachines are simply automatically controlled fine positioners designed to solve these problems. Although their features may be substantially bigger than a micron, the motion resolution sought is micron level or smaller. Active magnetic levitation (electronically controlled magnetic levitation) seems appropriate for this application. This is because the main object of such operations is to get high precision and to damp any high frequency vibrations or noise that may arise, while asymptotically tracking any command signal that moves the robot from one place to another. With electronic feedback control all those requirements can be achieved if the controller is well designed. Several different approaches to micromachines are available in the literature. For example, in Jeong and Busch-Vishniac [1] a magnetic levitation micro-actuator with end point friction is discussed. Fujita and Omodaka [2] have examined electrostatic fine motion positioners. Hollis *et al* [3] use a magnetic approach. In this paper, a new idea for a three-degree-of-freedom pure magnetic levitation micro-actuator will be discussed. A robust H_∞ controller designed to stabilize the system while allowing it to achieve the desired performance requirements is presented.

System description

A schematic diagram for the system is shown in Fig. 1. It consists of two U-shaped rectangular electromagnets (identical in their structure) and a manipulator constructed of two iron pole pieces connected together with a brass bar. Both the electromagnets and the iron pole pieces are made of ferromagnetic material. The forces generated by the electromagnets and exerted on the manipulator have two components [4]: one in the vertical direction (Z-direction) and the other in the axial direction (X-direction). The vertical components control both vertical and tilting (pitching) motions, while the axial components control the axial motion.

Expressions for the lift and transverse forces f_r and f_t between two closely spaced rectangular pole pieces have been derived mathematically in Brzezina and Langerholc [4] in terms of the coil current i, gap length g, axial clearance s, pole face area A, pole width h, and the number of turns of the magnet coil N. The assumptions were made that the field is uniform and passing perpendicularly between the opposing pole surfaces, and that the magnet cores are made of high permeability nonsaturated material. The force expressions are given below:

$$f_r = \mu_0 \left(\frac{N}{2}\right)^2 A \left(\frac{i}{g}\right)^2 \left(1 - \frac{|s|}{h} + \frac{2g}{\pi h} + \frac{2s}{\pi h} \tan^{-1}\left(\frac{g}{s}\right)\right) \qquad (1)$$

† A. Mohamed is currently a postdoctoral fellow at the Mech. Eng. Dept., University of Texas, Austin, on leave from the Elect. Eng. Dept. Assiut University, Assiut, Egypt.

$$f_t = \frac{2\mu_0 A}{\pi h}(\frac{N}{2})^2(\frac{i^2}{g})\tan^{-1}(\frac{s}{g}). \tag{2}$$

Model and dynamics

The equations of motion of the gravity center for the three degrees-of-freedom are

$$m\ddot{z} = -f_{lr} - f_{rr} - f_{dz} + mg \tag{3}$$

$$J\ddot{\theta} = (f_{lr} - f_{rr} + f_{d\theta})l \tag{4}$$

$$m\ddot{x} = f_{lt} - f_{rt} + f_{dt} \tag{5}$$

where m is the manipulator mass, J is its moment of inertia, f_{lr} and f_{lt} are the lift and transverse forces on the left-hand side, f_{rr} and f_{rt} are the lift and transverse forces on the right hand-side, and f_{dz}, $f_{d\theta}$, and f_{dt} are either real physical disturbance lift, tilt and transverse forces or can be considered as modeling errors. Linearizing equations (3)–(5) around the equilbrium point yields

$$m\ddot{z} = -2c_1 z - c_3(i'_l + i'_r + i_{n1}) + f_{dz} \tag{6}$$

$$J\ddot{\theta} = (-2c_1 l\theta - 2c_2 x + c_3(i'_l - i'_r + i_{n2}) + f_{d\theta})l \tag{7}$$

$$m\ddot{x} = -2d_1 l\theta - 2d_2 x + d_3(i'_l - i'_r + i_{n2}) + f_{dt} \tag{8}$$

where i_{n1}, i_{n2} represent actuator noise or model uncertainties, and $c_1, c_2, c_3, d_1, d_2, d_3$ are the linearization constants of the force equations (1) and (2). Equations (6)–(8) show that the Z-motion can be controlled separately from the (Θ-X)-motion.

Equations (6)–(8) can be formulated in the following state space form as follows: let $x_1 = z$, $x_2 = \dot{z}$, $u_1 = (i'_l + i'_r)$, $x_{g1} = (x_1, x_2)$. Then the Z-motion can be described by the following SISO linear control system

$$\dot{x}_{g1} = A_{g1}x_{g1} + b_{g1}u_1 + e_{g1}d_{o1}, \quad y_1 = c_{g1}x_{g1} + n_1, \tag{9}$$

where $y_1 = z$, n_1 represents the sensor noise, and $d_{o1} = (f_{dz}\ i_{n1})'$.

Let $x_3 = l\theta$, $x_4 = x$, $x_5 = l\dot{\theta}$, $x_6 = \dot{x}$, $u_2 = (i'_l - i'_r)$, $x_{g2} = (x_3, x_4, x_5, x_6)$. Then the ($\Theta$-X)-motion can described by the following single input-dual output (SIDO) linear control system

$$\dot{x}_{g2} = A_{g2}x_{g2} + b_{g2}u_2 + e_{g2}d_{o2}, \quad y_2 = c_{g2}x_{g2} + n_2, \tag{10}$$

where $y_2 = (l\theta, x)$, n_2 represents the sensor noise, and $d_{o2} = (f_{d\theta}\ f_{dt}\ i_{n2})'$.

Control system design

In control system design a satisfactory controller can not be obtained by considering the internal stability objective alone. Robustness to plant uncertainties and other performance specifications must be incorporated in the framework of controller design. The following performance requirements must be achieved: robust stability against various model uncertainties, disturbance/noise attenuation, asymptotic tracking to command

signals, avoidance of saturation of the actuators, achievement of good stiffness to get high precision, limiting closed loop bandwidth to achieve good robustness, and noise rejection. H_∞ synthesis has been used to design a controller for the 3-DOF magnetic micro-levitation, so that the closed loop system is internally stable and the above requirements are achieved. H_∞ synthesis methods based on state space solution techniques [5]-[6] provide powerful new tools for the design of linear control systems in a frequency domain setting, because the above requirements can be incoroporated in the framework of the controller design. Design specifications and goals are usually reflected by weighting the appropriate closed loop transfer functions in the H_∞ synthesis procedure.

Consider the standard H_∞ control problem shown in Fig. 2., where $\mathbf{w}$ represents all exogenous input signals such as (command signals, disturbances, sensor noises ...etc), $\mathbf{z}$ represents the error vector (all variables that need to be regulated), $\mathbf{u}$ represents the actuators input, $\mathbf{y}$ is the measured outputs, $\mathbf{P}$ is the standard plant (plant model plus the weighting functions that reflect the design specifications and goals).

Having set up the appropriate input output weightings, the H_∞ problem may be stated as follows [5]: Find a stabilizing controller, $\mathbf{K}$ such that $\|\mathcal{F}_L(\mathbf{P},\mathbf{K})\|_\infty \leq \gamma$, for some prespecified $\gamma \in \Re$. $\mathcal{F}_L(\mathbf{P},\mathbf{K}) = \mathbf{P_{11}} + \mathbf{P_{12}K(I + P_{22}K)^{-1}P_{21}}$ represents the transfer function from the exogenous input $\mathbf{w}$ to the regulated output $\mathbf{z}$. The solution to this problem is given in Glover and Doyle [5].

The most difficult part of the H_∞ problem is the choice of the appropriate weighting functions that reflect the design goals. Consider the augmented system shown in Fig. 3 for the $(\Theta - X)$ motion. The following set of weighting functions can be used to reflect the required performance

[1] $W_1(s) = \gamma_1 I_3$ to reject disturbance and model uncertainties and also achieve good stiffness.

[2]

$$W_2(s) = \gamma_2 \begin{pmatrix} \frac{100(1+0.004s)}{(1+100s)} & 0 \\ 0 & \frac{0.01(1+1000s)}{(1+10s)(1+s)} \end{pmatrix}$$

to achieve asymptotic tracking. Note that we can only achieve tracking for one motion because the system is a SIDO system, and in this case, it is the $\Theta-$motion. Another controller can be designed to achieve tracking for the X-motion.

[3] $W_3(s) = \gamma_3(10^{-8})$ to avoid actuator saturation.

[4] $W_4(s) = \gamma_4 \frac{s^2}{(2\pi 100)^2} I_2$ to limit the closed loop bandwidth and achieve good robustness and noise rejection at high frequency.

[5] $W_5(s) = \gamma_5 I_2$ to reduce the effect of noise.

The above set of weighting functions is not unique; several other choices will be tried. The design parameters $\gamma_1, \gamma_2, \gamma_3, \gamma_4, \gamma_5$ are varied during the control design process to achieve the best performance possible. Using the same procedure we can design an H_∞ controller for the SISO $Z-$motion system. The system is being implemented for experimental demonstration.

References

[1] Jeong, M. C., and Busch-Vishniac, I., "A Magnetic Micro-Levitation Robot," Proc. ASME Winter Meeting, Dec. 1-5, 1990, Dallas, TX.

[2] Fujita, H. and Omodaka, A., "Electrostatic Actuators for Micromachines," IEEE Micro Robots and Teleoperators Workshop, Hyannis, MA, Nov 9-11, 1987.

[3] Hollis, R. L., Allan, A. P.,and Salcudean, S.,"A Six Degree-of-Freedom Magnetically Levitated Variable Compliance Fine Motion Wrist," 4th International Symposium of Robotics Research, Santa Cruz, CA, Aug. 9-14, 1987.

[4] Brzezina, W. and Langerholc, J.,"Lift and Side Forces On Rectangular Pole Pieces In Two Dimensions", Journal of Applied Physics Vol. 45, No. 4, April 1974.

[5] Glover, K. and Doyle, J. C.,"State Space Formulae For All Stabilizing Controllers That Satisfy an H_∞-Norm Bound And Relations To Risk Sensitivity" Systems and Control Letters Vol. 11 1988.

[6] Maciejowski, J. M.,"Multivariable Feedback Design," Addison-Wesley, New York, 1989.

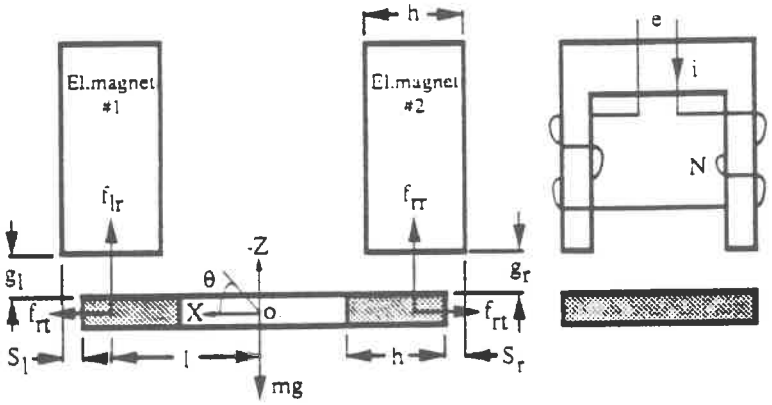

Fig. 1. Three DOF Magnetic Levitation System

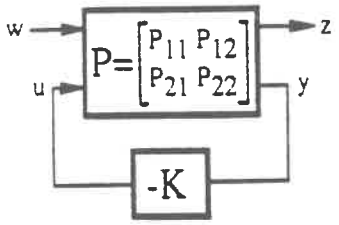

Fig. 2. Standard H_∞ Configuration

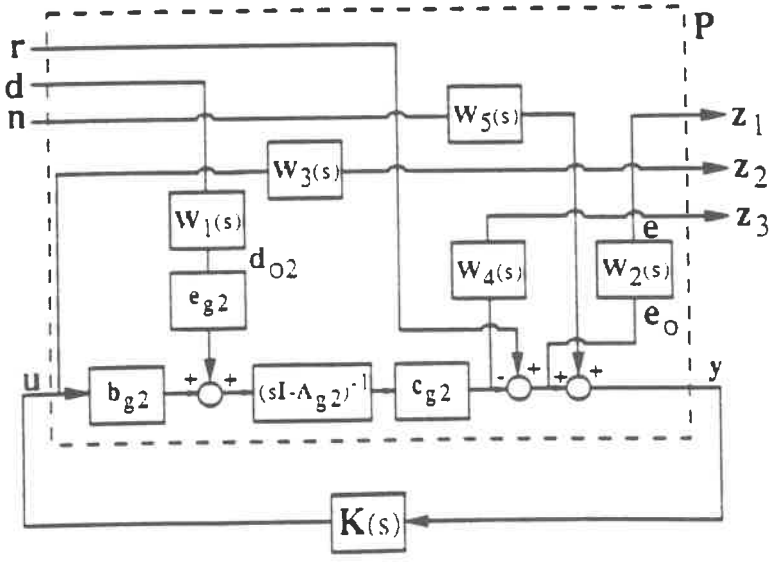

Fig. 3. Block Diagram of the Augmented System

Precise Positioning Mechanism with Surface Motor

Yoshiyuki Tomita, Fumiaki Sato and Yasushi Koyanagawa

Systems Engineering Laboratory
Sumitomo Heavy Industries, Ltd.
2-4-15 Yato-cho, Tanashi-City, Tokyo 188, Japan

1. Introduction

A new precise positioning system incorporating surface motor (SFM) drive, called the "SFM positioning system", has been developed, and its performance experimentally evaluated. This system utilizes a triangular-shaped positioning stage which is guided along a base plate by three air bearing pads. The positioning and guidance of the stage's planar motion is accomplished via the simultaneous operation of three identical force-controlled servo systems. Advantageous features include three-axis in-parallel direct drive, a compact and lightweight structure, and almost no friction. This system enables high positioning resolution and rapid response to be obtained in comparison with conventional positioning methods. The present paper describes the design features employed, the fundamental configuration and operating principles of the positioning stage mechanism, its servo control system, and some experimental results.

2. Design Features

The following design features were used to obtain system high positioning resolution and rapid response capabilities:

(1) Direct drive method- Direct drive enables precise motion control to be achieved since it provides an accurate force transmission method that does not include nonlinear behavior such as backlash, hysterisis, and dead zones [1].

(2) In-parallel actuation with three degrees of freedom- An in-parallel drive method is beneficial because it allows obtainment of guidance and positioning with three degrees of freedom using three identical force-controlled servo system [2].

(3) Non-contact levitated drive- A positioning mechanism constructed with a hydrostatically lubricated air bearings and employing an electro-magnetic drive method are useful to achieve precise motion control and smooth sliding, while also maintaining drive mechanism cleanliness.

3. System Configuration and Operation Principles

Figure 1 shows the configuration of the SFM positioning system. Main components of the system include an aluminum stage plate, the SFM drive unit, three air bearing pads, and a steel base plate. The positioning stage weighs 5.9 kg and has an x and y travel range of 30 mm each. It is kinematically constrained in the z, θ_x, and θ_y directions by the air bearing pads, whereas in the x, y, and θ_z directions by the SFM's servo system. The position and yaw angle of

the stage is measured by a three-axis laser-interferometer system having 5-nm resolution for x and y and 0.06 μrad for θ_z.

The SFM consists of three drive elements (X, Y_1 and Y_2) which use brush-less-type linear DC motors (Fig. 2). The stage is driven in the x-direction primarily by the x-element-produced thrust force F_x, and similarly driven in the y- and θ_z-directions by a combination of F_{y1} and F_{y2}. Each element has coil pairs (A and B) mounted on the bottom side of the stage plate and corresponding permanent magnet pairs on the base plate (1-mm air gap). The permanent magnet pairs of Y_1 and Y_2 are symmetrically located with their length running in the y-direction, while those of X are perpendicularly located between Y_1 and Y_2. Each magnet pair has a pole pitch of 12 mm, with Nd-Fe rare earth magnets being used to obtain a high magnetic flux density. The coil pairs have twin winding pairs that are aligned parallel to the magnets. Coils (A) and (B) have different phases to enable a long travel stroke to be obtained. Each coil (0.5-mm dia. × 86 turns) has a non-magnetic core to minimize actuator-produced force ripple and absorption force which decrease stage positioning resolution and accuracy. The electric time constants are about 0.1 ms for X, Y_1, and Y_2. Figure 2 shows the x-directional thrust force F_x which is generated when the energized coils are within the permanent magnet field. The thrust forces F_{y1} and F_{y2} are similarly generated. These resultant forces, i.e., a maximum force of 9 N for X and 6 N for Y_1 and Y_2 at a 5-A current, are used by the SFM to drive the stage.

4. Servo Control System

The servo control system employs PID control, decoupling compensation and two-phase current excitation for the drive element coils. Figure 3 shows a block diagram of the control system, with its main features being described as follows:

(1) Servo control compensation- The stage positions (m_x, m_{y1}, m_{y2}) are detected by the laser-interferometer system and transformed to a base-plate-referenced rectangular coordinate system and fed back to a closed-loop control system. Tracking errors between a reference command (x_r, y_r, θ_{zr}) and the actual position (x, y, θ_z) are compensated for by the PID controller. The resultant force commands (f_x, f_y, τ_z) represented in the rectangular coordinate frame are transformed to actuator-produced thrust forces (F_x, F_{y1}, F_{y2}) by a decoupling compensation process. This compensation method effectively suppresses the mutual dynamic interference behavior among the three degrees of freedom, which is caused by the distance between the drive locations and the center of gravity of the stage, as well as by inherent thrust force variations of the actuators.

(2) Coil excitation- The voltage of each coil ($u_{xA,B}$, $u_{y1A,B}$, $u_{y2A,B}$) is determined by a two-phase (A and B) energizing function, where Fig. 4 shows the measured thrust force of the X drive element versus its coil displacement in the x-direction. It should be noted that the thrust forces from phases A and B respectively vary in an approximate sine and cosine distribution, and also that its characteristics are dependent only upon the coil's x-position and

not on its y-position. The Y_1 and Y_2 elements have similar force characteristics; hence, each element provides thrust force with respect to a single position variable.

(3) Control system configuration- The servo control compensation and coil excitation are executed by a multi-transputer system (T800, Inmos, UK). The complex matrix calculations for three-axis motion control mentioned above are executed by a parallel processing system in a 450-μs sampling period.

5. Experimental Results

The positioning capability of the newly developed SFM positioning system was experimentally tested. Figure 5 shows the directional response of the stage mechanism for a 25-mm step motion command to only the y-direction. The maximum velocity of the command was 150 mm/s. The transient deviations in the x- and θ_z-directions were respectively less than ±0.1 μm and ±10 μrad. These are believed to be caused by dynamic interference primarily due to decoupling compensation errors or a force ripple produced by the actuators. Figure 6 shows the response to 10-nm stepwise commands in only the y-direction. Although the measured position shows variations due to the resolution of the laser-interferometer measurements, the mean value of the stage position tracks to the command without occurrence of a dead zone or hysterisis. Consequently, resultant positioning variances (3σ) were 15.7 nm, 9.4 nm, 0.11 μrad for the x-, y- and θ_z-directions, respectively.

6. Conclusions

A surface motor driven precise positioning system was newly developed and some experimental results were presented. A positioning resolution of 10-20 nm and maximum velocity of 150 mm/s were obtained. These results indicate that the proposed positioning method is useful to accomplish high resolution positioning with a long travel range at a high velocity. The SFM positioning system is expected to be applicable to several micro-machining systems.

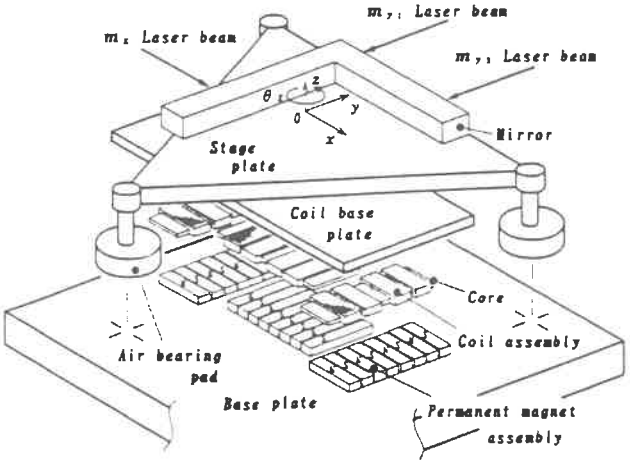

Fig. 1 A schematic of the SFM positioning system.

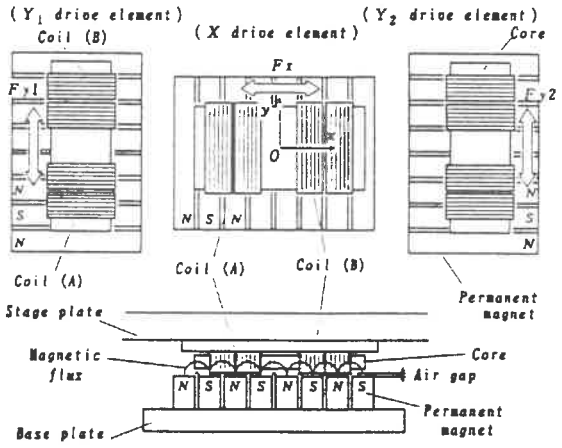

Fig. 2 Arrangement of the SFM's drive element coil and magnet pairs.

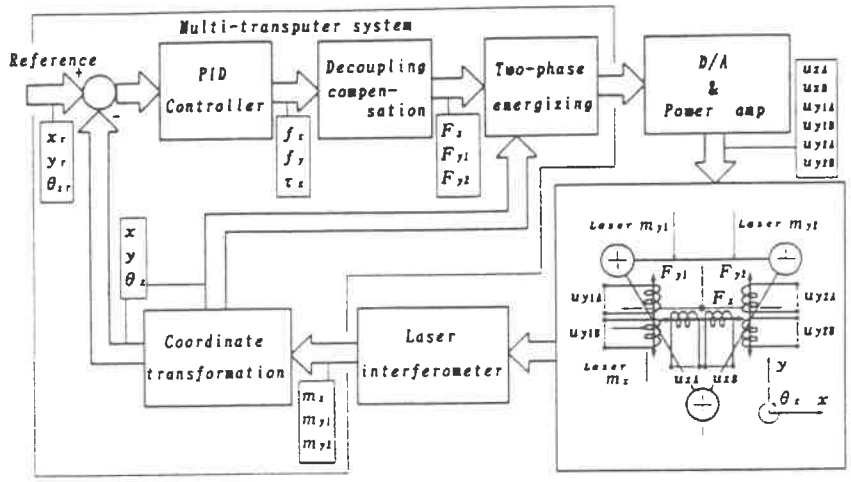

Fig. 3 Block diagram of the servo control system.

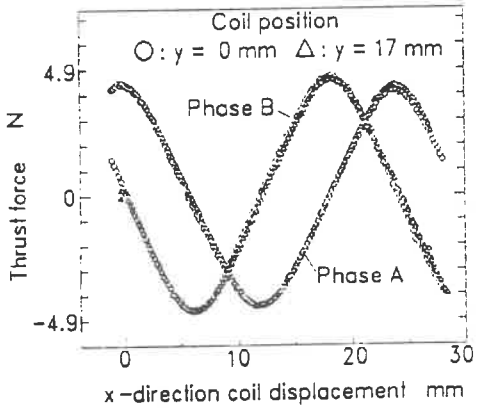

Fig. 4 Measured thrust forces of the X element versus it coil displacement under a 2.5-A current.

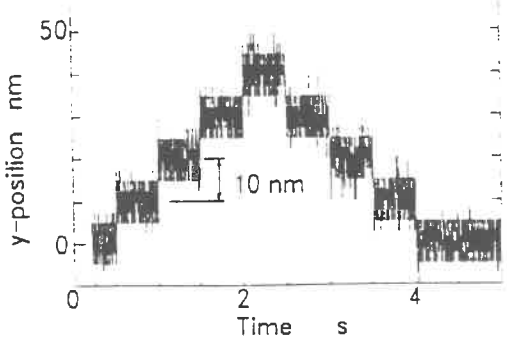

Fig. 6 Response of the SFM positioning stage for 10-nm stepwise commands in the y-direction.

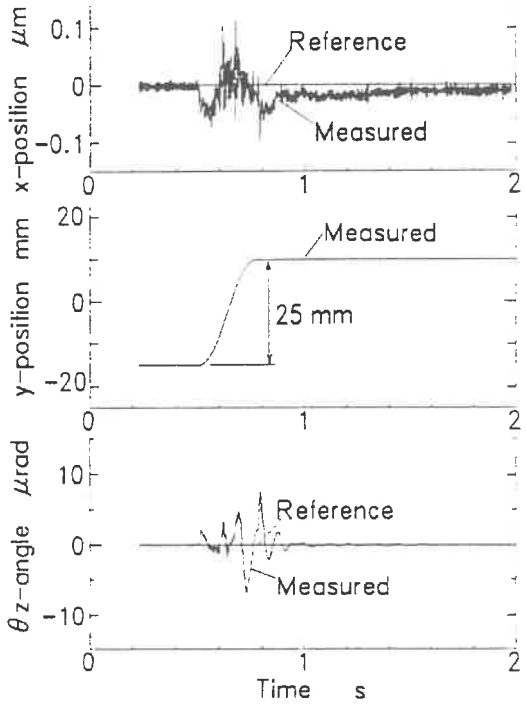

Fig. 5 Directional response of the SFM positioning stage for a 25-mm motion command in the y-direction.

References

[1] S. Futami and A. Furutani, "Ultra-precise AC Linear Motor for Nanometer Position Control", Proc. 1991 ASPE Ann. Conf., ASPE, 1991.

[2] R. Kendall, "Servo-guided Planar Stages and Other X-Y Stages for Microlithography : A Review", Proc. 1991 ASPE Ann. Conf., ASPE, 1991

ANALYTICAL/EXPERIMENTAL METHODS SUPPORTING AN "ERROR BUDGET"-BASED DESIGN OF THE PATS/PFMS

Joel G. Bennett, Richard L. Rhorer and Robert R. Stevens
Los Alamos National Laboratory
Los Alamos, New Mexico, 87544

The design of a Precision Automated Turning System (PATS) for use in the Department of Energy weapons complex is being carried out under the umbrella of the Precision Flexible Manufacturing System (PFMS) at the Los Alamos National Laboratory. From the beginning of this project, the design has been based on a finished part "error budget" concept that allows the contribution of the elastic displacements from the PATS machine-base to be included in the machining error and the spindle-to-spindle part transfer error.

Thus, a number of different analytical models have been used to perform studies of the displacements of key points when the base is subjected to the loadings that occur during movement of the slides on the way system. Finite Element (FE) models have been used in parameter studies and one of them is illustrated in Fig. 1. This model has pointer "beams" at the part-machining position along the spindle centerline and at the spindle-to-spindle part transfer position. These rigid pointers indicate the difference in the actual displacements, as opposed to the assumed displacements (thus, the "error"), at these points caused by the base deformation. For example, one of their uses was to study the effects of the locations and the number of base supports. The maximum relative pointer displacements, when the model is loaded by the way system for 3, 6, 11, and a crippled 11-point support scheme, were studied. Using this information, a decision was made to depart from the conventional 3-point ("milkstool") support concept, and support the base at 5-points.

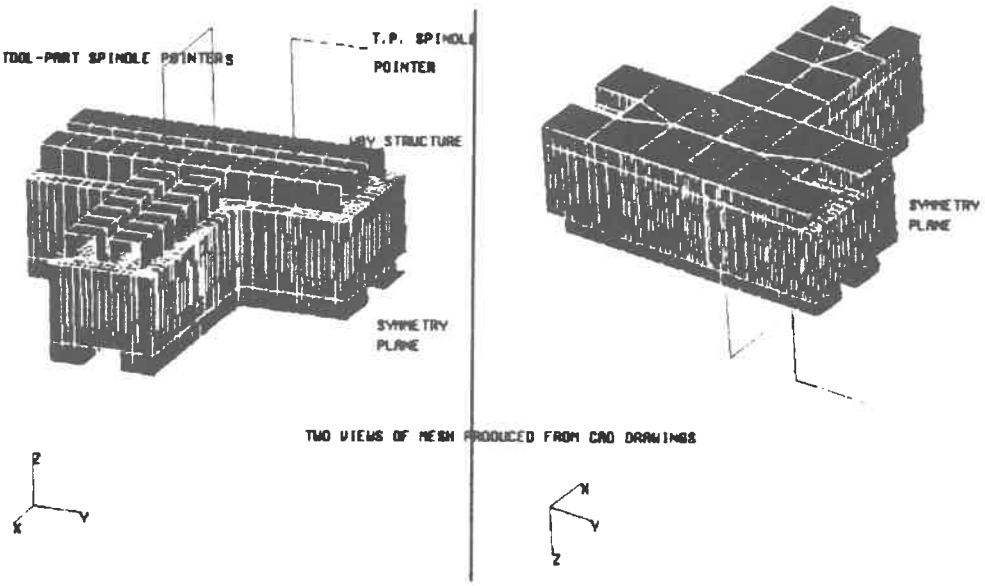

Fig. 1 Two views of the finite element (FE) mesh produced from the CAD drawings.

The preliminary design studies included parameter studies on the weldment geometries and base thicknesses. This information led to a final design and to a set of CAD drawings being produced. Next, a set of neutral files of the drawings were used with the PATRAN system to produce an FE mesh.(1). Because of the requirements of matching the geometry of the bottom support pockets, triangular webs, sides, top-plate, and way system, while maintaining nodal compatibility, the mesh becomes large (~ 35,000 dofs for a half-model), and the use of symmetry was deemed appropriate.

This model (Fig. 1) was run twice to produce the needed set of displacements: once with symmetry boundary conditions and again with asymmetry boundary conditions applied on the plane of geometric symmetry. Asymmetry boundary conditions imply that "downward" loads in the left half-model are "upward" loads in the right-half (unseen) portion of the model. By properly superimposing the results of these runs, the result for any of the applied loads taken separately can be found.

Figure 2 shows a set of four local coordinate systems located at the "home" positions of each way table. If Table 1, for example, is allowed to move full travel from $S_1 = -1$ to $S_1 = 1$, and likewise for all other tables, the entire range of positions of the movement of the tables can be represented by the set of vectors $\{S_1,S_2,S_3,S_4\}$ if the displacements for each table at $S_i = \{-1,0,1\}$ are known. Thus, 12 load cases are run (see Fig. 4). Once the displacements for the way tables in their extreme and home positions are known, i.e., for the 12 load cases, then the displacements {u}, of the nodes in the model for any combination of table positions at any coordinate S_i can be shown to be found from $\{u\} = \{pCNV\}$, where C is the matrix of displacements for the nodes involved for the these load cases, $N(S_i)$ are the set of shape functions that interpolate for any position of S_i between -1 and +1, V is the load vector for these load cases, and p is a vector of scalar multipliers for the load magnitudes (if unit pressures are used in the analysis). Software was developed to perform all of the necessary operations to get relative pointer displacements for the loads in any position using the above scheme.

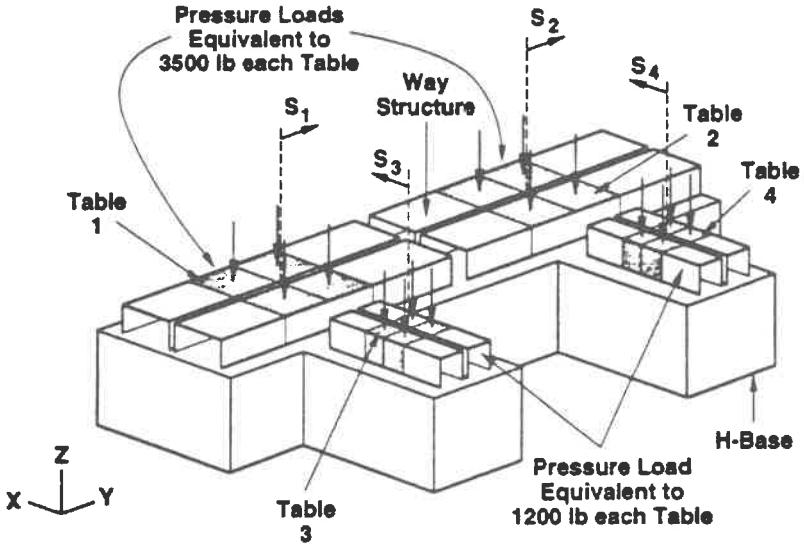

Fig. 2 Schematic representation of the base and way tables 1-4 with the normalized local coordinates definition S_1 through S_4. Full table motion is from $S_i = -1$ to +1, with $S_i = 0$ being the "home" positions shown. The upper structure is represented as table pressure loadings.

To illustrate, Fig. 3 shows the relative displacement of the pointers as Table 1 moves from $S_1 = 0$ to $S_1 = 1$, Table 2 moves from $S_2 = 1$ to $S_2 = -1$, Table 3 from $S_3 = +1$ to $S_3 = -1$, and Table 4 from $S_4 = -1$ to $S_4 = 0$, all simultaneously. This combination of moves represents a typical operation of finishing machining at station 1, so Table 1 moves from the machining station to the transfer point, while Table 2 has placed a finished part off the end and moves to the center for part transfer, Table 3 moves back from the machining point to pick up a new tool, and Table 4 moves from picking up a tool to its "home" position.

Simulations like those above, from the output of the FE models with and without bottom plates, have been studied. The conclusion from these studies is that the base either needs no bottom plate or only a partial bottom plate. Although this recommendation is too late for Base No. 1, the second weldment will likely have only a partial bottom plate if the finite element model verification proves adequate. Such a feature will make the decommissioning process easier at the end of the useful life of the PATS.

Several methods can be used to verify FE models, but at Los Alamos the comparison of the predicted modal frequencies from the finite element model to an experimentally determined set of modal frequencies has proved to be particularly useful. To ensurebe that meaningful data can be obtained from an experimental modal analysis for a structure as large and as stiff as the PATS base, a pretest was performed on a salvaged T-base lathe bed.

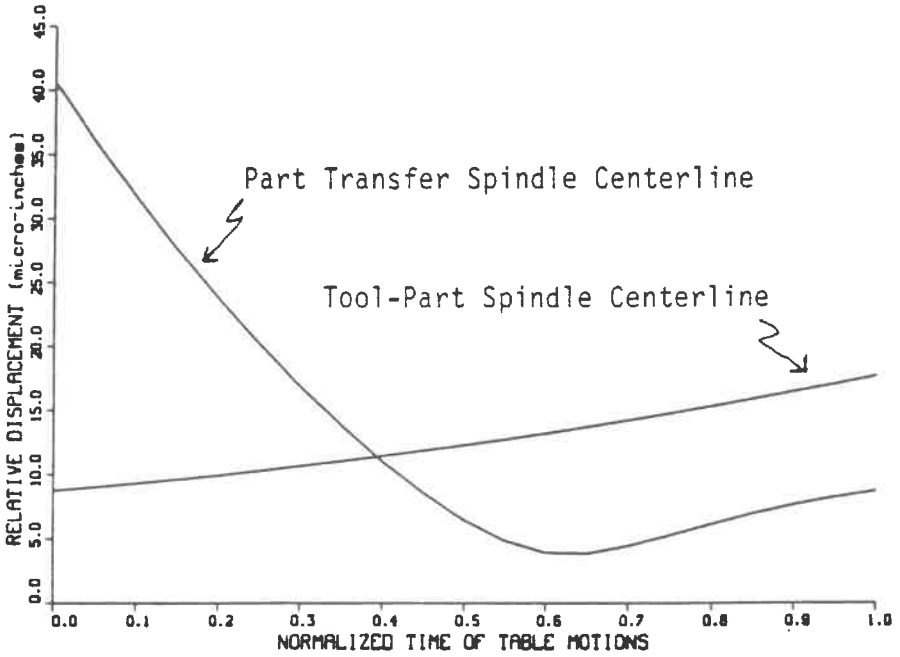

Fig. 3 Pointer movement for simultaneous table motions in text.

The bed was placed on air bags so the test could simulate totally free boundary conditions. Table I summarizes the results of this test. Figure 4 shows an example of the modal deformation for Mode 3. Testing of the first PATS base for model verification purposes is scheduled for August 1992. Predicted modal frequencies for the PATS H-base, without the ways attached, are given in Table II.

Table I

Natural Modes of Vibration
Moore T-base Lathe Base

Mode	Frequency (Hz)	Damping (% crit)	Description
1	235	0.84	1st bending mode, x axis.
2	270	0.71	1st bending mode, x axis.
3	303	0.28	1st bending mode, z axis.
4	329	0.39	1st bending mode, x axis with y-axis torsion
5	414	0.57	Shear (racking) of entire structure, with spindle bending about z axis.
6	693	0.34	Spindle bed walls bulging in x direction (in phase).
7	702	0.47	Work bed z-axis bending. Spindle point 40 y-direction motion.
8	743	0.33	Spindle bed walls bulging in x direction (out of phase). Work bed z-axis bending.
9	761	0.29	2nd mode of spindle bed walls (in phase).

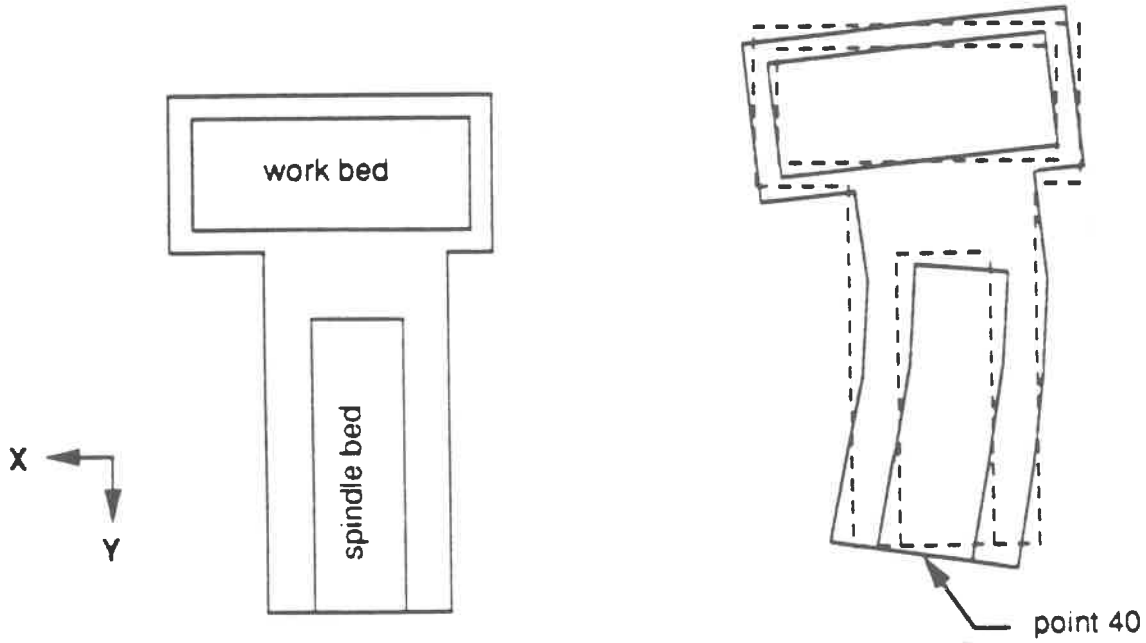

Fig. 4 Measured mode 3 for a T-base lathe bed.

Table II

Analytical Modal Predictions for Pats H-Base
Without Ways Attached

Mode	Frequency (Hz)	Description
1	38.8	Asymmetric web torsion.
2	85.7	Asymmetric bending mode x-z plane.
3	92.0	Symmetric bending mode y-z plane.
4	107.0	Symmetric bending mode x-y plane.
5	140.1	Asymmetric bending mode y-z plane.

In conclusion, analytical support has contributed heavily to the final design of the new PATS base. Experimental verification of the model will instill confidence that additional contributions can be made in designing the PFMS tools of the future and that future designs can truly make them precision machine tool systems.

1. PATRAN PLUS USER MANUAL, PDA Engineering, Costa Mesa, CA 92626.

Poster Papers

Analysis of the Kinematics and Workpiece Quality in Rotation Grinding of Monocrystalline Silicon

Ekkard Brinksmeier, Martin Klein
Institute for Production Engineering and Machine Tools
University of Hannover, Germany

Progress in wafer process technology is aimed at two main goals: The first and most important is cost reduction because of the international market situation. Second is improving of wafer quality. This is because of the decrease in line width of semiconductor devices which in turn translates into the need for ultraflat wafers to accomodate the limited depth of focus of advanced projection aligners. Conventional wafer production is based on the use of several lapping or grinding processes. Because of the high normal forces when grinding brittle materials, unavoidable elastic deformation of the tool and workpiece occur. This is due to the kinematics of the grinding process, i.e. that relative trajectories and speeds of the abrasive grains vary along the arc of contact with time. The elastic deformations caused by high normal forces effect faults of geometry, surface finish and sub-surface damage. With conventional grinding methods wafer quality is limited by the mentioned facts. With the new rotation grinding method it is possible to suppress these disadvantages. The novel method consists of rotaring the workpiece relatively to a cup wheel also rotating about its own axis. In this way

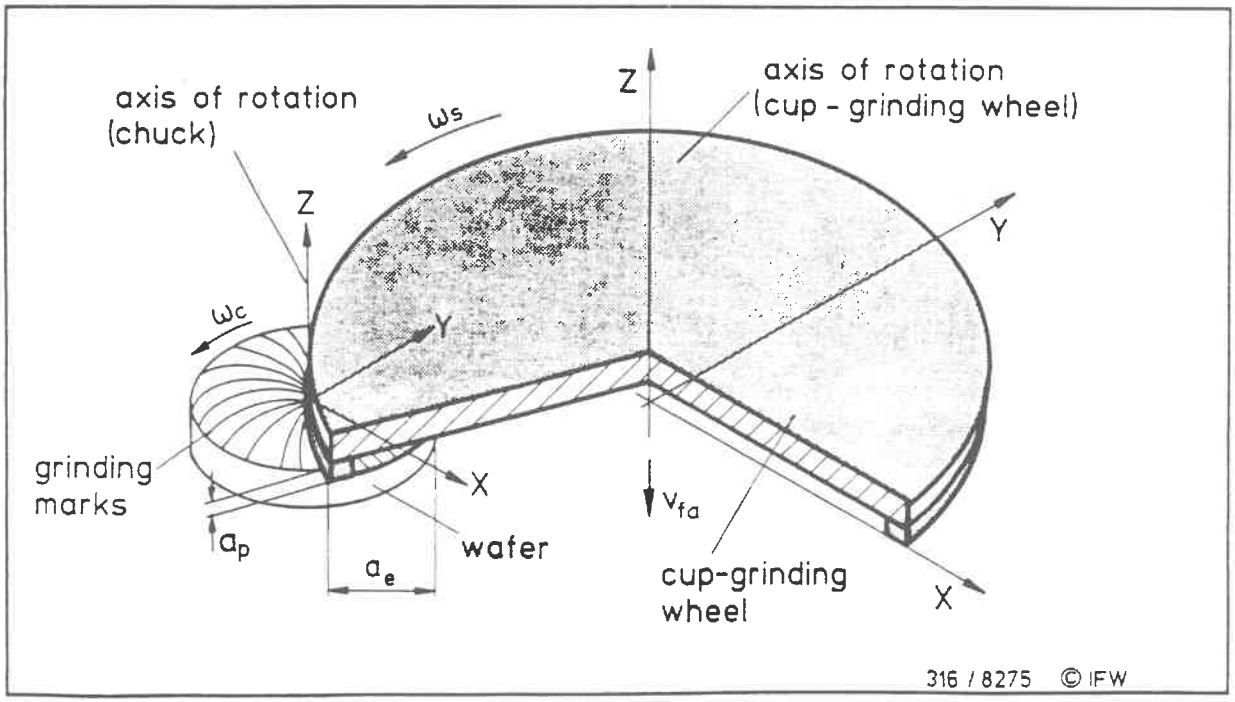

Fig. 1: Principle of Rotation Grinding

every point of the wafer surface comes into contact with the grinding wheel and on an average there is no difference in grinding speed and contact length. Material removal is carried out by the axial movement of the cup-grinding wheel (fig. 1). It is characteristic for grinding that the processed surface is not absolutely homogeneous, but shows a pattern of grinding marks. Their orientation is determined by the kinematics of the process. In rotation grinding they have the shown (fig. 1) typical geometry.

The surface profile of the ground workpiece depends on the relative position of tool and workpiece plane. For the determination of the surface profile the workpiece vacuum-chuck can be considered to be a plane surface. It coincides with the x-y-plane of the coordinate system and serves as a reference. The origin of coordinates is identical with the center of the grinding wheel (fig. 2). The position of the grinding wheel in space is defined by the direction angle ψ and the inclination angle ξ. ξ results from the position of the normal vector of the effective plane and it can be engaged in all angular positions on the direction plane.

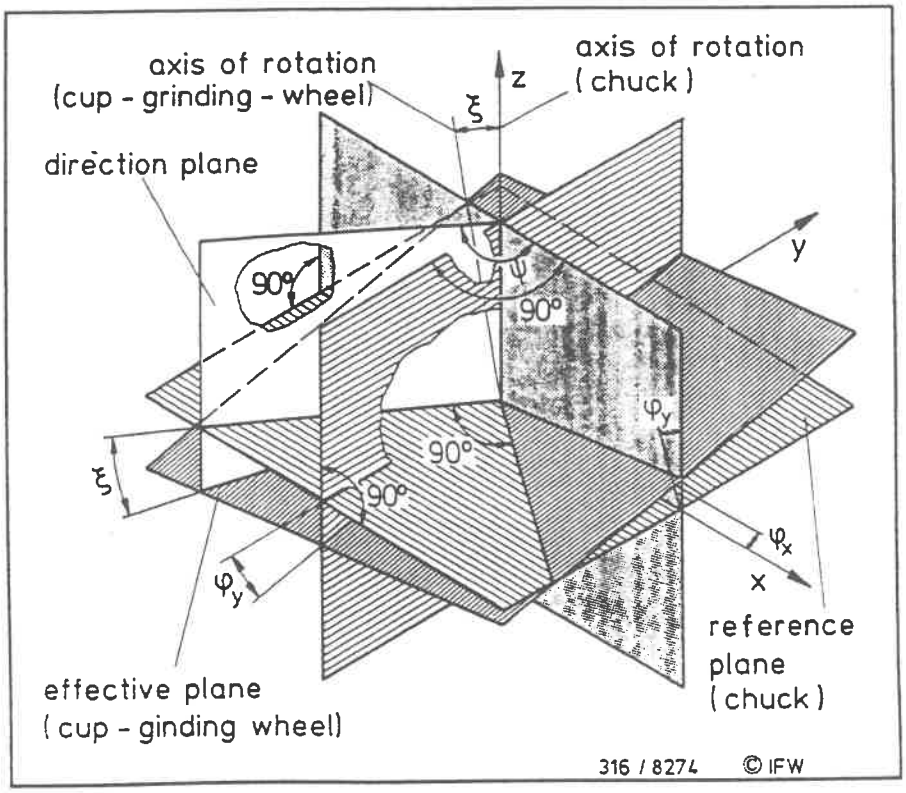

Fig. 2: Model of Planes in Rotation Grinding

Based on the angles ψ and ξ, the tool, and the workpiece radius it is possible to calculate wafer profile and wafer topography. To measure the angles ψ and ξ, Matsui /4/ used a precision indicating gauge which was positioned under the grinding wheel. Based on the ground wafer profile Hinzen /5/ calculated the position of the tool ex-post. The new measuring method described in this paper uses a laser scanner. With a parallel laser beam moving perpendicular to the beam direction the gap between grinding wheel and vaccuum-

chuck can be determined in different radial positions. By choosing suitable measuring positions a calculation of the position of the effective plane and the wafer profile is possible (fig. 3). The advantage of this method is the measuring of ψ and ξ in the working position without the influence of a preliminary wafer machining.

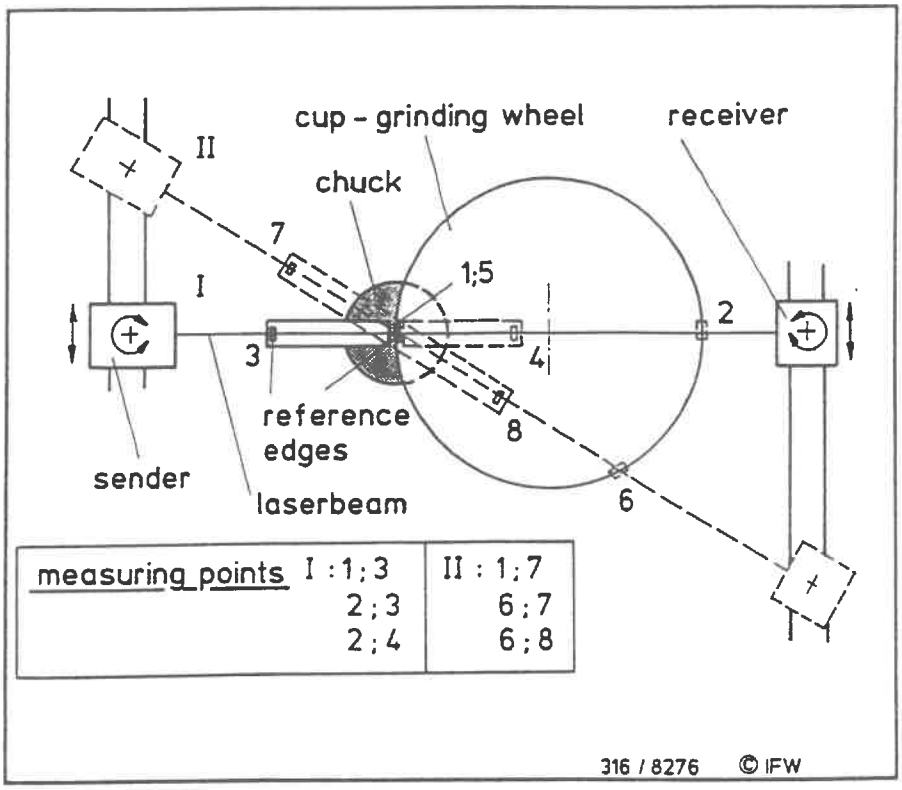

Fig. 3: Measuring Strategy with Laser Scanner

The comparison of the calculated and the measured profiles is shown in fig. 4. The 150 mm-wafer ground by a direction angle of $\psi = -166°$ and an inclination angle of $\xi = 27''$ has a profile height of 3 µm whereas calculated profil has only a height of 2,5 µm. The difference between the two profiles results from swelling of the machine components during grinding and from the sag of the vacuum-chuck because of underpressure.

An adapted measuring strategy is a precondition for producing high quality semicoductor wafers. With the described method the position of the effective tool plane is measurable from which the wafer profile can be calculated. In further investigations the grinding forces and their influence on wafer profile and the sub-surface properties will be analysed to find new starting points for further improvement of rotation grinding.

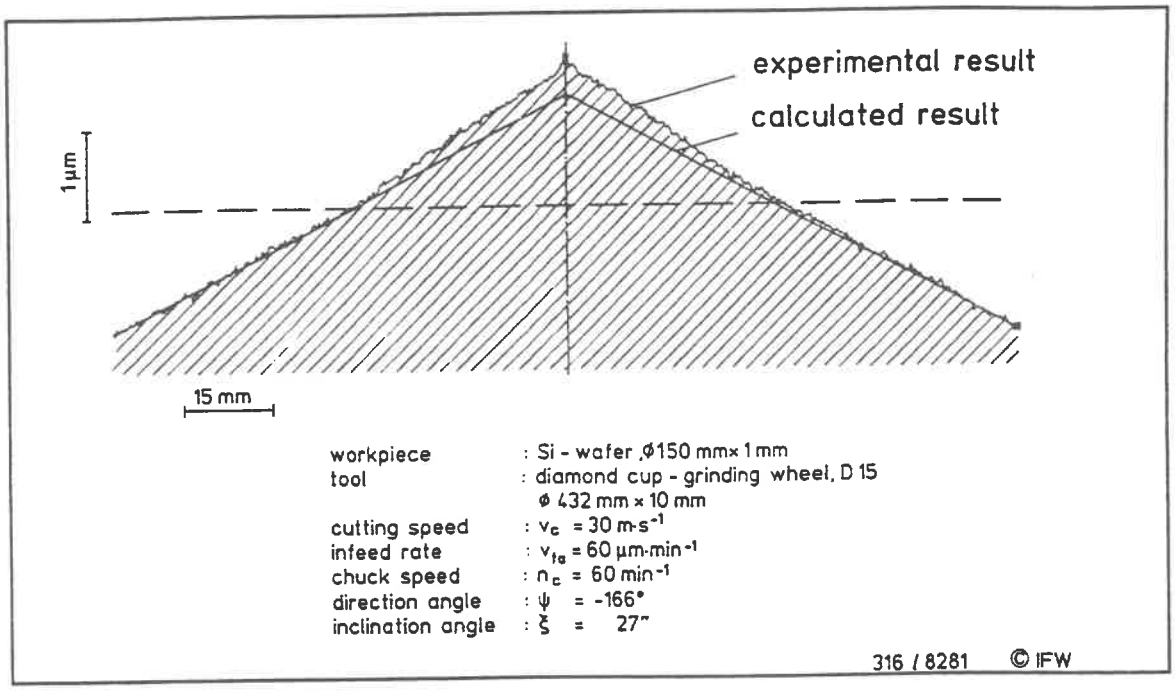
experimental result
calculated result
1 µm
15 mm
workpiece : Si - wafer ,Φ150 mm× 1 mm
tool : diamond cup - grinding wheel, D 15
Φ 432 mm × 10 mm
cutting speed : v_c = 30 m·s^{-1}
infeed rate : v_{fa} = 60 µm·min^{-1}
chuck speed : n_c = 60 min^{-1}
direction angle : ψ = -166°
inclination angle : ξ = 27°
316 / 8281
© IFW

Fig. 4: Comparison of Calculated and Measured Profiles

References

/1/ Tönshoff, H.K., W.v. Schmieden, I. Inasaki, W. König, G. Spur — Abrasive Machining of Silicon. Annals of the CIRP, 39 (1990) 2, pp 621-635

/2/ Tönshoff, H.K., M. Klein — Präzisionsbearbeitung von monokristallinem Silizium. Tagungsbericht Werkstoffe der Mikrotechnik, VDI-Berichte, Nr. 933, pp 29-78, VDI-Verlag, Düsseldorf

/3/ Brinksmeier, E. — State of the art of nondestructive measurement of sub-surface material properties and damages. Journal of Prec. Eng., 11 (1989) 4, pp 211-224

/4/ Matsui, S. — Study on Straightness of Ground Surface of Silicon Wafer. Journal of the Jap. Soc. of Prec. Eng., 53 (1987) 8, pp 1265-1270

/5/ Hinzen, H. — Flachschleifen von Halbleiterwafern. IDR 26(1992)2, pp 73-77

High Precision Turning of Hardened Steel - a Challenge for a New Generation of Machine Tools

M. Weck, J. Luderich, A. Wieners
Fraunhofer-Institut für Produktionstechnologie (IPT)
Aachen, Germany

In industrial applications an increasing number of high precision parts made of hardened steel are required. Typical examples of these workpieces are injection valves, hydraulic pistons, or forging tools. Demands are roundness errors in the order of 0.3 µm, dimensional accuracies of 1 to 2 µm and roughness values in the range of 0,5 to 1,2 µm (p-v) as shown in fig. 1. Due to the fact that these tolerances could not be achieved for hardened steel parts by turning, high precision grinding was used so far.

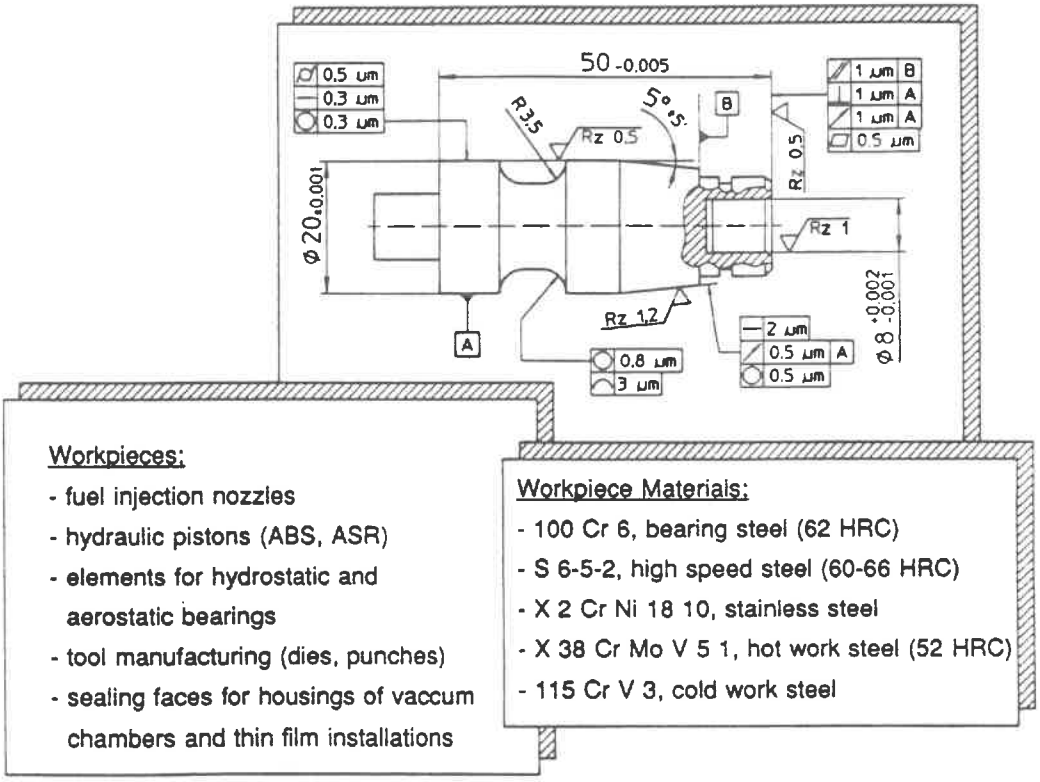

Fig. 1: Typical Specifications of High Precision Steel Parts

The continuous development in the field of hard turning enables the manufacturer to replace the grinding of high precision parts by cutting with geometrically defined tool geometry. As turning is much more flexible than grinding, the manufacturing of complex high precision steel parts is becoming much more cost effective.

After hard turning process technology had reached an acceptable state, it was necessary to develop new machine tools, that met the requirements. Because of their low stiffnesses and load capacities existing ultraprecision lathes could not be applied. By using conventional turning

machines the recommended accuracies could not be achieved (fig. 2). New machine concepts with special features combining high stiffness and high geometric accuracies were necessary.

Compared to ultraprecision turning, hard turning is connected with some basic problems, that make it much more difficult to handle.

- Process forces, heat development and so the related displacements are much greater.
- Not only form accuracies, but dimensional accuracies as well are demanded.
- If hard turing should be an alternative to grinding, accuracies have to be guaranteed even under mass production conditions.

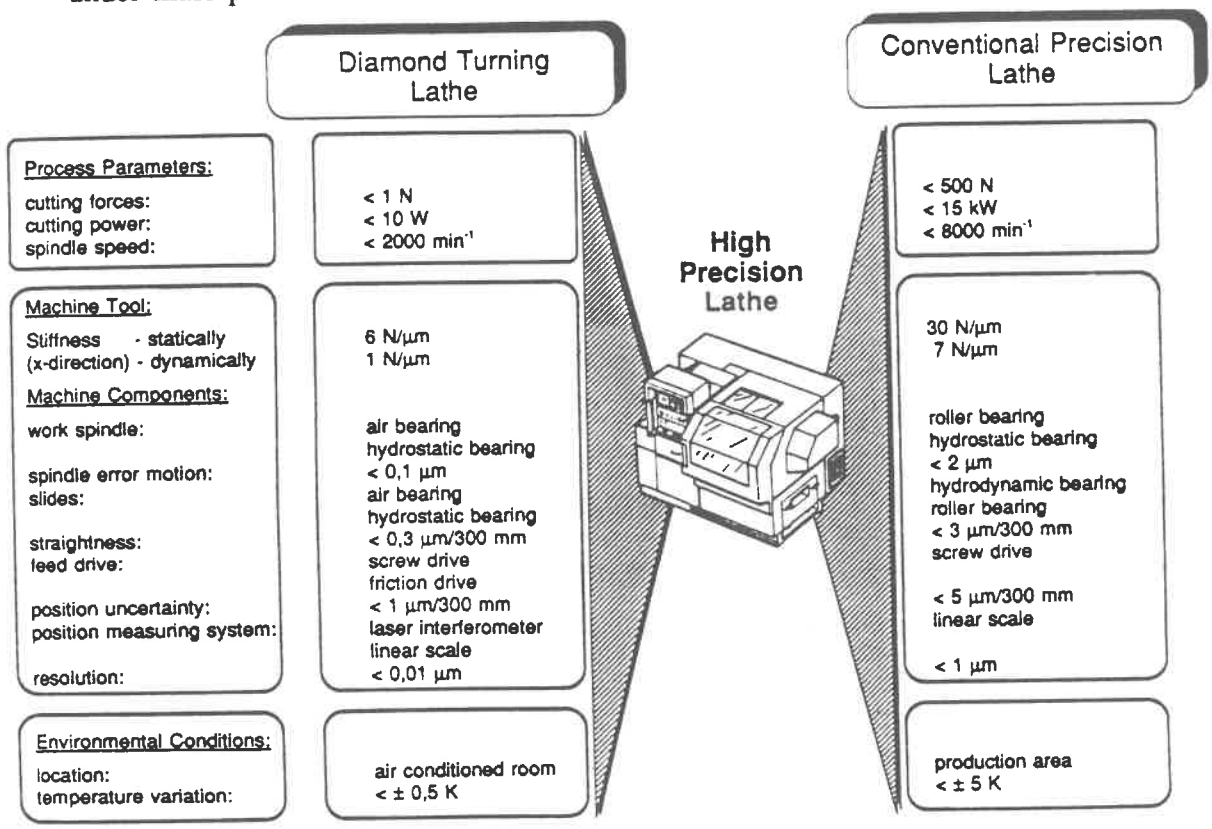

Fig. 2: Characteristic Elements and Parameters of Precision and Ultraprecision Lathes

As fig. 3 shows by the high passive forces, the machine tool compliance is a limitation for the dimensional accuracy. During turning with varying infeed a good correlation between depth of cut, passive force and diameter deviation has been detected. At an infeed increase of 0,1 mm passive force shifts of 25 to 50 N were measured that led from step to step to errors in diameter of 1 to 3,5 µm. Because of the tool geometry (stabilizing chamfer at the first face) and the degressive gradient of the machine tool compliance as a function of load, this relation is not linear.

One possibility to take this phenomenon into account, is to remove the last chip with constant infeed. A more flexible alternative is to compensate the relative displacements between tool and workpiece. For that the passive process force has to be measured during the turning process. With this and other influencing parameters (machine compliance, workpiece geometry, process location) a correction parameter can be calculated and delivered to the NC-controller.

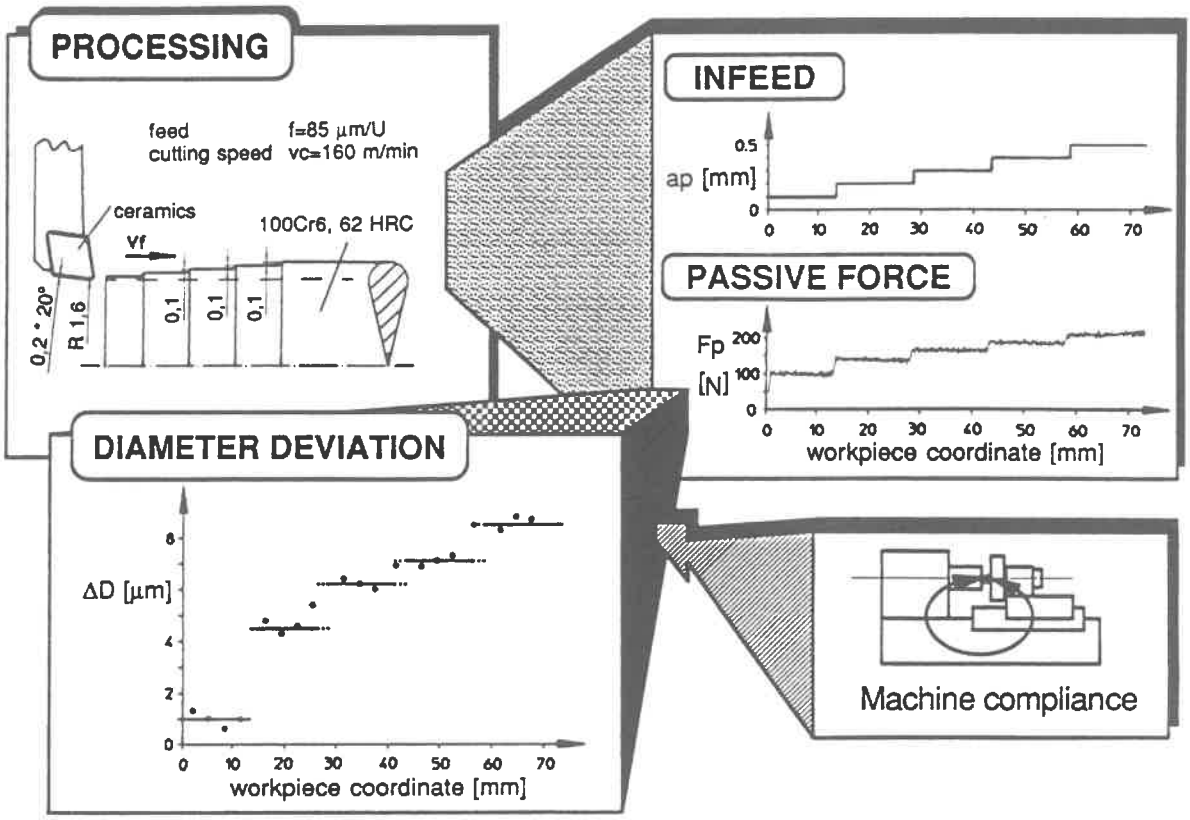

Fig. 3: Correlation between Passive Force and Diameter Deviation

Another influence has the thermal behaviour of the machine tool and the heat development of the process. In order to cause a chip softening during cutting, shear zone temperatures of 800 to 900 °C are necessary. At these temperatures a longer tool life can be reached. So a dry cut should be preferred to using cooling lubricant. In spite of that, a great disadvantage of dry cutting is, that the process heat cannot be carried away and leads to an expansion of workpiece and tool. Fig. 4 shows the temperature rise at the rear side of the indexable insert (tool) and the tool shank close to the clamping device (toolholder) during hard turning. A temperature rise of 12,5 K at the insert and of 3,3 K at the tool holder has been measured. It can easily be calculated, that for a tool shank lenth of 30 mm the thermally caused diameter error would be more than 2 µm. In reality not only the tool shank but the whole machine tool expands and so the diameter errors become even larger.

As the mentioned examples demonstrate, high precision turning contents many more problems than ultraprecision machining. In order to gain more experience about what is necessary for such machines, a basic research program has been established at the Fraunhofer-Institute for Production Technology, Aachen/Germany. In a joint venture with German manufacturers of machine tools, machine components and users new lathes are in development (fig. 5). The properties and the application potential of hydrostatic, aerostatic and roller bearings for the high precision turning are being analysed. Besides that, compensation strategies and temperature stabilising devices are being developed in order to achieve a further improvement of the manufacturing accuracy of hardened steel.

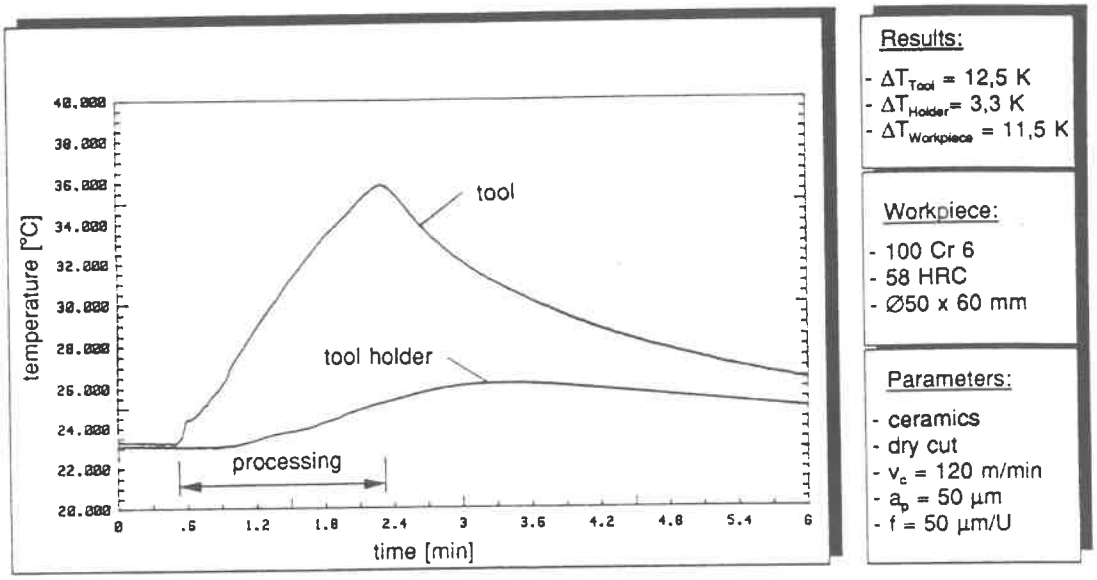

Fig. 4: Temperature Rise of a Tool during Hard Turning

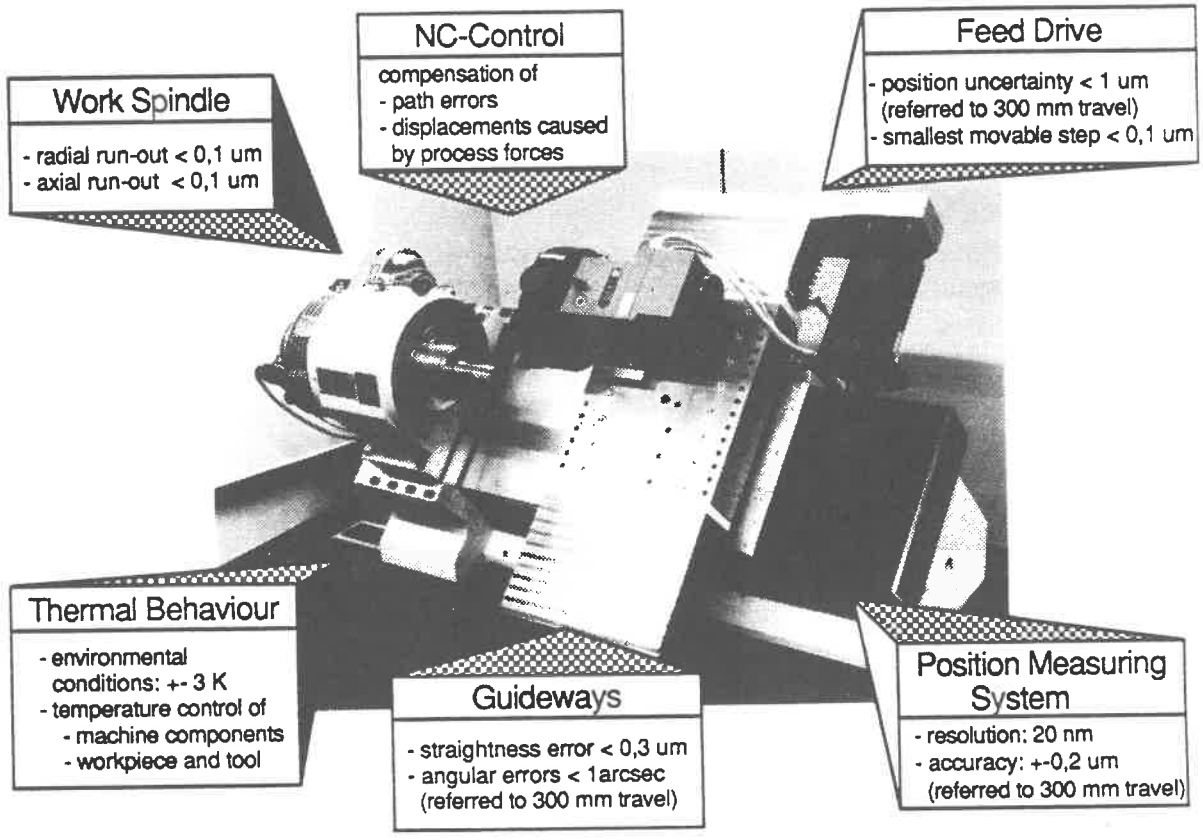
NC-Control
compensation of
- path errors
- displacements caused by process forces
Feed Drive
- position uncertainty < 1 um (referred to 300 mm travel)
- smallest movable step < 0,1 um
Work Spindle
- radial run-out < 0,1 um
- axial run-out < 0,1 um
Thermal Behaviour
- environmental conditions: +- 3 K
- temperature control of
- machine components
- workpiece and tool
Guideways
- straightness error < 0,3 um
- angular errors < 1arcsec (referred to 300 mm travel)
Position Measuring System
- resolution: 20 nm
- accuracy: +-0,2 um (referred to 300 mm travel)

Fig. 5: Parameters of a High Precision Lathe

Orthogonal Ultra-Precision Machining of Single Crystal Germanium

D. A. Lucca and T. R. Oquin
School of Mechanical and Aerospace Engineering
Oklahoma State University
Stillwater, OK 74078

Significant interest in the "ductile-regime" machining and grinding of brittle materials has resulted in several investigations aimed at identifying the mechanisms of material removal at depths of cut where there is the appearance of ductile cutting of an otherwise brittle material [1, 2]. These studies are based on a three dimensional facing operation, and examine the transition from a damaged to undamaged surface along the shoulder of a cut resulting from interrupted machining. The transition point, or critical depth, is seen to vary with feed rate, workpiece crystallographic orientation, tool rake angle and lubricant, and has been observed to be in the range of 50-300 nm for Ge [2]. Whereas the change from pitted to not-pitted region is apparent, there is still debate on the actual mechanism responsible for material removal [3, 4].

We report here some initial results of a study on the ultra-precision machining of Ge under orthogonal cutting conditions. A single point diamond flycutting geometry is employed, and cutting and thrust forces are measured as a function of depth of cut. The experimental set-up, described more fully elsewhere [5], consisted of rotating a flat nose single crystal diamond tool (0 degree rake, 5 degree clearance angle) off the spindle axis of a Rank-Pneumo ASG-2500 diamond turning machine, and infeeding a 15 mm x 1 mm rectangular workpiece. The rotational speed (cutting velocity) is held constant at 7.5 m/min, and the infeed rate corresponds to the depth of cut. For the initial series of experiments reported here, depths of cut ranged from 10 μm down to 0.2 μm, and no lubricant was used. Single crystal Ge, supplied by Eagle-Picher Research Laboratory, Miami, OK was oriented such that cutting was performed on the (110) plane in the <001> direction. Cutting and thrust forces were measured by a Kistler 9251A piezoelectric dynamometer placed directly beneath the workpiece. Measurement of the resultant forces allowed for the calculation of the specific energy.

The measured cutting and thrust forces for two different specimens of (110) oriented Ge are shown in Fig.1. Also included are cutting and thrust forces measured in the orthogonal ultra-precision machining of OFHC Cu [6]. Unlike ductile materials (aluminum or copper), Ge does not exhibit a cross-over of cutting and thrust force in the several micrometer depth of cut range. Thrust force is seen to dominate in the micro-cutting of Ge, consistent with it's high indentation hardness. After each depth of cut, the resulting surface was examined by both Nomarski microscopy and a Zygo laser interferometric microscope. For both specimens of Ge, over all depths of cut (0.2 - 10 μm), pitting of the surface was observed. This is consistent with the critical depth of cut range of 50 - 300 nm for surface pitting when machining Ge reported in the literature [2]. Fig. 2 shows the thrust to cutting force ratio vs. depth of cut for both Ge and Cu. The rotation of the resulting force vector downwards towards the workpiece which is observed for ductile materials is also seen to occur in the machining of Ge over this depth of cut range. Fig. 3 shows the specific energy dissipated for the Ge machined in these initial experiments. Also included is the specific energy measured by Furukawa [7] when machining polycrystalline Ge, and that of OFHC Cu. It is well established that when machining ductile materials at large depths of cut, the specific energy is constant. However, both the present work and that of Furukawa [7], do not show constant specific energy up to 10 μm depth of cut. Our current efforts are directed towards extending the depth of cut range downward, to enable assessment of the specific energies resulting below the critical depth of cut at which pitting is observed.

Acknowledgements

The authors gratefully acknowledge the kind support of the Oklahoma Center for the Advancement of Science and Technology, Eagle-Picher Research Laboratory, and the Department of Energy. In particular, we thank Messrs. Gene Cantwell, Mike Hailey, and Bob Haskins of Eagle-Picher for their technical help and support, and Mr. Y.W. Seo of OSU for assisting with the data analysis.

References

1. Chao, C.-L. and Gee, A. E., "Material Removal Mechanisms Involved in the Single-Point Diamond Turning of Brittle Materials", Proc. of the ASPE Annual Conference, Santa Fe, NM, Oct. 13-18, 1991, pp. 112-115.

2. Blake, P. N. and Scattergood, R. O., "Ductile-Regime Machining of Germanium and Silicon", J. Am. Ceram. Soc., 73, 1990, pp. 949-957.

3. Shaw, M. C., Shafer, H. G. and Adler, M., "Chip Formation in Single Point Diamond Turning", Proc. of the 1990 Annual Meeting of ASPE 2, 1990, pp. 212-215.

4. Taylor, J. S., Syn, C. K. and Donaldson, R. R., "Observations of Brittle-to-Ductile Cutting Mode Transition During Diamond Turning Tests of Single Crystal Silicon", Presented at the 2nd Annual ASPE Conf., Columbus, OH, 1987.

5. Lucca, D. A., Seo, Y. W. and Rhorer, R. L., "Energies in the Ultra-Precision Machining of Ductile Materials", Proceedings of the 1992 NSF Design and Manufacturing Systems Conference, Georgia Institute of Technology, Atlanta, Georgia, Jan. 8-10, 1992, pp. 123-129.

6. Lucca, D. A., Rhorer, R. L. and Komanduri, R., "Energy Dissipation in the Ultraprecision Machining of Copper", Annals of the CIRP, 40, 1, 1991, pp. 69-72.

7. Furukawa, Y. and Moronuki, N., "Effect of Material Properties on Ultra Precise Cutting Processes", Annals of the CIRP, 37, 1, 1988.

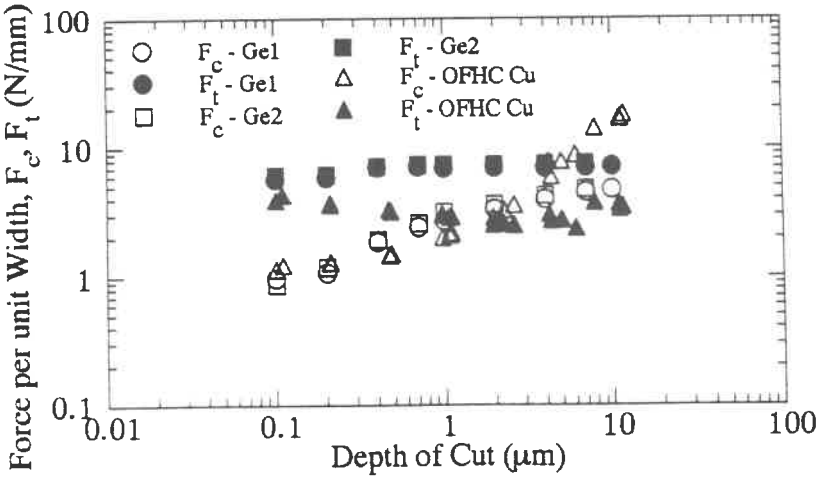

Fig.1 Effect of Depth of Cut on Force Components in Orthogonal Flycutting of Germanium and OFHC Copper

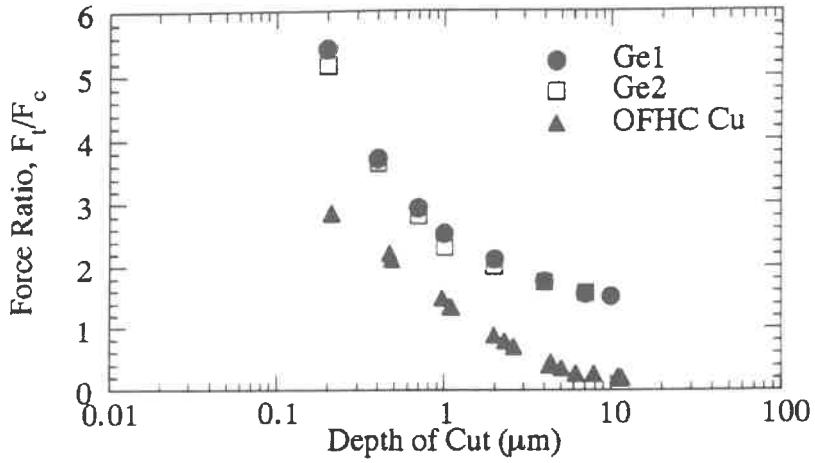

Fig.2 Effect of Depth of Cut on Force Ratio in Orthogonal Flycutting of Germanium and OFHC Copper

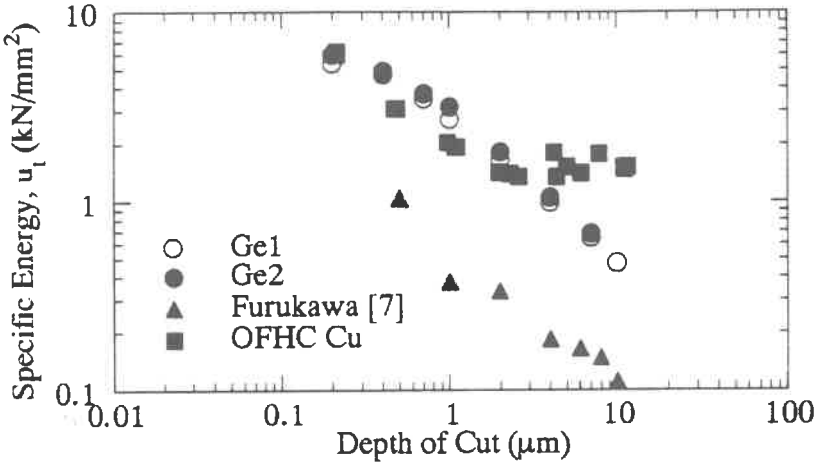

Fig.3 Effect of Depth of Cut on Specific Energy in Orthogonal Flycutting of Germanium and OFHC Copper

Single Point Diamond Turning of (111) CdTe for Epitaxial Film Growth

D.A. Lucca and Y.W. Seo
School of Mechanical and Aerospace Engineering
Oklahoma State University
Stillwater, OK 74078

Introduction

CdTe is used as a substrate material for the epitaxial growth of HgCdTe thin films. These films, produced by liquid phase epitaxy (LPE), are used in the production of infrared detectors and detector arrays. Epitaxially ready CdTe substrates require that no subsurface damage be present in order to allow for the proper lattice matching required for growth. Subsurface plastic deformation of the single crystal CdTe caused by mechanical material removal creates a damaged layer which requires elimination by the time consuming operation of chemical polishing/etching [Weirauch, 1985]. There is also the possibility of preferential etching due to non uniform subsurface plastic deformation. Whereas various chemo-mechanical [Chin, 1988] and hydroplane [Gormley, 1981] polishing techniques exist for attaining nanometer level surface roughnesses of these crystals, controlling flatness is a problem. In a pure mechanical material removal process, it is hard to conceive of a scenario whereby no subsurface plastic deformation will occur. However, the ultra-precision machining process offers the potential for minimum, uniform subsurface damage, with well controlled form accuracy.

Use of diamond milling for the preparation of CdTe wafers has been reported in the literature [Mroczkowski, 1981]. This work investigated optimum cutting directions in terms of quality of surface finish generated when diamond flycutting oriented CdTe wafers at nominal depths of cut between 12.5 - 50 μm at a maximum feedrate of 12.5 μm/rev. We report here some initial results of a study aimed at assessing the performance (in terms of achievable surface finish and extent of sub-surface damage) of single point diamond turning for preparing epitaxially ready CdTe substrates.

Experimental Study

Oriented CdTe wafers, manufactured by Eagle-Picher Research Laboratory, Miami, OK were used in the present study. CdTe, grown by the modified-Bridgman technique was prepared into 5 mm x 6 mm x 1 mm wafers. The 5 mm x 6 mm face was parallel to the (111) plane (within ± 0.5 degrees). For the initial series of experiments, no distinction was made between the A and B face. The $<10\bar{1}>$ direction (within ± 2 degrees) was oriented parallel to one of the edges. The wafer surfaces were mechanically lapped with 9 μm Al_2O_3 on a cast iron plate, using an undercutting technique, on a Logitech LP30 lap-polisher.

The wafers were glued with instant adhesive to a diamond-turned aluminum substrate which was in turn held on a vacuum chuck of a Rank-Pneumo ASG-2500 diamond turning machine. A facing operation, using a single crystal diamond tool with a 6.4 mm nose radius, was performed on the wafers in two orthogonal directions, i.e., $<10\bar{1}>$ and $<\bar{1}2\bar{1}>$. The wafers were positioned approximately 20 mm off the spindle axis, and as a result the cutting direction varied ±10 degrees with respect to the crystallographic direction. The nominal depth of cut was 0.5 μm and the feedrate used was 2.5 μm/rev. Multiple passes at the final depth of cut (0.5 μm) were taken to assure that any previous subsurface damage from prior lapping was removed. Typically, greater than 30μm in thickness was removed.

Initial Results

Our first attempt has consisted of machining (111) surfaces at the modest feedrate and depth of cut conditions cited above. Two orthogonal cutting directions of $<10\bar{1}>$ and $<\bar{1}2\bar{1}>$, which were expected to yield differences in resulting surface finish, were chosen. Surfaces roughnesses measured with a Zygo laser interferometric microscope were compared for both cases, and no discernible differences were observed. Both conditions resulted in average surface roughnesses of 1.9 - 2.0 nm R_a. This was larger than the 1.2 nm R_a achieved when a HgCdTe film was diamond turned using the same set-up under identical conditions. After the surface topography was characterized, the CdTe substrates were cleaved to expose their cross-section. (CdTe readily cleaves on the (110) plane.) Both the mechanically lapped (111) and the diamond-turned (111) faces for both cutting direction conditions were examined by SEM and Nomarski microscopy for gross subsurface damage in the way of microcracks and pits. The subsurface of the lapped side exhibited microcrack damage to an average depth of 2 μm with a maximum depth of about 4 -5 μm. The subsurface of the lapped side bore close similarity to the results of Weirauch [1985] for mechanically lapped (111) CdTe using SiC abrasives with grit sizes of 47 and 28 μm. In counter-distinction to the lapped subsurface, the diamond-turned subsurface for wafers machined in both the $<10\bar{1}>$ and $<\bar{1}2\bar{1}>$ directions showed no visible microcracks when viewed under magnifications up to 5000X in the SEM. Due to the nature of the cleaved surface we were unable to examine distances closer than 0.5 μm from the machined surface. Our present efforts are directed towards a closer assessment of the subsurface of the diamond-turned substrates by near surface etching techniques. HgCdTe films grown on these machined surfaces are also being examined. Performance of the diamond turning process over a range of cutting conditions is being investigated.

Acknowledgements

The authors gratefully acknowledge the kind support of the Oklahoma Center for the Advancement of Science and Technology, Eagle-Picher Research Laboratory, and the Department of Energy. In particular, we thank Messrs. Gene Cantwell, Mike Hailey, and Bob Haskins of Eagle-Picher for their technical help and support, and Mr. William Edwards of OSU for assisting with the cutting experiments.

References

Weirauch, D. F., "A Study of Lapping and Polishing Damage in Single-Crystal CdTe", J. Electrochem. Soc. :Solid-State Science and Tech., 132, 1, 1985, pp. 250-254.

Chin, B. H. and Barlow, K. L., "Bromine/Methonal Polishing of ‹100› InP Substrates", J. Electrochem. Soc. :Solid-State Science and Tech., 135, 12, 1988, pp. 3120-3125.

Gormley, J. V., Manfra, M. J. and Calawa, A. R., "Hydroplane Polishing of Semiconductor Crystals", Rev. Sci. Instr., 52, 8, 1981, pp. 1256-1258.

Nouruzi-Khorasani, A., Lunn, M. A., Jones, I. P. and Dobson, P. S., "Surface Damage of CdTe by Mechanical Polishing Investigated by Cross-Sectional TEM", J. Cryst. Growth, 102, 1990, pp. 1069-1073.

Mroczkowski, J. A., "Polishing of CdTe Surfaces by Diamond Milling", J. Electrochem. Soc. :Solid-State Science and Tech., 128, 12, 1981, pp. 2688-2690.

Nanometer Tool Centering for Diamond Turning Applications

Arthur C. Miller and Joseph P. Cunningham
Optics MODIL, Oak Ridge National Laboratory
Oak Ridge, Tennessee †

"The submitted manuscript has been authored by a contractor of the U S Government under contract No DE AC05-84OR21400 Accordingly the U S Government retains a nonexclusive royalty-free license to publish or reproduce the published form of this contribution or allow others to do so for U S Government purposes"

Introduction

Single point diamond turning technology is capable of producing highly accurate surfaces in a wide range of optical geometry if several sources of error are adequately controlled. Many of the well characterized error sources are associated with machine setup, repeatability and accuracy, part support, environment, and tooling accuracy. This paper will discuss a solution to a common source of error due to misalignment of the diamond tool center with respect to the spindle axis of rotation. A chamfered post technique is presented that allows on-machine, deterministic centering of a diamond tool to nanometer tolerances with a minimum of external equipment and testing.

Tool centering must be performed in both the vertical and horizontal directions. Tool height can be adequately set by using a microscope to inspect a test cut, since a small vertical displacement merely creates a cosmetic defect at the center of the mirror. Any tool decenter in the horizontal direction, however, creates a figure error over the entire optical surface. The resulting optical peak-to-valley error depends on the f# and surface slope. Gerchman has described an "Ogive surface of revolution" error present in spheres and aspheres [1]. Advanced, steeply curved (f# < 1) optical designs made possible with diamond turning technology may suffer significant figure errors produced by as little as 250 nm tool center misalignment. Figure error caused by tool decenter becomes much more serious in systems that achieve alignment when mechanically assembled ("snap-together" systems). In these systems, the spacing between mirrors defines the base radius of curvature and prevents a best fit analysis of surface errors.

Background

Several techniques have been developed for ultraprecision tool centering. Some require the use of machine mounted interferometry [2]. Tool set stations using displacement measuring devices such as air bearing LVDTs can be positioned a fixed distance from the spindle axis and used to probe the tool edge and calculate its center. Mechanical probing at the tool edge presents the risk of damaging the diamond edge if not done carefully. Probing just below the edge is considered safer and effective for centering purposes. Some probing geometries are performed on the tool nose which is insensitive to the location of the center since the contour approaches a flat. The distance from the tool set station to the spindle axis must be accurately established and verified periodically by auxiliary techniques. Also, many mirror fixtures, when mounted on the machine, are too large to allow access to tool set stations. Recently, an automated tool centering system has become available where the X and Z slides of a diamond turning machine are used in conjunction with the tool set station LVDT to probe the diamond tool, calculate the radius, and determine center.

Other techniques involve cutting test objects such as a small mirror or cylinder which are then measured to determine the tool center. An interferometric technique developed by Rasnick and Yoder [3] entails cutting a small spherical mirror and measuring tilt fringes caused by a decentered "Ogive" surface. If interferometer beam divergers around f# 1 are not available, the measurement can suffer from low resolution. Also, other errors such as tool wear, tool waviness, fixturing, or

† *Research sponsored by the Strategic Defense Initiative Organization, through the System Integration, Command and Control Directorate, Integration Support Division, under Interagency Agreement No. 1855-1562-A1 under Martin Marietta Energy Systems, Inc. contract DE-AC05-84OR21400 with the U.S. Department of Energy.*

stressed substrates can disrupt the measurement and result in confusing, iterative and sometimes subjective testing.

Cutting a small cylinder will yield the spindle center axis through measurement of the part diameter, but relies on a precise determination of the tool radius. The diameter of the cylinder is measured either on-machine or externally, 1/2 of which when added to the tool radius equals the distance to the spindle center. Normally, centering errors are much more significant than radius compensation errors, and it is seldom necessary to know the tool radius to the limits of decenter allowance. Also, the tool must be mounted at an angle to cut the cylinder, which is not always convenient. The Chamfered Post technique overcomes the problems of standard centering methods.

Description of the Chamfered Post Technique

The chamfered post technique uses the ultra sharp precision edge of the diamond tool as a sensor in combination with the machine slides to calculate tool horizontal center. The technique relies on the rotational symmetry of the workpiece spindle and the fabrication symmetry of the diamond tool edge radius. It is similar to the cylinder method except that by using the tool as a probe, the radius measurement is made twice and drops out of the calculation.

First a point is defined near the center of the chamfer, and a toolpath is chosen that will machine the desired angle on some part of the optic or an auxiliary piece. After the chamfer is machined, the point is set to X_0,Z_0 (usually 0,0) in Figure 1. The tool is then moved to the opposite side (Figure 2.) of the chamfer at the same Z_0 coordinate some safe distance past the cut surface. The spindle rotation is reversed, and the tool is stepped toward the chamfer with high resolution, Δs, until a slight cut is detected at position X_1. Tool center is 1/2 the difference in the two X coordinates.

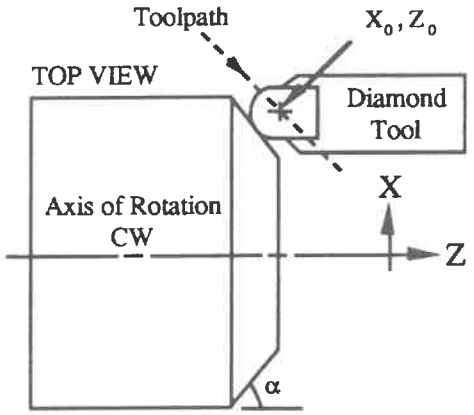

Figure 1. Chamfered Post Turning

Accuracy in the chamfered post method is limited only by 1/2 the deviation in symmetry of the diamond tool, any spindle shift, the machine slide accuracy, and the resolution step size used to locate the chamfered surface. Tool radius does not need to be accurately known, nor does the tool need to be circular. Tool edge asymmetry is generally the largest of the uncertainties and will result in a decenter of 1/2 the asymmetric error. A diamond machined chamfered post is shown in Figure 3.

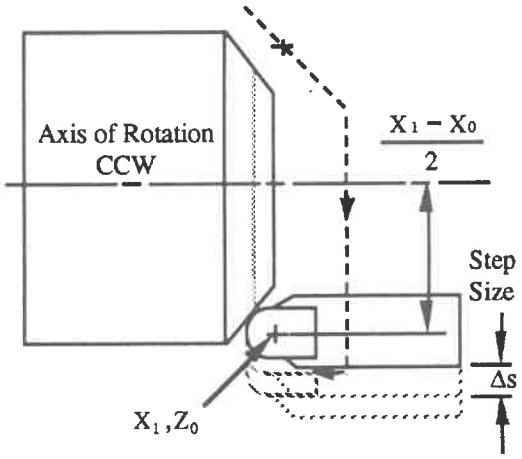

Figure 2. Chamfered Post Measurement

Application of the Chamfered Post Centering Technique

Several methods are available for detecting the surface of the chamfer. The simplest is by merely observing the chamfer while spinning without coolant as the tool approaches the surface. If a small step size (0.1 - 0.5 μm) is used, hundreds of steps must be executed before a chip or cut is visible. One way to accelerate this process is to use a 30x microscope and position the tool edge much closer to the chamfer initially. Preferably, an acoustic emission sensor or sensitive accelerometer can be located on the tool or holder to indicate when the diamond edge touches the chamfer. This technique can be interfaced to most machine controllers and allows a

programmed stop in the Δs infeed after detection. To date, aluminum and copper chamfers have been used for centering, and either a chip or small cut are easily visible. Other materials may require an acoustic emission sensor to reliably locate the chamfered surface.

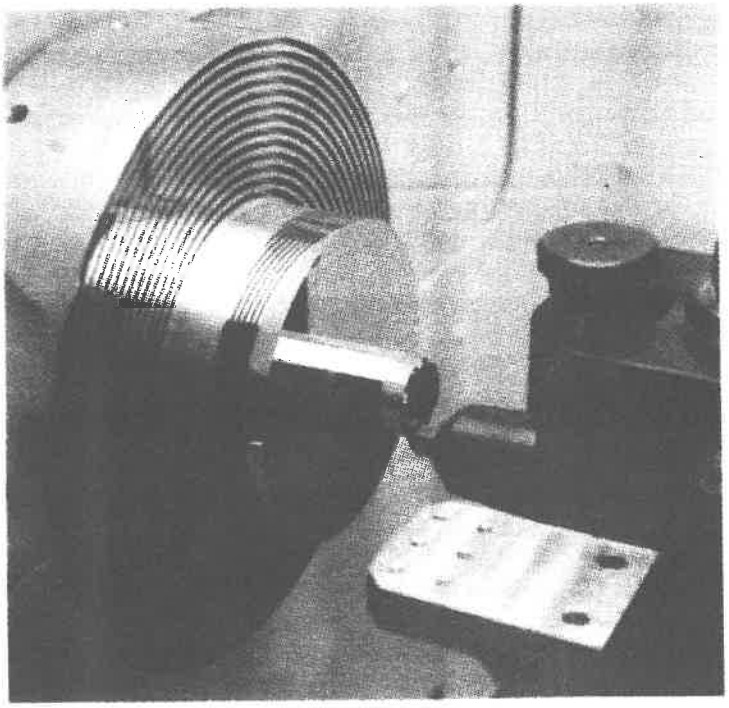

Figure 3. Machined Chamfered Post

Any horizontal shift in the spindle axis of rotation from clockwise to counterclockwise rotation will introduce a centering error with the chamfered post technique. Measurements were made on the Nanoform 600 ultraprecision turning machine in the Optics MODIL test bed to quantify this effect.

A capacitance probe positioned at the side of the chuck was used to measure spindle shift with respect to the X slide. Figure 4. shows that although there are different levels for increasing spindle speeds, the relative shift is negligible for rotation at the same speed and small at different speeds. We suspect that the different levels result from centrifugal growth of the chuck or that the air speed changes the dielectric constant in the probe gap. In any case, chamfered post measurements should be made at the rotational speed intended for cutting the optic, and spindle shift should be characterized and subtracted from the calculation for tool center.

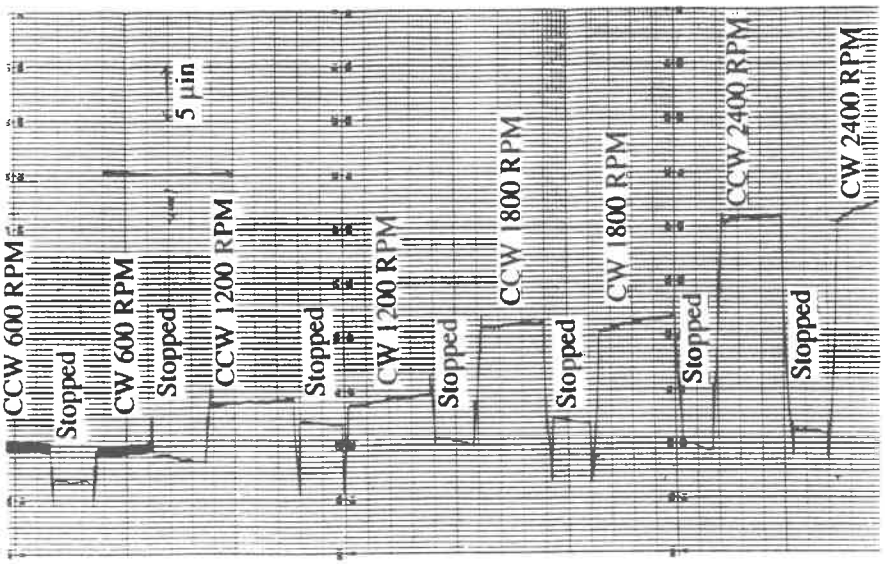

Figure 4. Spindle Axis Shift from CW rotation to CCW rotation

The chamfer angle is not particularly important, but smaller angles will utilize more of the available tool arc and provide more sensitivity to the technique. Typical values range from 45° to 65° depending on the tool orientation and available tool arc. Ideally, if more than 180° of tool sweep were available, a cylinder would be probed with alternate sides of the tool for highest accuracy. Best results are achieved when a light finish cut is used on the chamfer to minimize cutting forces, and careful attention is paid to tool wear. Although roundness errors and tool wear effects are cut in half by using the technique, they

can limit accuracy in setup as well as imprint directly in the figure of the optic. The Chamfered Post technique requires that the tool holder be positioned with respect to the X axis so that the tool can reach both sides of the chamfer. This means that a chamfer can be conveniently located on the outer edge of the part if the X slide travel exceeds the optic diameter.

Figures 5. and 6. show interferograms of 90 mm diameter aluminum mirrors diamond turned using the Chamfered Post centering technique. The first mirror was cut on-center and the second with a 10 μm not-to-center displacement. Both mirrors were analyzed with the Ogive method for determining tool center. An f# 3.38 was chosen due to an f# 3.0 diverger limitation on the MODIL test bed Twyman-Green interferometer. The on-center mirror exhibited a 0.18 wave Peak-to-Valley (λ=0.633 μm) accuracy with no measurable Ogive or decenter error. A 10 μm displacement from Chamfered Post center will produce 9.35 fringes of tilt. In the interferogram of the measured part (Figure 6.) around 9.5 fringes are visible.

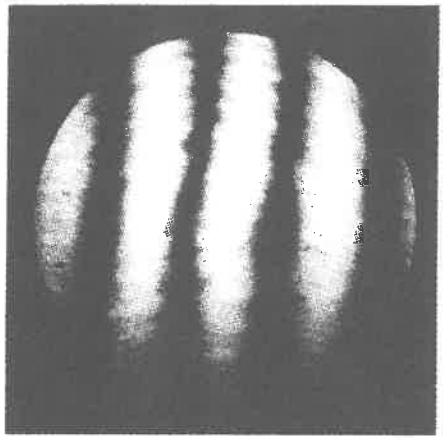

Figure 5. Spherical mirror with tool center set by Chamfered Post technique

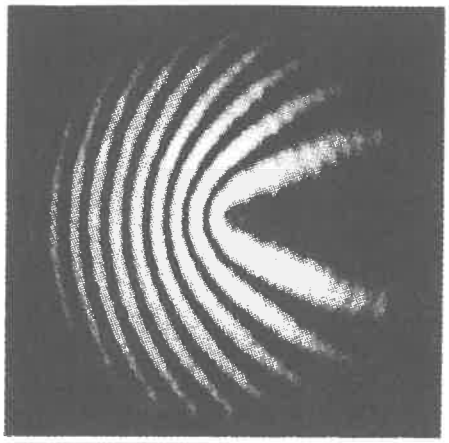

Figure 6. Spherical mirror cut with 10 μm offset from Chamfered Post center

Summary

The Chamfered Post tool centering method overcomes many of the inconveniences and errors of standard techniques. It is a simple and fast technique which is independent of tool radius. A rotationally symmetric surface is diamond turned on the optic or a test part, and the diamond tool is used as a sensor to locate coordinates on this surface which determine the horizontal center.

The method can be used to quickly check center after delays in the machine process setup or before critical cuts. The center of the tool is measured on-machine using the sides rather than the nose where sensitivity is lowest. No additional sensors are needed to set center precisely, and the method can be automated with an acoustic emission sensor or used manually by visually looking for a chip or a slight cut which appears as a scratch. Lengthy off-line interferometric checks are avoided as well as sometimes subjective alignments in evaluating Ogive surfaces. With the Chamfered post technique, tool centering becomes a one-time, nanolevel, deterministic process.

[1] Gerchman, M.C. Rank Taylor Hobson, Inc., "Optical Tolerancing for Diamond Turning Ogive Error", SPIE Vol 1113, pp 224, 1989.
[2] Parker, R.A. British Aerospace, "In-Process Analysis of Optical Components Machined on a Diamond Turning Lathe", SPIE Vol 954, 1988.
[3] Rasnick, W.H., and Yoder, R.C. "Diamond-Turning tool setting by Interference Analysis", US Govt. Contract W-7405-ENG-26, available from the National Technical Information Service Pub. No PB 81970767, 1980.

EVALUATION OF ENVIRONMENTALLY SAFE CLEANING AGENTS FOR DIAMOND MACHINED OPTICS

Lonnie A. Theye, Robert D. Day, Marion L.Scott
Los Alamos National Laboratory
Los Alamos , NM 87544

BACKGROUND

Single point diamond machining has increased in technological importance rapidly over the past few years because it has become a cost effective method for generating accurate complex shapes with very good surface finishes. The last step in the production of a diamond machined surface is that of cleaning. A procedure often used in cleaning the surface was that of cutting fluid removal with Trichloroethane (TCA) followed by an ethanol rinse. Since the Montreal Protocol TCA has fallen out of favor to the extent that it will not be produced in a few years. As a result, a number of environmentally safe solvent substitutes for TCA have been marketed recently. However, tests had not previously been conducted on these solvents to determine their effectiveness in cleaning diamond machined surfaces. Therefore it was decided to conduct a series of tests so the effectiveness of each solvent could be quantitatively derived.

OVERALL TESTING PLAN

The materials chosen from which to produce the samples for these tests were Oxygen Free High Conductivity Copper and 6061 Aluminum. These materials were chosen because they are commonly used in diamond machining applications. A fixture was made which would allow 18 samples to be machined at one time. All samples were machined using mineral oil as the cutting lubricant. Seventy two samples were made from a single bar of each material and immediately set into a mineral oil bath for storage until they could be cleaned and tested.

The cleaning procedure consisted of removing the specimen to be tested from the mineral oil and immersing it in the appropriate solvent. Then it was ultrasonically cleaned for five minutes. If the tests required an Ethanol rinse, the specimens were taken from the solvent and immersed in Ethanol. They were once again ultrasonically cleaned for five minutes. After cleaning, the specimens were dried with clean pressurized air.

Ten solvents were tested, including TCA, on copper samples. This paper only reports the data obtained on the copper samples since no data has been gathered on the aluminum samples.

DIAGNOSTICS

Ellipsometry was chosen as the primary diagnostic tool for evaluating surface cleanliness. It was chosen because it can be used in ambient air (the environment that most diamond machined surfaces are used in), it is capable of submonolayer sensitivity [1,2], and it will give us a quantitative value for the film thickness on the specimen surface. The film thickness is directly related to surface cleanliness.

Ellipsometry measures the state of polarization of a light wave. This state changes abruptly as it is reflected at the interface of two optically dissimilar media. For a copper substrate, four factors affect this change: 1) the angle of incidence of the light beam, 2) the index of refraction of the air through which the light passes, 3) the index of refraction of the surface layer, and 4) the thickness of the surface layer. For these measurements, the angle of incidence was fixed at a known value, and the index of refraction of the residual solvent and mineral oil mixture was measured independently. By knowing these two values, a model can be made which uses the ellipsometer data to calculate the thickness of the residual film left on the sample after the cleaning process.

TESTING RESULTS

The copper samples were cleaned with the environmentally safe solvents and rinsed with ethanol. A model of polarization state changes assuming that mineral oil was the major constituent in the surface film was used to determine the residual film thicknesses. Data was gathered at three places on each sample and then averaged. To acquire this data as a function of time, the samples had to be removed and replaced on the ellipsometer table many times. Therefore the exact location of the three probing locations will not be duplicated. A test was made to determine how well the data at a location could be repeated when the sample was removed from the instrument, replaced, and remeasured ten times. It was concluded that the film thickness measurement could be repeated to a standard deviation of about 0.5 nm.

The average values for each solvent are plotted as a function of time in figure 1. Most of the data is contained in the 5 to 8 nm region which indicates that many of the solvents clean about as well as the others. The data for TCA is also contained in this region. Therefore, it is concluded that many of the solvents tested clean diamond machined copper as well as TCA. A notable exception is X-Caliber® which consistently left a surface film which was from one third to one half as thick as the other solvents. It is clearly the best solvent for cleaning these surfaces. A listing of the solvents tested and the manufacturers name and address is listed in Table I.

CONCLUSIONS

Ellipsometry has been shown to be a very effective method for determining surface cleanliness. It has been a quick (a single point measurement can be made in about 10 minutes) and relatively easy method to use for these studies. For single angle measurements, it requires that the index of refraction be measured independently [3] and that a model based upon these measurements be developed. This model can be developed in a rather straight forward manner by using a commercial software routine, such as Filmstar® by FTG software.

All of the solvents left a surface film which appeared to retard oxide growth on the surface. The data indicate that there are environmentally safe solvents which will clean diamond machined copper as well as TCA. One solvent tested, X-Caliber®, performed much better than the other solvents.

ACKNOWLEDGMENTS

The authors appreciate the helpful discussions with Stephen Seiffert of Benchmark Environmental Corporation, and Jeffrey Weinrach of LANL. This work was sponsored by the Department of Energy under contract W-7405-ENG-36.

REFERENCES

[1] Scott, M. L., Optical Measurements of Surface Oxide Layer formation on Metal Films, Proceedings of Symposium on Laser Induced Damage in Optical Materials: 1987, pp. 361-367, NIST SP 756.

[2] Scott, M. L., Arendt, P. N., Cameron, B. J., Saber, J. M., Newnam, B. E., Extreme Ultraviolet Reflectance Degradation of Aluminum and Silicon from Surface Oxidation, Applied Optics, vol. 27, no. 8, April 15, 1988, pp. 1503-1507.

[3] The authors used a method outlined on page 8 of Polarized Light Microscopy, McCrone W. C, McCrone, L.C, Delly, J.G., Ann Arbor Science, Ann Arbor, Mich. 48106, 1978. These measurements were made on a Nikon Shadowgraph.

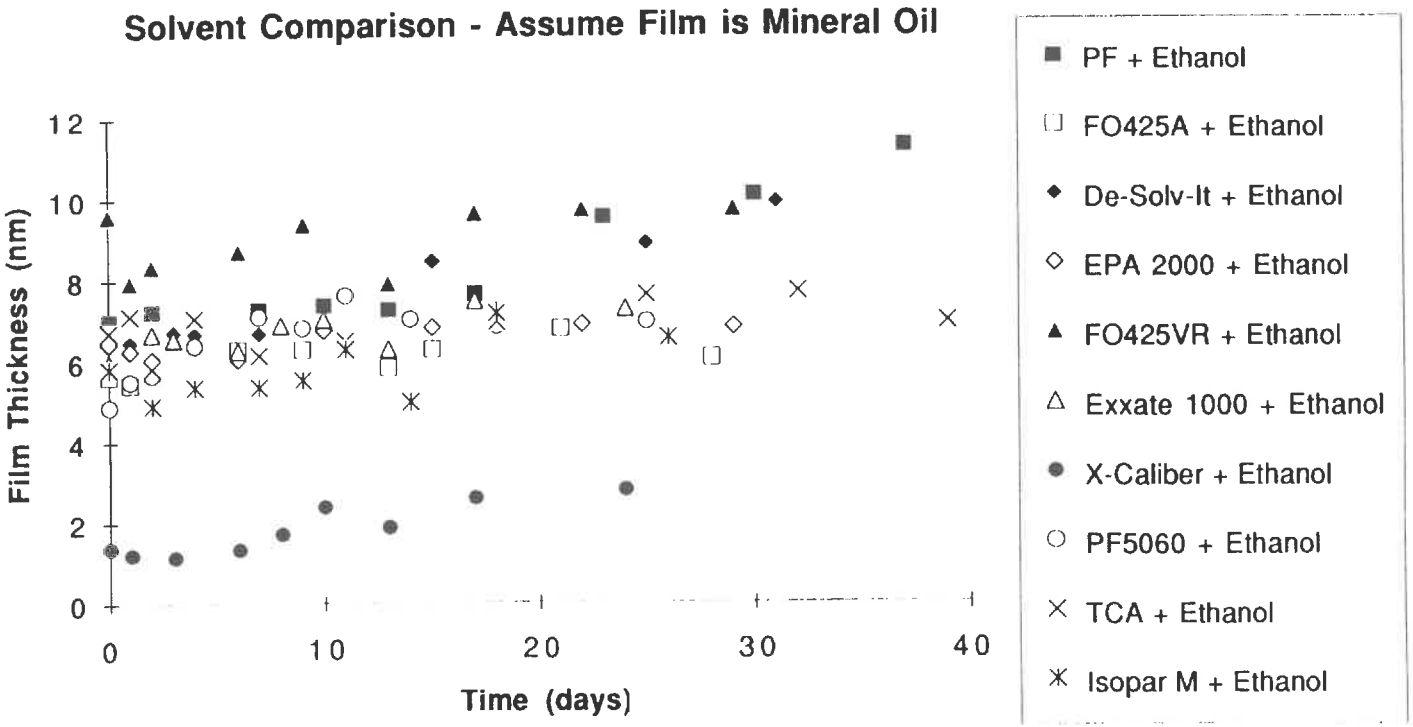

Figure 1- Plot of Ellipsometer Data for All Solvents Tested

Table I - List of Solvents and Suppliers

Name	Supplier	Name	Supplier
De-Solv-It	Orange-Sol, Inc. P. O. Box 306 Chandler, AZ 85244 (602) 497-8822	EPA 2000	Western Chemical Int. 2939 North 67th Place Scottsdale, AZ 85251 (602) 990-9487
Exxate 1000	Exxon Chemical Americas P. O. Box 3272 Houston, TX 77001 (713) 870-6000	FO 425 A	Fine Organics Corporation 205 Main Street Lodi, NJ 07644 (201) 472-6800
FO 425 VR	Fine Organics Corporation 205 Main Street Lodi, NJ 07644 (201) 472-6800	Isopar M	Exxon Company P. O. Box 2180 Houston, TX 77252-2180 (713) 656-2443
PF 5060	3M Ind. Chemical Prod. Div. 3M Center St. Paul, MN 55144-1000 (612) 733-1110	PF	P-T Technologies, Inc. 800 N. Belcher Rd., Suite 2 Clearwater, FL 34625 (800) 441-7874
Trichloroethane	J. T. Baker, Inc. Phillipsburg, NJ 08865 (201) 859-2151	X-Caliber	Inland Technology, Inc 2612 Pacific Highway East Tacoma, WA 98424 (206) 922-8932

INVESTIGATION OF TOOL WEAR IN METAL CUTTING USING ACOUSTIC EMISSION

H.V.RAVINDRA Research Scholar
Y.G.SRINIVASA Associate Professor
R.KRISHNAMURTHY Professor
Department of Mechanical Engineering
Indian Institute of Technology
Madras - 600 030, India

ABSTRACT

Acoustic Emission (AE) generated during turning was detected and analyzed in order to study tool wear phenomenon during machining. The sensitivity of AE signal to tool fracture was studied by using many quantifiable characters like rise time, RMS voltage level, energy, etc. Experiments were carried out on medium carbon steel using coated carbide tool. The influence of flank wear on AE activity was examined and results are presented in the paper. The analysis of AE vs time curves correlates with the wear vs time curve, which is an useful indicator of wear status. The methods can be used to identify the initiation for the change of tool in unattended manufacturing systems as well.

INTRODUCTION

The automation and optimization of manufacturing processes play an important role in improving the productivity and requires techniques for on-line monitoring. Monitoring the condition of the cutting tool in the machining process is very important since tool wear will affect the part size and quality and an unexpected tool failure may damage the workpeice, tooling and sometimes the machine tool itself. Hence sensor based monitoring and diagnostic systems have become increasingly useful in improving the efficiency of a manufacturing systems. Several methods have been investigated for monitoring tool wear either directly or indirectly\1\. Most of these techniques have been applied successfully to a certain extent with limitations. At present, the research has tended towards the use of multiple sensors, mainly, AE and cutting forces \2\for the study of tool wear\3\, tool fracture \4\ and metal cutting processes\5\. The primary and unique advantage of an AE based sensing technique is that the output AE signal is directly related to the basic mechanisms of the operation.

The present paper summarizes the key points of various approaches to tool wear monitoring using various types of AE signals. The critical technical issues relating to the use of AE signals for monitoring machining conditions are also discussed.

EXPERIMENTAL PROCEDURE

Carbon steel (C-60) bars were turned using coated carbide tool. Turning tests were carried out in a VDF high speed, precision lathe for different cutting conditions. Five different cutting speeds (in the range of 300 - 450 m/min), depth of cut (1 - 2 mm) and feed of 0.1 mm/rev were used. Tool flank wear was measured for every 60 - 80 seconds of cutting. A 1000 kHz piezoelectric AE transducer was fixed on the top of the tool holder. Between transducer and tool holder surface, a layer of couplant was interposed to ensure good coupling. The pencil lead break test has been used in the calibration of acoustic emission to estimate the attenuation factor of the AE signal when the signal is transmitted from the workpiece to an insert. Electrical signals produced by the transducer are of very low amplitude and high frequency content and need to be first amplified with a low noise pre-amplifier. Most pre-amplifiers have a gain of 40-60 db. The detected signals based on the threshold of 60 db were amplified and filtered through high-pass filter(cut off frequency 30 kHz); the conditioned signals were recorded in the computer for further analysis.

RESULTS AND DISCUSSION

Figures 1 and 2 present the wear curves at different cutting conditions. It can be observed that the wear curves have clearly defined regions of running-in, steady state and rapid wear. It can be inferred that the wear mechanisms are predominantly thermally controlled due to the fact that wear-rate increases with increase in speed and depth of cut. The parameters of the AE signal recorded like rise time, RMS value were plotted with respect to time. From the fig. 3, it can be seen that the variation in rise time resembles the three stages of wear usually associated with cutting tool flank, i.e. rapid run-in wear of cutting wedge, a stage corresponding to tool wear with minimum rate of propagation and a third stage of rapid wear including tool chipping/ catastrophic failure. This trend is found consistent for different cutting conditions as well(fig. 4). Here, we can observe the steep decrease in the rise time during spalling/chipping of the tool. In this study, the threshold has been fixed as 60 db, since the chipping/catastrophic failure of tool is associated with higher order deformation, cracking and subsequent spalling of the tool material which results in an emission of around 60 db\6\. The strength of the AE signal in terms of RMS values or power is a good indication of the tool wear. The RMS value depends on the severity of wear, which depends on the specific cutting pressure and there by the area of contact between the tool tip and workpiece. There is an increase in RMS value during the initial and rapid wear stages (fig. 5 & 6); but it remains constant during steady state of wear. The RMS value and rise time were minimum at higher speeds. The influence of events, energy, ringdown count, peak amplitude of AE signal have also been studied at different stages of tool wear. There is not much variation in events and ringdown count. However, the peak amplitude and energy increases

as wear progress. Hence, it can be concluded that AE signals such as RMS voltage and rise time can be reliably used for tool-wear monitoring and subsequent process control.

CONCLUSIONS

The detection and analysis of AE generated during machining with coated carbide tool has been carried out in order to monitor the tool wear. The possibility of applying AE methods as on-line tool wear monitoring techniques has been studied. Quantifiable characteristics of AE signal viz., rise time, energy, ringdown count, events and RMS voltage level were studied and an attempt has been made to correlate the above parameters with tool wear and cutting conditions. The parameters - rise time and RMS voltage level seem to respond more to the wear rate and cutting conditions. Chipping of the cutting tool causes a substantial change in the RMS value, but a steep decrease in rise time. The results of this study suggest that AE signal analysis is sensitive to tool wear and can be used for on-line monitoring the failure of a cutting tool.

REFERENCES

1. Lister, P.M., and Barrow, G., ''Tool condition monitoring systems'', Proce. 27th IMTDR Conf., 1986, pp 271 - 302.

2. Dornfled, D.A., '' Monitoring of cutting process by means of AE sensors'', Proc. IMTDR Conf., 1988, pp

3. Iwata, K. and Moriwaki, T., ''An application of acoustic emission measurement to in - process sensing of tool wear'', Annals of the CIRP, Vol.26, No.1, 1977, pp 21-26.

4. Kakino, Y., ''In-process detection of tool breakage by monitoring acoustic emission'', Proc.IMTDR Conf. 1980, pp 29 - 33.

5. Dornfled, D.A. and Kannatey-Asibu, E., ''Acoustic emission during orthogonal metal cutting'', Int. J. Mech. Sci., Vol.22, No.5, 1980, pp 285 - 296.

6. Dungar, H.L., ''AE-for when you absolutely cannot afford a failure of a critical pressure boundary'', J. of AE., Vol.8, No.1-2 (Jan-June 89) pp. 571-574.

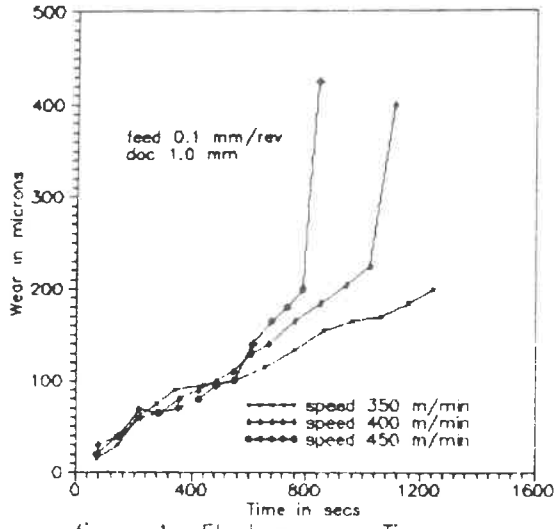

figure 1 Flank wear vs Time

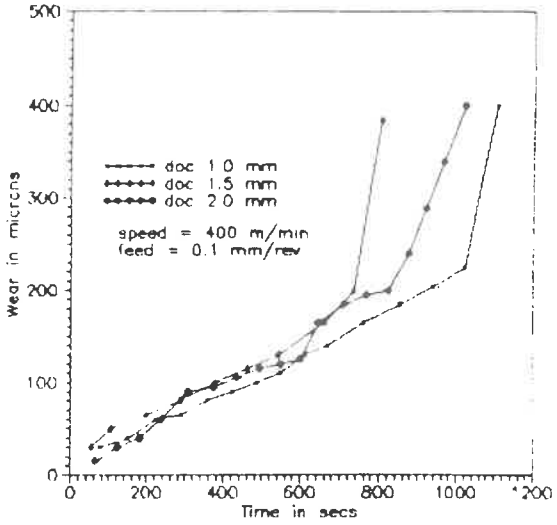

figure 2 Flank wear vs Time

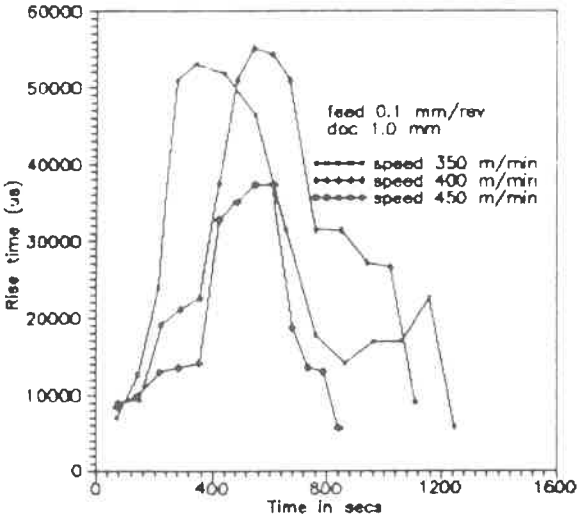

figure 3 Rise time vs Time

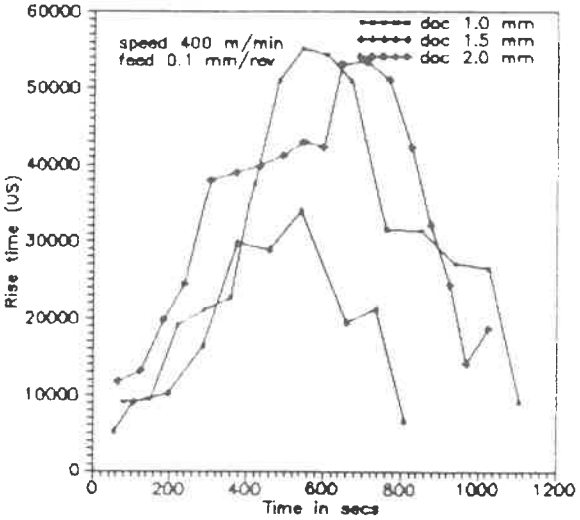

figure 4 Rise time vs Time

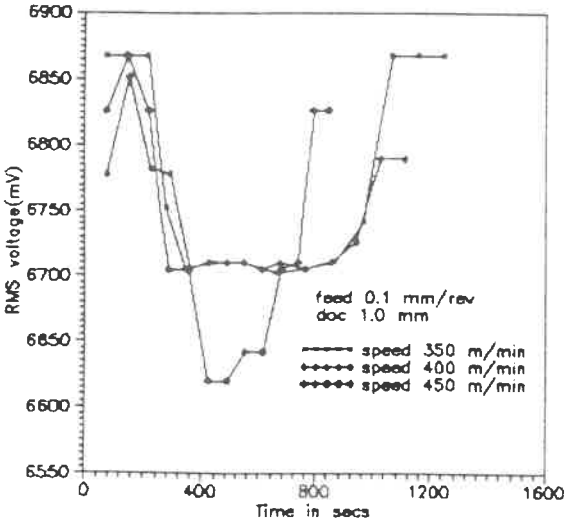

figure 5 RMS voltage vs Time

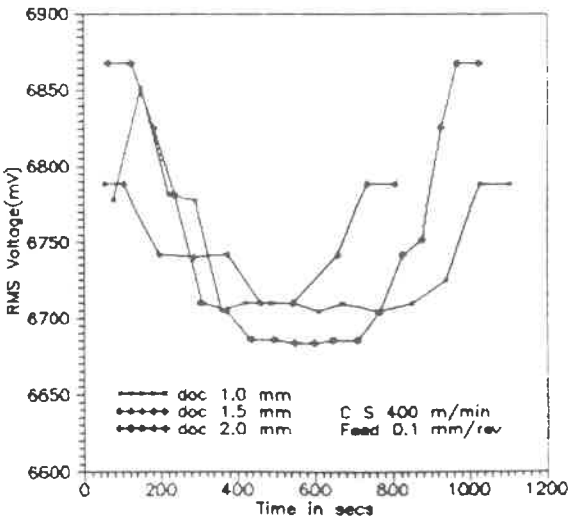

Fig 6 RMS voltage vs time

PRESSURE-CONTROLLED MICROPOLISHING OF GLASS

Yoshinori Yamada, Toshiji Kurobe :
Department of Mechanical Systems Engineering,
Faculty of Technology, Kanazawa University.
Kodatsuno 2-40-20, Kanazawa Ishikawa, 920, Japan

1. INTRODUCTION: Needs for fine scale finishing have recently been increased in the field of mashining of optical parts such as a lens of stepper in LSI lithography and X-ray reflective mirror in synchrotron orbital radiation (SOR). Fine polishing in nano-meter scale is very difficult because of being necessary to control precisely the movement of machine and applied load, and so on. Some kinds of polishing machines have hitherto been developed to achieve severe demands of finishing. However, there is yet some problem to obtain superior finished surface.

Polishing characteristics may be controlled by both of relative motion of workpiece and polishing pad, and the applied pressure. It is well known that the polishing rate is represented by the convolution of pressure and relative speed, since Preston has proposed semi-empirical formula for polishing characteristics. Pressure-controlled fine finishing method has been newly-developed. Fine pressure yielded by repulsive magnetic force between an electromagnet and permanent one, has proved to be excellent polishing performence on the optical glasses. Present study is focused on the reduction of surface waviness and roughness in nano-meter scale.

2. EXPERIMENTAL:

2.1 Polishing machine: Fine pressure controlled polishing machine has been developted by using magnetic repulsive force. Schematics of polishing setup is shown in Fig. 1. This machine is consisted of three main components, that is, repulsive force generator, rotational equipment and polishing vessel. Polishing pressure has yield by repulsive magnetic force between the electromagnet and the permanent one. Repulsive force is detected using beam-type load cell as shown in Fig. 1.

Permanent magnet shaft with a polishing pad can be rotated

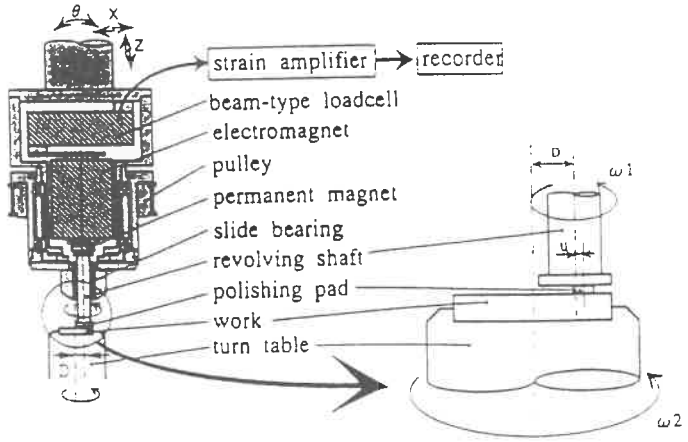

Fig.1 Micropolishing machine and contact geometry of a pad and a work

Table 1 Polishing conditions

variable	circular pad	triangular pad
Revolving speed of a shaft, ω_1	120 ~ 240 rpm	60 ~ 140 rpm
Revolving speed of a work, ω_2	0 rpm 50 rpm	0 rpm 25 rpm
Polishing time, t	10 ~ 30 min	20 min
Load, P	2 ~ 10 g	20 ~ 60 g
Eccentricity, u	0.5 mm	0.5 mm (for pad A) 0.87 mm (for pad B)
Distance between two axes of revolution, D	3 ~ 7 mm	3 ~ 7 mm

by stepping motor, and polishing pad is glued onto one end surface of the shaft. This polishing head has the capability of controlling precise positioning of X, Z and θ direction. Workpiece mounted on a turn table is set into the the vessel.
2.2 Polishing pad and slurry: Mirror polishing of silicon wafer is usually conducted using vesicant polyurethane sheet. Similar pad with dimension of vesicant layer thickness of 0.4 mm is used in polishing of glass. Three kinds of shapes of polishing pads were prepared to evaluate the polishing characteristics of glass. One of them is a circular pad of 2 mm in diameter and the others are regular triangular pads of 1.73 or 1.5 mm in side length. Those pads punched from the sheet were glued onto one end surface of the shaft as shown in Fig. 2.

Polishing of glass was performed by pouring continually the slurry onto the surface of workpieace. Slurry was made with the suspension of grains into the distilled water. Cerium Oxide grain of about 1 μm was used as a abrasive. Optical glass of BK-7 was used in polishing experiments, whose dimension is 20 mm in diameter and 2 mm in thickness.

2.3 Polishing procedure: Experimental conditions are listed in Table 1. Schematical drawing of polishing is shown in Fig. 2. The turn table and the shaft can be revolved independently. The shaft with a pad can be moved to set any position on the workpiece by adjusting X-Z-θ system shown in Fig. 1. Before experiment, polishing pad and workpiece is contacted carefully with zero polishing pressure.

Surface profiles are measured by means of non-contacting optical profilometer (TOPO-3D, WYKO Co.). Gross stock removals in the entire polished region are calculated from the cross-sectional area of measured profiles.

3. RESULTS AND DISCUSSION: Typical examples of profile of polished surface are shown in Fig.3. Experiments were conducted under the conditions shown in the figure 3. Figs. 3(a) and (b) are taken with and without revolving the work, respectively. With revolving the work, the waviness and roughness of finished surface are less than 100 nm and 5 nm in peak-to-valley value, respectively and reduced to lower values than those without revolving the work.

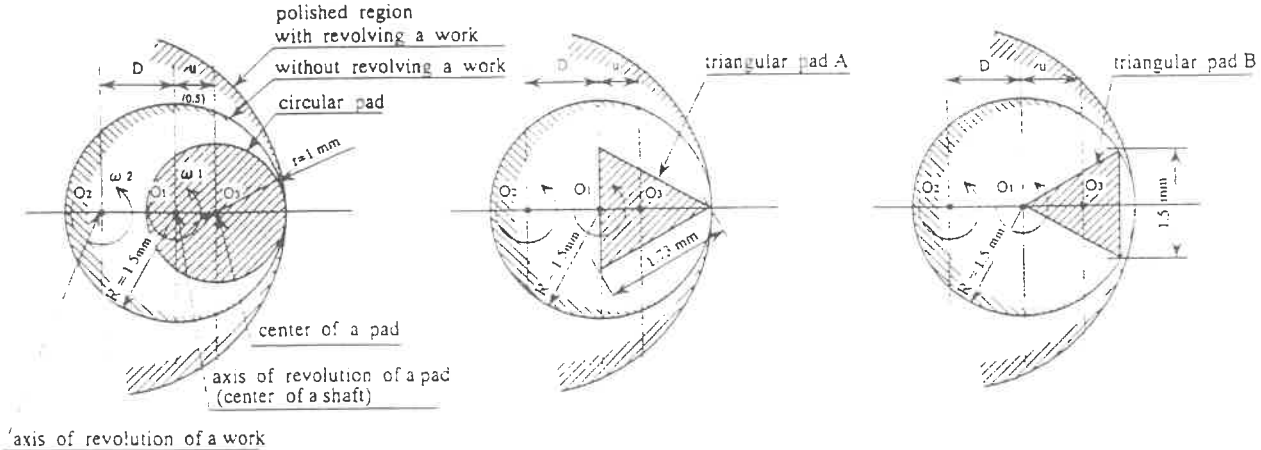

Fig.2 A shape and geometry of pads

Relation between the stock removal and the load is shown in Fig. 4. Figs. 4(a),4(b) and 4(c) indicate the results of circular pad, triangular pad A and pad B, respectively. As can be seen, stock removal increases with increasing load. It is found that data of ω_2 of zero speed are very smaller than those of higher speed and that stock removal is influenced considerably by the geometry of polishing pad.

Fig. 5 shows the relation between stock removal and polishing time. It is found the stock removal increases with increasing the finishing time. Relation between stock removal

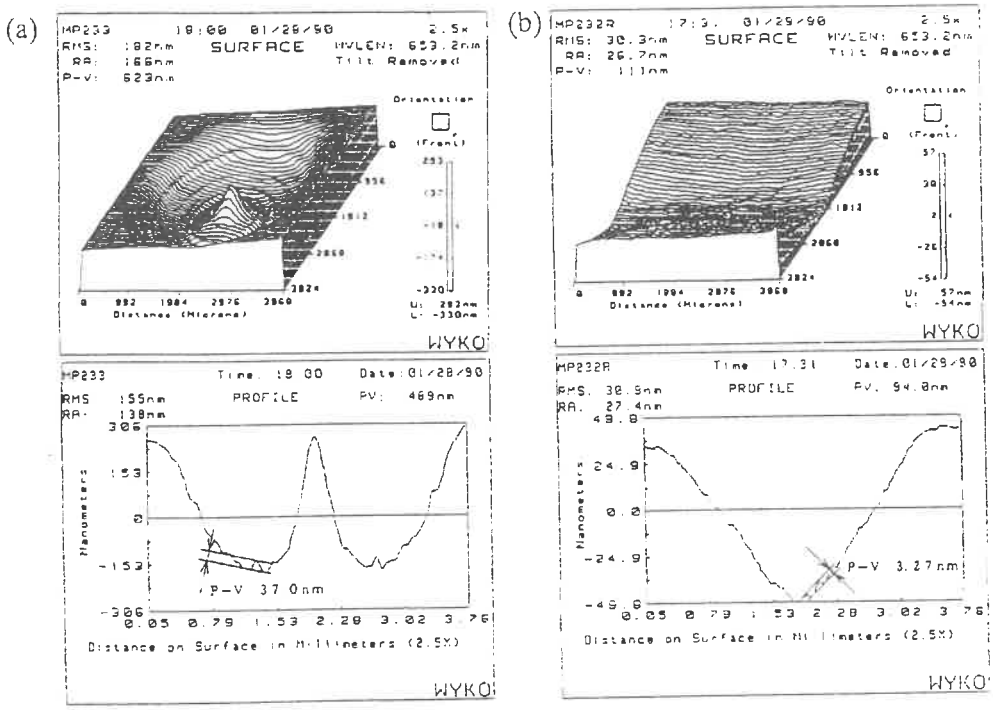

Fig.3 Typical examples of profiles of polished surfaces : circular pad , ω_1=120 rpm , P= 6 g, t =20 min. ; (a) ω_2=0 rpm , (b) ω_2=50 rpm , D= 5 mm

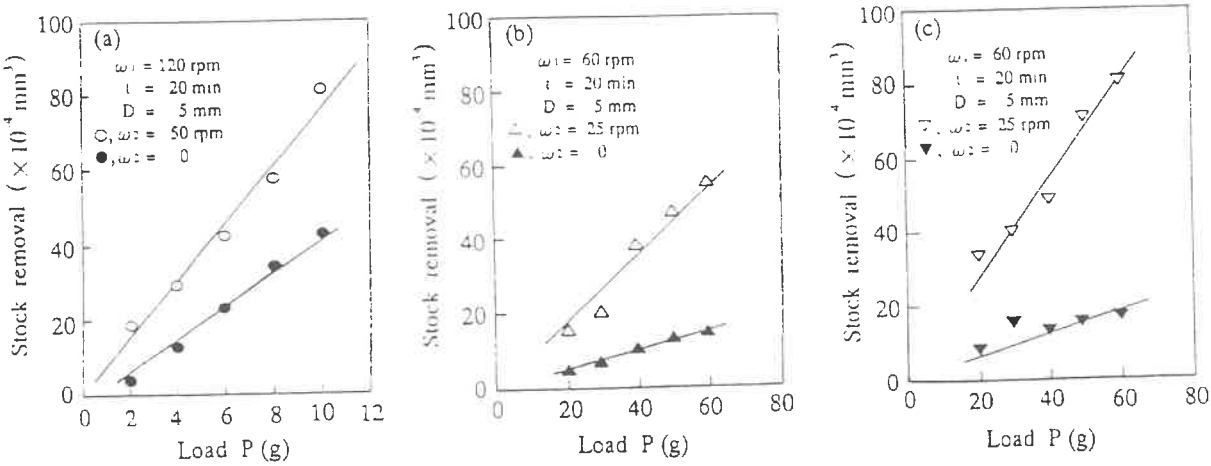

Fig.4 Load dependence of gross removal : (a), circular pad ; (b), triangular pad A ; (c), triangular pad B

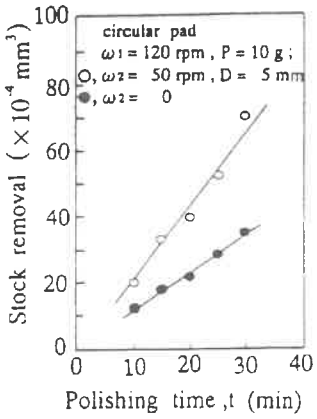

Fig.5 Polishing-time dependence of stock removal

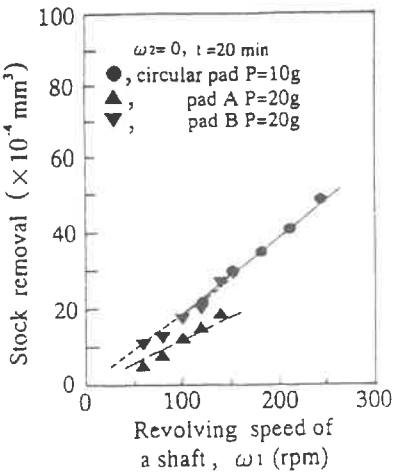

Fig.6 Relationship between stock removal and revolving speed of a shaft

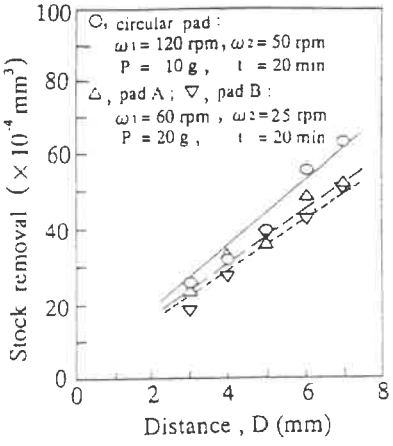

Fig.7 Dependence of stock removal on the distance between two revolving axes

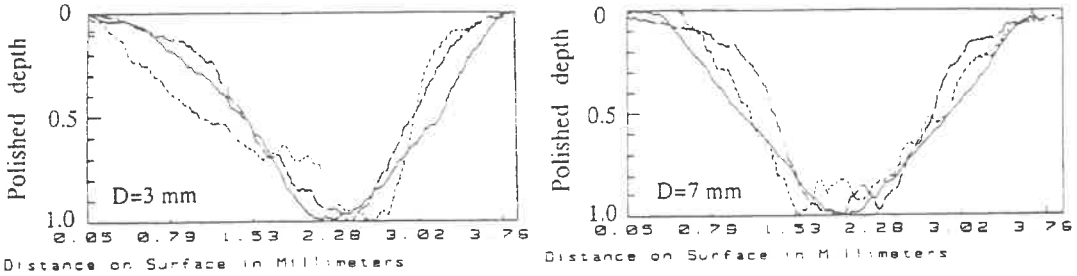

Fig.8 Profiles of polished surfaces with various shapes of pads :
_____ ; circular pad, ω_1=120 rpm, ω_2=50 rpm, P=10 g, t=20 min.
_ _ _ _ ; triangular pad A, ω_1=60 rpm, ω_2=25 rpm, P=20 g, t=20 min.
- - - - - - - ; triangular pad B, ω_1=60 rpm, ω_2=25 rpm, P=20 g, t=20 min.

and ω_1 is shown in Fig. 6. It may be said to be small effect of ω_1 for triangular pad A. Data of the relation between stock removal and D is shown in Fig. 7. Stock removal of circular pad seems to be somewhat greater than that of triangular one. As shown in Figs. 4 to 7, it is found that stock removal is approximately proportional to load, polishing time, revolving speed of a shaft and the distance between two axes of revolution.

The profiles of polished surface with three types of pads are shown in Fig. 8. In order to compare the shape of the profiles, they are shown in normalized form. It is found that the profile is influenced considerably by the shape of pad, that is, the profile for the triangular pad A is sharper than those for the other pads. Such a observed phenomena may suggest that the effectual reduction of micro waviness of surface should be achieved by choosing accurately the shape of a pad.

4.CONCLUSION: Fine pressure controlled polishing method has been newly-developed. This polishing method proved to be excellent performence for fine scale order polishing. It was found that the reduction of micro waviness of surface could be controlled effectively by choosing a proper shape of the polishing pad. Developed technique may be useful for the modification of surface profile in nanometer scale.

A STUDY ON CORRECTING TECHNIQUES FOR RECOVERING ACCURACY OF DETERIORATED LAPPING PLATE USING A CORRECTING CARRIER

Koh-ichiro ICHIKAWA*,Ken-ichi ISHIKAWA**,Hitoshi SUWABE**,Atsushi KAJIKURA*
* Fujikoshi Machinery Co.1650 Kiyono, Matsushiro, Nagano 381-12, Japan
** Kanazawa Institute of Technology, 7-1 Ohgigaoka, Nonoichi, Knazawa 921,Japan

1. Introduction

At present, lapping using a correcting carrier is one of the methods that recover accuracy of a deteriorated lapping plate, and is simpler than the grinding method. However, as the deteriorated condition of the lapping plate changes with machining conditions, the best correcting conditions must be selected in order to recover the deteriorated lapping plate. Therefore, we have been studying on corrective processing using a correcting carrier theoretically and experimentally.

This report deals with a method using a rectangular correcting carrier. Consequently, this method enables to carry out corrective processing regardless of a wear state of the lapping plate.

2. The method using a rectangular correcting carrier

Until now, we have been studying on corrective processing using a correcting ring carrier. As a result, this method enables to carry out corrective processing using a correcting carrier that has wear characteristic opposed to wear state of a deteriorated lapping plate. And, it needs to be measured the wear state of the deteriorated lapping plate. However, in view of wear characteristic of the lapping plate, it became clear that the lapping pressure changed according to wear state of the lapping plate and the lapping pressure reduces at a progressing part of wear. In this paper is considered a method which makes possible to carry out corrective

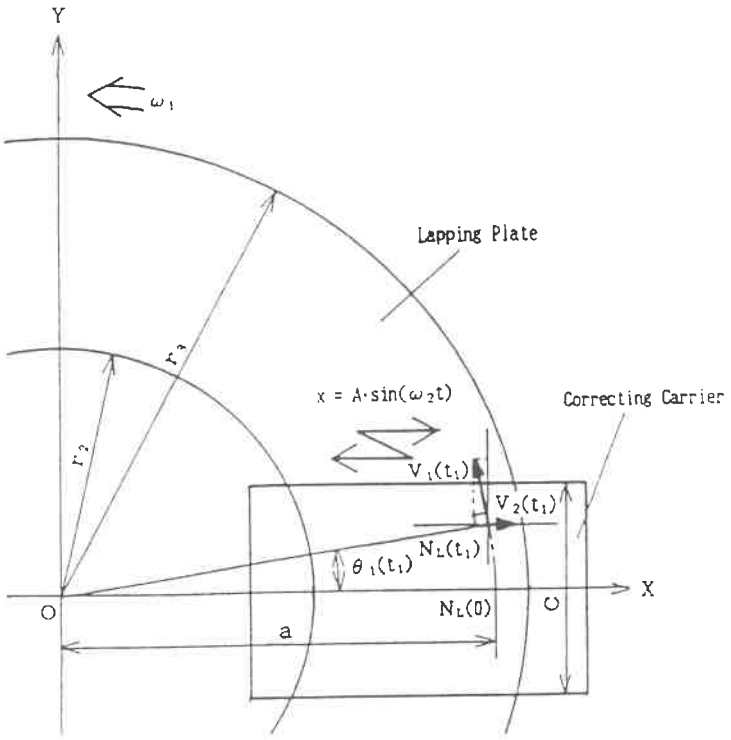

Fig.1 Components of velocity at an arbitrary point

processing regardless of wear state of the lapping plate. We study the method using a rectangular correcting carrier as shown Fig.1.

The lapping plate rotates around a point O at an angular velocity of ω_1. The correcting carrier vibrates approximately sinusoidally X-axis direction ($x=A\sin\omega_2 t$). Now, the components of relative velocities at an arbitrary point N(t) on the lapping plate are discussed. When the lapping time t is 0, an arbitrary point N(t) exists on X axis. Next, when the lapping time t is t_1, an arbitrary point N(t) moves to the point $N(t_1)$. Velocity of $V_1(t_1)$ obtained by ω_1 is

$$V_1(t_1) = \omega_1 \cdot a \qquad (1).$$

Velocity of $V_2(t_1)$ obtained by vibration applied is

$$V_2(t_1) = A \cdot \omega_2 \cdot \cos(\omega_2 \cdot t) \qquad (2).$$

If the velocity components of $V_1(t_1)$ in X and Y directions are respectively $V_{1X}(t_1)$, $V_{1Y}(t_1)$, relative velocity $V_G(t_1)$ is

$$V_G(t_1) = \sqrt{\{V_{1X}(t_1)-V_2(t_1)\}^2+V_{1Y}(t_1)^2} \qquad (3).$$

Therefore, the frictional distance $L_{(a)}$ at an arbitrary point N(t) is obtained by integrating Eq.(3), and is obtained as follows:

$$L_{(a)} = 2 \cdot \int_0^{t_a} V_G(t)dt \qquad (4).$$

where, t_a = lapping time when an arbitrary point N(t) on the lapping plate passes through the half of the correcting carrier. Lapping time t_a is derived as follows,

$$\pm C/2 = a \cdot \sin\theta_1(t_a) \qquad (5).$$

C:width of rectangular correcting carrier. Lapping time t_a is obtained when the conditions of Eq.(5) are satisfied. Fig.2 shows characteristics of the friction distance on the lapping plate. In this graph, the horizontal axis is the distance from center of the lapping plate and the vertical axis is the friction distance. As shown Fig.2, characteristics of the friction distance is theoretically flat from an internal circumference to an outer circumference.

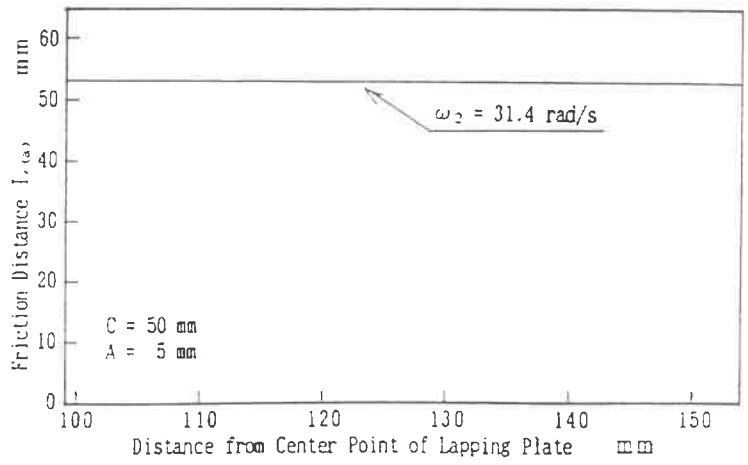

Fig.2 Characteristics of friction distance on lapping plate

3. Experimental Apparatus and method

Fig.3 shows an outline of the experimental apparatus. In this lapping machine is install an arm on which a carrier holder and a crank are set. The arm is possible to be vibrated with revolution of the crank. The lapping plate and the correcting carrier are initially prepared with a total waviness of less than 1μm by means of grinding. A working fluid is uniformly supplied to the processing part by means of a slurry device. Table 1 shows the main experimental conditions.

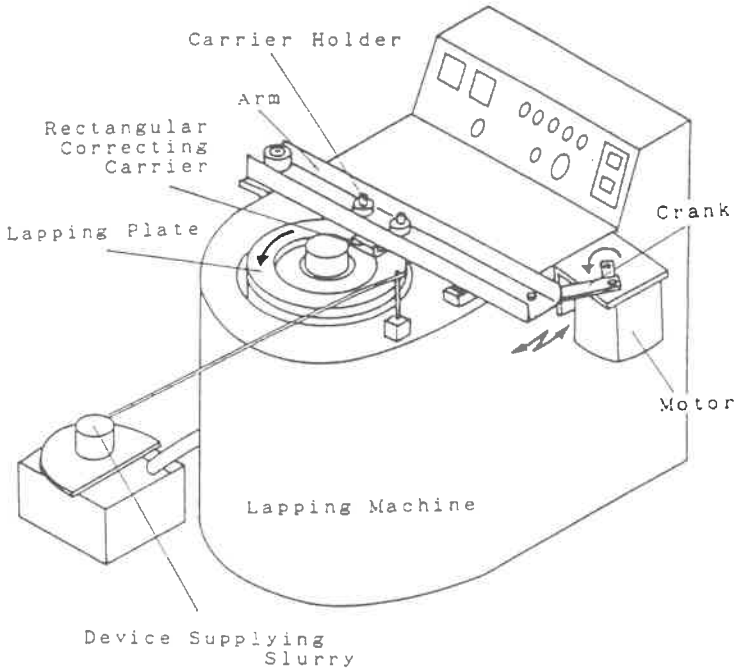

Fig.3 Schematic drawing of experimental apparatus

Table 1 Experimental conditions

Lapping Pressure		P_0	5	kPa
Lapping Plate	Material		FC300	
	Inner Radius	r_2	99.0	■■
	Outer Radius	r_3	154.0	■■
	Angular Velocity	ω_1	-4.82	rad/s
Correcting Carrier	Material		FC300	
	Width	C	50.0	■■
	Amplitude	A	5.0	■■
	Vibrational Angular Velocity	ω_2	31.4	rad/s
Slurry			GC#600 + Water	
Concentration			35	wt%
Working time			3.5	h

4.Experimental results

Fig.4 shows the experimental results of wear characteristics of the lapping plate when the rectangular correcting carrier is used. The following measurements were obtained. The thickness of the lapping plate was measured with an electronic micrometer both before and after lapping processing. Next, the surface profile was measured with a surface roughness tester, and finally, these were combined to produce the graphic results. In each graph, the horizontal axis shows the distance from the center of the lapping plate, and the vertical axis shows the wear height of the lapping plate. Fig.4 shows profiles of the initial condition and the surface after 5 hours. As shown Fig.4, both surface profiles are approximately flat.

Next, we carry out corrective processing. Fig.5 shows examples of

the corrective processing. Each graph shows surface profile of the deteriorated lapping plate and the surface profile after corrective processing. Fig.5-(a) is a profile of the worn surface shaped concave. Fig.5-(b) is a profile of the worn surface shaped convex. As shown Fig.5, after the corrective processing of 3 hours, both surface profiles of the lapping plate become approximately flat.

5. Conclusions

This report treats with the rectangular correcting carrier. This method is possible to carry out corrective processing regardless of wear state of the lapping plate.

Reference

1) K.ICHIKAWA, K.ISHIKAWA, H.SUWABE, A.KAJIKURA : A Study on Recovering Techniques of Deteriorated Lapping Plate Used Correcting Carrier, PROCEEDINGS OF CIRP CONFERENCE ON PRECISION ENGINEERING AND MANUFACTURING SYSTEM, 1991

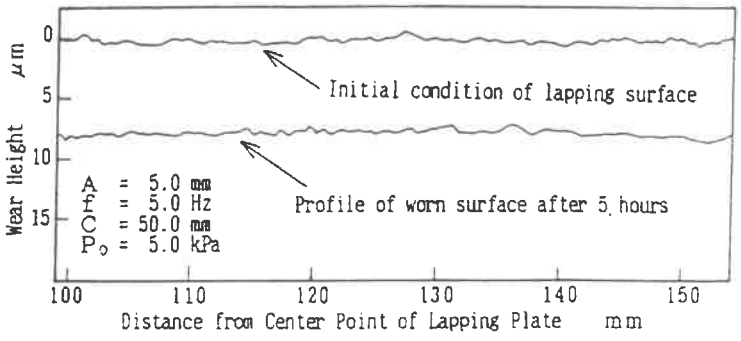

Fig.4 Wear characteristics of lapping plate

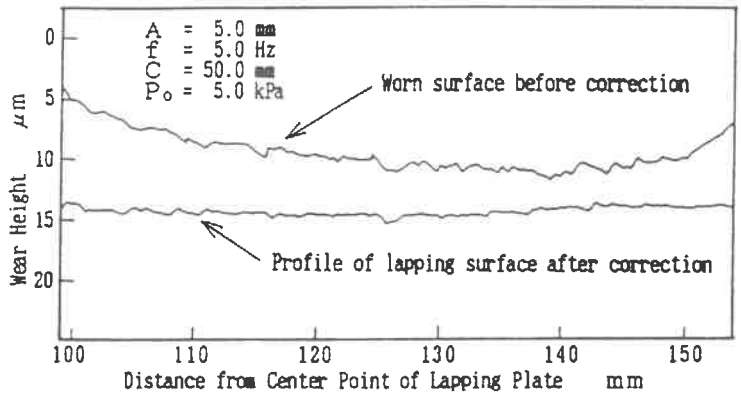

(a) Worn surface shaped concave

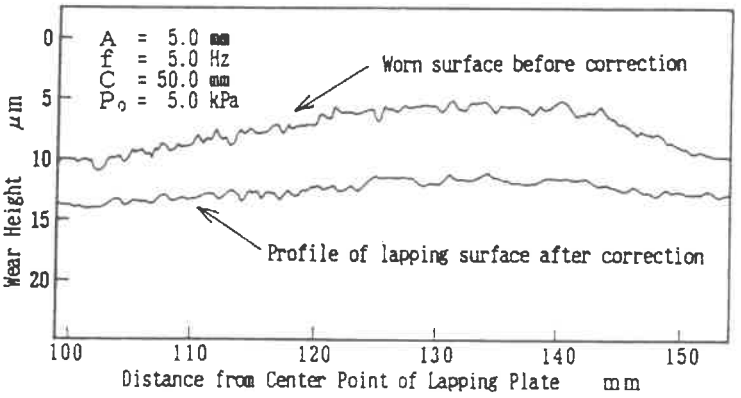

(b) Worn surface shaped convex

Fig.5 Corrective processing of deteriorated lapping plate

Observations on the mechanisms of polishing

R.E. Parks[a] and C.J. Evans[b]

Diamond turning can produce aspheric optics with good figure accuracy cost effectively. The finish obtained, however, is generally inadequate for use in the visible or shorter wave-length regions due to objectionable light scattering. Optimum post polishing techniques improve finish without materially changing the figure.[1,2,3] We report on a simple polishing method successfully used on diamond turned electroless nickel and bare aluminum; some quantitative results on finish improvement as a function of process parameters are presented.

The post polishing method relies on subaperture laps approximately 1/6th the diameter of the work. The laps have a metal backing or pin plate of the same base radius as the surface to be polished and a self adhesive Pellon 3480[c4] surface. On the laps that worked best, a layer of self adhesive closed cell foam tape[5] was inserted between the Pellon and backing plate. Polishing was done with a small quantity of diamond paste rubbed into the Pellon and kept lubricated with a few drops of a polyglycol based diamond paste "extender."[6]

The samples used were 125 mm diameter diamond turned aluminum disks that were subsequently plated with 80 micrometers of electroless nickel.[7] Some were diamond turned again to create various finishes and features to simulate the slope changes that would be encountered in the polishing of aspheres and others were polished immediately after plating. Some tests were performed on unplated aluminum. In no case were the starting surfaces representative of good diamond turning practice but were surfaces specifically designed to provide a range of experimental conditions.

---

[a]Optical Sciences Center, University of Arizona

[b]Precision Engineering Division, National Institute of Standards and Technology, Gaithersburg, MD 20899

[c]Specific commercial items are identified only to provide a complete description of the test system and does not imply an endorsement of the products.

The polishing was done on a conventional polishing machine with a part rotation of 4 rpm and an average stroke velocity of 160 mm/sec. Except where noted, the lap load was 1.1 g/mm^2 and the lap was stroked from side to side through the center of the specimen so that the center got proportionately more polishing time than the edges. The many polishing time data points shown in Fig. 1 result from a small number of polishing runs but data are taken at various radial increments to determine the finish at shorter "effective" polishing times than the center of the sample. Note that this procedure does not account for the sinusoidal variation of lap speed across the work, but this does not appear to affect the results significantly.

Figure 1[d] shows the rms surface roughness as determined with a WYKO TOPO 3-D with a 20X objective versus effective polishing time for several different sets of polishing parameters. The data plotted in Fig 1(a) is for 3 micrometer and 0.25 micrometer diamond on a foam backed Pellon lap. Fig 1(b) compares a foam backed lap with a lap made with Pellon mounted directly on an aluminum plate. In both cases 1 micrometer diamond was used but one lap was more flexible than the other because a layer of foam tape was used between the Pellon and the backing plate. For Fig. 1(c), foam backed laps were used at two different lap loads.

Several features of the data in Fig. 1 should be noted. In all cases, the finish improves with polishing time until a knee or plateau is reached; for very long polishing times there is a suggestion that finish in fact deteriorates. For similar lap construction, the ultimate finish is related to diamond size. Although not shown here, our data suggests that there is a difference in the polishing rate when the lap motion is parallel with, rather than at an angle to the lay of the diamond turning marks. This, we believe, is a major contributor to the scatter in Fig. 1.

More data is needed to determine the precise relationship but clearly finish improvement is faster with larger diamond grit size. Also the flexible lap construction, the Pellon backed by foam tape, gave a faster polishing rate and a better ultimate finish. This is important in its own right but more so when it is realized that the importance of the technique applies to the greatest extent to aspherics. Increased forces give more rapid polishing but a worse ultimate finish. Ultimate finish may also be limited by plating quality.

Surfaces have been studied at various stages of polishing using Mirau interference and Nomarski objectives. By the time the curves in Fig. 1 reach the knee, all traces of the original diamond turning tool feed marks have been replaced by a fine, isotropic network of scratches left by the diamond polishing abrasive. A study of various stages of tool mark removal shows that the laps have a great height discrimination in that they remove material only from the peaks and not from the valleys even when the

---

[d] The broken lines shown in this figure are intended as a guide to the eye for the trends in the data; they are not least squares fits to the data

valleys are only 0.1 micrometer below peaks separated by several hundred micrometers. Also, the diamonds seem to be firmly socketed in the Pellon and work as individual diamond tools, each removing a continuous depth of material relative to the lap and not the work. That is, if the diamond passes over a void or valley, the diamond does not fall into the void but continues cutting on the opposite side of the void at the same depth as before the void. Similar results are obtained on bare aluminum, although the limiting surface finish is worse; here the limitation appears to be material defects.

Although work is continuing on this project, we conclude here by saying that we have outlined a simple method of improving the finish of nickel surfaces which were diamond turned either before or after being electroless nickel plated. The process uses a synthetic polishing material, Pellon, that is not dissolved by common lubricants, and a little, readily available diamond paste. Perhaps most important, the technique incorporates a flexible lap backing that makes it applicable to many aspherics including those used in grazing incidence optics. A further extension of the work, now under way, is to post-polishing of surfaces produced by "ductile" grinding" or "low-damage micro-grinding".

Acknowledgements

We would like to acknowledge the contributions of numerous colleagues at NIST, Gaithersburg, where this work was done. In addition to financial support from NIST, this work was initially funded by a grant from Oak Ridge Associated Universities, Inc.

References

1. P.C. Baker, et. al., "Finishing of Precision Generated Metal Optical Components," Proc. SPIE, 65, 42-7 (1975).

2. N.J. Brown, et. al., "Fabrication of Machined Optics for Precision Applications," Proc. SPIE, 381, 48-62 (1983).

3. R.E. Parks, "Finish Improvement of Micro-machined Surfaces," Proc. SPIE, 1015, 68-72 (1988).

4. Available from Universal Photonics, Inc., 495 West John St., Hicksville, NY 11801.

5. Scotch Brand Tape, Core Series 2-0300.

6. Buehler Ltd., 41 Waukegan Rd., Lake Bluff, IL 60044.

7. Supplied by Acteron Corp., 851 Shasta St., Redwood City, CA 94063.

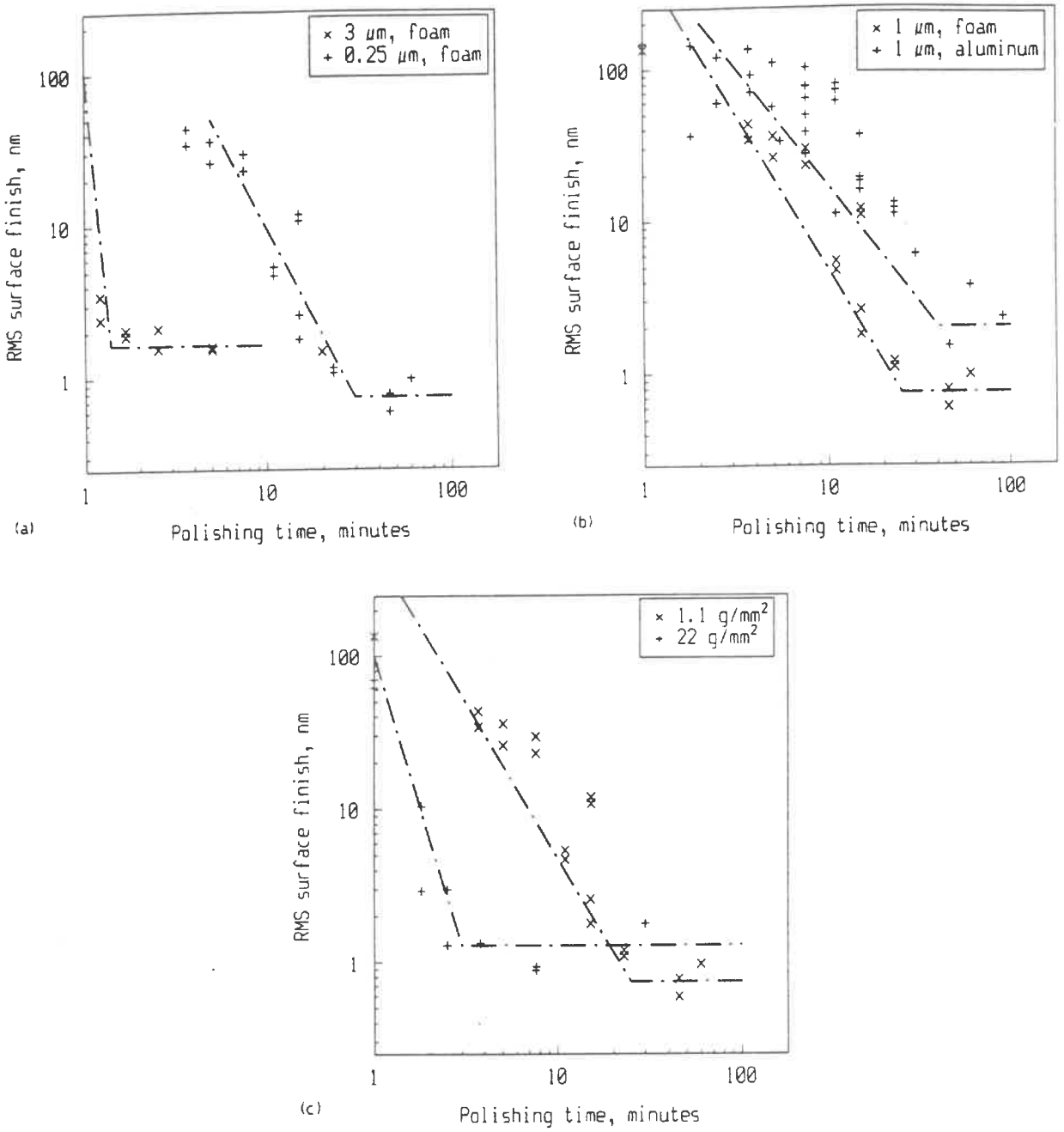
× 3 μm, foam
+ 0.25 μm, foam
RMS surface finish, nm
100
10
1
1
10
100
(a)
Polishing time, minutes
× 1 μm, foam
+ 1 μm, aluminum
RMS surface finish, nm
100
10
1
1
10
100
(b)
Polishing time, minutes
× 1.1 g/mm²
+ 22 g/mm²
RMS surface finish, nm
100
10
1
1
10
100
(c)
Polishing time, minutes

Figure 1

THE EFFECTS OF POLISHING PARTICLE SIZE ON THE FINISH AND SUB-SURFACE DAMAGE OF GLASS

Chi M. Lee
Department of Materials Engineering and Materials Design
University of Nottingham, NG7 2RD, England

David J. Bell
Optical Surface Technologies
Fullerton Road, Rotherham, S60 1DL, England

Introduction

Glass components used in precision optics and optoelectronics applications need to be polished to a high degree of surface conformity and surface finish. The way in which these aims are achieved can influence the way in which the components will behave when used in their final design situation. It is therefore very important to achieve predictable and reproducible results during the manufacture of such components. The degree of sub-surface damage in optical elements and other components can have an important bearing on their performance. Commercial glass polishing is carried out using cerium oxide based polishing media. Speed of polish is usually important in commercial glass polishing but higher polishing speeds can lead to increased sub-surface damage. It is possible to achieve similar degrees of surface finish by various polishing regimes but the degree of sub-surface damage may be influenced to a large degree by the type of polishing medium used and the polishing regime adopted. It is useful to have methods of estimating the extent of this damage so that the development and production of improved polishing media and processes for these critical applications can be advanced.

Sub-surface Damage in Grinding and Polishing

Much work has been done on the mechanism of sub-surface damage which arises from two sources during the surfacing operation, grinding and polishing. The initial grinding stage using either loose or bound abrasive is needed to produce the optical form required in the component within a reasonable time span. This results in a matt surface needing further polishing and also leaves a residue of deep cracks which are not removed during the initial polishing stages. The polished layer merely serves to hide the underlying defect layer. Surface roughness measurements indicate the quality of the polished surface but do not show the quality of the material underlying the surface. This because of its cracked and highly stressed nature causes light scattering which can affect the performance of critical optical components. Prolonged polishing can remove the sub-surface damage due to grinding but gives rise to the second form of sub-surface damage caused by the polishing medium itself. This cannot be removed by prolonged polishing and will approach a constant value depending on the polishing regime used. The selection and use of the polishing medium will therefore have a direct bearing, not only on the surface finish but also on the total performance of the optical surface by influencing the degree of residual sub-surface damage in the component.

Investigation of the Polishing Process

The aim of this work was to assess and improve the total surface quality produced during commercial glass polishing operations. Here time is an important factor and hence the work has looked at producing higher quality surfaces in the minimum time. All the surfacing operations were carried out on a Speedfam 12B single sided polishing machine. The test pieces were soda-lime float glass slides 35mm x 35mm x 1mm and were pre-ground using corundum in a two stage loose abrasive system using a nominal 12μm grit for 2 minutes followed by a nominal 9μm grit for a further 2 minutes. This produced a matt surface of Ra 670 nm.

Polishing operations were carried out using a polyurethane polishing pad and Regipol cerium oxide powders. These had nominal particle sizes of 2.3μm and 0.3μm. Surface roughness measurements were carried out on a Wyko TOPO-3D interferometric microscope except for the roughest specimens which were measured on a Surfcom stylus profilometer. Etching of polished specimens was done in a 3% solution of ammonium hydrogen difluoride and the samples examined on a JEOL 6400 scanning electron microscope.

Effects of Polishing Load

Glass removal rates for the 2.3μm polishing powder were measured at applied loads of 50g cm^{-2}, 100g cm^{-2}, and 200g cm^{-2}. The rate increases were approximately linear with applied load. Surface roughness measurements were made on the 50g cm^{-2} and 200g cm^{-2} samples as a function of time. Both samples reached the same limiting Ra value of about 1 nm but the 50g cm^{-2} sample took 4 times longer to reach it than the 200g cm^{-2} sample. This provides further evidence of the relationship between load and glass removal rate. **(Fig. 1)**

Fig.1 Roughness vs Load & Polishing Time

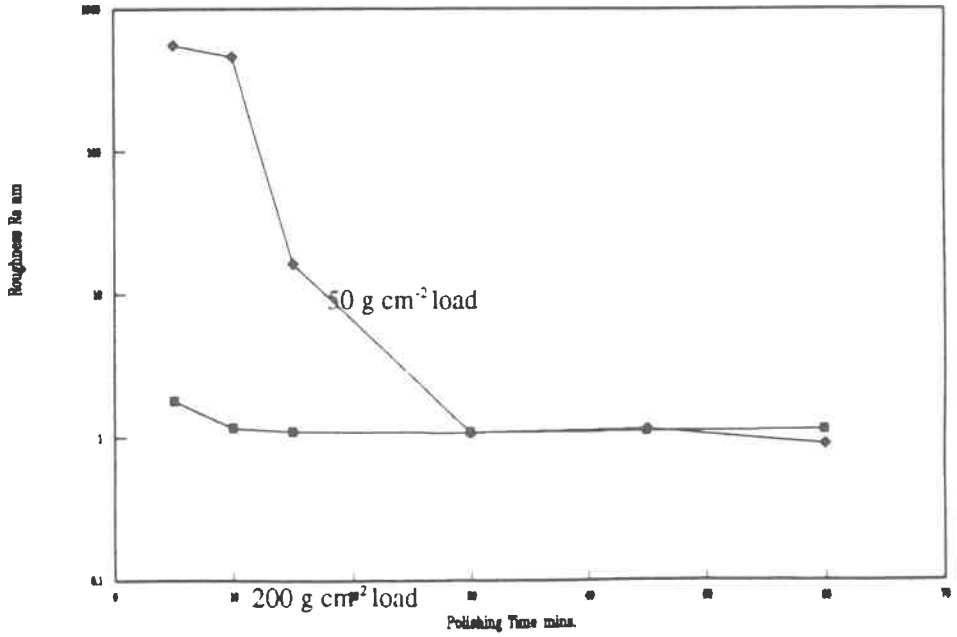

Effect of Particle Size

The glass removal over a 60 minute period for both 2.3μm and 0.3μm powders is shown in Figure 2. This shows no significant difference in the glass removal for the two samples and implies that the removal rate is independent of the particle size within this range.

Surface roughness measurements show that the 2.3μm sample achieves a final Ra of 1.1nm

Fig. 2 Glass Removal vs Particle size

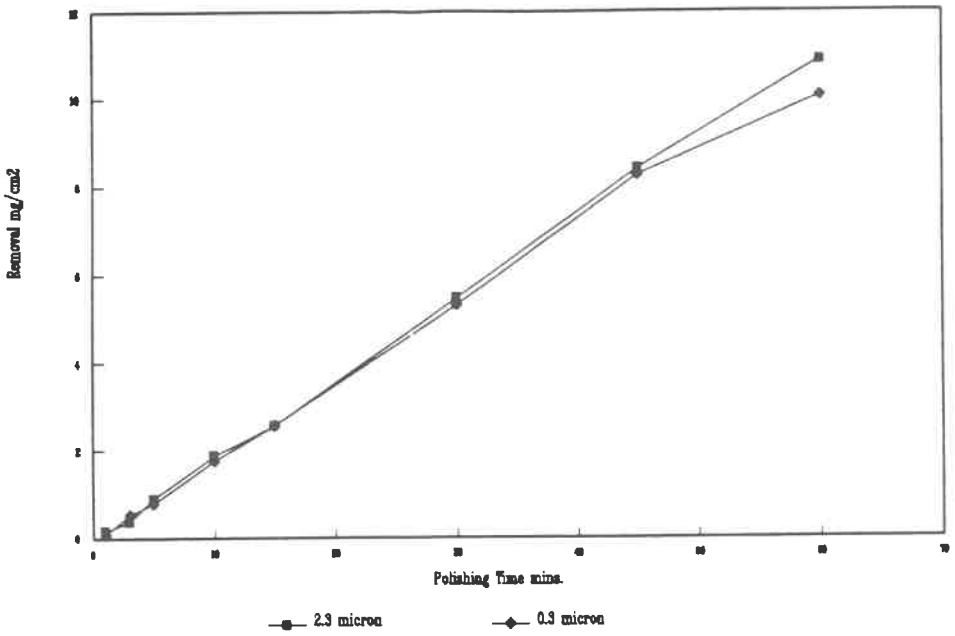

whilst the 0.3μm sample achieves a final Ra of 0.8nm. This difference is not great compared to the size difference between the two polishes. The Rt values for the two samples however are 20nm and 9nm respectively.

The differences between the two polishes however is clearly seen when etched surfaces are examined. Surfaces polished with the 2.3μm powder show a rapid decrease in the number of revealed defects over the first 10 minutes after which the density of defects remains more or less constant when all the grinding damage has been removed but the polish is then generating its own sub-surface damage. Surfaces polished with the 0.3μm powder show a gradual reduction of defects with increasing polishing time and show very few sub-surface defects after 30 minutes.

Figures 3 and 4 show the etched surfaces of samples polished with 2.3μm and 0.3μm powders for 30 minutes showing clearly the decrease in sub surface damage between the two polishing regimes.

Fig. 3 2.3μm polished 30 mins. etched

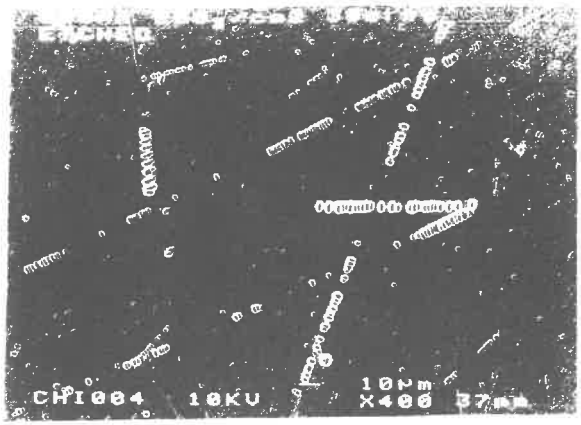

Fig. 4 0.3μm polished 30 mins. etched

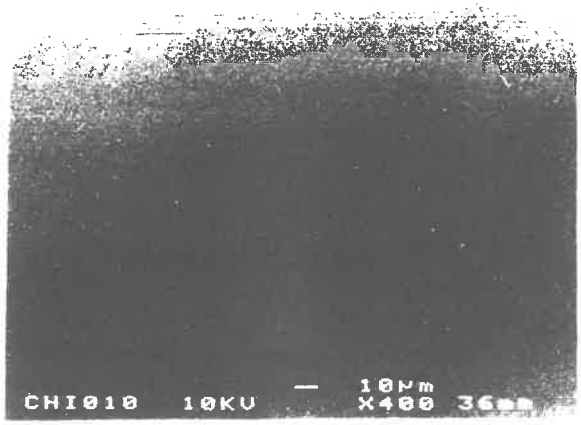

Conclusions

The work so far carried out indicates that a substantial improvement in total surface quality can be achieved by the use of sub-micron cerium oxide polish. Although a modest improvement in surface finish (Ra) is attainable compared to the coarser polish, the most dramatic improvement is in the reduction in sub-surface damage. The sacrifice in polishing speed is small under the conditions of these experiments although work at higher pressures and speeds, not reported here, indicates that the coarser polish can be about 40% faster than the finer one. Faster total polishing times can be achieved in a 2 stage process in which a pre-polish under high pressure using the coarser powder is followed by a finishing polish with the fine powder.

Ion Figuring System for Segmented, Adaptive Optics

Steven C. Fawcett and Robert W. Rood

Optical Systems Branch, EB23
National Aeronautics and Space Administration
Marshall Space Flight Center, AL 35812

Introduction

A new precision fabrication facility is currently being implemented at NASA's Marshall Space Flight Center (MSFC). One of the technologies which is being evaluated to complement the standard fabrication techniques is ion figuring. The use of neutral ion beams to remove selected material has been developed and is currently in use at commercial installations and research facilities. These implementations typically use the process for final figure correction on meter class optical components. The new facility at MSFC will focus on using the technique for the primary figuring of centimeter scale optics. The process under development will produce large radius of curvature mirror segments from polished flats of single crystal Si, fused silica and CVD SiC. These segments have a hexagonal shape and will used to form a segmented, adaptive optic, mirror. This mirror will form the primary of a 12 meter class beam expander to direct laser energy through the atmosphere. The adaptive system will be used to compensate for the phase perturbations caused by atmospheric turbulence. This paper will present a general discussion of the system requirements, the preliminary design concepts and the development of the ion figuring technique to produce the mirror segments.

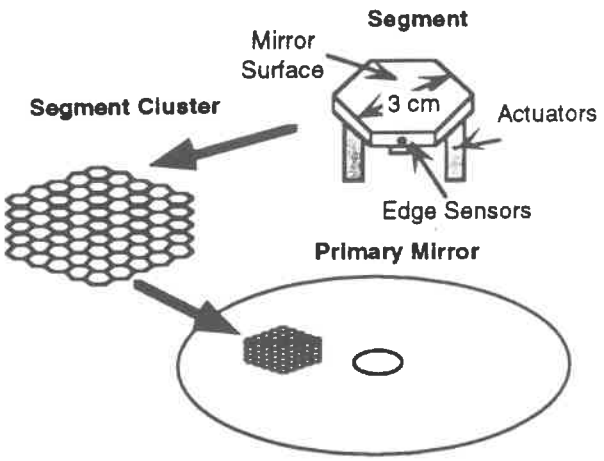

Figure 1 Laser beam expander made of segmented adaptive optics.

Segmented Mirror System

The segmented primary mirror being considered for this project is based on a design developed by Kaman Aerospace Corporation. The project was funded by the Strategic Defense Initiative Organization (SDIO) and the Defense Advanced Research Projects Agency (DARPA). The designation for the patented technology was PAMELA™ for Phased Array Mirror, Extendible Large Aperture (US patent #4,825,062). Figure 1 depicts the basic layout of the concept. The individual mirror segments are hexagonally shaped substrates with integral edge sensors on the six edges (3 active and 3 passive) and with three actuators on the backside. The actuators respond to the commands issued by the wave front control system to compensate for the phase aberration. This is achieved by differential piston movements that give the required tip and tilt of the mirror surface. The active edge sensors couple with adjacent passive sensors to maintain the continuity of the mirror surface.

The individual segments are joined into multiple segment clusters that form the primary mirror surface. The clusters are to be removable to aid in the maintainability of the system. Also, the cluster support structure may be actively controlled to remove the low frequency, large wavelength, large departure surface errors and aberrations. This will significantly reduce the range requirements of the segment actuators. The type of segment shown in Figure 1 is totally reflective and is designated as Type I. This configuration would be used in a system where the wave front sensor is located in the beam path prior to arriving at the beam expander. The segment would be made of an opaque material such as silicon carbide to provide for structural stiffness or single crystal silicon so that the sensors and processor could be integrated into the segment with lithographic patterning techniques.

An alternate configuration for the mirror segments will include the wave front sensor as an integral part. This segment is Type II and is shown if Figure 2. The segment's mirror surface will be made of a transparent material such as fused silica and will allow transmission and subsequent diffraction and refraction of both the beacon light and the laser light. Beneath the mirror is a miniature telescope made of a high index polymer with a diffraction grating made into the upper surface. This internal optical system will use a particular mode of the diffraction pattern for wave front correction. This system will continuously track the incoming beacon light and adjust the mirror surface to aim the outgoing laser beam towards the beacon. The wavelength dependent laser coating on the mirror surface will permit only a small percentage of the high energy laser light to reach the nulling detector while passing the majority of the beacon light. Because the orientation angles of the segments with respect to the beacon and laser beams vary as a function of radius on the primary, a diffraction grating will be required to ensure that one mode from the beams will constantly be incident on the detector. This angle varies from near normal incidence at the center of the primary to almost 10 degrees off normal at the mirror periphery.

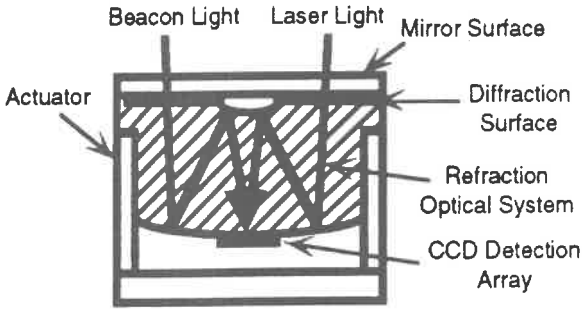

Figure 2 Schematic of refractive mirror segment (Type II).

These segments will also incorporate edge sensing and actuation devices as depicted in the first configuration. Provided that the optical system will perform the desired wave front sensing, this integrated configuration could transfer some of the system complexity to the segment level and greatly reduce the alignment and computational considerations with respect to the Type I segments.

The two configurations are being analyzed to determine the feasibility of each design. The choice of mirror substrate material will depend on which configuration is selected. The opaque mirror segments for Type I will use either single crystal silicon (Si) or Chemical Vapor Deposited silicon carbide (CVD SiC). The

CVD SiC offers many benefits in durability and specific stiffness while the Si can easily be doped as a semiconductor and patterned into microcircuits and sensors. If Type II is selected, the material choices will be limited to transparent media such as borosilicate glass (for example BK-7) or fused silica. For these materials the specific stiffness drops considerably when compared to the CVD SiC. In the configuration II design, the optical system for wave front detection will probably be fabricated from an optical polymer.

Segment Fabrication

The choice of the mirror substrate depends heavily on the fabrication procedures necessary to create the required surfaces. Preliminary designs for the mirror surfaces have specifications for 3 cm hexagonal segments with concave, 30 m radius of curvature surfaces. These surfaces will need figure accuracy tolerances of approximately $\lambda/40$ RMS and surface tolerances of approximately $\lambda/300$ RMS. At an operating wavelength of 840 nm this corresponds to allowable figure errors of 21 nm RMS and surface errors less than 28 Å RMS. These figures will be used in a baseline configuration but are preliminary and will need to be verified by an analysis of the complete optical system. The manufacturing tolerances on the edges of the segments will primarily depend on the edge sensor and actuator development.

To achieve the extremely tight tolerances, the fabrication procedures will be developed and optimized for these particular requirements. A fabrication test program is currently underway to develop the techniques. This program includes traditional polishing and figuring with loose abrasives, figuring with an inert ion beam and CVD replication techniques.

Traditional Polishing and Figuring

This procedure of optics fabrication is well developed and will be compared directly with the new ion figuring and replication procedures. This technique involves blocking the mirror substrates together and creating the desired curvature and surface characteristics by frictional abrasion and chemical reactions with a diamond slurry. It should be noted that the ion figuring technique will also require that the mirror segments are polished to the angstrom level prior to figuring. Also, the CVD replication procedure requires the formation of a mandrel to these exacting tolerances. This will be done with the traditional procedures. Therefore, all the candidate fabrication techniques rely on loose abrasive polishing in some manner.

Neutral Ion Figuring

The use of neutral ion beams to remove selected material currently in use at commercial installations typically use the process for final figure correction on meter class optical components. The process involves a kinetic energy transfer form inert gas molecules that results in molecular level sputtering of the substrate material. The basic operation is depicted in Figure 3.

A Small Business Innovative Research (SBIR) phase I program on ion figuring of optical components has recently been successfully completed under the sponsorship of the Optical Systems Branch at MSFC. A phase II program has been initiated to continue this effort. The information gained from these projects will significantly benefit the development of the

experimental ion figuring program for the mirror segments.

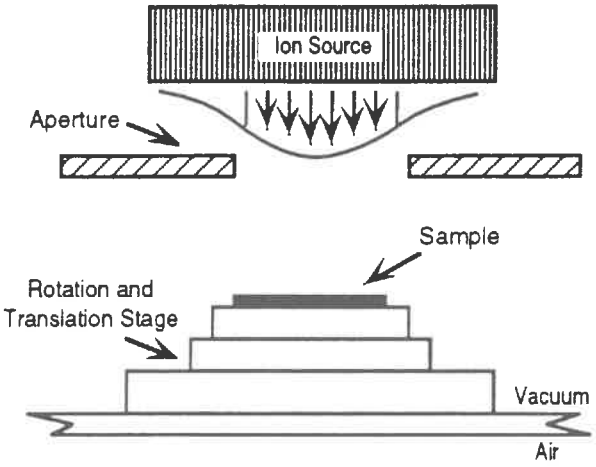

Figure 3 Schematic of ion figuring system.

The new facility at MSFC will focus on using the technique for the primary figuring of these centimeter scale optics. This facility was constructed around a surplus sputtering chamber obtained for this program. This chamber was retrofitted with a 3 cm, filament type ion source from Ion Tech Incorporated. This source is driven by a programmable power supply which can provide current densities to 10 mA/cm^2. The mirror substrates are attached to a two axis translation and rotary stage. The stage, manufactured by Klinger Scientific, has X-Y ranges to 100 mm and 360 degree rotation at speeds up to 15 RPM. The motion of the system as well as the ion source will be controlled by a 80486 based personal computer. The basic system is schematically depicted in Figure 4.

In this procedure, the optic is first measured with a Zygo Mark IV interferometer system. This surface profile is then mathematically convolved with a Gaussian ion distribution. This convolution results in the appropriate raster control algorithm to achieve the desired final contour.

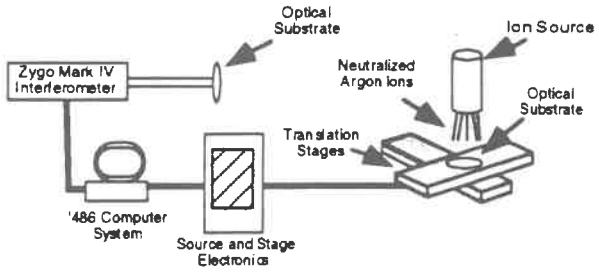

Figure 4 Schematic of the ion figuring procedure.

There are many benefits to using the ion figuring process. The process is relatively deterministic and should lend itself to automated manufacturing. Since the technique is noncontact, the edge distortion and support structure print through problems associated with traditional contact polishing are eliminated. The process can also enhance the application, adhesion and durability of the optical coatings if they are applied prior to breaking vacuum. Also, an additional benefit may be the application of lithographic sensor and controller patterns while still under vacuum. This could potentially lead to a complete fabrication procedure where the segment mirrors are lithographically patterned and etched with edge sensors and controllers, figured with the desired mirror surface and finally, coated with the high energy laser coating while in the vacuum environment. The current investigations at MSFC will be evaluating the ion figuring potential for the mirror segments. Future investigations will evaluate lithographically patterned sensors and controls as well as the application of wavelength specific laser coatings.

A Basic Study on Cutting Characteristics and Lifetime of Wire Tool Electrodeposited Diamond Grains

Ken-ichi ISHIKAWA, Hitoshi SUWABE and Kazunori KANAYAMA
Kanazawa Institute of Technology
7-1 ohgigaoka, Nonoichimachi, Ishikawa 921 Japan

1. Introduction

In recent years, a wire tool electrodeposited diamond grains on piano wire[1),2)] has been paid attention in a field of cutting for ceramics. In this study, the wire tool is made by means of a high speed nickel electrodeposited bath. This report describes about torsional strength and slicing characteristics of the wire tool.

2. Plating method of diamond grains

Figure 1 shows a model of a plating system. Figure 2 shows a mechanism of a plating pool. Diamond grains are plated on piano wire by a nickel sulfamate bath. In the plating, nickel boards are anode and wire is a cathode. Piano wire sent out from a wire bobbin is removed fat by aceton and activated by hydrochloric acid. Next, the wire is sentin the plating bath. First, basic plating is practiced on wire surface to increase fixed force of diamond grains. Grains pool is set in the nickel plating bath and is filled with diamond grains. There are some holes(ϕ10) on the side plates of the grains pool and teflon (polytetrafluoroethylene) net(the mean hole size is 3.0μm) is stuck on the inside of both plates. The teflon net is used to aim that diamond grains is bound in the grains pool and plating bath can flow into the pool. The diamond grains are fixed on wire in this pool andthe next plating stage. Wire fixed diamond grains is further plated to get adequate fixed force of diamond grains. The main plating

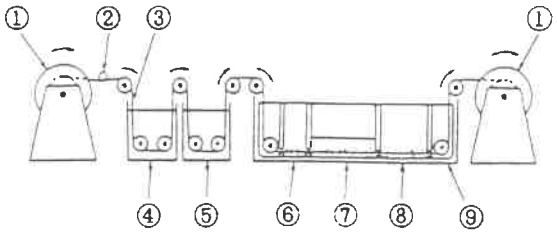

① Drum
② Cu-electrode
③ Wire
④ Degrease by aceton
⑤ Pickling by HCl
⑥ The 1st pool
⑦ The 2nd pool
⑧ The 3rd pool
⑨ Plating pool

Fig. 1 Model of plating system for diamond grains

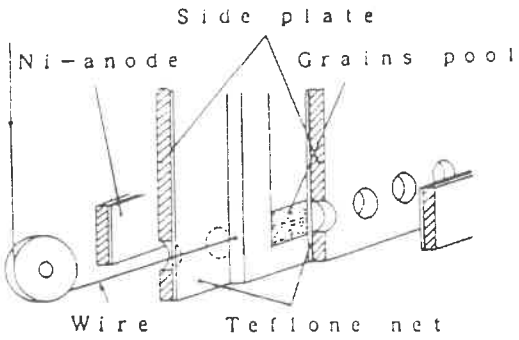

Fig. 2 Inside of plating pool

Table 1 Plating conditions

	Nickel Sulfamate bath		Copper Pyrophosphate bath	
Composition of electrolytic solution	$Ni(NH_2SO_3)_2 \cdot 4H_2O$	715g/l	$Cu_2P_2O_7 \cdot 2H_2O$	90g/l
	$NiCl_2 \cdot 6H_2O$	12g/l	$K_4P_2O_7$	420g/l
	H_3BO_3	42g/l	NH_3	6ml/l
			KHO_3	12g/l
Diamond size	30~40μm		30~40μm	
pH	4.0		8.8	
Wire velocity	80~200 mm/min		15 mm/min	
Temperature	70℃		60℃	
Current density	38 A/dm^2		5 A/dm^2	

conditions are shown in Table 1.

3. Torsional strength of wire tool

When we use a wire tool in slicing, the wire tool breaks during the slicing process whether many diamond grains are fixed on a wire surface or not. Therefore, we examined about torsional strength of the wire tool model during the slicing process as shown in figure 3. In general, when twisting moment:Mt acts on the wire tool, the relationship between twisting moment and an angle of twist: $d\phi$ is as follows;

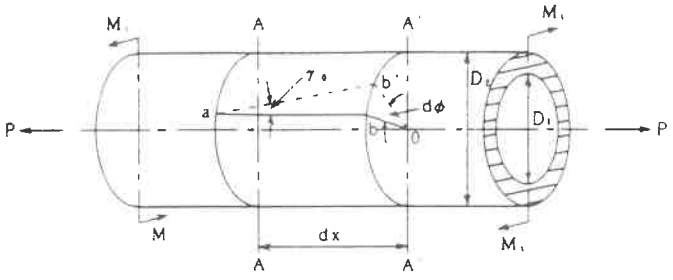

Fig. 3 Twist of wire

$$d\phi=\frac{32M_t}{\pi G_1}\cdot\frac{1}{D_1^4}\cdot dx \qquad (1).$$

Where, G_1 is the modulus of transverse elasticity of core wire, dx is minute length and D_1 is diameter of core wire. But torsional and tensile force act on the wire tool during slicing. In this case, when equivalent twisting moment of torsion and tensile, and the composite modulus of shearing elasticity between core wireand nickel plating are substituted for Eq.(1), the equation of twisting moment during slicing is obtained. The equivalent twisting moment of core wire is as follows;

$$M_e=\sqrt{\left(\frac{PD_1}{8}\right)^2+M_t^2} \qquad (2).$$

Where, P is tension. Breaking equivalent twisting moment is got owing to multiply ratio of breaking force of the wire tool to breaking force of core wire for P of Eq.(2).

$$M_e=\sqrt{\left(\frac{D_1^3P}{8}\cdot\frac{\delta_1A_1+\delta_2A_2}{\delta_1A_1}\right)^2+M_t^2} \qquad (3)$$

Where, A_1 is a cross-sectional area of the core wire, A_2 is a cross-sectional area of plating layer, σ_1 is breaking stress of the core wire and σ_2 is breaking stress of the plating layer.

Next, we describe about composite modulus of shearing elasticity. As the wire tool is made by the combination of solid and hollow materials, the equivalent twisting moment of the wire tool is equal to the sum of solid and hollow equivalent twisting moment. Therefore, the composite modulus of shearing elasticity:G is composed of the relationship shown in Eq.(4).

$$2\pi G\theta\int_0^{D_2/2}r^3dr=2\pi G_2\theta\int_{D_1/2}^{D_2/2}r^3dr+2\pi G_1\theta\int_0^{D_1/2}r^3dr \qquad (4)$$

The composite modulus of shearing elasticity is as follows;

$$G=\frac{G_2(D_2^4-D_1^4)+G_1D_1^4}{D_2^4} \qquad (5).$$

Where, G_2 is the modulus of shearing elasticity of nickel and D_2 is the diameter of the wire tool.

When the modulus of shearing elasticity is small, it is clear that torsional strength becomes large from Eq.(1). As the modulus of shearing elasticity of copper is smaller than the modulus of shearing elasticity of nickel or steel, Multiplating wire tool that one part of plating layer plates by copper pyrophosphate bath is made. Torsional strength of the multiplating wire tool is examined. The modulus of shearing elasticity of the multiplating wire tool is shown in Eq.(6).

$$G=\frac{G_3(D_3^4-D_1^4)+G_2(D_2^4-D_3^4)+G_1D_1^4}{D_2^4} \qquad (6).$$

Where, D_3 is a diameter of the multiplating wire tool and G_3 is the modulus of shearing elasticity of copper.

Figure 4 shows the relationship between a breaking twist angle and a diameter of the wire tool. In figure 4, theoretical twisting strength of the wire tool (nickel plating)shows a doted line and theoretical twisting strength of the multiplating wire tool(copperand nickel plating) shows solid lines. And the plotted points show experimental results. The theoretical value is agree with the experimental value. As shown in figure 4, when the wire tool is plated by nickel plating bath on core wire of ϕ0.2, it is clear that a breaking twist angle decreases suddenly within the range from ϕ0.2 to ϕ0.24. In case of the multiplating wire tool, a breaking twist angle increases in proportion to increase of the ratio of copper plating parts.

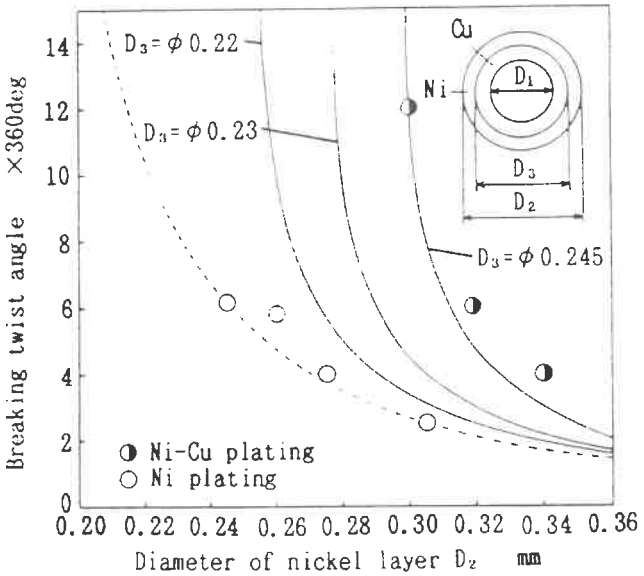

Fig.4 Relationship between breaking twist angle and diameter of nikel layer D_2

4. Slicing ability of wire tool

The wire tool made by nickel sulfamate bath is set at the device built as a trial (as shown in figure 5), and experiment of slicing ability is practiced. Table 2 is main slicing conditions.

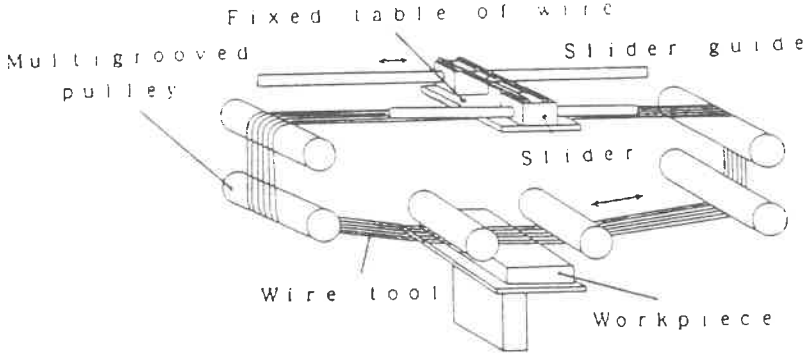

Fig.5 Model of slicing machine

Figure 6 shows SEM observations of wire tools. It is clear that the wire feed velocity has direct effects upon change of amount of diamond grains on the wire tool surface. When the wire feed velocity is from 80mm/min to 200mm/min, the wire tool can slice brittle materials to the full.

Figure 7 shows experimental results.

Table 2 Slicing conditions

Working load		1.96N/Wire
Wire running speed		100m/min
Wire tension		19.6N
Working fluid		Gas oil
Workpiece	Material	Glass
	Size	50×30×10
Cutting time		15min

The plotted points of △ and ○ show the nickel plating wire tool. The plotted points of ▲ are slicing results used the copper plating wire tool. Symboles of ▲ and △ are the wire tool of the same diameter. However, machining efficiency of the copper plating wire tool shows a tendency to decrease when compared with the nickel plating wire tool. As copper is softer than nickel, the copper plating wire tool becomes small fixed force of diamond grains.

The plotted points of ● show slicing results of the multiplating(copper and nickel) wire tool. This multiplating wire tool is plated by copper until ϕ0.24 (thickness of plating layer is 0.02mm) and is plated by nickel until ϕ0.30 (thickness of plating layer is 0.03mm). Behavior of machining efficiency by the multiplating wire tool shows the similar tendency of the nickel plating wire tool. But, cutting number of the multiplating wire tool increases to be compared with the nickel plating wire tool. As breaking twist strength of the multiplating wire tool is stronger than the nickel plating wire tool, the tool life (cutting number of break) increases to the nickel plating wire tool.

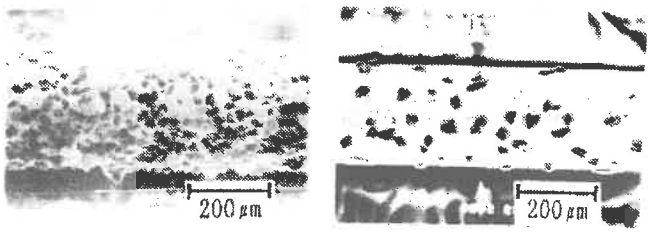

(a) 80 mm/min (b) 200 mm/min

Fig. 6 Surface of wire tools

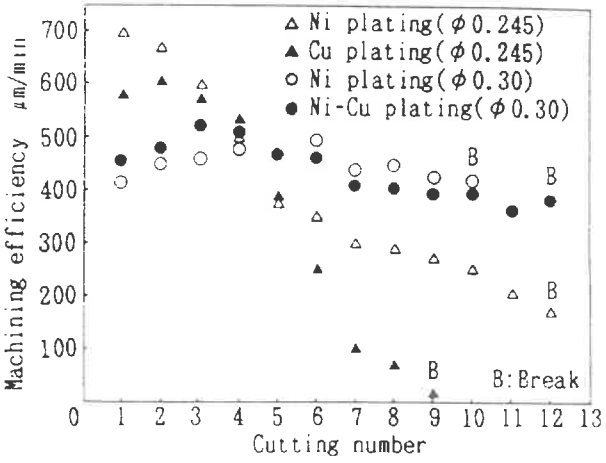
△ Ni plating(φ0.245)
▲ Cu plating(φ0.245)
○ Ni plating(φ0.30)
● Ni-Cu plating(φ0.30)
B:Break
Machining efficiency μm/min
Cutting number
0 1 2 3 4 5 6 7 8 9 10 11 12 13
100 200 300 400 500 600 700

Fig. 7 Relationship between machining efficiency and cutting number

4. Conclusions

As theoretical and experimental results of this paper, the followings are clear;

(1) Torsional strength of the wire tool becomes feeble as the plating layer becomes thicker.

(2) In case of torsional strength, the multiplating wire tool is stronger than the nickel plating wire tool.

(3) As the results of slicing, the copper plating wire tool shows the short tool life to be compared with the nickel plating wire tool.

(4) The multiplating wire tool is the longer tool life than the nickel plating wire tool.

Reference

1)Ken-ichi ISHIKAWA, Hitoshi SUWABE: A Basic Study on Vibration Multiwire Sawing using Wire fixed Diamond Grains, Bull. of J.S.P.E, 21, 3 (1987) P214.

2)Suguru NAKAYAMA, Masanori YOSHIKAWA, Hitoshi TOKURA, Jyunichi SATO: The adhering Method of Diamond Grains to Wire Tool, Journal of J.S.P.E, 53, 7 (1987) P1045.

3)Kaoru AOTANI : Practical plating for Engineer (1), Makisyoten (1978) P150.

Laser Photo-etching Method for a Maskless Fabrication of a New Type Amorphous Silicon Solar Cell Submodule

S.Kiyama, Y.Yamamoto, H.Hosokawa, R.Suzuki, M.Osumi, H.Nishiwaki*,
S.Sakai*, S.Matsumi*, M.Ohnishi*, S.Tsuda*, S.Nakano* and Y.Kuwano*
Control & Systems R.C., *Functional Materials R.C.,SANYO Electric Co.Ltd.
1-18-13 Hashiridani ,Hirakata-City ,Osaka ,Japan

Abstract

A laser photo-etching method was investigated as a fabrication technique for microscopic holes on a new structure, called the Through-Hole Contact (THC) , integrated-type amorphous silicon (a-Si) solar cell submodule which achieves the further improvement of output performance.

Microscopic holes, which were key components of the THC structure ,were fabricated by the laser photo-etching method. By optimizing conditions, no damage to the photovoltaic performance was observed.

Based on this technique, we fabricated 10cm x 10cm THC integrated-type a-Si solar cell submodules and obtained a high conversion efficiency of 10.55%.

1.Introduction

Solar cells have recently been in the limelight as a clean energy source. The world's highest module efficiency of 11.1% has been achieved for a 10cm x 10cm a-Si solar cell submodule[1].

However in order to acceralate the practical use of a-Si solar cells, further improvements in conversion efficiency are required. We have therefore proposed a new structure , Through-Hole Contact (THC), integrated-type a-Si solar cell submodule[2].

In this paper, we will first describe the summary of the THC integrated-type a-Si solar cell submodules. Next, we will describe the laser photo-etching method. Finally, we will discuss the optimization of preparation conditions of microscopic holes and report on the output performance of the THC integrated-type submodule.

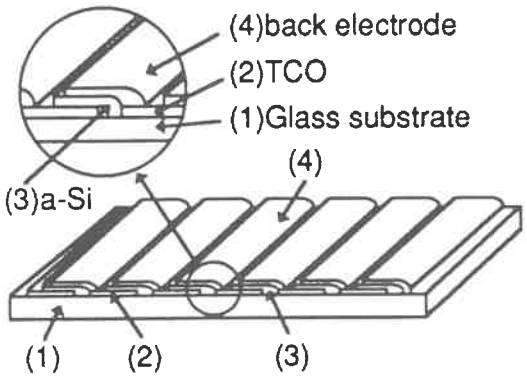

Fig . 1 The structure of a conventional integrated-type a-Si solar cell submodule

2.THC Integrated-type a-Si Solar Cell

Fig.1 shows the structure of a conventional integrated-type a-Si solar cell submodule which was developed by taking advantage of a-Si characteristics to generate a high output voltage from a single substrate.

Based on this conventional structure, we newly developed the THC integrated-type a-Si solar cell submodule shown in Fig.2.

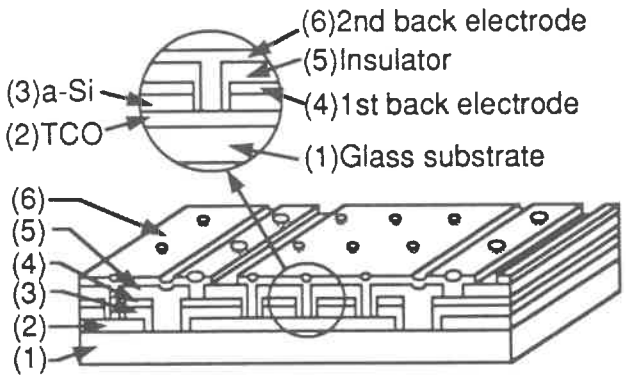

Fig . 2 The structure of a THC integrated-type a-Si solar cell submodule

The 2nd back electrodes are connected to the TCO (Transparent Conductive Oxide) through the multiple microscopic holes which collect photo-generated current.

The features of the THC structure are as follows :

1) The average length of the current flow path through the TCO is short. Therefore, power loss due to the resistance of the TCO is reduced.

2) It is possible to achieve separation and connection of each cell on the back of the cells. Therefore, the effective area can be increased.

In order to evaluate the output performance of the THC integrated-type submodule, we have developed a numerical simulation[3].

The output performance of the THC integrated-type submodule can be calculated by Eqs. (1) (2) and (3).

$$i(r)=i_{ph}-i_0[\exp\{q(V(r)+Rs\cdot i(r))/nkT\}-1] -(V(r)+Rs\cdot i(r))/Rsh \quad (1)$$

$$\frac{dV(r)}{dr}=I(r)\cdot\frac{Rst}{2\pi r} \quad (2)$$

$$Iout=2\pi\int r\cdot i(r)dr \quad (3)$$

r : The radius of the current collection area
i : The photocurrent , V(r) : The voltage
i_0 : The saturated reverse current
q : The electron charge
n : The diode quality factor
k : The Boltzmann factor
T : The absolute temperature
Rs : The series resistance
Rsh : The shunt resistance

Fig.3 shows the simulation results. The conversion efficiency of the THC integrated-type is about 10% greater than that of the conventional structure, and an output power of 1200 mW can be expected from the 10cmx10cm THC integrated-type submodule.

3.Laser Photo-etching Method

To apply laser photo-etching to the fabrication of the THC integrated-type a-Si solar cell submodules, the film quality of each layer must not be deteriorated due to the patterning of an adjacent layer.

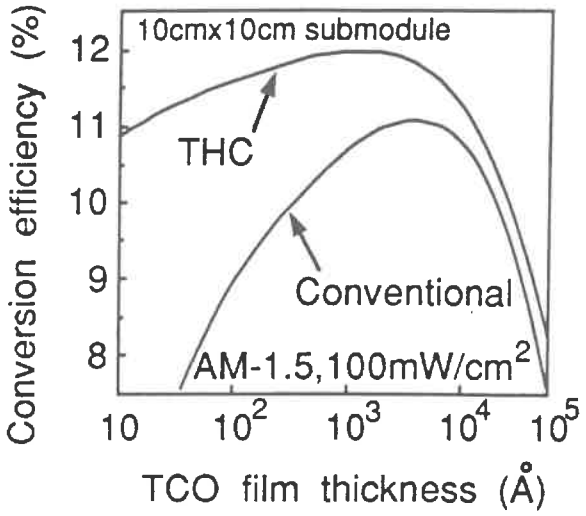

Fig . 3 Simulation results of conversion efficiency as a function of TCO film thickness

This laser photo-etching technology is based on bond breaking by absorption of photons of ultraviolet wavelength[4].

Fig.4 is a schematic diagram of impact of laser pulse on a material surface. If the fluence E exceeds a certain threshold value Eth, then the material is removed to the depth Z. The relationship between E and Z can be expressed by Eq.(4) which is known as Beer's law:

$$Eth = E\cdot\exp(-\alpha\cdot z) \quad (4)$$

where E and Eth are the intensities of the laser beam before and after transmission through a slice of material of thickness Z, and where α is the absorptivity.

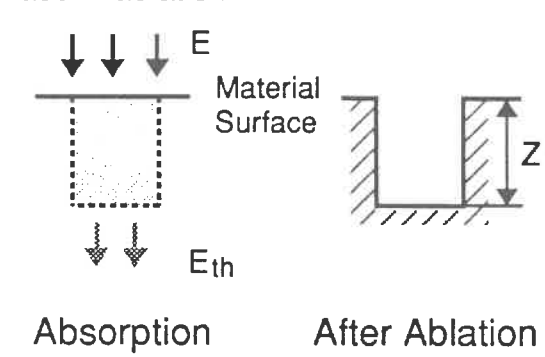

Fig.4 Schematic diagram of impact of laser pulse on a material surface

The removal rate of the insulator film (polymer) as a function of the XeCl laser energy density is shown in Fig.5. It is found that the removal rate is proportional to the logarithmic laser energy density and that the threshold energy density exists. The theoretical results calculated by Eq.(4) correspond well to the experimental results. This process is characterized by the control to be exercised over the depth of etching by the laser energy density, and also by the lack of detectable thermal damage.

In order to investigate the selective scribing for an insulator film and a TCO film, an insulator film deposited on a TCO film was scribed by a XeCl laser at a laser energy density of 0.4J/cm^2. A SEM image and element maps measured by EPMA , are shown in Fig.6. It was found that a clean surface on a TCO film was observed as shown in the SEM image (a), and that an insulator film composed of C was removed and a TCO film composed of Sn existed in a hole from chemical element maps (b) and (c) respectively. From these results, it was confirmed that the good selectivity between the TCO and the insulator could be achieved by using XeCl laser photo-etching.

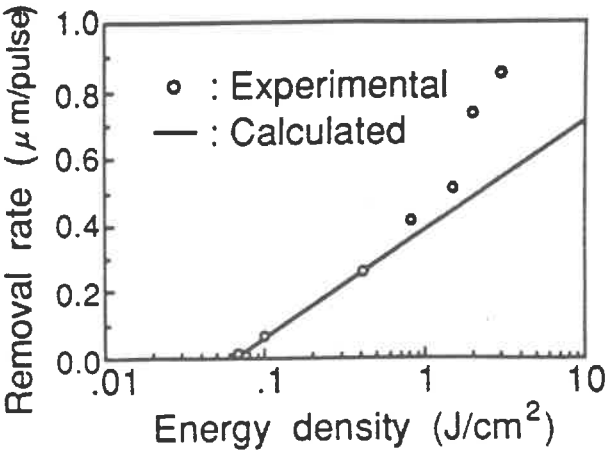

Fig.5 Removal rate of an insulator film (polymer) as a function of XeCl laser energy density

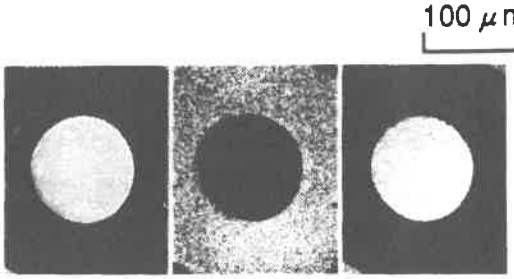

(a) SEM (b) C (c) Sn

Fig.6 A SEM image (a) and element maps of microscopic holes measured by EPMA ((b):C (c):Sn)

4.Resistance of Microscopic Holes

To improve output performance of the THC structure, it is important to reduce the resistance of microscopic holes[5].

Fig.7 shows the changes in the resistance of the microscopic hole formed by a XeCl laser for the different energy densities of 0.4J/cm^2, 1.5J/cm^2, 3.0J/cm^{2}as a function of the pulses. The resistance was mesured by the 4-terminals method illustrated in Fig.7. Above an energy density of 1.5J/cm^2, the conditions for good photo-etching are very narrow and it is difficult to keep this condition because of the distribution of the film thickness. On the contrary , at the energy density of 0.4J/cm^2, it was confirmed that a stable resistance below 5 Ω could be achieved even if the pulses increased.

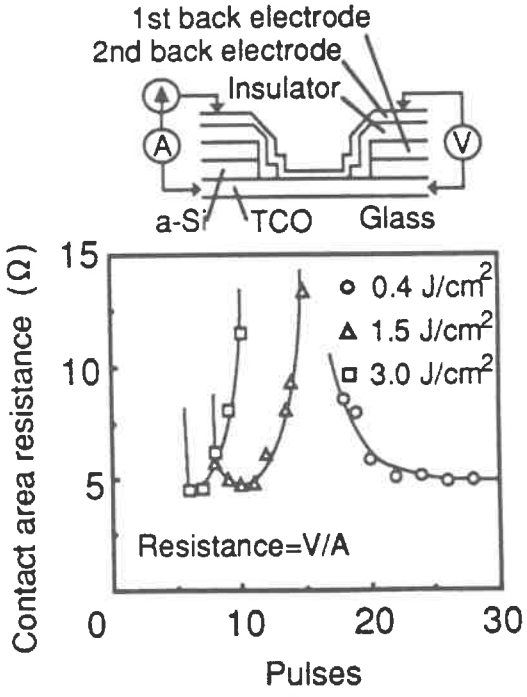

Fig.7 Changes in the resistance of the microscopic hole as a function of the pulses

5.Output Performance

Based on these investigations, 1cm^2 THC cells were fabricated using a laser photo-etching method.

Fig.8 shows the changes in the maximum output power of 1cm^2 THC cells as a function of the effective area ratio for various diameters of the microscopic holes. The maximum output power is normalized by that of the reference with a conventional structure.

According to this figure, the simulated results correspond well to the experimental results and thus we can find the optimum effective area ratio for each hole diameter. The smaller the hole diameter becomes, the larger the optimum effective area and the higher the maximum output power obtained. The maximum output power of the 1cm^{2}THC cell was found to be about 6% larger than that of the 1cm^{2}conventional cell using a hole diameter of 200 μm and an effective area ratio of 98%.

Furthermore, we fabricated a 10cmx10cm THC integrated-type a-Si solar cell submodule in which 10 cells were connected in series. The maximum output power of 1055 mW and a conversion efficiency of 10.55% , was obtained under AM-1.5, 100mW/cm^2 with an effective area ratio of 97% (Fig.9).

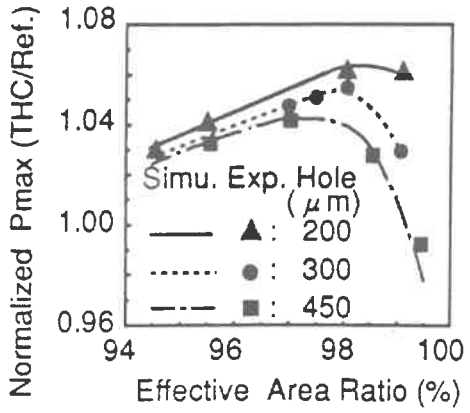

Fig.8 Changes in the maximum output power of 1cm^2 THC cells as a function of the effective area ratio

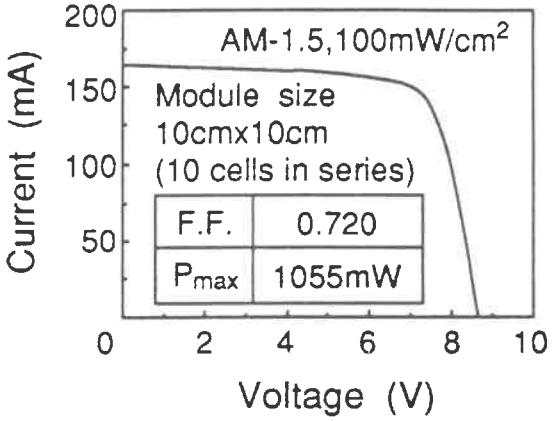

Fig.9 Illuminated I-V characteristics of the THC integrated-type a-Si solar cell submodule

6.Conclusion

The laser photo-etching method has been investigated as a new fabrication technique for microscopic holes on a THC integrated-type submodule in order to achieve further improvements in output performance. Microscopic holes can be fabricated without any significant damage to the TCO. Good selectivity between the TCO and the insulator can be achieved.

Based on this technique, a THC integrated-type a-Si solar cell submodule has been developed. The maximum output power of the 1cm^2 THC cell was found to be about 6% larger than that of the 1cm^2 conventional cell at a hole diameter of 200 μm and at an effective area ratio of 98%.

Furthermore, a conversion efficiency of 10.55% was obtained from a 10cmx10cm THC integrated-type submodule with an effective area ratio of 97%.

Acknowledgement

This work was supported in part by the New Energy and Industrial Technology Development Organization (NEDO) as a part of the Sunshine Project under the Ministry of International Trade and Industry.

References

1) H.Nishiwaki et al., Proc. 6th Int.PVSEC, New Delhi(1992), 469.
2) M.Ohnishi et al., Proc. 4th Int. PVSEC, Sydney (1989), 633.
3) M.Ohnishi et al., Proc. ISES Solar World Congress, Kobe (1989).
4) R.Srinivasan., Appl. phys. Lett.,51 (1978) , 1285.
5) H.Shibuya et al., Proc. 5th Int. PVSEC, Kyoto (1990), 383.

HIGH SPEED MILLING IMPROVES MACHINING RESULTS.

M.A.Shimanovich
New Jersey Institute of Technology
Newark, NJ

R.L.Pessolano
General Machine & Instrument Co., Inc.
Wayne, NJ

Contactless (hydrostatic, aerostatic or magnetic) bearings provide the basis for high-speed, high-precision, vibration-resistant compact spindle units featuring slide speeds of the spindle bearings up to 200 m/sec. With a milling cutter diameter 3 times more than spindle bearing journal, the cutting speed can reach 600 m/sec. However in practice mills are used with an outside diameter of the same order as the spindle bearing journal. The use of contactless spindle units together with natural (diamond) or artificial (composites) superhard cutting material mills allows the use of highly-efficient high-speed high-precision high-frequency milling technology. The major advantage of the milling method is the reduction of forces on the workpiece. Cutting forces, centrifugal forces, and workpiece temperatures are reduced. For example, regular turning of a main journal or crankpin of a crankshaft performed by a wide cutter can cause the cutting force to exceed 3,000 kg. The initial torque is so high, that a workpiece must be driven from both ends, therefore the machine tool requires two leading headstocks. Dealing with just one headstock can lead to the breakdown of a workpiece. The process of "lathe milling" involves replacing the turning tool with a milling tool driven by a contactless bearing spindle. The milling spindle can provide power up to 40 KW with rpm up to 30,000. The mill diameter would be the width of the turning tool. The material removal rate can be equal or better than the turning tool with a reduced cutting force of only about 3 kg or lower. Due to the formula P=F*V, where P - cutting power, F - tangential cutting force, V - cutting speed, if the power is a constant, the more the speed the less the force. By this technology of crankshaft machining not only roughing milling of raw crankpins is possible but finish milling of hardened crankpins can be also performed instead of grinding.

Contactless, especially hydrostatic, bearings ensure submicron precision of rotation (nanometers), suppressed cutting vibrations, decreased disbalance effect and drive influence, and therefore they assure high surface quality, minimum damage of subsurface layer of the hard-to-cut materials, increase service life period of superhard cutters.

In the 1970's a series of electric spindles ranging from n=30,000 rpm, P=30 KW to n=120,000 rpm, P=1.5 KW as well as series of spindles driven by belt or coaxial shaft coupling and ranging from n=12,000 rpm, P=100 KW to n=28000 rpm, P=10 KW. Some illustrations of industrial and experimental milling based on these

spindles are described hereafter.

Case 1. Rough turning of a large cast iron sleeve was attempted using a heavy duty chuck. The cutting force was so large that the sleeve bodies lost stability and broke away from the chuck. In the best case the sleeve remained in the chuck, but the cutting force (more than 1,500 Kg) deformed it so much that the precise dimension could not be achieved. The turning tool was replaced by an electric spindle (n=30,000 rpm, P=30 KW) with a mill, so that mill axis was perpendicular to the blank axis. When using single pass milling the cutting force was decreased to 10 Kg and machining efficiency doubled. By varying the relationship between rotation rates of a workpiece and a mill you can control the size and shape of a chip and also control the surface finish.

Case 2. In a second application aluminum pistons were machined by diamond face mill (10 mm diameter) rotated at 100,000 rpm by the use of an electric spindle (P=1.5 KW) mounted on a support of a special diamond-turning machine tool. The workpiece was rotated 10 times slower than during conventional turning. The resulting machined piston was held to higher accuracy with improved form and finish in significantly less machining time.

Case 3. For more than 20 years industry has utilized flat side diamond-milling, to produce a polygon from a 100 mm diameter single crystal of NaCl. This polygon crystal was part of an ultrasonic optics system, employed in electronic devices. The machining was improved by using a mill rotated by a contactless spindle rotating at 5,400 rpm, supported by hydrostatic bearings. Comparing the results with the results of customary machining of such parts, diamond-milling increased the accuracy and surface quality. It also considerably reduced the damage to subsurface crystal lattice during machining. Tests by ultrasound signal reflection inside the polygon proves the power dissipation became smaller by an order of magnitude. The rejection rate of crystals produced was decreased from 80% to 20%.

Case 4. An internal grinder was used to produce a Morse #5 taper in the hardened steel spindle of lathes. The machined part and spindle of the abrasive wheel were supported by contactless hydrostatic bearings. The abrasive wheel was replaced by a mill. The part was rotated at 150 rpm, the mill at 10,000 rpm. After milling hole surface was checked by blueing (the fit observed was around 75%-85%). The time to produce the taper was reduced several times by milling. The build up heat of the machined part was practically negligible. Eight spindles were cut by one mill without the use of coolant. The diameter of the milling (grinding) spindle journals was 45 mm, the housing of the grinding spindle had a bearing diameter 100 mm. The contactless spindle used a belt drive and contactless seals.

Case 5. A process was developed for high-precision machining of planes on a lathe. The lathe had an aerostatically supported electric spindle. The spindle was fitted with a high-precision

high-speed diamond mill rotating at 18,000 rpm. The mill was used to machine plane surfaces of aluminum, brass and copper blanks. The process yielded surfaces with a degree of roughness of 0.01 mkm, flatness was 0.2 mkm. Measurement resolution was 0.01 mkm. These results were obtained employing either natural or polycrystal diamond cutting tools.

The results of our experience show that high-speed milling can provide advantage for high-accuracy machining of workpieces made from various materials. The high-speed milling process decreases the harmful effect of machining on the workpiece quality. Spindle units with contactless spindle bearings combined with new tool technology of hard materials provide the tool for high-speed milling. Essential expertise exists. Future experiments are planned to create high-speed high-frequency mills, with specially combined face-and-end mills for precision machining of hardened steel. The significant centrifugal force and small dimensions of these mills rise some considerable difficulties, which may be overcome by additional experience testing. A two-tip end mill can be employed. When precision milling - just one tip is actually cutting, the second is used for better balancing and as a reserve. High-speed milling can open new ways for the production of complicated-shaped parts using CNC-controlled machine tools. High-speed milling on a lathe or "lathe-milling" eliminates the major tooling problems and associated problems of chip breaking by removing the chip (and heat) in a more efficient less damaging process.

A Comparison of Stylus, Interferometric and Scanning Probe Measurements

T. H. McWaid, J. Fu, T. V. Vorburger and J. F. Song
National Institute of Standards and Technology
Gaithersburg, MD 20899

Surface texture and feature sizes have traditionally been measured with stylus profiling instruments. Phase measuring interferometry (PMI) and scanning probe microscopy (SxM) are now becoming standard tools for the measurement of precision surfaces. All three techniques can achieve a vertical resolution on the order of 0.1 nanometer. Both stylus profilers and PMI microscopes are limited by a lateral resolution on the order of a micrometer. Scanning probe microscopy, however, offers the potential for obtaining a much higher lateral resolution than either of the other two measuring techniques.

Phase measuring interferometric microscopes allow one to obtain a three-dimensional surface map that is highly resolved in the vertical direction. The technique is inherently nondestructive; moreover, the commercially available instruments are relatively quick and easy to use. The use of various power objectives enable one to obtain data over different fields of view (FOV).

Scanning probe instruments allow one to obtain topographical data down to atomic dimensions over very small fields of view. The resolution of the instruments decreases as the FOV is increased. Although scanning tunneling microscopes can only measure conducting surfaces, the development of the atomic force microscopes has enabled one to image nonconducting surfaces as well.

The goal of this project was to determine the relative performance of a STM, a stylus instrument and a PMI microscope for the measurement of small features. Measurements have been made on a commercially available STM calibration standard. The standard consists of a 12 x 8 mm silicon die with three nominally 100 nm thick silicon dioxide grid patterns spaced 100 μm apart. Each grid pattern measures approximately 270 x 270 μm. The nominal pitches are 3, 10 and 20 μm. The entire die is over-coated with nominally 40 nm of platinum.

The platinum overcoat was deposited in order to enable one to make accurate vertical measurements across the standard using phase measuring interferometry. In order to obtain accurate height measurements with an PMI microscope the effective optical properties across the specimen surface must be uniform at the wavelength of the microscope. The 40 nm thick platinum overcoat may not have been sufficient to ensure that the PMI measurements were extremely accurate. As discussed in [1], an 80 nm overcoat of either chromium or platinum is recommended in order to make very accurate PMI height measurements across a specimen comprised of dissimilar materials.

The PMI microscope was equipped with a 100X objective lens. The numerical aperture of the lens is 0.90. Each set of surface heights measured with the PMI microscope was multiplied by an appropriate obliquity correction factor (numerical aperture factor) to correct errors associated with the oblique incidence of the light. An approximately 100 x 100 μm field of view was imaged onto the 256 x 256 element CCD. The detector element center-to-center spacing was therefore approximately 0.4 μm. The microscope utilized 651.9 nm wavelength light from a halogen lamp for illumination. The optical (diffraction limited) resolution of the microscope is 0.35 μm based on the Rayleigh criterion. The lateral resolution of the microscope is therefore limited by the detector sampling.

The long-range STM used in this study has been described in the literature [2]. A commercial STM head has been interfaced to a PZT controlled flexure stage, allowing one to make large field of view measurements by scanning the stage and small FOV measurements by scanning the microscope head. All measurements reported herein consisted of an array of 400 x 400 points. The sampling interval is thus the x- or y-dimension of the FOV divided by 400.

Each instrument was used to measure the three grid patterns on the calibration standard as well as individual defects on the standard surface. Several of these defects consisted of small scratches or divots incurred during handling of the standard. Additionally, the stylus profiler was used to create a set

of four scratches across a portion of the specimen. These scratches were made by dragging a diamond stylus under a relatively large contact force back and forth across the surface several times.

Both the stylus profiler and the STM imaged the grid patterns very well. The PMI microscope was not capable of measuring the grids accurately. Even the largest, 20 μm pitch, grid appeared rounded in the images obtained using the PMI microscope. Figures 1a, b and c present profiles of the 3 μm grid as obtained using the stylus profiler, PMI microscope and STM, respectively.

The stylus profiler utilized a horizontal magnification of 2000X and a vertical magnification of 100000X to obtain the profile presented in Fig. 1a. A 0.3 μm radius diamond stylus was used in order to minimize the convolution of the tip and the specimen.

The profile obtained with the PMI microscope includes a portion of the substrate and also six cells across the grid. Note that the bottom of the grid appears to be over 10 nm above the substrate, although in reality the bottom of the grid is co-planar with the substrate. In addition, the optically measured height from the substrate to the top of the grid walls is approximately 67 nm, well below the actual height of 94 nm.

The actual grid height was measured using the stylus profiler, which was calibrated using a standard reference step. The first STM measurements indicated that the grid height was about 147 nm. The vertical piezoelectric (PZT) actuator was re-calibrated so that the STM measured the correct grid height. The reasons for the large discrepancy between the vendor-quoted PZT calibration value and our calibration value are not fully understood.

The images of the largest stylus scratch that were obtained using a scanning electron microscope (SEM), the PMI microscope and the STM are shown in Figs. 2a, b and c, respectively. Fig. 2a shows the scratch on the substrate and on a portion of the raised pattern; the raised portion is in the foreground. Fig. 2b and c show the scratch only across a region of the substrate. A portion of the raised pattern is visible in the background of Fig. 2b; however, the top of the structure has been cropped from the image in order to highlight the scratch across the substrate.

The fact that the scratch is comprised of several fine scratches, each of which corresponds to a single pass of the stylus, is apparent from the images obtained using the SEM and the STM (Figs. 2a and 2c). The image obtained with the PMI microscope does not reveal the fine structure of the scratch. Both the SEM image and the PMI microscope image show the scratch penetrating below the substrate surface. Convolution of the probe and the valley walls apparently prevented the STM probe from imaging the lower regions of the valleys.

The STM's failure to resolve the scratch valleys is somewhat surprising. The probe radius is believed to be much smaller that the approximately 100 nm wide valleys. It is possible that the tip was damaged when these data were obtained. In the future the scratch will be imaged again using the STM. This time the probe will be imaged using a SEM subsequent to acquiring the surface data.

The scratch was also measured with the stylus profiler. The stylus profiler was not able to resolve the small-scale structure of the scratch. The profiler measured the scratch to be a ridge approximately 16 nm high and 0.95 μm wide. The scratch valleys could not be resolved, presumably due to convolution of the tip with the valley walls.

References

1) T. H. McWaid, T. V. Vorburger, J. F. Song, and D. Chandler-Horowitz, "The effects of thin films on interferometric step height measurements," to be published in Proc. SPIE Conf./Vol. 1776, 1992.

2) J. Fu, R. D. Young and T. V. Vorburger, "Long-range scanning for scanning tunneling microscopy," Rev. Sci. Inst., 63(4), April, 1992.

a. Stylus Profiler

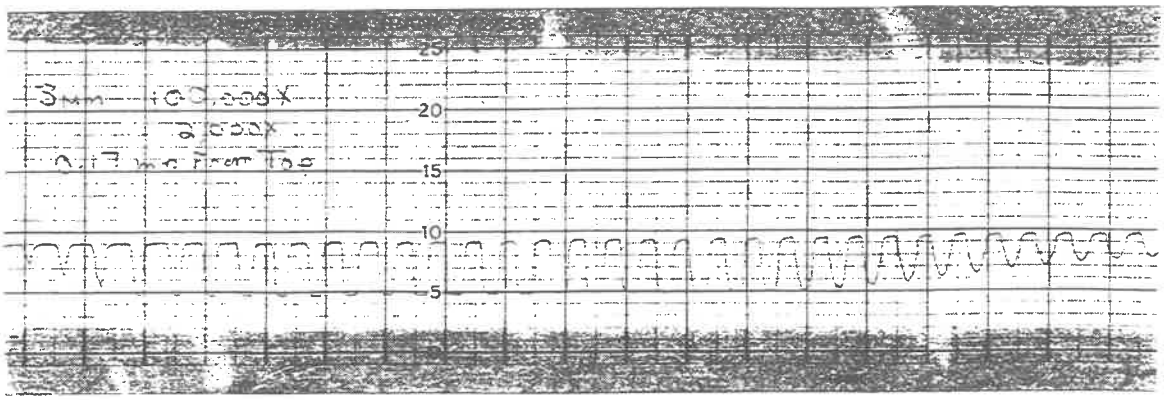

b. PMI Microscope

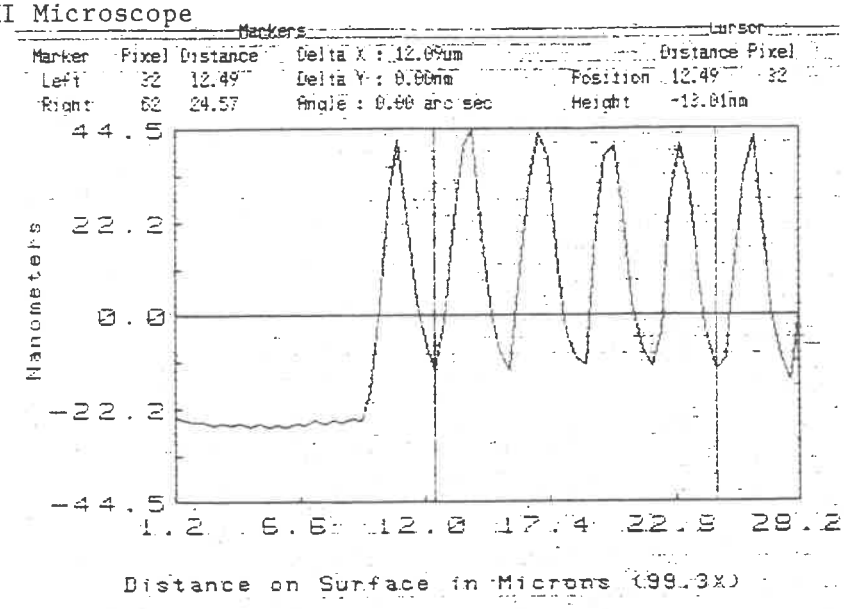

c. STM

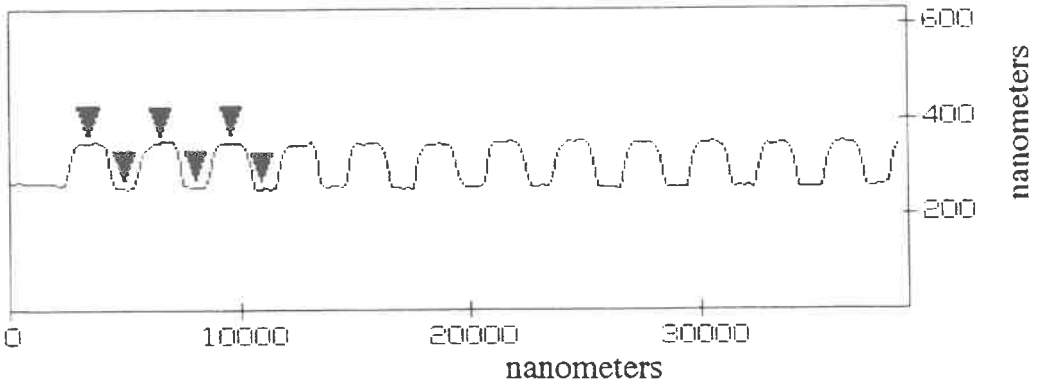

Fig. 1. STM Calibration Standard, 3 micrometers Pitch Grid.

a. SEM

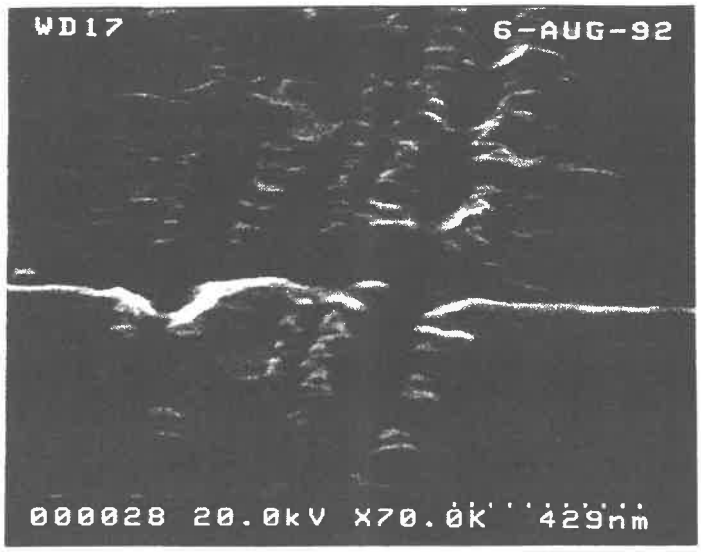

b. PMI Microscope

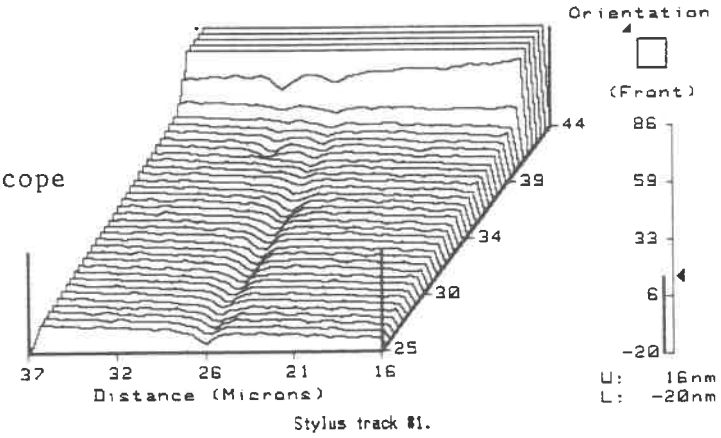

c. STM

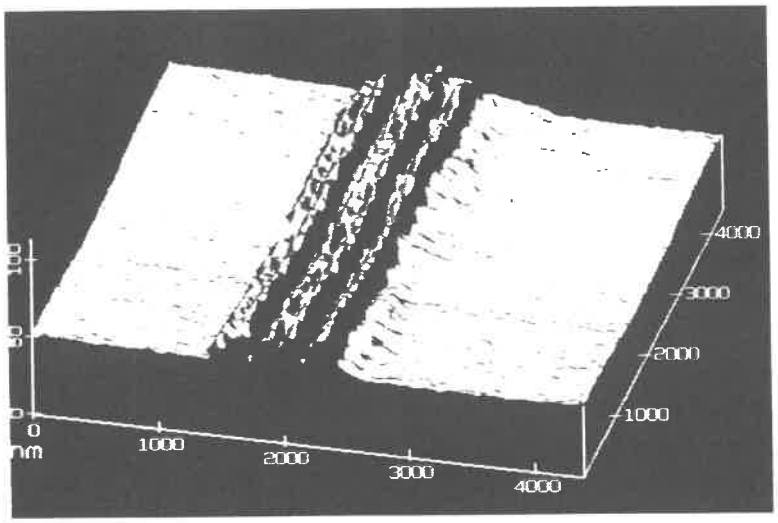

Fig. 2. Scratch.

Comparison of Optical Figure Measurements by Mechanical and Interferometric Methods

Richard F. Schenz
Robert R. Donaldson
Douglas D. Owens
Steven R. Patterson

Lawrence Livermore National Laboratory

Abstract

The authors used the Large Optics Diamond Turning Machine (LODTM) to measure the figure of an eight inch Zerodur optical flat. Point-to-point contact measurements were made using an air-bearing LVDT with low noise electronics. The data was then analyzed by means of linear regression and systematic machine errors were removed. Three dimensional plots were made of the corrected data and compared to measurements made with a commercial phase shifting interferometer.

Both the LODTM and the interferometric measurements showed the figure of the optical flat to meet its 1 microinch p-p certification, and the longer wavelength figure errors within this range were in good agreement.

Introduction

LODTM is a 1.6 meter capacity turning machine at Lawrence Livermore National Laboratory and has been described in several papers in recent years[1,2]. It has an accuracy of 1 μin p-p as certified by the old National Bureau of Standards.[3] The eight inch Zerodur optical flat was certified to 1 microinch p-v deviation. The present experiment demonstrates LODTM's ability to measure optical figure as a metrology machine where the accuracy of the measurement is required to be approximately equal to or better than the error motions of the machine and its fixturing.

The eight inch flat was placed on the vertical axis spindle and a displacement transducer was positioned on a polar coordinate grid by the radial X-axis and the angle of the spindle. Point to point contact measurements were made using an air-bearing Linear Variable Displacement Transducer (LVDT) with low noise electronics. Diametral sets of data consisting of vertical Z-axis measurements were taken. The data was then analyzed and systematic errors consisting of part setup tilt, machine squareness and one theta spindle piston were subtracted out. Three dimensional plots were made of the corrected data.

The figure of the optical flat was also measured by means of a Zygo Mark IV phase shifting interferometer. The results were then compared to measurements made with LODTM.

---

*This work was performed under the auspices of the U.S. Department of Energy by Lawrence Livermore National Laboratory under Contract No. W-7405-ENG-48.

Measurement Technique

An LVDT was mounted vertically on the tool bar in order to measure deviations in the Z direction. The LVDT was moved from point to point by raising the tool bar a small amount so that the LVDT probe was separated from the surface of the flat. The lateral machine motion was completed and the LVDT probe was lowered onto the flat. Once the probe was in position, the output of the LVDT sensing electronics was measured by averaging 1000 readings at a one Khz rate in order to reduce the effects of noise. The LVDT used here was an air-bearing design with special low noise electronics developed in our laboratory. The uncertainty for a single measurement due to noise was 0.1 microinches (p-p)(2.5 nm).

Data was obtained every 0.25 inches along diametral lines separated by 30 degrees. The data along any single diametral line was recorded beginning at the center of the flat, moving to the edge, then back along the diameter to the opposite edge and finally returning to the center. Figure 1 shows a plot of uncorrected deviation vs. radial position for a typical single diametral data set. The overall slope reflects a setup error of about 1.2 microradians nonparallelism to the X-axis. The p-p nonrepeatability for this run is 0.35 microinches (closure error between the first and last data points). For the most part it consists of a transient that decays out over the first several inches, and is thought to be a thermal interaction involving the lift-lower cycle of the aluminum shaft in the airbearing LVDT.

The optical flat was supported at three points, 2.5 inches from the center of the flat with 120 degrees separation. A finite element analysis of the plate supported by the three points was done to determine the amount of sag to be expected. The sag was calculated to be about 0.35 microinches p-v. We were not able to detect it in the data.

Data Reduction

The data was corrected for systematic errors inherent in the machine and the mechanical setup of the part. The major contributing errors include machine squareness, part tilt and fundamental axial spindle motion. The errors were identified by means of linear regression analysis and subsequently subtracted from the raw data. In addition, obvious outliers were removed from the data.

The errors are given by:

$$PartTilt = \alpha r Sin\Theta + \beta r Cos\Theta$$

$$MachineSquareness = \gamma r$$

$$OneThetaPiston = \xi Sin\Theta + \zeta Cos\Theta$$

Where r is the radius and Θ is the angular coordinate of the system. α, β, γ, ξ ,ζ and k are constants whose values are obtained from the regression analysis.

$$TotalError = \alpha r Sin\Theta + \beta r Cos\Theta + \gamma r + \xi Sin\Theta + \zeta Cos\Theta + k$$

The one theta piston error could be a part error as well as a systematic machine error. In order to separate the two errors, a reversal technique was used. The part was rotated 180 degrees on the spindle where new data was acquired and compared with the previous data. No one theta piston error was detected in the optical flat.

The regression analysis and correction of the raw data was done on a PC with a spreadsheet program. After the data had been corrected for the above systematic errors, a coordinate transformation from the polar coordinates to cartesian coordinates was made. Linear interpolation was used to fill out an array with equally spaced X and Y coordinates. The reason for doing this was to allow the use of a commercially available three dimensional plot routine. Figure 2 shows the result from one of our sets of data.

The results of the data taken interferometrically are shown in Figure 3. They can be compared visually to the results in Figure 2 where it can be seen that there is a general agreement as to the shape of the figure. There is also agreement in the rms and peak to valley values.

Conclusions

Both the LODTM and the interferometric measurements showed the figure of the optical flat to meet its 1 microinch p-v certification, and the longer wavelength figure errors within this range were in good agreement. The principal difference appeared to arise from the disturbance of the LVDT measurements by fine surface particulates. For flats, interferometry has a clear advantage in terms of testing time and cost. However, the exercise was motivated by the fact that it contains the dominant LODTM errors that would arise in the measurement of figure errors for a long-radius aspheric surface, an arena of much greater difficulty for interferometry.

References

1. R. R. Donaldson and S. R. Patterson, "Design and Construction of a Large, Vertical Axis Diamond Turning Machine", Lawrence Livermore National Laboratory UCRL-89738, and SPIE Proceedings, Vol. 433 *Ultraprecision Machining and Automated Fabrication of Optics*. Bellingham, WA, 1983.

2. S. R. Patterson, "Development of Precision Turning Capabilities at Lawrence Livermore National Laboratory", Lawrence Livermore National Laboratory UCRL-94719 and Proceedings of the Third Biennial International Machine Tool Technical Conference, Chicago, Ill., September 3-10, 1986.

3. W. T. Estler and E. B. Mcgrab, "Validation Metrology of the Large Optics Diamond Turning Machine", report NBSIR 85-3182(R), National Bureau of Standards, Center for Manufacturing Engineering, Automated Technology Division, Gaithersburg, MD (1985).

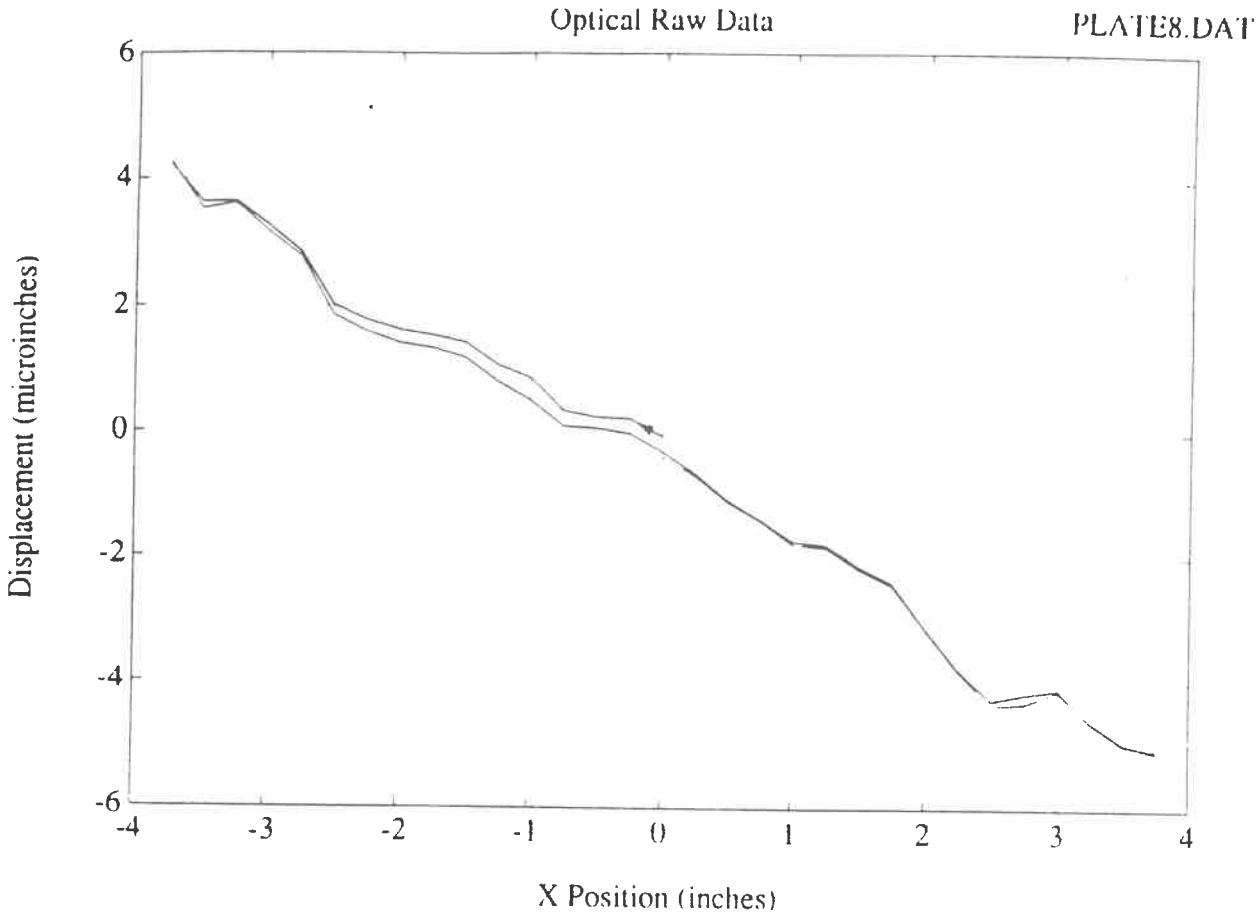

Figure 1 - Deviation vs. Radial Position for a Diametral Data Set

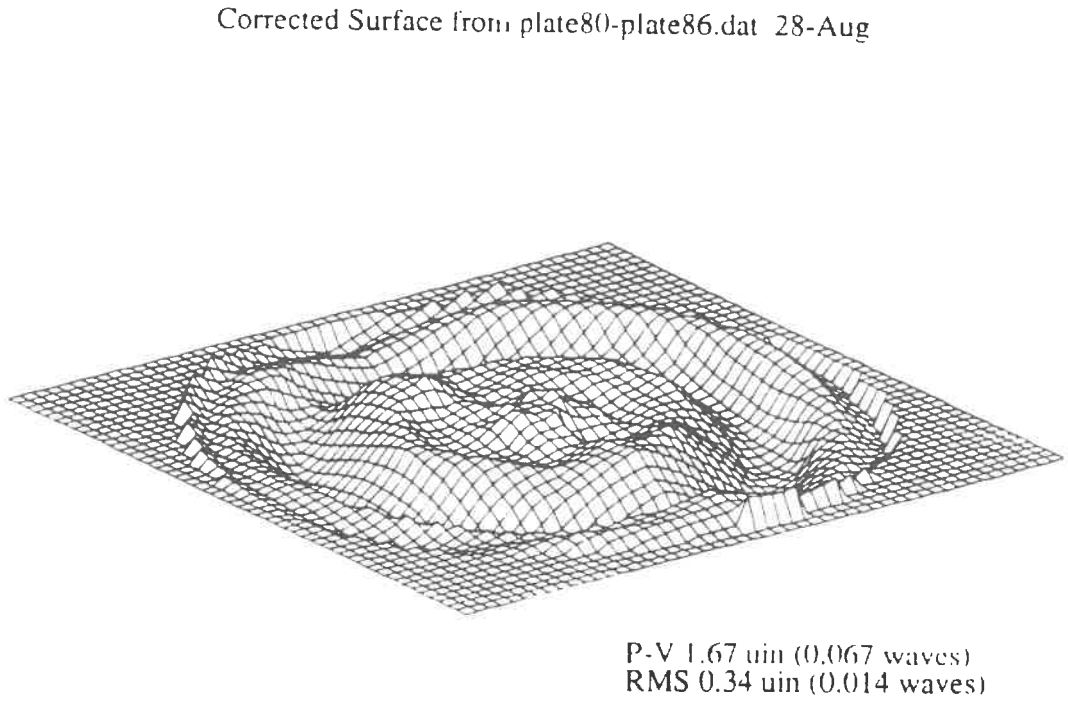

Figure 2 - Plot of Corrected Data Showing the Surface

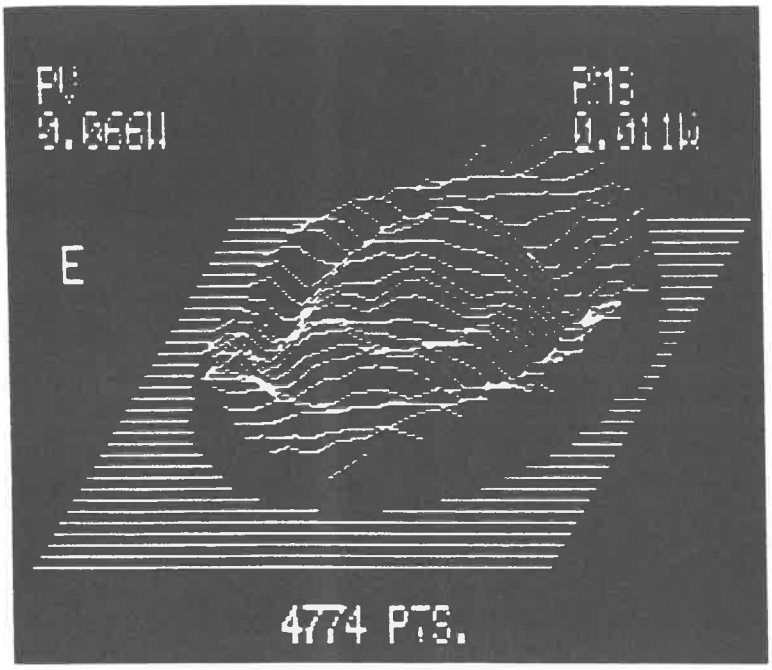

Figure 3 - Results of Measurement by Phase Shifting Interferometry

A scanning differential interferometer to measure index heterogeneity

Norman Bobroff, Alan E. Rosenbluth, Michael Hatzakis Jr.
IBM Thomas J. Watson Research Ctr.
P.O. Box 218 Yorktown Hts. NY 10598

Introduction

To ensure diffraction-limited performance in an optical system, index nonuniformity in the glass must be characterized at a resolution exceeding the ratio of the wavelength to the total optical path. The physical relationship between index inhomogeneity and local mass density is also used to infer the mass distribution of precision glass rotators for gyroscopes [1, 2]. Schlieren and interferometric methods to measure index heterogeneities [1, 3-6] have been developed, with interferometric techniques demonstrating fractional resolutions in optical path length (OPL) better than 10^{-6}. For highly corrected refractive optics used in microlithography, a uniformity in OPL $\lesssim 10^{-6}$ is required. We have developed a scanning interferometric technique which resolves fractional OPL changes to $\simeq 2 \times 10^{-8}$ in samples of fused silica 50mm on a side and larger. This corresponds to an OPL sensitivity of about 2nm. The differential measurement configuration of this optical system is highly immune to vibration and laboratory temperature changes. Variations in OPL caused by surface figure are separated from those due to bulk index heterogeneity through the use of a thin film of index matching liquid. Surface tension localizes the liquid between the scanning sample and the fixed interferometer optics.

Instrument

An overview of the instrument showing the path of the glass sample as it scans through the measurement and reference beams of the differential interferometer is presented in Fig.1. In the differential measurement configuration, the sample OPL gradient is measured at a grid of points in the X-Y plane. The X-Y scan motion is controlled by DC servo motors and data is automatically acquired while the stage is scanning. First, the path difference between the measurement (M) and reference (R) beams is measured with the cube in an initial orientation, designated as the X orientation for convenience. The cube is then rotated 90° and rescanned to acquire the orthogonal Y gradient. Reconstruction algorithms discussed later in the paper use the X and Y gradient data to produce an OPL map of the sample.

The interferometer optics are described with reference to Fig.2. A frequency stabilized Zeeman laser (Hewlett-Packard 5501) produces orthogonally polarized frequency states which are separated into parallel measurement and reference probe beams by a commercial differential interferometer optic [7] (Hewlett-Packard 10715A). The 1 e diameter of each beam is 1.5mm, and the beams are separated by 10mm. In the differential configuration, both beams are transmitted to the sample through a rigidly mounted laser window which defines the top of the scan cavity. The upper view of the Fig.2 inset shows the laser window used in the differential OPL gradient measurement. The HP 10715A interferometer optics directs both the M and R beams through the transmitting left half of the window in the first up-down pass. After reflecting from a mirror at the bottom of the scan cavity, and returning to the HP unit, both beams are again directed downwards in a second pass, where they are re-emitted symmetrically reflected about the optical axis as indicated in the Fig.2 inset. The beams enter the right side of the laser window which has a mirror coating on the surface above the sample. The beams return to the HP 10715A where they are recombined and sent to the receiver. The phase of the receiver signal relative to a reference provided by the laser head is measured by an HP 3575A gain-phase meter with

a noise limited resolution of about $\pm 0.2°$ of phase. The accuracy of the phase meter is better than $\pm 4°$ over 360°. 360° is one fringe or 316.5nm of OPL for a 633nm HeNe laser and the conversion from nanometers of OPL to degrees of phase is $0.9°/nm$. The measurement configuration is converted from differential OPL gradient to single beam operation by substitution of a three quarters mirrored window, shown in the lower view of the Fig.2 inset, for the half mirrored window. This window passes a single measurement beam into the sample.

An important feature of the differential measurement configuration is that linear motions of the mirrors and changes in cavity length do not introduce phase shifts between the probe beams. Also, because both the measurement and reference arms of the interferometer are reflected from each mirror surface, tilt movements of the cavity window and mirror do not introduce phase shifts between the beams. For optics which are kinematically mounted or are not stressed to the point of nonlinear deformation, the instrument is insensitive to structural perturbations introduced by vibrations or thermal gradients. This immunity extends to motions of the test specimen as well. Translations of the sample along the cavity do not affect the measurement. Small rotations of the sample about an axis in the X-Y plane, as might be caused by imperfection in the scan motion, introduce a phase change proportional to the product of the OPL gradient and the square of the rotation angle. The scan stage straightness is less than 1.0 mrad and the rotation effect is thus less than 0.1nm for a sample 100mm on a side, with a local OPL gradient of $10^{-3} nm.^{-1}$. OPL changes in the HP 10715A are less than 1nm in the presence of ambient thermal variations as rapid as $4K\,hr^{-1}$. [8].

The surface figure of the sample is isolated from bulk index heterogeneity by index matching the cavity window and mirror to the test specimen. Surface tension supports thin films of index liquid at the specimen-laser window and specimen-cavity mirror interfaces. The ability of the index matching liquid to isolate surface figure from bulk variations is illustrated in the data of Fig.3. Fig.3a shows scan data from a SiO_2 sample with an evaporated calibration step of SiO_2 which is 25 nm high. The phase step height is (n-1) × 25nm × 0.9 degrees/nm, or 10° for a thin film SiO_2 index of n = 1.44. The step is well resolved in the raw phase meter data. Fig.3b shows the same step scan, but with a 75um film of index matching liquid. The step is no longer visible and the data shows the index heterogeneity of the bulk sample. Liquid films from 50um to 150um were used with indistinguishable results. For comparison, Fig.3c shows the short term instrument noise level by displaying as a surface 600 data points acquired at a fixed sample position.

Although the HP10715A differential optics are environment insensitive, the thermal coefficient of refractivity of the fused silica specimens is large [9], $\frac{\partial n}{\partial T} \simeq 1 \times 10^{-5} K^{-1}$, and thermal gradients must be suppressed. A local temperature fluctuation of 10 mK introduces an index change between beams of $\delta n/n \simeq 10^{-7}$, or 10nm in OPL. The instrument is placed in a insulating polystyrene enclosure and button type negative temperature coefficient thermistors fitted with a teflon sheath (Yellow Springs 44036) are used to monitor the temperature at several locations on the sample cube and the instrument frame. The thermistors have a resistance, R, of about 10KΩ at 20°C, and a temperature sensitivity $dR/dT = -420\Omega\,K^{-1}$. A test for parasitic temperature dependence and noise in the resistance measurement was made by substituting 10kΩ reference resistors for the thermistors. The temperature sensitivity, dR/dT, of the foil resistors (Vishay model VH102K) is less than $10^{-5}\Omega\,K^{-1}$ from 20°C to 30°C and the parasitic influence of temperature on resistance measurement is less than the multimeter noise of 0.4Ω. Temperature gradients are measured to about + -2mK.

Data Analysis and Sample Reconstruction

Though the instrument provides greatest accuracy in two-beam mode, the differential format of the resulting data may not be immediately useful. Instead, one usually seeks a map of the sample OPL as a function of position across the aperture. The simplest way to reconstruct the OPL profile from measured two-beam difference data is by direct integration or summation. Unfortunately, as the number of measurements in each scan line increases, summation of low-level noise in the data leads to unacceptable fluctuation in the reconstructed OPL map. In the presence of noise, more sophisticated reconstruction algorithms are required. Some of the noise arises from instrument drift, and may have a correlation time longer than the interval between successive difference readings. If the sample is also of sufficient quality that the underlying OPL change between adjacent scan lines is smaller than the noise fluctuation, the scan data will show a more rapid fluctuation in the cross-scan direction than along the scan. Fluctuation between scan lines causes OPL profiles reconstructed by simple integration to show significant up-down noise oscillations on the scale of the scan spacing. These fluctuations can be eliminated by suitably filtering the data or reconstruction, but we have found that fairly extensive smoothing is needed for good results.

A better approach is to exploit the redundancy in the data. The OPL is a single valued function (to within an undetermined constant), so the change in OPL between any two points can in principle be calculated by integrating the OPL gradient along any path between the points. An equivalent statement is that the curl of noise-free OPL gradient data must be zero. Noise that takes the form of fluctuations between adjacent scans will usually have a curl departing substantially from zero, and can in principle be distinguished from the underlying OPL gradient by exploiting the redundancy in the full x and y datasets. A simple approach along these lines is to integrate the x and y difference data along multiple paths, and to average the result.

Though multiple path integration filters much of the noise, the reconstructed OPL profile would typically require additional smoothing to be suitable for use in optical fabrication. While such smoothing is commonly resorted to, e.g. by Zernike polynomial fits, a more elegant approach is to treat the OPL map as an unknown, and then find the solution which best fits the full x and y datasets together. This fully exploits the measurement redundancy, and is similar to the approach taken by Rimmer to evaluate shearing interferograms [10]. This approach is equivalent to obtaining the best fit solution to

$$\nabla^2 OPL_{i,j} = \nabla \cdot \nabla OPL_{i,j} \quad (1)$$

The right side of eq.1 is the divergence of the measured OPL gradient, formed as the vector sum of the x and y difference maps. The OPL reconstruction problem is regarded as a potential problem governed by Poisson's equation, with the measured gradient serving as a source term. Eq.1 is satisfied by definition in the absence of noise. According to Helmholtz' theorem, the vector field represented by the noise in the x and y scans can always be written as the sum of a gradient and a curl. The curl noise component is automatically filtered out of the solution by the divergence operator on the right of eq.1, since $\nabla \cdot \nabla \times \equiv 0$. The gradient component of the noise constitutes a physically acceptable OPL, and cannot be filtered from the data without additional a priori information. A detailed development including boundary effects is given Rosenbluth[11].

Three sets of x-y scan data, reduced by eq.1, are shown in Fig.4. Data are taken from the same sample over several weeks to quantify the long and short term repeatability of the instrument. Fig.4a is a reconstructs a sample scan with no index matching liquid, so that residual surface contributions are included. Fig.4b shows the departure from 14a in a reconstruction made from data taken a few minutes later, while Fig.4c shows the change associated with a third dataset taken after a 10 day delay.

Reconstructions from five scans, taken over the same 10 day period, show a maximum departure from one another of 0.2 ppm, and an RMS departure of 0.06 ppm = 10^{-7} = 9nm.

Acknowledgments

R.Myer was responsible for the portions of the mechanical design and fabrication. S.Lovas prepared the samples. We thank Dr. H. Harary of NIST for his advice on thermistor temperature measurement.

[1] M. A. Player, Quartz homogeneity studies, Stanford contract PR4590, report #25., June 1989.

[2] J. P. Turneaure, C. W. Everitt, B. W. Parkinson, D. Bardas, J. V. Breakwell, S. Buchman, W. S. Cheung, D. E. Davidson, W. M. Fairbank, S. Feteih, D. Gill, R. Hacker, G. M. Keiser, J. M. Lockhart, B. Muhlfelder, R. T. Parmley, X., "The gravity-probe-B relativity gyroscope experiment development of the prototype flight instrument," *Adv. Space Res.*, vol. 9, pp. 29-38, 1989.

[3] D. Tentori, "Homogeniety testing of optical glass by holographic interferometry," *Applied Optics*, vol. 30, pp. 752-755, 1991.

[4] J. Schwider, R. Burow, K. E. Elssner, R. Spolaczyk, and J. Grzanna, "Homogeniety testing by phase sampling interferometry," *Applied Optics*, vol. 24, pp. 3059-61, 1991.

[5] E. E. Roberts and P. Langenbeck, "Homogeniety evaluation of very large disks," *Applied Optics*, vol. 8, pp. 2311-14, 1969.

[6] L. W. Tilton, E. W. Rosberry, and E. T. Badger, "Refractive uniformity of a borosilicate glass after different annealing treatments," *J. Res. Natl. Bureau of Standards*, vol. 49, pp. 21-32, 1952.

[7] R.R. Baldwin and G.J. Siddall, "A Double Pass Attachment for the Linear and Plane Mirror Interferometer," *Proc. Soc. Photo. Instr. Eng.*, vol. 480, pp. 78-84, 1984.

[8] C. R. Steinmetz, "Displacement measurement repeatability in tens of nanometers with laser interferometry," *Proc. Soc. Photo. Instr. Eng.*, vol. 921, pp. 406-420, 1988.

[9] I. H. Malitson, "Interspecimen comparison of the refractive index of fused silica," *J. Opt. Soc. Am.*, vol. 55, pp. 1205-1209, 1965.

[10] M.P. Rimmer, "Method for Evaluating Lateral Shearing Interferograms," *Applied Optics*, vol. 13, pp. 623-629, 1974.

[11] N. Bobroff and A.E. rosenbluth, "A scanning differential interferometer to measure index heterogeneity," *Applied Optics*, vol. 31, p. In Press, 1992.

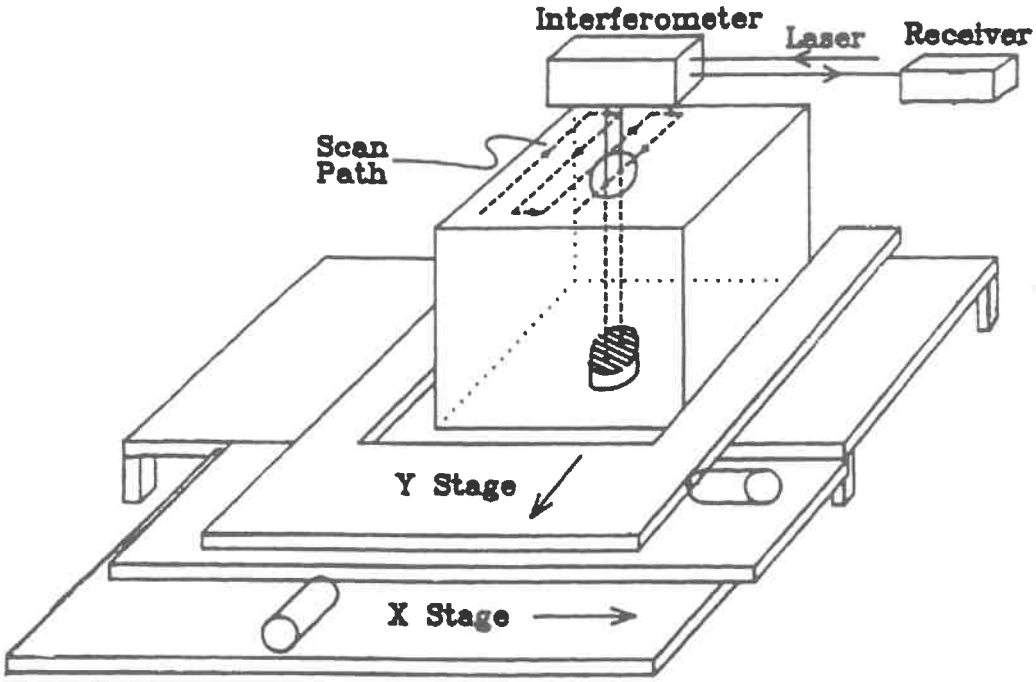

Fig.1 Mechanical configuration of the scanning interferometer. The sample is scanned through fixed optics.

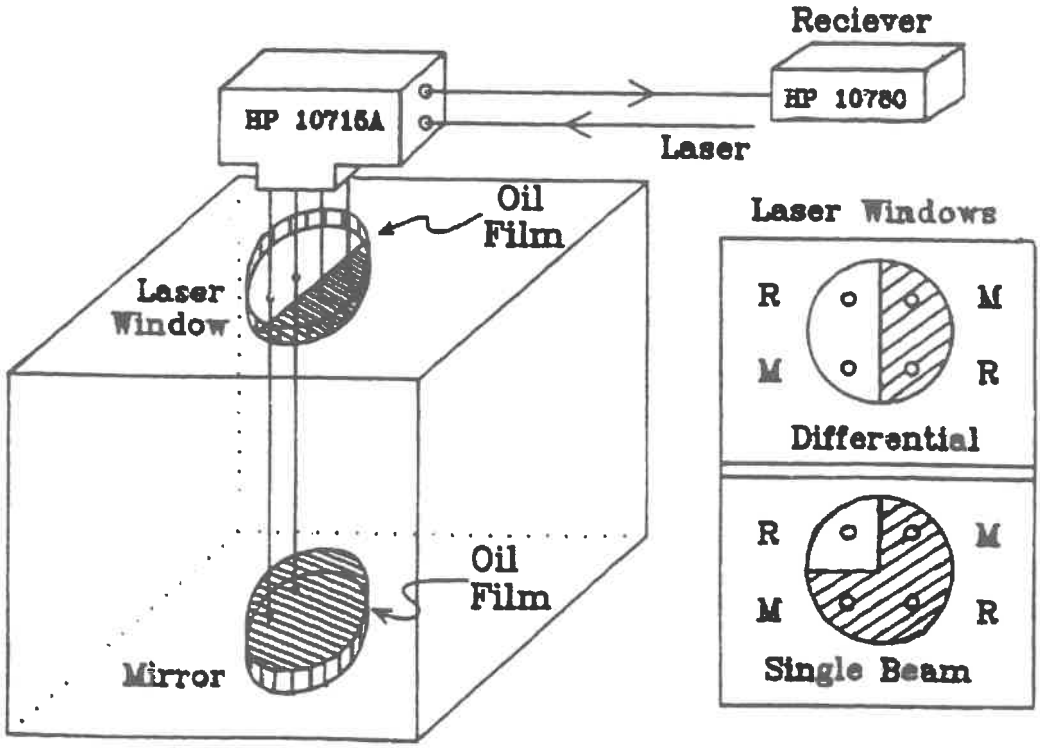

Fig.2 Instrument optics. The upper inset shows the cavity window for differential mode, where two of the four beams are reflected, the lower shows the window for single beam mode, where three beams are reflected.

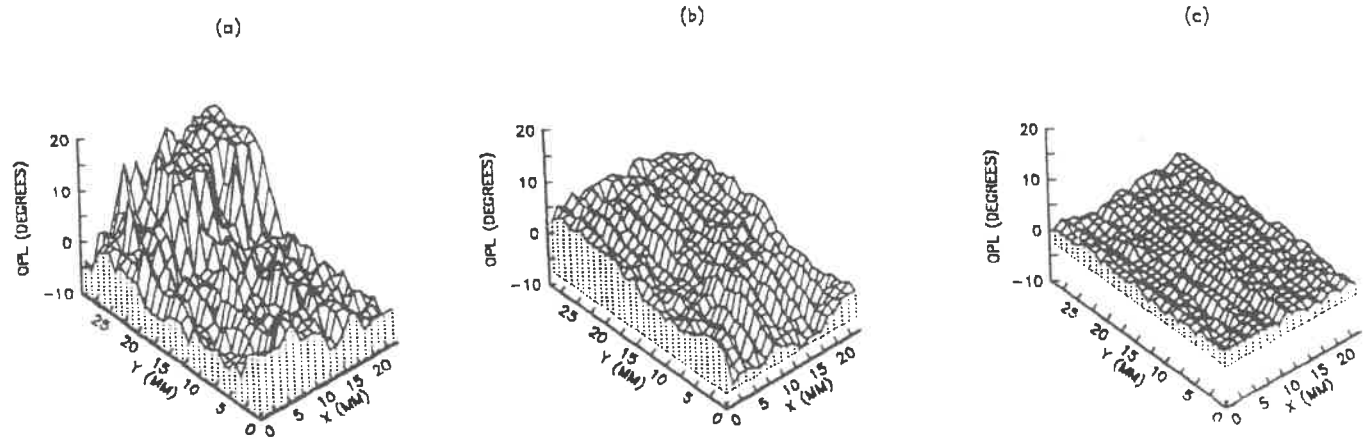

Fig.3 a) A differential mode scan over a 10° surface phase step without index matching. b) Scan with index matching. c) Instrument noise floor.

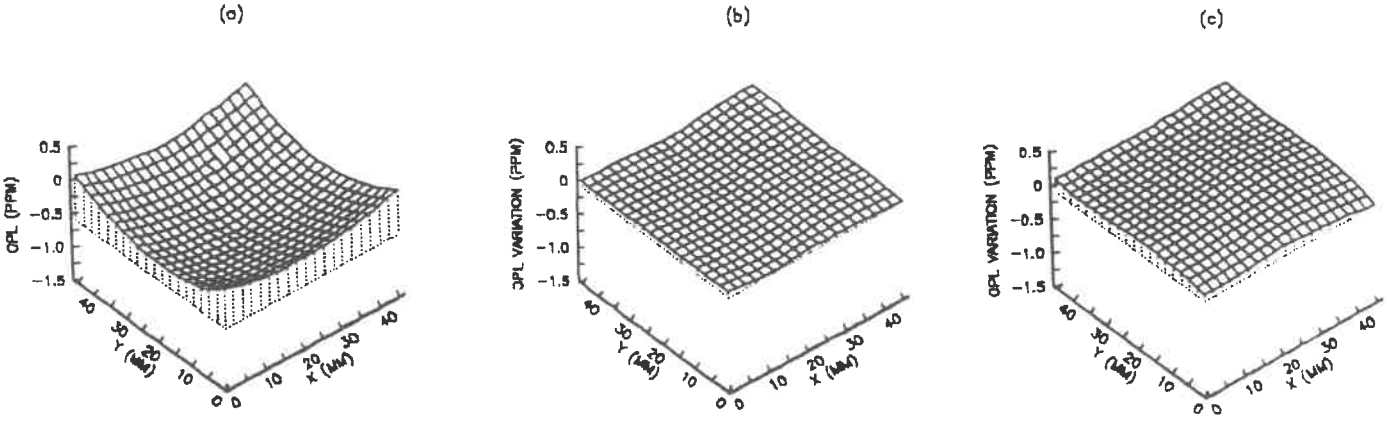

Fig.4 a) Reconstructed OPL surface of Fig.11. b) Difference between OPL reconstructions from data sets taken with 30 minutes of each other. c) Difference between OPL reconstructions from data sets taken several weeks apart.

DIRECT PHASE CONVERSION FOR VERY LOW FREQUENCY MEASURAND DETECTION IN A FIBEROPTIC INTERFEROMETRIC SENSOR

Lisa C. Giulianelli, A.J.Seltzer, and A.B.Buckman
Research Applications, Inc., and
University of Texas at Austin, Electrical and Computer Engineering Department,
Austin, Texas, 78712

1. Introduction

Two difficulties often encountered by designers of fiberoptic interferometric sensors are the detection of very low frequency measurands and the extraction of unambiguous phase information at imposed phase shifts which are larger than 2π radians. A signal processing technique which addresses both problems, the Direct Phase method [1], is presented here. The technique addresses the aforementioned difficulties to extract unambiguous phase information at extremely low frequencies. The implementation discussed in this paper is a prototype chemical sensor; a fiberoptic interferometric sensor is used for photacoustic spectroscopic detection. Photacoustic spectroscopy (PAS)[2] is a technique used to detect trace chemical concentrations of gases, as well as solids and liquids.

If a chopped light source irradiates a sample gas, the molecules in the gas will absorb the radiation in the form of increased vibrational energy. This increased vibrational energy is then converted to thermal energy, which, in a chamber of constant volume, becomes an increase in pressure. The exceedingly high sensitivities of fiberoptic sensors [3], make them ideal for detecting miniscule pressure changes in a PAS system.

In order to stay within the linear range of operation of a PAS system, the chopping frequency of the incident light must be well below the frequency of the gas molecules' relaxation rates (rates of vibrational-to-thermal energy transfer). Usually, this translates into chopping frequencies of a few hertz. Low-frequency signal processing detection has always been problematic because of the appearance of 1/f noise (that is, the sharp increase in noise at frequencies approaching zero hertz). Extracting a signal at frequencies as low as several hertz is difficult in this region because the signal-to-noise ratio (S/N) is lowered by the high 1/f noise floor. If the signal of interest is somehow moved to a higher frequency (where the noise floor is lower), the S/N increases. A popular solution has been that of heterodyne detection [4] in fiberoptic sensors. The Direct Phase technique uses a unique optical configuration [5] to obtain a heterodyne output directly from the transmittance of the fiberoptic sensor, and employs simple phase detection circuits to extract phase information. This phase information may be at frequencies as low as one hertz; the signal processing

scheme extracts the phase unambiguously. The dual-loop interferometer itself also offers a reduction in common-mode noise response[6].

The optical transmittance of the interferometer is

$$T = \frac{1}{2}[\ 1 + \sin \Phi \sin P\ ] \qquad (1)$$

where Φ is the phase difference of the first loop, and P, of the second loop (see Figure 1). The second loop is where the sensing takes place. A phase shifter is modulated in each of the loops with a time dependence of the form

$$\Phi = \Phi_0 + \Phi_1 \sin(\omega t) \qquad (2)$$

$$P = P_0 + P_1 \sin(2\omega t) \qquad (3)$$

where Φ_0 is a dc phase bias and P_0 is the measurand phase shift. Equations (2) and (3), when substituted into (1), give a time-dependent transmittance resulting in infinite series of Bessel functions. The resulting series have terms which take the form,

$$\begin{bmatrix} \sin \\ \cos \end{bmatrix}(n\omega t)\begin{bmatrix} \sin \\ \cos \end{bmatrix}(2m\omega t) \qquad (4)$$

where n and m are any non-negative integers and either trigonometric function in the sets of square brackets may occur in any combination. Products for many combinations of n and m will produce difference frequencies at ω and 2ω which contribute to the total amplitudes at these frequencies. The Direct Phase method makes use of the harmonic information to extract phase information in the form of a phase modulated carrier.

2. Experimental Setup

The fiberoptic sensor, electronics, and data acquisition portions [7] of the chemical sensor are shown in Figure 1. The entire chemical sensor is a superset of this arrangement, where the PAS system acts as the optrode of the fiberoptic sensor. The data acquisition system was used for signal processing in addition to obtaining raw data; both processing schemes were implemented entirely within this system. A 1-MHz, four-channel input/output board acquired the data, and all digital signal processing (DSP) was performed in software for maximum flexibility. This DSP system, in addition to acquiring live data, was also able to simulate data for calibration purposes.

The fiberoptic interferometer used was the dual-loop Mach-Zehnder Interferometer (or 1.5 MZI) invented at the University of Texas, which offers a reduction of or elimination of common-mode noise such as temperature drifts, vibration, erroneous pressure differences, etc. The phase shifters consisted of piezoelectric transducers around which optical fiber from one of each of the two loops was wrapped tightly. For

modulation, a sinusoidal voltage was applied to the phase shifters and the piezoelectric transducers stretched the fiber accordingly. Thus, a phase modulation over a large dynamic range could be applied to the interferometric sensor.

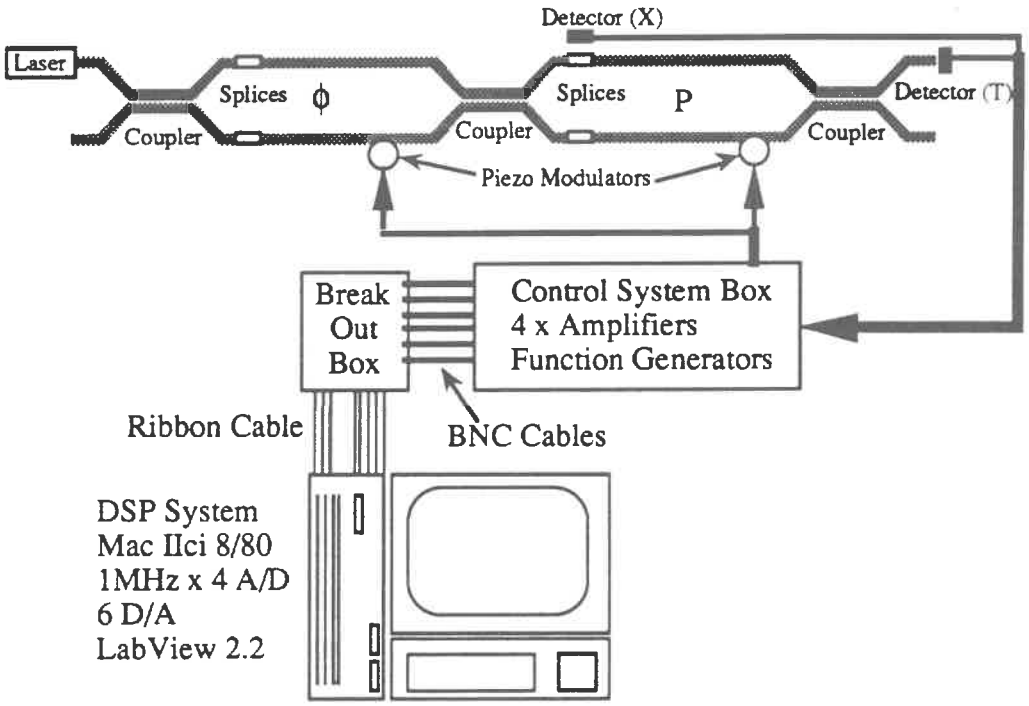

Figure 1: The dual-loop interferometric sensor, control electronics, and data acquisition/DSP system used for measuring the photoacoustic effect.

The chemical sensing optrode portion of the entire system used nitrous oxide as the sample gas to be detected and argon as the carrier monatomic gas. As a broad-band infrared source was strobed at frequencies from one to eight hertz on the gas sample cell, the pressure change in the cell was detected via the fiberoptic sensor. As a new chemical concentration of the sample gas was to be detected, the entire chemical optrode chambers were emptied and then re-filled with the new ratio of sample to carrier gas. The signal processing schemes then were used to read the new concentration as a pressure difference.

3. Results

As a simple demonstration of the signal processing scheme, a simulated sinusoidal measurand input of 4 Hz was used. Figures 2 and 3 show the input measurand and the demodulated output, respectively.

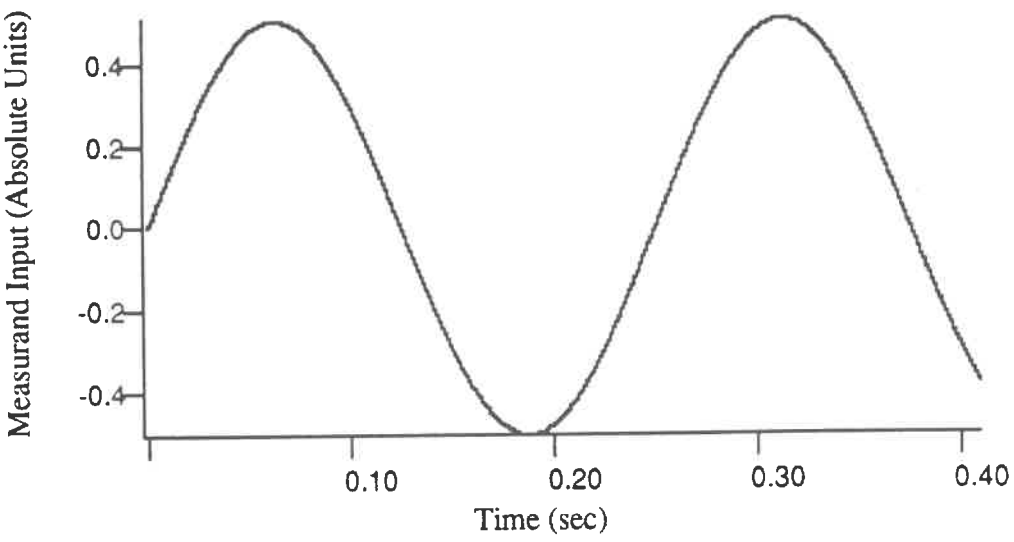

Figure 2: Sinusoidal measurand (test signal) at 4 Hz input to fiberoptic sensor.

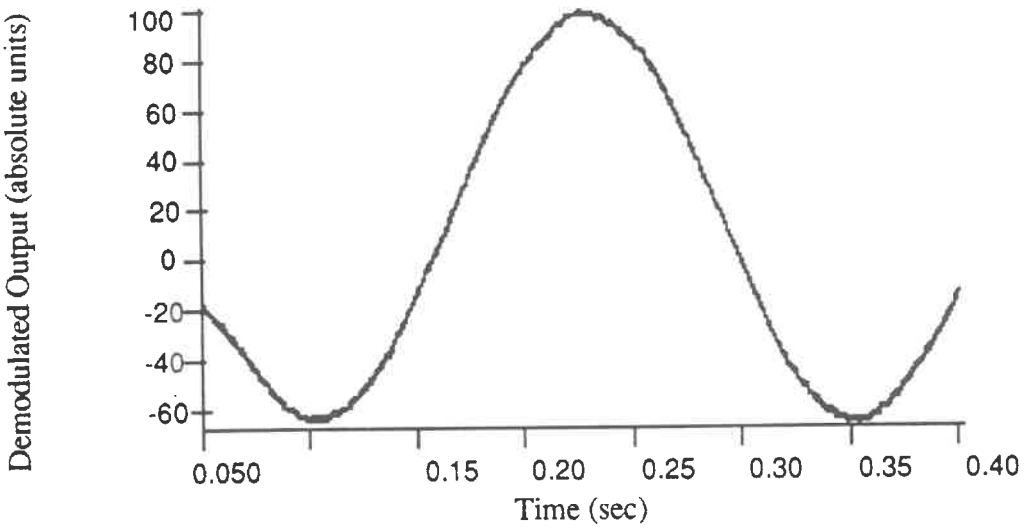

Figure 3: The resulting demodulated output as obtained by the Direct Phase method.

To obtain this demodulated output, the transmittance acquired by the data acquisition system was digitally filtered at the fundamental of a sinusoidal modulation signal of 1100 Hz imposed upon the first loop (the ϕ-loop) of the interferometric sensor. When compared to a reference signal at the modulation frequency, a pulse-width-modulated signal resulted.

This signal was then digitally low-pass filtered, giving the demodulated signal.

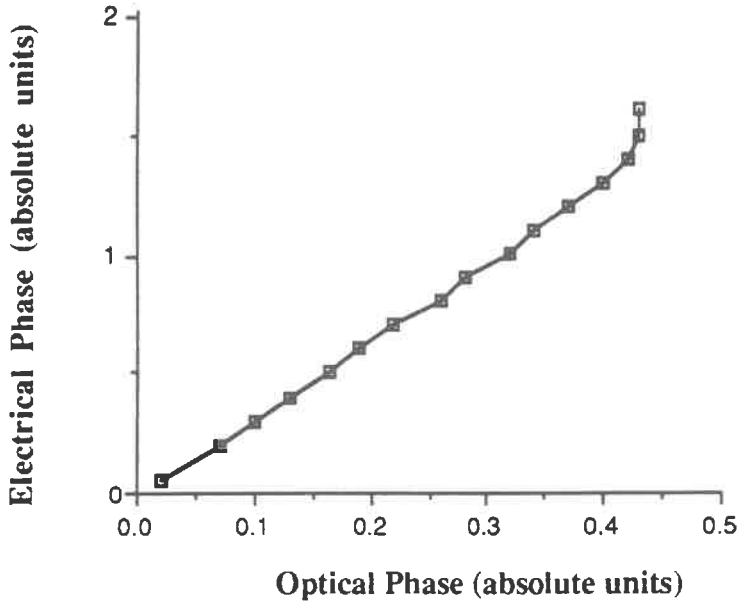

Figure 4: Linearity of the Direct Phase method.

To determine the linearity of the method, the sinusoidal measurand amplitude was swept from 0.1 to 1.6 Vpp and the resulting electrical phase versus optical phase is shown in Figure 4.

Chemical concentrations, as determined via the fiberoptic sensor's pressure measurements, will be presented. The chemical concentration of nitrous oxide in a carrier gas of argon is determined according to the extent of the acoustic (pressure) changes induced when irradiated with the broadband infrared source. In addition, an overview of the chemical sensing optrode using the photoacoustic effect will be given.

4. Conclusions

In conclusion, we have demonstrated the operation of a prototype chemical sensor using the Direct Phase technique for the fiberoptic interferometer used at the detection end of the PAS system. The method allows the user to obtain very low frequency data without the associated low-frequency noise resident near dc. In addition, linearity over a dynamic range greater than that of the conventional interferometer was demonstrated, and was linear, as shown in Figure 4.

References

[1] L.C.Giulianelli, A.B.Buckman, *Direct Optical-to-Electrical Phase Conversion in a Fiber Optic Interferometer*, **Proceedings of Precision Interferometric Metrology**, 1992 Spring Topical Meeting, April 7-9,1992, ASPE, 22-26 (1992).

[2] Yoh-Han Pao, ed., **Optoacoustic Spectroscopy and Detection**, Academic Press, New York, 1977.

[3] B.H.Tyrone, *The Analysis of a Stabilized 1.5 Mach-Zehnder Interferometric Sensor with Enhanced Sensitivity and Common-Mode Compensation,* Dissertation, University of Texas at Austin, 1991.

[4] J.H. Cole, B.A.Danver, and J.A.Bucaro, *Synthetic-Heterodyne Interferometric Demodulation,* IEEE Journal of Quantum Electronics, Vol. QE-18, No. 4, pp. 694-696, April 1982.

[5] A.B.Buckman, *Analysis of a Novel Optical Fiber Interferometer with Common-Mode Compensation,* IEEE Journal of Lightwave Technology, Vol. 7, No. 1, pp. 151-157 (1989).

[6] A.B.Buckman, *General sensitivity enhancement and common-mode compensation principle for interferometric fiberoptic sensors,* IEEE Journal of Lightwave Technology, Vol. 8, pp. 1456-1460 (1990).

[7] A.J.Seltzer, *Low-Frequency Measurand Detection in Interferometric Fiber Optic Sensors*, Dissertation, University of Texas at Austin, 1992.

A New Strategy for Inspecting Roundness Features

L. C. R. Carpinetti and D. G. Chetwynd

Department of Engineering - University of Warwick
Coventry CV4 7AL England

Algorithms for estimating reference figure fits for shape measurement use either a least squares approach or a constrained optimization of a geometric parameter of the figure. Both because it is an important class in its own right and because it is a good vehicle for studying algorithmic approaches, there has been a strong concentration in the literature on roundness measurement, where fits to minimum radial zone, minimum circumscribing radius and maximum inscribing radius are all of interest. Highly efficient solution techniques for these use a local parameter linearization within an "exchange algorithm" [Chetwynd and Phillipson, 1980]. Other approaches have been tried, for example non-linear weighted least square iterations [Goto and Iizuka, 1977], and Monte Carlo, Simplex and Spiral search techniques for non-linear parametrizations [Murthy, 1980], but not widely adopted.

Partly for historical reasons and partly because of computing efficiency, the methods specified in metrology standards [e.g. BSI, 1987] differ from the approach to the specification of tolerances in design standards [e.g. BSI, 1972]. This does not matter for simple circularity measurement, but there may be conflicts when several tolerances are used in combination, for example circularity, centre position and absolute radius. Inspection of geometric features of components in the context of a manufacturing process requires only that it be established that the measured features are contained within an acceptable tolerance zone. It does not require necessarily that any form of "best fit" be found. However in practice it is usual, to first find an optimal reference and then to test its parameters and the deviation of the features from it against the design specification. Consider, for example, the ring limacon reference [Reason, 1966; Chetwynd, 1979] . Common practice seeks to minimize the reference radius R while maintaining the condition that the profile is enclosed, that is subject to mathematical constraints $a\cos\theta_i + b\sin\theta_i + R \geq r_i$ **(1)** for N data points where (a, b) and R are the reference centre coordinates and radius respectively, and (θ_i, r_i) are the instrument polar coordinates of the profile.

The design specification for out of roundness actually imposes that the deviation of any data point r_i from the limacon reference must be less than the tolerance value specified in design, say t_r. This can be expressed by $(a\cos\theta_i + b\sin\theta_i + R) - r_i \leq t_r$ **(2)**. On combining this set of constraints with those imposed by the circumscribing reference condition, the existence of at least one feasible solution shows that the out of roundness is within tolerance and the workpiece passes inspection, without any need to optimize the parameters. Otherwise, the out of roundness is larger than that specified in design and the workpiece fails inspection. This formulation is directly comparable to the manual use of an annular template trying to enclose the profile.

There are many situations where not only the out of roundness but also the centre position of the cross section of a circular component is to be controlled. This would be specified by a geometric tolerance of concentricity or position besides the roundness tolerance. The specification tends to ignore the fact that these two features are interrelated. When the section is not perfectly circular, the definition of centre becomes to some extent a matter of interpretation and in practice the reference centre is used. Consequently, as the reference changes the measured centre position also changes.

It is better, therefore, to extend the previous approach with yet a further set of constraints. To satisfy the geometric tolerance this set should place a circular boundary central on the nominal position within which the trial centre must lie. In practice we have sought local linearization to ease

the computation and here a regular polygon is suggested as an approximation to the circle. The constraint set then relates to a set of lines of pre-defined slopes each having the same perpendicular distance from an origin corresponding to the nominal position of the feature. To illustrate, a square boundary region would be generated by the constraints $-t_c/2 \leq a \leq t_c/2$ **(3)** and $-t_c/2 \leq b \leq t_c/2$ **(4)**, where t_c is the concentricity or centre position tolerance value specified in design. This method is readily-extended to an octagonal boundary which will often be adequate while keeping the number of constraints small.

If the combination of constraint sets **1**, **2**, **3** and **4** results in unfeasibility, there is no reference figure with centre limited within a pre-defined position and out of roundness within tolerance. Consequently, the workpiece fails inspection. The ideas outlined above attempt to simulate the action of a GO-NOGO gauge in software.

This reformulation is of little practical significance unless there is an efficient method of testing for feasibility. The exchange algorithm approaches are not applicable but Fletcher, 1970, provides a simple algorithm for calculating a feasible vertex for optimization problems subject to linear constraints. This method does not use ideas of adding artificial variables, as in the two phase simplex technique (see for example Hadley, 1962) which are computationally expensive for the problems of concern here.

The general problem is to find a feasible solution of the set of linear constraints. As with Simplex, the method seeks a vertex, that is a point at which the zero contours of n constraints intersect, where n is the number of variables. It iterates from one vertex to another by interchanging one constraint at a time, until either a feasible vertex is found or until it is possible to say that no feasible point exists. An initial vertex must be chosen to start the process. Each iteration consists of moving along the half-line which is generated when one inequality constraint is removed from the basis, in an attempt to reduce the number of constraint violations.

A start up algorithm, based on the geometry of the fit, is used to select an initial vertex likely to be not grossly infeasible and so, on average, reduce the number of iterations required. The index of the point in the data array with the largest positive value will define the index of the constraint with largest slope. If this point lies in the first quarter of the data points array, then the upper bounds of variables a and b are used as an initial vertex. Else, if the point lies on the second quarter, then the upper bound of variable b and the lower bound of variable a are used. Else, if the point lies on the third quarter, then the lower bounds of variables a and b are used. Finally, if the point lies on the fourth quarter, the upper bound of variable a and lower bound of variable b are used. The initial vertex is then defined by the intersection of the plane with largest slope with the planes corresponding to the selected upper or lower variable bounds.

These algorithms have been implemented for the ring and radial zone limacon cases and tested for efficiency, using a set of 10 profiles, digitized and stored, from nominally circular components. The parts included ground and turned shafts, in carbon steel and aluminium, with radii between 15 and 40 mm. Measurements were made on a Rank Taylor Hobson Talyrond 200 instrument under typical operating conditions. Samples were taken by a 12-bit analogue to digital converter at equal intervals of time corresponding to 512 nominally equiangular positions around one revolution of the instrument spindle.

The out of roundness according to the ring and minimum zone limacon references was measured by running a direct implementation of the standard exchange algorithms. Examples of tolerance values for the out of roundness as well as the centre position were defined as fractions of the mesasured error and reference centre respectively, so as to map the efficiency and the result of inspection (pass/fail) in comparison with the ring and minimum zone exchange algorithms. Taking Z as the out of roundness, values of $0.7, 0.8, 0.9, 1.0, 1.1, 1.2, 1.3$ of Z were used as roundness tolerances. In the case of the centre position tolerance, a square zone equaly spaced around the

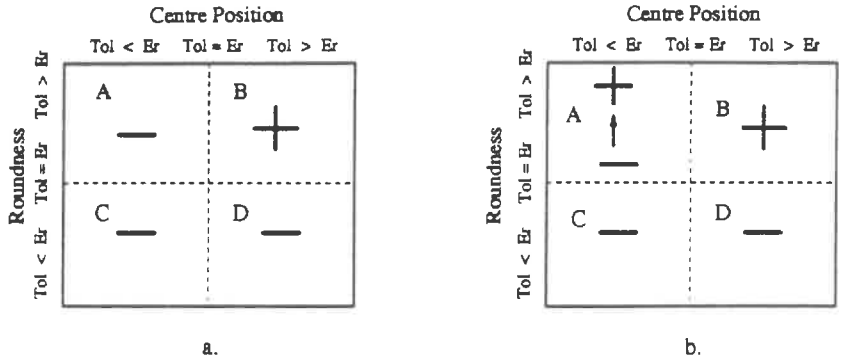

Figure 1: Pass/fail regions for exchange **a.** and gauge algorithms **b.**

instrument coordinate system origin was defined. Values of $0.7, 0.8, 0.9, 1.0, 1.1, 1.2, 1.3$ of the maximum reference centre coordinate $max(a, b)$ were used to define the perpendicular distance from the origin to the upper and lower bounds. Therefore, for each testpiece, and for each reference figure (either ring or zone limacon), a set of 49 different tolerance zones were fed to the algorithm, which returned a pass/fail flag.

The efficiency was measured in terms of execution time, number of iterations and number of floating point operations. The routines were written in C language, single precision floating point, and run under Unix, on a SUN 4/330, with 48 Mbytes of RAM (Random Access Memory) and speed of 16 MIPS (Milions of Instructions Per Second).

Figures 1a and 1b present a graphical illustration of the pass/fail regions according to the exchange and gauge algorithms, where the plus/minus signs indicate pass/fail inspection. Figure 2 presents the average number of iterations for the ring limacon. The pattern for the minimum zone is similar. The number of iterations when the tolerance is assumed to be the same as the actual error is slightly higher due to round-off errors.

In order to check whether the roundness error and centre position are satisfactory by directly using the ring and minimum zone references, tolerance values for both would have to be compared with the reference parameters. Note however that if the inspection fails because the reference centre position eccentricity is larger than the tolerance, there is no routine means of evaluating whether it is possible to define a new reference with its centre and out of roundness both within tolerance. This can be seen in figure 1a, where the pass status to a inspection procedure using the exchange algorithms is confined to region B only. This reveals a major disadvantage of the exchange algorithms if we attempt to use them in the inspection of several geometric features.

The formulation of the inspection problem as an extended linear programming problem with a test for feasibility overcomes this limitation. Refering to figure 1b, when the eccentricity of the minimum circumscribing or minimum zone reference (defined by the exchange algorithm) exceeds the design tolerance, it is possible to find a new reference such that the out of roundness as well as the reference centre position are within tolerance provided that the out of roundness obtained using the exchange algorithm is sufficiently less than the allowed out of roundness. This is illustrated by the change in sign in region A, figure 1b.

The gauge algorithm takes on average less than 2 iterations to get to the solution and the number of arithmetic operations is approximately $15N$ per iteration. The exchange algorithms take on average 3 to 4 iterations to get to the solution and the number of arithmetic operations is approximately $6N$ per iteration, where N is the number of data points, in this case 512. Although the gauge algorithm is not as fast as the exchange algorithms, the difference is not very significant because the computation time is of the order of one second. The new approach is thus quite practicable.

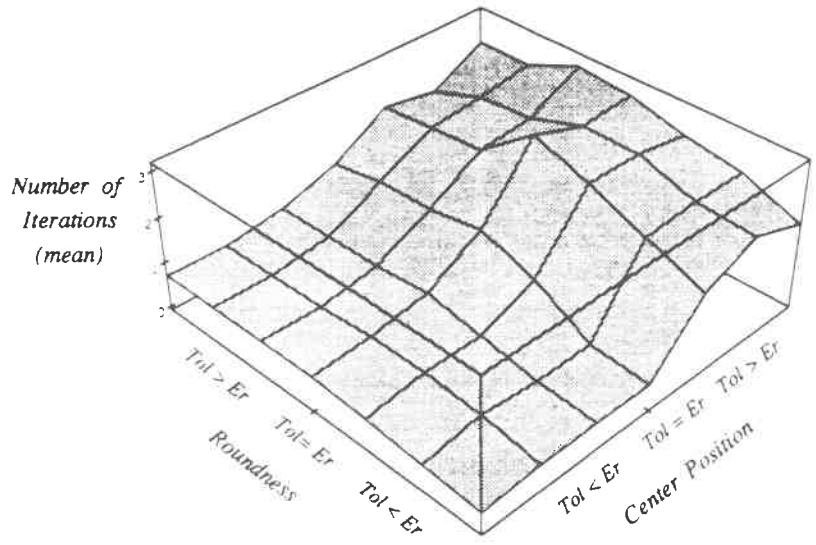

Figure 2: Average number of iterations of the gauge algorithm routine for the ring limacon

Finally, we note that neither the exchange nor the present method can be applied if local linearization is not possible, so more general techniques may be needed for fully automated inspection. Nevertheless, the present work illustrates a new line of approach that can well be applied in other shape inspection problems.

References

BSI. 1972. *Engineering Drawing Practice*, Part 1-3. London: British Standard Institution. BS308:1972.

BSI. 1987. *Assessment of Departures from Roundness*, Part1. London: British Standard Institution. BS3730:Part1:1987.

Chetwynd, D. G. , 1979. Roundness Measurement Using Limacons. *Precision Engineering*, vol. 1. pp. 137-141.

Chetwynd, D. G. and Phillipson, P. H., 1980. An Investigation of Reference Criteria used in roundness measurement. *J. Phys. E: Sci. Instrum.*, vol. 13, pp. 530-538.

Fletcher, R., 1970. *The Calculation of Feasible Points for Linearly Constrained Optimization Problems*. Harwell, UK: Atomic Energy Research Establishment Report AERE-R 6354.

Goto, M. and Iizuka, K., 1977. An Analysis of the Relationship Between Minimum Zone Deviation and Least Squares Deviation in Circularity and Cylindricity. *Proc. Int. Conf. Prod. Eng.*, New Delhi, India, pp. x61-x70.

Hadley, G., 1962. *Linear Programming*. Addison-Wesley Pub. Company: Reading, Massachusetts.

Murthy, T. S. R., 1982. A Comparison of Different Algorithms for Cylindricity Evaluation. *Int. J. Mach. Tool. Des. Res.*, vol. 22, pp. 283-292.

Reason, R. E., 1966. *Report on the Measurement of Roundness*. Leicester: Rank Taylor Hobson.

A NEW MEASURING METHOD OF CENTRAL POSITION OF SPINDLE ROTATION(1st Report:Steel Ball Method)

N.Ozawa, K.Takeuchi and T.Sugano
Mechanical Engineering Laboratory
Namiki 1-2,Tsukubashi,Ibaraki,JAPAN

Summary

In this paper a new measuring method of central position of spindle rotation (CPSR) is described. The principle of the new method is first discussed. Then, results of fundamental experiments on the CPSR of the hydrodynamic bearing spindle and hydrostatic bearing spindle are presented.

1.Introduction

The CPSR is affected by the spindle structure, the spindle bearing, rotational speed, machining conditions, external forces and so on. Especially with machine tool spindles, a change in the CPSR affects the machining accuracy of the workpiece. Therefore,it is necessary to measure the CPSR during the machining process and to minimize the amount of fluctuation in the CPSR. Matsuda and Eiju have developed an optical measuring method for the CPSR based on laser Doppler velocimetry /1/. We have also developed a new method of measuring the CPSR. This paper deals with the principle of the new method and the results of basic experiments.

2. New CPSR measuring method

2.1 Measuring principle

A precision steel ball is attached to the workpiece and an electronic capacitance-type transducer mounted on the tool slide on a three-dimensional sliding stage, as shown in Fig.1. The relative displacement is measured by detecting the fluctuation in gap distance between the ball and the transducer. Figure 2 shows principle of the new measuring method. The CPSR is on the Z axis and the steel ball is mounted at a distance "e" from the Z axis.

In the case of the axial error motion equal to zero, the ball shifts to the "broken line" position after a half-rotation of the spindle. The distance between points D and E i.e. the magnitude of z varies like a sine wave in synchronization with the spindle rotation. Then the magnitude changes with the same period as the spindle rotation. The closer the distance between the transducer and the CPSR, the smaller the magnitude of z becomes. The magnitude of z

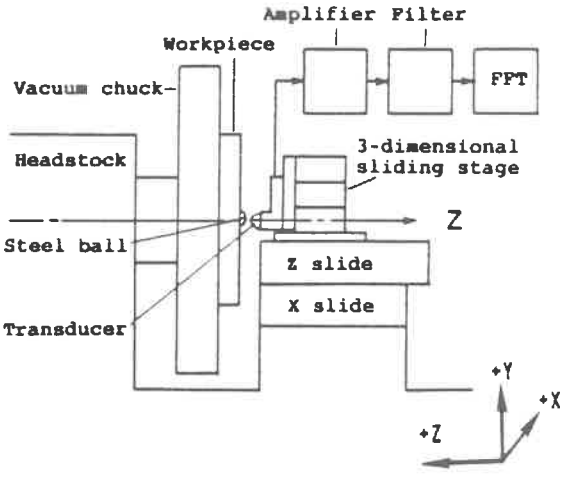

Fig.1 New measuring method

reaches a minimum value at the central position of rotation.

Assuming the ball is an ideal sphere, the magnitude of z can be expressed by the following equation :

$$z^2 + 2z\sqrt{r^2 - (y+e)^2} - 4ey = 0 \qquad (1)$$

Since the value e and y are very small as compared with radius r of the ball.Therefore,the value of z is proportional to the value of y.The larger the value of e,the larger the value of z becomes.

2.2 Results of the preliminary experiment

The steel ball was bonded with adhesive to the center of the workpiece. The ball used has an roundness of 0.025 μm. The output signal from the transducer is amplified and the undulation component synchronized with the rotation z is filtered out using a band-pass filter.

At the beginning of the experiment, the relation between amplitude of the output signal of the transducer and the gap distance, i.e., the displacement between the ball and the transducer, was investigated. As a result, the gain of the output signal is 1.25 times the case of the measurement of the relative displacement between the flat plane and the transducer. Figure 3 shows the result of the preliminary experiment. In this figure, the horizontal axis represents the transverse displacement of the transducer which was measured by another displacement transducer with a resolution of 0.1μm. The transducer was first moved in the +Y direction and then in the negative direction. Consequently, characteristics of the z exhibited a " V " shape, as illustrated in Fig.3. The magnitude of z is directly proportional to the displacement y. The minimum value of z is about 4nm. It may be considered that the residual component of z was caused by the effect of axial error motion and vibrations. Results of the experiment may be summarized as follows : 1)The CPSR exists in the region where the z falls

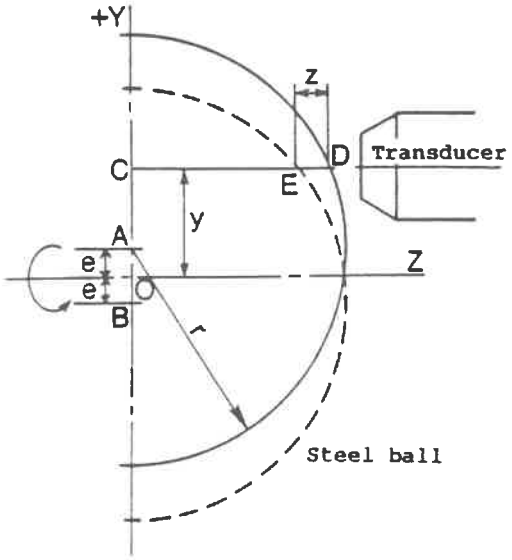

Fig.2 Measuring principle

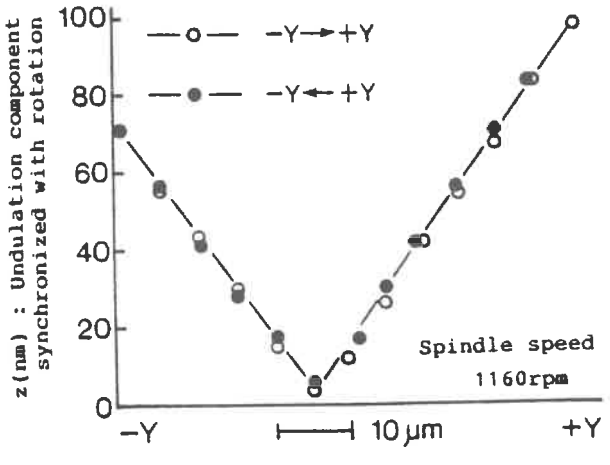

Fig.3 Relation between distance from the center and value z

below a few nanometers. 2) The measuring resolution of the CPSR depend upon the accuracy of the three dimensional sliding stage.

3. Measurement of the CPSR

3.1 The CPSR of the hydrodynamic bearing spindle

This bearing made by FAG Corp.,type HDKO, and is separated into 6 peripheral segments. In the journal bearings, a wedge-shaped oil film generally fills up the gap between the bearing and the spindle during rotation. The spindle rotates in the position where the resultant of the oil film pressure is balanced with external forces. Therefore, it may be assumed that the CPSR in this spindle fluctuate according to rotational speed, external forces, and so on.

From these factors, we tried to clarify the relation between the CPSR and the rotational speed of the spindle. Measurements of the CPSR were carried out at 200 rpm speed increments in the range from 400 rpm to 1200 rpm. Figure 4 illustrates the locus of the CPSR in the X-Y plane. The CPSR moves in the same direction as spindle rotation with increasing rotational speed, except at 1000rpm. Obviously, these behaviors are due to the effect of hydrodynamic pressure.

At 1000rpm, CPSR locus exhibited a very singular behavior, so the CPSR measurement between 800rpm and 1200rpm were carried out in 100rpm speed increments. Figure.5 shows the results of the measurements. The locus of the CPSR becomes like a circle around at 1000rpm .

In order to clarify the reason of this phenomenon, measurements of vibration amplitude on the headstock versus rotational speed of the spindle were carried out. Vibration amplitudes measured on the headstock revealed a maximum value at 980rpm (16.3Hz). This is a resonance vibration of the headstock. Therefore, it is thought that the resonance vibration has a significant influence on the locus of the CPSR at 1000rpm.

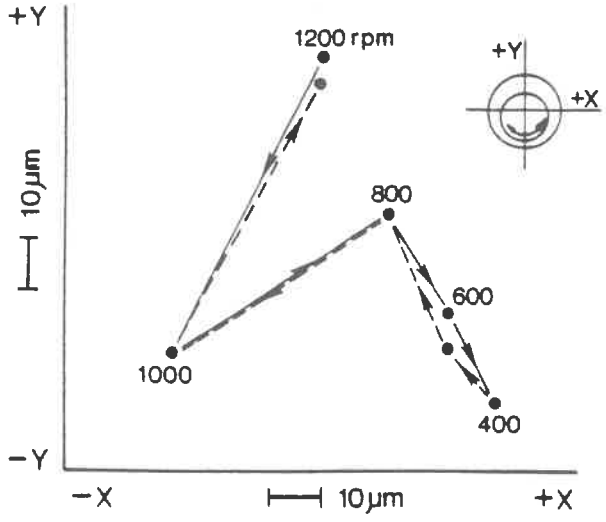

Fig.4 Locus of the CPSR on the hydrodynamic spindle

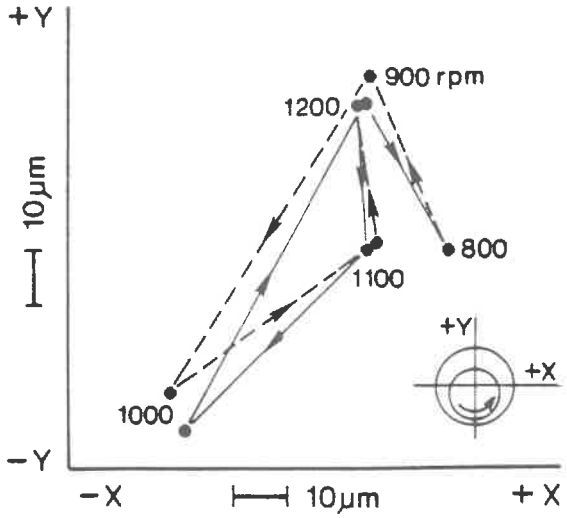

Fig.5 Locus of the CPSR on the hydrodynamic spindle

3.2 The CPSR of the hydrostatic bearing spindle

In this experiment, we used a high precision CNC turning machine employing a oil hydrostatic bearing spindle and slideways. We investigated dependence of the CPSR on the rotational speed of the spindle, rotational direction, mass of the workpiece and pressure of the supply oil. The rotational speed were changed in the range from 400rpm to 2000rpm. Two kinds of workpieces used, i.e. a heavy workpiece (copper : 8.2kg) and a light workpiece (aluminum : 0.2kg). Changing of the supply oil pressure were carried out in the range from 7kg/cm^2 to 14kg/cm^2.

Figure 6 shows the locus of the CPSR on X-Y plane in case of a heavy workpiece. And Fig.7 is in case of a light workpiece. The results of these experiments are summarized as follows : 1) The locus of the CPSR of this spindle moves in the same direction as spindle rotation with increasing rotational speed. 2) In the case of chucking a heavy workpiece, magnitude of the locus of the CPSR is larger than light workpiece. 3) The CPSR of this spindle does not depend on the pressure of supply oil. It is indicated that the CPSR of the hydrostatic bearing spindle are also affected due to the effect of hydrodynamic pressure.

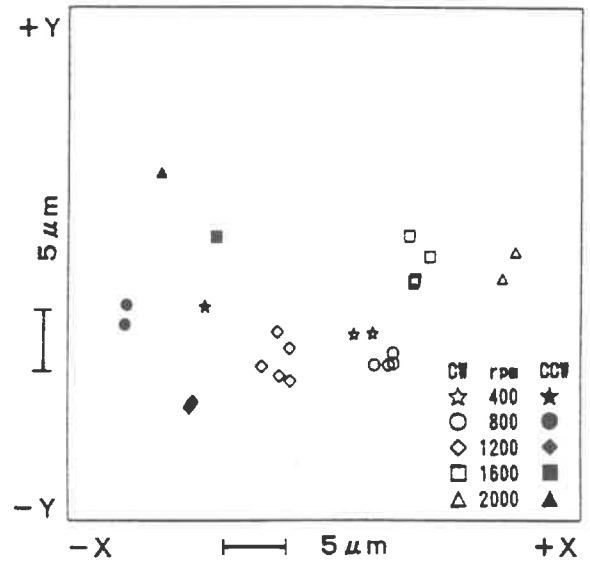

Fig.6 Locus of the CPSR in case of a heavy workpiece

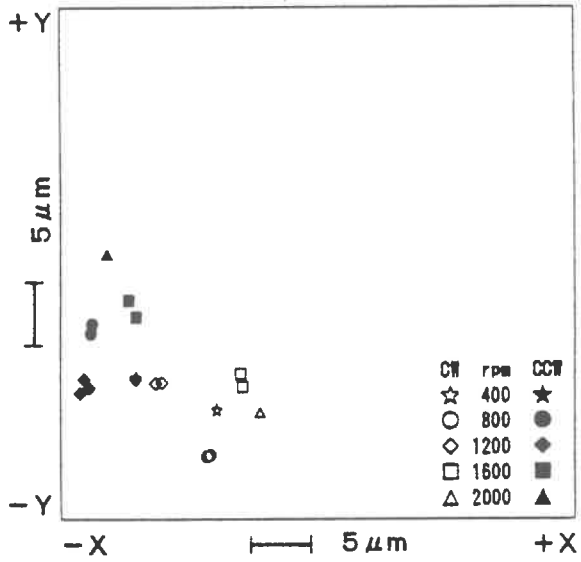

Fig.7 Locus of the CPSR in case of a light workpiece

4. Conclusions

(1)The new measuring method developed is capable of detecting the CPSR with a resolution of 0.5 μm.

(2)The CPSR is affected due to the effect of hydrodynamic pressure not only hydrodynamic bearing spindle but also hydrostatic bearing spindle.

Reference

/1/ T. Eiju and K. Matsuda : Determination of the Central Position of Rotating Object by Laser Doppler Velocimetry, Optical Engineering, Vol.30 No.11(1991) 1825.

Linear detection of high-precision optical surface sensor and its function of optical skid

Tsuguo Kohno, Shinichi Mutoh, Tsuneo Miyai
Tokyo Metropolitan Institute of Technology
6-6 Asahigaoka, Hino, Tokyo, 191 Japan
and Eiichi Satoh Olympus Optical Co. Ltd.
2951 Ishikawa-cho, Hachioji, Tokyo, 192 Japan

Abstract

Linear illumination and detection are applied to a critical angle method optical stylus, HIPOSS. The linear profile of surface microfigure can be obtained without mechanical scanning. For compensation of mutual displacement or vibration between the sensor and the surface to be measured, a function of skid is introduced to the L(linear)-HIPOSS. The optical skid is formed using several pixels of both sides of the center pixel which serves as an optical stylus for surface roughness measurement. Preliminary experiment showed the effectiveness of the skid function of vibration compensation.

Introduction

It should be essential to measure the machined surfaces with in-process or on-machine mode in the near future manufacturing system. The optical surface sensors with various methods, such as, interference, scattering, focus detection, will play important roll in this field. They are now all in use and have the vertical sensitivities of sub-nanometer orders[1]. The optical heads of focus detection or optical stylus have some advantages of high accuracy, small in size, stability, good correspondence with the diamond stylus profilometer, and availability for in-process micro-displacement measurement. According to the progress of measurement accuracy, however, some problems of the optical stylus are becoming appear. They are such that the relatively long time is needed for 2-dimensional scanning with the point detection, the micro-instability of the mutual position between the optical head and the surface under test, and also that the datum is not accurate enough for long scanning range.

A linear detection high precision optical surface sensor (L-HIPOSS) has been developed to overcome these problems by modification of the HIPOSS[2], which is based on the critical angle method. The L-HIPOSS illuminates the measuring surface linearly and detects that dimension with linear array sensors. So the L-HIPOSS is expected to be used as a fast scanning profilometer, an in-process micro-displacement sensor with free of surface roughness, or as a stable roughness measuring instrument for super smooth surfaces using an optical skid method.

In this article, we report the principle and characteristics of the L-HIPOSS and the result of preliminary experiment as a skid type profilometer.

Structure and characteristics of L-HIPOSS

In the standard HIPOSS, as shown in Fig. 1, a laser diode illuminates one point as optical stylus on the surface to be measured and the reflected light is detected by splitted photo-diodes through critical angle prisms. A half mirror is employed to split the optical path so as to avoid any effects of object surface inclination on the measured results. Since the optical path of the HIPOSS is arranged in a flat plane, the linear detection can be realized by stacking up the structure vertically.

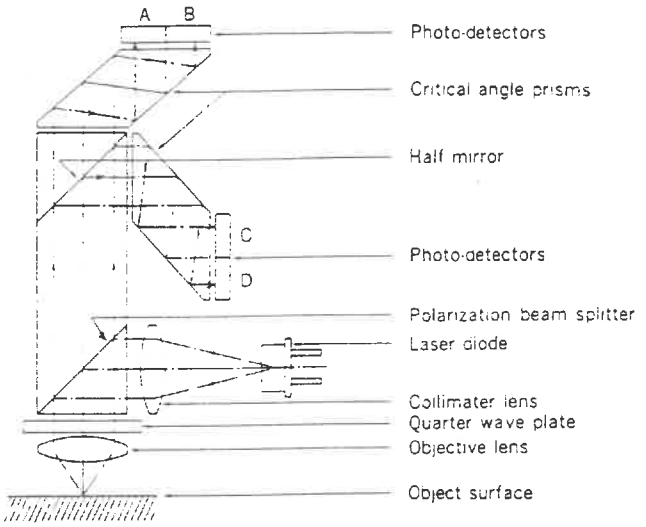

Fig.1 Optical path of the HIPOSS

Figure 2 shows the optical path of L-HIPOSS in its cut model and it is basically same as traditional HIPOSS but some additional cylindrical lenses and dual-line sensors in place of split photo-diodes. For the free and random read out, the MOS type of dual - line sensor with 2 x 128 pixels is specially developed . The area of each N - type photo - diode pixel is 21μ m x 11000μ m and the space between pixels is 24μ m.

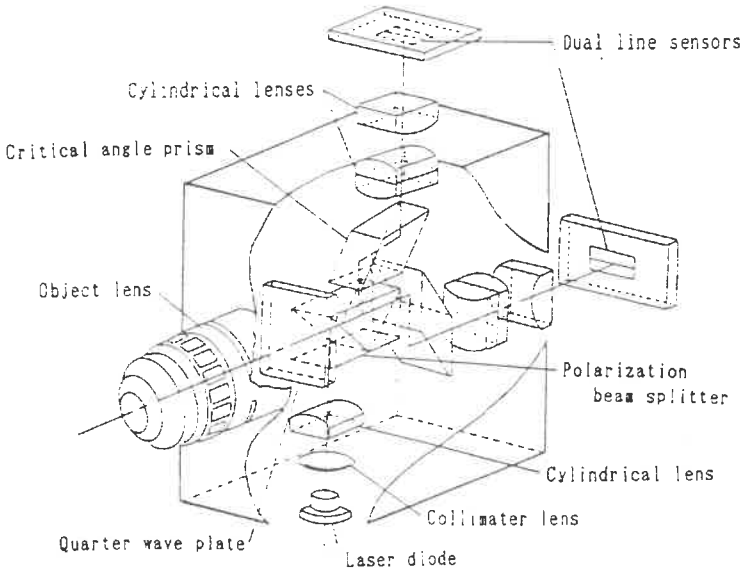

Fig.2 Cut model of the L-HIPOSS

Microfigure measurements are conducted using the L-HIPOSS. The recorded curve of three-stripe sample as an example shown in Fig.3 extends slightly of the sample. This may be due to unsatisfactory optical or mechanical alignment. Table 1 summarizes the present states of the L-HIPOSS.

L-HIPOSS as a skid plofilometer

For stable surface roughness measurement, a skid is sometimes employed to remove unwanted mutual displacement between the stylus and the surface under test as well as removing the waviness component of the surface. In the non-contact measure-

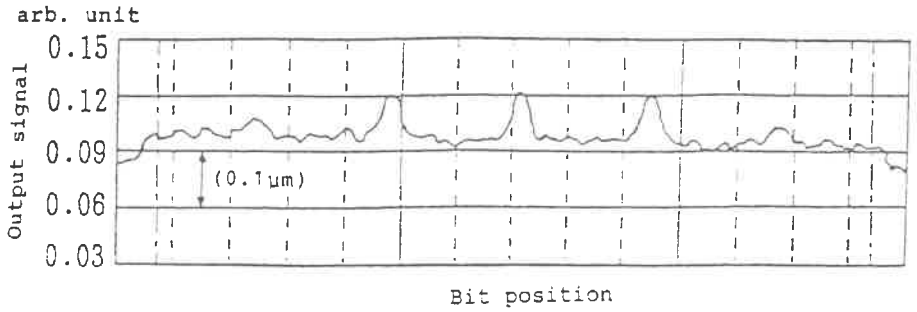

Fig. 3 Recorded curve of three-stripe sample

Table 1 Characteristics of L-HIPOSS

Vertical resolution	2 3 n m
Lateral resolution	5.5 μ m
Illuminating length	1.1 m m
Working distance	8.1 m m
Numerical aperture	0.4
Wavelength of Laser diode	780 n m
Size	78 x 45 x 78 (m m)

ment such as optical stylus, the skid should also be non-contact. For the L-HIPOSS, the optical skid can be formed using several pixels of both sides of the center pixel which is selected as an optical stylus for surface roughness measurement.

Fig. 4 shows the principle of the skid measurement [3]. ha, hb and hc are the distances between two broad areas A , B and a point C on the measuring surface M and the corresponding detector surface D, respectively . They can fluctuate caused by vibration or thermal drift. The amount (ha+hb)/ 2 means an averaged distance of M and D, and basically insensitive to the surface roughness. A difference between the center pixel and the averaged skid signals, i.e.,

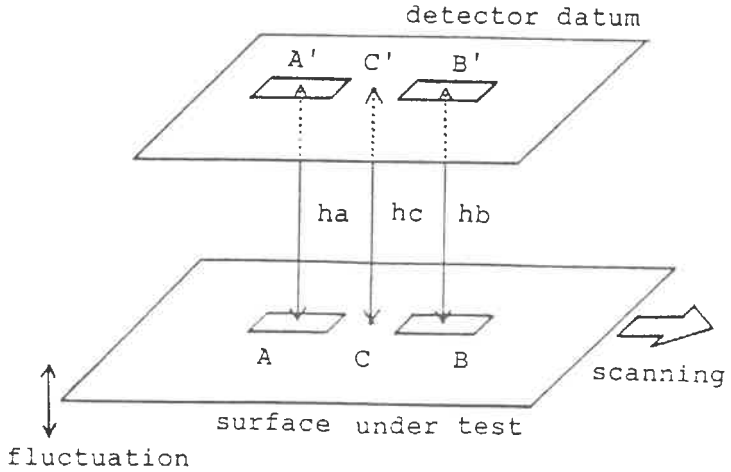

Fig.4 Principle of the skid measurement

$$Xc=hc-(ha+hb)/2,$$

is insensitive to the fluctuation and indicates the pure surface roughness component at point C which as well as areas A and B is scanned along A - B direction mechanically.

Experiments for verifying the effect of the optical skid was carried out under the condition of some vibrations. Figure. 5 shows the result of the experiment. It is shown that the influence of the vibration over the measured value is reduced up to one-eighth with skid function.

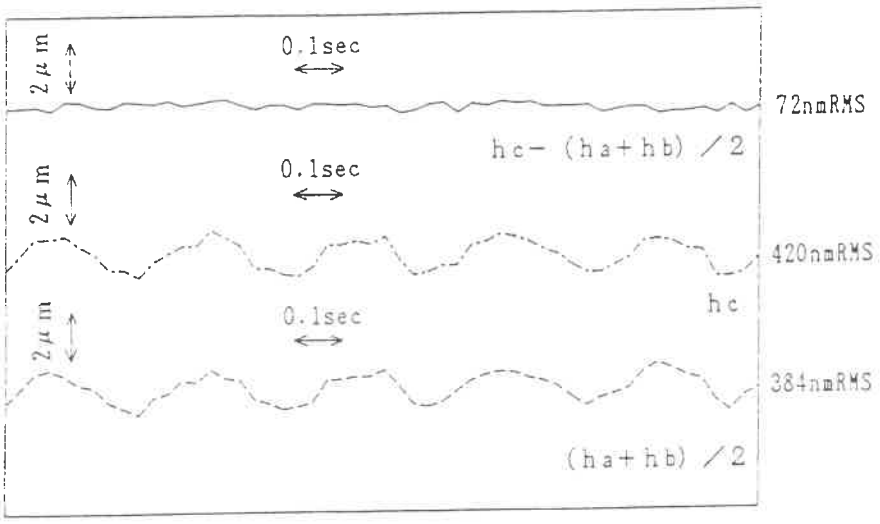

Fig. 5 Result of the skid experiment

Conclusion

High precision optical surface sensor with linear illumination and detection is developed and its skid function is showed to reduce the vibration effectively. This kind of arrangement should be difficult to the astigmatism method optical stylus by the principle. Progressing more downsizing and complete adjustment, L-HIPOSS profilometer or displacement sensor will be used for a high speed and reliable profilometer or a stable in-process displacement sensor.

References

[1] M. Stedman, Proc. SPIE, No.1009, P.56 (1988).
[2] T. Kohno, et al, Applied Optics, Vol.27, P.103 (1988).
[3] M. Adachi, et al, Opt. Lett., Vol.12, P.792 (1987).

ON-MACHINE MEASUREMENT OF LARGE MIRROR PROFILE

Wei GAO and Satoshi KIYONO

Department of Mechatronics, Faculty of Engineering
Tohoku University, Sendai, 980 JAPAN

1. Introduction

In scanning methods of profile measurements, displacements or inclinations relative to a datum line are sampled. Therefore, the accuracy of the measurement is dependent on that of the datum line and the sensor detecting the displacement or the inclination. The displacement sensor and the angle sensor with advanced sensing technique may have the resolution of high enough to the purpose. However, it is not so easy to get a datum line with sufficient accuracy for measurements. Especially in an on-machine measurement, because the guide of the machine is used as a datum line, large datum errors are introduced by scanning stage, vibration and thermal drift. In order to measure the profile of machined surface accurately under on-machine conditions, these datum errors must be decreased to a level lower than the machined error of the surface. For this purpose, some differential methods, such as the 2-point method[1], the 3-point method[2] and the laser autocollimation method[2][3], have been developed. In these methods, probes take displacements or angles at more than two points simultaneously and get the real profile from their data processing. The proposed mixed method combines the laser autocollimation method with the 2-point method. The sensor in this method takes two displacements and an angle at two points on the profile simultaneously. A differential operation of them cancels the datum errors and a deconvoluting operation of the differential data gives the real profile. Comparing with the 2-point method, the mixed method can reduce more remarkably the datum errors. This method has also an important advantage of expressing high frequence components in the probed profile accurately.

2. Principle

Figure 1 gives the principle of the mixed method schematically. Three probes are set on a stage which can scan a surface when the stage moves. The fixed co-ordinate axes XYZ are taken as in the figure. The surface is described by function f(x). Let C_0 be the representative point of the stage, and d_A, d_B, d_C be the distance from probe1,2,3 to point C_0 respectively.

Probe1 measures the displacement m_A at point A.

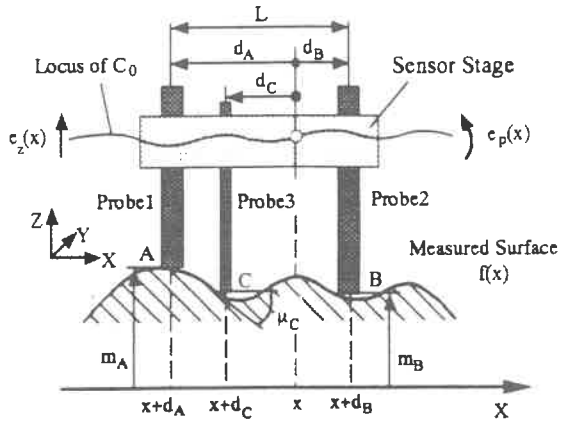

Figure 1 Principle of measurement

Probe2 measures the displacement m_B at point B. Probe3 measures the inclination angle of tangents μ_C at point C. m_A,m_B and μ_C can be described as follows:

$$m_A=f(x+d_A)+e_Z(x)+d_A \cdot e_P(x), \quad (1)$$

$$m_B=f(x+d_B)+e_Z(x)+d_B \cdot e_P(x), \quad (2)$$

$$\mu_C=f'(x+d_C)+e_P(x), \quad (3)$$

where $e_Z(x)$ is the z-directional error of the scanning motion and the $e_P(x)$ is the pitching error. Eliminating the term $e_Z(x)$ and $e_P(x)$, these equations are reduced to the differential output m(x) of the mixed method by Equation (4):

$$m(x)=m_A-m_B-(d_A-d_B)\,\mu_C. \quad (4)$$

Expressing the Fourie transform of the function f(x) and m(x) as F(ω) and M(ω) respectively, the relation between them can be expressed by the following transfer function :

$$H(\omega)=M(\omega)/F(\omega)$$
$$= e^{j\omega d_A} - e^{j\omega d_B} - (d_A - d_B)\, e^{j\omega d_C}. \quad (5)$$

When $d_C=d_A$, the transfer function becomes:

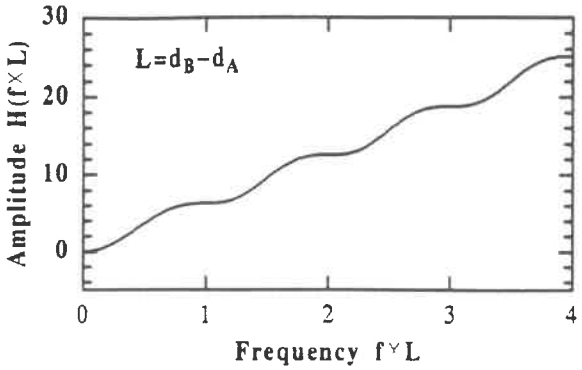

Figure 2 Frequence response of the mixed method

$$H(\omega)=\omega L\sin(\omega L/2)+j[\omega L\cos(\omega L/2) -2\sin(\omega L/2)]. \quad (6)$$

Here $d_A=d_B=-L/2$, and L is the probe interval. In this case, the sensor becomes the most compact size.

Figure 2 is the graph of the transfer function of Equation (6). From Figure 2, it can be seen that the amplitude of the transfer function doesn't become zero except the case of $\omega=0$. This is an advantage of the mixed method, which may not be found in other differential methods.

3. Multi-sensor

3.1 Principle of the sensor

As mentioned above, the sensor for the mixed method is needed to detect the displacement and the inclination angle of tangents simultaneously. Such a sensor can be constructed optically by using the imaging system and the laser autocollimater.

Figure 3 shows the optical structure of the multi-sensor which can measure the displacement and the angle of two points at the same time. A collimated laser beam with 45° linear polarization is split into two parallel beams whose polarization is perpendicular to each other, by the splitting component made of the Prism, PBS1 and PBS2. Both beams are reflected by point A and B of the measured surface, and are split once more by the PBS3 according to the polarization, and then accepted by the detector1 and the detector2 respectively. The each detector can detect the displacement and angle as in Figure3. The detector1 consists of the lens L1, PSD1 and PSD2, and the detector2 consists of the lens L2, PSD3 and PSD4. In this scheme, the autocollimater lens of the angle meter is also used as the imaging lens of the displacement meter.

Lens L1 and L2 have a diameter of 15 mm and a focal distance of 30 mm. Sensitive area of the PSD is 3mm×1mm and its resolution is 0.1 μm. The

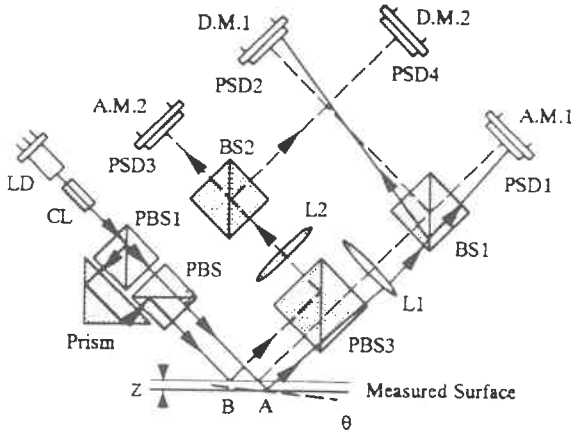

Figure 3 Principle of the multi-sensor

magnification of the displacement meter is 2 and the distance between the measured surface and the lens is 45 mm. According to the geometrical relation and the performance of the PSD, the displacement meter has a measurement range of ±700 μm and a resolution of 0.07 μm, the angle meter has a range of ±61 minutes and a resolution of 0.34".

To avoid the influence of the miscellaneous lights under the on-machine conditions, a modulation technique is used. The power of the laser diode is modulated by a sine wave with a frequency of 20 kHz.

In the rest of this paper, the displacement meter and angle meter of detector1 are named as displacement meter 1 and angle meter 1 respectively, those of detector2 are named as displacement meter 2 and angle meter 2 respectively.

3.2 Performance of the sensor

3.2.1 Calibration

A displacement sensor of the capacitance type (Microsense) with a range of ±50 μm is used to calibrate the displacement meters. Figure 4 shows calibration curves of the displacement meter 1 and their fitting error to the linear approximation. The repeated results of 2 times are plotted in the figure. The fitting error in the graph is about 0.2 μm. The fitting error of the meter 2 is about 0.3 μm in the range of ±50 μm. It is also confirmed that the displacement meters can work linearly in the range of ±600 μm.

A photoelectric autocollimeter with a resolution of 0.1" and a range of ±10 minutes is used to calibrate the angle meter. Figure 5 shows calibration curves of the angle meter 1 and their fitting errors to the linear approximation. The repeated results of 2 times are plotted in the figure. The fitting error in the graph is about 3". The fitting error of the angle

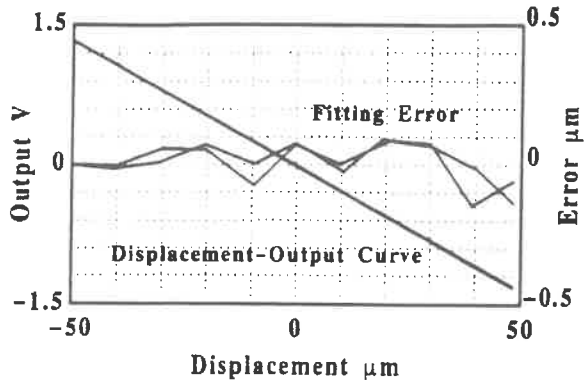

Figure 4 Calibration curve of the displacement meter

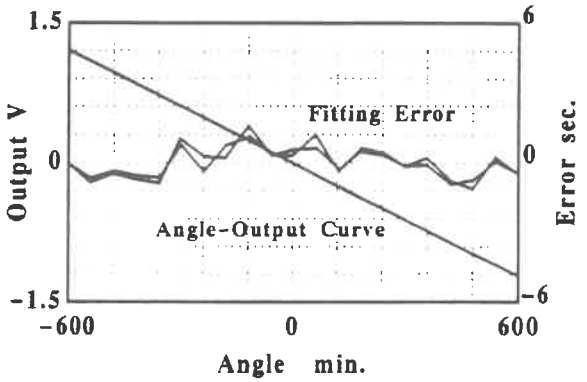

Figure 5 Calibration curve of the angle meter

meter 2 is about 4" in the range of ±10 minutes. It is also confirmed that the angle meters can work linearly in the range of ±1 degree (angle).

By evaluating from the ratio of S/N, the trial multi-sensor used in this paper has a resolution of 0.1 μm and 1".

3.2.2 Thermal drift behavior

The multi-sensor in a circumstance without temperature control is tested about its drift behavior. The result of the test is shown in Figure 6. Although the output of the individual displacement meter varies 15 μm and the angle meter varies 20" with a temperature change of 2° C, the drift of the differential output is remarkably decreased.

3.2.3 Cancellation of vibration

The characteristics of the differential output against vibrational noise is investigated. Figure 7 shows the output of displacement meters when impulsive stimulations are given to the specimen. The output of individual displacement meter varies 25 μm and the angle meter varies 15" due to the stimulation, but the differential output is just about 0.8 μm, which is reduced to 1/30 of individual outputs.

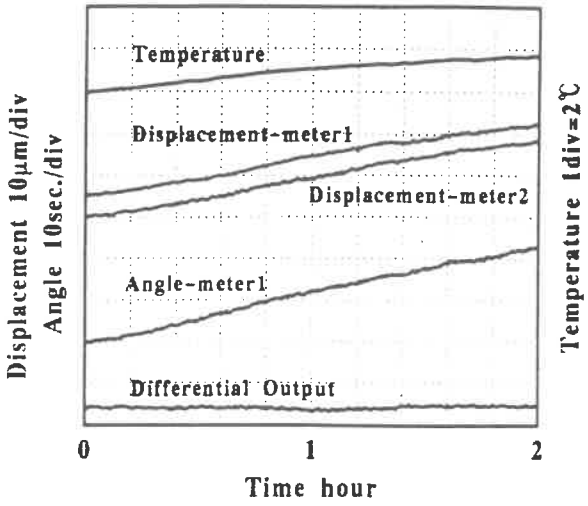

Figure 6 Thermal drift of the multi-sensor

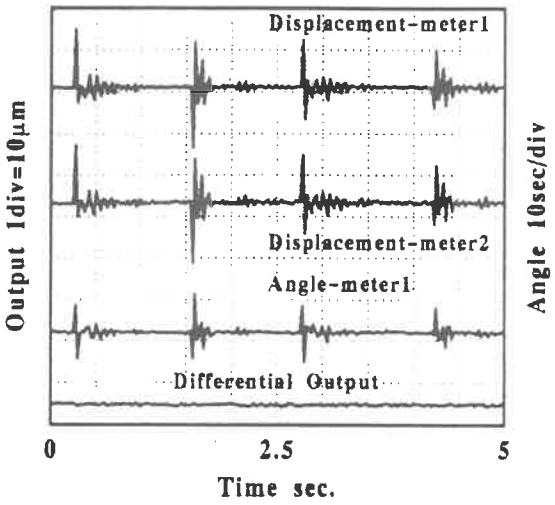

Figure 7 Vibration reduction of the multi-sensor

4. Profile measurement

4.1 Measurement system

A measurement system is constructed by a scanning stage and the multi-sensor as shown in Figure 8. The measured workpiece is mounted on two v-blocks and can be moved in XYZ directions so that the relative position to the sensor can be adjusted. The stage can carry the sensor over 1 meter for measurements. It is driven by a motor in the X-direction. To determine the position of the stage in the X-direction, a pulse generator is equipped. The positional signal from the pulse generator is sent to a personal computer as a trigger signal. The computer reads the outputs of the sensor via a A/D converter. It takes about 30 minutes to measure the whole movement range of the stage.

4.2 Measurement of mirror profiles

A flat mirror is measured with the system. The

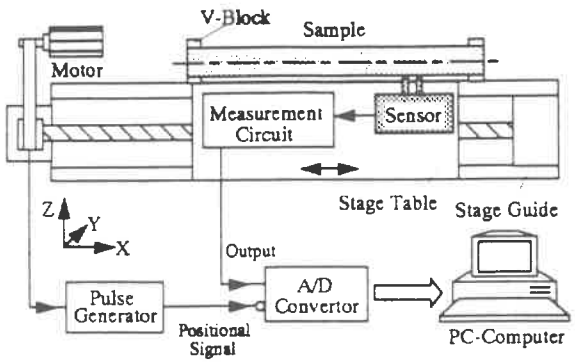

Figure 8 Measurement system

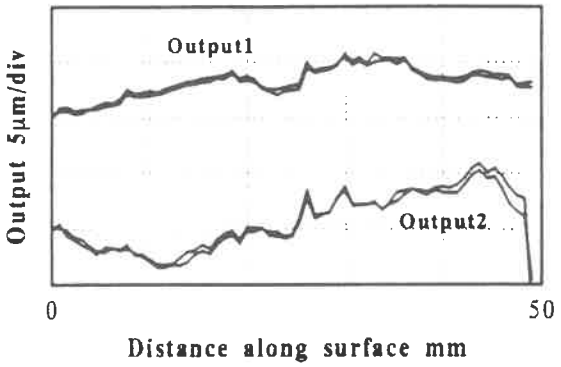

Figure 9 Output of the displacement meter

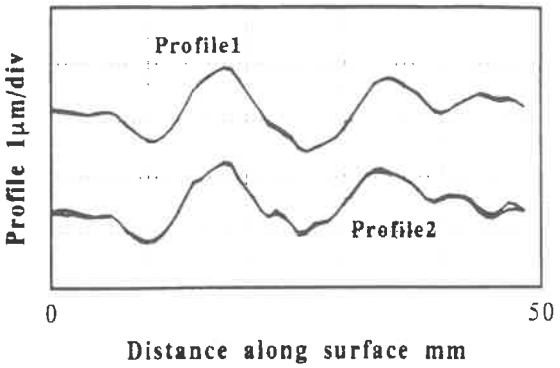

Figure 10 Resulted profile1 of the mixed method

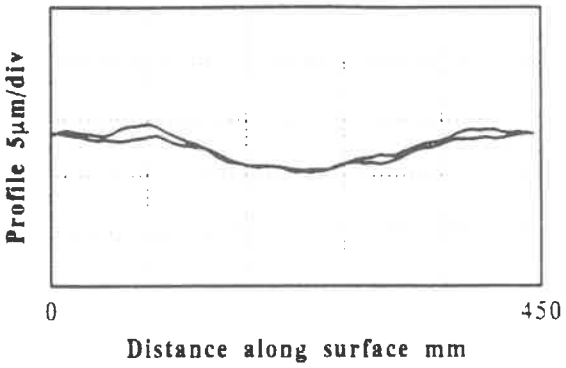

Figure 11 Resulted profile2 of the mixed method

probe interval is 7 mm and the measurement length is 49 mm. The Output1 in Figure 9 shows the raw output of the displacement mete The Profile1 in Figure 10 shows the resulted profiles after data processing of the mixed method. The repeated results of two times are overlaid in the figure. The repeatability errors are less than 0.1 μm.

In order to identify the effectiveness of the mixed method, another scanning stage is used to measure the same flat mirror. The Output2 in Figure 9 shows the raw output of the displacement meter obtained by using this stage. The Profile2 in Figure 10 shows the result of data processing of the mixed method of these data. The two curves in Figure 9 are different from each other. It is because that the motion error of the stages is different. However, the two curves in Figure 10 are agree with each other well.

The system is also used to measure the straightness of a cylindrical mirror whose diameter is 90 mm.

The measurement is performed repeatedly with the measurement length of 450 mm. Figure 11 shows the resulted profile after data processing of the mixed method. The repeatability error is about 1 μm. The measurement which the measurement length is longer than 450 mm was also performed. However, so good result as in Figure 10 couldn't been gotten. This is because the resolution of the displacement meter is not sufficient for this long profile with a good straightness. It should be also noted that the influence of thermal drift in the differential output becomes strong as the measurement length increases.

5. Conclusion

(1) The mixed method which combines with the 2-point method and the laser autocollimation method has been proposed.
(2) A new sensor which can measure the displacement and angle of two points on a surface simultanously has been designed and made. The resolution of displacement meter and angle meter is 0.1 μm and 1" respectively. And the errors due to thermal drift and vibration are decreased by 30 dB.
(3) The mirror profiles have been measured with the mixed method to confirm the performance of the method.

References

1, G.Makosch and B.Drollinger, Applied Optics, Vol.23, No.24, pp.4544-4553, (1984)
2, S.Kiyono, P.Huang and N.Fukaya, Int. Conf. of Advanced Mechatroics, pp.467-472, (1989)
3, S.Kiyono, etc., Int. J. of the JSPE, Vol.25, No.2, pp.148-149, (1991)

INVESTIGATION OF AN OPTICAL NONCONTACT MEASURING SYSTEM FOR GEAR GEOMETRY

— Measurement of pitch errors and tooth profiles —

Eiki Okuyama*, Satoshi Kiyono** and Hitoshi Moritoki*

* Department of Mechanical Engineering, Akita University
Tegata-gakuen-machi, Akita-shi, 010, Japan
** Faculty of Engineering, Tohoku University
Aoba, Aramaki, Aoba-ku, Sendai-shi, 980, Japan

1. Preface

Since gear has complex features, there are many difficulties in the measurement of geometrical shapes of a gear. Some of them can be avoided by using a noncontacting feeler. For examples, demands for shortening measuring time and difficult problems of putting feeler between small teeth are easily solved by means of an optical probe.

However, there is no effective noncontacting feelers that can be used for measurements of gear shapes. From the above point of view, noncontact system using optical probes to measure the shape of the gear was developed. The development of the measuring system was carried out in two steps.

In the first step, a system to measure pitch errors was developed. It has two optical probes that are equivalent respectively to a fixed probe and a measuring probe in the well known system of contact probe. The probe corresponding to a fixed probe is to detect the moment that every tooth of the rotating gear passes a triggering point made with a laser beam. The other probe is to measure a displacement of tooth surface from a determined position. During the rotation of the test gear, displacement of each tooth surface is sampled on the every moment that the tooth passes the triggering point. In this system, there is no mechanical interference between probes and a test gear, therefore, high speed measurement is possible.

In the next step, a system to measure the tooth profile was developed. In this system, the optical probe corresponds to the measuring probe in the pitch measurement system moves in the radial direction of the test gear. And it detects the displacements of all surfaces of teeth. At each sampling point fixed on a radial position, displacements of teeth surface are sequentially detected. Therefore, sampling time of this system is almost independent of the number of the tooth of a test gear.

2. Principle and structure of the system of pitch measurement

Fig.1 shows a principle of the system of pitch errors measurement. A test gear rotates around an axis O. Two optical probes of laser beams cross the tooth spaces in the tooth trace direction. The optical prove which contains a focus A is equivalent to a fixed probe in a contact measuring system. The other optical prove contains a focus B is a measuring probe. In this paper, the optical prove which contains the focus A is called a trigger part, and the other is called a detecting part. At the moment when a tooth surface passes the focus A, deflection of the next tooth from the focus B is detected. The distance between focus A and B should be adjusted by relating to circular pitch of the test gear.

A block diagram of the system is shown in Fig. 2. In the trigger part, current signals that are output of PDs are transformed into voltage signals. These four signals are bound into two signals to detect only the movement of the spot sensitive to the tooth deflection. The difference of them is divided

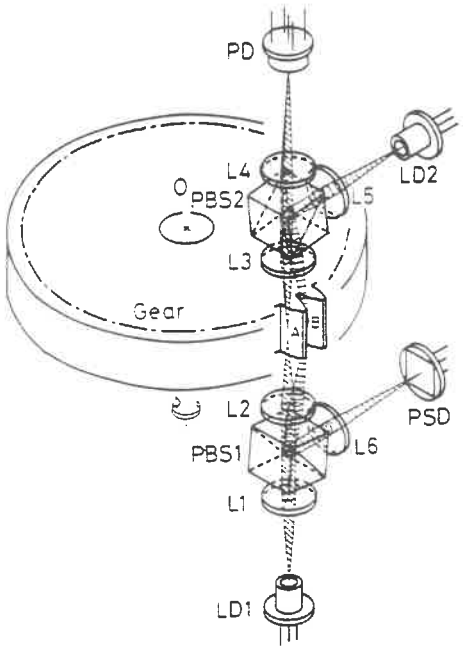

Fig.1 Principle of the pitch measuring system

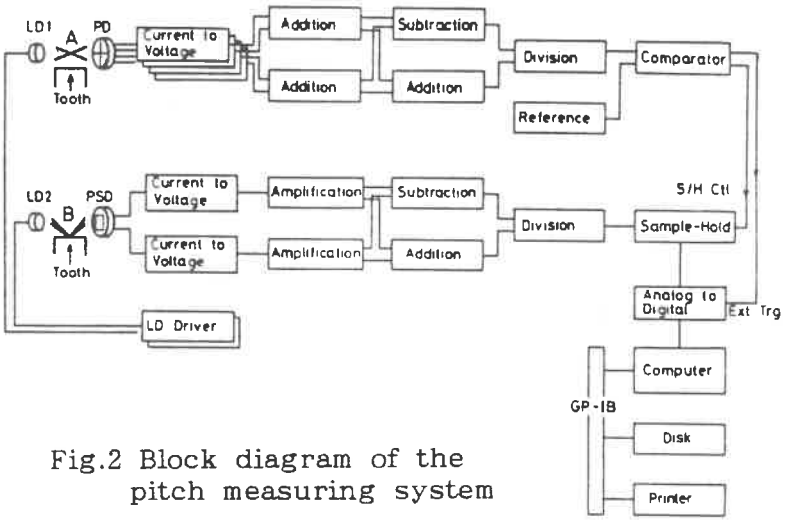

Fig.2 Block diagram of the pitch measuring system

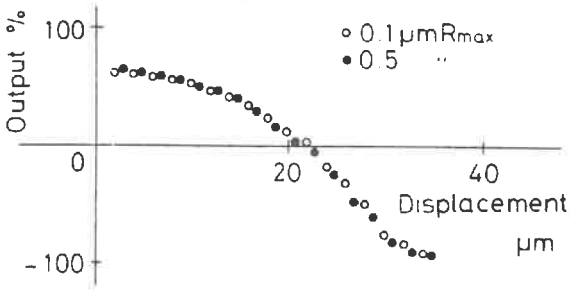

Fig.3 Experimental output of the divider

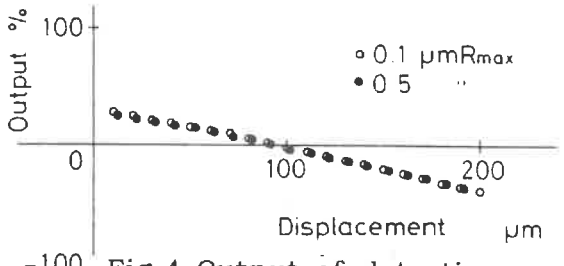

Fig.4 Output of detecting part

Table 1 Coefficients of least squares

Data No.	Coefficient 0th	1st	2nd	3rd	Rmax μm
1	97.616	-2.9199	$-1.4509*10^{-2}$	$-2.5522*10^{-4}$	0.5
2	98.832	-2.7384	$-0.9177*10^{-2}$	$-2.0841*10^{-4}$	0.1
3	95.073	-2.7515	$-1.0308*10^{-2}$	$-2.5793*10^{-4}$	0.1
Average	97.174	-2.8033	$-1.1331*10^{-2}$	$-2.4052*10^{-4}$	

by the addition of them. At its zero cross point, trigger signal is generated. Output of the detecting part is send to a sampled hold circuit. Synchronizing to trigger signals from the trigger part, deflection from the focus B is held. And held datum is read into a computer according to an external trigger hitting the AD converter. This sequence is repeated at every crossing of the focus A with surfaces of tooth.

3. Characteristics of the trigger part and detecting part

3.1 Trigger part

A measurement system for pitch errors according to the principle in Fig.1 was made for experimental investigation. Characteristic of each part of the probe was tested. Sensitivity and repeatability of triggering part are examined by using samples of different roughness. Roughness of them was 0.1 micrometer in Rmax, 0.5 micrometer in Rmax respectively. Results are shown in Fig.3. Output of the divider is independent of the surface roughness, if it is smaller than 0.5 micrometer in Rmax. It is found that the output curve crosses the zero line with an inclination of about 8%/micrometer.

3.2 Detecting part

Sensitivity and reliability of detecting part are examined by using the samples above. The result is shown in Fig.4. Output is independent of the surface roughness within 0.5 micrometer in Rmax. Coefficients of a 3rd order polynomial obtained with the least squares method that is applied in 200

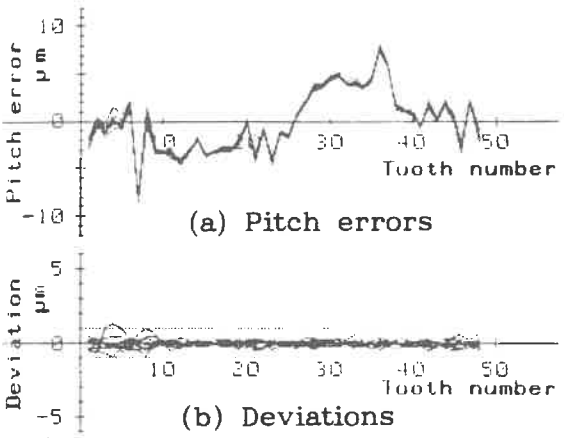

(a) Pitch errors

(b) Deviations

Fig.5 Result of pitch measurement

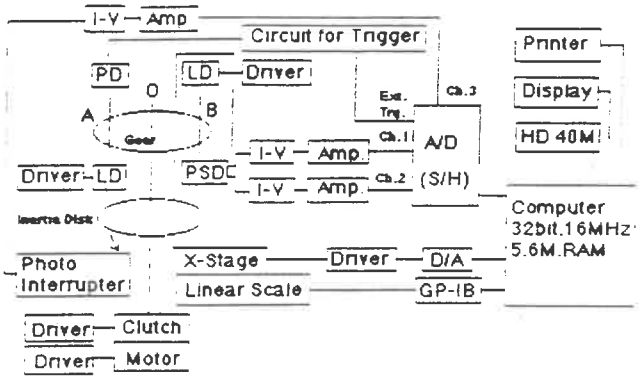

Fig.6 Block diagram of the profile measuring system

micrometers measured range are shown in Table 1. The worst case of deviation of the first coefficient that is the most significant one in the polynomial is 5% from average. In the case that variations of pitch are within 10 micrometers, deviation of 5% is not important. In following measurements of pitch errors, this 3rd order polynomial of averaged values will be used as the calibrated curve.

4. Measurements of pitch error

A test gear was set to the axis of an inertia disk. After obtaining initial velocity, the disk put into the free rotation and pitch errors are measured in the state of decreasing velocity. The test gear is a spur gear that has 0.8 module, 48 tooth number and tooth width of 10mm. The results of measurements repeated ten times are shown in Fig.5(a). Fig.5(b) shows the deviations from the average. Dashed line means +-1 micrometer range. Though most parts of this data are within +-0.5 micrometer, there is a part where the deviation exceeds over 1 micrometer. During continuous repetition of measurements, rotational speed of the tested gear becomes slow gradually. But the significant difference has not been found among measured pitches under different rotational speeds.

5. Principle and structure of the profile measuring system

In this system, the detecting part moves in the radial direction of the gear to trace the tooth profile.

Block diagram of the system is shown in Fig. 6. A test gear is fixed to a rotary axis driven by a motor. Also, an inertia disk is fixed to this axis. And a mark to show a starting point is fixed on the disk. When the mark is detected by a photo interrupter, the sequence of the measurement is to start. The Trigger part is equal to the pitch measuring system. The detecting part is set on a linear stage movable in a radial direction. This stage is able to be controlled by the computer with open loop through a D/A converter. In addition, the displacement of the stage is measured by a liner scale and is sent to the computer through GP-IB.

6. The experiments of tooth profile measurement

6.1 The measurement of tooth profile

The measurement of tooth profile was performed. The sample gear has module 2.5 and 40 teeth. Tooth surfaces of the gear are ground. When the measurement is finished, profiles of all teeth are shown in the computer display. After the display of all tooth profiles, an extended tooth profile of chosen number can be shown, as in Fig. 7. The abscissa means the displacement of the detecting part, the left hand of it corresponds to the

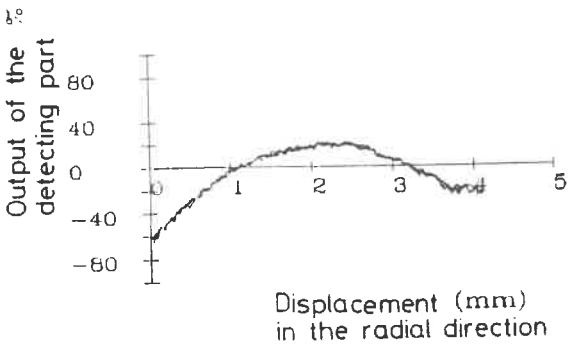

Fig.7 Extended display datum

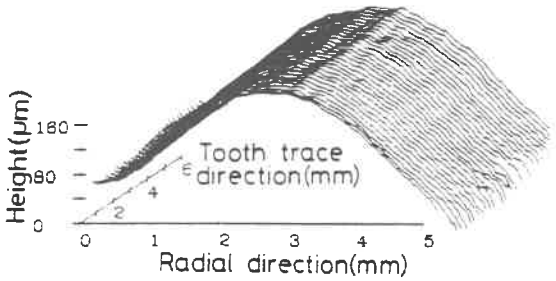

Fig.8 Tooth surface measured by the detecting part

dedendum and the right hand corresponds to the addendum. The ordinate is height of the tooth surface. To take 100 sampling points on every tooth profile, 20 minutes was needed to measure all tooth profiles. In this figure, three results are shown. The three results in Fig. 7 are coincided with each other well as a whole, but some small deviations due to high frequency components are also found. The radial deflections of the rotary axis may cause these deviations of the repeated results. In each optical probe, the amount of error due to a radial deflection is proportional to the part of the deflection in each sensitive direction of the probe. The angle between the sensitive directions of the two probes is about 90 degrees. Therefore, the maximum amount of the error due to a radial deflection attains that of the deflection itself. This maximum occurs when the direction of it is coincident with the sensitive direction of the either probe.

6.2 Measurement of tooth surfaces using the detecting part

A tooth of the measured gear mentioned above section was cut out and put on to another method of measurement. The detecting part used above was set on an X-Y stage. The detecting part was used as a displacement probe and moved in two dimensional area to measure the tooth surface that is fixed on a table. The result is shown in Fig. 8. The left hand side of the X axis corresponds to the dedendum of the gear, and the right hand side is the addendum. The Y axis is the tooth trace direction. The outline is similar to that in Fig. 7. Because there is no effect like to the radial deflection in the rotating system, the curve of the result has no high frequency component.

7. Conclusion

A noncontact measuring system using optical probes has been developed, which may be applied to measure pitch errors and tooth profiles of a gear rapidly and with high accuracy. The following characteristics have been obtained.

1) In this system, there is no mechanical interference between probes and a test gear, therefore, high speed measurement becomes possible.

2) In the pitch measuring system, 3 to 4 seconds measuring time was needed to measure pitch errors of a spur gear with module 0.8, 48 teeth. Estimating the maximum value of deviation from average as (average + standard deviation), it was (0.74 + 0.22) micrometers.

3) In the tooth profile measuring system, it took 20 minutes to measure all tooth profiles, having 100 sampling points on every tooth surface.

Acknowledgment

We thank Katutoshi Nara and Koresuke Matuda for the help in designing and trial manufacturing of apparatus. We also thank Tuneo Takaku, Takumi Saka, Yoshitomo Suzuki and Kazuhiro Mizumiya for supporting the experiments.

COMPUTER INTEGRATED ERROR CALIBRATION SYSTEM FOR A CMM OF CNC TYPE USING CALIBRATED MECHANICAL ARTEFACTS AND TOUCH PROBE

HEUIJAE PAHK and JONGHOO KIM
POSTECH (Pohang Institute of Science and Technology),
PO BOX 125, POHANG, KOREA

1. Introduction

Error calibration and frequent reverfication of working accuracy of coordinate measuring machines and machine tools are currently acknowledged as essential processes in order to maintain high performance of the equipments and high quality of products.

Mechanical artefacts such as ring gauges and step gauges were conventionally used for quick acceptance tests, but their geometric inaccuracies limited the application to the precision error calibration of machines. The concept of gauge compensation can be applied in that the error calibration data of the gauges can be stored in a computer and be used for correction of gauge measurement. The advantage of gauge measurement is that they can assess the real measuring accuracy with touch probe and that they can be located easily in any orientation in a working volume of machines.

The development of micro computer and CNC controller technology enables a new error calibration system using calibrated mechanical artefacts, where the data of the geometric inaccuracy are stored from error calibration. Then the measurement paths are generated for the probing of the mechanical artefacts, and error terms are evaluated from the comparison between the stored and probing data of specific gauges. High degree of computer integration is achieved, and thus the whole measurement/calibration procedures are computer controlled and driven by the developed user friendly software.

2. Error calibration of gauges

The geometry of inside cylinder is of special metrological importance, and consists of inside diameter and roundness. The inside diameter is calibrated with precise ring gauge comparator, and the roundness is calibrated with a roundness tester (TALYROND). The inner diameter and roundness data along the inside circle form the geometry of ring gauge and are stored in a datafile in the micro computer. Fig. 1 shows the calibrated profile of 200mm nominal dia.

For the step gauge, the real distance between the reference block and respective blocks are of metrological importance, thus a specially designed length calibration system with laser interferometer is used to calibrate the distances between the blocks. Both sides of the block are calibrated and they are stored in a data file. Fig. 2 shows the practical calibration data of 600mm step gauge.

3. Path plan module for gauge measurement

Many modern CMMs of CNC type have vector driving functions, with which target positions can be programmed in CNC commands, then the machines move to the target points, thus 3 dimensional motion can be planned. The gauge path plan is automatically performed in the computer and the corresponding CNC codes are generated, then downloaded unto the commercial CMM of CNC type. Fig.3,4 ahows the planned path for the ring gauge and the step gauge in use.

4. Error evaluation module

4.1 Circular error from Ring gauge measurement

Lobing error and effective radius of probe stylus

The lobing error can be incurred in multidirectional measurement such as ring gauge probing, and it is apparent that equal amount of the lobing error of the probe stylus are incurred in both small ring and large ring gauge probing. Therefore the lobing error and the effective radius of the probe stylus can be successfully measured by probing along a ring gauge of relatively small radius. Let Rm, Em(q) be the mean radius and deviation of probing data of the ring, and Rc, Ec(q) be the radius and roundness data of the calibrated ring gauge. Thus the error of probe stylus is

Error of probe stylus = Rc + Ec(q) - (Rm+Em(q))
= Reff + Lobing(q) (1)

Circular error

The influence of the machine errors on the ring test has to be assessed, which is circular error. The circular error can be evaluated when the ring of relatively large radius is assessed. The circular error , DR, is

DR=ring gauge geometry - (gauge probing data + effective radius)
= Rc + Ec(q) - (Rm + Em(q) + Reff) (2)

where ring gauge geometry=Rc+Ec(q)
gauge probing data=Rm+Em(q)

Eq(2) gives the circular error , which is from the machine's geometric errors.

Calculation of systematic errors

The X scale error can be calculated as the deviation of the circular error from the nominal radius in 0, 180 degree direction, and the Y scale error as the deviation from the nominal radius in 90, 270 degree direction. The squareness error can be calculated from the deviation from the nominal radius in 45, 135, 225, 315 degree direction, noting the squareness error is double of the mean deviation.

4.2 Linear displacement error

The linear displacement accuracy or length measurement error can now be calculated from the measurement data and the calibration data of the step gauge.

Let M2i-1, j(X2i-1-1, Y2i-1, Z2i-1), M2i, j(X2i, Y2i, Z2i) be the jth measurement data at (2i-1)th and (2i)th block side respectively, and S2i-1, S2i be the actual distance of (2i-1)th, (2i)th block side from a reference point, respectively, which can be obtained from the calibration file of the step gauge. Then the errors at (2i-1)th , (2i)th sides can be evaluated as follows.

Let XF2i-1, j , XB2i, j be the jth forward and backward positional error at (2i-1), (2i)th step, respectively.

F2i-1, j = (S2i-1- Sref) - ¦(M2i-1, j- Mref) C1C2¦/¦C1C2¦ (3)

B2i, j = (S2i- Sref) - ¦(M2i, j- Mref) C1C2/¦C1C2¦ (4)

where Mref is the position of reference point, and Sref is actual distance of the reference point from the step gauge origin. It is noted that the measurement data are decomposed into the normal vector C1C2 direction in order to exclude any mispositional errors of the measuring probe on the block sides.

5. Practical application of the developed system and discussions

Ring gauge measurement

Fig.3 shows the ring gauge probing data before probe compensation, giving 46.7 um roundness error with 11.234 um repeatability from 3 repetitive measurement. Fig.4 shows the circular error of CMM on XY plane, giving 19.2um roundness error, which is combination of systematic machine errors.

The scale error of the X axis was found to be -7.8um/100mm, that of the Y axis as 4.1um/100mm, and the squareness error between the XY axis as -0.1um/100mm.

Step gauge measurement

A step gauge is located and measured in a working volume of a CMM. For the X axis calibration, the step gauge is located from (350,40,196) to (119,40,196) position, and the measurement operation has been performed accoring to the calculated path plan. Fig.14 shows the X positional errors, giving -8.5 um bandwidth, 5.0 um repeatability over 230 mm measurement span, where the repeatability is two standard deviation of 5 repetitive measurements. It was found that the X positional error value from the step gauge measurement is very close to that from the ring test. Fig.6 shows the linear displacement error along diagonal direction on the machine working volume.

6. Conclusion

(1) Calibrated mechanical artefacts are found to be useful for assessing geometric errors in terms of total measuring accuracy.

(2) Lobing error of the probe stylus was successfully evaluated from the ring test of small radius.

(3) The circular error was possibly obtained from the calibrated ring test.

(4) Scale errors and squareness error was successfully calculated from the ring test, and the scale error showed very closeness to that of the step gauge measurement.

(5) A complete algorithm for linear displacement accuracy (length measurement) along any direction in the working volume of a commercial CMM has been implemented with a calibrated step gauge.

(6) Path plan module for gauge measurement has been found to be efficient, where measurement paths have been planned, simulated, then executed for real measurement operation

(7) The developed system has been found to be fast and efficient system, where practical error measurement / calibration are performed in very short time, thus it is applicable to day-to-day calibration or frequent reverification of CMMs.

References

[1]BS 6808:1987

[2]ANSI/ASME B89.1.12M-1985

[3] VDI/VDE 2617

[4] Knapp,W., Test of three dimensional uncertainty of machine tools and measuring machines and its relation to the machine errors, Annals of CIRP Vol32/1/1983

[5]Kakino,Y., Ihara,Y., and Nakatsu,Y., The measurement of motion errors of NC machine tools and diagnosis of their origins by using telescoping magnetic ball bar method, Annals of CIRP, Vol36/1/1987

[6]Bryan,J., A simple method for testing measuring machines and machine tools, Precision Engineering,Vol4 No2,1982

[7] Kunzmann,H., and Waeldele,F., On testing coordinate measuring machines with kinematic reference standards (KRS), Annals of CIRP, Vol 32/1/1983

[8] Pahk,H., KIM,J. Development of computer integrated system for error diagnosis of a CMM using calibrated mechanical artefacts, Int.J.Mach.Manu,accepted for publication.

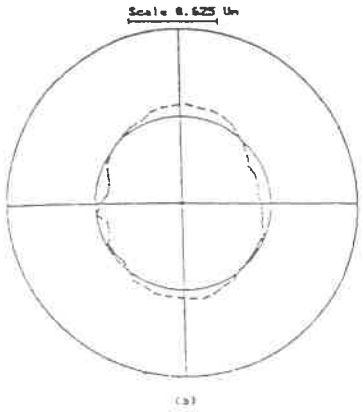

Fig.1 calibrated profile of 200mm dia. ring gauge

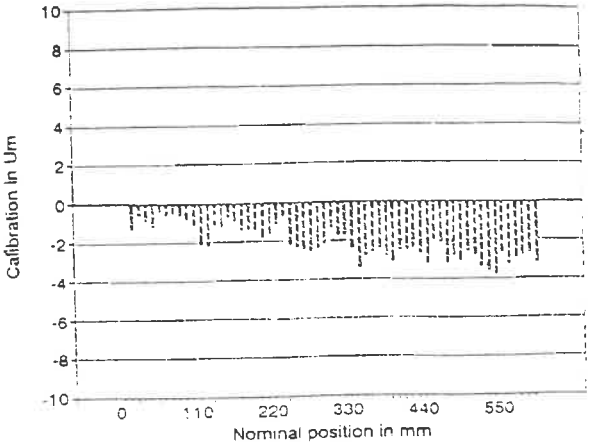

Fig.2 step gauge calibration

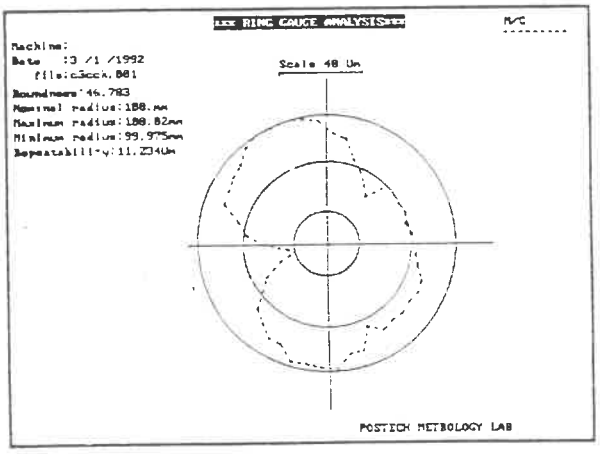

Fig.3 200mm ring probing

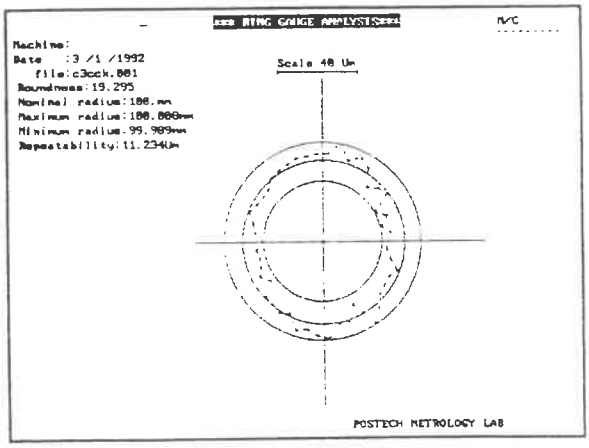

Fig.4 Circular error of CMM on XY plane

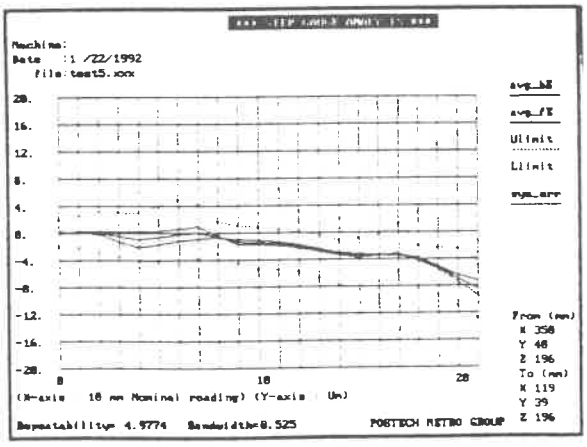

Fig.5 X axis calibration

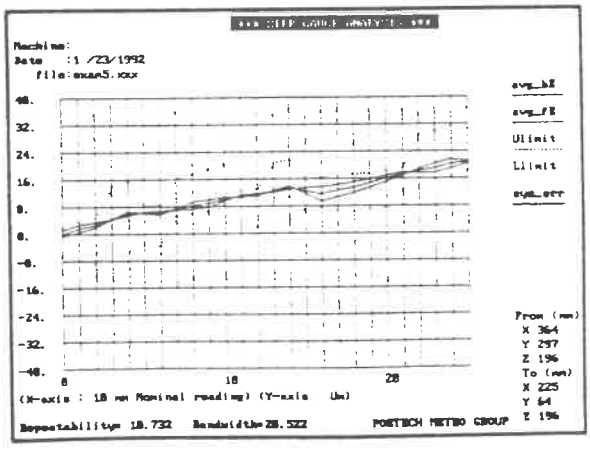

Fig.6 Diagonal calibration

Self Calibration of Displacement Sensors

S.Kiyono K. Morishima and T. Sugibuch
Tohoku University, Sendai, Japan

1. Introduction

In precision engineering, self correction of flat planes, and self proving of a rotary scale are well-known techniques, which are very important to improve the accuracy of measurements. However, any other self-correcting method applicable to the displacement sensors is not known.

The calibration of sensitivity of sensors can be performed by using some references such as gauge blocks or specimens of step-wise profiles. These references are very reliable and stable and also can be brought easily to any places needed. Therefore calibration of the average sensitivity without any reference is not desired so strongly.

When a sensor is used in a wide measuring range and the highest resolution of its performance, it is necessary to know the detailed linearity errors of the sensor. The detailed calibration curve of a sensor is obtained usually by means of the comparing measurement with a reference instrument which is more accurate and stable than the calibrated one. However, we can not get any reference instrument so easily for detailed calibrations of sensors whose resolution and accuracy are better than 1 micrometer. It is of course true that the sensors can be calibrated by comparing with a laser interferometer system. It may be, however, too expensive to prepare the system only for the calibration. Furthermore it is not easy for the interferometer system to present its highest performance in usual circumstances of measurements. Therefore it will be very useful to establish the method to calibrate the detailed linearity error without any accurate reference.

In the new method named as self calibration method, two sensors are compared with each other and no accurate sensor for the reference is needed. The accuracy of the calibrated result is limited only to the noise level of the sensor signals and the amount of thermal drift of the calibration system including the sensors. Capacitance type displacement sensors are calibrated by means of the proposed method to confirm its performance.

2. Principle of the self calibration and its process

Figure 1 illustrates the outline of self calibration

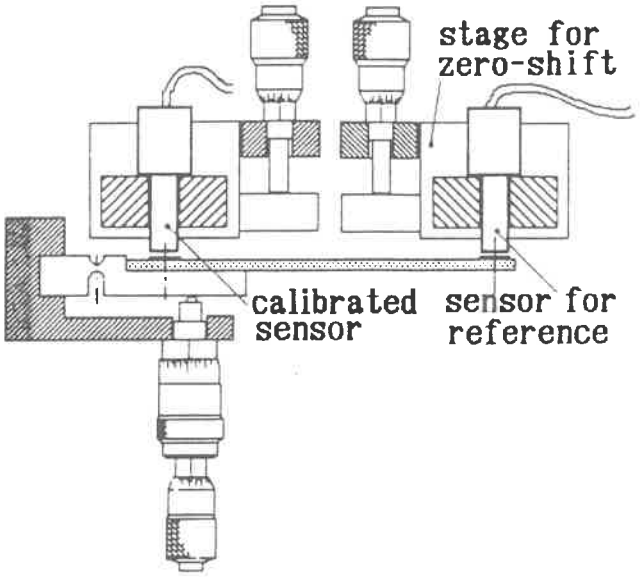

Fig .1 Mechanical structure of the calibration system

system of displacement sensors. The system is constructed from two sensors A and B and a lever system. One of the sensors is fixed at the reference side and the other is fixed at the calibrated side. Owing to the magnification of the lever system, the displacement of the target at the reference side is n times as large as that at the calibrated side. The sensor at the reference side is fixed on a linear stage. Its position can be shifted to cover the displacement wider than its range.

The calibration is proceeded in the following steps.

STEP (1) Calibration over a whole measuring range of the reference side sensor

The displacement of the target at the reference side is increased from the lower limit to the upper limit of the range of the sensor, while readings of both sensors are sent to the computer.

STEP (2) Shifting of the linear stage

When the reading attains to the upper limit of the range in the reference side, the sensor is sifted by means of the linear stage so that its reading resumes approximately the original value at the lower limit.

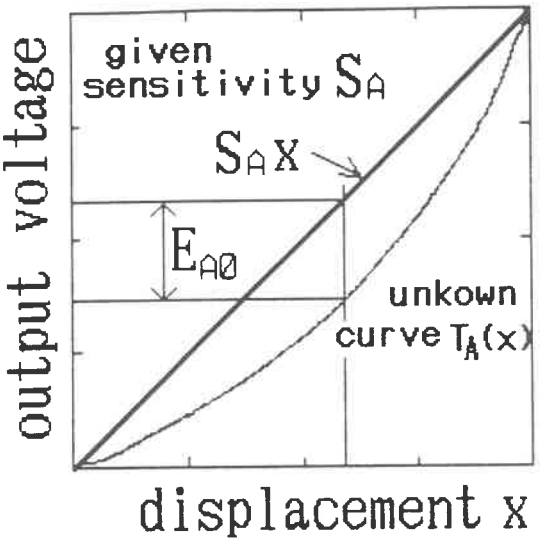

Fig. 2 Input-output relation of a displacement sensor

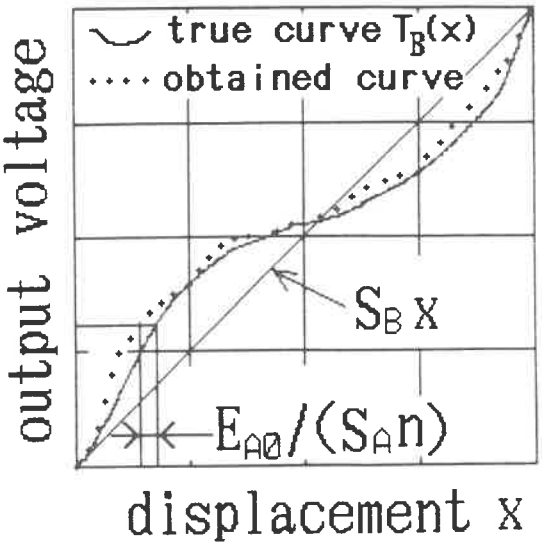

Fig. 3 Reduction of the uncertainty after the step(3)

STEP (3) Data acquisition over full range of the calibrated sensor

The cycles of STEP (1) and (2) are repeated n times until the displacement of the target at the calibrated side reaches to the upper limit of the range of the sensor.

We begin the calibration process by putting on the reference side the sensor A whose sensitivity is known beforehand. The sensor has unknown linearity error $E_{A0}(x)$ as shown in Fig. 2.

Using the mean sensitivity S_A of the sensor A, the displacement of the target at the calibrated side can be estimated. Therefore a calibration curve of the sensor B can be plotted as in Fig. 3 with the data obtained in the above process.

The amount of original uncertainty in the ordinate in Fig. 2 is reduced to 1/n in the abscissa of Fig. 3. The relation is expressed in the following equation:

$$E_{B1}(x)= E_{A0}(x)(S_B/S_A)/n, \qquad (1)$$

where the term S_B is the mean sensitivity of the sensor B. In most cases we can assume $S_B/S_A=1$. In general, the calibration data are expressed approximately by a polynomial obtained by the least squares method. Then the error of the calibration curve is given as follows:

$$F_{B1}(x)=E_{A0}(x)S_B/(nS_A) + f_{B1}(x), \qquad (2)$$

where the second term is the fitting error of the least squares approximation.

STEP (4) Exchange of roles of two sensors

The positions and roles of both sensors are exchanged and the same processes (1) to (3) are followed once more. In this case the calibration curve of the sensor B (reference side) has been obtained in the above process. The uncertainty in the resulted calibration curve of the sensor A is presented as,

$$F_{A1}(x)=E_{A0}(x)/n^2 + f_{B1}(x)S_A/(nS_B) + f_{A1}(x). \qquad (3)$$

Thus the uncertainty is reduced to about $(1/n)^2$ of the original one.

STEP (5) Correction of estimated magnification of the lever

In most cases the magnification of the lever system initially estimated is not accurate enough. If the estimated value and its true value are n' and n respectively, the sensitivity obtained in the step (4) becomes as follows:

$$S_A' = S_A (n/n')^2 \qquad (4)$$

Since the sensitivity of the sensor A is given and should be fixed, the true magnification n can be reestimated as:

$$n = n' \sqrt{S_A'/S_A}. \qquad (5)$$

STEP (6) Converging calculation

The procedure (1) to (4) is repeated until the calibration curves of both sensors approach to the final converging ones. Really, only one set of data of cali-

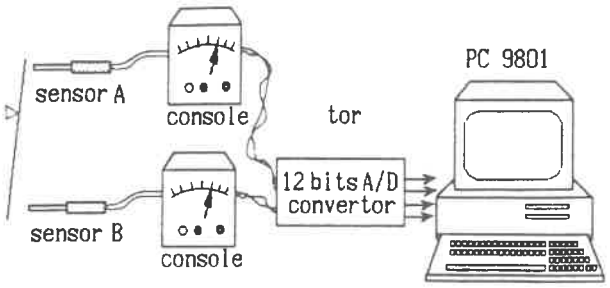

Fig. 4 Experimental system

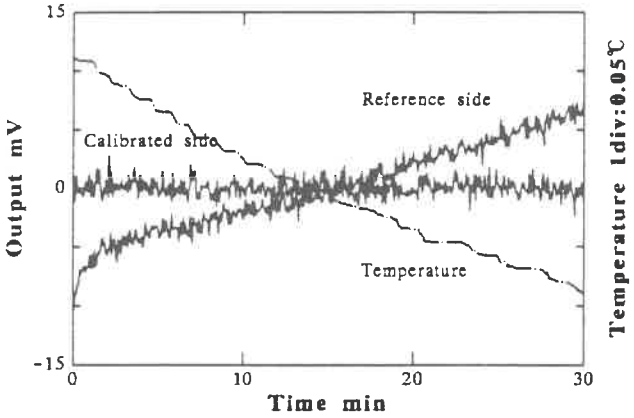

Fig. 5 Thermal drift of the outputs of sensors

bration for each sensor should be acquired. The converging calculation can be proceeded by only correcting the reference values of the abscissa repeatedly. The correction is progressed by applying the last calibration curve of the reference sensor in the present stage.

3. Experiment

3.1 Experimental Systems

Fig. 4 illustrates the experimental system. The analog outputs of the consoles are converted to digital value through a A/D converting board of 12 bits and sent to a personal computer (NEC 9801). Exactly speaking, a system made up of a sensor, a console of microsense and the A/D board is to be calibrated. The result may changes when the A/D converting element is changed.

Outline of the mechanical construction is shown in Fig. 1. A cantilever made of an elastic hinge is deflected by a micrometer head and its inclination is converted to the displacements of the targets of the sensors. Targets are gauge block fixed on the lever plate. The ratio of the displacements of two targets is

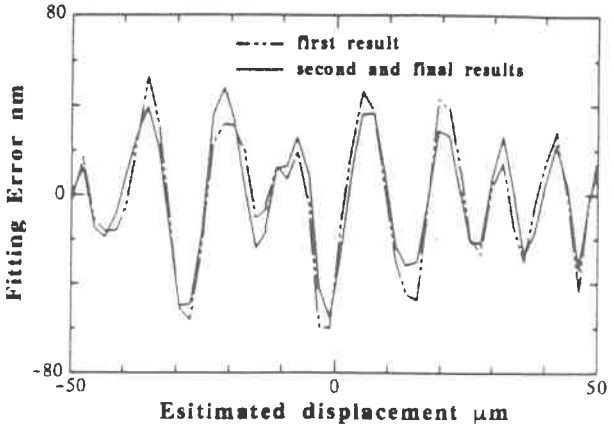

Fig. 6 Process of the convergence

about 5.0. The material of all components excepting the gauge block and sensors is aluminum.

The sensors calibrated are capacitance type displacement sensors (microsense). The calibrated range is ± 50 micrometers and voltage output is ±10 V. The zero adjusting knobs on the console are fixed.

Figure 5 shows a result of drift test of sensors in the system. It is seen that the amount of the drift in the reference side is much larger than that in the calibrated side. This tendency does not change when the sensors are exchanged their positions each other. If the material of the lever plate is changed to bronze, the amount of drift increases. This tendency may ,therefore, be caused by some distortion at the joint of the lever plate and the cantilever with elastic hinge.

About 5 minutes are necessary to get a set of calibration data of a sensor in this system. The amounts of drifts of two sensors during 5 minutes are about 0.5 mV (3 nm) and 5mV (25 nm) in the calibrated side and the reference side respectively. The noise level is about 6 mV (30 nm) in p-p value, to which the stability of the calibrating system will be limited.

3.2 Results of experiments

Figure 6 shows linearity errors of the sensor A in each end of STEP (4). The linearity error converges to the final value after three times of repetition. The result of convergence corresponds to the original uncertainty of the sensor A.

Figure 7 shows the repeatability of the converged linearity errors. The maximum deviation among three measurements is about ±10 nm, which is within the stability limit of the calibration system. It should be noted that the calibration data have been fitted to the 9th polynomials by the least squares approximation and used as a calibration curve of the next step. The maximum fitting errors of the polynomials are

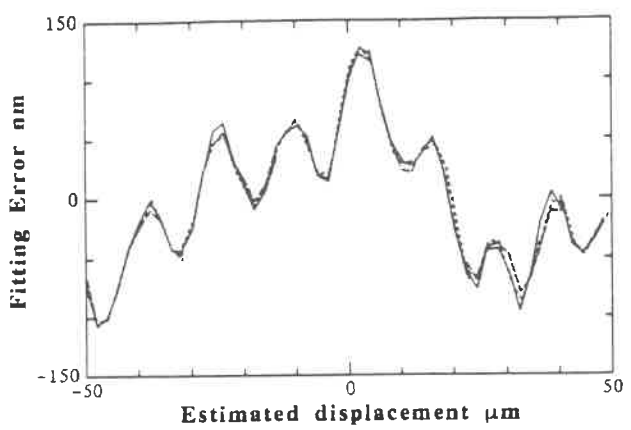

Fig. 7 Obtained linearity error of the sensor A

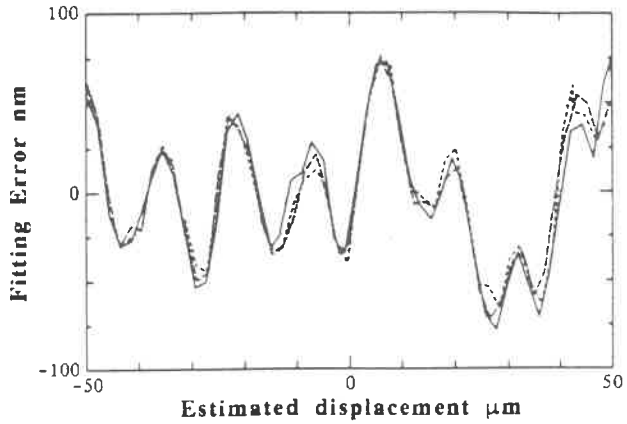

Fig. 8 Obtained linearity error of the sensor B

Table 1 Estimated sensitivity S_B

	sensitivity mV/μm	deviation %·10²
1	0.20258621	-4.477
2	0.20275482	3.842
3	0.20270238	1.255
4	0.20260082	-3.756
5	0.20274048	3.135
ave.	0.20267694	(σ) 3.873

Table 2 Estimated sensitivity S_A

	sensitivity mV/μm	deviation %·10²
1	0.19863687	3.766
2	0.19860950	2.388
3	0.19859784	1.801
4	0.19846574	-4.852
5	0.19850047	-3.103
ave.	0.19856208	(σ) 3.752

about 20 nm, therefore, one fifth of this value (4 nm) is included in the converged calibration data. This value may decrease when a more accurate fitting curve, for example, a curve made by a spline function, or a curve expressed with connected broken lines, is applied.

Figure 8 shows the linearity error and its repeatability of the sensor B. The shapes and values of linearity errors in the sensor B are different from those in the sensor A. The amount of repeatability errors in the sensor B is also within the stability limit of the system. Furthermore the magnification of the lower system estimated from Eq.(5) was 4.94 .

Since the sensitivity of the sensor B is not given at first, it can also be calibrated. Table 1 gives the sensitivity of the sensor B in five measurements. The maximum deviation of the sensitivity from its mean value is about 0.05 %. The amount of standard deviation corresponds to the value of 20 nm at the limit of the measuring range (= 50 micrometers).

If the sensitivity of the sensor B is given, that of the sensor A can be experimentally estimated. The results of this case are given in Table 2.

It has been also confirmed that the same calibration curve of each sensor is obtained when the sensitivity of the sensor B is given and used in the reference side in the first step of the calibration.

4. Summary

1) A new calibration method which does not need any accurate reference sensor has been proposed. In the system, two same kind of sensors and a lever system are used.

2) As an example, two capacitance type displacement sensors were calibrated by each other. For the range of ±50 micrometers, the repeatability error of the calibration curves was within ±10 nm. Its value is within the limit of stability of the system which is dependent on the noise level and the thermal drifts of sensors in the system.

3) Unknown sensitivity of one of the sensors is also calibrated with a similar accuracy.

Reference

1)Wayne R. Moore; Foundation of mechanical accuracy, the Moor special tool company,(1979)

A Fully Automatic High Precision Length Measuring Machine For Calibrating Optical Line Scales.

M B McCarthy[1] and A E Gee[2]

[1] Division of Mechanical and Optical Metrology, National Physical Laboratory, Teddington, Middlesex, TW11 0LY. UK.

[2] School of Industrial & Manufacturing Science, Cranfield Institute of Technology, Cranfield, Bedford, MK43 0AL. UK.

Introduction: Origins and Requirement

This work has origins in a 150mm scale measuring machine built at NPL (Sears 1923), essentially a well-engineered travelling microscope hand-driven through a calibrated precision lead-screw.

Lead-screw generation had received much attention in preceding decades through ruling-engine work of Rowland and Michelson in the USA and Blythswood, (with the help of Hilger) in the UK, [see Stroke (1967) or Palmer et al (1975)], the Blythswood machine having been transferred to NPL. A half-century later the technology became a basis for VLSI microlithography equipment.

Progressively modified and improved, finally to incorporate laser-interferometric stage displacement measurement, the NPL scale-machine achieved ±0.5μm repeatability in certain applications but by 1985 microelectronics industry demands exceeded its capability. In integrated microelectronics manufacture, production quality is dependent upon the accuracy of photomask feature generation. For this and other industrial requirements, a new NPL linear measuring machine has been built with the aims of fully automatic measurement of the separation line-centres with overall placement calibration to improved accuracy (±0.1μm), increased range (400mm) and versatility in respect of scale artefacts.

Machine Mechanics

On the new machine (Fig.1), the scale is Bessel-point mounted on a short-range, low-inertia upper carriage, which in turn is flexure mounted on a lead-screw driven long-range carriage, a design approach enunciated by Michelson for ruling-engines; see Stroke (1967), Loewen et al (1970). Full

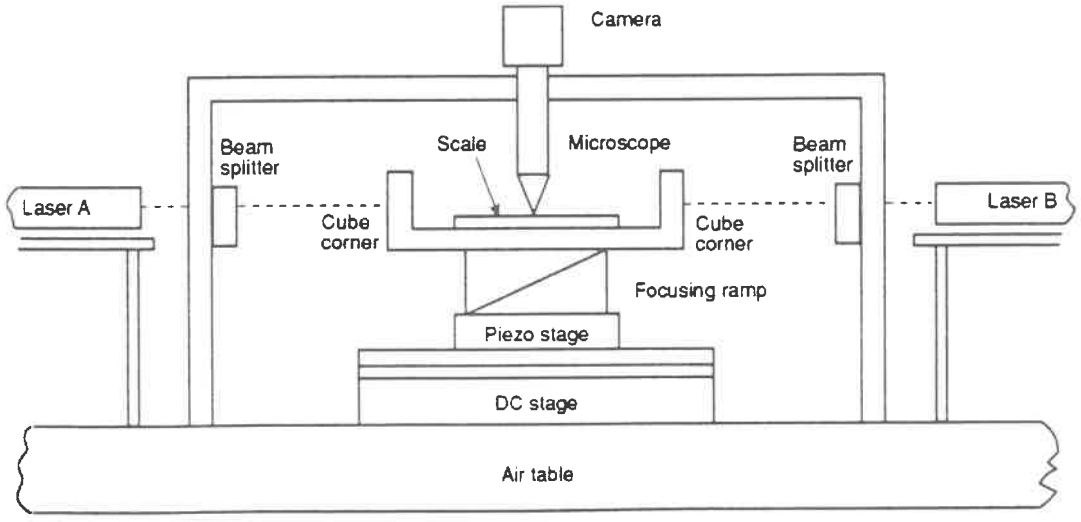

Linear 400 mm Interferometric Measuring Machine (NPL)

Figure 1.

400mm range motion is provided by a dc servo motor driving through a 5mm pitch lead-screw; fine (sub-micrometre) motion is provided by a piezoelectric actuator.

Double-Interferometer Carriage Displacement Measurement

Motion is measured by two colinear independent Michelson type laser interferometers through cube-corner reflectors on either end of the upper carriage. Following the Abbe principle, the common axis of the interferometers lies in the plane of the scale to be calibrated and passes through the measuring point. Separation of the corner cube reflectors (one flexure mounted) is maintained by a fused silica (five-degree-of-freedom) 'wobble-pin' (see Jones 1951). The two beam splitter units are each flexure-mounted on the frame of the machine, separated from the measuring head by further silica wobble-pins.

The two interferometers employed are a Hewlett-Packard type HP 5528A (see Dukes and Gordon 1970) based upon Zeeman frequency-splitting and beating and the other a single frequency unmodulated system constructed at NPL (Downs and Raine 1979).

Although each interferometer is of two-beam Michelson form, they were chosen for differences in principles of operation in their laser sources and fringe counting and fractioning electronics. Whereas frequency-stabilisation in the H-P instrument is piezoelectric, the NPL instrument uses thermal length variation (Bennett and Rowley 1973). A combination of the two measurements obtained greatly reduces the chances of common-cause error in displacement-measurement and the configuration provides an indication of accuracy and repeatability.

Image Processing and Automatic Scale Measurement

For viewing a scale-line, a binocular turret microscope, incorporating a CCD camera, is mounted on the machine-frame. The scale may be viewed by either the (usual) reflected illumination or by transmission (which gives greater image contrast but requires illumination from beneath the carriage). The upper fine motion stage is arranged to overhang the lower carriage, permitting access from beneath for a fibre-optic bundle carrying filtered white light from a remote source.

From any one scale line to the anticipated position of the next, the machine is programmed to advance open-loop, followed by a small correction from the fringe-count, both using the lead-screw. This brings into view the next scale line whose image (a spatially noisy rectangle) is processed to produce a centre-of-gravity line which is then centred on a specified pixel field grid by the piezo-driven stage. The process is monitored absolutely by the interferometers' mean fringe-count to provide measurements of both line-to-line increments and of line position with respect to the scale zero.

Environment and Atmospheric compensation: Wavelength Effects

The instrument is housed in a Class I (UK) clean-room with temperature maintained to ±0.1°C by a single-stage heater/chiller and humidity control to ±5%; an air-cascade provides a room volume change every 20s. An interference air refractometer (Downs & Birch 1983) provides a correction to the laser wavelength for displacement calculations.

The stabilities of the lasers employed have been shown to be better than a few parts in 10^8 (Wallard 1973, Rowley 1986). A 0.1 deg C temperature change would be expected to cause a refractivity wavelength error of 6.33×10^{-14}m and thence, with average air-path difference of 400mm, a position error of 40nm (or 80nm in the longest path condition). The 5% maximum humidity change would cause a wavelength error of 3.165×10^{-14}m and an average length error of 20nm. Pressure variation of 1mb causes a length error of 11nm over the full 400mm travel of the stage.

Results

The repeatability of the measuring machine in automatically locating and measuring the position of lines on an 80mm optical scale (chromium-on-silica) is shown in figure 2. The scale has been measured five times in its initial orientation and positional deviations of the lines from their design calculated; standard deviations are of the order of ±40nm.

The scale was also physically reversed on the stage and the measurements repeated. The difference between the five-measurement averages are shown in figure 3 indicating repeatability to ±50nm.

Intercomparisons with similar measuring machines are in hand and results will be made available.

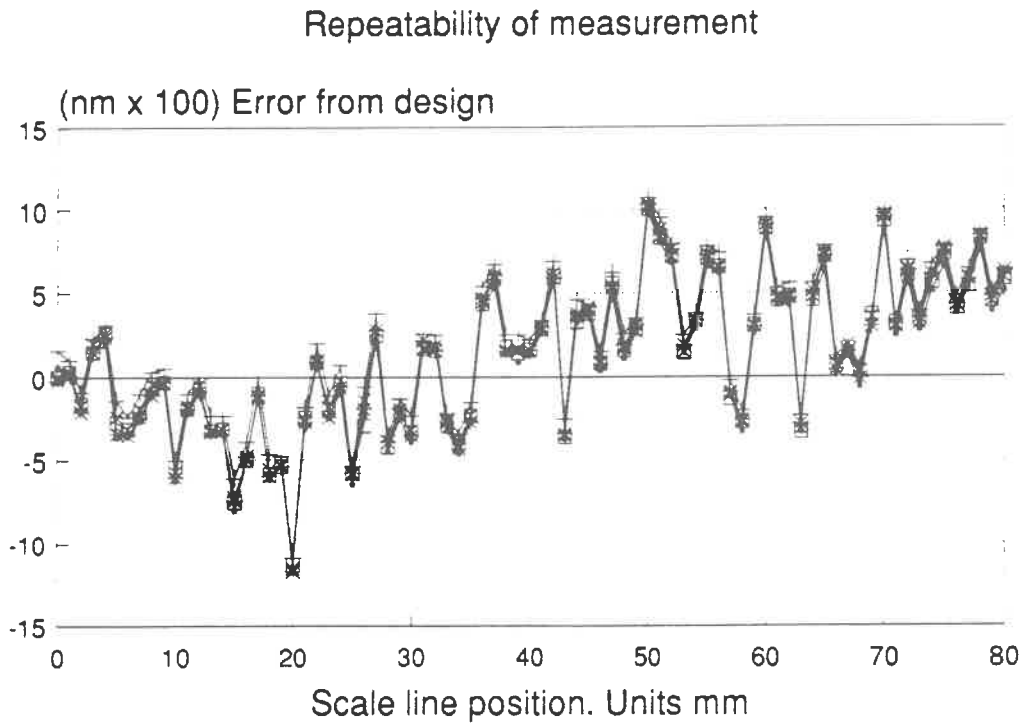

Fig 2. The repeatability of the machine to automatically locate the position of lines on an 80mm optical scale.

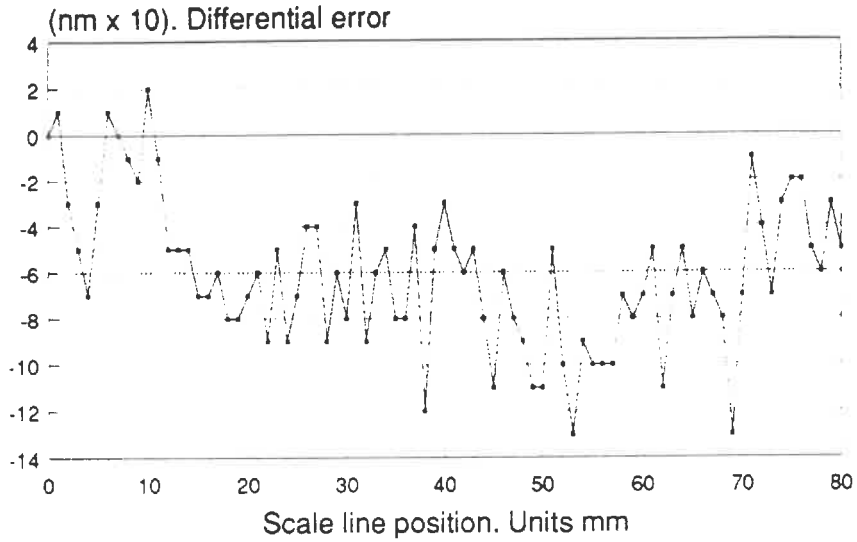

Fig 3. Difference between measurements taken on an 80mm scale when calibrated in two orentations (West/east-East/west)

References

Bennett S J and Rowley W R C. 1973 J Phys E vol 6 pp963-964
Downs M J and Birch K P. 1983 Precision Engineering vol 5 p105
Downs M J and Raine K W. 1979 Precision Engineering vol 79 pp85-88
Dukes J N and Gordon G B. 1970 Hewlett-Packard J vol 21(12) pp2-8
Jones R V. 1951 J.Sci.Instrum. vol 28 pp38-41
Loewen E G. et al 1970 *Diffraction Grating Handbook*, Bausch & Lomb, Rochester, NY
Palmer E W, Hutley M C, Franks A, Verrill J F and Gale B 1975 *Diffraction Gratings*, Rep Prog Phys vol 38 pp975-1048
Rowley W R C. 1986 *NPL Report MOM 78* pp1-2,&35
Sears J E. 1923 *NPL Annual Report 1923* (Metrology section) pp122-124
Stroke G W. 1967 in Flugge S (ed) *"Handbuch der Physik"*, Springer, Berlin pp426-754
Wallard A J. 1973 J Phys E vol 6 pp802-807

COMPARISON OF THE CONFORMITY OF SURFACE TOPOGRAPHY MEASURED BY OPTICAL AND STYLUS INSTRUMENTS

W.P. Dong L. Blunt K.J. Stout

School of Manufacturing and Mechanical Engineering
The University of Birmingham, Birmingham B15 2TT, UK

1. Introduction

Although some comparisons between optical instruments and stylus instruments have been made recently, these were mainly confined to the comparisons of 2-D profile and some general characteristics, such as vertical and horizontal measurement ranges, resolutions and some of statistical average parameters. To date, it appears that little work has been carried out in the field of conformity of 3-D topography assessment between the two techniques. Thus, this paper deals with the nature and origin of inherent measurement differences of 3-D surface topography between the well known phase shifting interferometric instrument and the stylus instrument. The instruments used are a WYKO TOPO-3D and a self-constructed stylus system composed of a commercial stylus pick-up and a set of linear translation X-Y stages. Besides a comparison between general characteristics of the two kinds instruments, the emphases of the paper is concentrated on (i) the conformity to map uni-directional and multi-directional surfaces; (ii) consideration for the influence of small indents; (iii) consideration for the influence of measurement direction; (iv) consideration for surface reflectivity and specimen material. The results obtained should give a suggestion for the conformity of the two instruments and their inherent differences, which is of interest in engineering applications.

2. Experimental Setting Up

The experiments were carried out under following conditions.

Instruments: WYKO TOPO-3D (equipped with a x10 objective head) and DSAGE TOPO-3D (a self-constructed stylus instrument). They were calibrated with testing standard specimens before the experiment.

Specimen:
a). Multi-directional polished steel.
b). Uni-directional polished steel.
c). Multi-directional polished perspex polymer (blue colour).
d). Multi-directional polished perspex polymer (transparent colour).
N.B. All the surfaces were polished with 10μm diamond paste. Specimen c) and d) were bounded together and polished at exactly the same polishing condition.

Data Sampling: Sampling interval 4μmx4μm. Number of data points 256x256.

3. Comparison of General Characteristics of the Optical and the Stylus Instruments

The common difference of all kinds of optical instruments from the stylus instrument is the non-contact measurement. In addition, different optical instruments which are based on different optical principles have their own different characteristics. In particular, the WYKO TOPO-3D, used in the present study, which is a phase shifting interferometric instrument has following distinctive characteristics in comparison with the DSAGE TOPO-3D (the stylus instrument) for the particular measurement conditions of the experiment.

- **Measurement resolution.** The WYKO TOPO-3D has a vertical resolution of 0.1nm and a lateral resolution 4μm depending on the selected objective head. The DSAGE TOPO-3D has a vertical resolution 1.6nm and has a lateral resolution 0.785μm. (NB. for this experiment the stylus instrument used a 4μm lateral resolution)
- **Measurement range.** The vertical range of the WYKO TOPO-3D is 625nm which is much smaller than 6.8μm adopted for the DSAGE TOPO-3D.
- **Time for instrument and specimen setting-up.** Unless operated by a skilled user the WYKO set-up time can be excessive when detecting fringes compared to the stylus instrument.
- **Data logging time.** The WYKO takes about 15 seconds to map an area of 256x256 data points, while it takes 30 minutes or more to map the same area for the DSAGE.
- **The influence of specimen tilt.** The WYKO is sensitive to the specimen tilt due to its small vertical range.
- **The influence of dynamic movement.** No specimen or sensor movement is required for the WYKO. The dynamic movement of the stage of the DSAGE does have influence on the measurement results.
- **The choice of measurement condition.** There is flexiblibility in choosing sampling interval and sampling length for the DSAGE, whereas the two parameters for the WYKO are fixed except by changing the objective head.

4. Comparison of the Conformity of the Measurement Results

The comparison is conducted and the results are given at following aspects.

- **The ability to map uni-directional and multi-directional surfaces.** Fig. 1 and 2 present the isometric plots mapped on specimen a) and b) by the two instruments respectively. Both techniques exhibits the features of original surfaces. Table 1 gives the averaged arithmetic mean height, S_a, and its standard deviation (SD) from several mapped areas. The S_a obtained by the DSAGE are bigger than those obtained by the WYKO.

Table 1. Measurement condition and parameters

			WYKO		DSAGE	
Specimen	Map Direction	No. of Areas	S_a(nm)	SD(nm)	S_a(nm)	SD(nm
(a)		7	26	7.7	34	9.3
(b)	Direction 1	7	23	8.7	30	4.2
(b)	Direction 2	7	18	9.7	32	5.9
(c)		7	7.8	0.52	28	6.7
(d)		7	6.1	0.50	27	1.6

- **The ability to map indents (i.e. to map a steep slope surface).** Fig. 3 shows the results mapped on the indent area of specimen a). Both instruments can detect the irregularity of the indents. But rather than detecting the depth of the indents, the WYKO mainly detects the pile-up of the indents. The typical profiles detected by the two instruments are shown in Fig. 4.
- **Measuring uni-directional surface in orthogonal directions.** This was carried out in order to check the influence of the specimen orientation on the mapping of the optical instrument. Fig. 5 presents two contour maps where the specimen was orientated in two orthogonal directions relative to the lay b). It seems that the measurement direction has

little significance on the results. Row 2 and 3 in Table 1 lists the parameters obtained. The stylus results were measured across (orthogonal direction 1) and along (orthogonal direction 2) the lay.

- **The influence of reflectivity.** Fig. 6 shows a grey scale contour map of the specimen c) and d) measured within one image. Row 4 and 5 in Table 1 lists the parameters obtained. It is difficult to tell the difference between the two parts despite the difference in reflectivity of the transparent and coloured zones.
- **Consideration for the materials.** Although all the specimen were manufactured at the same manufacturing conditions, the S_a on the steel is much larger than the one on the polymer for the WYKO, whereas there is a little difference for the DSAGE. This large inconsistency for the WYKO may be partly due to the material characteristics and partly due to different optical properties for the steel and the polymer. In addition the mechanical response of moving the stylus across the surface of two vastly different materials may be significant in masking genuine difference in surface roughness.

5. Conclusions

Generally speaking, the stylus instrument is a traditional, versatile, reliable and robust instrument. The major disadvantage is the contact measurement, low speed and the influence of dynamic movement on the 3-D measurement. Thus it best suited for measuring common engineering surfaces. It is proved that the WYKO is reliable and fast when measuring smooth surfaces, the influence of surface lay features and the measurement direction on the measurement result are not the so significant. When considering comparisons across differing instruments the results obtained from different materials need to be carefully interpreted.

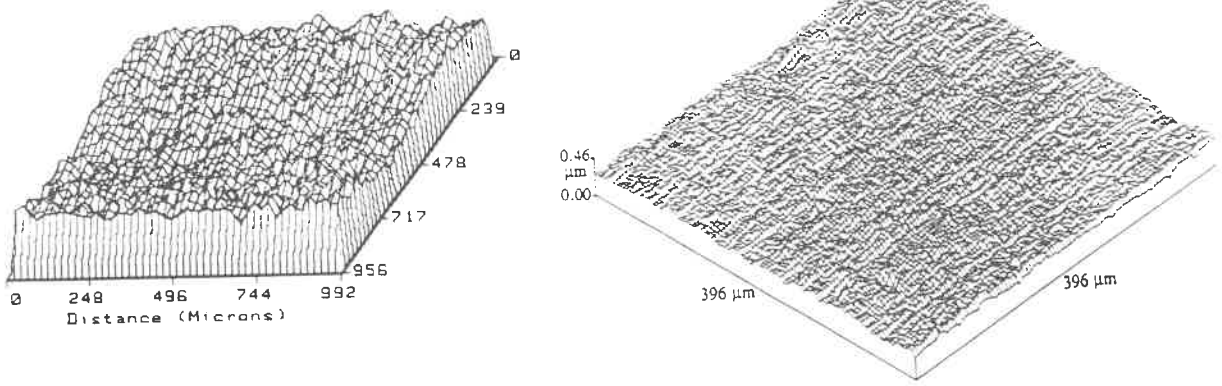

(a) Mapped by WYKO (b) Mapped by DSAGE

Fig. 1 Isometric plots of Multi-directional surface.

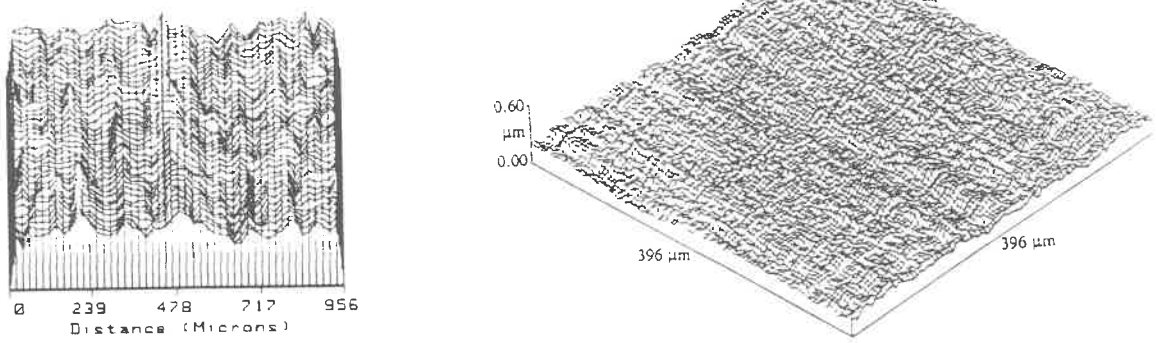

(a) Mapped by WYKO (b) Mapped by DSAGE

Fig. 2 Isometric plots of Uni-directional surface.

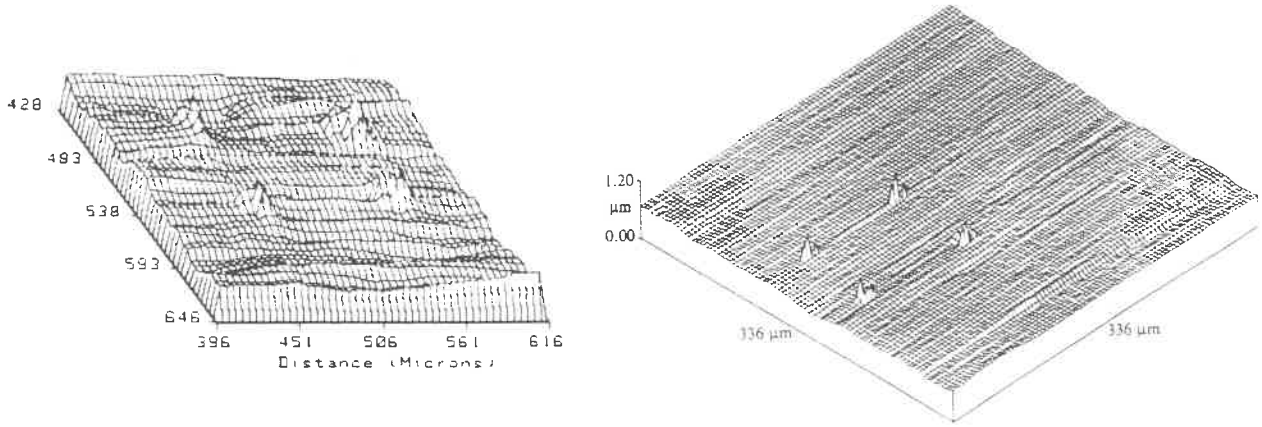

(a) Mapped by WYKO (b) Mapped by DSAGE

Fig. 3 Isometric plots of the indentation surface.

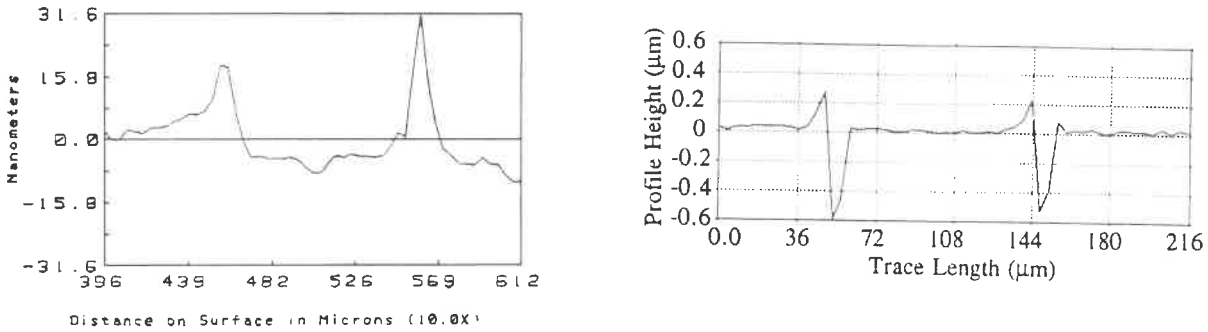

(a) Mapped by WYKO (b) Mapped by DSAGE

Fig. 4 Profiles across the indentation

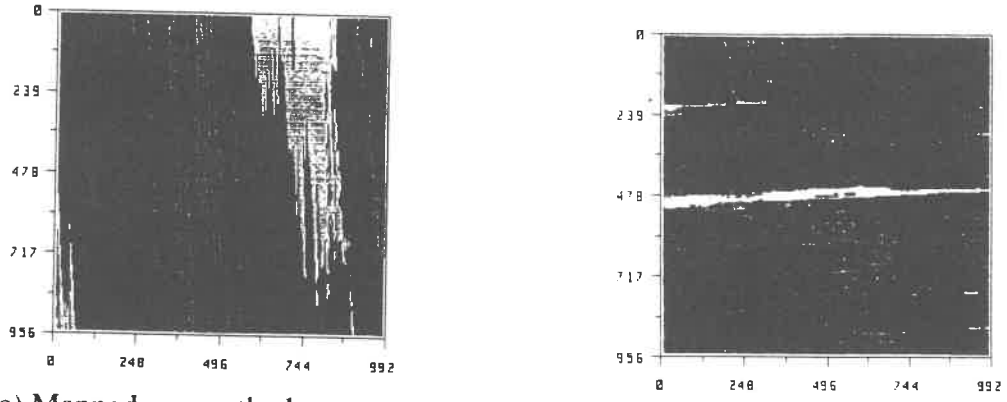

(a) Mapped across the lay (b) Mapped along the lay

Fig. 5 Contour map of the Uni-directional surface obtained by the WYKO

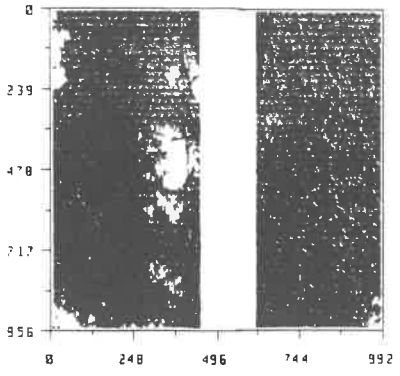

blue colour trans. colour

Fig. 6 Contour map of two polymer surfaces obtained by the WYKO

"The Specification of a Flexible File Format for Storage and Retrieval of Engineering Topographic Data"

by
P.J. Sullivan[1] and K.J. Stout
School of Mechanical and Manufacturing Engineering,
University of Birmingham, Birmingham B15 2TT, UK

Abstract

This paper presents a summary of considerations for, and the basis of, a specification for a flexible disk file format for storing 3D topographic data. It is intended to generate discussion with users and manufacturers of 3D topographic measurement systems and, as such, forms the basis of a poster paper to be presented at the ASPE meeting.

1.0 Introduction

There are a number of commercially available and in-house developed 3D (so-called) surface measurement instruments. They operate on a variety of principles (e.g. mechanical contact, light scatter) but due to the complexity of the data acquisition technique and the subsequent data analysis, almost all of the instruments are microcomputer-based and store/retrieve the topographic data from data files held on disk. Each measurement system usually has its own data characterization system capable of graphical analysis, numerical representation (such as through statistical parameters) and processing routines (e.g. filtering, data inversion). In addition, there are a wide variety of commercial software packages suitable for analyzing surface data such as MatLab™, Mathcad™, AutoCad® and image analysis packages as well as conventional spreadsheets. However, as any user is aware, each package has its own unique data file format which results in an expensive file conversion procedure (in terms of time and disk storage) when converting from one data file format to another. This often results in many, in essence, identical versions of the same data file being stored. This leads to confusion and a full disk!

Many standard file formats already exist for interchange of other popular computer based data such as PCX for image files, DXF for drawing files, and ASCII for text files. The specification for a surface data file (SDF) format is proposed here, for consideration of use by manufacturers and users, to enable straightforward interchange of topographic data between different software packages. In addition to simplifying data storage, the acceptance of a standard file format for 3D data would provide a useful step towards the development of "soft artifacts". i.e. it would be possible to verify software routines through the use of artifact surface files which would be generated with known properties.

This work forms part of an EC project currently underway at the University of Birmingham examining current trends in 3D surface measurement and characterization.

2.0 Scope of specification

For the purposes of this specification the data points represent a rectangular area of a surface using a rectangular sampling lattice with equal lattice spacing along each axis (see Fig. 1). Let the sampling lattice consist of NP data points per profile (each point separated by a distance Xscale) and NT profiles (separated by a distance Yscale). Using a Cartesian co-ordinate system, the individual data points correspond to the measured height, $Z_{i,j}$, (where $1 \leq i \leq NP$; and $1 \leq j \leq NT$) of the surface at the sampling location. Assuming $Z_{1,1}$ is at $x = 0$ and $y = 0$, each number triple is specified exactly by (i-1)*Xscale, (j-1)*Yscale, and $Z_{i,j}$. Thus, provided the values of $Z_{i,j}$ are stored in the data file in a deterministic fashion (e.g. sequentially profile by profile), it is necessary only to store the Xscale and Yscale values to reconstruct the data triples. A more complete data reference is obtained by the

[1]Currently at the Precision Engineering Division, National Institute of Standards and Technology, Gaithersburg, MD 20899, USA. Tel: (301) 975 6386

additional storage of X, Y, and Z offset values which define the offsets from the measured zero datum of all the Z values. N.B. SI units (m) are used throughout.

The present scope of the file specification is to provide a data format for files to be stored on an IBM PC-based (or equivalent) machine i.e. those using 8088 through 80486 processor. The specification is not machine specific but due to variations in the way in which different processors store and manipulate numbers (in particular real numbers), data file transfer between different platforms may not be possible without some conversion.

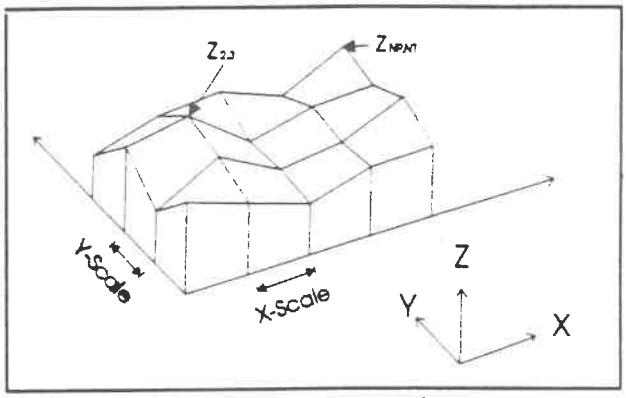

Figure 1 Co-ordinate system used

Note, although there already exist some de-facto image formatting file specifications, i.e. PCX, GIF, TIFF, there are several limitations to their use for storage of topographic data and thus a purpose-specified format is necessary.

3.0 Formatted disk storage

As previously mentioned, the amount of information necessary to store surface data is relatively large. Thus, the most efficient storage type, in terms of file size and speed of access, is so-called binary (as opposed to ASCII). Also, to maintain flexibility the format should be free format (i.e. it should allow a combination of storage of different types including CHAR, INTEGER, and FLOAT). Appendix 1B describes the supported data types. In order to ease file searching a common file extension should be used (.SDF).

The format for the data files is divided into three sections (a schematic of the SDF storage layout is shown in Appendix 1D).

(1) Header - fixed length
(2) Data area - variable length
(3) Trailer - variable length descriptive area

3.1 Header

The proposed header format is described below and defined in Appendix 1A.

(i) **Version Number.** A version number (e.g. V3D92A) for the file specification is essential so that modifications to the file format may be easily implemented. Although the version number could be coded and stored as a single UNSIGNED CHAR, utilizing a 6 character version number almost eliminates the possibility of mistakenly attempting to read a non-SDF file. N.B. For obvious reasons, it is essential that a central source should be responsible for control over issuing version numbers and specifications of the file format.

(ii) **Measurement instrument manufacturers identifier.** This provides the source of the data and might include hardware and software identifiers. It is anticipated that 10 characters is sufficient to identify a machine/gauge/software-version type.

(iii) **Original creation date and time.** This is a 10 UNSIGNED CHAR field (DDMMYYHHMM) to store the date and time that the measurement was completed. Redundant separator characters are not stored. Thus, 1207921421 is interpreted as the 12th July 1992 at 2:21pm .

(iv) **Last modified date and time.** This field is similar to that in (iii) but defines the last date and time that the SDF was modified.

(v) **Number of points per profile, NP.** It is anticipated that one UNSIGNED LONG value is more than sufficient to store the maximum possible number of points in a profile. (i.e. 2,147,483,647).

(vi) **Number of profiles or traces, NT.** See (v).

(vii) **X scale**. For flexibility, and to maintain accuracy, the scaling factors are stored as type DOUBLE (floating point double precision) values. The three scaling factors then provide scaling to the standard unit of the meter. Thus an Xscale value of 1.00E-6 represents a sample spacing of 1μm.

(viii) **Y scale**. See (vii)

(ix) **Z scale**. See (vii)

(x) **Z resolution**. When dealing with digital data it is important to recognize the problem of quantisation rounding. After certain processing operations (e.g. removal of datum) the data type may have changed or be re-scaled such that the original quantised data has been re-quantised. Thus, the inclusion of this value enables the user to be aware of the original base resolution of the measurement instrument. The units of the resolution value is in meters. The resolution value is stored as type DOUBLE. A specification for the method of calculation of Z resolution is also required.

(xi) **Xoffset**. Xoffset, Yoffset and Zoffset values enable a reference data triple to be maintained between surfaces. Thus, for example, if a portion of a surface is windowed and stored it is possible to maintain the spatial reference between it and the original surface. These values are stored as type DOUBLE.

(xii) **Yoffset**. See (xi).

(xiii) **Zoffset**. See (xi).

(xiv) **Compression type**. This single UNSIGNED CHAR value gives a coded correspondence to the compression type used on the data. The list of types implemented is given in Appendix 1C. See section 3.2.2.

(xv) **Data type**. This single UNSIGNED CHAR value gives a coded correspondence to the base data type used. The list of types implemented is given in Appendix 1B. (See section 3.2.1).

(xvi) **Number of data matrices**. This single UNSIGNED CHAR value determines the number of data matrices that are contained within the data area. (See 3.2)

3.2 Data Area

The data area of the data file contains the coded height information of the number of surface matrices for the number of points, NP, and number of profiles, NT, defined above. The actual height values are obtained by scaling the coded values by the Zscale factor and adding the Zoffset value defined in the file header. The data is stored trace-by-trace starting with $Z_{1,1}, Z_{2,1} \ldots Z_{NP,1}, Z_{1,2}, \ldots$ and finishing with $Z_{NP,NT}$.

The data area may contain data matrices for more than one surface. In general, for the simple case of a single surface the number of matrices is set to 1. There are occasions, however, when it is desirable to store a number of associated data matrices within the same data area. Consider the following examples: (i) Two matrices are required to store a measured surface along with a reference surface, (ii) It may be desirable to store several measurements of the "same" surface for statistical analysis purposes, and, (iii) It is possible, after processing surface data, to require the storage of complex data e.g. after a 2D Fourier transform. This means that the data area must contain both the real and imaginary parts of the data. In this case the number of data matrices is set to 2. Clearly, the maximum number of matrices is 255 and all the stored matrices share the same header attributes (number of points, scaling factors etc.). If there is more than one data matrix the matrices are stored successively in the data area (see Appendix 1D).

3.2.1 Data types

Due to variations in output resolution of different measurement gauges (i.e. numbers of bits), memory and storage considerations (see 3.2.2), and consequential changes in data types due to processing, it is necessary to incorporate some flexibility in the base data type. The base data type (i.e. FLOAT, INTEGER etc.) of the coded height information is also specified in the header and the base types utilized here are given in Appendix 1B. The data formats can be machine specific thus it is important to utilize available standards (ANSI C IEEE) and "de facto" standards (e.g. Microsoft® and

Borland C®, Turbo Pascal®).

3.2.2 Data compression methods

Topographic data files can occupy considerable disk storage space. For example, using INTEGER storage of individual data points, a 1mm square area mapped at 1μm sample spacing occupies approximately 2MB of disk space. Recently, largely due to the increased use of high resolution computer video images, there has been an emergence in the development of compression algorithms. Using compression techniques can considerably reduce the storage requirements of many different data types. For example, typical Wyko and Rank Taylor Hobson data files can be compressed by over 50% with zero information loss.

Briefly, data compression schemes may be classified into two categories (i) information preserving and (ii) lossy compression algorithms. Information preserving, or error free, compression includes techniques such as variable length coding, bit plane coding, and lossless predictive coding. Lossy (or destructive) compression algorithms include the use of the discrete cosine function and fractal compression and are being implemented on an increasing number of hardware (where a considerable increase in speed of compression/decompression is achieved) as well as software systems. Lossy compression techniques have key applications in cases such as surface databases where the high compression ratio is favorable to a small loss in data integrity.

Another compression scheme (which may be either "lossy" or not) is the simple re-casting of data type. For example if the data is type UNSIGNED INT i.e. 16-bit, but the range of the actual data is 0-200 then the data may be re-cast to type UNSIGNED CHAR which will halve the storage requirements. This situation may occur quite often when a surface is high pass filtered or levelled. Clearly, this is an example of an error free compression. The scheme may be lossy when converting from FLOAT to INTEGER, for example.

The use of compression schemes, including "lossy", in topographic analysis needs to be investigated further. Thus, at this stage only uncompressed and run-length limited (RLL)[1] compression has been included in the specification. It was felt necessary, however, to include the ability to store other compression types as this clearly will be an important future issue.

3.2.3 The treatment of NULL data

Certain topography measurement systems, as a consequence of the measurement process (in particular phase measuring interferometers), produce data points within the complete measurement map that are not measurable. These data points may be referred to as "bad" or NULL data and should be distinguished from outlier data whose representation is functionally specific. As a consequence of this, it is necessary to implement procedures which enable the analysis software to take appropriate action when encountering such data. Typically, for example, this may mean simply ignoring the values of the NULL data points in a parameter calculation or representing them in a different colour when plotting.

The identification of such NULL data points may be achieved by setting them to a particular value within the data range which is not allowable for any valid data points. For example, when using a measurement process that acquires data using a 12 bit digitisation process (i.e. produces decimal values in the range 0-4095) the data is typically stored in 16-bit words. Thus, any NULL values may be represented by the value 65,535. Clearly this is merely a representation issue but one which needs to be standardized. The use of the maximum value for the particular data-type used, provides an acceptable solution.

3.3 Trailer

The trailer part of the data file contains useful historical information associated with a particular measurement. Consider the following examples (i) when a measurement is made, information such as the operator name, measurement conditions, and sample specification might be stored with the data file (ii) after processing the data file in a particular way such as filtering or a data inversion the process parameters may be attached to the data file. In order to maintain flexibility of extendibility it is

important that the trailer be of variable length and, for simplicity, exist at the end of the data file. The trailer is thus stored at the end of the file as a series of UNSIGNED CHAR values.

4.0 Soft artifacts and other issues

Other issues in topographical analysis software design and data exchange are the design of algorithms and "soft calibration". There is increasing demand for the availability to the user of procedures for verification of the performance of surface characterization algorithms. This verification may be achieved through the use of soft artifacts i.e. data files representing a particular set of surface characteristics. These data files may be mathematical test matrices with known attributes generated using simulation or analytical techniques.

5.0 Conclusions

A specification is given here of a flexible extendible file format for the storage of topographic engineering data, for consideration by others (manufacturers of equipment and users) involved in the measurement and analysis surface topography. It is hoped that following discussions with interested parties a suitable specification can be agreed upon which will then be published in an appropriate journal for reference.

APPENDIX 1

A. Header description showing field types and lengths

See Section 3.1	Information	Data Type	Total Length (BYTES)
(i)	Version Number	UNSIGNED CHAR	6
(ii)	Manufacturers ID	UNSIGNED CHAR	10
(iii)	Original Date and Time	UNSIGNED CHAR	10
(iv)	Last Modified Date and Time	UNSIGNED CHAR	10
(v)	Number of points per profile	UNSIGNED LONG	4
(vi)	Number of profiles	UNSIGNED LONG	4
(vii)	Xscale	DOUBLE	8
(viii)	Yscale	DOUBLE	8
(ix)	Zscale	DOUBLE	8
(x)	ZResolution	DOUBLE	8
(xi)	Xoffset	DOUBLE	8
(xii)	Yoffset	DOUBLE	8
(xiii)	Zoffset	DOUBLE	8
(xiv)	Compression Type	UNSIGNED CHAR	1
(xv)	Data Type	UNSIGNED CHAR	1
(xvi)	Number of Data Matrices	UNSIGNED CHAR	1
TOTAL			103

B. List of supported base data types

Data Type Number	Data Type	Length	Decimal Minimum Value	Decimal Maximum Value (NULL)
0	UNSIGNED CHAR	1	0	255
1	UNSIGNED INT	2	0	65535
2	UNSIGNED LONG	4	0	4294967295
3	FLOAT	4	3.4E-38	3.4E+38
4	SIGNED CHAR	1	-128	127
5	SIGNED INT	2	-32,768	32,767
6	SIGNED LONG	4	-2147483648	2147483647
7	DOUBLE	8	1.7E-308	1.7E308

C. List of supported compression types

Compression Type Number	Compression Type
0	None
1	Run Length Limited

D. Schematic of SDF data format

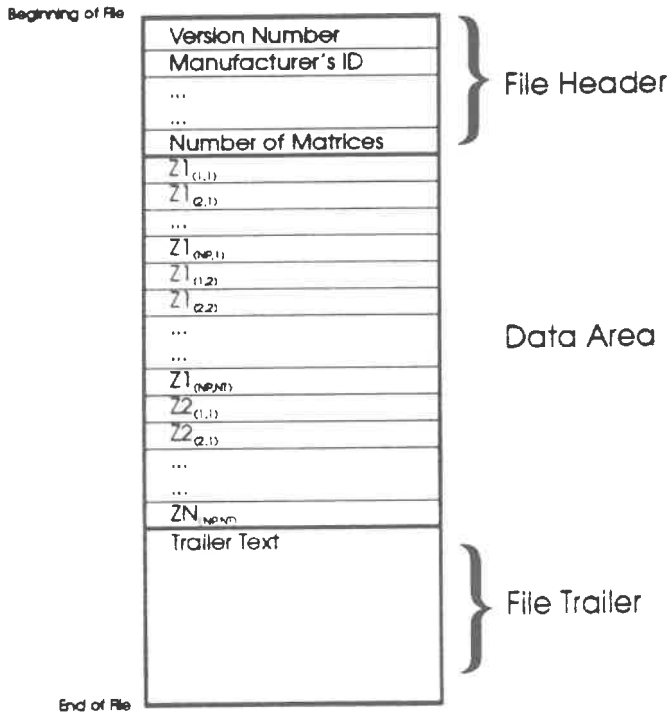

Reference

1. See for example Lindley, C.A., "Practical Image Processing in C", Wiley, 1991.

DETERMINATION OF PROPER SAMPLING SPACING FOR 3D TOPOGRAPHY MEASUREMENT OF MACHINED SURFACES USING POWER SPECTRAL ANALYSIS

T Y Lin, K J Stout and P J Sullivan
School of Manufacturing and Mechanical Engineering, University of Birmingham
Edgbaston, Birmingham B15 2TT, UK

1.0 Introduction

The determination of sampling spacing (or sampling interval) is essential in the digital measurement of surface topography. For instance, sampling spacing must be selected together with sampling length before a profile measurement can be made, although in some measuring systems the sampling spacing is pre-set by the manufacturers of the systems. The spacing of ordinates in a sample determines the highest frequency that can be identified in the acquired data.

1.1 Two dimensional (2D) power spectral analysis

Surfaces exist in three dimensions (one dependent and two independent variables). A dependent surface height $h_{j,k}$ is the function of two independent coordinates x_j and y_k along two Cartesian axes x and y. The two dimensional discrete Fourier transform (as conventionally called) of surface heights is defined as

$$H_{r,s} = H(f_r, f_s) = \frac{1}{NM} \sum_{k=0}^{M-1} \sum_{j=0}^{N-1} h_{j,k} \exp\left[- i2\pi \left(\frac{rj}{N} + \frac{sk}{M} \right) \right]$$

N and M are the number of data points in x and y axes respectively.

The 2D spectral coefficients $H_{r,s}$ of a surface sample are normally used to compute the power spectrums of the sample. Circular power spectrums by periodogram estimation can be defined by

$$P_{r,s} = P(f_r, f_s) = |H_{r,s}|^2 + |H_{N-r,M-s}|^2 + |H_{N-r,s}|^2 + |H_{r,M-s}|^2$$

$$f_r = \frac{r}{N\Delta_x}, f_s = \frac{s}{M\Delta_y} \qquad 0 < r < N/2, 0 < s < M/2$$

$P_{r,s}$ may be interpreted as the accumulation of power spectrums distributed around the four quadrants of a spectral matrix $H_{r,s}$ for a given frequency $f = \sqrt{fr^2 + fs^2}$. Δ_x and Δ_y are the sampling spacing along x and y axes respectively. Frequency components f_r and f_s along two coordinate axes are defined only for the positive frequencies up to the Nyquist limit of $1/2\Delta_x$ and $1/2\Delta_y$. The definition of power spectrums above is mainly due to the fact that there are no negative frequencies in the measurement of engineering surfaces.

2.0 Considerations of sampling bandwidth in surface measurement

In choosing sampling spacing, aliasing problem and computing efficiency as well as memory capacity of a computer used should be considered. Sampling at ordinates that are too close together will produce correlated and highly redundant data, and this will in turn lead to a long time computing and an increasing data processing difficulty arising from computer memory. On the other hand, a too large sampling spacing may lead to the confusing folding in the original data of high frequency components with low frequency (aliasion problem). As in the case of stylus instruments, a stylus acts in the same manner as a low-pass analogue filter. One of the approaches to overcome aliasing is to choose a sampling interval as small as the size of the stylus, therefore any frequency components with a wavelength shorter than the stylus can not be acquired. However, heights of data collected from engineering surfaces by using such a small sampling interval is inevitable to be highly correlated. Some researchers present their analytical formulae as using various criteria for the determination of "optimal" sampling spacing. These criteria usually presume that the tolerance between a parameter calculated from a measured (discrete and digitised) surface and the true value of a real (continuous) surface does not exceed a pre-set limit. The limit of the use of these analytical formulae is due to their idealised analytical assumptions and the ignorance of the aliasing effect.

3.0 Scope and results of this investigation

The work reported in this paper attempts to develop an approach for determining a proper sampling spacing for three dimensional (3D) topography measurement of an engineering surface. Based on the proper sampling interval, a reasonable number of ordinates can be used to express the main geometric features of the surface, which are usually represented by characteristic parameters.

In this research, 2D power spectral analysis is employed to analyse the frequency constituents of a surface. The influence of the aliasing problem on surface measurements is evaluated by the circular spectrum of the surface. The quantity of surface geometric features contained in a surface sample is assessed by the plot of accumulation spectrum against frequency, which is used to study the effect of the sampling spacing. A reasonably large sampling interval can be obtained using the principle that the difference between the estimates of a 3D parameter computed from a measured surface and the most accurate realisation of the actual surface does not exceed a prescribed limit. The principle is enhanced in use of the criterion that the spectral constitutes of a measured sample do not deviate from its accurate realisation to a certain extent. Although the concept of the principle is similar to other previous work, the approach of the research has in essence several advantages: such as, influence of aliasion distortion is considered by the spectral analysis mentioned above; without the limitation of theoretical assumptions, such as surface heights as a stochastic process and Gaussian distribution of Ra estimates.

The results of the determination of proper sampling spacing above are useful in some studies, such as the selection of low frequency cut-off and its influence on area surface parameters. Some results of this investigation are shown in the following figures.

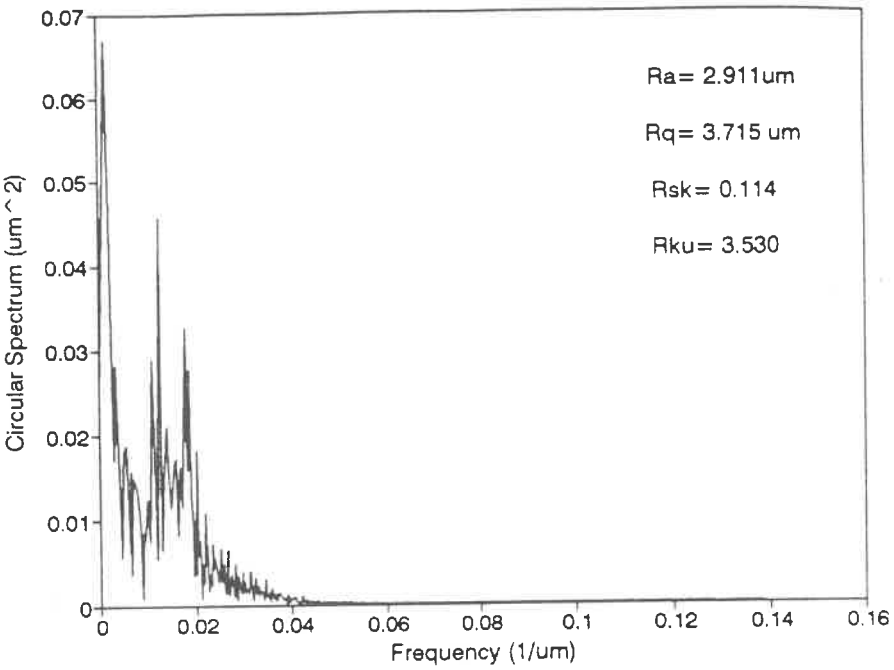

(a)

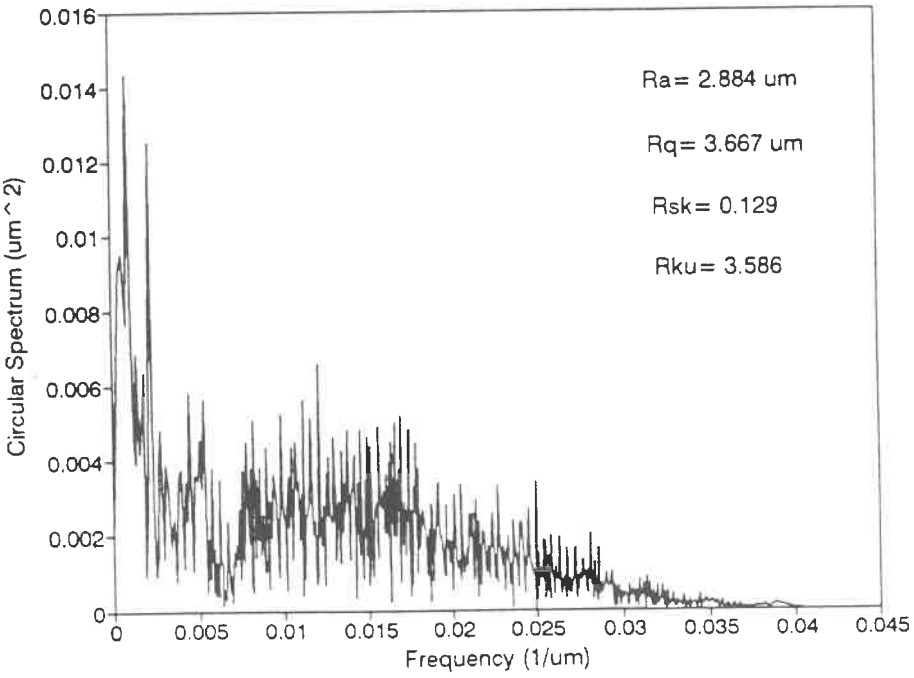

(b)

Fig 1 Circular spectrums of a spark eroded surface measured by 128 x 128 data points (a) sampling spacing = 5 μm; (b) sampling spacing = 17.5 μm

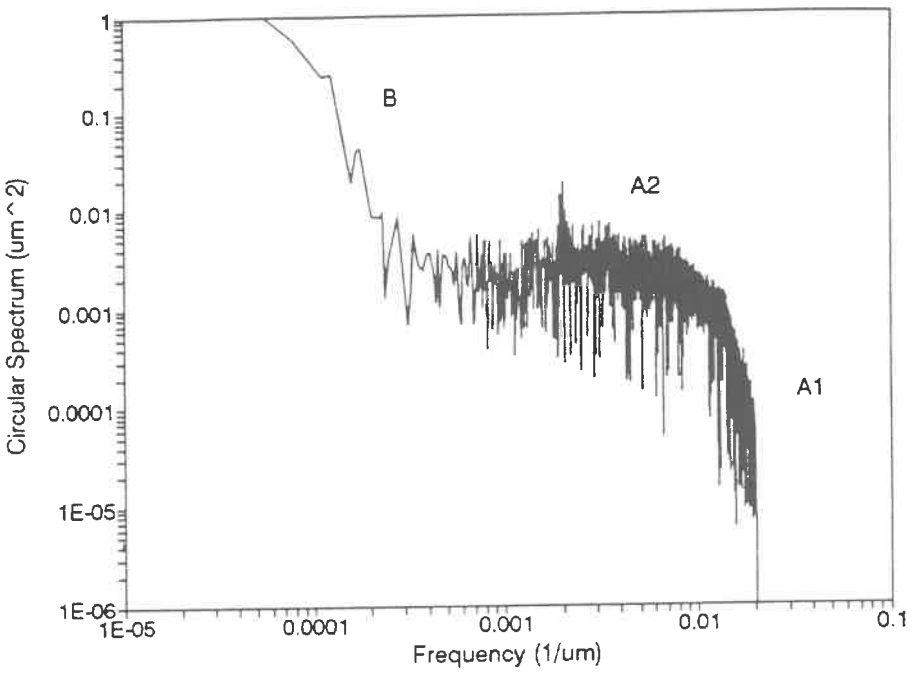

(a)

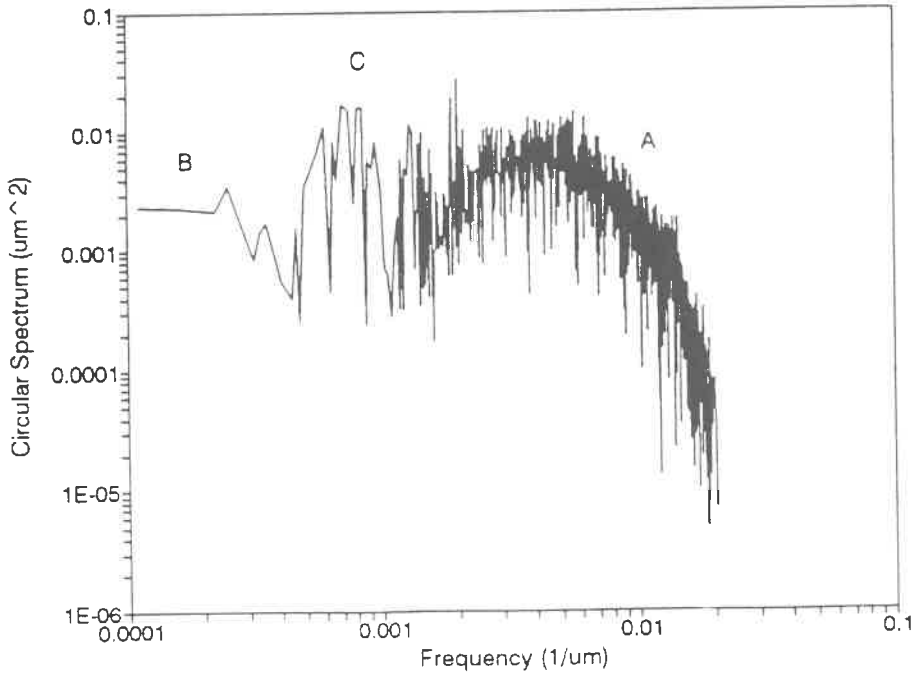

(b)

Fig 2 Typical spectrums of sample surfaces from (a) spark eroded specimens; (b) shot blasted specimens

Non-contact Surface Roughness Measuring System for Magnetic Disk

You Zheng
Dept. of Precision Instruments. Tsinghua University
Beijing, P.R.China
Li Zhu
Dept. of Mech. Eng.(1),Huazhong Univ. of Sci. & Tech.
Wuhan, P.R.China

I,INTRODUCTION

During recent years, several methods of determining surface characteristics of extremely smooth surfaces have been presented. The principles of these methods are total-integrated and angle-resolved scattering, stylus profilometry, and heterodyne profilometry.

The scattering methods are noncontact and give statistical information about the surface , not a profile. Stylus profilometers contact the sample with a stylus, risking surface damage, however, they offer 1 Å sensitivity and excellent spatial resolution. Heterodyne profilometers can give height resolutions comparable with stylus profilometers,while their lateral resolution is limited by diffraction to 1-2 um if the light source operates in visible region. This is also noncontact method, and scan length has no theoretical limitations.

II, PRINCIPLE OF OPERATION

The system is based on the heterodyne interferometry with a common optical route . The surface of the workpiece is illuminated by two laser beams with slightly different frequencies. One of the beams is focused as the measuring optical probe to scan the surface of workpiece. The other is used as a reference optical beam. the above two reflected beams are allowed to interfere. The optical phase difference of signal is in proportion to the variation of surface height. The lateral resolution is less than 2 um and the vertical resolution is less 1 nm .No extensive alignment of the sample is needed and the sample is also used as the reference surface also.

A, Optical System

The schematic of the optical system is shown in Fig. 1 . The laser is 2.8mw He-Ne laser. The laser beam is divided into two beams with a beam splitter. Each arm of the system contains an acoustooptic (AO) modulator operating at slightly different frequencies (100 and 100.1MHz). The beams from L1-BS-AO1-CP1 and L1-

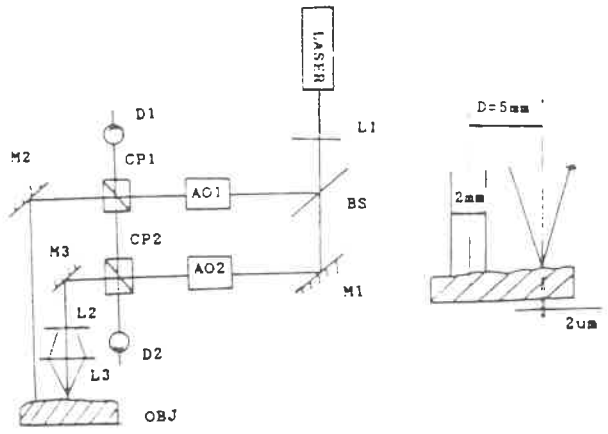

Fig.1 The schematic of optical system

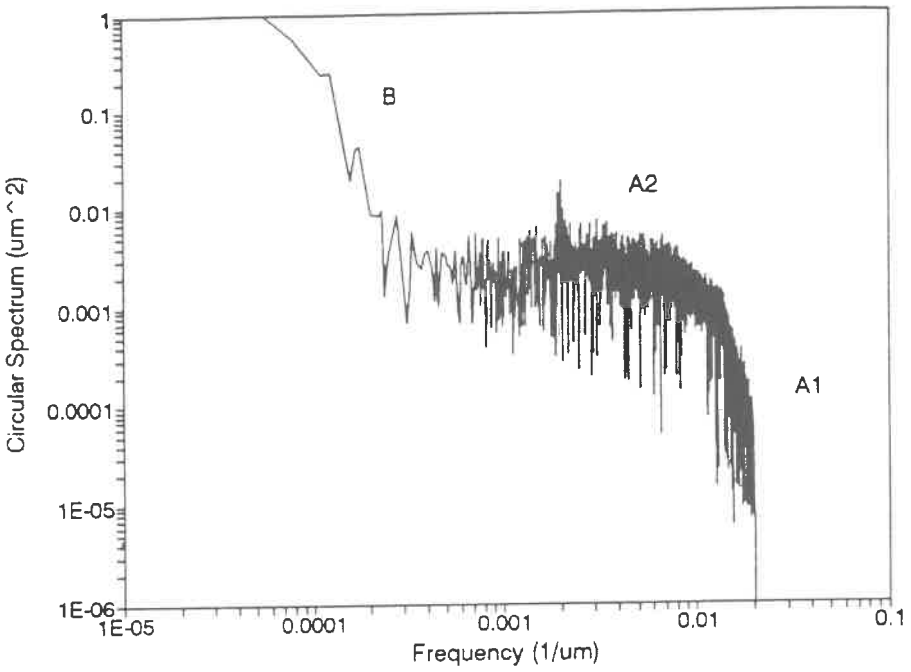

(a)

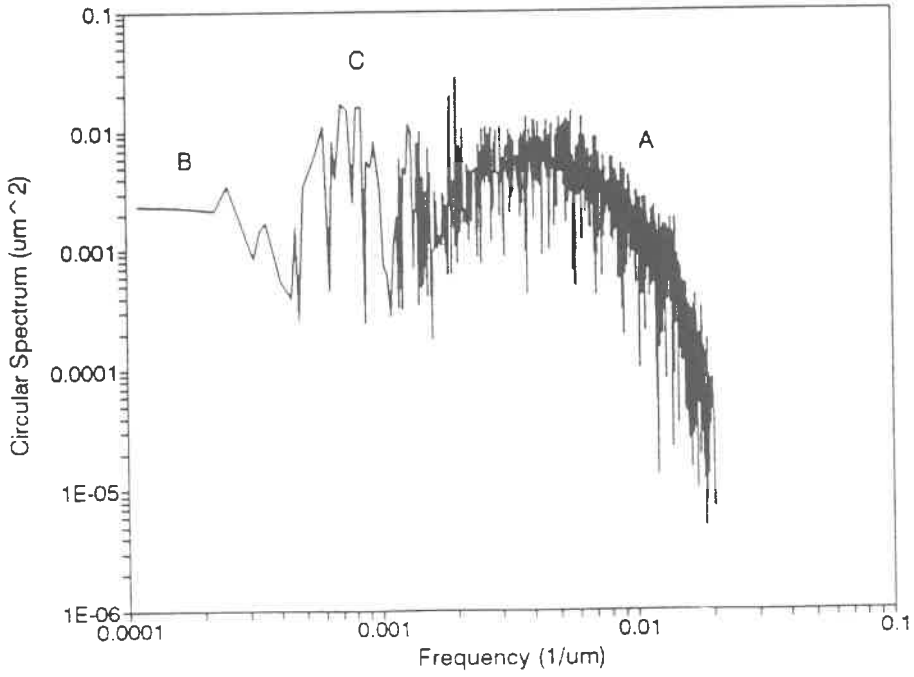

(b)

Fig 2 Typical spectrums of sample surfaces from (a) spark eroded specimens; (b) shot blasted specimens

Non-contact Surface Roughness Measuring System for Magnetic Disk

You Zheng
Dept. of Precision Instruments. Tsinghua University
Beijing, P.R.China
Li Zhu
Dept. of Mech. Eng.(1),Huazhong Univ. of Sci. & Tech.
Wuhan, P.R.China

I,INTRODUCTION

During recent years, several methods of determining surface characteristics of extremely smooth surfaces have been presented. The principles of these methods are total-integrated and angle-resolved scattering, stylus profilometry, and heterodyne profilometry.

The scattering methods are noncontact and give statistical information about the surface , not a profile. Stylus profilometers contact the sample with a stylus, risking surface damage, however, they offer 1 Å sensitivity and excellent spatial resolution. Heterodyne profilometers can give height resolutions comparable with stylus profilometers,while their lateral resolution is limited by diffraction to 1-2 um if the light source operates in visible region. This is also noncontact method, and scan length has no theoretical limitations.

II, PRINCIPLE OF OPERATION

The system is based on the heterodyne interferometry with a common optical route . The surface of the workpiece is illuminated by two laser beams with slightly different frequencies. One of the beams is focused as the measuring optical probe to scan the surface of workpiece. The other is used as a reference optical beam. the above two reflected beams are allowed to interfere. The optical phase difference of signal is in proportion to the variation of surface height. The lateral resolution is less than 2 um and the vertical resolution is less 1 nm .No extensive alignment of the sample is needed and the sample is also used as the reference surface also.

A, Optical System

The schematic of the optical system is shown in Fig. 1 . The laser is 2.8mw He-Ne laser. The laser beam is divided into two beams with a beam splitter. Each arm of the system contains an acoustooptic (AO) modulator operating at slightly different frequencies (100 and 100.1MHz). The beams from L1-BS-AO1-CP1 and L1-

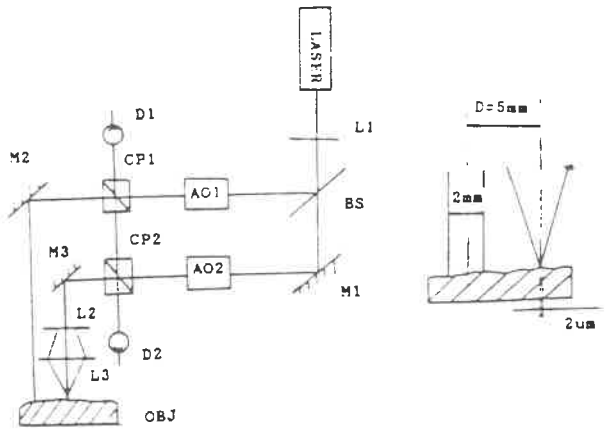

Fig.1 The schematic of optical system

BS-M1-AO2-CP2-CP1 are directed toward a photodetector D1 allowing the beams to interfere, and the signal from this detector is used as a phase reference singal. The beams from L1-BS-AO1-CP1-M2-OBJ-M2-CP1-CP2 (The diameter of the beam is 2mm) and L1-BS-M1-AO2-CP2-M3-L2-L3-OBJ-L3-L2-CP2 (The diameter of the focused beam is less than 2 um) are directed toward a photodetector D2 allowing the beams to interfere, and signal from this detector is used as the measuring singal, The focused beam serves as a probe beam measuring the height of this spot compared to the large spot area.

B, Phase Detection

The detectors D1 and D2 detect a beat frequency equivalent to the difference in the frequencies of the AO modulators operate, i.e.,100 KHz. The phase difference between the two detector signals carries information about the surface profile and is affected by system parameters such as mechanical instability, thermal drift and laser cavity detuning. In following paragraph, the influence of these system parameters is examined.

The reference signal from the detector D1 can be expressed:

$$Sr \sim Isr = |Er|^2$$
$$= |A*\cos(2*\pi*f1*t+k1*z1)+A*\cos(2*\pi*f2*t-k2*z2)|^2$$
$$= 2*A^2*\{1+\cos[2*\pi*(f1-f2)*t-(k1*z1-K2*z2)]\}$$

The measuring signal from the detector D2 can be expressed:

$$Sp \sim Isp = |Esp|^2$$
$$= |A*\cos(2*\pi*f1*t+k1*z3)+A*\cos(2*\pi*f2*t-k2*z4)|^2$$
$$= 2*A^2*\{1+\cos[2*\pi*(f1-f2)*t-(k1*z3-K2*z4)]\}$$

Where f1,f2 = the shifted optical frequencies;
k1,k2 = the wave numbers associated with f1 and f2;
z1,z2 = the optical path lengths in the reference route;
z3,z4 = the optical path lengths in the measuring route.

The phase difference between these signal is detected by the electronics:

$$\Phi = \Phi p - \Phi r = [2*\pi*(f1-f2)*t-(k1*z1-K2*z2)] - [2*\pi*(f1-f2)*t-(k1*z3-K2*z4)]$$
$$= k2*(z4-z2)-k1*(z3-z1)$$

Introducing z4-z2 = z6, z3-z1 = z5, z'=z6-z5, where z' is the optical path difference (OPD) between the reference signal and measuring signal.

Because ki=2*π*fi/c, f2=f1+f'.

$$\Phi = 2*\pi/c(f1*z'+f'*z5+f'*z')$$
$$\Delta\Phi = 2*\pi/(\Delta f1*z'+f1*\Delta z'+\Delta f'*z5+f'*\Delta z5+\Delta f'*z'+f'*\Delta z')$$

In this expression $\Delta f1*z'$ represents cavity detuning of the laser; $f1*\Delta z'$ and $\Delta f'*z'$ are related to surface height of the sample; $\Delta f'*z5$ and $\Delta f'*z$; are related to drift of the beat frequency and $f'*\Delta z5$ represent the mechanical instability of the measuring system. The term $f1*\Delta z'$ represent changes in the OPD of the system, mainly surface height variations. Changes in refractive index caused by air turbulence and temperature variations are also included in this term. To be able to resolve 1 Å, the temperature has to kept constant with 0.01° C between two sample points(1ms or so). This requirement is readily met. Tab.1 shows the typical magnitudes of the system parameters.

Tab.1 The typical magnitudes of the system parameters

Parameter	Value	Variation	
f1	$0.5*10^{15}$Hz	Δf1	10^{6} Hz
z5	0.2 m	Δz5	10^{-3}m
f'	$100*10^{3}$Hz	Δf'	10^{-6}Hz
z'	10^{-3}m	Δz'	10^{-10}m

Phase contribution	Value (rad)
$2*\pi/c(\Delta f1*z')$	$2*10^{-5}$
$2*\pi/c(f1*\Delta z')$	$1*10^{-3}$
$2*\pi/c(\Delta f'*z5)$	$4*10^{-8}$
$2*\pi/c(f'*\Delta z5)$	$5*10^{-7}$
$2*\pi/c(\Delta f'*z')$	$2*10^{-7}$
$2*\pi/c(f'*\Delta z')$	$2*10^{-12}$

If all the terms are sufficiently small compared with the second term,they can be neglected. The following expression is the differential phase difference between the detector signals:

$$\Delta\phi = 2*\pi/c*f*\Delta z'$$

The relationship between surface height and OPD can be expressed:

$$\Delta z' = 2*\Delta h$$

Using this expression and the relation $c=\lambda*f$. Thus the relative surface height can be expressed as a function of the differential phase as:

$$\Delta h = \lambda/(4*\pi) * \Delta\phi$$

C, Traversing Table and Focusing

The sample is translated by a traversing table powered by a steper-motor with variable speed, thus allowing different scan length. The table initially has to be carefully aligned for motion perpendicular to the axis of the incident beam. This alignment need only be checked occasionally. The sample is mounted on the traversing table and the focus is adjusted by moving the position of the object lens with steper-motor. The focusing method is based on the astigmatism principle. Fig. 2 shows the schematic layout of the astigmatism focusing system. Fig. 3 shows the relation between the position (Δl) of the focus spot and measuring voltage signal ,S. A minimum will occur in the signal, S, when the surface is in focus.

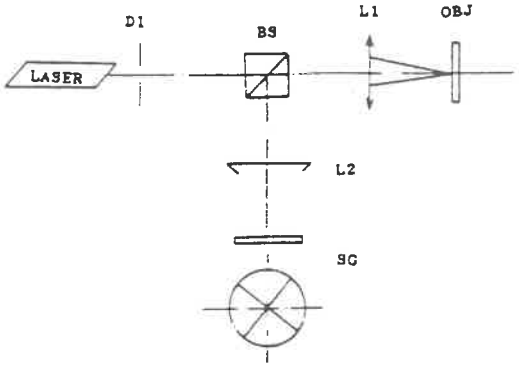

Fig. 2 The schematic layout of the astigmatism focusing system.

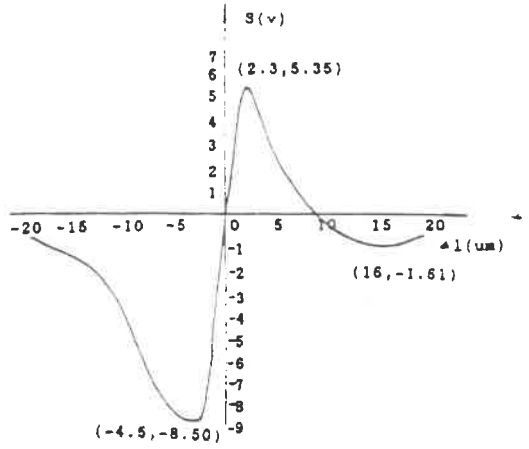

Fig. 3 The relative curve betweem Δl and s

III. RESULTS

The phase difference between the two detector signals is measured by a microcomputer. The phase difference is measured in both the positive and negative zero crossings of the signals according to the relationship between OPD and surface height, The microcomputer can fast accomplish calculates, displays and prints the profile graph, Abbott curve, and the surface roughness evaluation parameters.

The result of a measuring standard grooved sample which was offered by NIM ,(National Institute of Metrology, standard value Ra = 0.088 um) is shown in Fig.4. Fig.5 shows the results of measuring a glassy surface(Ra=0.005um measured by Talysurf5-120). The Abbott bearing ratio curve of Fig. 5 is shown in Fig.6.

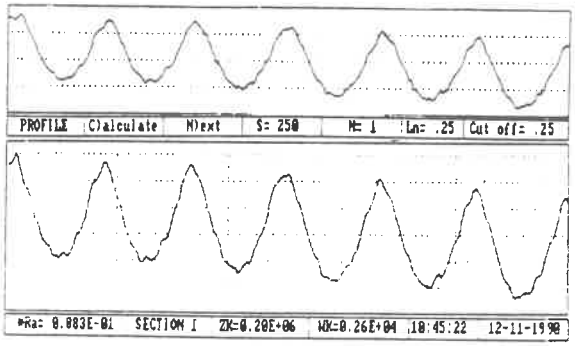

Fig.3 Profile of a standard grooved sample(Ra=0.088um)

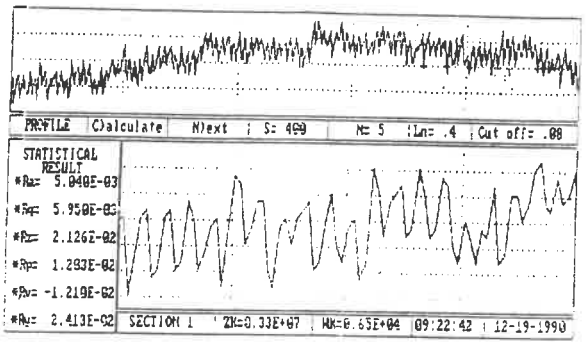

Fig.5 Profile of a glassy surface (Ra = 0.005 um)

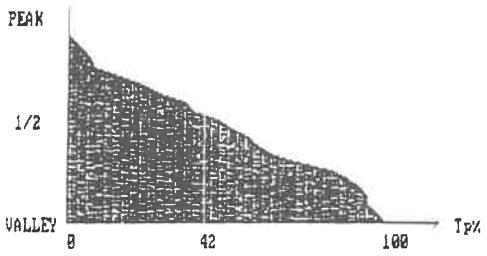

Fig. 6 The Abbott bearing ratio curve of Fig. 5

IV. CONCLUSION

A noncontact optical heterodyne Profilometer for measuring surface profiles without need of an extra reference surface has been developed. The lateral resolution of the tester is less than 2 um,while theoretical height is 1 Å. The actual height resolution is limited to 8 Å by mechanical instabilities in the tester. The tester exhibits good repeablities and ease of alignment. Measurements with scan lengths of 80 um to several millimeters can be performed with no changes in the instrument, and data can be treated by microcomputer programs for obtaining information about surface roughness. Now the tester has been used as Noncontact Surface Roughness Tester of Magnetic Disk.

A SPHERE AND CYLINDER ALIGNMENT SYSTEM

Richard Rhorer
Los Alamos National Laboratory
Los Alamos, New Mexico 87545

Introduction

In designing an automatic manufacturing system for spherical shell components, it was necessary to develop an alignment system for two high precision air-bearing spindles. One spindle holds the shell during machining of the outside. When the outside is complete, the shell is transferred automatically to the other spindle which contains a vacuum pot-chuck. The vacuum pot-chuck then holds the shell while the inside surface is machined. To prevent damage to the shell surface during this spindle-to-spindle transfer, it is necessary to have good alignment between the two spindles.

The slide ways that carry the spindles are mounted on a common base, and mechanical alignment within 2 or 3 micrometers could be achieved under ideal conditions. The problem occurs when a heavy fixture or part is held on one spindle, and the natural deflection of the air bearing would allow one spindle to droop, then the alignment could be 5 to 10 micrometers. With a significant misalignment, delicate parts can be damaged during the spindle-to-spindle transfer because the part itself works as an alignment device. The force necessary to align the spindles is then carried by the component.

The design of the alignment device discussed in this report protects the part by preventing it from touching the receiving fixture until alignment is guaranteed. The design is based on a hard spherical surface mounted on one spindle and a cylindrical surface mounted on the other. The basic concept is illustrated in Figure 1. The spherical surface constrains the two spindles to be aligned in the plane perpendicular to the axes, but allows angular and axial motion. Angular and axial motion are constrained separately.

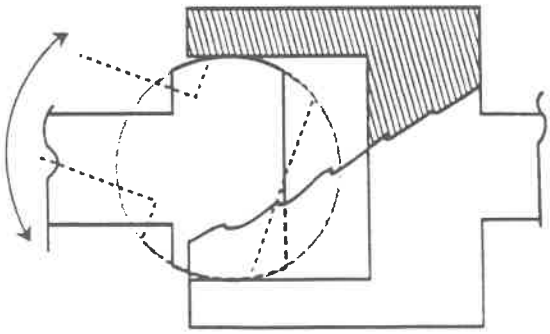

Fig. 1. Sphere and Cylinder

The idea of a spherical surface sliding into a cylindrical surface has been used for many different applications. The author first saw this type of alignment system demonstrated for ultraprecision chucking applications by Richard Clouser[1].

Background

The manufacturing of toxic or radioactive parts is being automated to minimize exposure to the workers. A project to build an automated system for machining spherical shells was initiated within the US Department of Energy in 1986. This project is called the Precision Automated Turning System (PATS). The PATS project is part of the larger program called the Precision Flexible Manufacturing Systems (PFMS)[2].

To automatically manufacture a shell component it is necessary to transfer the part from the outside machining operation to the inside machining operation. In current practice this operation is done by a skilled operator who "feels" the fit of the shell into the holding fixtures. Our goal in the PATS project is to make this transfer integral to the controlled machining operation -- the system is designed to make a good part every time. The system design requires that all significant variables be monitored with appropriate sensors to insure that the process is under control at all times.

To transfer the parts during the machining operations, several different approaches were considered. We decided to use a precision engineered mechanical alignment approach instead of an adaptive feed-back or robotics approach. The approach of transferring parts in the PATS is a displacement controlled process.

As automatic handling is applied to more and more precise manufacturing processes, the traditional approach from robotics becomes difficult. In general, robotics -- devices with human like motions -- uses force controlled motions for very precise positioning. Whereas, precision engineering has been concerned with precise displacement controlled motion. In other words, a robotic device would have a rather crude displacement control, rather flexible components, and a very sensitive force feed back. A robotic device could move a component until it "hits" something and then stop, or change directions.

A displacement controlled device such as an ultraprecision machine tool has very precise motion control, very stiff components, and no force feed back. An ultraprecision machine tool would move a tool to its programmed point with all the force available in the drive motors regardless of what forces it encounters. Of course, machining has to be a displacement controlled process rather than force controlled -- producing a constant thickness chip would be possible with a robotic machine tool, but the accuracy would be no better than the blank.

The PATS basic machine is composed of two very high precision machine tools built on a common base, providing the best possible built-in alignment of the two spindles. Therefore a displacement controlled system can be used for transferring the parts, without the added complications of a force feed back system. The sphere-in-cylinder alignment system has been added to the spindles to guarantee the alignment to within the last 2 micrometers, even when one of the spindles may be drooping due to a heavy load. The axial and angular

alignment is produced by three hard surface buttons after the spherical surface has been fully engaged in the cylindrical surface.

Alignment System Design

The sphere-in-cylinder alignment system has been designed for the PATS as illustrated in Fig.2. The rings are large enough in diameter to allow the fixtures for the largest parts to be contained inside. The design calls for the spherical element to be a segment of a sphere, not part of a torus. If the segment is not part of a sphere centered on the axis, then binding can occur.

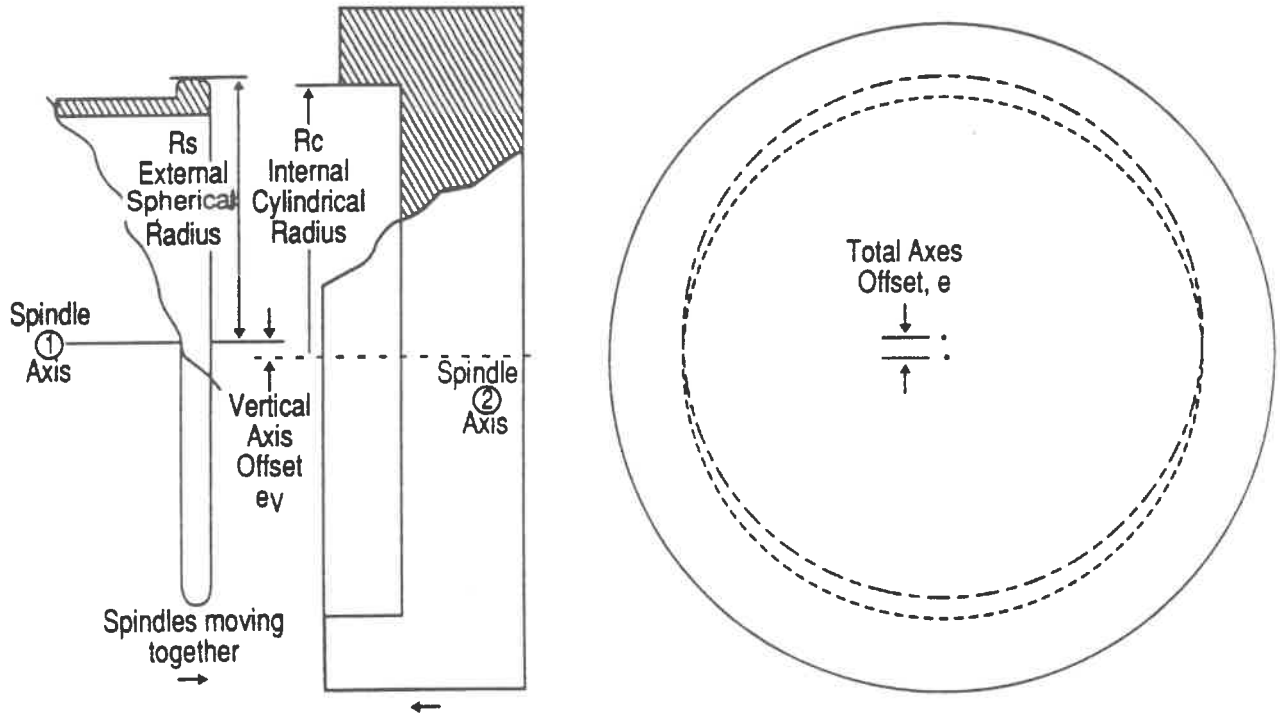

Fig. 2. Sphere and Cylinder Alignment System for PATS

As shown in Fig. 3, the width of the spherical segment needs to be calculated so that the edge of the segment does not touch the mating ring at the very greatest misalignment anticipated in service. The spherical surface touches the edge radius of the cylinder, r_2 in Fig. 4, as the two spindles are brought together. The small radius at the edge of the sphere, r_1, should never touch if the width of the spherical segment is great enough to handle the misalignment, e, in Fig. 2. It is

tempting to make the spherical segment actually part of a torus (by making the radius of curvature less than the radius of the ring); however, this could theoretically cause binding as the spindles are brought into angular alignment.

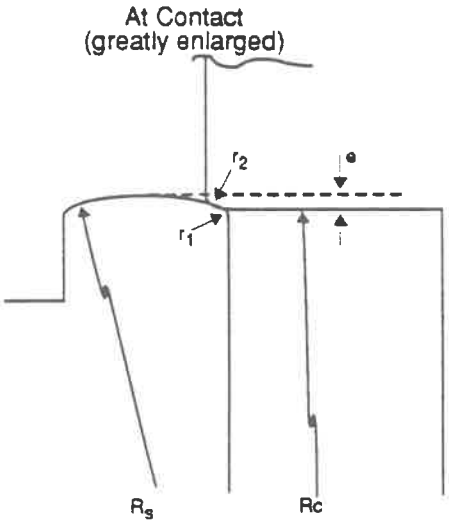

Fig. 3. Effect of Spindle Misalignment

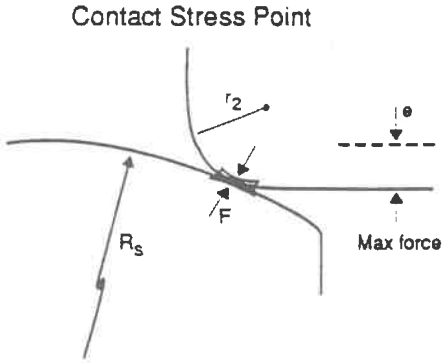

Fig. 4. Contact Point for Sphere and Cylinder

The initial contact of the two spindles would, therefore, be between a sphere of radius R, and a torus with a cross section radius of r_2. The contact stress, or hertzian stress, would be distributed across the elastically deformed intersection of the sphere and torus. As the spindles are moved together to the point where the spherical surface slides into the cylinder, the force goes up because of the radial stiffness of the spindles (and the overall stiffness of the machine); however, the contact area also goes up as the misalignment goes down, thereby lowering the contact stress. When the sphere is engaged in the cylinder, the stress can be distributed over close to half of the cylinder, lowering the wear of the surfaces.

Conclusions

The sphere-in-cylinder alignment method theoretically allows the spindle-to-spindle transfer of parts in a displacement controlled system. Calculations of the stresses, and experimental verification, for the PATS spindle alignment system geometry are being carried out.

---

[1]Clouser, R., In a presentation at the 1978 SME Diamond Turning Meeting in Williamsburg, VA.
[2]U.S. Department of Engery Precision Flexible Manufacturing Systems (PFMS) Program, LALP-89-40, Feb 1990, Los Alamos National Laboratory.

A STUDY ON THE STATIC AND DYNAMIC CHARACTERISTICS OF EXTERNALLY PRESSURIZED AIR BAERINGS

Dong-Chul Han, Professor
Sang-Shin Park, Graduate Student
Woo-Jung Kim, Graduate Student
Jongwon Kim, Research Associate

Department of Mechanical Design & Production Engineering
Seoul National University
San 56-1, Shilim-Dong, Kwanak-Ku, Seoul, KOREA

The recent rapid research activities in the area of electronics and optics are partly based on the development of ultra-precision machining equipment. One of most important factors which determine the overall performance of the ultra-precision machine is the spindle unit, and air bearings are usually used as the main spindle bearings of the machine tools for small and light workpieces. Especially, externally pressurized air bearings are very effective for obtaining accurate run-out of a light rotor shaft. For the design of high-speed accurate spindle with the externally pressurized air bearings, the analysis of dynamic characteristics such as bearing stiffness and damping coefficients are very important as well as that of static characteristics such as bearing load capacity and required air flow rate. To find out the static dynamic characterisitics of the rotor-bearing system, the Reynolds' equation must be solved. The Reynolds' equation for compressible fluid is presented as follows.

$$\frac{\partial}{\partial\theta}\left(PH^3\frac{\partial P}{\partial\theta}\right)+\frac{\partial}{\partial\zeta}\left(PH^3\frac{\partial P}{\partial\zeta}\right)=\Lambda\frac{\partial}{\partial\theta}(PH)+2\Lambda\frac{\partial}{\partial\tau}(PH) \tag{1}$$

Unlike other researches, using direct numerical method that is based on the conservation property of mass flux, iteration method is applied to solve the Reynolds' equation that includes the external air supply sources with a constraint condition. For this, assuming the small motion in the vicinity of the steady state point of rotor shaft, the perturbed Reynolds' equation is obtained through perturbing the film thickness and the pressure term.

$$\nabla\cdot\left(P_oH_o^3\nabla P-\underline{\Delta}P_oH_o\right)=0 \tag{2}$$

$$\nabla\cdot\left[P_0H_0^3\nabla P_k+3P_0H_0^2H_k\nabla P_0+H_0^3P_2\nabla P_0-\underline{\Delta}\left(P_0H_k+P_kH_0\right)\right]=2\Lambda i\left(P_0H_k+P_kH_0\right) \tag{3}$$

Integrating the equation (2) and (3) along the lubricated surface which encompass the arbitrary point (i,j), then Gauss' divergence theorem is applied to obtain line integral equation. If the functions of pressure and clearance are assumed to be linear in the finite minimal domain shown in Fig.2, then by using a central difference equation, following simple algebraic equation is obtained for each mesh point.

$$A_{ki,j}P_{ki,j}=A_{ki-1,j}P_{ki-1,j}+A_{ki+1,j}P_{ki+1,j}+A_{ki,j-1}P_{ki,j-1}+A_{ki,j+1}P_{ki,j+1}+A_{dk}-I_k \tag{4}$$

At the mesh points located on air supply restrictors, the continuity condition for mass flow rate is used. The dimensionless mass flow rate through the inherent compensated air supply restrictor is obtained assuming the isotropic process for compressible fluid[1]:

$$Q_s=\Gamma_sP_sH\Phi \tag{5}$$

The perturbed flow rate equation for the finite minimal domain can be obtained as the governig equation.

$$Q_s=Q_o+Q_1\Delta x+Q_2\Delta y \tag{6}$$

By solving the equation (4), the perturbed pressures are obtained, and then the stiffness and damping coefficients are calculated by integrating these perturbed pressures along bearing width and each coordinates.

$$\gamma_{ij}=\frac{K_{ij}\cdot C}{p_a\cdot B\cdot D} \tag{7}$$

$$\beta_{ij}=\frac{D_{ij}\cdot C\cdot\omega}{p_a\cdot B\cdot D}\qquad ,i=1,2,j=1,2 \tag{8}$$

The forces exerted from air film are then obtained :

$$\bar{F}_x = 0 + \gamma_{11}(\varepsilon,\theta)\cdot\Delta x + \gamma_{12}(\varepsilon,\theta)\cdot\Delta y + \beta_{11}(\varepsilon,\theta)\cdot\Delta\dot{x} + \beta_{12}(\varepsilon,\theta)\cdot\Delta\dot{y} \quad (9)$$

$$\bar{F}_y = \bar{F}_{st} + \gamma_{21}(\varepsilon,\theta)\cdot\Delta x + \gamma_{22}(\varepsilon,\theta)\cdot\Delta y + \beta_{21}(\varepsilon,\theta)\cdot\Delta\dot{x} + \beta_{22}(\varepsilon,\theta)\cdot\Delta\dot{y} \quad (10)$$

where $\Delta x = \Delta\varepsilon\sin\Delta\theta$, $\Delta y = \Delta\varepsilon\cos\Delta\theta$

In the coordinate system shown in Fig.3, O_{js} is the steady-state position of rotor shaft center around which O_{jd} spins with the unbalance of $0.5m_we_\rho$. The nonlinear equation of motion of the rigid rotor-bearing system is as follows where all the variables are in dimensionless forms:

$$\bar{F}_{st}\left(\frac{\omega}{\omega_0}\right)^2\left[\ddot{\varepsilon} - \varepsilon\dot{\theta}^2\right] = -\bar{F}_\varepsilon + \bar{F}_{st}\cos\theta + \bar{F}_{st}\left(\frac{\omega}{\omega_0}\right)^2\varepsilon_\rho\cos(\tau-\theta) \quad (11)$$

$$\bar{F}_{st}\left(\frac{\omega}{\omega_0}\right)^2\left[\varepsilon\ddot{\theta} + 2\dot{\varepsilon}\dot{\theta}\right] = -\bar{F}_\theta - \bar{F}_{st}\sin\theta + \bar{F}_{st}\left(\frac{\omega}{\omega_0}\right)^2\varepsilon_\rho\sin(\tau-\theta) \quad (12)$$

where $\varepsilon = \frac{e}{C}$, $\varepsilon_\rho = \frac{e_\rho}{C}$, $\bar{F}_{st} = \frac{m_w g}{2p_a BD}$, $\omega_0^2 = \frac{g}{C}$ and bearing forces $\bar{F}_\varepsilon$ and $\bar{F}_\theta$ are

$$\bar{F}_\varepsilon = \bar{F}_x\cdot\sin\theta + \bar{F}_y\cdot\cos\theta \quad (13)$$

$$\bar{F}_\theta = \bar{F}_x\cdot\cos\theta - \bar{F}_y\cdot\sin\theta \quad (14)$$

The equation (11) and (12) can be solved applying Runge-Kutta method with initial conditions for ε_o and θ_o obtained at each static equilibrium point, and those for $\dot{\varepsilon}_o$ and $\dot{\theta}_o$ are assumed to be zeroes. The iteration dimensionless time interval $\Delta\tau$ is 0.001.

The theoretical analysis methods are applied to an air bearing with its major dimensions B/D=38/60 and C=20 μm. The supply restrictors are assumed to be located at equal distance with each other along the circumference. The mesh for difference equation is generated such that the circular angle is divided by 60 and axial length by 16.

Principal stiffness and damping coefficients γ_{11} and β_{11} are shown in Fig.4. In this case, the supply pressure is $0.6MPa$ and the eccentricity ratio is 0.1. It is verified that there exist a set of design parameters which yield a maximum stiffness for a given supply pressure. However, the damping coefficient reaches its minimum value with this set of design parameters. Hence there is no way to get simultaneously both of maximum stiffness and damping in case of externally pressurized air bearing.

Fig.5 presents the stiffness coefficients γ_{11} according to the number of air supply restrictors. The supply pressure is $0.6MPa$, $\Lambda = 1$ and $\varepsilon = 0.1$. As the number of air supply restrictors is incresed, the stiffness gets higher. However, the differences between maximum stiffness are within 10 % when the number of restrictors is more than 8. The stiffness also gets higher as the supply pressure is increased as shown in Fig.6. $\Lambda = 1$, $\varepsilon = 0.1$ and the number of restrictors is 12. The maximum stiffness coefficients are linearly proportional to supply pressures. However, the values of feeding parameter which result in maximum stiffness are different for each supply pressure. Fig.7 shows the stiffness and damping coefficients, respectively, according to the eccentricity ε. In this case, compressibility number is 1.0, feeding parameter is 2.4 and attitude angle is 0 . If the ε is relatively small, the principal coefficients are almost same with each other and the coupled coefficients have same magnitude with each other even though the sign is reversed. As the ε increases, γ_{22} becomes larger than γ_{11} since the eccentricity is given to the y direction only. In case of damping coefficients, β_{22} increases rapidly as the ε becomes larger due to the squeeze effect.

This section deals with the comparison between the theoretical prediction of the orbit of rotor shaft center and the experimental result. In general, the orbit of rigid rotor-bearing system supported by air bearing is smaller than the geometrical error of the rotor shaft including the roundness of sensor mounting fixture. For this reason, three-point measuring method[2] is used to measure the accuracy of spindle rotation.

Fig.8 shows the schematic diagram of experimental set-up. Prior to the measurement of the accuracy of spindle rotation, the field balancing of spindle is done according to the procedure proposed by Ozawa[3]. Three of the capacitance type gap sensors PDG-210 are attached to each end of bearing supports and the gains are adjusted to be 1.5748 V/μm. Initially, the balancing of spindle is set to be within 0.1 g at the radial distance of 38.1 mm with 2000 rpm.

The dimensionless orbits (solid lines) of rotor shaft center calculated from the theoretical analysis are compared with the measured orbits (dotted lines) resulted from the experimental study as shown in Fig.9 and Fig.10. In case of Fig.9, F_{st} is 0.21224, each revolution per minute is 1000 and 1500 rpm, the clearance is 20 μm, and the diameter of supply restrictors is 0.25 mm. The magnitudes of the orbits

are proportional to the spining speed of the rotor shaft. Fig.10 presents that the magnitudes of the orbits are also incresed as the unbalance gets larger. In this case, F_{st} is 0.5306 and the other conditions are same as those in previous case.
The differnece between the orbits from the analytical analysis and experimental study is within 5 %. This is largely based on the actual roundness of air bearing, which is 2 μm. The actual roundness results in the difference of air film thickness, which gives the inevitable error between analysis and experiment. So, by using these schemes from this paper, the accuracy of precision surface can be predicted.

1. A.H. Shapiro, "Compressible Fluid Flow", Vol.1, The Ronald Press Company, N. Y., 1953.
2. Kimiyuki Mitsui, J. JSME(C), Vol.48, No.425 (1983)
3. Norimitsu Ozawa, Akinori Yui, Kimiyuki Mitsui, J. JSPE,1987,4.

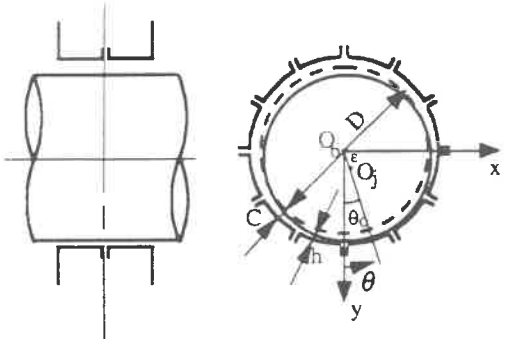

Fig.1 Schematics of the externally pressurized gas journal bearing

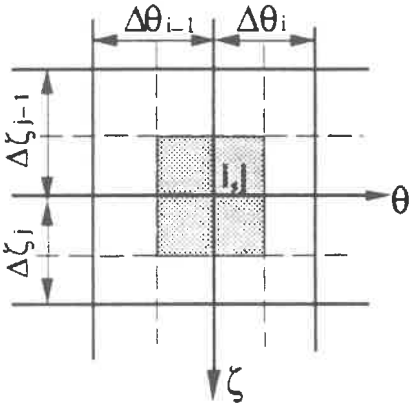

Fig.2 Mesh defined for analysis

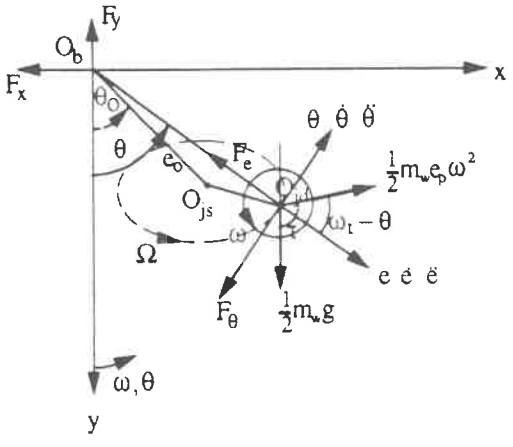

Fig.3 Coordinate system for nonlinear equation of rigid rotor motion

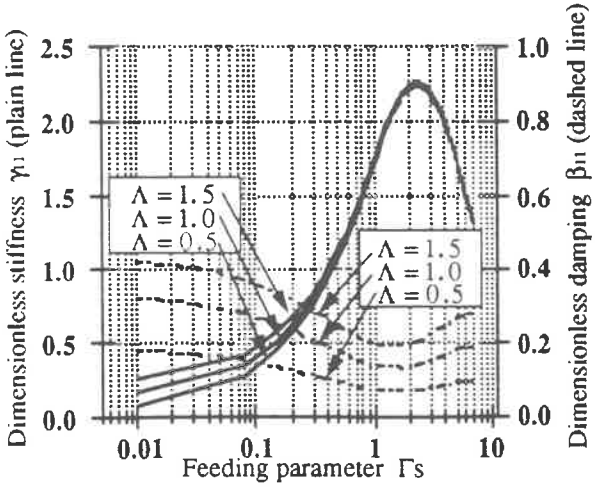

Fig.4 Feeding parameter vs. dimensionless dynamic coefficients

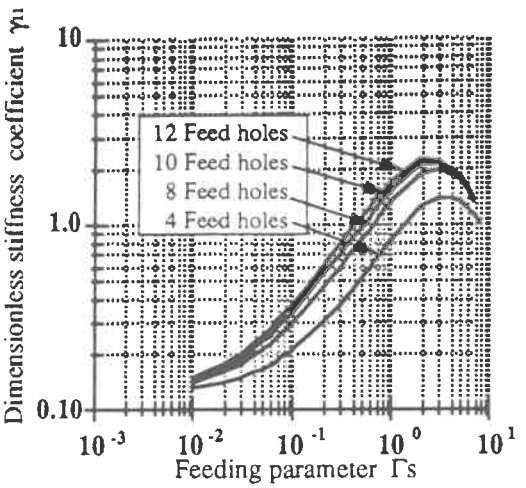

Fig.5 Influence of the number of feeding holes
(Λ =1.0 , Ps = 0.6 Mpa)

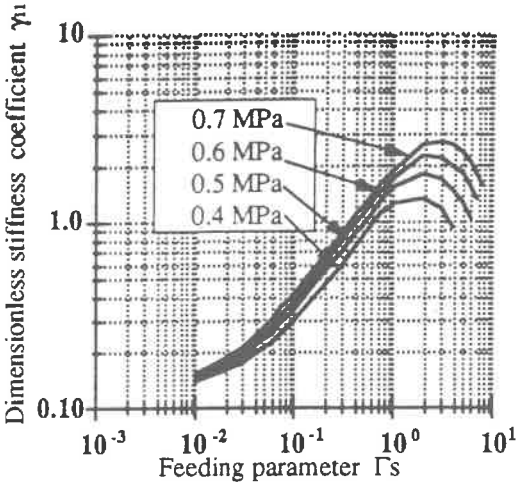

Fig.6 Influence of supply pressure
(Λ =1.0 , n = 12)

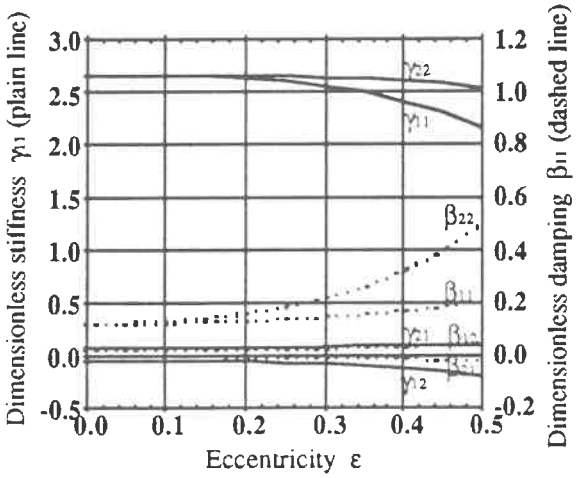

Fig.7 Eccentricity vs dynamic coefficients

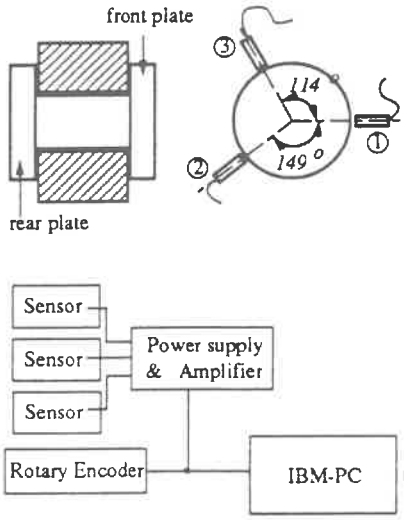

Fig. 8 Experimental set-up

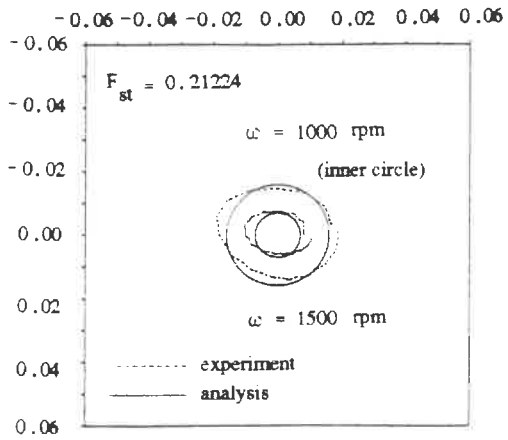

Fig. 9 Comparison between analysis
and experiment of orbits of rotor shaft center

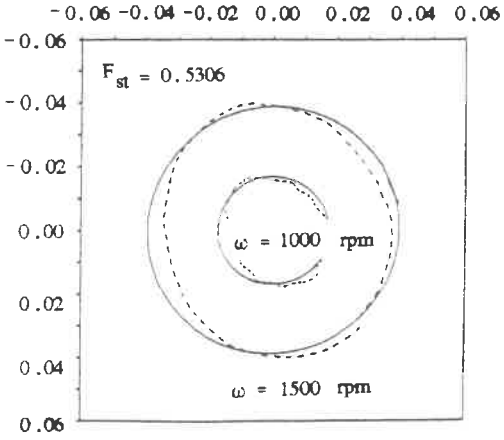

Fig. 10 Comparison between analysis
and experiment of orbits of rotor shaft center

Evaluation and Improvement of Thermal Characteristics of a Thrust Air Spindle

Nozomu Mishima,Kiyoshi Mizuhara and Yuichi Okazaki
Mechanical Engineering Laboratory,AIST
1-2 Namiki,Tsukuba,Japan

Summary
In this study, numerical analysis and control methods of thermal deformations of static air spindles are mentioned. For the purpose of analyzing the deformations theoretically, Thermohydrodynamic Lubrication Theory (THL) is applied. And to control them, precise temperature control method of air supply to spindles, is discussed experimentally. As the result of the analysis, it was able to foresee the thermal deformations of the spindle, and of the experiments, thermal properties of the spindle, such as the quantity of the thermal deformations and the settling time of the deformations, were improved evidently. So that, this report will be a proposal for completing the higher accuracy of static air spindles.

Introduction

Static air spindles has some advantages such as high stability and low heat generation. Because of those advantages, they are often applied to ultra precision machine tools. But even an air spindle is not free from certain quantity of thermal deformations. For example, thermal deformations of our spindle amounted more than 6μm under some severe conditions, large size, narrow clearance and high revolving speed. And those quantity of deformations are not negligible especially for ultra precision machining, so that analysis and control of thermal deformations have to be discussed.

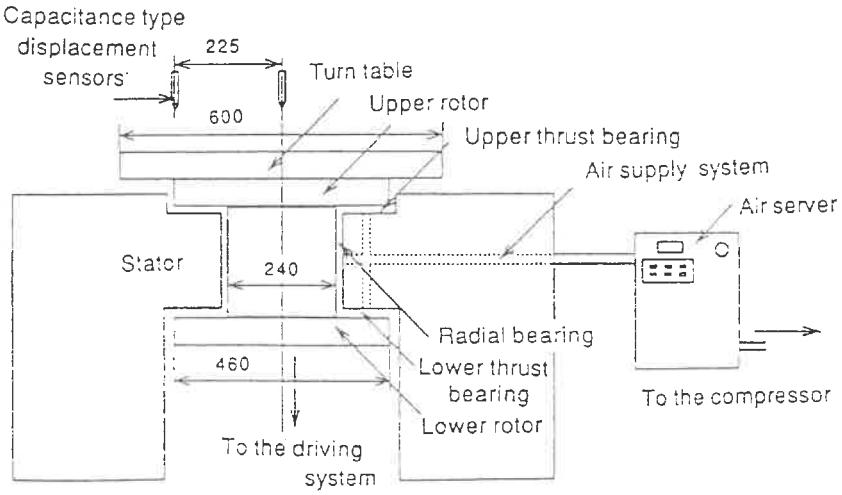

Fig.1 Schematic view of the experimental set-up

Experimental Set-up and Measurements

The overview of the experimental set-up is shown in Fig.1 with measuring points for displacements. Thermal deformations were measured as growth of the spindle to Z direction at

three various revolving speeds by capacitance type displacement sensors, Fig.2. In the figure, "Edge" shows displacements of a point which apart from the center with a radius of 225mm. From fig.2, it is concluded that the heat generation of motor and driving system, such as coupling, is not the primary cause of the deformation. Because, if the heat spreads into the rotor through the axis, deformations of the rotor must be larger at the bearing center than the bearing edge. In this case, the "bowl-like" deformation shown in Fig.2, which means that the deformation of the edge is larger than that of the center, will not rise. So it is supposed that the cause of the deformation is viscosity friction of air film of the bearing. Results of these measurements, two problems became clear, one is quantity of the deformations itself and the other is extremely long time to its saturation witch amounted more than 8 hours.

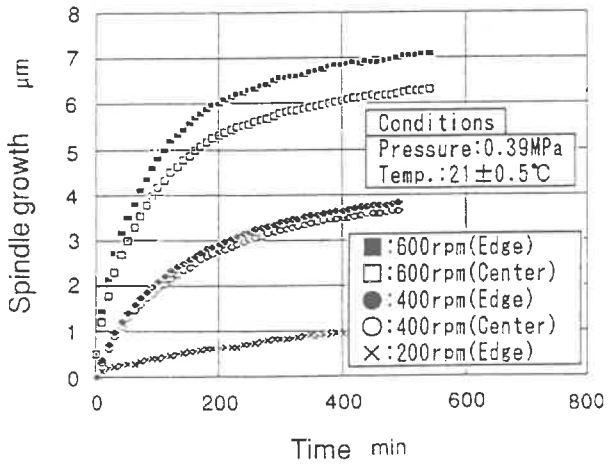

Fig.2 Thermal deformations of the spindle

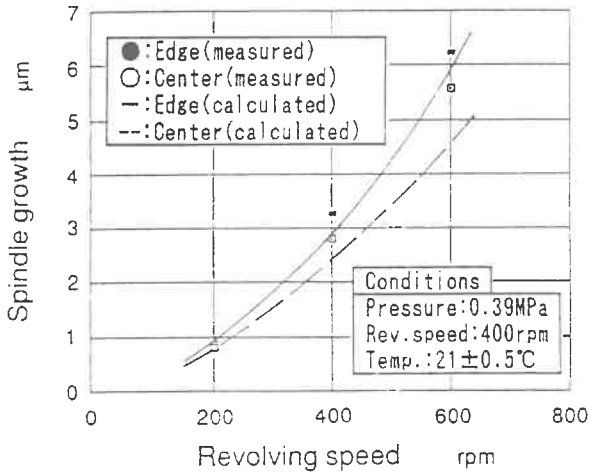

Fig.3 Thermal deformations(comparison between calculations and measurements)

Numerical Analysis

As it was mentioned above, the cause of the thermal deformations is supposed to be viscosity friction, so THL can be applied to estimate and foresee numerically the thermal deformations [1]. In THL, The Reynolds equation, the energy equation and the equation of heat conduction of the bearing metal are considered, and they have to be solved as simultaneous equations under certain boundary conditions. And these ordinal equations are simplified by introducing some assumptions. Important assumptions are shown as follows.

1.Flow of the air is constant layer flow

2.Inertia force of the fluid is extremely smaller than viscosity force.

3.Pressure distribution of the fluid is homogeneous to the thickness direction.

4.Coefficients of heat conduction and heat capacity of metal are constant.

5.Velocity and temperature distributions have the axial symmetry.

As a result of simplification, the velocity and pressure distributions within the air film are solved at once [2], and the energy equation of the air film and the equation of heat conduction are simplified and also the boundary conditions are. Putting the pressure and the velocity distributions into the energy equation, the temperature distribution of air film is obtained. And then, temperature distributions of the bearing metal are obtained. These temperature distributions become the boundary conditions of the energy equation and the energy equation is solved again. Last two steps are repeated until the all equations and the all boundary conditions are satisfied. To be more concrete, those calculation is realized by FDM and computer calculations. The computer program is written in FORTRAN and put into practice on a super computer. As the results of this calculation, the temperature distributions of the rotor and the stator surface are calculated, and from these temperature distributions, deformations of the rotor are obtained. Fig.3 is a comparison between the calculated value of the thermal deformations and the measured value. According to the figure, the calculated value matches the measured value well at the bearing edge.But at the bearing center, the calculated value are substantially small. The error factors are supposed as follows.

1.There was a heat generation at the motor and it spreads into the rotor
2.There were changes of the coefficient of heat conduction and the thermal capacity of the bearing metal
3.Supposed value of the coefficient of heat transfer was not suitable.
4.The shape of the air film changed with the deformations of the rotor.

Except for those shortages, it is able to foresee the thermal deformations of an air spindle by THL and numerical calculations.

Control Method of Thermal Deformations

In ordinal cases, an ultra precision machine tool is settled in a thermo-static chamber, and air is supplied with the same temperature as the chamber. But there must be certain quantity of heat generation in the bearing, because of the viscosity friction, and it causes thermal deformations. So, for the purpose of decreasing thermal deformations, it is not enough to cool whole the machine in the thermo-static chamber. And many investigations have been carried out and many methods have been developed to keep accuracy of machining [3-5]. But against the inner heat source, such as main spindles, it is said that one of effective methods is to cool the heat source directly [6]. We also tried a simple direct cooling method to decrease the thermal deformations. It is to supply air to the bearing with lower temperature than that of the chamber. Fig.4 shows effects of the low-temperature air supply. As shown in the figure, far lower deformations were obtained. Advantages of this method is that any special equipment except an air controller and any reconstruction of the spindle is not necessary. But one of the problem left is long settling time of the thermal deformations. To shorten this, we proposed more progressive method of controlling. It is to heat the spindle from the beginning of the rotation, by higher temperature air

supply than the chamber, and after a proper time pasts, change the temperature to the lower level and cool the spindle.

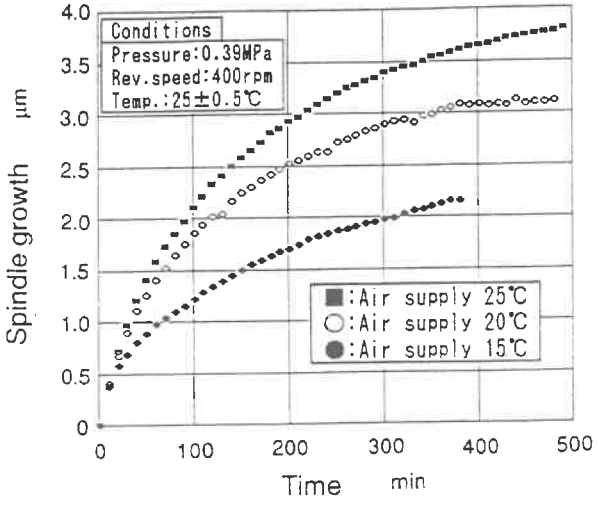

Fig.4 Effect of the low-temperature air supply

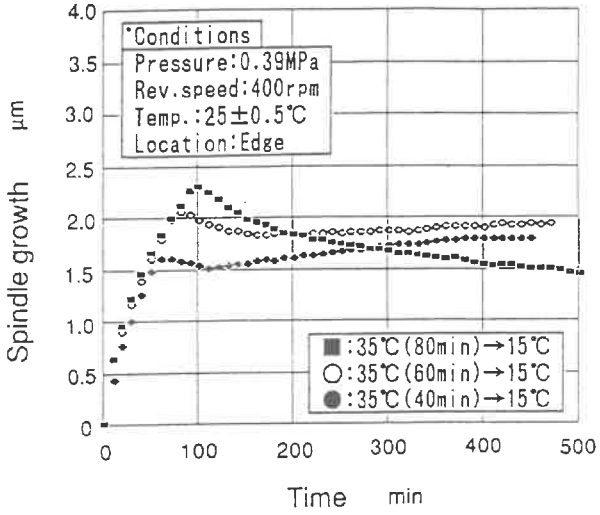

Fig.5 Improved hysteresis of the thermal deformations

Result of this method, the thermal deformations increased rapidly from the beginning of the rotation and then kept the similar level. As shown in Fig.5, when the heating temperature and the heating time was suitable, the settling time of the deformation was shortened to about one and a half hour and the incremental displacement after the rapid increase of the deformation finished, was suppressed to less than 0.3 μm.

Conclusions

In this work, it is proved that THL and numerical analysis is suitable to foresee the thermal deformation of an air spindle. And our method to decrease the thermal deformation utilizing a temperature difference between supplied air and atmosphere, was easy to realize and very effective. In addition, changing the temperature of air supply suitably, it was able to obtain the improved transient properties. The rest theme is to improve the accuracy of the numerical calculation and develop a method of in-process controlling of thermal deformations by measurement of tthe deformations themselves and control of air supply.

References

1. Dawson,D and et al,"A thermohydrodynamic analysis of journal bearings", Lubrication & Wear Fifth Convenion, 1967, 117-126
2. V.N.Constantinescu,Gas Lubrication,ASME,New York, 1963, 74-90
3. Bryan,J.B., and et al,"A Practical Solution to the Thermal Stability Probrem in Machine Tools", SME Paper, 1972, MR72-138
4. Nishiwaki,N and et al, Trans. of JSME, Vol.53, No.495C, 1987, 2408-2413
5. Hattori,M, and et al, Preprint of Spring Conf. of JSPE, 1992, 161-162
6. Nishiwaki,N and et al,"A New Precise Temperature Controlling Method for Machine Tool", MSET-21, 1990, 69-74

STUDY ON TIGHTENING TECHNIQUES OF PLASTIC PARTS BY MEANS OF TAPPING SCREWS

K. Ishikawa, R. Hori and N. Unno
Kanazawa Institute of Technology, Japan

ABSTRACT

This paper describes the screw tightening for plastic parts by means of tapping screws. In the present study, a harmonic vibration (frequency: 25 Hz, angular displacement: 2 deg) was applied to tapping screws during ordinary unidirectional rotation screw tightening in ABS resin, a thermoplastic, using a DC motor. Also a heating screw tightening was carried out by means of tapping screws which were heated beforehand. And then, a loosening torque test was performed. As a result, the following matters are clarified.

(1) The theoretical analysis of driving torque can be proved by experiments.
(2) The driving torque is decreased in order of theheating screw tightening, the vibration screw tightening and the unidirectional rotation screw tightening.
(3) Appropriate tightening force increased according to the order of the heating screw tightening, the vibration screw tightening and the unidirectional rotation screw tightening.
(4) The loosening torque ratio in vibration screw tightening and the heating screw tightening is increased than unidirectional rotation screw tightening.

The above results confirm that the reliability of assembly of OA appliances made with plastics may be greatly improved using these methods.

INTRODUCTION

Tapping screws are commonly used in the assembly of office automation appliances made with plastics. Unfortunately, they exhibit considerable non-uniformity in driving torque and tightening force. [1]

In this study, as regards the tapping screw tightening, a relationship between the driving torque required when the female screw is formed, and the tightening force when tapping screw is tightened are studied. And the tightening characteristics in the unidirectional rotation screw tightening, the vibration screw tightening and the heating screw tightening are investigated. [2] , [3]

ANALYSIS OF DRIVING TORQUE [4]

Now, assuming the forming of female screw thread is performed by a thread of the driving torque: Td can be obtained as the sum of torque: Tf which required to form the female thread and the friction torque: Tp which applied on the surface of screw thread

$$T_D = T_F + T_P \tag{1}$$

Considering the yield condition of Von-Mises, the torque which required to form the thread can be expressed as Eq.(2);

$$T_F = (\sigma/\sqrt{3})[(d-d_0)\tan\alpha + 2\sqrt{\{(d-d_0)/2\}^2 (1+\tan^2\alpha)}] \cdot \sqrt{[\{(d+2d_0)/3\}\pi]^2 + P^2} \quad \{(d+2d_0)/6\} \tag{2}$$

where, σ is the tensile yield stress of ABS resin.
d is the nominal diameter of tapping screw.
d0 is the hole size for tapping screw.
p is the pitch of screw.
α is the half angle of screw.

Next, the torque owing to friction resistance which applies to the surface of thread can be obtained as taking into consideration such a semi-infinite block of plastic-rigid material which is pressed in by a smooth rigid body. [5]

As the constant stress produces along the constant surface between a tapping screw and female thread, all normal force on the thread surface can be expressed as the product of the compressed stress and the surface area of contact surface of ABS resin. Consequently, the torque by means of friction resistance is expressed as follows:

$$T_P = \mu N \cdot r \tag{3}$$

$$= \mu \sigma' \sqrt{\{(d-d_0)/2\}^2 (1+\tan^2\alpha)} \cdot \sqrt{[\{(d+2d_0)/3\}\pi]^2 + P^2} \quad \ell/p)\{(d+2d_0)/6\} \tag{4}$$

where, N is the normal force applied on the surface of screw thread.
μ is the coefficient of friction between a tapping screw and ABS resin.
r is the flank radius of screw thread.
σ is the normal stress.
ℓ is the driving distance of tapping screw.

TIGHTENING METHODS

The tapping screw (M4×40), clamped member (Material: SPCC) and member formed female thread (Material:ABS) were set through a load cell as shown in Fig.1. In this study, screw tightening was performed as follows;

(1) Unidirectional rotation screw tightening: Rotations; 10 - 500 rpm.
(2) Vibration screw tightening: Frequency; 25 Hz, Angular displacement; 2 deg.
(3) Heating screw tightening: Room temperature, Temperature at start of driving; 318 K.

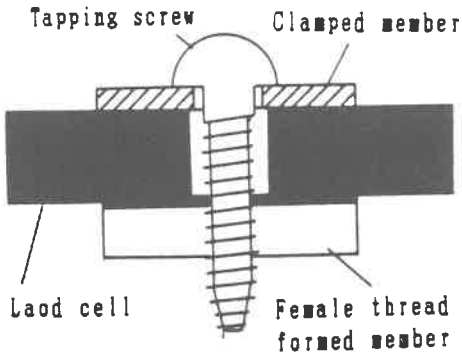

Fig.1 Condition of Set of Driving and Tightening Test

EXPERIMENTAL RESULTS AND CONSIDERATIONS

Fig.2 shows the relationship between hole size for tapping screw an driving toque. The driving torque in an each hole size for tapping screw is calculated from Eq.(2) and Eq.(4). The solid line is theoretical value using Eq.(1). In this experiment, it is found that the experimental value nearly agrees with the theoretical value. The driving torque shows a tendency to reduce as the hole size for tapping screw increases. It can be seen that the vibration screw tightening is lower than the unidirectional rotation screw tightening for each hole size for tapping screw. This is considered that the driving torque in the vibration screw tightening is slightly less than that in the unidirectional rotation screw tightening resulting from repeated friction between thread faces of the tapping screw and female screw thread on forming because micro vibration repeatedly operates during forming.

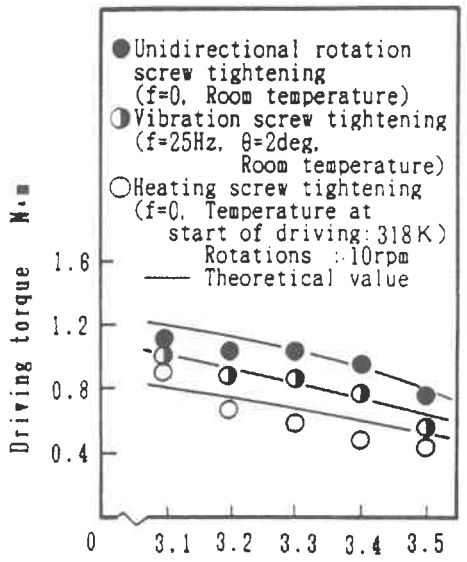

Fig.2 Relationship between Hole Sizes for Tapping Screw and Driving Torque

Fig.3 shows the comparison of tightening force by means of the tightening method. It can be seen that the value for tightening force in the vibration screw tightening is highter than that for the unidirecional rotation screw tightening. This is considered that the tightening force increases in the coefficient of kinematic friction of the thread surface as the result of moothed thread surface resulting from repeated friction between thread surfaces. And then, the tightening force in the heating screw tightening shows a higher tendency than in both unidirectional rotation screw tightening at room temperature and vibration screw tightening.

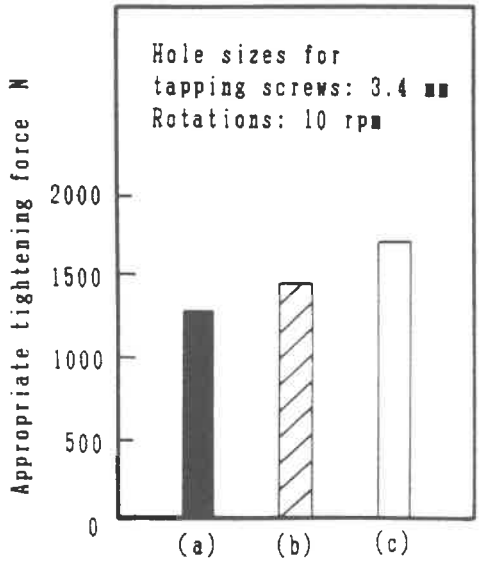

(a) Unidirectional rotation screw tightening (f = 0, Room temperature)
(b) Vibration screw tightening (f = 25 Hz, θ=2 deg, Room temperature)
(c) Heating screw tightening (f = 0, Temperature at start of driving: 318 K)

Fig.3 Relationship between Tightening Method and Tightening Force

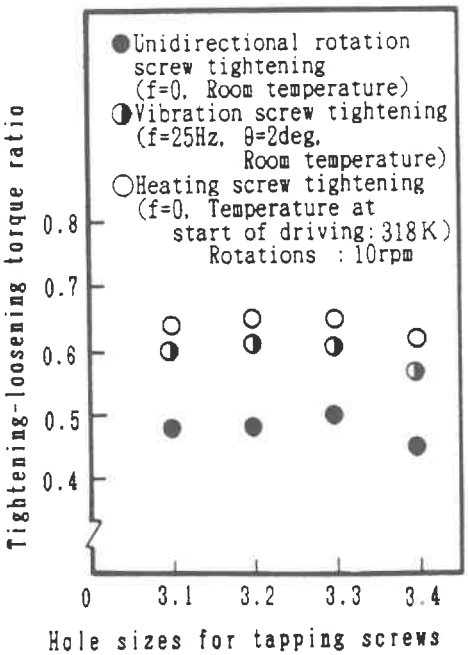

Fig.4 Relationship between Hole Sizes for Tapping Screws and Tightening - Loosening Torque Ratio

Fig.4 shows the results of tightening-loosening torque test for tapping screw. Comparing the unidirectional rotation screw tightening with heating screw tightening, it has been known that the loosening torque increases in heating screw tightening, and the torque ratio of tightening-loosening also increases. From this fact, the performance of tapping screw could be improve.

CONCLUSIONS

In conclusions, vibration screw tightening and heating screw tightening were performed for plastic parts, and the following matters have been clarified compared with the unidirectional rotation screw tightening:

(1) The driving process of a female screw when forming and tighteng the tapping screw has been clarified.
(2) In both the vibration screw tightening and heating screw tightening, the value for driving torque is lower than that in the unidirectional rotation screw tightening.
(3) In the heating screw tightening, a better female screw can be formed than in the unidirectional rotation screw tightening.
(4) A apropriate tightening force can be obtained by heating screw tightening than by the unidirectional rotation screw tightening.
(5) In the heating screw tightening and vibration screw tightening, the tightening performance of tapping screw could be improved because the torque ratio of tightening-loosening is greater than in the unidirectional rotation screw tightening.
(6) Therefore, these methods are considered to ensure assembly operation of office automation appliance by means of tapping screws.

ACKNOWLEDGEMENT

The authors also would like to express their gratitude to Original Trading Co., Ltd. for providing the many test pieces in carrying out these experiments.

REFERENCES

[1] Lincoln, B,; Gomes, K.J.; and Braden, J.F. 1984. " Mechanical Fastening of plastics, " An Engineering Handbook, Marcel Dekker, Inc. New York: 117
[2] Ishikawa, K,; Hori, R,; and Unno, N. 1991. " A basic Study on Vibration Tightening of Tapping Screws, " International Journal of the Japan Society for Precision Engineering, Vol.25, No.3 (September) 235-237.
[3] Ishikawa, K.; Hori, R,; and Unno, N. 1991. " A Study on Tightening Characteristics of Tapping Screws," Preprint of Autumn Meeting, Japan Society of Precision Engineering, 759-760.
[4] Ishikawa, K.; Hori, R,; and Unno, N. 1992. " A Study on Screw Tightening Technique of Plastic Parts by means of Tapping Screws " ,Symposium on Design and Processing of Functions Elements of Plastics, JSME Machine Design and Trybology Division, (No.920-29) 125-129.
[5] Hill, R., 1971. " The Mathematical theory of Plasticity, " Oxford at the Clarenden Press, 215.

CHARACTERISTICS IDENTIFICATION OF A MECHANICAL DYNAMIC SYSTEM

J. Mandak
Slovak Metrological Society
Lipt.Mikulas, Czechoslovakia

ABSTRACT

Further improvement of utility properties of mechanical dynamic systems cannot be separated today from wide employment of advanced mathematical procedures and using of modern measuring and computing instruments. This holds true for the construction design as well as for the analysis of utility properties which are determined by their characteristics in the course of their operation. In determining the characteristics of a mechanical dynamic system procedures, based on the theory of frequency analysis, are used that are mathematically defined by Fourier integral transform. Less attention has been so far payed to the employment of the theory of the so called AutoRegressive Moving Average models which brings certain priorities over the frequency analysis. Both approaches to the identification of characteristics of mechanical dynamic system are briefly theoretically circumsribed. Comparison of results achieved by both procedures is given at the end of the paper. The results prove an evident advantage of using the so called AutoRegressive Moving Average models for modal analysis /characteristics determination/ of mechanical dynamic systems. Their greatest advantages are ability of effective filtering noisy scanned signals and obtaining results in a short time. Further direction of research will therefore be oriented to the study of possibilities to connect the advantages of given methods with the methods of elasticly stressed conditions of a continuous mechanical continuum, under its loading already in the stage of its design proposal.

INTRODUCTION

In identifying the characteristics of the mechanical dynamic system an input signal $a(t)$ - excitation, is being fed to the input of the system. The response of the mechanical dynamic system to the received input signal $a(t)$ appears in the course of the output signal $b(t)$ - response.
Practical calculation of instantaneous spectrum, spectrum envelope, natural spectrum, mutual spectrum, frequency response functions, coherence, signal-to-noice ratio, coherent spetrum or others, as a rule start from using of Discrete Fourier Transform by use of Fast Fourier Transform /FFT - algorithm/, /Rem. FFT analysers work on the basis of the Discrete Fourier Transform/. Moreover this method demands relatively much time, in spite of high-quality computing devices.
One possible way of removing these shortcomings is creating statistically adequate models of mechanical dynamic systems on the basis of modelling in the time domain.

The problems of finding statistically adequate model of the given time series values leads to the employment of nonlinear method of least squares that minimizes the sum of squares of residual deviations $\Sigma\varepsilon_t^2$.

SOLUTION

In order to compare both methods in practice, there was established an experimental working place consisting of a mechanical dynamic system with a piezoelectric acceleration scanner mounted at its output and connected by cabling to a charge amplifier. Its input impedance of the order of several gigaohms excluded the necessity of using a separate preamplifier and it was followed by an integrator determining time behaviour of speed and deviation. Built-in low-pass and high-pass filters were set so that the operation frequency range corresponded to the frequency range of the scanned vibration, while at the same time noises with low and high frequency were effectively suppressed. The amplified signal was further rectified in a proper way in a rectifier and as directcurrent it was connected to the circuits of indication equipment and outer registering devices /level recorder, memory oscilloscope or others/. After digitalization of the obtained signal, the letter was numerically processed in harmony with the introduced methods. The shape of the signal /Fig. 1/ as it is evident from the picture, is in

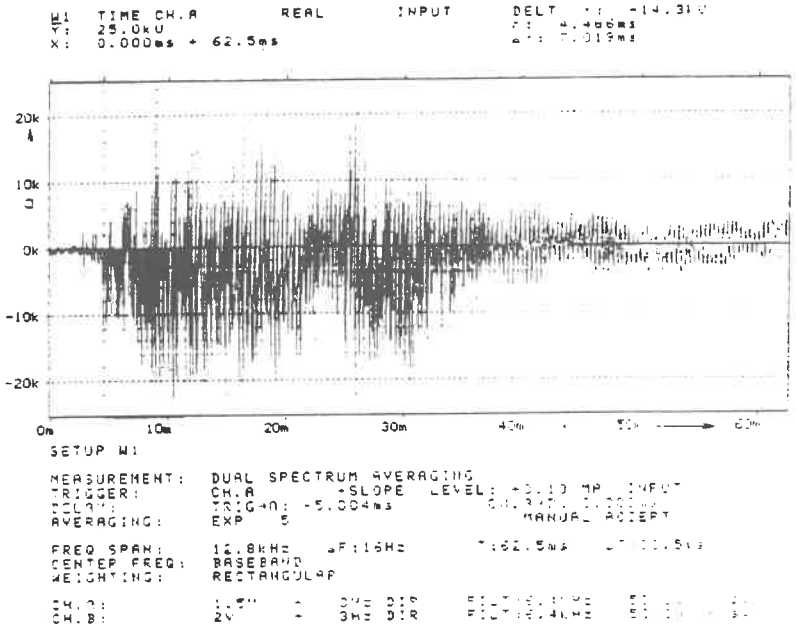

Fig. 1 Experimentally recorded time behaviour of the acceleration signal $a(t)$

the length of duration 0 beginning up to 36 ms of an impuls character, in the length of duration 36 ms to 62 ms - end of record - is expressively stationary. The Autospectrum /often called Power Spectrum/ $A(f)$ of signal $a(t)$ from Fig. 1, determined by FFT - algorithm, is given in Fig. 2 and 3.
In using the method of ARMA(n, n-1) models with an input time series of 521 values discretizing the signal in range from 36 to

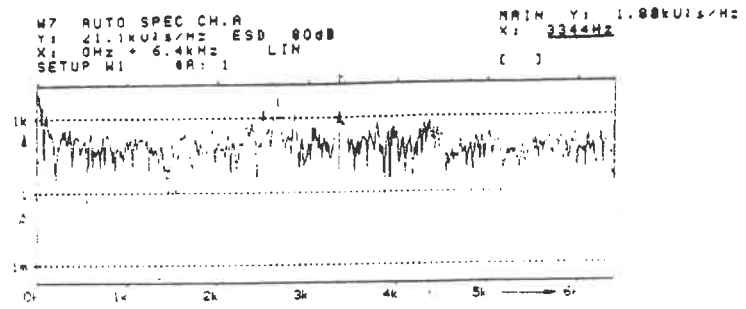

Fig. 2 Estimation of Autospectrum A(f) of signal a(t) from Fig.1

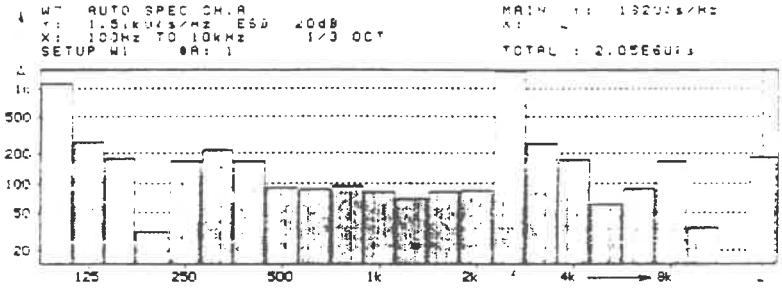

Fig. 3 Estimation of Autospectrum A(f) of signal a(t) from Fig.1 - 1/3 octave analysis

62 ms with the step of $\Delta t = 0.05$ ms, an adequate discrete model of the time series of the type ARMA(8, 7) was statistically calculeted with the coefficient vector of the left-hand side

$$a = [4{,}981\ ;\ -12{,}663\ ;\ 20{,}9772\ ;\ -24{,}2713\ ;\ 19{,}792\ ;\ -11{,}263\ ;\ 4{,}088\ ;\ -0{,}7852]\ ,$$

and right-hand side

$$b = [2{,}172\ ;\ -4{,}184\ ;\ 6{,}128\ ;\ -7{,}453\ ;\ 5{,}777\ ;\ -2{,}221\ ;\ 0{,}8331]\ .$$

In harmony with relation for computation of natural frequencies Ω_i and with relation for computation of relative dampings ξ_i

$$\Omega = \frac{1}{\Delta t}\sqrt{\frac{[\ln(\lambda_i \bar{\lambda}_i)]^2}{4} + \left[\arccos\left(\frac{\lambda_i + \bar{\lambda}_i}{2\sqrt{\lambda_i \bar{\lambda}_i}}\right)\right]^2}\ , \qquad \xi = \sqrt{\frac{[\ln(\lambda_i \bar{\lambda}_i)]^2}{[\ln(\lambda_i \bar{\lambda}_i)]^2 + 4\left[\arccos\left(\frac{\lambda_i + \bar{\lambda}_i}{2\sqrt{\lambda_i \bar{\lambda}_i}}\right)\right]^2}}\ ,$$

in which independent variables λ_i, $\bar{\lambda}_i$ are conjugate roots of characteristic equation of Frequency response function /Fig.4/

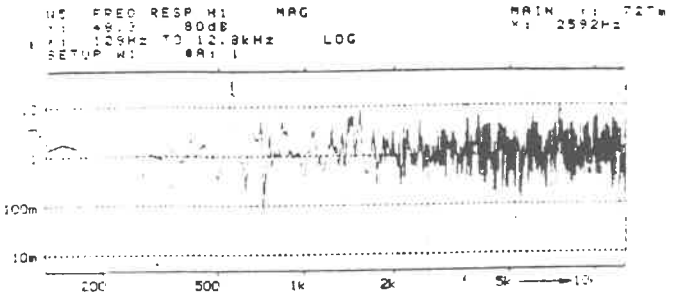

Fig. 4 Magnitute of Frequency Response Function $H_1(f)$ /log-lin scale/

of mechanical dynamic system, correspond to the given values summarized in Table 1.

Table 1

Ordinal number	Ω rad.s^{-1}	ξ -
1	15 708	0,0812
2	16 462	0,0353
3	17 718	0,0187
4	20 986	0,0112

By their calculating once more and comparing with the results from Fig. 2 it is evident that values given in Table 1 are in good accordance with expressive extremes of frequency time behaviour from Fig. 2.

CONCLUSION

The presented results prove an evident advantage of using the so called ARMA models also for modal analysis of mechanical dynamic systems. Their greatest advantages are ability of effective filtering noisy scanned signals and obtaining results in a short time. Further direction of research will therefore be oriented to the study of possibilities to connect the advantages, of the given methods with the methods of elasticly stressed conditions of a continuous mechanical continuum, under its loading already in the stage of its design proposal.

REFERENCES

1. Mandak, J.: The Methods for the Solution of Motion Equation of a Mechanical System, Proc. of the 30th Int. Conf. on Parts and Mechanisms of Machines, Liberec - CSFR, /1989/, /in czech/.
2. Maca,J. at al, Identification, Modelling and Control of Mechanical Dynamic Systems, Research report of VSDS Zilina - CSFR, /1988/, /in slovak/.
3. Maca, J., Identification and Modelling of Mechanical Dynamic Systems with Employment of Time Series Theory, Proc. of the Random Processes and Identification of Mechanical Dynamic Systems 89, House of Technology Zilina - CSFR, /1989/, /in slovak/.
4. Mandak, J., Simulation of Dynamics of Mechanical System Excited by Shocks, Proc. of the European Congress on Simulation, Academia Publ., Czechoslovak Academy of Sciences with Cosponsorship of IMACS, Prague - CSFR, /1987/,
5. Mandak, J., On the Possibility of Employing Representative Mathematical Methods for Diagnosing Mechanical Dynamic Systems, Proc. of the 8th International IMEKO Symposium on Technical Diagnostics, Dresden - Germany, /1992/.
6. Mandak, J., at al, Identification of Statistically Significant Natural Frequencies of a Mechanical Dynamic System Excited by Shock, Proc. of the VSDS - Zilina, CSFR, /1989/, /in czech/.
7. Mandak, J., Characteristics Identification of a Mechanical Dynamic System, Proc. Ist Int. Conf. on Motion and Vibration Control, Yokohama - Japan, /1992/.

A Study of the Characteristics of Herring Bone Air Bearings for Polygon Mirror Laser Scanners

Gang Lin,* Robert O. Warrington**, Yoshihiro Ue***, Tadaatus Satomi****
*Assis.Prof., ** Head, Institute for Micromanufacturing, Louisiana Tech University, Ruston LA 71272
***Graduate Student, ****Prof., Ind. Eng. Dept. Tokyo Denki University, Saitama 350-03 JAPAN

1. Introduction

Polygon mirror scanners have been widely used in computer peripheral equipment and office automation within the last few years. In the scanners' spindle design to date, high-precision roller bearings have been generally used, however, higher spindle speeds and higher scanning quality have been difficult to achieve. Self-acting air bearings have been, therefore applied due to their superior performance in terms of rotational speed and rotational errors.

In this paper the characteristics of the journal air bearing for the spindles will be discussed. Among various self-acting air bearings, the herring bone type shown in Fig.1 has been considered as one of the best bearings for the spindle of the scanners due to its high efficiency and high stability. For the best possible bearing design, the relationships between design specifications and bearing characteristics such as load capacity and stability have to be known. However, the design data and information available so far from various sources (e.g., references [1,2]) give only several design examples, which are in most cases insufficient for design optimization. Therefore, the design of herring bone bearings still depends mainly on the experiences.

In order to analyze the bearing performance, several FEM programs have been developed in this study. The influences of the design specifications on the loading characteristics of the herring bone bearing over the most commonly used ranges have been investigated. Consequently the design optimization of the bearings has been made possible.

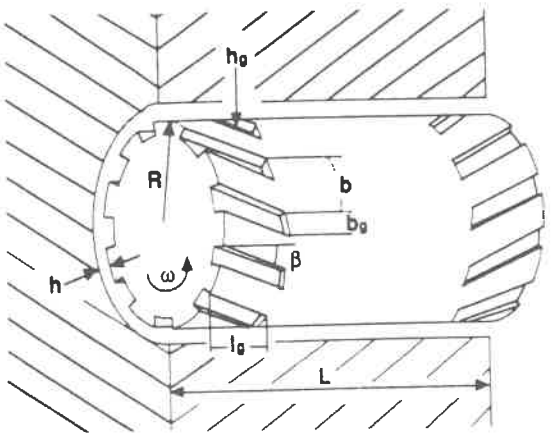

(a)

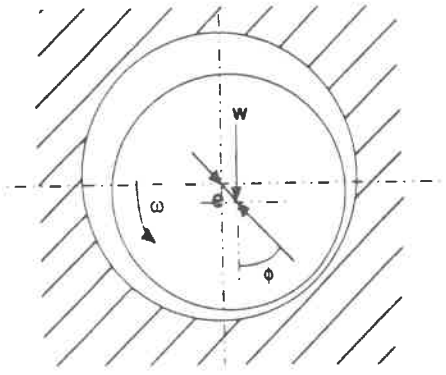

(b)

Fig.1 Configuration of herring bone bearing

2. Nomenclature (see Fig.1)

b_g: width of a groove
b: sum of a groove width and a land width
e: eccentricity of bearing
D: diameter of bearing, $D=2R$
h: bearing clearance
h_0: average clearance over the land
h_g: depth of the grooves, $H_g=h_g/h_0$

L: length of the bearing
lg: length of the grooves in bearing longitudinal direction
n: number of the grooves
p: pressure within the clearance
p_a: ambient pressure
R: radius of the bearing
w: load capacity of the bearing, $W=w/(p_aLD)$
x: coordinator on bearing surface in circumferential direction, $X=x/R$
y: coordinator on bearing surface in longitudinal direction, $Y=y/L$
Z: normalized groove length, $=2l_g/L$
α: width ratio of the grooves, $=b_g/b$
β: pump-in angle of the grooves
ε: eccentricity ratio, $=e/h_0$
ϕ: attitude angle
Λ: bearing number, $=6v\omega(R/h_0)^2/p_a$
v: viscosity of air
ω: rotational speed

3. Method of analysis

The normalized Reynolds equation, which governs the air flow within bearing clearance, is given by Eq.1,

$$\frac{\partial}{\partial X}(H^3P\frac{\partial P}{\partial X})+\frac{\partial}{\partial Y}(H^3P\frac{\partial P}{\partial Y})=\Lambda\frac{\partial PH}{\partial X} \quad (1)$$

Generally, the strict solution of Eq.1 is not possible, so the FEM is employed to obtain a numerical solution. Once the solution, i.e., pressure distribution over the bearing surface is obtained, the bearing performance such as load capacity and attitude angle can be derived [3,4]. The reliability of the FEM programs has been confirmed in references [3,4].

4. Bearing load performance

The performance of herring bone bearings are determined by design specifications such as the groove depth h_g, the groove width b_g, etc.. The following discussions on the influence of these specifications on bearing performance are carried out over the ranges of the most commonly used values [1,2]. The characteristics used to show the bearing performance are normalized load carrying capacity W (see Nomenclature for definitions) and attitude angle ϕ (see Fig.1). The former gives a loading capacity per unit area ratio and the latter gives indirectly the stability of the bearings (bearings with a large attitude angle are often likely to become instable [5]). The rotation of the spindle, however, must be in the direction that pumps air into the bearing clearance. Otherwise the pressure within the clearance will drop down below ambient pressure.

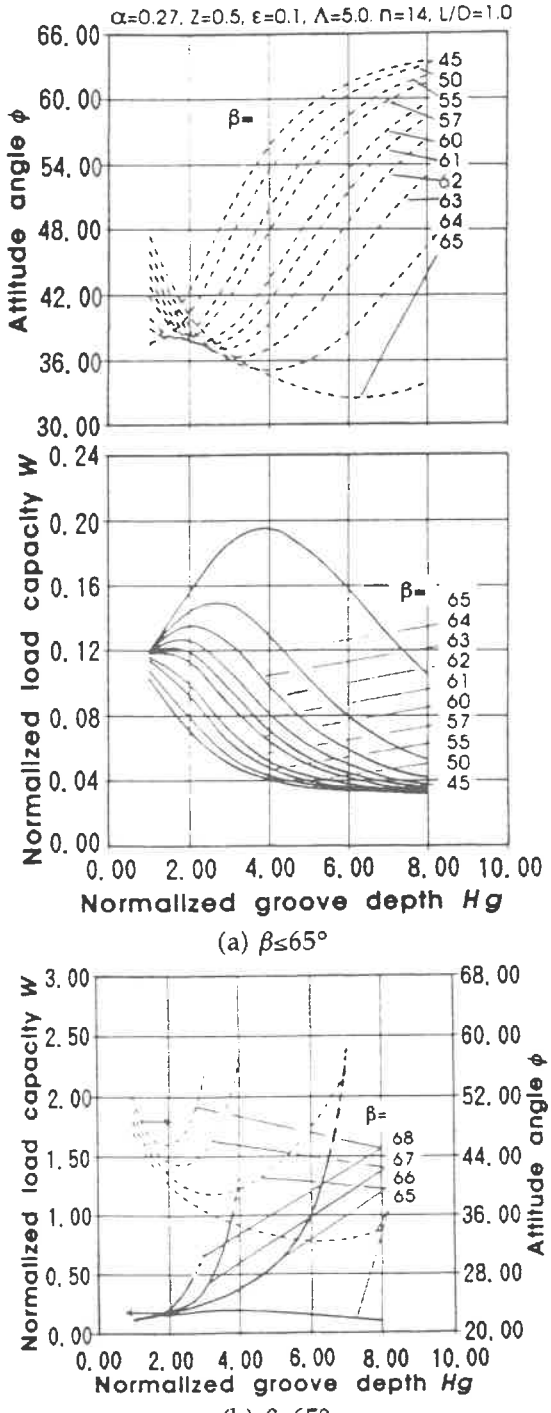

Fig.2 Influences of the groove pump-in angle β

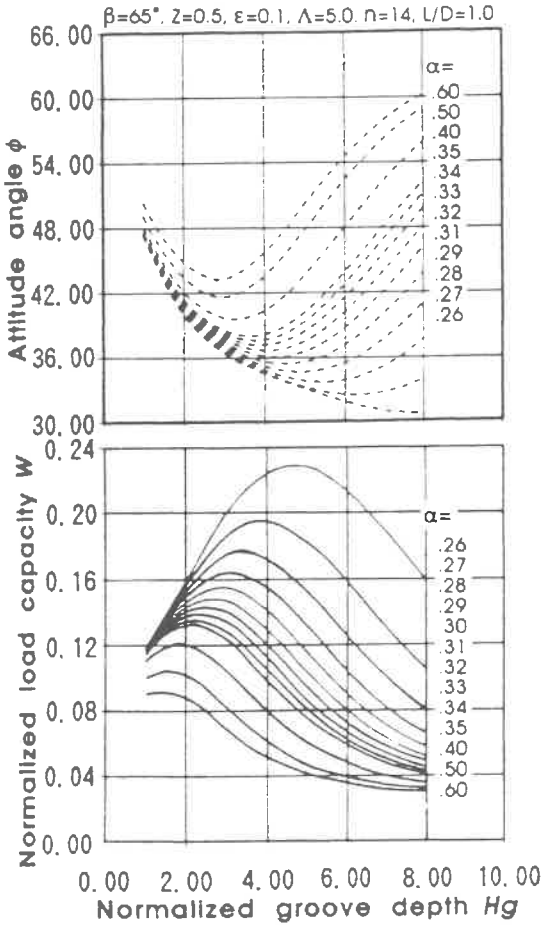

(a) $\alpha \geq 0.26$

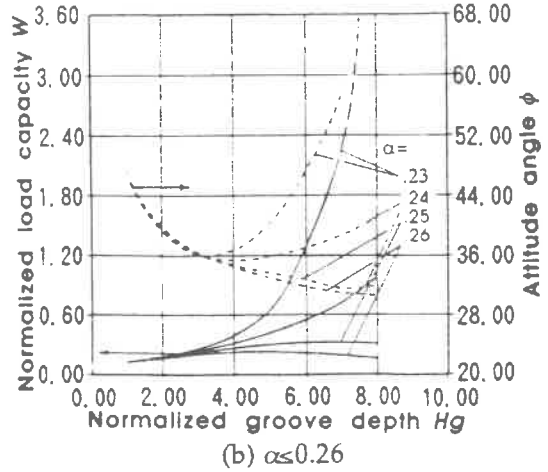

(b) $\alpha \leq 0.26$

Fig.3 Influences of the groove width ratio α

Figure 2 is a relationship between the pump-in angle β and the bearing performance obtained by the computed results. It shows that increasing pump-in angle β can increase bearing load capacity W The minimum value of ϕ are obtained at about β= 65 with respect to groove depth Hg=2.0. The computed results also show that increasing β can further increase$W$, but it may drastically increase the attitude angle ϕ which often deteriorates the stability of the bearings.

The effect of the groove width α has been shown in Fig.3. According to the computed results, decreasing the α can increase the W. The smallest ϕ is obtained at α=0.26. Further decreasing in pump-in angel ϕ can further increase the load capacity W but also quickly increases the attitude angle ϕ. For best overall performance, the value of α=0.27 is often recommended.

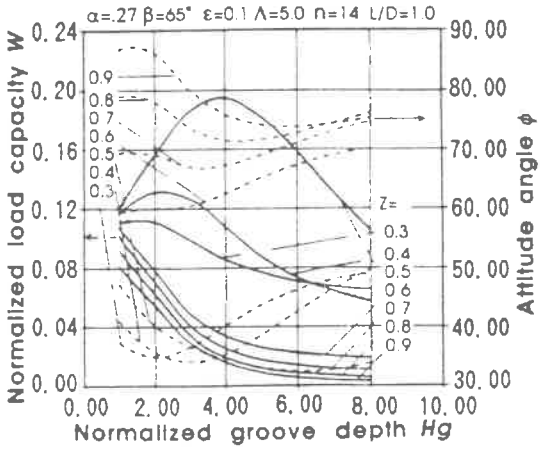

Fig.4 Influences of the groove length ratio Z

In Fig.4, the influence of the length of the grooves Z is shown. Since the β and α have been optimized with respect to Z=0.5, both maximum load capacity W and minimum attitude angle ϕ are obtained at Z=0.5.

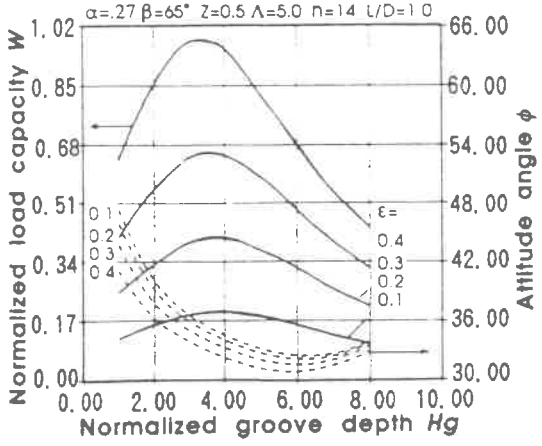

Fig.5 Influences of the eccentricity ratio ε

Figure 5 shows the relationship of eccentricity ratio of the bearing ε to the bearing performance. Naturally the load capacity W increases with an increase in eccentricity ratio ε while the attitude angle ϕ decreases.

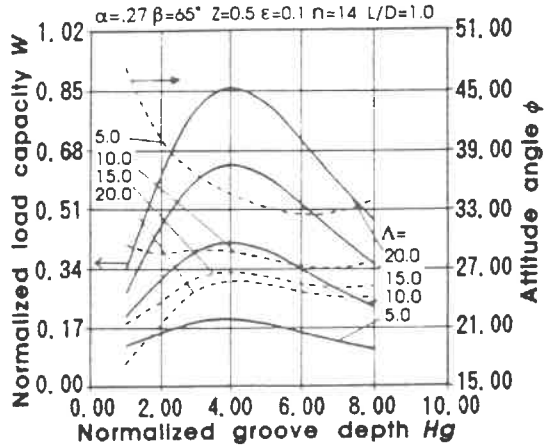

Fig.6 Influences of the bearing number Λ

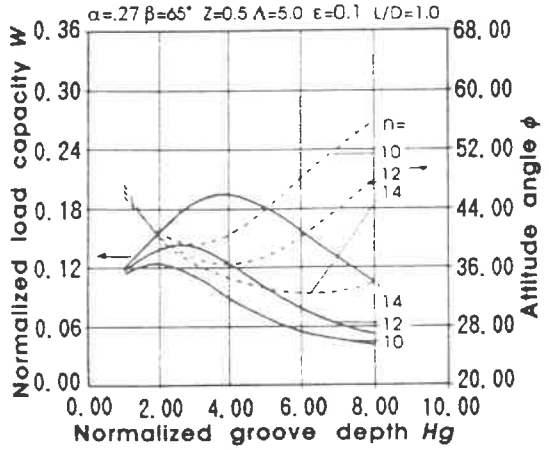

Fig.7 Influences of the groove number n

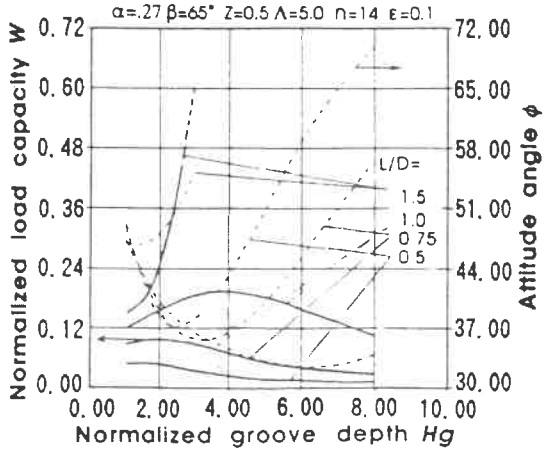

Fig.8 Influences of the slenderness ratio L/D

Figure 6 shows that bearing load capacity W increases approximately in proportion to the bearing number Λ, while the attitude angle ϕ decreases. However, the designer should notice that the instability caused by factors other than attitude angle ϕ increase with the bearing number.

The influence of number of grooves n is shown in Fig.7. Apparently, the load capacity W increases, while the ϕ decreases with the number of the grooves n. The load capacity W approaches to a constant when the groove number n reaches a certain value. This value, which varies from 20 to 40, has to be determined by the combination of other design specifications.

The variation of bearing performance with respect to the L/D ratios is shown in Fig.8. Although it is usually true that the bearings with smaller L/D ratio have a smaller attitude angle ϕ, it is seen in the figure that the bearing with an L/D=1.0 has the best overall performance due to the influences of β, α and Z. In other words, different values of optimal design specifications have to be given for bearings with different L/D ratios.

5. Conclusion

Based on the computed results and foregoing discussions, the influences of the design parameters on the load capacity W and attitude angle ϕ within most commonly used range have been known. Therefor the design optimization of the bearings, especially when the bearing slenderness ratio L/D=1.0, has become possible.

6. Acknowledgment

The authors would like to express their appreciation to the National Center for Supercomputing Applications for its support.

7. References

1) Togo J., Gas bearings. Kyoritsu Pub. 1984, pp32-34, (in Japanese)
2) MTI text book, design of gas bearings. 1967, pp6.1.1
5) Lin G. Aoyama T. and Inasaki I., Wear, Vol.126, 1988 pp307-319
4) Lin G. and Satomi T., Trans JSME, Vol.57, No.541, Ser.C, 1991, pp2971-2977 (in Japanese)
5) Fuller D.D., Trans ASME, Ser.F, 1969, pp1-16

L: length of the bearing
lg: length of the grooves in bearing longitudinal direction
n: number of the grooves
p: pressure within the clearance
p_a: ambient pressure
R: radius of the bearing
w: load capacity of the bearing, $W=w/(p_aLD)$
x: coordinator on bearing surface in circumferential direction, $X=x/R$
y: coordinator on bearing surface in longitudinal direction, $Y=y/L$
Z: normalized groove length, $=2l_g/L$
α: width ratio of the grooves, $=b_g/b$
β: pump-in angle of the grooves
ε: eccentricity ratio, $=e/h_0$
ϕ: attitude angle
Λ: bearing number, $=6\upsilon\omega(R/h_0)^2/p_a$
υ: viscosity of air
ω: rotational speed

3. Method of analysis

The normalized Reynolds equation, which governs the air flow within bearing clearance, is given by Eq.1,

$$\frac{\partial}{\partial X}(H^3P\frac{\partial P}{\partial X})+\frac{\partial}{\partial Y}(H^3P\frac{\partial P}{\partial Y})=\Lambda\frac{\partial PH}{\partial X} \quad (1)$$

Generally, the strict solution of Eq.1 is not possible, so the FEM is employed to obtain a numerical solution. Once the solution, i.e., pressure distribution over the bearing surface is obtained, the bearing performance such as load capacity and attitude angle can be derived [3,4]. The reliability of the FEM programs has been confirmed in references [3,4].

4. Bearing load performance

The performance of herring bone bearings are determined by design specifications such as the groove depth h_g, the groove width b_g, etc.. The following discussions on the influence of these specifications on bearing performance are carried out over the ranges of the most commonly used values [1,2]. The characteristics used to show the bearing performance are normalized load carrying capacity W (see Nomenclature for definitions) and attitude angle ϕ (see Fig.1). The former gives a loading capacity per unit area ratio and the latter gives indirectly the stability of the bearings (bearings with a large attitude angle are often likely to become instable [5]). The rotation of the spindle, however, must be in the direction that pumps air into the bearing clearance. Otherwise the pressure within the clearance will drop down below ambient pressure.

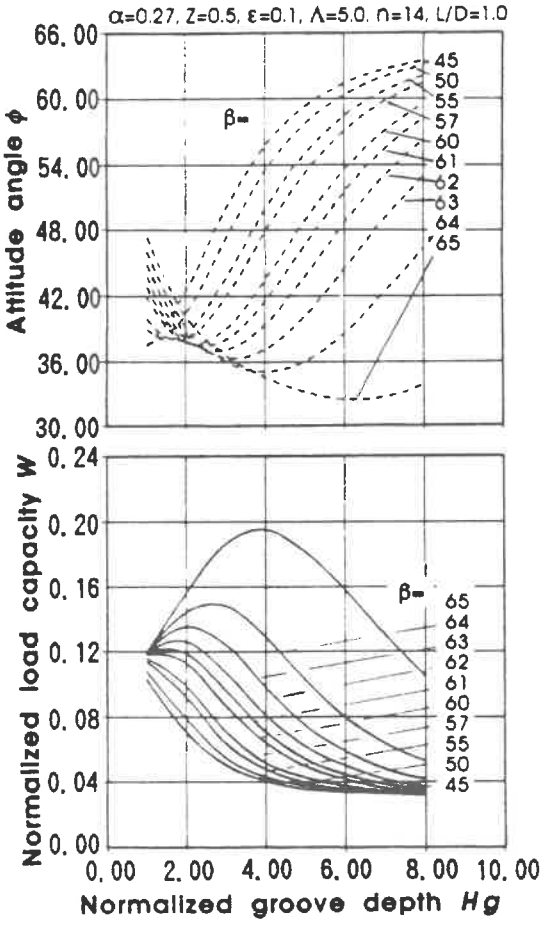

(a) $\beta\leq65°$

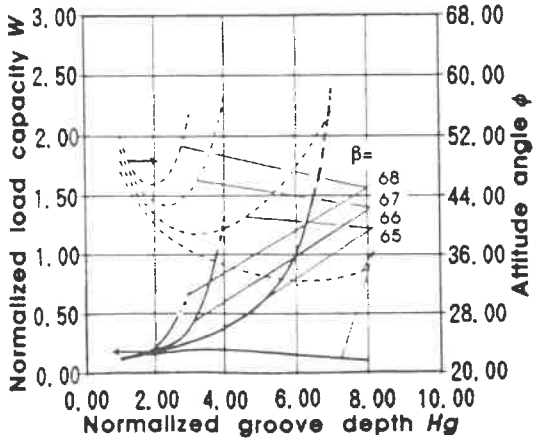

(b) $\beta\geq65°$

Fig.2 Influences of the groove pump-in angle β

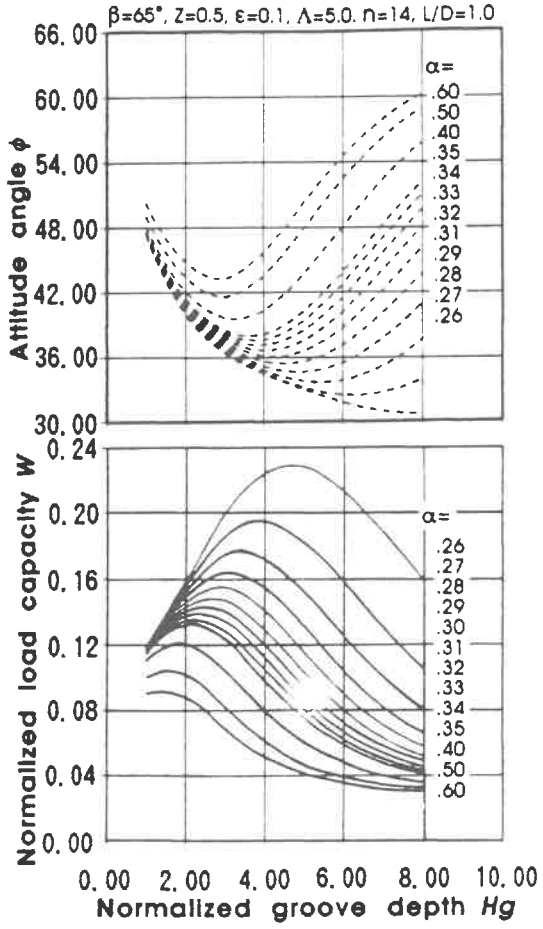

(a) $\alpha \geq 0.26$

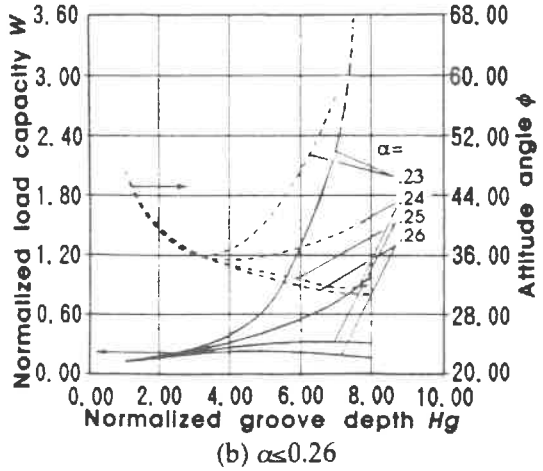

(b) $\alpha \leq 0.26$

Fig.3 Influences of the groove width ratio α

Figure 2 is a relationship between the pump-in angle β and the bearing performance obtained by the computed results. It shows that increasing pump-in angle β can increase bearing load capacity W The minimum value of ϕ are obtained at about β= 65 with respect to groove depth Hg=2.0. The computed results also show that increasing β can further increase$W$, but it may drastically increase the attitude angle ϕ which often deteriorates the stability of the bearings.

The effect of the groove width α has been shown in Fig.3. According to the computed results, decreasing the α can increase the W. The smallest ϕ is obtained at α=0.26. Further decreasing in pump-in angel ϕ can further increase the load capacity W but also quickly increases the attitude angle ϕ. For best overall performance, the value of α=0.27 is often recommended.

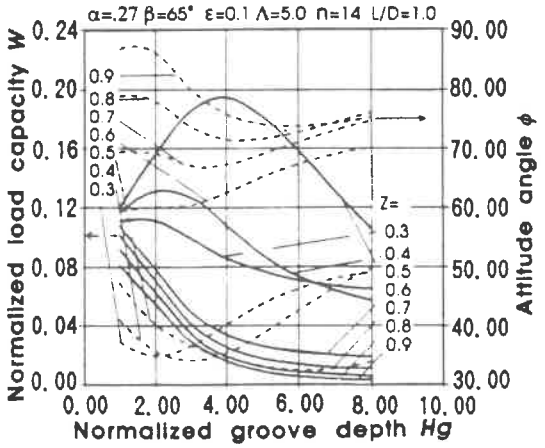

Fig.4 Influences of the groove length ratio Z

In Fig.4, the influence of the length of the grooves Z is shown. Since the β and α have been optimized with respect to Z=0.5, both maximum load capacity W and minimum attitude angle ϕ are obtained at Z=0.5.

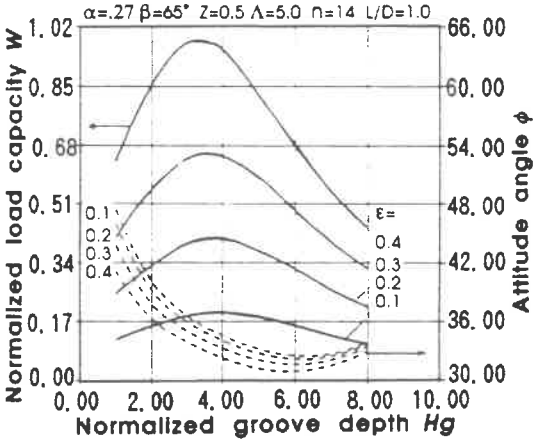

Fig.5 Influences of the eccentricity ratio ε

Figure 5 shows the relationship of eccentricity ratio of the bearing ε to the bearing performance. Naturally the load capacity W increases with an increase in eccentricity ratio ε while the attitude angle ϕ decreases.

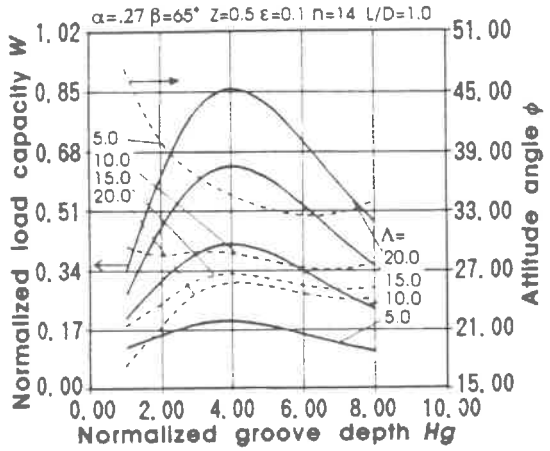

Fig.6 Influences of the bearing number Λ

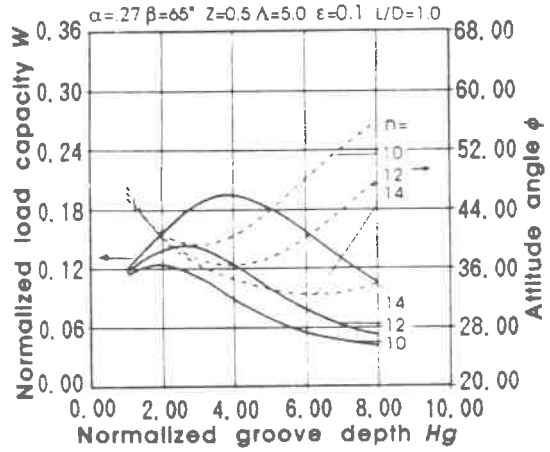

Fig.7 Influences of the groove number n

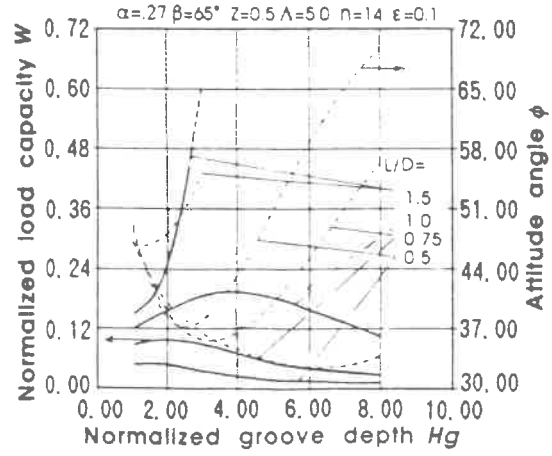

Fig.8 Influences of the slenderness ratio L/D

Figure 6 shows that bearing load capacity W increases approximately in proportion to the bearing number Λ, while the attitude angle ϕ decreases. However, the designer should notice that the instability caused by factors other than attitude angle ϕ increase with the bearing number.

The influence of number of grooves n is shown in Fig.7. Apparently, the load capacity W increases, while the ϕ decreases with the number of the grooves n. The load capacity W approaches to a constant when the groove number n reaches a certain value. This value, which varies from 20 to 40, has to be determined by the combination of other design specifications.

The variation of bearing performance with respect to the L/D ratios is shown in Fig.8. Although it is usually true that the bearings with smaller L/D ratio have a smaller attitude angle ϕ, it is seen in the figure that the bearing with an L/D=1.0 has the best overall performance due to the influences of β, α and Z. In other words, different values of optimal design specifications have to be given for bearings with different L/D ratios.

5. Conclusion

Based on the computed results and foregoing discussions, the influences of the design parameters on the load capacity W and attitude angle ϕ within most commonly used range have been known. Therefor the design optimization of the bearings, especially when the bearing slenderness ratio L/D=1.0, has become possible.

6. Acknowledgment

The authors would like to express their appreciation to the National Center for Supercomputing Applications for its support.

7. References

1) Togo J., Gas bearings. Kyoritsu Pub. 1984, pp32-34, (in Japanese)
2) MTI text book, design of gas bearings. 1967, pp6.1.1
5) Lin G. Aoyama T. and Inasaki I., Wear, Vol.126, 1988 pp307-319
4) Lin G. and Satomi T., Trans JSME, Vol.57, No.541, Ser.C, 1991, pp2971-2977 (in Japanese)
5) Fuller D.D., Trans ASME, Ser.F, 1969, pp1-16

Design Concept of Ultraprecision and High Stiffness Feed System Based on Differential-Force Operation, and the Application

M. Miyasita*, A. Kanai* and J. Yoshioka**

* Ashikaga Institute of Technology, Ashikaga, Tochigi 326, Japan, ** NUTR K.K.

1. Classification of absolute and relative values operated servo systems and the applications

1.1 Concept of absolute value and relative value operated servo systems

Fig. 1 is a typical example of hydraulic feed system defined as an absolute value operated servo system. The system is characteristic of a combination of flow rate control servovalve and the conventional hydraulic motor, that is, flow rate integrated displacement transmission actuator. The model gives the following characteristics :

(1) The resulted lost motion from reversing feed direction is not avoidable due to the combination of displacement transmission, backlash and compliance.

(2) Applied load in feed direction to the carriage is balanced with the driving force induced by the displacement transmission actuator through the compliance. Accordingly, the stiffness is not high.

Fig. 2 is a typical example of hydraulic feed system defined as a relative value operated servo system. The system is characteristic of a combination of differential pressure control servovalve with two pressure outputs--- nozzle-flapper servovalve--- and differential force operated force transmission actuator. The model gives the following characteristics:

(1) In reversing feed direction, no lost motion occurs due to a direct transmission of the driving force.

(2) Applied load in feed direction to the carriage is directly balanced with the driving force. Accordingly, the stiffness is high.

1.2 Classification of key elements of servo system and definition of relative value operated servo system

In viewpoint of the definition of absolute value and relative value operated servo systems, the key elements of the system are an operation signal generator for error correction and a signal operated actuator. They are classified in function into the following categories:

(1) Operation signal generator,
  (a) absolute value operation signal generator
  (b) relative value operation signal generator

(2) Signal operated actuator,
  (a) displacement transmission actuator
  (b) force transmission actuator.

Several examples are shown in Figs. 3 and 4.
Generally, a system composed of a relative value operation signal generator and a relative value operated actuator, that is, a force transmission actuator is defined as relative value operated servo system.

1.3 Technical merit of relative value operated servo system

A differential force operated actuator is a force transmission unit. A loss of transmitted force is caused by inertial and viscous resistances and accordingly the actuator is preferable in functional accuracy in a range of lower feed rate.
Comparing with a flow rate control srevovalve in viewpoint of a resolution, a differential pressure control servovalve is easy to get a high resolution of pressure difference, while the former is difficult to get extremely small flow rate control capability. Therefore, a differential

pressure control servovalve has a high resolution in a range of lower feedrate similar to a differential force operated actuator.
Accordingly, a relative value operated servo system has generally a high resolution as far as a position feedback sensor has sufficiently high resolution.
Conclusionally, a relative value operated servo system has the following characteristics:

(1) high resolution, (2) high stiffness, (3) lost motion free

and is functionally preferable to be applied in a range of lower feed rate.

2. Practical applications of relative value operated servo system

2.1 Workrest with differential force operated actuator – Fig. 5 (a), (b), (c)

2.2 Feed system of 845 kg carriage on plain bearing guideways with load compensation unit – Fig. 6 (a), (b)

2.3 Cam copying truing unit with differential force operated actuator – Fig. 7 (a), (b)

2.4 Feed system of 200 kg carriage on plain bearing guideways with differential force operated actuator – Fig. 8

3. Conclusion

Feed control systems are classified into an absolute value operated and relative value operated servo systems, of which characteristics are compared. And it is discussed that a relative value operated servo system is generally characteristic of the following performances in a rage of lower feed rate:

(1) high resolution, (2) high stiffness, (3) lost motion free.

The practical applications applied the new concept support experimentally the above discussion. As a result, for example, the 200 kg carriage feed system achieve a high resolution of 1 nm/step, a high stiffness of more than 60 N/nm and also lost motion free feed in the range of nanometer.

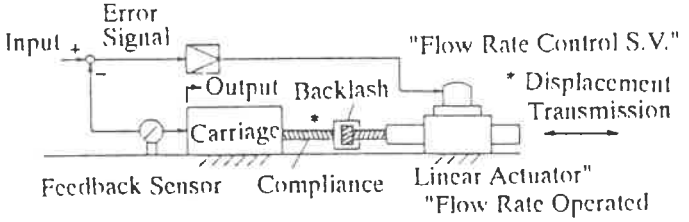

Fig.1 Flow rate operated servo system.

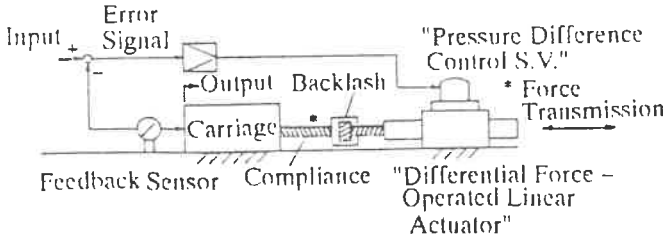

Fig.2 Differential force operated servo system.

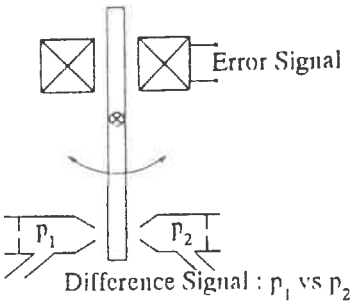

(a) Nozzle-flapper servovalve

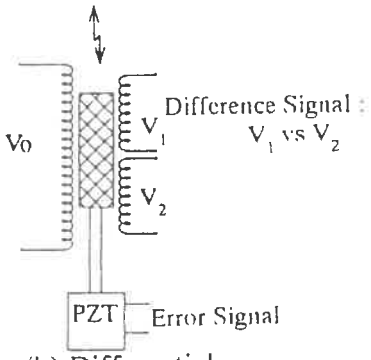

(b) Differential transformer + PZT actuator

Fig.3 Differential operation signal generators.

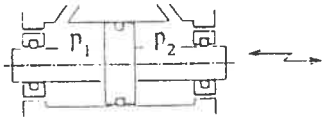

(a) Differential force operated hydraulic actuator

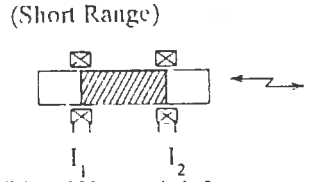

(b) Differential force operated voice coil actuator

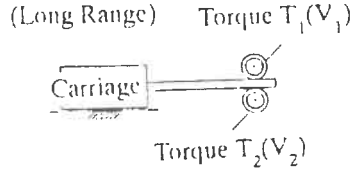

(c) Differential torque operated gear drive actuator

Fig.4 Differential signal operated actuators.

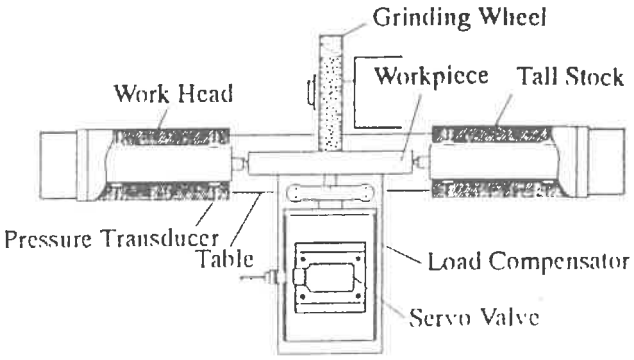

(a) Construction of the system

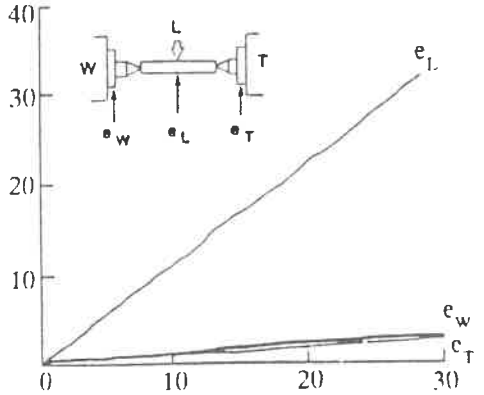

(b) Work support stiffness without load compensation unit

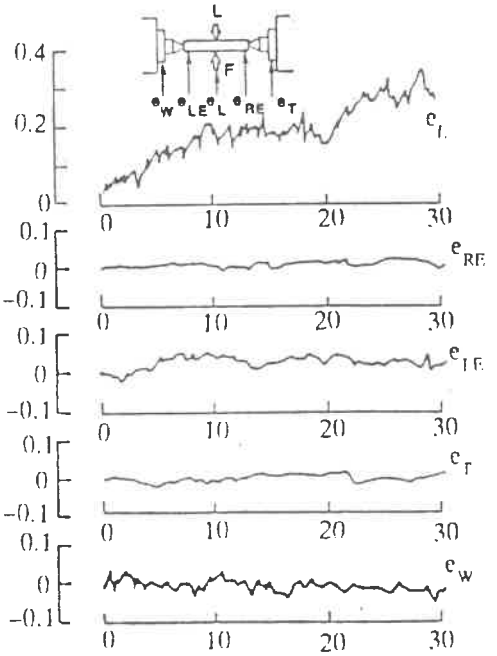

(c) Work support stiffness

Fig.5 Workrest with differential force operated actuator.

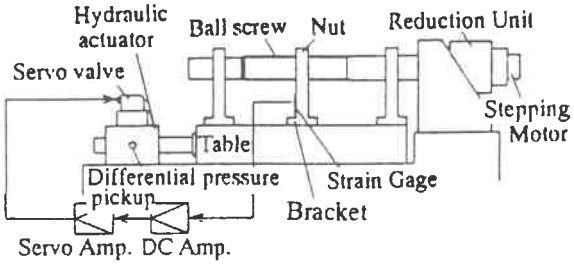

(a) Construction of the system

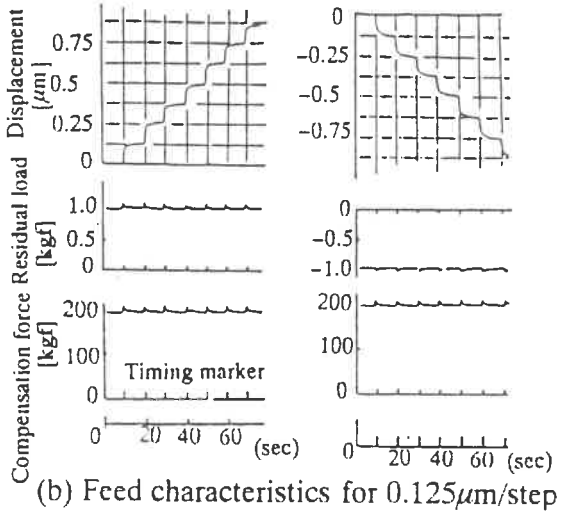

(b) Feed characteristics for 0.125μm/step feed

Fig.6 Feed system of 845kg carriage of plain bearing guideways with load compensation unit.

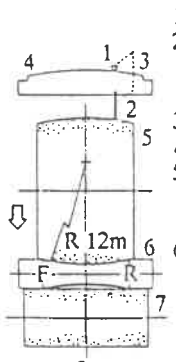

(a) Layout of cam copying truing unit and centerless grinding

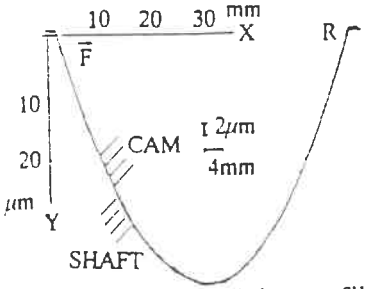

(b) comparison of the profiles of the cam and the ground workpiece

Fig.7 Cam copying truing unit with differential force operated actuator.

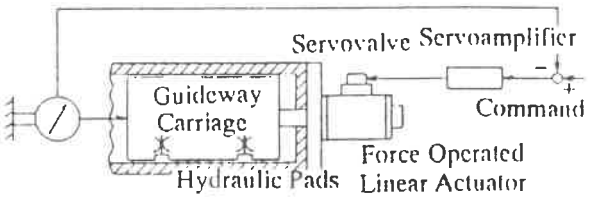

(a) Construction of the system

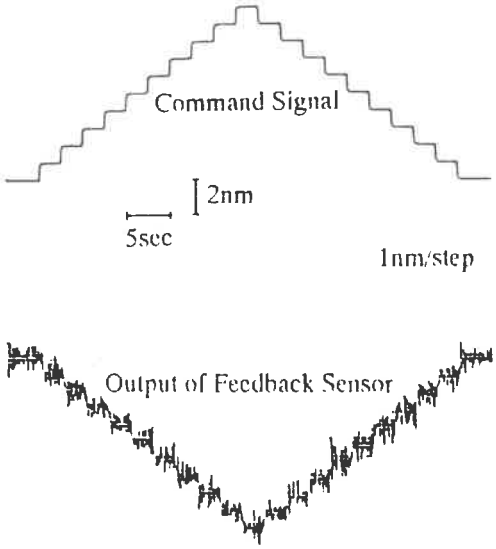

(b) 1nm/step feed characteristics

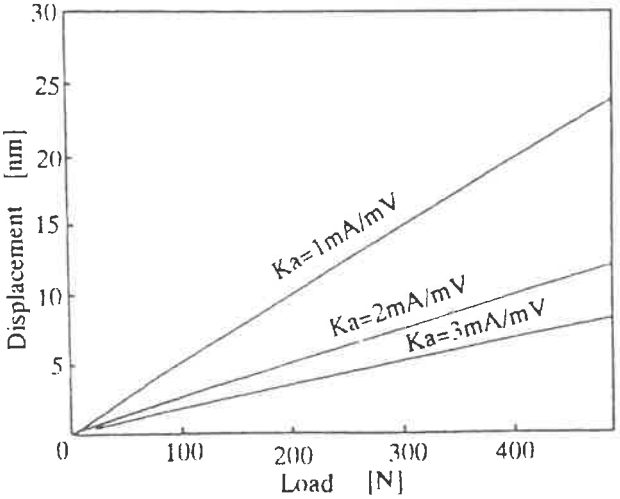

(c) Stiffness in feed direction

Fig.8 Feed system of 200kg carriage on plain bearing guideways with differential force operated actuator.

Power-Efficient Linear Motor for Precision Motion Control

David L. Trumper, Tiep Nguyen, Mark Williams
Precision Engineering Laboratory
Univ. of N. Carolina at Charlotte
Charlotte, NC 28223

The first author has previously reported on the use of magnetic bearings for precision motion control of a linear stage [1]. In this stage, the magnetic bearings constrain five degrees of freedom of a 10.7 kg platen measuring 125 mm by 125 mm by 350 mm. This stage has demonstrated 3 nm short-term stability in our laboratory as shown in Figure 1. The figure shows the response of the stage to a commanded 10 nm lateral step. Note that the step settles to within 3 nm of final value within approximately 10 msec. Note also that the negative-going step returns to essentially the initial position, and thus the actuator is free of hysteresis within the nanometer resolution limits of the observed data. The noise present on the response is dominated by a 430 Hz component of about 3 nm peak-to-peak. A high-sensitivity accelerometer (100 V/m/sec^2) has been used to confirm that the noise is due to floor vibrations transmitted onto the un-isolated optical table on which the experiment rests. Integrating the accelerometer output twice yields an estimate of the vibration amplitude which is within a factor of two of the amplitude measured by the capacitance probes. This provides an independent confirmation of the scale of the position measurements which we are reporting. The source of these vibrations is believed to be the air conditioning equipment located in the sub-basement of our building.

Travel of 50 mm in the sixth degree of freedom (axial) is provided by a novel permanent magnet linear synchronous motor. This motor consists of permanent magnets attached to the moving platen and stator windings attached to the machine base. The motor in present operation utilizes a conventional magnet array. The geometry and field pattern for this magnet array are shown in Figure 2. Under laser interferometer feedback in the axial direction, this motor is used to control the axial position of the platen. The resulting positioning stability is shown in Figure 3. This data shows the position error over one second of observation. The vertical axis represents position with a sensitivity of 10 nm per division. The quantization seen in the error signal is due to the quantization of the plane mirror interferometer of approximately 5 nm per least significant bit. Note that the peak-to-peak error is three least significant bits or about 15 nm. This data verifies that such a motor can be used to position a magnetic bearing with sufficient accuracy for the envisioned photolithography application. The axial step response of the linear bearing is shown in Figure 4. This trace shows the response of the bearing to a commanded 200 nm axial step. Note that the response settles to final value in approximately 15 msec. This data demonstrates that the bearing can exhibit sufficiently fast settling time.

In the future, we intend to adopt a Halbach magnet array configuration [3]. The geometry and field pattern for this array are shown in Figure 5. Analytical calculations show that the use of this magnet array doubles the motor power efficiency in comparison with a conventional magnet array of the same volume. In addition, an analytical solution for the power-optimum stator thickness has been derived. Using this optimum thickness, preliminary design calculations indicate that such a properly-sized motor is capable of providing 30 N force for 2.2 W power dissipation, and 50 N force for 6.1 W power dissipation.

In the intended photolithography application, with a 10 kg platen, this translates to accelerations of 0.3 and 0.5 times the acceleration of gravity, respectively. Such acceleration allows a significant reduction in the stage step-and-settle time, and thereby an increase in machine throughput, with attendant economic advantages. In addition, the power dissipation is low enough to be readily compatible with the wafer stepping environment. The envisioned motor structure is single-sided and planar; the stator is to be fabricated on an aluminum substrate to provide highly efficient cooling of the stator windings. We anticipate that the stator temperature rise in steady-state operation can be limited to less than 0.5 °C.

[1] Trumper, D.L., and Slocum, A.H., "Nanometer Motion Control via Magnetic Suspension," ASPE 1991 Annual Conference, Oct. 13–18, 1991.

[2] Trumper, D.L., and Queen, M.H., "Control and Actuator Design for a Precision Magnetic Suspension Linear Bearing," SPIE Optical Engineering/Aerospace Sensing, Marriot's Orlando World Center, Orlando, PL, April 20–24, 1992.

[3] Halbach, K., "Design of Permanent Multipole Magnets with Oriented Rare Earth Cobalt Material," Nuclear Instruments and Methods, 169, 1980, pp. 1–10, North-Holland Publishing Co.

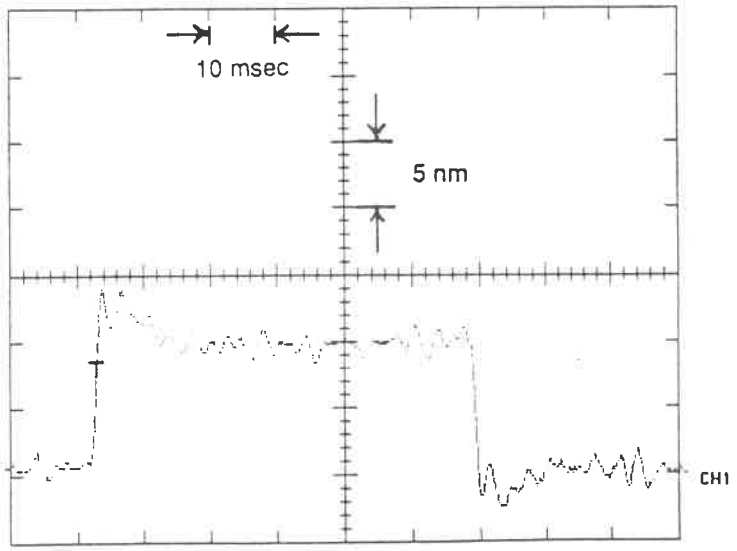

Figure 1. Response of bearing to a commanded 10 nm lateral step. The step settles to within 3 nm of final value within approximately 10 msec.

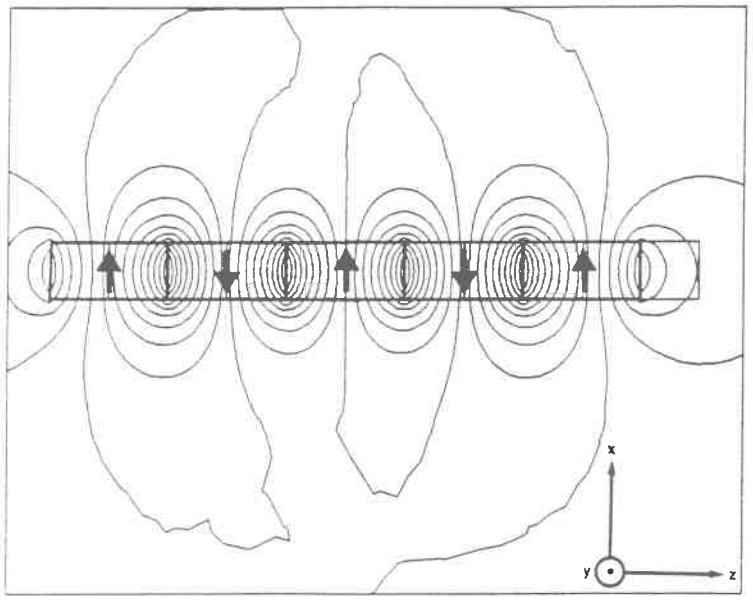

Figure 2. Conventional magnet array.

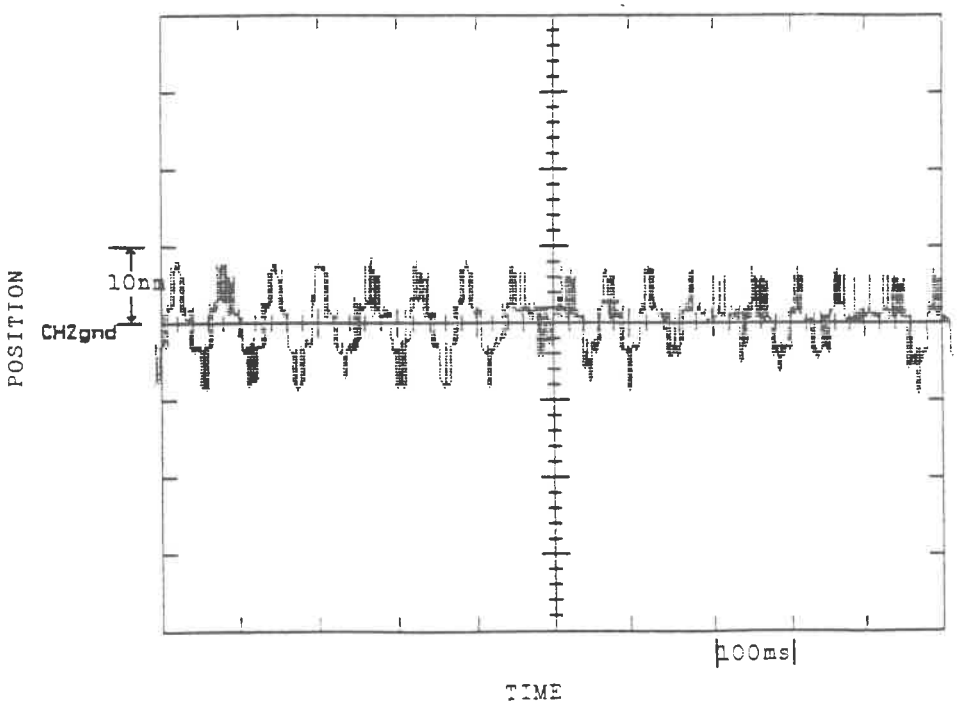

Figure 3. Axial position stability of linear bearing. Vertical scale is 10 nm per major division. Horizontal scale is 100 msec per major division.

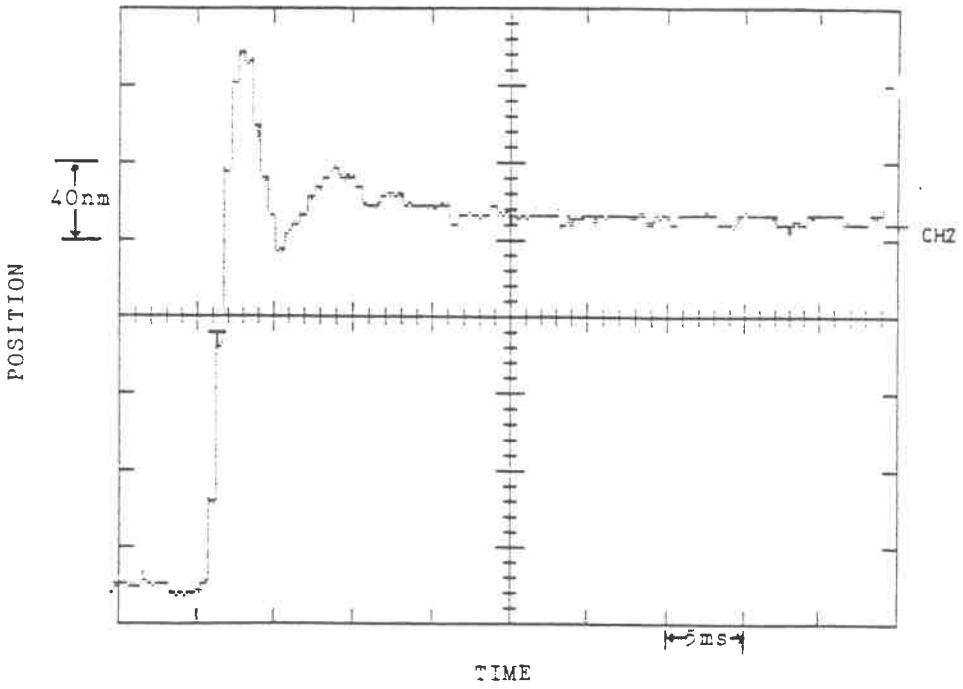

Figure 4. Axial step response of linear bearing. Vertical scale is 40 nm per major division. Horizontal scale is 5 msec per major division.

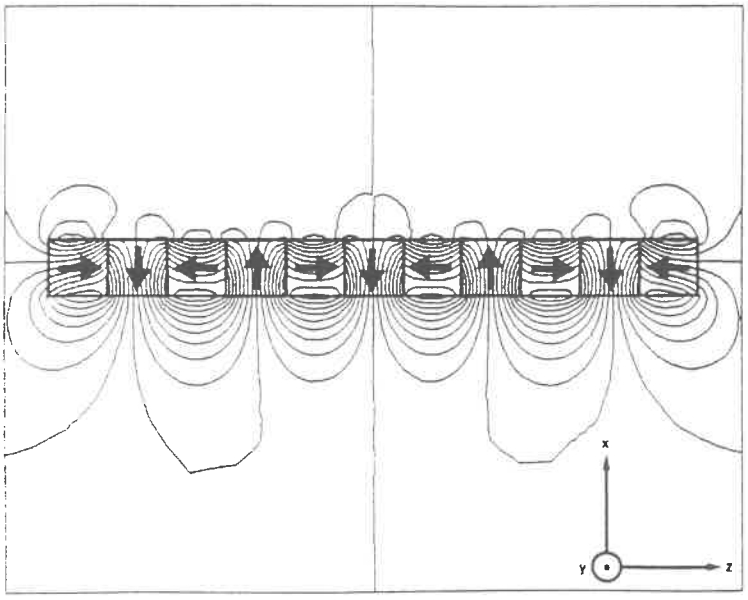

Figure 5. Halbach magnet array.

BALL SCREW NONLINEARITY AND DYNAMIC SLIDEWAY PERFORMANCE

James F. Cuttino — Graduate Student
Thomas A. Dow — Professor
Precision Engineering Center
North Carolina State University
Raleigh, NC 27695-7918

INTRODUCTION

Many high volume components such as optical assemblies, copier drums, and microelectronics components rely on precision machinery such as diamond turning machines (DTM) and step-and-repeat cameras to achieve increasingly tighter design tolerances at reasonable cost. The accuracy of these manufacturing machines depends heavily on the ability to provide repeatable and accurate slide motion.

One of the most common precision slide actuators is the ball screw. A ball screw is usually considered a fixed gain device in a control system where the gain is represented by the pitch of the screw. However, previous studies have shown that, for displacements on the nanometer scale, the output displacement vs. input angle is not always linear. This nonlinearity is due to frictional forces in the nut which in turn result in windup of the shaft and couplings as the screw is turned. Both experimental measurements of this phenominon as well as theoretical predictions have been performed on a test bench using a commercial ball screw [1]. The objective of this section is to describe recent efforts to extrapolate these results to a DTM and explain the consequences of this behavior on the machined components.

EXPERIMENTAL PROCEDURE

The DTM slideways are driven by ball screw actuators as shown in Figure 1. Input to the amplifier is a commanded velocity in digital-to-analog converter (DAC) bits, which in turn sends a signal to the motor which produces the angular velocity of the screw. The nut is attached to the slideway by a non-influencing coupling which is stiff in the translational direction and compliant in the directions perpendicular to the slideway travel. Slide displacement is measured using a laser interferometer with 2.5 nm resolution.

Amplitude ratio and phase diagrams between the commanded input velocity and the output displacement for the Z slide of the DTM are shown in Figure 2. The input signal was a generated

sinusoidal velocity command centered around zero with varying amplitudes. The amplitude ratio (output displacement/input velocity) in the left hand figure decreases with frequency due to the integration process (velocity in and displacement out) and has a peak at 65 Hz resulting from the natural frequency of the slide. As the input amplitude is reduced, the amplitude ratio is reduced at any given frequency. This means that the output motion is not proportional to the input command and the systems behaves nonlinearly. The spread in the frequency response for the range of amplitudes studied is about 20 db and the spread in phase is 20-30 degrees except near the natural frequency.

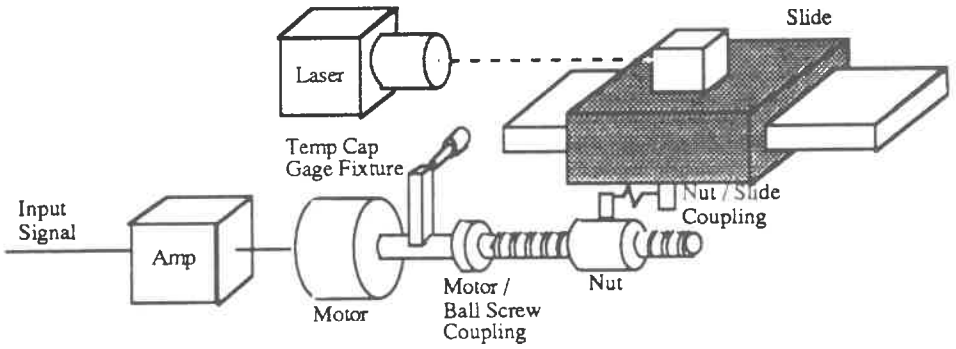

Figure 1: Diagram of DTM Slideway and Ball Screw Actuator System.

Tests were also conducted where a DC offset was applied to the input signal such that the velocity was always positive. The results from these tests indicated negligible spread in frequency response and phase as a function of input amplitude. It was concluded that motion reversal was the source of the nonlinearity. For the sine wave excitation, the elastic windup increases with rotation until a steady state value is reached and the screw pitch is realized. This nonlinearity occurs each time motion of the ball screw is reversed because residual strain must be released and reversed.

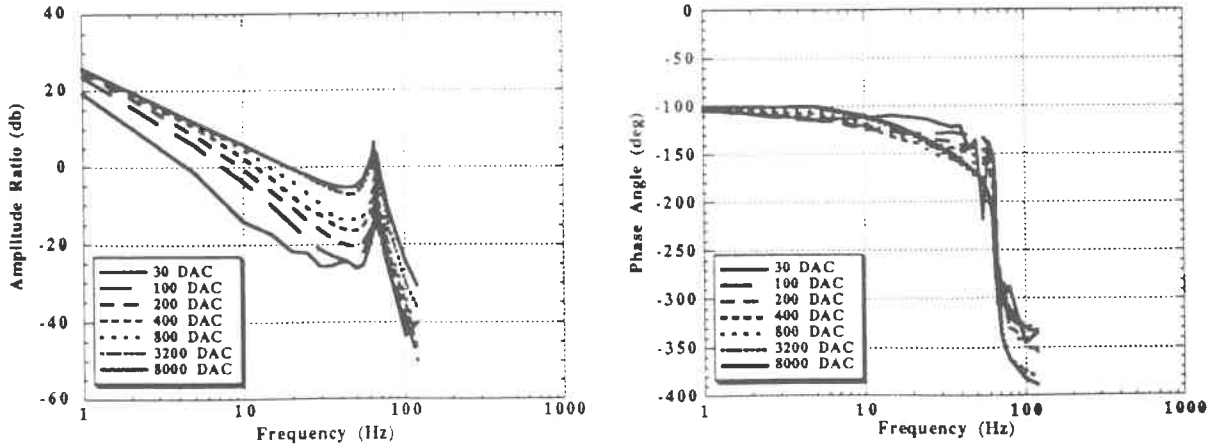

Figure 2: Amplitude and Phase Diagrams for Z slide at input amplitudes from 30-8000 DAC bits

To identify the source of the nonlinearities in the DTM, the motor tachometer was used to indicate the position of the motor shaft. Transfer functions and phase diagrams were obtained for the amplifier/motor assembly by measuring the output displacement as a function of the input signal. This function was then subtracted from the whole system response to obtain the response of the ball screw. In this way, the total transfer function (Figure 2) can be separated into the contributions from the amplifier/motor (Figure 3) and the ball screw/slide (Figure 4). Because of the noise in the tachometer signal at amplitudes less than 100 DAC bits, data at the lowest experimental condition (30 DAC bits) was not included on these graphs.

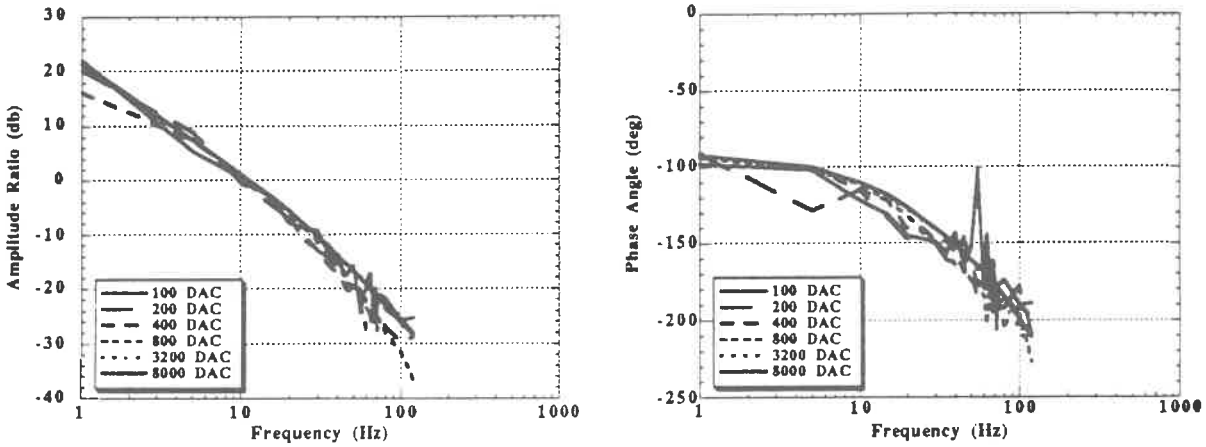

Figure 3: Amplitude and Phase Diagrams for Amplifier/Motor Assembly.(100-8000 DAC bits)

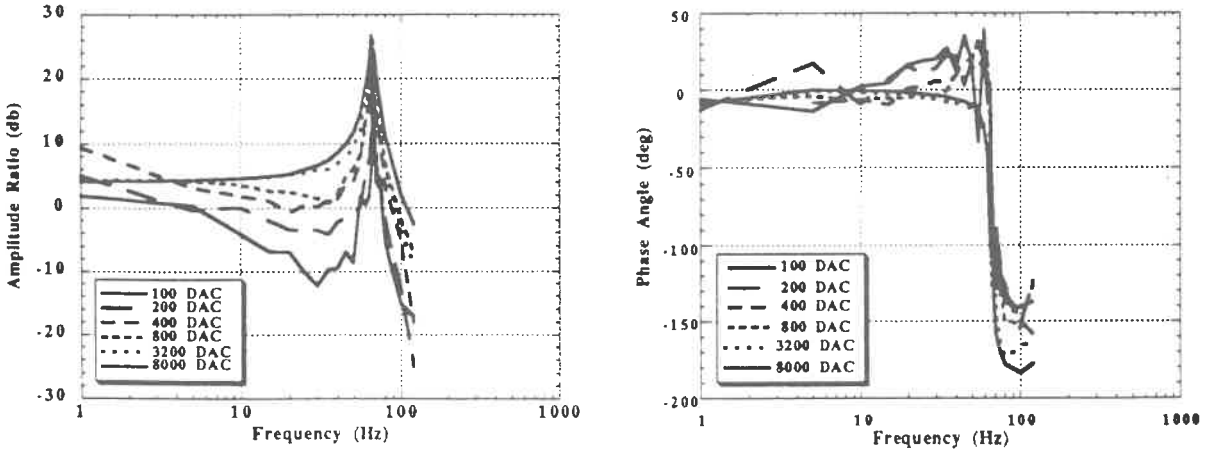

Figure 4: Amplitude and Phase Diagrams for Ball Screw/Slide Assembly (100-8000 DAC bits)

Figure 3 shows the transfer function between the computer and the motor shaft. The integration resulting from a velocity command input and an angular displacement output results a 20 db per decade slope of the amplitude ratio curve and the initial 90° lag in phase. The feedback controller in the motor has been adjusted for a high level of damping and has a break frequency of

approximately 50 Hz. This increases the slope of the amplitude ratio curve for frequencies above about 5 Hz and moves the phase angle toward 270°. For this amplifier/motor combination, there is little change in output as a function of input with changes in the input amplitude and thus it behaves as a linear system.

Figure 4 shows the features of the transfer function between the motor drive shaft and the slide linear motion through the ball screw. This response exhibits the classical shape of a second order system with low damping and a natural frequency of ~70 Hz at the high input amplitudes . The phase stays close to zero until the frequency approaches the natural frequency where it shifts 180°. However, the amplitude of the input has a significant impact on the resulting amplitude ratio. At small amplitudes, the output can be down 10 db which translates to only $\frac{1}{3}$ of the expected motion. This nonlinearity as a function of input amplitude can have an important impact on the control system design and the performance of the slide.

MODEL OF BALL SCREW DYNAMICS

To understand if the influence of the elastic windup in the ball screw was responsible for the measured frequency response, the model of the ball screw developed previous was applied to the DTM slide. Because the geometry of ball screw was not known in detail, the elastic response was measured directly. A fixture was attached to the output shaft of the motor to measure the motor angular displacement. Referring to Figure 1, the fixture consisted of an arm attached to the shaft and a capacitance gage mounted to the DTM base. The cap gage was used to measure the angular input to the ball screw.

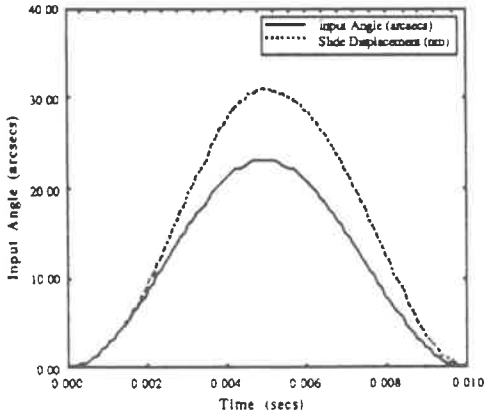

Figure 5: Input Angle and Output Displacement vs. Time (100 DAC input at 100 Hz)

A plot of output slide displacement vs. input angle to the screw was obtained, and a empirical curve was fit to the data. For any given input angle to the ball screw shaft, a relative angular windup could be calculated from the last point of reversal and a theoretical slide displacement could

be predicted from the curve fit. Figure 5 shows an example output for a 100 Hz sine wave input (100DAC bits). This plot reveals several features. First, the ball screw pitch (3.92 nm/arcsec) is not realized since the maximum slide displacement is only about 35% of the 90 nm expected. Secondly, the output displacement curve is delayed in time due to the screw windup. This effect is more pronounced as input amplitude is decreased or as frequency is increased.

An FFT analysis was used to predict the dynamic performance of the the ball screw for different input amplitudes. The theoretical response plots are shown in Figure 6. The characteristic spread in the frequency response shown in Figure 4 is predicted with reasonable accuracy in Figure 6. The theoretical spread is on the order of 10 db, which is still somewhat less than the measured value (the measured data did not contain a transfer function at an input of 30 DAC bits). Comparing the phase plots in Figures 4 and 6, the model seem to provide an reasonable picture of system but with the observation that the measured response has more noise.

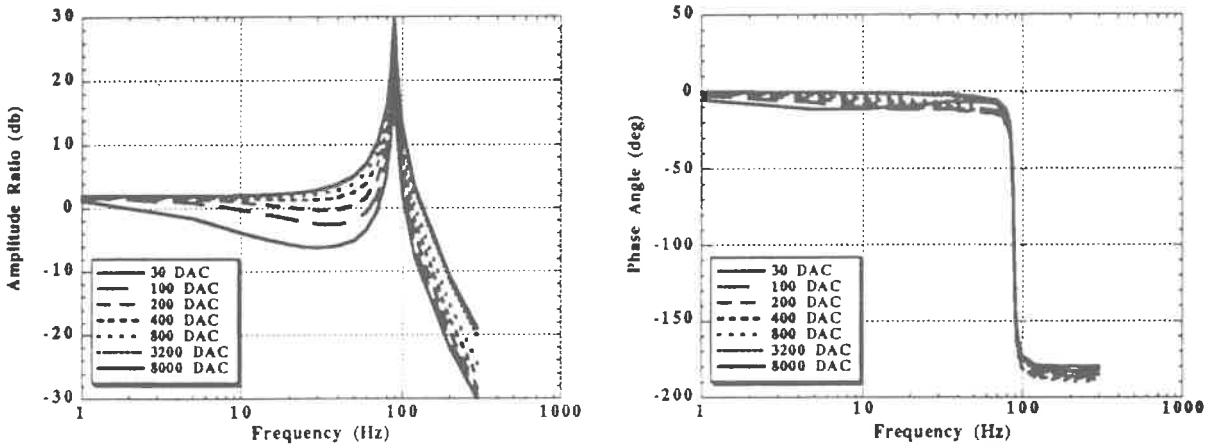

Figure 6: Theoretical Amplitude and Phase Diagrams for Ball Screw / Coupling Assembly with Slide Dynamics.

CONCLUSIONS

The frequency response and phase of the DTM slideway have been separated into contribution from the amplifier/motor system and the ball screw/coupling. Amplifier dynamics created a lag in phase and a change in amplitude ratio with frequency, but were not greatly influenced by the amplitude of the input signal. The model of the ball screw motion developed over the last several years has been applied to the dynamics of the slide and predicts the measured performance as a function of the input amplitude. Work in continuing to develop strategies to control such a system with nonlinear characteristics.

A Study On Dynamic Performance Of Closed-loop Commuted Stepping Motor To Improve Precision Motion Control

Kai-leung Yung* and Hong Liu†
* Dept. of Manufacturing Engineering, Hong Kong Polytechnic
Hung Hom, Kowloon, HONGKONG
† Dept. of Precision Instruments, Tsinghua University
Beijing 100084, P.R.CHINA

1. Introduction

The design of many precision machines required that the axis not only be able to position accurately, but also to describe a profile or contour precisely. To describe a profile or contour precisely, the machine drive is required not only to stop accurately at the designed position, but to move accurately at the desired speed and acceleration. This accurate speed and acceleration requirement can only be achieved by a motor ideally with no torque ripple and speed ripple. That is, for a set excitation, the motor should be able to deliver a constant amount of torque which is independent of the angular position of the rotor.

Due to the physical constrain of the motor windings and the magnetic pole pieces, actually designing a motor which has no torque ripple is very difficult. Many precision d.c. servo motors have addressed this problem by: increase the number of poles so as to increase the torque ripple frequency and minimise the inter-pole dip in torque; increase the size of the communication ring and hence the number of segments so that the position of the conducting windings can be controlled more precisely; arrange the position of the brushes so that the torque generated at different angular position of the rotor are averaged out. Or in the case of brushless DC servo motor, use digital signal processors to compensate for the imperfection of the motor[1]. The result of all these efforts makes the motor very expensive.

An alternative to all these expensive torque/speed ripple reduction methods is to use a *low cost* hybrid stepping motor and commute it in such a way that it becomes a multi-pole d.c. motor[2].

2. Motor Commutation

There have been many attempts, such as micro-stepping, to drive the stepping motor smoothly and make it position between steps. Nearly all of this methods involve open-loop commutation of the stepping motor, which, requires the stepping motor to work well under its maximum torque to avoid slipping and missing steps. Similar to a.c. servo motors, the rotor of open-loop commutated stepping motor produce a force according to its position within ± 1 step. This represent compliance in the part of the servo system and affect the performance of the servo loop.

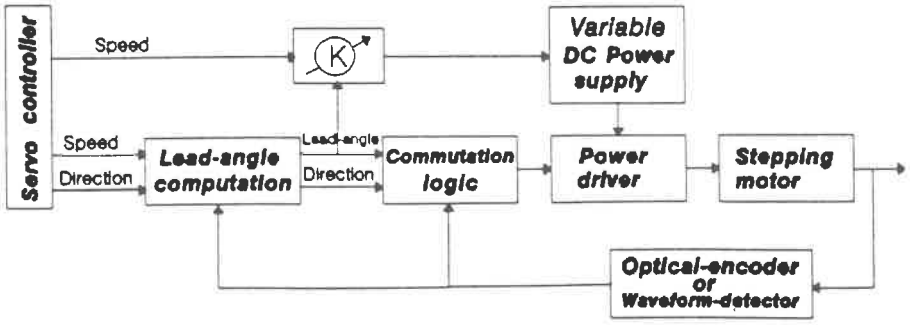

Fig.1 Block diagram of a typical closed-loop commuted stepping motor

To eliminate compliance the motor characteristic has to resemble that of the d.c. servo motor. It is achieved by using positional feedback and/or velocity feedback to determine the proper phase

switching with respect to the rotor position (Fig. 1). The optimal commutation control for this method relies on the apriority knowledge of the stepping motor in terms of a mathematical model and the rotor position feedback.

Throughout this paper, reference will be made to a typical stepping motor of the brand name VEXTA, model PH264-01B manufactured by the Oriental Motor Co. Ltd. It is a two-phase, bifilar-wound, hybrid type stepping motor with 50 rotor teeth (1.8 degrees per step). This motor is driven in half step mode and an optical encoder with resolution of 1600 pulses per revolution is used for feeding back the rotor position.

3.Developments & experimental results:

Traditionally, the d.c. power voltage applied to the stepping motor control system (Fig.1) is fixed on the rated value and the motor speed is adjusted by the lead angle in closed-loop control. This and the equivalent method are limited in precision motion control because they produce considerable speed ripple and torque ripple under most conditions.

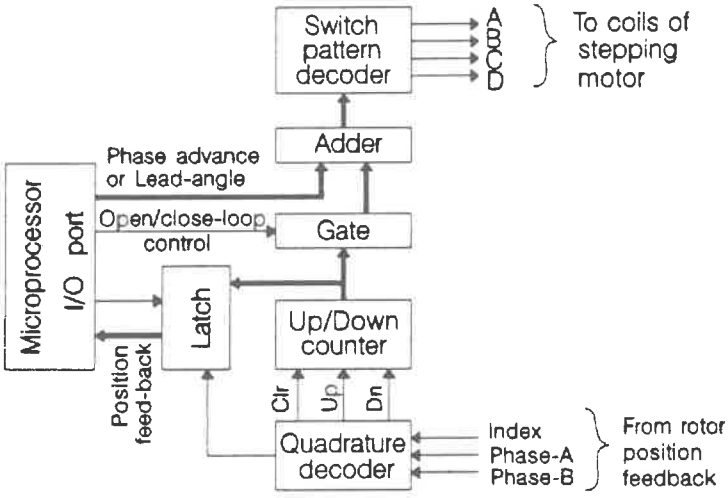

Fig.3 Schematic diagram of implementation of closed-loop commuted stepping motor

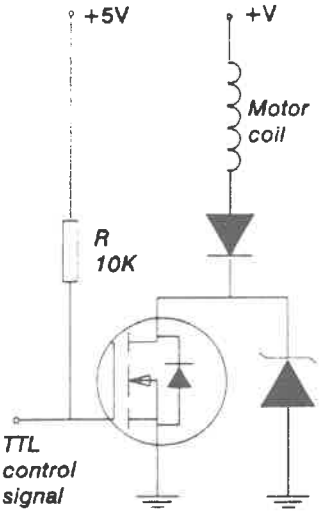

Fig.2 Drive circuit for closed-loop control

In our system both the lead angle and the power voltage are used to adjust the motor speed. By omitting the overdriving scheme usually used in open-loop control, the power voltage $+V$ in the drive circuit shown in Fig.2 can be used to adjust the phase current and then the motor speed. It can either be provided by a variable magnitude d.c. power source or a pulse-wide-modulation (PWM) supply.

The implementation of closed-loop commutation scheme is shown in Fig.3. *Index, Phase-A & Phase-B* signals come from the optical-encoder while *A, B, C & D* signals are connected to motor coils as shown in Fig.2. The microprocessor can monitor the position feed-back and adjust the lead angle at any time. With proper control algorithm in the processor, the stepping motor can be set to an optimum operating condition.

Fig.4 shows the steady-state average speed versus power voltage characteristics at different lead angles. The almost linear relationship between the motor speed under no load condition and the power voltage suggests that having determined the appropriate lead angle for speed range selection and ripple minimization, the motor speed can be controlled by varying the voltage supplied.

To derive a method of determining the optimal

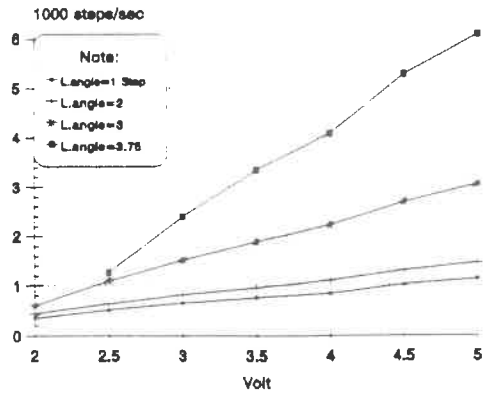

Fig.4 Average speed vs power voltage characteristics

relationship between lead angle and motor speed for the lowest possible speed ripple, an accurate dynamic model of the system is required.

4.Dynamic model:

The following dynamic model can be derived for the hybrid type stepping motor described earlier.

$$\frac{d\theta}{dt} = \omega$$

$$\frac{d\omega}{dt} = -\frac{K_T}{J}\left[i_{ac}\,Sin(N_r\theta) + i_{bd}\,Sin\left(N_r\theta - \frac{\pi}{2}\right)\right] - \frac{B}{J}\omega - \frac{T_D}{J}$$

$$\frac{di_{ac}}{dt} = \frac{1}{L_1 + \frac{dL_1}{di_{ac}} i_{ac} + \frac{dk_a(i_{ac})}{di_{ac}} Cos(N_r\theta)} \left[\frac{V_{ac}}{2} - \frac{r i_{ac}}{2} + k_a(i_{ac})\, N_r \omega\, Sin(N_r\theta)\right]$$

$$\frac{di_{bd}}{dt} = \frac{1}{L_1 + \frac{dL_1}{di_{bd}} i_{bd} + \frac{dk_b(i_{bd})}{di_{bd}} Cos\left(N_r\theta - \frac{\pi}{2}\right)} \left[\frac{V_{bd}}{2} - \frac{r i_{bd}}{2} + k_b(i_{bd})\, N_r \omega\, Sin\left(N_r\theta - \frac{\pi}{2}\right)\right]$$

Where the motor phases are assumed to be identical and alternate phases (Eg. phase *a* and *c*) are 100% coupled; and

θ	= motor position	L_1	= phase inductance
ω	= motor angular speed	N_r	= rotor teeth number
T	= motor torque	i_{ac}	= i_a-i_c
B	= viscous damping coefficient	i_{bd}	= i_b-i_d
J	= rotor & load inertia	V_{ac}	= V_a-V_c
r	= Phase resistance	V_{bd}	= V_b-V_d

K_T is coefficient depending on the motor geometry, the PM flux and the respective phase current. When the magnetic circuit is linear, which is true when not saturated, they vary linearly with respect to the phase current. k_a, k_b are coefficients depending on the phase permeance, the number of turns, the strength of the permanent magnet and phase current. When the effect of magnetic saturation exists, the phase inductance L_1 and the coefficients k_a, k_b are functions of the respective phase current.

5.Computer simulation:

Obviously, it is fairly difficult to study the dynamic performance of the model derived above analytically, and very seldom does the system have a closed-form solution. One of the methods of obtaining realistic solutions to the analysis and studies of stepping motor system is computer simulation.

The dynamics of the drive circuit and the type of suppression used must be taken into account. When the TTL control signal in Fig.2 changes to zero volt, the transient phase current will be large in magnitude but decays very rapidly through the zener suppression circuit. However, this switching method makes the computer simulation difficult because, the large equivalent resistance makes the dynamic model become a stiff system. Attempts to use common numerical methods and techniques, such as Runge-Kutta method, to solve such problems encounter the requirement of absolute stability. Thus, the Rosenbrock methods for the initial value problems of stiff system are used in the simulation program. A particular method from Calahan is used here, which is a two stage, A-stable method with order 3. Furthermore, the dual-step scheme is used in solving the differential equations which helps to achieve higher accuracy without greatly slowing down the simulation process.

To test the dynamic model and simulation program, the waveforms from numerical solution are compared with the measured current. The matched characteristics give good verification and reliability of the dynamic model.

6.Torque ripple minimization method:

Although there are other methods to reduce the speed ripple, such as micro-stepping technique or couple the motor with large inertia, they suffer disadvantages of inherent compliancy and slow response respectively. This paper focuses on the relationship between speed ripple and lead angle,

and attempts to minimize speed ripple by adjusting lead angle in conjunction with supply voltage.

Having fixed the required lead angle, target velocity is reached by adjusting the power voltage. A group of results about the relationship between speed ripple and lead angle is derived from computer simulation as shown in Fig.5.

Tab.1 Best lead angle for various motor speed

MOTOR SPEED (Steps/sec)	LEAD ANGLE (Step)	K	VOLTAGE (Volt)	SPEED RIPPLE
167	1.50	K1	1.02%	20.8
333	2.75	K2	0.96%	13.1
500	3.00	K3	2.01%	9.5
667	3.50	K4	1.29%	7.7
800	3.50	K4	1.67%	3.8
1000	3.50	K4	1.98%	2.9
1333	3.75	K5	1.72%	2.1
2000	3.75	K5	2.74%	1.8
2667	3.75	K5	3.38%	1.2
4200	3.75	K5	5.00%	0.6

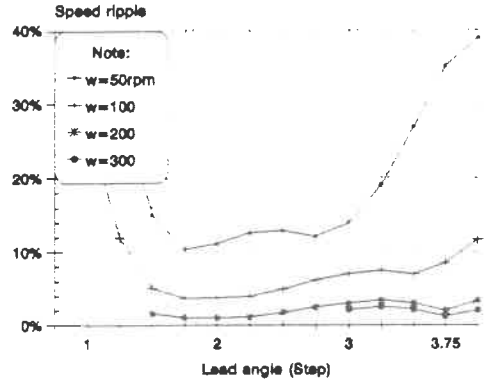

Fig.5 Speed ripple vs lead angle at fixed speed

It can be seen that there are two minimum speed ripple points at low motor speed. The one located at smaller lead angle and larger power voltage has less speed ripple than another. A stepping motor working at this point will show minimum speed ripple. However, this optimum point disappears at high motor speed because of voltage limitation (For example, 5V). Furthermore, according to Fig.4, larger lead angle gives higher speed sensitivity. Therefore, another minimum ripple point located at larger lead angle is chosen as working point.

Table 1 shows the best lead angle for various motor speed, which is extracted from the computer simulation results in Fig.5. The constants K1 to K5 in the table express the different gain K at the speed output to the variable power supply as shown in Fig.1. It is used for matching the speed-voltage curves at different lead angle (Fig.4).

7.Conclusion:

The dynamic model for the closed-loop commuted hybrid type stepping motor, which takes into account the drive circuit and the effect of magnetic saturation, was established and verified by the computer simulation. The dynamic performance of the motor system, including the torque ripple and speed ripple were studied. The ripple minimization method by adjusting the lead angle was found. The stepping motor under this speed ripple minimization scheme shows linear relationship between the motor speed and power supply voltage. Its characteristic is similar to that of a brushless d.c. servo motor. Therefore, it has strong potential for application in precision motion control.

With the model of the motor derived, accurate control law can be developed which utilizes the rotor position feedback to control the power supply to the motor for further minimization of the speed ripple at low speed.

8. References:

[1] *Low, T.K., Lee, T.H., Tseng K.J., and Lock, K.S.* Servo Performance of a BLDC Drive with Instantaneous Torque Control, IEEE Transactions on Industry Applications, Vol.28, No.2, 1992.

[2] *Yung, K.L. and Cheng, K.W.* Conversion of Stepping Motor to Precision Servo-motor, CAI Symposium '90, Hong Kong, 1990.

[3] *R.D.Slater, R.R.S.Simpson and H.A.F.Ibrahim*, Theoretical Analysis of Two-phase Permanent Magnet Machines, Modellin: Simulation and Control A, Vol.20, Pt.1, p19-30, 1988

[4] *P.J. Clarkson and P.P. Acarnley*, Closed-loop Control of Stepping Motor Systems, IEEE Transactions on Industry Applications, Vol.24, No.4, 1988

[5] *B.C.Kuo*, «Incremental Motion Control: Step Motors and Control Systems», 1979

Accuracy Improvement of Machine Tool by Workpiece-Refered Control

T.Kohno* Y.Uda** A.Morita* H.Nagano*
* Tokyo Metropolitan Institute of Technology
6-6 Asahigaoka, Hino, Tokyo 191 Japan
** Nikon Corporation
1-6-3, Nishi-Ohi Shinagawa-ku,Tokyo140,Japan

Abstract

To improve an accuracy of machine tool, the authors proposed a new system, named the workpiece-refered form accuracy control (WORFAC)[1], and confirmed an effectiveness of this manufacturing method. On this report, we try to apply this method to an ordinary NC machine tool, and we can get a higher accuracy with a simple mechanism. Here, we find out the new function of corrective servo by the change of feed-back volume that the error is multiplied by some coefficient m ($0 \leqq m \leqq 1$). This character is confirmed by both simulation on computer and experiment of cylindrical turning.

Introduction

On the ultra-precision machining technology, manufacture of more precise and larger elements is expected. In the case of turning, the machined form accuracy is determined by the so-called mother principle, where a copy is made of the accuracy of the machine tool. Of course, it is important to improve the accuracy and stiffness of machine tool and the machining conditions. In the previous report. the authors proposed WORFAC, and confirmed an effectiveness of this manufacturing method. On this report, with aim of accuracy improvement, we try to apply this method to a cylindrical turning using an ordinary NC machine tool, not to an ultra-precision machine tool. First, we turned a cylinder without this method and measured the form accuracy. We found that the workpiece has a 0.5 μ m p-p error of 6mm pitch and a large slope. For correcting the error of the tool slide motion by the WORFAC, we simulated this system and then examined by turning.

Principle of the research

The WORFAC is based on a concept that a form accuracy is determined by the relative distance between the workpiece and the cutting tool. So this method is a way to control the depth of micro - cutting by in - process measurement of the distance. Fig.1 is showing the WORFAC principle. If the tool-holder moves away from the workpiece surface,

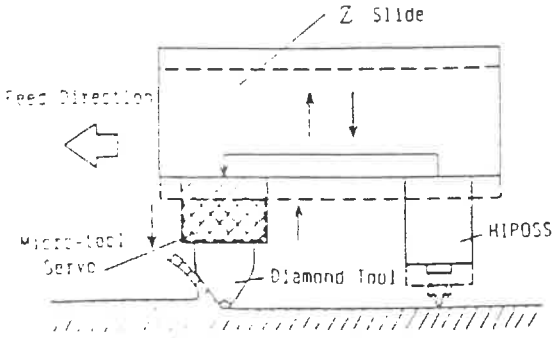

Fig.1 Principle of WORFAC

the micro-tool servo (MTS) pushes the tool by the same amount as the gap detected, and vice versa. A system of experiment of cylindrical turning is illustrated in Fig.2. MTS and the non-contact optical surface sensor (HIPOSS)[2] are attached on the same post rigidly, and the workpiece is put between MTS and HIPOSS. MTS consists of parallel leaf springs, a piezoelectric actuator, and strain gauges. Digital servo control is employed for changing the parameter of control freely.

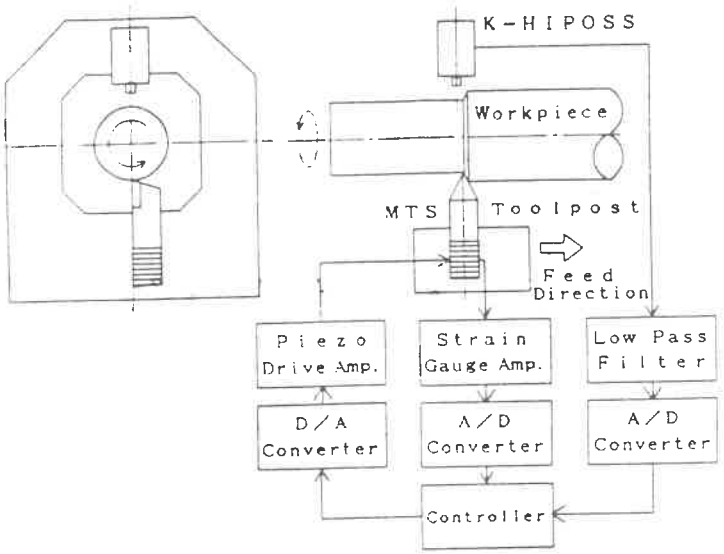

Fig.2 Block Diagram of WORFAC

Simulation of WORFAC

For simulation of the WORFAC on a computer, the mechanism of cylindrical turning is modeled and showed in Fig.3. X-axis is defined in the direction of workpiece's axis, and x means the position of cutting point. The tool post motion in the radial direction of workpiece will be appeared as an error $T_0(x)$. In the case of non-servo turning , and that amount is denoted as $T_0(x)$. The motions of the cutting tool, and the sensor as well as the workpiece figure are all same as $T_0(x)$. Since a subscript means the number of servo-loop, 0 means a case of non-servo, and n is n'th loop. If the axial distance between the cutting point and the sensing point is x_g, the sensing volume $S_n(x)$ is written by the equation (1).

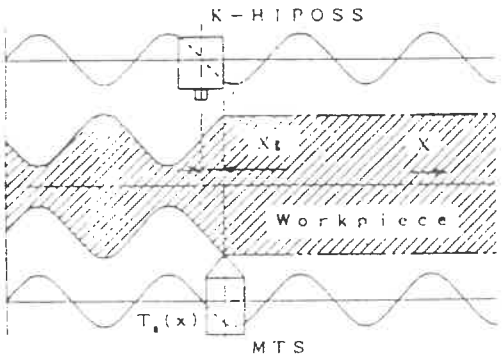

Fig.3 Simulation model of equipment

$$S_n(x) = T_n(x) + T_n(x-x_g) + C \qquad \cdots\cdots (1)$$

Where C means the off-set volume of the sensor in the radial direction. And it is set so that $S_1(x_1)$ becomes zero at point x_1. Here, using the advantage of digital control, the volume of feedback to MTS is determined that which is $S_n(x)$ multiplied by a coefficient m (the corrective servo coefficient). Controlling MTS, both the motion of the tool edge and the form of workpiece are $T_0(x)+mS_n(x)$. Fig.4 shows the results of simulation in the case of x_g=0.2mm at m=0.5 and m=0.9.

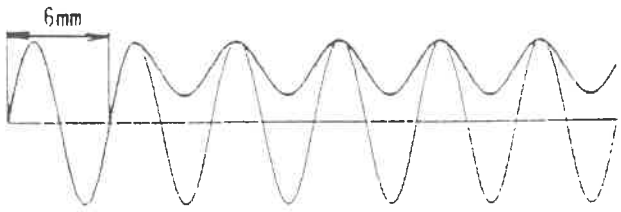

(a) m = 0.5

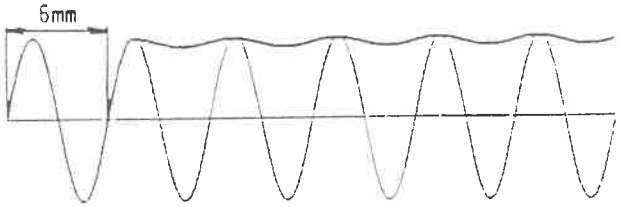

(b) m = 0.9

Fig.4 Results of Simulation

If we choose x_g to a feed per revolution which is small amount comparing to the pitch of $T_0(x)$, we can regard $T_0(x-x_g)$ as $T_0(x)$, and get the equation (2).

$$T_n(x) = (1-m)T_0(x) - mT_{n-1}(x) - mC \quad \cdots\cdots (2)$$

In the case of $0 \leqq m \leqq 1$ and $n \to \infty$, we obtain the equation (3).

$$T\infty = \frac{(1-m)T_0(x) - m\,C}{1+m} \quad \cdots\cdots (3)$$

Suppose the ratio M is an amplitude ratio of remained error and $T_0(x)$, it is converged to $(1-m)/(1+m)$. Fig.5 is the diagram of the relationship between m and M.

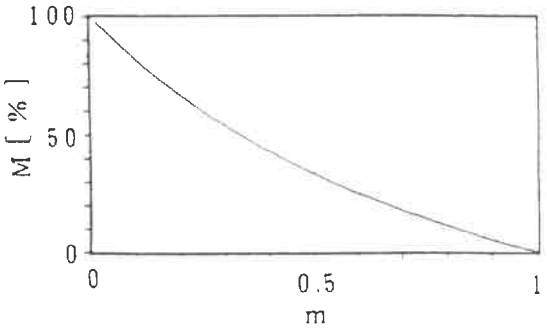

Fig.5 Relationship between m and M

Experiment of cylindrical turning

For the experiment of cylindrical turning, CNC lathe (TC-2MII by Takisawa) and a diamond tool of 1mm nose radius, are used. The cutting condition is as follows:
spindle speed 1000rpm , d=10μ m , f=20μ m/rev.
Changing the corrective servo coefficient m, the experiments carried out three times, (a) m=0 , (b) m=0.5 , (c) m=0.9 . The form accuracies are measured by a form tester (Surfcom 204B by Tokyo Seimitu), and the results are shown in Fig.6. In the case of (b), one third of the original error is remained. In the case

of (c), the remained error is as small as less than surface roughness. They are the same results as indicated by simulation.

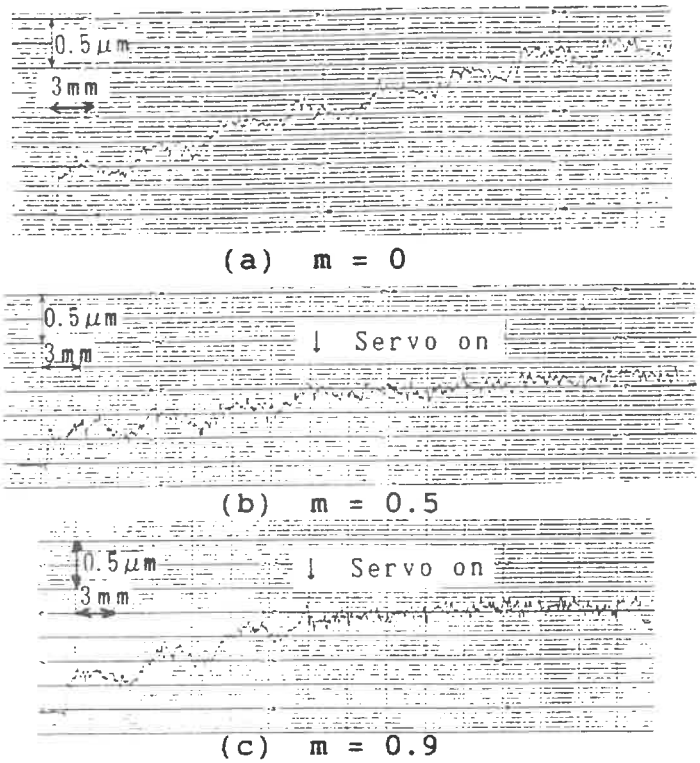

Fig.6 Results of cylindrical turning

Conclusion

Workpiece-referred form accuracy control (WORFAC) is applied an ordinary NC machine tool, and the results of both simulation on a computer and experiment of cylindrical turning are compared and investigated.

(1) The accuracy improvement by WORFAC is confirmed by cylindlical turning with an ordinary NC machine tool, not an ultra-precision machine tool.

(2) The new function of corrective servo is found by changing the feed-back volume that the error is multiplied by some coefficient m ($0 \leq m \leq 1$).

① So far, the method of WORFAC has a weak point that the form accuracy is determined be the error of the reference. Using the corrective servo coefficient m, the error of referred surface can be reduced and converged.

② Suppose the ratio of remained error M is the proportion of amplitude with control to without control. The closer to 1 the corrective servo coefficient m increases, the closer to 0 M decreases.

Reference

[1]T.Kohno, et al. Precision Engineering, P.9, Vol.11, No.1, 1989
[2]T.Kohno, et al, Applied Optics, P.103, Vol.27, No.1, 1988

USING A SINGLE CHIP MICROPROCESSOR TO COMPENSATE THE TRANSMISSION ERROR OF GEAR HOBBING MACHINES

Yongjia LI, Zhixiang CHEN
Department of Mechanical Engineering (1st)
Huazhong University of Science & Technology
Wuhan, Hubei, China

Abstract

The dividing transmission error between the hob and worktable in a gear hobbing machine, is the major factor causing the gear manufacturing error. In order to improve the accuracy of the machined gear, decrease the influence of the transmission error on the machined gear, this paper proposes a method of using a single chip microprocessor to compensate the dividing transmission error of gear hobbing machine. Through the dynamic transmission error measuring instrument attached on worktable, which constantly measures out the transmission error and sends signal to the single chip microprocessor, after the microprocessor receives the 'zero bit' pulse signal emitted by the photoelectronic converting switch attached at the edge of the worktable, and waits the synchronous phase compensating interval arriving from the photoelectronic encoder fixed on the hob shaft, then the microprocessor begins to drive the stepping motor run to generate the compensating movement, so the system performs the compensation. The hardware and application software of actual compensating system are introduced in this paper. When this compensation system was applied in a type Y38-A precision gear hobbing machine, it is shown that the transmission error of this machine can be reduced more than 50% .

Keywords: the single chip microprocessor; gear hobbing machines; transmission error; compensation.

1.INTRODUCTION

In the process of cutting gear on a gear hobbing machine, the transmission ratio between the hob and worktable must be constant. But in fact, as each driving medium in the transmission chain from the hob to worktable has the machined allowance and assembly error, these errors cause the transmission ratio between the hob and worktable changing from instant to instant, so it will affect the working accuracy of cutted gear. In order to machine out a high accuracy and high performance gear, there are two methods to realize, that is :

(1) To improve the manufacturing and assembling accuracy of each machinery parts in the transmission chain of machine tools;

(2) Using the technique of compensation, to adjust the transmission ratio, and to decrease the influence of transmission error on the working accuracy of the cutted gear.

Using the first method will increase the cost of machine tools, and it may be very difficult to carry out in technology. But using the technique of compensation, it is very easy and effective to increase the accuracy of machined production. this paper mainly discusses the method of using the microprocessor to compensate the transmission error .

2.THE WORKING PRINCIPLE AND COMPOSITION OF THE COMPENSATION SYSTEM

In the process of cutting the gear on a gear hobbing machine, the exist

of the transmission error causes a instantaneous velocity ratio deviation, reduces the accuracy of the transmission ratio, causes a instantaneous position deviation on the cutting position between the hob and cutted gear. according to this principle, this transmission error can be measured out and compensated.

If we use the hob shaft as reference position, then the theoretical position deviation of the worktable rotation relative to the hob shaft must be the transmission error of the driving chain between the hob and worktable. As the displacement movement of each driving medium in the transmission chain is relative to the rotation angular displacement of the hob or worktable by a transmission ratio, the transmission error is the resultant error of each driving medium transmit to the worktable, and the transmission error must be the function of the worktable angular displacement . By the periodicity of the transmission error[1], we adopt the FOURIER SERIES to expand it as following:

$$f(\phi)=\sum A_k \cdot \sin(B_k\phi+\phi_{k0}) \qquad (1)$$
$$=A_w \cdot \sin(\phi+\phi_{w0})+A_h \cdot \sin(B_h \cdot \phi+\phi_{h0})+\cdots$$
$$+A_g \cdot \sin(B_g \cdot \phi+\phi_{g0})+\cdots$$

A_k — The error amplitude of the k transmission piece;
ϕ_{k0} — The satrt phase angle of the k transmission piece;
B_k — The times of the transmisson ratio beween the k transmission piece and worktable.
The footing margin: w—worktable; h hob; g gear.

In the compensating system, we use the dynamic transmission error measuring instrument to measure out the transmission error in each compensating position constantly, and send this error to the microprocessor to handle, then the microprocessor drives the compensating mechanism running to generate compensating movement.

This compensation system is composed by a dynamic transmission error measuring instrument, a photoelectric-encoder, a single chip microprocessor controller instrument, a stepping motor and the stepping motor driving power. The fig.1 showing is the structure schematic diagram of this compensation system constitution.In this system, the single microprocessor depends on the pulse signal of the firing or stopping rotation and clockwise or counter clockwise rotation of the main electric motor in machine tool, to identify the status of the machine working, if it finds the cutting process have begun, then to wait the arrival of the worktable 'zero bit' pulse signal. after the 'zero bit' signal arriving, the microprocessor adopts the transmission error data measured out by the instrument, controlled by the synchronous phase compensating interval pulse signal emitted from the photoelectric-encoder fixed on the hob shaft, then starts to drive the stepping motor run, to generate the movement of compensation. This compensating movement and the hobbing movement are synthesized by the differential device, then to drive the worktable rotation, so this system performs the compensation of dividing transmission error between the hob and worktable in gear hobbing machine.

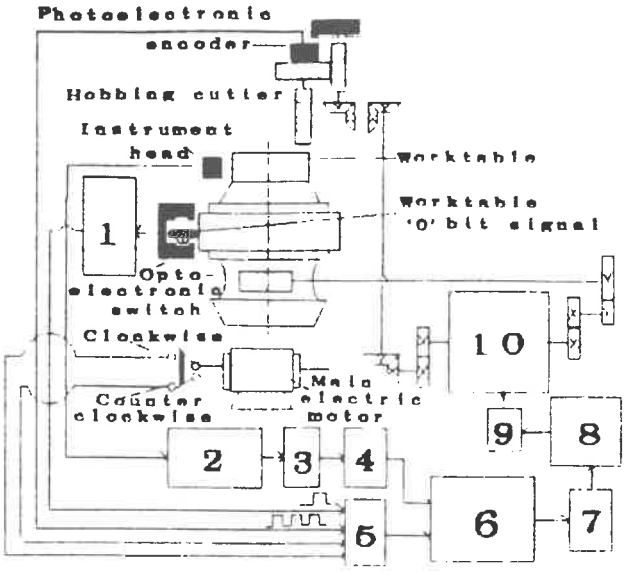

1- Pulse reshaping 2-The dynamic measuring instrument 3-Filter
4- A/D transfer conversion 5, 7- Photoelectronic isolator
6-The microprocessor control system 8-The step motor driving power
9-The stepping motor 10- The differential synthesizing device

Fig.1 The structure schematic diagram of this compensating system

In this compensation system, the error signal is measured out by the instrument, after filtered, this analogue signal was sent to A/D conversion to transfer it into digital value. If the error data is $f(\phi_i)$ when sampling in this moment, the last compensating position error data is $f(\phi_{i-1})$ according to the cumulative character of transmission error, we select the cumulation compensating method, then the error value must be compensated in this moment is:

$$D=f(\phi_i)-f(\phi_{i-1}) \quad (") \qquad (2)$$

When in compensating, the microprocessor must transfer the error value to the stepping number to drive the stepping motor rotating. If the stepping motor run a step can compensate the error value is d (in this system, d=0.125"), then the stepping number of stepping motor must rotate with correspond to the error value D is:

$$P=D/d \quad (step) \qquad (3)$$

3.THE HARDWARE AND SOFTWARE OF THE COMPENSATION SYSTEM

In the compensation system of the figure 1, the microprocessor receives the transmission error data sent by the instrument and handles it, monitors the working status of machine tool and controls the compensating movement of the stepping motor running. Therefore, the microprocessor applying hardware and software system is very important part in this compensation system. The Fig.2 showing is the schematic diagram of this compensation system applying hardware.

In this microprocessor controlling system, we adopt the 8255 PA port has the ability of latching the input data, to latch the "zero bit" signal emitted by a photoelectronic converting switch attached on worktable, and

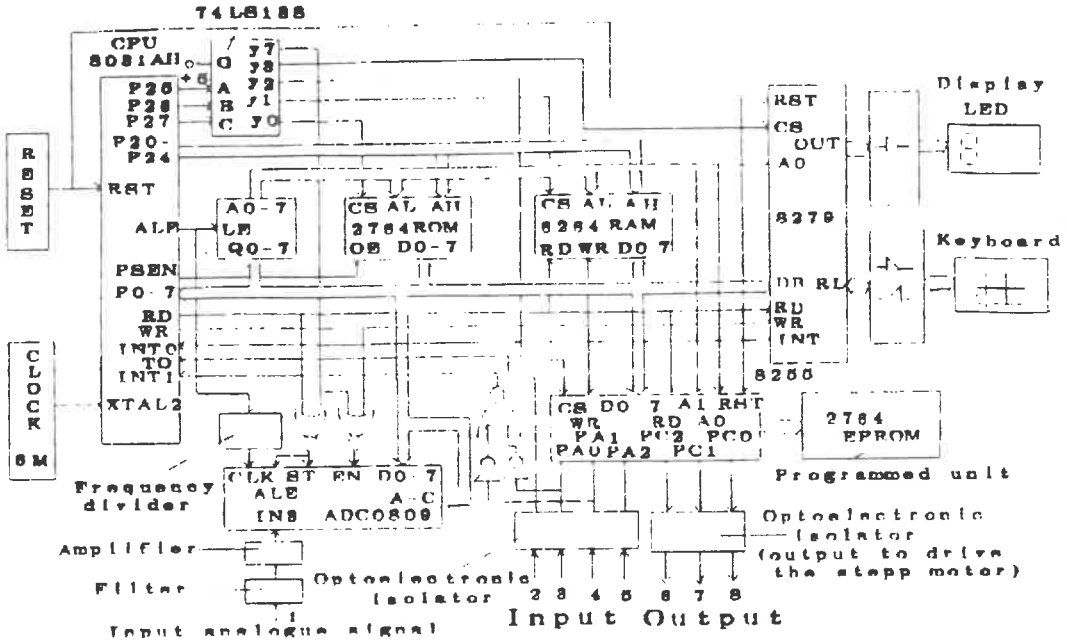

1-Transmission error signal 2-Photoelectronic encoder pulse
3- The firing or stopping signal of the main electric motor
4-The worktable "zero bit" signal 5-The clockwise or counter clockwise signal of the main electric motor 6-Reset step motor
7-Control step motor rotating on clockwise or counter clockwise
8-The pulse of controlling the step number.

Fig.2 the schematic diagram of applying hardware

to latch the rotation status of the main electric motor (including the firing or stopping signal, and clockwise or counter clockwise rotating direction of the main motor), so as for the microprocessor to identify the machine working status according to these latched data. We use the 8255 PC port having the SET/RESET bit function, to control the stepping motor rotate on the correct direction and needed speed,, so as to compensate correctly according to the plus or minus value of the transmission error D. In this hardware system, through the interrupted signal which produced by the firing /stopping rotation signal of the main electric motor OR the "zero bit" signal of worktable, when the "zero bit" signal of worktable arrived, the microprocessor can control the compensation system to compensate from the start position, and to synchronize the phase at the start position of compensation with that in sampling; and when the microprocessor finds the machine stop cutting gear, then stops the compensating process immediately, until it finds the machine start to work again, then the microprocessor controls the system returns to the compensating status. In order to keep the compensation system works in good status even in the bad environment,the hardware adds the measures to eliminate the disturbance. The photoelectronic isolator is used to isolate the input/output signal when the microprocessor exchanges the data and control signal with the external device, so as to decrease external disturbance, and improve the ability of the microprocessor system antijamming

(2) APPLICATION SOFTWARE OF THE SYSTEM

In order to gain the best effect of compensation, not only the error value measured out must be compensated in the largest limitation by using the compensating software, but the phase position of compensation point must be the same with that in sample. In this compensation system, we select a proper compensating interval to synchronize the phase position of compensating point with that in sample except for the "zero bit" position, and selecting a proper compensating interval can drive the stepping motor run on a adequate speed, this can compensate the high frequency cyclical error parts, it is more benefit to improve the accuracy of compensation. In this paper, we use the pulse emitted by the photoelectronic-encoder fixed on the hob shaft, counted by the counter T_0 to get the compensating interval.

The selection of the compensating interval is relative to the number of the compensated point, the teeth number of the cutted gear. If the hob teeth number is K, the teeth number of the cutted gear is Z, and the number of the compensated point is M; and when the photoelectronic encoder rotates a cycle, it sends out the pulse number is N, then the counting number of counter T_0 is:

$$T=(N\cdot Z)/(M\cdot K) \qquad (4)$$

In this system, K=1, Z=90, N=2048, and we select M=1440, then the value of counter T_0 is:

$$T=2048*90/1440=128 \qquad (5)$$

When in compensating, the system must compensate the error value D in the time that the counter T_0 counts T pulse. and in this time, the stepping motor must perform rotating P steps, therefore, the counting number of counter T_0 when the stepping motor rotates one step is:

$$\Delta T=T/P \qquad (6)$$

Assume the hob rotating speed is n (rpm), the time costing in a compensating interval is:

$$t=60/(n*M) \quad (S) \qquad (7)$$

Then the stepping motor rotating a step costs time is:

$$\Delta t=t/P \quad (S) \qquad (8)$$

The frequency of the stepping motor rotation is:

$$f_i=1/t=P/t \quad (step/s) \qquad (9)$$

In the process of compensation, the maximum frequency f_{max} ($f_{max}=\max\{f_i\}$) must not bigger than the rated frequency f_0 of the stepping motor rotation. In this system, the stepping motor type is 90BF002, its rated frequency is $f_0=16000HZ$, so we can select the proper compensating interval according to the frequency of this stepping motor rotation and the request of compensation.

In the process of compensating control, the stepping motor sometime may lose the step, especially in the transmission chain of gear, the backlash error of the driving chain may "eat" the pulse step sent by the stepping motor. but in the process of cutting gear, the cutting movement is unidirectional and constant, so the force born and rotation of each driving medium is mono-directional also, then the backlash error doesn't appear in the cutting process in spite of the existence of the running empty angular in the transmission chain. The backlash error only exists in the transmission chain between the stepping motor and differential device, in this short transmission chain, the direction of force born and rotation is bidirectional. however, in this compensating system, we use the fine machined gear and assembling method of decreasing the side gap to improve the accuracy of mesh in this compensating driving chain, and to increase the practical effect of compensation.

4. THE CHARACTER OF THIS COMPENSATION SYSTEM

(1) It can compensate in real time. From figure 1, in the process of cutting gear, after the instrument measured out the data of transmission error, then sends these data to the microprocessor to handle. When the microprocessor waiting the arrival of signal synchronizing with the main transmission rotating motion, then the microprocessor begins to drive the stepping motor running immediately, to perform the compensating movement.

(2) It can realize the function of digital cam. When the machined gear is sameness, and the number is a great lot, then the dynamic measuring instrument may be not used in this compensating system. because the transmission error is similar when cutting the same gear, then we can store the error data in a EPROM memory of microprocessor. when this compensating system works in the status of compensation, the microprocessor adopts the error data stored in the EPROM to correct the transmission ratio, depends on the signal of worktable "zero bit" and compensating interval to synchronize the phase position of compensation with that in sample, so the system realizes the function of digital cam. Adopting the keyboard of the compensating instrument in this system, we can read out the outline value of digital cam (means error data) from the EPROM, and may correct these data according to the practical measuring value of machined gear pitch error or profile error, then can write these data back to the EPROM.

5.CONCLUSION

(1) It is very effective that using the single chip microprocessor compensate the transmission error of gear hobbing machine, it can decrease the transmission error and improve the accuracy of machined production. After this compensation system was applied in a type Y38-A precision gear hobbing machine, when cutting the worm wheel with teeth number Z=90 the long cyclical transmission error between the hob and worktable can be reduced form 23" to 7", and the short cyclical transmission error can be reduced from 8" to 3", so the effect of compensation is very obvious, and the transmission error of machine can be reduced more than 50%.

(2) The compensating instrument can be made smaller, and can be used very widely in the compensation of transmission error in machine tool, and it is very properly to be used in reforming the old machine tool in our country.

(3) This compensation system not only can be applied in gear hobbing machine, but also in other type machine tool to decrease its transmission error, and in precision NC machine tool to control its working process.

REFERENCES

(1) Zhu mingshen. Analysis of the Dividing Transmission Error for Gear Hobbing Machines. MACHINE TOOL, No.10,1981,P_{2-7}. (In chinese)

(2) Hidata Teruaki. Dynamic Behavior of Differential Gears. Transaction of the Japan Society of Mechanical Engineering (C), 1988, 54(498): $P_{467-473}$.

(3) H.yagishita, Method for Measuring the Dynamic Transmission Error in Large Gear Hobbing Machines. PRECISION ENGINEERING, July 1990, Vol.12,No.3,$P_{144-150}$.

(4) Chiu Hua, Umezaki Yoji. Improvement of Gear Accuracy in Hobbing Translation of the Japan Society of Mechanical Engineering (C),1988, 54(503): $P_{1515-1523}$.

(5) Elms D. Replacing Cams with Software. Machine Design, 1981, NO.26: P_{95-98}.

(6) INTEL. Embedded Controller Handbook, 1988.

Depth of Reluctant Uncut and Deformed Part in CFRP cutting

Toshiaki Kaneeda
Okayama University of Science
Ridai-cho, Okayama, JAPAN

1. Introduction

CFRP(Carbon Fiber Reinforced Plastics) cutting has inevitable problems such as poorly machined surfaces and severe tool edge wear. Fundamental research of unidirectional and cross ply CFRP cutting mechanism have been performed. The research demonstrated unidirectional CFRP laminates cutting has three types of chip formation which were determined by rake angle and fiber angle[1].

The research which dealt with surface generation mechanism[1] established that the machined surfaces were dependent on fiber angle and rake angle as well as chip formation types, however damaged layer that is one of the typical surface texture have not entirely been investigated yet. This layer will be referred hereafter to as deformed part. Depth of reluctant uncut, that markedly controls accuracy of dimension, have not been measured either. The former may be closely related to fatigue strength, wear properties, while the latter is equivalent to depth of uncut that should have been cut.

This paper deals with typical machined surface texture of CFRP, namely, depth of reluctant uncut and deformed part from the view of surface generation mechanism.

2. Experimental Procedure

2.1 Work Material

Work material is unidirectional laminates "Torayca 3052" having 8 plies. The carbon fiber is PAN(Polyacrylonitrile) based high tensile strength type "Torayca T300". The carbon fiber contents are 60 volume %. Mechanical properties of the laminates are shown in Tab.1. Dimensions of the work material are 15×12×2.28 mm. Fiber angle θ (will be referred hereafter to as θ) is defined as an angle between the cutting direction and the fiber orientation.

2.2 Tool

Cemented carbide tool K10 (WC+Co, H_RA more than 90.5) was used. Rake angle α markedly controls CFRP cutting process[1], then rake angle ranged from -10° to 30°. A relatively larger relief angle ε=10° was adopted, because relief angle significantly affects cutting forces, and smaller angle permits heavier brushing action from the fiber cut on the machined surface. Sharp edge tools ground by diamond abrasive #800 were chosen by inspection of an optical microscope with Nomarski differential interference contrast. Thus sharp edged tools with 2 μm radius edge roundness were employed and their sharpness was effectively small for diameter of the fiber.

2.3 Experimental Setup

The orthogonal cutting experiments by the lathe were carried out for a range of depth of cut from 30 to 250 μm. Cutting speed 0.02 m/min was extremely low to minimize temperature and strain rate effects. Tab.2 lists the cutting conditions.

3. Measurement of Depth of Reluctant Uncut and Deformed Part

Depth of reluctant uncut could be determined by measuring a step

between the last pre-cut surface and newly generated surface using an electric micrometer. All cutting operations unavoidably generate depth of reluctant uncut, it will be reduced as much as possible by cutting several times without giving any depth of cut such as spark-out action in grinding operation.

Depth of deformed part could be measured by an original method as described below. The work material was clamped with two aluminum plates in order to do cutting experiments under plain strain condition. The lateral surfaces were observed by an optical microscope with Nomarski differential interference contrast. Debonded area on the lateral surface that attributed to differences between the fiber and the matrix on mechanical properties in the cutting event should represent small irregularities, then the contrast device may actually detect the irregularities whose height is less than resolution of an objective lens as contrast.

4. Experimental Results

4.1 Depth of Reluctant Uncut

Fig.1 shows curves of depth of reluctant uncut Δt_1 for a range of fiber angle for three rake angles under 100 μm depth of cut. The results showed that every rake angle cutting condition evidently had different curve form and Δt_1 increased as rake angle become smaller. Most of them were much greater than those in conventional metal cutting process, thus significantly control dimensional accuracy of CFRP cutting.

Fig.3(b) shows curves of normal cutting force components[1] under the same cutting conditions as the experiments to determine Δt_1. It can be seen that the normal components varied with fiber angle and rake angle to a great extent. Every rake angle cutting condition provided different shapes of the curves on the graph. To compare with Δt_1, these normal component curves are of the same form as those for Δt_1 in Fig.1, hence Δt_1 presented a similar tendency to the normal force components on the effects of α and θ.

4.2 Depth of Deformed Part

Fig.2 shows curves of depth of deformed part for three rake angles under 100 μm depth of cut. From the results in Fig.2 it can be seen that d_d definitely increases with decreasing rake angle. Every rake angle cutting condition provided the curves with concave curvature like a letter "U" on the graph, unlike forms of Δt_1 curves. In fiber angle $15^\circ \leqq \theta < 90^\circ$ conditions where fiber cutting type occurs, the minimum value appeared at $\theta = 30^\circ$ or 45°.

Fig.3(a) shows curves of tangential cutting force components under the same cutting conditions[1] as to determine d_d. It can be seen that the tangential components markedly varied with fiber angle and rake angle. Tangential components increased with a decrease in rake angle as same as d_d described above. Comparisons were made between d_d and the tangential components, thereby the curves of d_d can be seen to be of the same general form as the tangential components curves. In a word, d_d offered the same tendency as the tangential force components on the effects of α and θ as a result.

Additional results showed that Δt_1 and d_d presented similar tendency to the normal, tangential force components respectively on the effects of α and θ even though at various kinds of depth of cut from 30 to 250 μm.

4.3 Generation Mechanism

Fig.4 shows schematic illustration of fiber cutting type chip formation this paper focuses on. Fiber cutting type that is produced for fiber angle $0^\circ < \theta < 90^\circ$ and every rake angle condition[1]. This chip

formation process can be divided basically into two stages:(1) bending deformation of the layer around the tool edge and cutting the fiber with the epoxy resin and (2) chip elimination process by the glide of the layers along the fiber orientation, being equivalent to shear deformation on the localized shear plane in continuous chip formation of conventional metal cutting, or forced chip elimination that flows with independent direction of the fiber orientation. The bending deformation results in deflection of the layer around the tool edge, hence the tool cannot split the fiber with the epoxy resin immediately at the initial contact to the fiber. As the cutting event proceeds, the fiber is finally crushed and split into two parts, namely, the chip and the machined surface.

Such cutting condition as rake angle and fiber angle are dominant factors in allowing the split point of the layer to occur under or over the tool edge trace line. The machined surface split by the tool edge greatly does elastic recovery after passing through of the tool edge because of low Young's modulus of elasticity in the matrix. Therefore the depth of uncut that should have been cut, namely depth of reluctant uncut is presented here. In elastic recovering, the layer split into the machined surface severely brushes the clearance face of the tool. This is "brushing action" shown in Fig.4.

Depth of reluctant uncut can be determined by the deflection and the split point in the layer contacted to the tool edge. These two factors definitely control contact area to the clearance face of the tool and the amount of the elastic recovery of the layer split into the machined surface. Brushing action that is inevitably controlled by the two factors can mainly determine the value of the normal cutting force components. Generally speaking, larger rake angle can provide smaller deflection and larger chip elimination space angle "γ", thus splitting point become in closer vicinity of the tool edge, which allows Δt_1 to be smaller. Chip elimination space angle "γ" is defined as an angle between tool rake face and fiber orientation in Fig.4.

The tangential force components consists of three stages:to deform the layer severely and cut down the fiber by the tool edge, and to eliminate the fiber with the epoxy resin as chips[1]. The first stage is positively characterized by difficulties in cutting into the layer, resulting in the extent of deformed zone, and therefore corresponds extent of the deformed zone under the cutting line, i.e. depth of deformed part. These facts suggest that depth of deformed part actually corresponds to the tangential force components qualitatively.

5.Conclusion

Depth of reluctant uncut, which was much greater than that in metal cutting, was significantly controlled by rake angle and fiber angle. The measured value, which had a close relationship with brushing action, was depend ent on deflection of the layer in contact with tool edge and location of split point. Depth of deformed part that is equivalent to damaged layer in metal cutting appear to be debonded area between the fiber and the matrix, then could be measured using an optical microscope with Nomarski differential interference contrast as the width of the contrast. The value obtained were markedly controlled by rake angle and fiber angle and corresponded to difficulties in splitting and cutting of the fiber in contact to the tool edge. Depth of reluctant uncut and deformed part had the same tendency as the normal, tangential force components respectively on the effects of rake angle and fiber angle. These relationship were recognized in even though 0.03~0.2 mm depth of cut.

Table 1 Mechanical properties of CFRP

0 ° Tensile strength	1950 MPa
Young's Modulus of Elasticity in tension	130 GPa
Elongation on fracture	1.3 %
Interlaminar shear strength	100 MPa
Percentage of fiber contents	60 vol%

All value are measured at 296 K

Table 2 Cutting conditions

Work material	Unidirectional laminates
Tool geometry	Tungsten carbide K10
Rake angle °	-10.0.10.20.30
Relief angle °	10
Cutting form	Orthogonal
Cutting speed m/min	0.02
Depth of cut mm	0.03 ~ 0.25
Cutting oil	Dry
Fiber angle °	0 ~165 (every 15°)

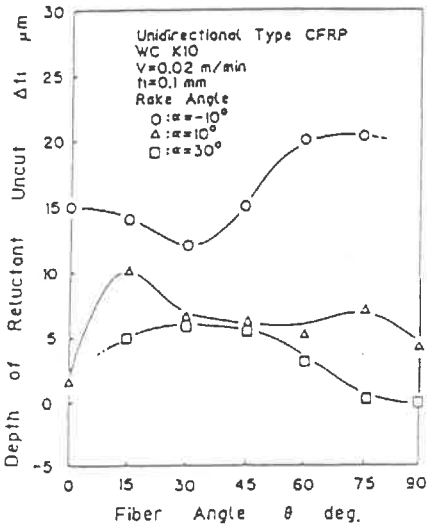

Fig.1 Depth of Reluctant Uncut

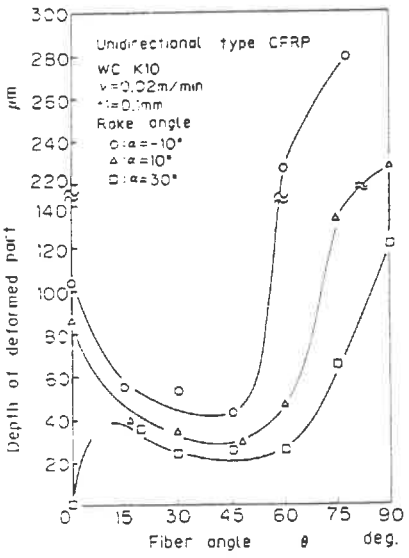

Fig.2 Depth of Deformed Part

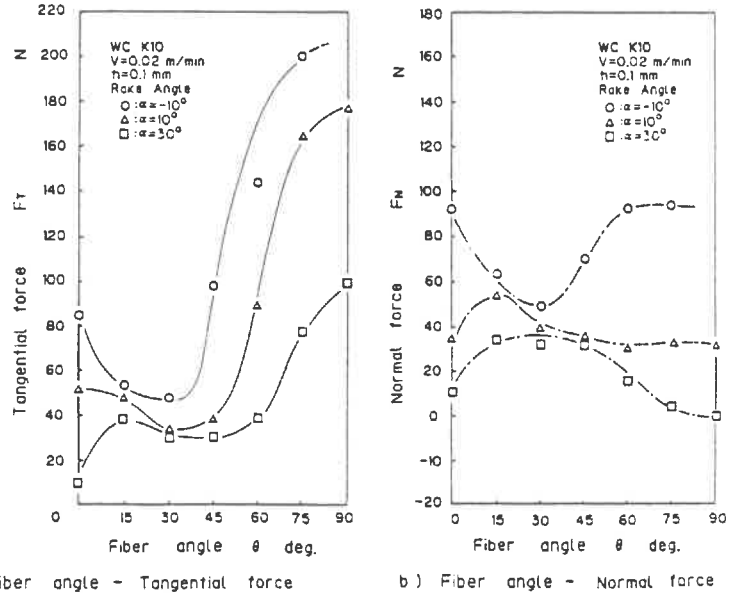

Fig.3 Cutting Force

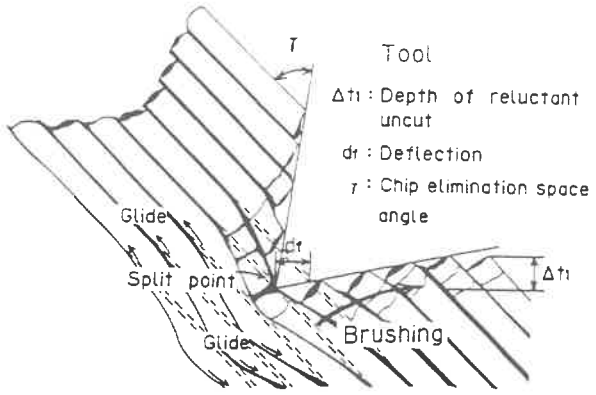

Fig.4 Cutting Mechanism of Fiber Cutting Type

Acknowledgement

The author would like to express appreciation to Toray Co. for supplying CFRP laminates and useful information.

References

1) T.Kaneeda,Trans.NAMRI(1989) 216.
2) K.Sakuma,J. of Machine and Tool(in Japanese), 29, 8 (1985) 105.

The Effect of the Interaction of Abrasive Grains on the Deformation and Fracture Behavior of Brittle Materials

N.MORITA, T.C.WU and Y.YOSHIDA

Chiba University

Chiba,JAPAN

To achieve the ductile mode grinding of brittle material with a grinding wheel of rough grain size, it is important to investigate the influence of stress field interaction produced by abrasive grains and machining hysterisis on the material surface integrity. However, the effect of micro interaction between abrasive grains and brittle material on the deformation and fracture behavior has not been crearly understood yet. This paper describes the stress field, the mechanism of micro deformation and fracture induced by the interaction between abrasive grains and the brittle material surface.

The stress distribution was calculated by the finite element method on the assumption of the elastic indentation model with Hertz's contact theory and plane strain condition. The analysis model is illustrated in Fig.1. The physical properties and parameters of a diamond indenter and a lime glass substrate are given in Table 1.

Figure 2 shows the distribution of maximum principle stress (σ_1) and the direction of minimum principle stress (σ_3). The compression stress field is distributed under contact circles. In the outside of contact edges, the tension stress field is formed and becomes highest at the

surface in the center between indenters. This suggests that the crack propagates and connects with each other. Figure 3 shows the distribution of equivalent stress (σ_E). The highest stress region exists under indenters.

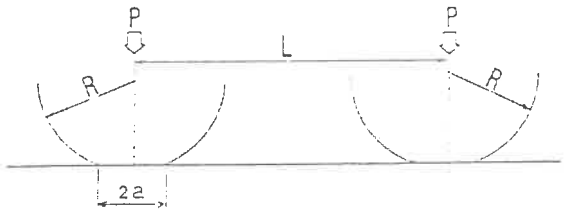

Fig.1 Analysis model

Table 1 The physical properties and parameters of a diamond indenter and a lime glass substrate

	DIAMOND	GLASS
Young's modulus E(GPa)	1000	67.6
Poisson's ratio ν	0.20	0.24
Vickers hardness H_v		540
Yield stress σ_y(GPa)		8.38
Fracture stress σ_f(GPa)		7.55
Indentator radius R(μm)	52.7	
Normal load P(10^5N/m)	4.00	
Contact circle radius a(μm)	20.0	

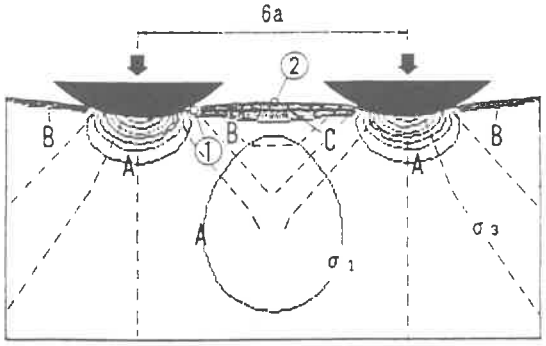

A:-37.6MPa B:810MPa C:1.66GPa

Fig.2 The distribution of maximum principle stress (σ_1) and the direction of minimum principle stress (σ_3)

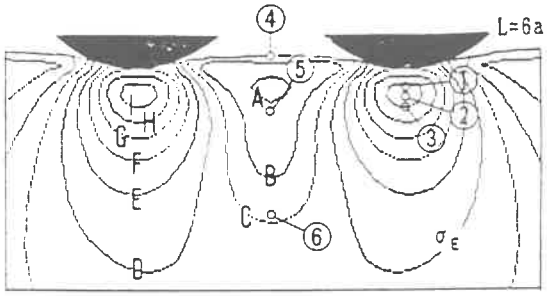

A:0.481 B:1.42 C:2.37 D:3.31 E:4.26 F:5.20
G:6.14 H:7.09 I:8.03 :GPa

Fig.3 The distribution of equivalent stress (σ_E)

Figure 4 shows the relationship between σ_1 and the distance between indenters (L). The σ_1 values at the contact edge and the center between indenters (①② shown in Fig.2) were plotted. σ_1 increase with a decrease in distance between indenters. Figure 5 shows the relationship between σ_E and the distance between indenters (L). The σ_E values at the center between indenters (④⑤⑥ shown in Fig.3) were plotted. σ_E increase with

a decrease in distance between indenters. These results explain that stress field interference between abrasive grains seems to be one of the mechanisms that cause the deformation and fracture of brittle material, which depend on both of the applied load (P) and the distance between indenters.

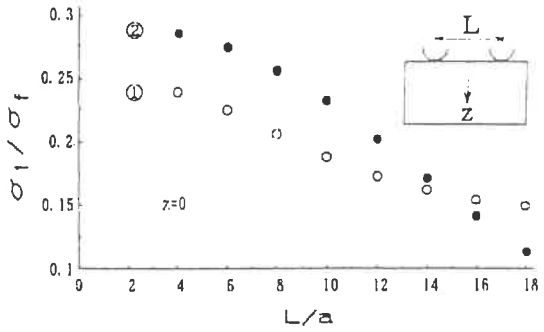

Fig.4 The relationship between σ_1 and the distance between indenters

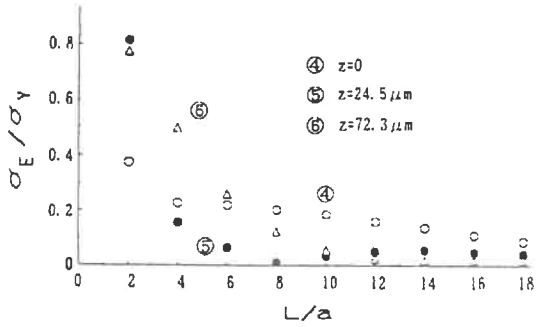

Fig.5 The relationship between σ_E and the distance between indenters

Figure 6 is the SEM photographs of cracks which are the results of intercaction between single point vickers indentations. The specific cracks, which were not observed in the single point indentation, were developed. This endorses the above simulated results experimentally. Figure 7 shows the SEM photographs of the interaction between the single point diamond grinding scratches. The ductile mode scratches did not interacted in the case of a distance of 15 μm between scratches. But, in the case of a distance of 5 μm between scratches, the deformation and fracture were generated between scratches. From the single point diamond grinding experiment and the vickers indentation test, the critical distance for chipping and crack propagation were obviously observed.

The sub-surface temperature and stress distribution in the single point diamond grinding was also simulated using the sliding contact indenter and

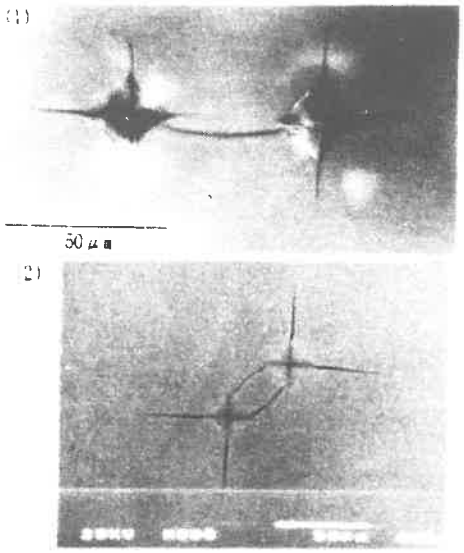

Fig.6 The SEM photographs of cracks which is the results of intercaction between the single point vickers indentation

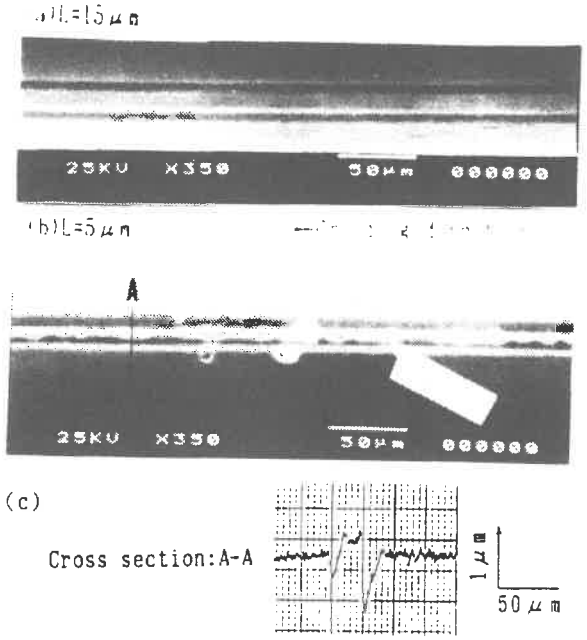

Fig.7 The SEM photographs of the interaction between the single point diamond grinding scratches

moving heat source model. From the detail simulation, it was found that the temperature of surface layer and the fracture mode depend on the applied load, the depth of indentation, the velocity of indenter and the coefficient of friction. It is concluded that, to achieve a ductile mode grinding surface, it seems to be essential to control not only the depth of cut but also the distribution of abrasive grains on the wheel, and necessary to consider the high peripheral velocity of wheel and lubrication.

ACKNOWLEDGMENTS

Special thanks for asistance in research are due to: Kawasaki Steel Corp., Okamoto Machine Tool Works,LTD. and Osaka Diamond Industrial Co.,LTD.,JAPAN. The help of Y.Fukutome and T.Kikuchi in this work is acknowledged.

Authors Index

Abe, Kohzo 83
Akabane, Masahiro 145
Armstrong, S. 130
Barbato, G. 161
Bartos, Jacob J. 130
Belak, James 45
Bell, David J. 240
Bennett, Joel G. 197
Bhandiwad, Manoj V. 157
Bifano, Thomas G. 33, 96
Blunt, L. 313
Bobroff, Norman 269
Boercker, David B. 45
Boudreau, Brian D. 173
Brinksmeier, Ekkard 73, 203
Buckman, A. Bruce 275
Busch-Vishniac, Ilene 185, 189
Carpinneti, Luiz C. R. 281
Carr, J. ..... *
Chen, K. 149
Chen, Zhixiang 380
Chetwynd, Derek G. 281
Cloninger, T. 173
Cunningham, Joseph P. 216
Cuttino, James F. 367
Damazo, Bradley N. ..... *
Day, Robert D. 220
Donaldson, Robert R. 45, 263
Dong, Wei-Ping 313
Dow, Thomas A. 22, 53, 367
Downs, Michael J. 142
Drescher, Joseph D. 22, 53
Drueding, Thomas W. 96
Duduch, J. G. 41
Egert, Charles M. 96
El-Ashkar, S. ..... *
Evans, Christopher J. 57, 236
Ezis, A. 92
Fawcett, Steven C. 96, 244
Forman, L. 130
Fu, J. 259
Gao, Robert X. 157
Gao, Wei 293
Garcia, Felix 100
Gee, Anthony E. 41, 309
Gerchman, Mark C. 15
Giulianelli, Lisa C. 275
Gobby, P. 130
Griffith, Joseph E. 178
Grigg, David A. 178
Han, Dong-Chul 336
Hannah, Philip R. 100, 130
Hashimoto, H. 11
Hatch, D. 130
Hatzakis, Jr., Michael 269
Henneke, B. 130
Hiatt, G. D. 29
Hocken, Robert J. 149, 173
Holmes, Mike 181
Hori, Ryuichi 344
Horio, Kenichiro 61
Hosokawa, H. 252
Howard, Lowell P. 153
Ichikawa, Koh-ichiro 232
Imada, Shigehiko 112
Ishikawa, Ken-ichi 232, 248, 344
Kajikura, Atsushi 232
Kanai, Akira 126, 359
Kanayama, Kazunori 248
Kaneeda, Toshiaki 386
Kasai, Toshio 61
Kim, Jonghoo 301
Kim, Woo-Jung 336
Kim, Jongwon 336
Kiyama, S. 252
Kiyono, Satoshi 293, 297, 305
Klein, Martin 203
Kochanski, G. P. 178
Kohno, Tsuguo 289, 376
Koyanagawa, Yasushi 193
Krishnamurthy, R. 224
Kuriyagawa, Tsunemoto 79
Kurobe, Toshiji 228
Kuwano, Y. 252
Larson, William C. 53
Lee, Chi M. 240
Li, Yongjia 380
Lin, T-Y. 324
Lin, Gang 352
Lingard, Philip S. 87
Liu, Hong 372
Lucca, Don A. 49, 211, 214
Luderich, Jörg 207
Lundin, Ralph L. 57
Mackay, David B. 87
Mai, Y-W. 87
Mandak, Josef 348
Matsumi, S. 252
McCarthy, Michael B. 309
McWaid, Thomas H. 259
Miller, Jr., Arthur C. 216
Mishima, Nozomu 340
Miyai, Tsuneo 289
Miyashita, Masakazu 126
Mizuhara, Kiyoshi 340
Mohamed, Abdelfatah M. 189
Molis, S. ..... *
Morantz, Paul 18
Morishima, K. 305
Morita, A. 376

* Paper not available at press time.

Morita, Noboru 69, 390
Moritoki, Hitoshi 297
Murari, G. 161
Murayama, Yoshihisa 112
Mutoh, Shinichi 289
Nagano, H. 376
Nagem, Raymond J. 33
Nakamura, K. 11
Nakano, S. 252
Nguyen, Tiep 363
Nishihara, H. 126
Nishiwaki, H. 252
Odayappan, O. 149
Ogata, Yoshiharu 61
Ohnishi, M. 252
Okazaki, Yuichi 340
Okuyama, Eiki 297
Oquin, T. R. 211
Osumi, M. 252
Owens, Douglas P. 263
Ozawa, Norimitsu 285
Pahk, Heui-Jae 301
Park, Sang-Shin 336
Parkin, R. ..... *
Parks, Robert E. 236
Patten, J. 173
Patterson, Steven R. 263
Paul, Edwin S. 57
Pessolano, Richard L. 256
Picotto, G. B. 161
Podda, G. 161
Polvani, Robert S. 57
Poovey, Tony L. 181
Powell, Martin 65
Pronko, Peter P. 92
Raja, Jay 149, 173
Rao, Ganesh S. 122
Ravindra, H. V. 224
Rhorer, Richard L. 26, 49, 197, 332
Ro, Paul I. 122
Rood, Robert W. 96, 244
Rosenbluth, Alan E. 269
Roth, Peter E. 73
Rowley, W. R. 142
Russell, Phillip E. 178
Sakai, S. 252
Salzer, Leander S. 130
Sandri, Guido V. 33
Sato, Kaiji 112, 145
Sato, Fumiaki 193
Satoh, Eiichi 289
Satomi, Tadaatus 352
Scagnetti, Paul A. 33
Scattergood, Ronald O. 37
Schenz, Richard F. 263
Scott, Paul J. 169
Scott, Marion L. 220
Seltzer, A. J. 275
Seo, Y. W. 49, 214
Shimanovich, Moisey A. 256
Shimokohbe, Akira 112, 145
Siekhaus, W. J. 45
Smith, Stanley M. 37
Smith, Stuart T. 153
Song, J. F. 259
Srinivasa, Y. G. 224
Stevens, David M. G. ..... *
Stevens, Robert R. 197
Stewart, Delbert D. 57, 100
Stout, Kenneth J. 313, 317, 324
Stowers, Irving F. 45
Strenkowski, John S. 29, 53
Struik, Klaas G. 165
Sugano, T. 285
Sugibuch, T. 305
Sullivan, Paul J. 317, 324
Suwabe, Hitoshi 232, 248
Suzuki, R. 252
Syoji, Katuso 79
Takeuchi, K. 285
Tang, Donglei 145
Theye, Lonnie A. 220
Tomita, Yoshiyuki 193
Trumper, David L. 181, 363
Tsuda, S. 252
Uda, Yutaka 376
Ue, Yoshihiro 352
Unno, Naotaka 344
Vasile, M. J. 178
Vestgaard, Bard 189
Visscher, Marnix 165
Vorburger, Theodore V. 259
Wang, Wanjun 185
Warrington, Robert O. 157, 352
Weck, M. 207
Whitenton, Eric 57
Wieners, A. 207
Williams, Mark 363
Wu, Tung-Chung 69, 390
Yamada, Yoshinori 228
Yamamoto, Y. 252
Yamazaki, Y. 11
Yasuda, Katsuhiko 145
Yasunaga, Nobuo 83
Yoshida, Yoshitaro 69, 390
Yoshioka, Junichi 126, 359
Youden, David H. 116
Yung, Kai-leung 372
Zhang, Enyao 145
Zheng, You 328
Zhou, Libo 79
Zhu, Li 328

* Paper not available at press time.